AFFDL-TR-77-61
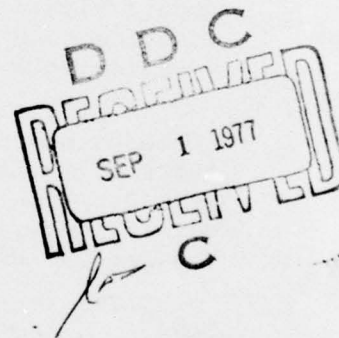
BOUNDARY LAYER EFFECTS — PROCEEDINGS OF THE 5TH U. S. AIR FORCE / FEDERAL REPUBLIC OF GERMANY DATA EXCHANGE AGREEMENT MEETING

DR. ANTHONY W. FIORE
AEROMECHANICS DIVISION

JULY 1977

TECHNICAL REPORT AFFDL-TR-77-61
Technical Proceedings Report for Period June 1975 — April 1976

Approved for public release; distribution unlimited.

AIR FORCE FLIGHT DYNAMICS LABORATORY
AIR FORCE WRIGHT AERONAUTICAL LABORATORIES
AIR FORCE SYSTEMS COMMAND
WRIGHT-PATTERSON AIR FORCE BASE, OHIO 45433

NOTICE

When Government drawings, specifications, or other data are used for any purpose other than in connection with a definitely related Government procurement operation, the United States Government thereby incurs no responsiblity nor any obligation whatsoever; and the fact that the government may have formulated, furnished, or in any way supplied the said drawings, specifications, or other data, is not to be regarded by implication or otherwise as in any manner licensing the holder or any other person or corporation, or conveying any rights or permission to manufacture, use, or sell any patented invention that may in any way be related thereto.

This report contains the proceedings of the 5th U.S. Air Force/Federal Republic of Germany Data Exchange Agreement Meeting covering many investigations conducted in both the United States and the Federal Republic of Germany as part of the Data Exchange Agreement number AF-68-G-7416 entitled "Boundary Layer Effects." The meeting was sponsored by the Air Force Flight Dynamics Laboratory and was held on 28/29 April 1976 in the Air Force Wright Aeronautical Laboratories' auditorium at Wright-Patterson Air Force Base, Ohio.

The contribution from the United States was research performed within the Air Force Flight Dynamics Laboratory and other agencies such as the U.S. Army, U.S. Navy, N.A.S.A., and various American Universities.

The contributions from the Federal Republic of Germany were research programs performed at various DFVLR laboratories such as those of Gottingen and Porz Wahn. In addition, data was presented on research carried out at Universities at Karlsruhe, Berlin, and Hamberg as well as various Aircraft Companies with the Federal Republic of Germany were also presented.

The research reported was conducted from June 1975 to April 1976.

This report has been reviewed by the Information Office (ASD/OIP) and is releasable to the National Technical Information Service (NTIS). At NTIS it will be available to the general public, including foreign nationals.

Requests for this report should be directed to: U.S. Department of Commerce, National Technical Information Services, Washington, D.C.   20230

This technical report has been reviewed and is approved for publication.

ANTHONY W. FIORE
USAF Project Officer

ROBERT D. McKELVEY, Col, USAF
Chief, Aeromechanics Division

REPORT DOCUMENTATION PAGE		READ INSTRUCTIONS BEFORE COMPLETING FORM
1. REPORT NUMBER AFFDL-TR-77-61	2. GOVT ACCESSION NO.	3. RECIPIENT'S CATALOG NUMBER
4. TITLE (and Subtitle) Boundary Layer Effects - Proceedings of the 5th U.S. Air Force/Federal Republic of Germany Data Exchange Agreement Meeting (5th), Held at Wright-Patterson AFB on 28-29 April 1976.		5. TYPE OF REPORT & PERIOD COVERED Technical Proceedings Rpt June 1975 — April 1976,
		6. PERFORMING ORG. REPORT NUMBER
7. AUTHOR(s) Dr. Anthony W. Fiore, Editor		8. CONTRACT OR GRANT NUMBER(s) MWDDEA AF-68-G-7416
9. PERFORMING ORGANIZATION NAME AND ADDRESS Aeromechanics Division Air Force Flight Dynamics Laboratory Wright-Patterson Air Force Base, Ohio 45433		10. PROGRAM ELEMENT, PROJECT, TASK AREA & WORK UNIT NUMBERS N/A
11. CONTROLLING OFFICE NAME AND ADDRESS Aeromechanics Division Air Force Flight Dynamics Laboratory Wright-Patterson Air Force Base, Ohio 45433		12. REPORT DATE July 1977
		13. NUMBER OF PAGES 527
14. MONITORING AGENCY NAME & ADDRESS(if different from Controlling Office) N/A		15. SECURITY CLASS. (of this report) Unclassified
		15a. DECLASSIFICATION/DOWNGRADING SCHEDULE

16. DISTRIBUTION STATEMENT (of this Report)

Approved for public release; distribution unlimited.

17. DISTRIBUTION STATEMENT (of the abstract entered in Block 20, if different from Report)

Approved for public release; distribution unlimited.

18. SUPPLEMENTARY NOTES

N/A

19. KEY WORDS (Continue on reverse side if necessary and identify by block number)

Turbulent boundary layers	Computer graphics
Numerical methods	Separated flows
Transonics	Boundary layer effects
High Reynolds Number	Supersonics

20. ABSTRACT (Continue on reverse side if necessary and identify by block number)

In 1968 the United States Air Force and the Federal Republic of Germany signed a Data Exchange Agreement numbered AF-68-G-7416 entitled "Boundary Layer Effects." The purpose was to exchange data in the area of boundary layer research. It includes both experimental and theoretical boundary layer research at speeds from subsonic to hypersonic in the presence of laminar, transitional, and turbulent boundary layers. The main effort in recent years has been on turbulent boundary layers which are both attached and separated in the presence of such

DD FORM 1473 1 JAN 73   EDITION OF 1 NOV 65 IS OBSOLETE

ABSTRACT CONTINUED

parameters as pressure gradients, wall temperature, surface roughness, etc.

The research presented in this report covers the period June 1975 - April 1976.

In the United States the research was conducted in various Departments of Defense laboratories, N.A.S.A., and private Universities.   In the Federal Republic of Germany it was carried out within the DFVLR Laboratories, Universities, and industry.

FOREWORD

The 5th U.S. Air Force/Federal Republic of Germany Data Ex-
change Agreement Meeting entitled "Boundary Layer Effects" numbered
M.W.D.D.E.A. AF-68-G-7416 was sponsored by the Air Force Flight
Dynamics Laboratory. It was held on 28/29 April 1976 in the Air
Force Wright Aeronautical Laboratories' Auditorium in Bldg. 450 at
the Wright-Patterson Air Force Base, Ohio. This report contains
the detailed proceedings of that meeting. It contains both theore-
tical and experimental data covering a great variety of topics in
the area of boundary layers. The speed range is from subsonic to
hypersonic Mach numbers. The types of boundary layers were lami-
nar, transitional, and turbulent; both fully attached and separated.
Some similar problems in the area of hydrodynamics are also in-
cluded.

The experimental research includes·investigations of Magnus
effects at supersonic speeds, high Reynolds numbers boundary
layers, shock-wave boundary layer interactions at transonic and
hypersonic Mach number, turbulent separated and reattached flows,
as well as the influence of turbulence levels in the free strain
on the development of boundary layers.

The theoretical work is mainly concerned with computer solu-
tions of the Navier Stokes equations higher order boundary layer
equations, and unsteady boundary layer equations. Also included
are new turbulence models and engineering approximation methods
for the three-dimensional boundary layer case.

One paper was not received in time to appear in these pro-
ceedings. The paper was titled "Heat Transfer From a Rotating
Disc" by Dr. Tuncer Cebeci of the Douglas Aircraft Company, Long
Beach, California.

The paper of Dr. Joseph Marvin of the Ames Research Center,
N.A.S.A.; Moffet Field California was originally presented as an
AGARD paper. The Air Force Wishes to thank NASA for permitting
Dr. Marvin's participation in this D.E.A. meeting.

iii

TABLE OF CONTENTS

TABLE OF CONTENTS (continued)

Session II - Chairman; Dr. D. J. Harney

Page

WELCOMING REMARKS

by

Demetrius Zonars
Air Force Flight Dynamics Laboratory
Wright-Patterson Air Force Base, Ohio

The Air Force Flight Dynamics Laboratory is most pleased to host this DEA meeting between the United States and the Federal Republic of Germany. The Laboratory is delighted with the progress under this DEA and often times it is referred to as the model Data Exchange Agreement because of its widespread activity in an area of great importance in aeronautics. The boundary layer continues to be a very important discipline in aerodynamics. Recent experiences of contemporary aircraft, while flying at high angles of attack, have indicated flow separation which can lead to many unexpected results. We have found aircraft departure characteristics to be influenced strongly by the asymmetrical shedding of vortices on the lea side of a symmetrical shape. This phenomena causes lateral forces which contribute significantly to the departure aspects of aircraft at high angle attack. May I suggest that personnel from both nations examine this particular phenomena as a part of this Data Exchange Agreement. Solutions to the asymmetrical loadings would be a significant contribution to understanding a phenomena which can plague the aircraft and missile design engineer. This, of course, is only one of many undertakings in this joint program. Many fine developments have come about as a result of this DEA and we encourage you to continue this effort with great vigor.

I would like to take this opportunity to welcome you all to this joint meeting and wish you a very successful symposium.

INTRODUCTORY REMARKS

by

K. H. Gronau
Bundesministerium der Verteidigung
Bonn, Germany

As the representative of the German Ministry of Defense and
the administrative project officer, I would like to thank Dr.
Zonars on behalf of all the German participants for his warm words
of welcome. This will be the fifth meeting held by both the Ger-
man and United States scientists under this Data Exchange Agree-
ment. It will be the first time a D.E.A. meeting has taken place
at Wright-Patterson Air Force Base. For eight years now we have
exchanged data in this particular field of science and I think it
is safe to say that the D.E.A. has been very good for both our
countries and both our scientists.

The proceedings of our last meeting, which took place in
Gottingen in June 1975 have been published and sent to all those
that are active participants in this D.E.A. The most important
six tasks to be considered in the future have been outlined in
that report by Professor Waltz, who is the German technical pro-
ject officer of the D.E.A.

As the spokesman of the German delegation, I should like very
much to thank Dr. Fiore and Dr. Harvey for the extensive prepara-
tions for this meeting. The present agenda indicates that the
meeting should be fruitful to everyone involved.

I hope that this two-day meeting will impart to all partici-
pants new ideas and orientations for current work through the
presentations and discussions. In addition, I hope it will deepen
existing personal contacts and occasion new ones.

INTRODUCTORY COMMENTS

by

Alfred Walz
Technaische Universitat Karlsruhe
Karlsruhe, Germany

I would like to add my comments to those of Dr. D. Zonars and Dr. K. Gronau by emphasizing the fact that in the case of actual lifting body designs the complex three dimensional flow phenomena encountered in flight can not be described either by potential flow theory or the boundary layer equations alone. Interacting separated flow fields which involve both the non-viscous outer region and the boundary layer appear to be the primary area of present interest for most D.E.A. activities. The tool to attack this problem and to bring together diverging results is without doubt the "Navier-Stokes Physics."

Details of the research accomplished under this D.E.A. will be used to determine the present state of the art so that new approaches to this problem can be defined and new work can then be initiated under the new D.E.A.

The present meeting will surely offer an opportunity to define the program achieved since the past year's meeting in Gottingen as well as the program for future activities.

LIST OF PARTICIPANTS

Name	Address	Phone No.
Dr. Ernest H. Hirschel	DFVLR Cologne, Germany	----
Dr. Jurgen Kux	Institute of Schiffban University of Hamberg Hamberg, Germany	----
Dr. George Inger	V.P.I. Blacksburg, Va.	(703) 951-6409
Dr. Klaus Gersten	Ruhr University Bochum, Germany	----
Dr. Robert L.P. Voisinet	Naval Surface Weapons Center Silver Springs, Md.	----
Dr. Arnold Palak	University of Cincinnati Cincinnati, Ohio 45221	----
Dr. E. Elsholz	Technical University Berlin Berlin, Germany	----
Dr. W. Haase	Technical University Berlin Berlin, Germany	----
Mr. B. Weinberg	Naval Surface Weapons Center Silver Springs, Md.	(202) 394-2283
Mr. W.C. Volz	Naval Air Systems Command Washington, D.C.	(202) 692-7417
Dr. A.H. Walz	Technical University Karlsruhe Karlsruhe, Germany	----
Dr. K.H. Gronau	Germany Ministry of Defense Bome, Germany	----
Dr. Gut R. Schneider	DFVLR-AVA Gottingen, Germany	----
Dr. Julius C. Rotta	DFVLR-AVA Gottingen, Germany	----

LIST OF PARTICIPANTS (continued)

Name	Address	Phone No.
Dr. Joseph G. Marvin	NASA Ames Research Center Moffett Field, Cal.	(415) 965-5390
Dr. D.J. Harney	Flight Dynamics Laboratory Wright-Patterson AFB, Ohio	(513) 255-6156
Dr. W.L. Hankey	Flight Dynamics Laboratory Wright-Patterson AFB, Ohio	(513) 255-3138
Dr. D.L. Whitfield	ARO Inc. Tullahoma, Tenn.	(615) 455-2611
Dr. J.C. Adams Sr.	ARO Inc. Tullahoma, Tenn.	(615) 455-2611
Mr. E.R. Thompson	U.S.A.F. AEDC Rash Div. Tullahoma, Tenn.	(615) 455-2611
Dr. W.B. Sturek	Ballistic Resch. Laboratory B-12 Aberdeen Training Grounds, Md.	(301) 278-4103
Dr. J.E. Danberg	University of Delaware Newart, Delaware	----
Dr. Hans Ulrich Meier	DFVLR-AVA Gottingen, Germany	----
Dr. H.W. Stock	Dornier Gmoh, 799 Friedrichshafen, Germany	07545/82328
Dr. A.W. Fiore	Flight Dynamics Laboratory Wright-Patterson AFB, Ohio	(513) 255-4150
Lt/Col Robert F. Lopina	EOARD, Box 14 FPO New York 09510	----
Maj David S. McRae	Flight Dynamics Laboratory Wright-Patterson AFB, Ohio	(513) 255-3138
Dr. Joseph S. Shang	Flight Dynamics Laboratory Wright-Patterson AFB, Ohio	(513) 255-3138
Lt./Col John R. Taylor	AECD/XOA Tullahoma, Tenn.	(615) 455-2611
Dr. D. Zonars	Flight Dynamics Laboratory Wright-Patterson AFB, Ohio	(513) 255-4012

LIST OF PARTICIPANTS (continued)

Name	Address	Phone No.
Dr. Joanna Schot	David Taylor Resch. & Dev. Center Code 1843 Bethesda, Md. 20084	(213) 593-8322
Dr. T. Cebeci	Aero. Research Douglas Aircraft Long Beach, Cal.	----
Dr. L. Boehman	University of Dayton Dayton, Ohio 45469	(513) 229=3221
Dr. J. Gross	University of Arizona Tucson, Arizona	(602) 884-2591
Dr. John Lee	The Ohio State University Columbus, Ohio	--

THEORETICAL INVESTIGATIONS OF THE THREE-DIMENSIONAL
TURBULENT BOUNDARY LAYER ON SWEPT WINGS

by

J.C. Rotta, G.R. Schneider

Deutsche Forschungs- und Versuchsanstalt
fur Luft- und Raumfahrt E.V.
Aerodynamische Versuchsanstalt Gottingen
D-3400 Gottingen, Bunsenstrasse 10, W-Germany

Abstract

The three-dimensional turbulent boundary layer on an infinite
swept wing is used as a test vehicle to study four different tur-
bulence models. The differential equations are solved by finite
difference procedures. The results are compared with the wind
tunnel measurements on an infinite swept wing model.

11

List of Symbols

C_f local skin friction coefficient, $C_f = 2(\tau/\rho)_w/u_{re}^2$

C_p static pressure coefficient, $C_p = 1 - (u_r/U_{ref})^2$

E   kinetic energy of turbulent fluctuations (per unit of mass

F   dimensionless correction function

H   shape parameter in the streamline coordinate system,
$$H = 1/\theta_{11} \int_o^\delta (1 - u_s/u_{re}) \, dy$$

$'\ell'$ corrected mixing length, $\ell = FL$

ℓ_{mix} mixing length, $\sqrt{\tau/\rho}/(\partial\bar{u}/\partial y)$

L   length scale

N_e ratio of eddy viscosities with respect to direction normal and paralel to local streamline

s,n   rectangular coordinates (s parallel to local mean streamline)

T_s, T_n multiplying functions for nonisotropic eddy viscosity

$\bar{u}, \bar{v}, \bar{w}$ mean velocity components (in x,y,z-direction)

u',v',w'   components of turbulent velocity fluctuations

U_∞ velocity of undisturbed flow

x,y,z   system of rectangular physical coordinates (z parallel to leading edge of wing, y normal to surface)

a angle between the u_r-direction and the x-axis, $a = \arcsin(w/u_r)$

o   sweep angle of the leading edge

β crossflow angle, $\beta = a - a_e$

δ boundary layer thickness (where $u_r/u_{re} = 0.995$)

ϵ scalar eddy viscosity

12

κ v. Kármán constant

θ_{11} momentum thickness parameter in the streamline coordinate system,

$$\theta_{11} = \int_{0}^{\delta} (1 - u_s/u_{re})u_s/u_{re}\, dy$$

ν kinematic viscosity

ρ density

τ_x, τ_z components of shear stress

τ resultant shear stress

φ_{grad} angle of mean velocity gradient

φ_r angle of resultant shear stress

Subscripts

e   outer edge of boundary layer

r   resultant value

re   resultant value at outer edge of boundary layer

s   parallel to the direction of u_{re} (external streamline)

w   wall

x   x-direction

z   z-direction

13

1. Introduction

With the computation of three-dimensional turbulent boundary
layers on bodies at incidence or on swept and yawing wings, one
is confronted with a two-fold problem. The one results from the
poor knowledge on turbulent flows and is to choose a proper tur-
bulence model, which is capable of describing the three-dimen-
sional boundary layers correctly. On the other hand, it is sus-
pected that the execution time for numerical solutions and the
storage requirements are orders of magnitude greater than for two-
dimensional flow and also for three-dimensional laminar boundary
layers. In order to arrive at useful solutions in practice, a
compromise is necessary, where simplified turbulence models will
be preferred at the expense of accuracy.

At the Euromech Colloquium No. 60, which was held at Trondheim,
Norway, in April, 1975 on the subject "Three-Dimensional Turbu-
lent Boundary Layers in External Flows", a systematic comparison
was made of the performance of available calculation methods [1].
This was achieved by selecting test cases prior to the meeting
and inviting the originators of various calculation methods to
compute the test flows, referred to as "Trondheim Trials". The
results were compiled and discussed by L.F. EAST [2].

It appeared desirable to us to test further turbulence models and
to make more detailed comparisons. The present investigations
are concerned with three-dimensional turbulent boundary layer cal-
culations on an infinite swept wing in incompressible flow, where
four different turbulence models were used. The work is not yet
completed, such that only preliminary results can be presented.

2. The Equations of Mean Motion

The equations of mean motion for the boundary layer on an infinite
swept wing are shown on Fig. 1. A Cartesian coordinate system is
introduced, in which the z-axis is parallel to the leading edge
of the wing and the y-axis is perpendicular to the surface. The
flow quantities are assumed to be constant in z-direction. We

14

have the momentum equations for x- and z-direction and the con-
tinuity equation. In the idealized case of an infinite swept
wing with irrotational free flow outside the boundary layer, the
velocity component in z-direction, w_e, is independent of x and
z. In a wind tunnel, however, the conditions of the infinite
swept wing can be approximated with more or less accuracy only.
In particular, with the experiment made at the National Aerospace
Laboratory of the Netherlands (NLF) 3 , the measurements indicate
a slight variation of w_e with x. This means actually that the
outer flow is either not completely irrotational or not indepen-
dent of the z-coordinate. For this reason, the term $u_e dw_e/dx$
is included in the second momentum equation.

3. The Turbulence Models

3.1 Survey

A survey of the four turbulence models, which have been included
in the investigations, is given in Fig. 2. The details of the
models will be described subsequently. The first column of the
table gives a brief symbol, by which the models are distinguished
in the graphs to be shown later. The first model uses Prandtl's
mixing length formula, extended to 3-D boundary layers. As an al-
ternative to this, the mixing length formula is applied in combi-
nation with a generalized eddy viscosity concept, such that dif-
ferent values for the eddy viscosity are used with respect to the
shear stresses in streamline and cross flow direction. The third
model is based on the partial differential equation for the kinetic
energy of turbulent fluctuations. The turbulent shear stresses
are determined from Prandtl's relations. With the fourth model
three partial differential equations are used, namely for the
kinetic turbulence energy and the two turbulent shear stresses.

3.2 The Mixing Length Formula (Model ML)

The mixing length model has been described by G.R. SCHNEIDER 4
already at the previous DEA Meeting in Göttingen, 1975 and calcu-
lated results have been discussed. The detailed assumptions are

15

compiled in Fig. 3. The two shear stress components are calculated with a scalar eddy viscosity, ϵ, which is determined from the mixing length formula. Michels model is used for the mixing length, which consists of a length, L , which is represented by a hyperbolic tangent function. $\mathcal{K}$ is the von Kármán constant of the logarithmic law of the wall and L_e is the value of L at the edge of the boundary layer. A multiplying correction function F is introduced to take into account the effects of the viscous sublayer. v is the kinematic viscosity.

3.3. The Generalized Eddy Viscosity (Model MLG)

With the mixing length model just described, the vector of the resultant turbulent shear stress has the same direction as the resultant of the mean velocity derivative with respect to the y-coordinate. Experiments indicate, however, that the two vectors may have different directions. This points to a reduced eddy viscosity in cross flow direction. Calculations with a reduced eddy viscosity perpendicular to the direction of the external streamline were presented by T.K. FANNELØP and D.A. HUMPHREYS [5]. With the generalized eddy viscosity concept of the model MLG, the eddy viscosity is presented as a second rank tensor in planes y = const with its principle axes in direction of local mean streamline and normal to it, Fig. 4. The coordinates of the eddy viscosity tensor are determined from the scalar eddy viscosity by multiplication with dimensionless factors T_s (=1) and T_n(=0.4). With respect to the shear stresses in the cartesian xz-coordinate system, the relationships shown on Fig. 4 are derived. The Fanneløp-Humphrey calculations are a special case to the MLG-model.

In the special case of isotropic eddy viscosity, characterized by T_s = 1 and T_b = 1, the model MLG reduces to the model ML.

3.4. The Kinetic Turbulent Energy Equation and Prandtl's Shear Stress Relation (Model EP)

The two remaining models both use the partial differential equation

16

for the kinetic energy of velocity fluctuations [6, 7], which is
given on Fig. 5. E denotes the kinetic fluctuation energy per
unit of mass, L is a characteristic length scale. The equation
has terms for turbulent production due to the work done by the
mean rate of strain, dissipation of kinetic energy due to vis-
cosity, convection of energy by the mean velocities, and diffu-
sion due to turbulent mixing. Two empirical coefficients, c
and k_q, appear in the equation, for which the values 0.165 and
0.6, respectively, have been used.

The shear stresses of the model EP are calculated from the
energy, E, and length scale, L, by relationships which were
proposed by PRANDTL in 1945. k is another coefficient, which is
related to the coefficient c by $k = c^{1/3}$. The model represents
a high Reynolds number approximation, and the contribution to the
shear stresses due to the molecular viscosity are completely ne-
glected. This means the model does not describe the flow within
the viscous sublayer. For the length scale L the same distri-
bution is assumed as for the function L of the mixing length.
A partial differential equation for L has been used neither
with the model EP nor with the model ET.

3.5. The Shear Stress Transport Equation (Model ET)

The model ET differs from the model EP in that Prandtl's rela-
tionships of the shear stresses are replaced by partial differen-
tial equations, the so called shear stress transport equations
[6,8], Fig. 6. Each of the equations has four terms of different
physical meaning. These is production due to interaction of mean
rate of strain with the turbulent motion, there is destruction of
turbulent shear stress due to the tendency of the turbulence to
isotropic distribution of velocity fluctuations, there is convec-
tion by mean motion, and finally there is diffusion due to tur-
bulent mixing. Three empirical coefficients occur in addition to
those which appeared already in the energy equation. $a_p = 0.2$
and $k_q = 0.6$ are chosen and k_{pr} is related to a_p and c.
The length scale, L, is the same as in the energy equation.

17

Like the model EP, this model ET does also not apply to the viscous sublayer.

3.6. Relations between the Turbulence Models

The turbulence models, except for the model with the generalized eddy viscosity concept (Model MLG), present a family of models, which can be derived one from the other. In order to show this, let us start with the most complicated model, the one which includes partial differential equations for turbulent kinetic energy and turbulent shear stresses (Model ET), Fig. 7. If the convection and turbulent diffusion terms are neglected in the transport equations for the shear stresses, the shear stress equations reduce to Prandtl's relations. Consequently, the model EP, which uses only a partial differential equation for the turbulent kinetic energy is obtained. If then the terms for convection and turbulent diffusion are neglected in the energy equation, one arrives at the mixing length formula. Since all four models are used with the same assumptions for the length scale, it is expected that the investigations will give detailed insight into the influences of the particular features of the models.

The equations are solved numerically by a finite difference method. Details of the methods are partly described in Reference [4].

4. Results

We have applied the calculations several of the Trondheim Trials. At this presentation we will report only on comparisons with van den BERG and ELSENAAR's swept wing experiment [3], which was denoted as case B1 at the Trondheim Conference. On a wind tunnel model measurements have been made in the incompressible turbulent boundary layer under infinite swept wing conditions. In the model a pressure gradient is induced on a 35° yawed flat plate by means of a suitably shaped body near the plate. The boundary

18

layer that develops on the surface of the flat plate starts off as a constant pressure two-dimensional boundary layer and changes slowly into a three-dimensional boundary layer leading to a three-dimensional separation close to the trailing edge. Extensive measurements have been carried out, including mean velocity profiles, flow angles, local skin friction coefficient and Reynolds stresses [9].

Fig. 8 gives the pressure coefficient as measured along the centre line of the model. The pressures as deduced from the measured dynamic head at the boundary layer edge deviate from the measured wall pressures near the separation line. The calculations are based on the approximation by a polynomial of degree 5 to the pressures deduced from the dynamic head measurements.

The flow angles at the edge of the boundary layer is seen from Fig. 9. The flow angles calculated from the assumptions of infinite swept wing are smaller for both pressure distributions than the measured angles. If one calculates the velocity, w_e, from the measured flow angle, one obtains a w_e slightly increasing in downstream direction. As already mentioned, this means that the idealized conditions of an infinite swept wing are not exactly met with the experiment. The polynomial approximation of degree 5 to the measured flow angles is used as input for the calculations in addition to the pressure distribution deduced from the dynamic head. With these data, the results of any calculation method comes closer to the experiments than with the assumption denoted by number 1 and 2.

In the following figures, the development of four characteristic parameters of the boundary layer will be shown.

The comparison of the calculated thickness of momentum loss in the direction of the external streamlines with the experiment of Reference 3 is presented on Fig. 10. Up to a value of $x = 1.0$ m the results of all four models agree well with the test data. Farhter downstream the agreement deteriorates.

More pronounced differences are observed with the angle between

19

the wall streamline and the streamline at the edge of boundary layer, β_w, as shown in Fig. 11. None of the models give satisfactory agreement with the experimental data. The models ML, EP, and ET show fair agreement up to $x = 1.0\,m$. But none of these three models predict separation of the flow, whereas the experiment shows separation at $x = 1.31\,m$. However, the models EP and ET give greater β_w at the large values of x and are thus closer to the experimental data.

The model MLG with the nonistropic eddy viscosity ($T_n = o.4$) displays an unexpected behavior with respect to the angle β_w. For small values of x, β_w develops to negative values and rises steeply downstream. It predicts separation at $x = 1.23\,m$. The overall agreement is not satisfactory. The model can not be recommended in its present form.

The ratio of displacement thickness to momentum thickness with respect to streamline direction, denoted as shape parameter, H, is a characteristic of the velocity profiles, which is known to be very sensitive to variations in the calculation methods. Fig. 12 presents the comparison with the experiment. There is a minor discrepancy of the initial values for the mixing length models and the models using the energy equation. This discrepancy, however, does not affect the comparison. For values $x > 1.0\,m$, the four models predict values of H, lower than the experimental values. The mixing length model ML gives the lowest values. The models EP and ET come gradually closer to the experiment. The model with the generalized eddy viscosity gives poor agreement with the experiment at lower values of x.

The calculated values of the local skin friction coefficient, given in Fig. 13, closely agree for the methods ML, EP, and ET, whereas the model MLG yields lower values. The calculated results follow the trend of the test data in general, but are too low for small values of x and too high farther downstream.

Further details of the calculated results as compared with the experimental data of A. ELSENAAR and S.H. BOELSMA [9] are

20

presented in the following figures. Fig. 14 gives the angle be-
tween local mean velocity and velocity at the edge of boundary
layer, β, the angle of mean velocity gradient, ϕ_{grad}, and the
angle of Reynolds shear stress, ϕ_r, versus the distance from
the surface, y, for the test station 4 (x = 0.795 m). The cal-
culated results of only the methods MLG and ET are plotted.
For the model ML and EP the angles ϕ_{grad} and ϕ_r have the same
values due to the physical assumptions. For the model ET, the
angles β and ϕ_{grad} agree well with the experiment. The angle
ϕ_r differs from ϕ_{grad}, but the iifference between the two
angles is considerably underestimated as compared with the ex-
periment. The agreement for the model MLG is poor. At the first
place, there is the unexpected behavior that the flow angle β
has a maximum value at y = 2.6 mm, whereas the experiment shows the
maximum of β at the surface. The condition $d\beta/dy = 0$ causes
the vector of mean velocity gradient and shear stress to assume
the same direction as the mean velocity. Therefore, the three
curves cross at the maximum of β. The angles ϕ_{grad} and ϕ_r,
as calculated with this model have also maximum values away from
the surface.

The same angles as in Fig. 14 are plotted for station 7 (x = 1.095 m)
in Fig. 15. For the model with generalized eddy viscosity the
maximum of   occurs now at the surface, in agreement with the
experiment. For both models, ET and MLG, β is smaller than
the measured values, but the model ET comes closer to the ex-
periment. The model ET agree also better with the experiment
with respect to the angle ϕ_{grad}. The difference between ϕ_r
and ϕ_{grad} is, however, again underestimated by the model ET
and overestimated by the model MLG. The fact that the differ-
ence between ϕ_{grad} and ϕ_r as predicted by the model ET is
entirely due to history effects, suggests that, in a real flow,
effect other than history effects may be responsible too for the
experimentally observed differences between ϕ_{grad} and ϕ_r.

The mixing length ration, ℓ_{mix}/δ, recalculated from the result-
ing shear stress and the resulting mean velocity gradient, is

21

plotted versus the dimensionless distance from the surface for the models MLG and ET in Fig. 16. This length is not identical with the length scale L. Especially, the mixing length according to the model ET is considerably lower than L, due to the convective and diffusive effects in the partial differential equations, but it is higher than the mixing length deduced from the experiment.

In Fig. 17 the ratio

$$N_e = \frac{\tan(\phi_r - \beta)}{\tan(\phi_{grad} - \beta)}$$

which corresponds to the ratio of the eddy viscosities in the transverse and streamline direction, is plotted versus the dimensionless distance from the surface. Outside the viscous sublayer the ratio $N_e = 0.4$ by supposition of the value $T_n = 0.4$ for the model MLG. For the model ET the ratio N_e is greater than unity closer to the surface and drops to about 0.9 in the outer part of the boundary layer. The experimental values are, on the average, 0.5 at station 4 and 0.7 at station 7.

Some test calculations were carried out in order to investigate the effect of the magnitude of the length scale, L_e/δ, on the results. The two most sensitive quantities, namely the wall streamline angle β_w, and the streamwise shape parameter, H, are plotted in Fig. 18 and 19. L_e/δ is varied between 0.075 and 0.085. Results are presented for the mixing length model ML (isotronic eddy viscosity) and the model ET. The predictions come closer to the measurements, if a smaller value of L_e/δ is chosen. With $L_e/\delta = 0.075$ the model ET predicts separation at $x \approx 1.10$ m.

5. Conclusions

The comparative application of several turbulence models to the infinite swept wing turbulent boundary layer reveals interesting facts. With respect to relevant boundary layer parameters, the predicted values agree with the experiment at least for a part of

the flow. If the region of separation is approached none of the models gives satisfactory results. The short comings are brought to light even more, if some further details of the boundary layer are considered. But the comparisons indicate that a model based on partial differential equationd has greater capability of correctly predicting the details of the flow, although to a greater expense. There is room for modifications of the models. In particular, variations in the length scale assumptions have strong effects on the results. Modifications of the models make no sense, unless there is evidence that the agreement with experiments is improved for many flow cases. ·Therefore, further comparisons are required, before final conclusions can be drawn.

6. References

[1] FANNELOEP, T.E.   Three Dimensional Turbulent Boundary
    KROGSTAD, P.A.   Layers in External Flows: A Report on
                        Euromech 60.

                        J. Fluid Mech. 71 (1975), pp. 815-826.

[2] EAST, L.F.   Computation of Three-Dimensional Turbu-
                        lent Boundary Layers.

                        FFA TN AE-1211 (1975), pp. 1-86.

[3] van den BERG, B.   Measurements in a Three-Dimensional
    ELSENAAR, A.   Incompressible Turbulent Boundary Layer
                        in an Adverse Pressure Gradient Under
                        Infinite Swept Wing Conditions.

                        NLR TR 72092 U (1972), pp. 1-31.

[4] SCHNEIDER, G.R.   A Finite Difference Method for the
                        Calculation of Three-Dimensional Boun-
                        dary Layers on Swept Wings.

                        BMVg-FBWT 75-21 (1975), S. 144-168.

[5] FANNELØP, T.K.   The Solution of the Laminar and Tur-
    HUMPHREYS, D.A.   bulent Three-dimensional Boundary Layer
                        Equations with a Simple Finite Differ-
                        ence Technique.

                        FFA Rep. 126 (1975), pp. 1-82.

[6] ROTTA, J.C.   Turbulente Strömungen.
                        Verlag B.G. Teubner, Stuttgart, 1972.

[7]   VOLLMERS H.   Similar Solutions for Turbulent Shear
      ROTTA, J.C.   Flows Described by Mean Velocity, Tur-
                              bulent Energy, and Turbulent Length
                              Scale.

                              BMVg-FBWT 75-21 (1975), S. 119-143.

[8]   ROTTA, J.C.   Recent Attempts to Develop a Generally
                              Applicable Calculation Method for Tur-
                              bulent Shear Flow Layers.
                              AGARD-CP 93 (1972), pp. A-1 to A-11.

[9]   ELSENAAR, A.   Measurements of the Reynolds Stress
                              Tensor in a Three-Dimensional Turbulent
                              Boundary Layer Under Infinite Swept
                              Conditions.
                              NLF TR, 74095 U (1974), pp. 1-41.

x-Momentum:

$$\bar{u}\,\frac{\partial \bar{u}}{\partial x} + \bar{v}\,\frac{\partial \bar{u}}{\partial y} = u_e\,\frac{du_e}{dx} + \frac{1}{\rho}\,\frac{\partial \tau_x}{\partial y}$$

z-Momentum:

$$\bar{u}\,\frac{\partial \bar{w}}{\partial x} + \bar{v}\,\frac{\partial \bar{w}}{\partial y} = u_e\,\frac{dw_e}{dx} + \frac{1}{\rho}\,\frac{d\tau_z}{\partial y}$$

Continuity:

$$\frac{\partial \bar{u}}{\partial x} + \frac{\partial \bar{v}}{\partial y} = 0$$
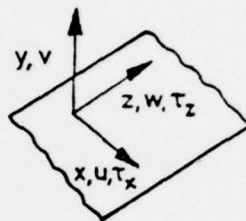
Fig. 1   Boundary layer mean velocity
equations for a swept wing

Model	Characteristics
ML	Mixing Length Formula
MLG	Mixing Length Formula Generalized Eddy Viscosity
EP	PDE for Turbulence Energy Prandtl's Relations for Shear Stresses
ET	PDE for Turbulence Energy PDE for Shear Stresses

Fig. 2   Turbulence models for three-
dimensional boundary layers

25

$$\frac{\tau_x}{\rho} = (\epsilon + v)\,\frac{\partial \bar{u}}{\partial y} \qquad \frac{\tau_z}{\rho} = (\epsilon + v)\,\frac{\partial \bar{w}}{\partial y}$$

Eddy Viscosity: $\displaystyle \epsilon = \iota^2 \left[\left(\frac{\partial \bar{u}}{\partial y}\right)^2 + \left(\frac{\partial \bar{w}}{\partial y}\right)^2 \right]^{\frac{1}{2}}$

Mixing Length: $\iota = F\,L$

$$L = L_e \tanh\,(xy/L_e) \qquad L_e/\delta = \text{const}$$
$$x \approx 0.4$$

Correction Function for Viscous Effects

$$F = 1 - e^{-\gamma}\,; \qquad = L\sqrt{\tau/\rho}\,/(10.66 \cdot v)$$

$$\tau = (\tau_x^2 + \tau_z^2)^{\frac{1}{2}} = \text{Resultant Shear Stress}$$

Fig. 3 Mixing length formula
(Model ML)

Coordinates of Eddy Viscosity

$$\epsilon_{ss} = \epsilon T_s \quad \text{in s-Direction } (T_s = 1)$$

$$\epsilon_{nn} = \epsilon T_n \quad \text{in n-Direction } (T_n = 0.4)$$

Cartesian xz Coordinate System

$$\frac{\tau_x}{\rho} = (\epsilon_{xx} + v)\,\frac{\partial \bar{u}}{\partial y} + \epsilon_{xz}\,\frac{\partial \bar{w}}{\partial y}$$

$$\frac{\tau_z}{\rho} = (\epsilon_{zz} + v)\,\frac{\partial \bar{w}}{\partial y} + \epsilon_{zx}\,\frac{\partial \bar{u}}{\partial y}$$

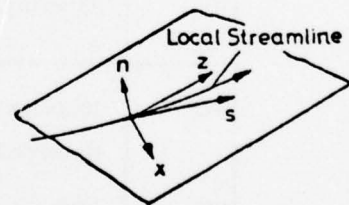$$\epsilon_{xx} = \epsilon\,(T_s \bar{u}^2 + T_n \bar{w}^2)/\bar{u}_r^2$$

$$\epsilon_{zz} + \epsilon\,(T_s \bar{w}^2 + T_n \bar{u}^2)/\bar{u}_r^2$$

$$\epsilon_{xz} = \epsilon_{zx} = \epsilon\,(T_s - T_n)\bar{u}\,\bar{w}/\bar{u}_r^2$$

$$\bar{u}_r = (\bar{u}^2 + \bar{w}^2)^{\frac{1}{2}} = \text{Resultant Mean Velocity}$$

Isotropic Eddy Viscosity (Model ML): $T_s = T_n = 1$

Fig. 4 Generalized eddy viscosity
(model MLG)

26

Kinetic Energy Equation $E = \frac{1}{2}(\overline{u'^2} + \overline{v'^2} + \overline{w'^2})$

$$\bar{u}\frac{\partial E}{\partial x} + \bar{v}\frac{\partial E}{\partial y} = \underbrace{\frac{1}{\rho}\left(r_x\frac{\partial\bar{u}}{\partial y} + r_z\frac{\partial\bar{w}}{\partial y}\right)}_{} - \underbrace{c\frac{E^{3/2}}{L}}_{} + \underbrace{k_q\frac{\partial}{\partial y}\left(\sqrt{E}L\frac{\partial E}{\partial y}\right)}_{}$$

$\underbrace{}_{\text{Convection}}$ $\underbrace{}_{\text{Production}}$ $\underbrace{}_{\substack{\text{Dissi-}\\\text{pation}}}$ $\underbrace{}_{\text{Diffusion}}$

$c = 0.165;\ k_q = 0.6$

Turbulent Shear Stresses, Model EP

$$r_x/\rho = -\overline{u'v'} = k\ \sqrt{E}\,L\ \partial\bar{u}/\ \partial y$$

$$r_z/\rho = -\overline{w'v'} = k\ \sqrt{E}\,L\,\partial\bar{w}/\ \partial y$$

$k = c^{1/3} = 0.548$

Fig. 5 Kinetic energy equation and shear stresses
after PRANDTL (model EP) for the swept
wing boundary layer

Shear Stress $r_x = -\rho\,\overline{u'v'}$

$$\bar{u}\frac{\partial r_x}{\partial x} + \bar{v}\frac{\partial r_x}{\partial y} = a_p\rho E\frac{\partial\bar{u}}{\partial y} - k_p c\frac{\sqrt{E}}{L}r_x + k_{qr}\frac{\partial}{\partial y}\left(\sqrt{E}L\frac{\partial r_x}{\partial y}\right)$$

$\underbrace{}_{\text{Convection}}$ $\underbrace{}_{\substack{\text{Produc-}\\\text{tion}}}$ $\underbrace{}_{\substack{\text{Destruc-}\\\text{tion}}}$ $\underbrace{}_{\text{Diffusion}}$

Shear Stress $r_z = -\rho\,\overline{w'v'}$

$$\bar{u}\frac{\partial r_z}{\partial x} + \bar{v}\frac{\partial r_z}{\partial y} = a_p\rho E\frac{\partial\bar{w}}{\partial y} - k_p c\frac{\sqrt{E}}{L}r_z + k_{qr}\frac{\partial}{\partial y}\sqrt{E}L\frac{\partial r_z}{\partial y}$$

$\underbrace{}_{\text{Convection}}$ $\underbrace{}_{\substack{\text{Produc-}\\\text{tion}}}$ $\underbrace{}_{\substack{\text{Destruc-}\\\text{tion}}}$ $\underbrace{}_{\text{Diffusion}}$

$a_p = 0.2\ ;\ k_{/p} = a_{/p}c^{-4/3} \approx 2.21\ ;\ k_{qr} = 0.6$

Fig. 6 Shear Stress transport equations (model
ET) for the swept wing boundary layer

```
┌────────────────────────────────────────────┐
│                Model  ET                    │
│                                             │
│    PDE  for Energy and Shear Stresses       │
└────────────────────────────────────────────┘
                      │
                      ▼
┌────────────────────────────────────────────┐
│                 Neglect                     │
│                                             │
│    Convection and Diffusion of Shear        │
│            Stress Equations                 │
└────────────────────────────────────────────┘
                      │
                      ▼
┌────────────────────────────────────────────┐
│                Model   EP                   │
│                                             │
│             PDE  for Energy                 │
└────────────────────────────────────────────┘
                      │
                      ▼
┌────────────────────────────────────────────┐
│                 Neglect                     │
│                                             │
│    Convection and Diffusion of Energy       │
│                 Equation                    │
└────────────────────────────────────────────┘
                      │
                      ▼
┌────────────────────────────────────────────┐
│                Model   ML                   │
│                                             │
│           Mixing Length Formula             │
└────────────────────────────────────────────┘
```
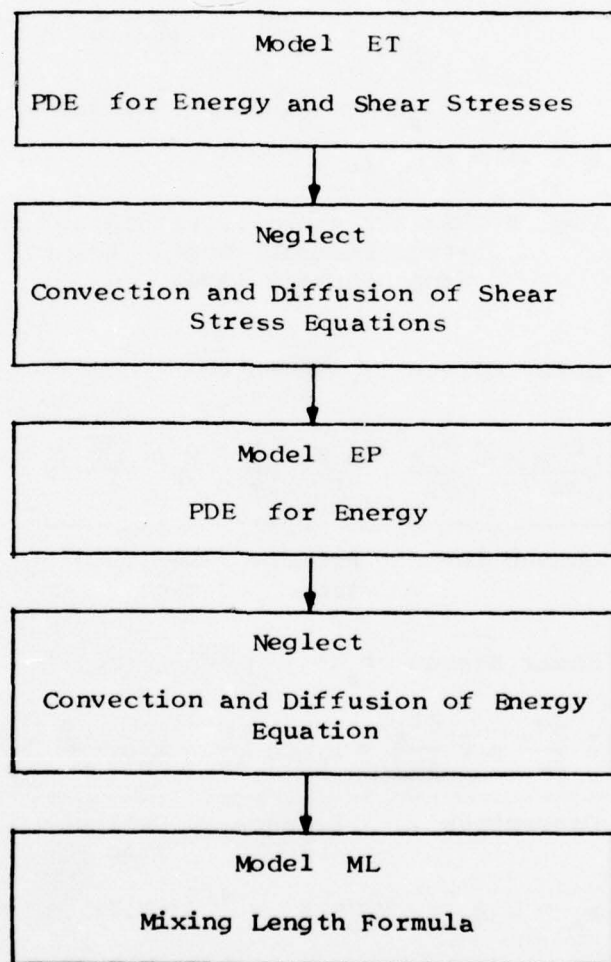
Fig. 7 Relations between the turbulence
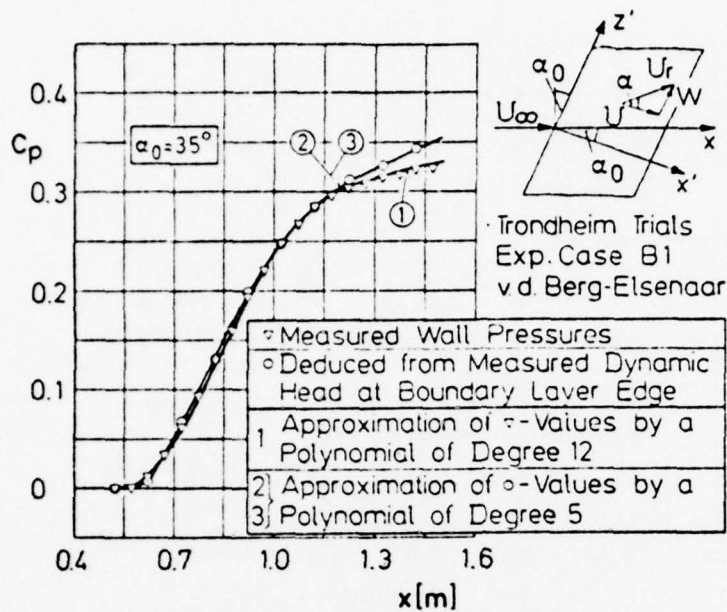   models

Fig. 8   Pressure distributions for the NLR
swept wing experiment
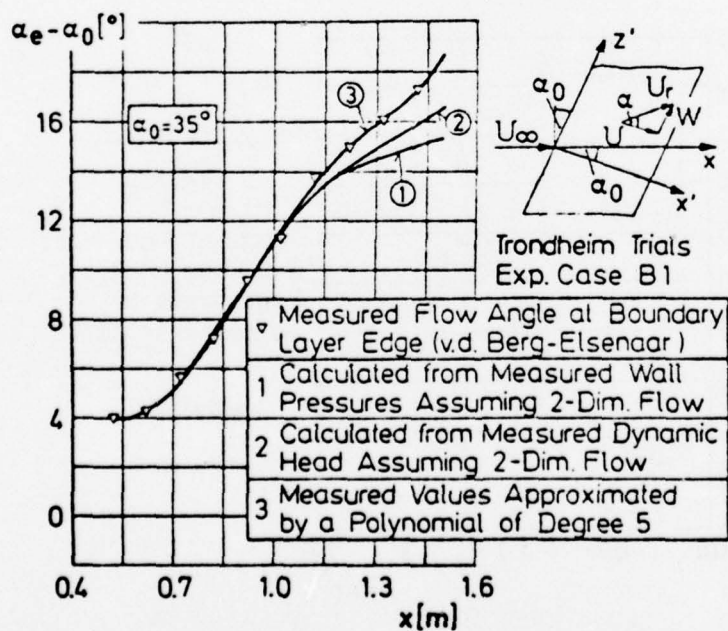

Fig. 9   The different development of the flow
angle at the edge of the boundary layer
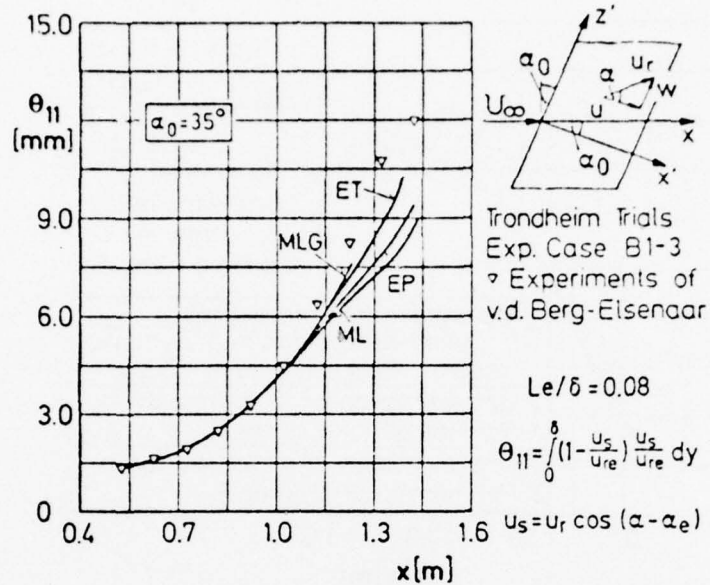for the NLR swept wing experiment

θ_{11} [mm]

$\alpha_0 = 35°$

15.0

ET

9.0

MLG

EP

6.0

ML

3.0

0

0.4   0.7   1.0   1.3   1.6

x [m]

U_∞

α_0

α u_r w

u

α_0 x'

z'

Trondheim Trials
Exp. Case B1-3
∇ Experiments of
v.d. Berg-Elsenaar

$Le/\delta = 0.08$

$$\theta_{11} = \int_0^\delta \left(1 - \frac{u_s}{u_{re}}\right) \frac{u_s}{u_{re}}\, dy$$

$u_s = u_r \cos(\alpha - \alpha_e)$

Fig. 10   Development of the streamwise momentum thickness

β_w [°]

45

Experiments
Wall Pitots
(Stanton)
∇ = 0.1 mm
$\alpha_0 = 35°$

MLG

35

EP

30

ML

25

ET

20

15

10

5

0

-5

0.4   0.7   1.0   1.3   1.6

x [m]

U_∞

α_0

α u_r w

u

α_0 x'

z'

Trondheim Trials
Exp. Case B1-3
Experiments of
v.d. Berg-Elsenaar

$Le/\delta = 0.08$

$\beta_w = \alpha_{wall} - \alpha_e$
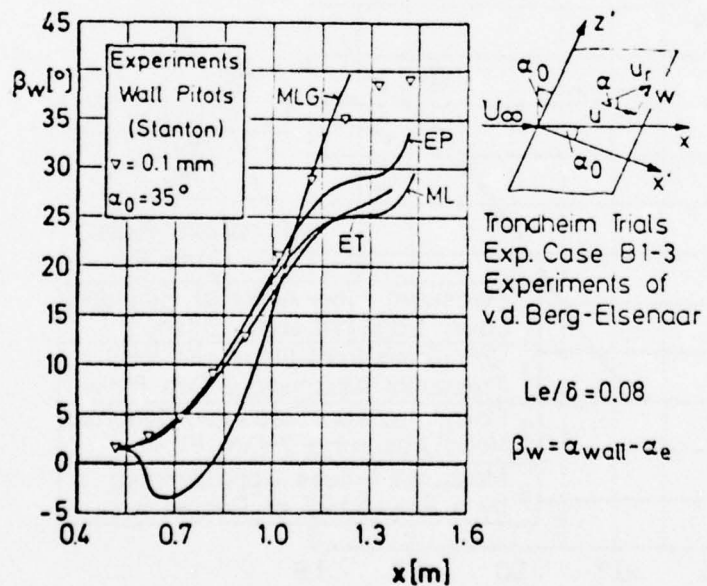
Fig. 11   Development of the cross flow angle at the wall
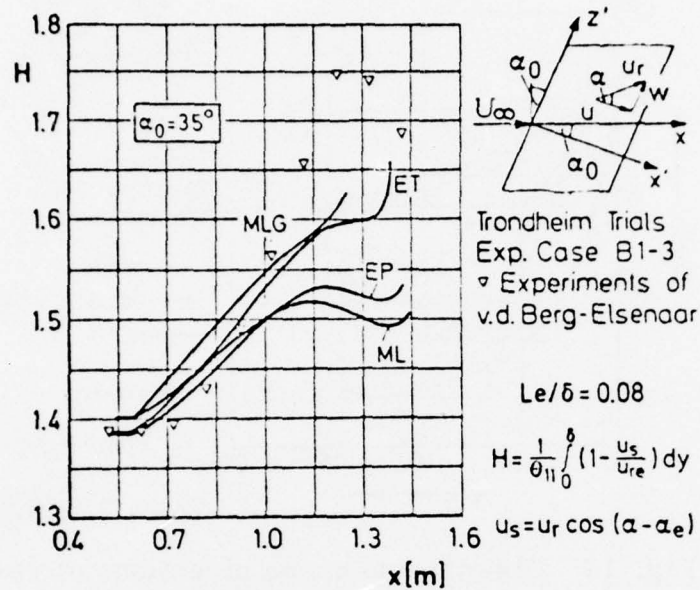
30

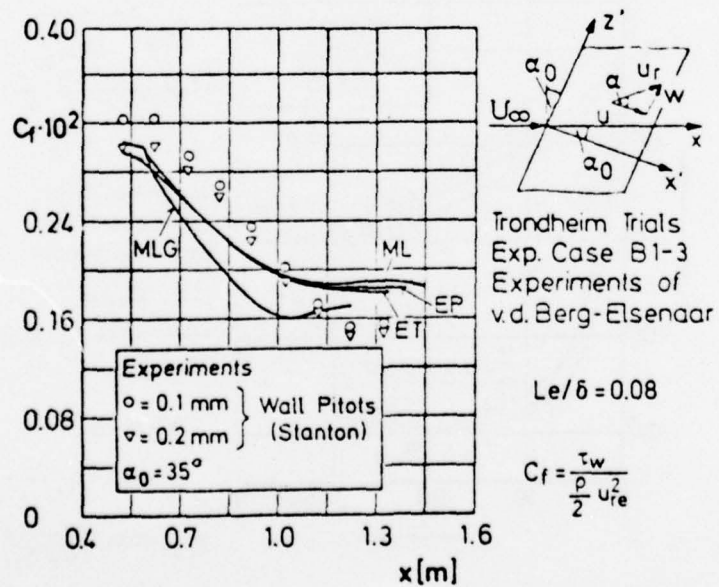Fig. 12 Development of streamwise shape
parameter

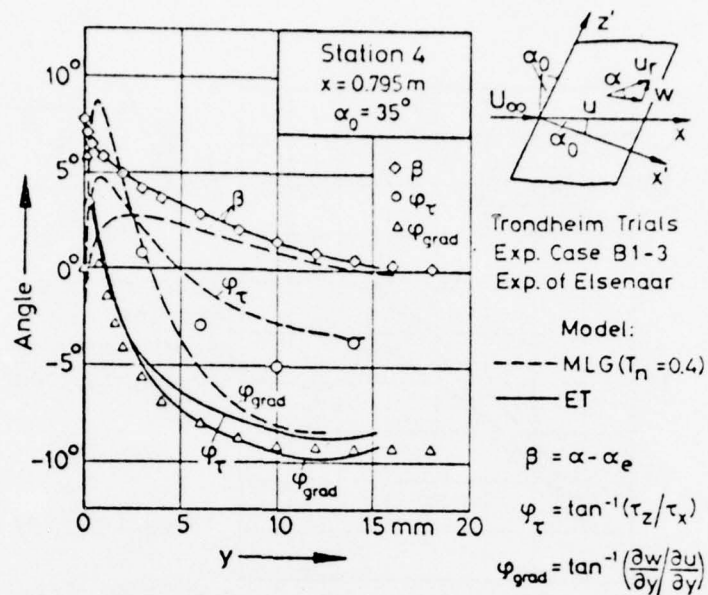Fig. 13 Development of local skin friction
coefficient

31

Fig. 14 Distribution of the directions of ve-. locity, velocity gradient and shear stress at measuring station 4
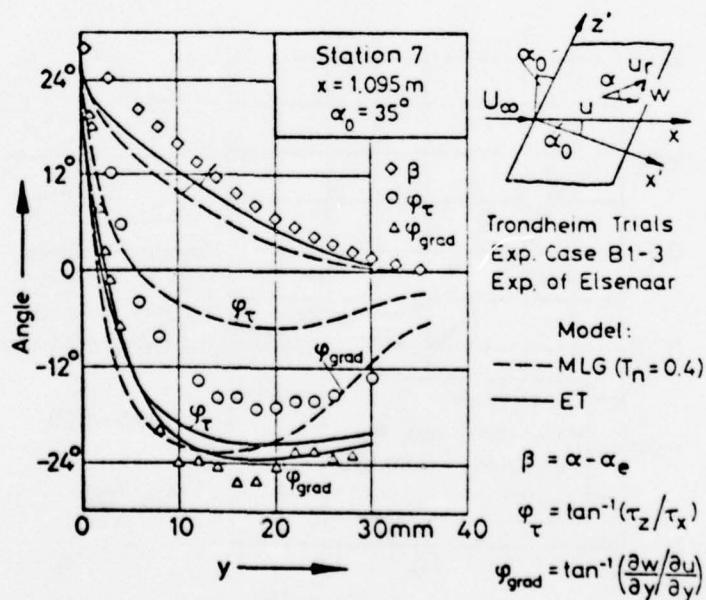

Fig. 15 Distribution of the directions of ve-locity, velocity gradient and shear .stress at measuring station 7
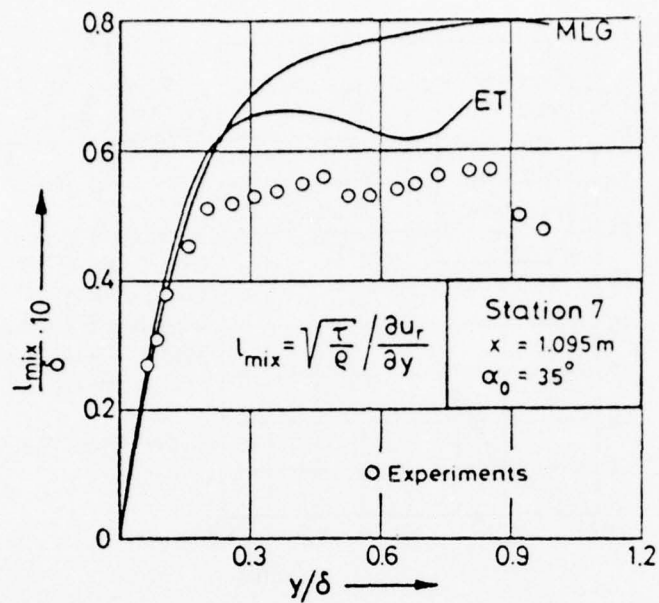
Fig. 16 Distribution of mixing length as calculated from the resultant shear stress
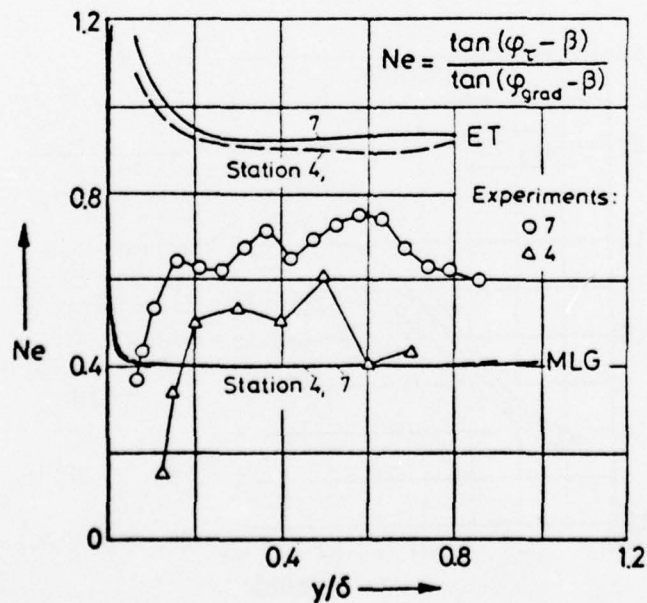

Fig. 17 Ratio of eddy viscosities with respect to direction normal and parallel to local streamline
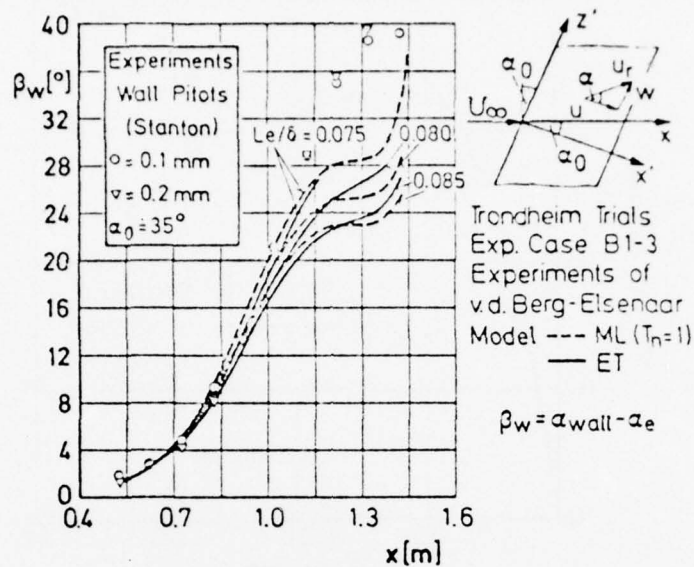
Fig. 18 Effect of the length scale on the development of the cross flow angle at the wall
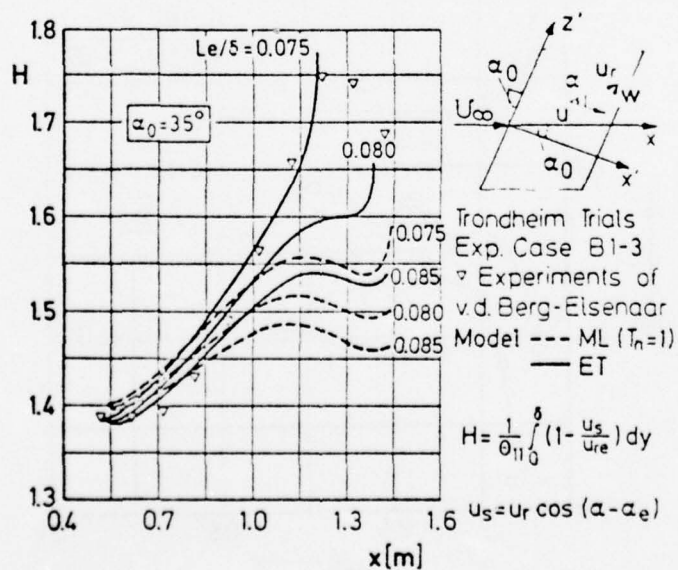

Fig. 19 Effect of the length scale on the development of the streamwise shape parameter

SKETCH OF AN ITERATIVE PROCEDURE FOR CALCULATING THE 3-DIMENSIONAL
FLOW AROUND A LIFTING BODY AT REALISTIC RE-NUMBERS INCLUDING
EFFECTS OF TURBULENCE.

by

Alfred Walz
Technical University of Karlsruhe
Karlsruhe, Germany

Numerically stable solutions of 3-dimensional steady-state NAVIER-
STOKES Flows provide information and fundamental interaction ef-
fects between separated and attached flow regions and the corres-
ponding pressure distribution on the solid body surface, up to
realistically high Re-Numbers (see the paper of ELSHOLZ-HAASE).
This result, however, can not be realistic insofar as for this
high Re-Number range turbulence will occur preferably in the at-
tached boundary layer (B.L.) part and also in the shear layer be-
tween the "Dead Water Body" and the quasipotential outer flow.
But the Elsholz-Haase pressure distribution may be used as a 1.
approximation for 3-dimensional Boundary Layer calculations in
the attached flow region, including transition criteria (see
HIRSCHEL's paper) and known turbulent Boundary Layer calculation
technics. As a main result, flow separation will be shifted down
stream and the "Dead Water Body" (D.W.B.) size and volume will be
decreased. The main shape features may be determined in analogy
to GRASHOF's 2-D. procedure (BMVg-FBWT-74-3, FRG) with the empiri-
cally justified assumption of constant pressure within this D.W.B.
and by repeated use of the ELSHOLZ-HAASE, NAVIER-STOKES-procedure.

Thus, a 2. approximation of the solid body pressure distribution may be obtained and used for a 2. approximation of the 3-D.B.L. calculation. An upstream shifting of the separation must be expected from this 2. iteration, because for a given angle of attack, a decrease of the D.W.B. volume and the corresponding vortex system will produce an increase of the circulation and of the positive pressure gradient in flow direction, hence, shifting the separation down stream again. Therefor, convergence of this iteration procedure may be expected, if a 3. iteration for the influence of this variation of the D.W.B. and vortex phenomenon on the surface pressure distribution will be taken into account.

Let me sketch some essential details about the sequence of steps to be done in this research program.

For simplicity, let me start with the 2-dimensional case, for which the procedure in question is already studied and realized successfully.

First, I want to state that there are three kinds of interaction between the outer quasi-potential flow filed and viscous effects:

1. Boundary layer (laminar and turbulent state)
   displacement effect, _slightly_ circulation decreasing,
   Fig. I.

2. Displacement by Flow separation with _strong_ circulation
   decreasing effect, Fig. II.

3. Flow Separation in 3 Dimensions, Displacement including the
   Induction Effects of Vortex Formations at small Aspect
   Ratios. Example: Axisymmetric Lifting Body, Fig. III.

The numerical calculations for such an iterative procedure are of course, time-expensive. But presently started simplifications in the physical and numerical concepts seem to promise an economic state for this direction of research.

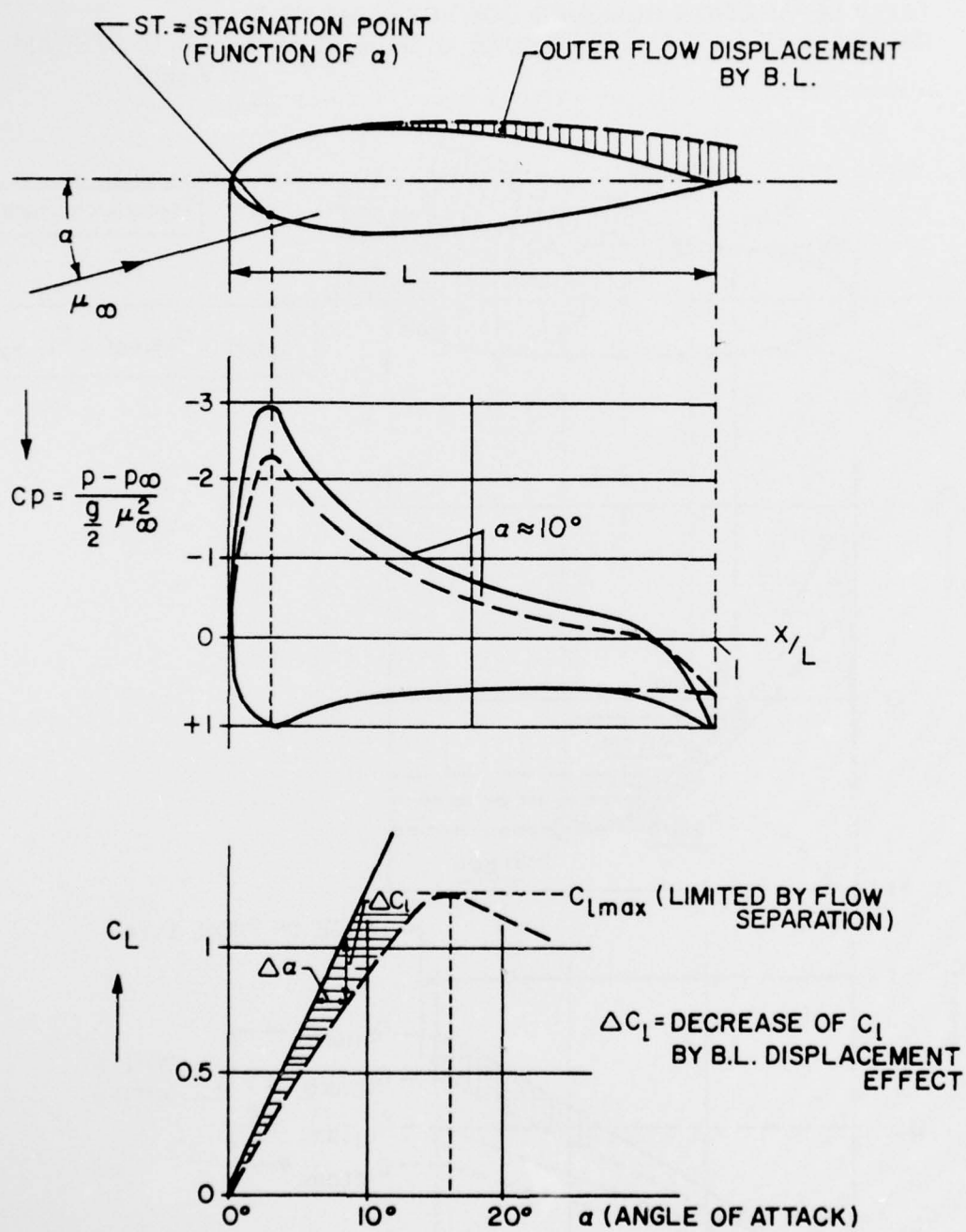Figure 1. Boundary Layer Displacement Effect (Slight Circulation
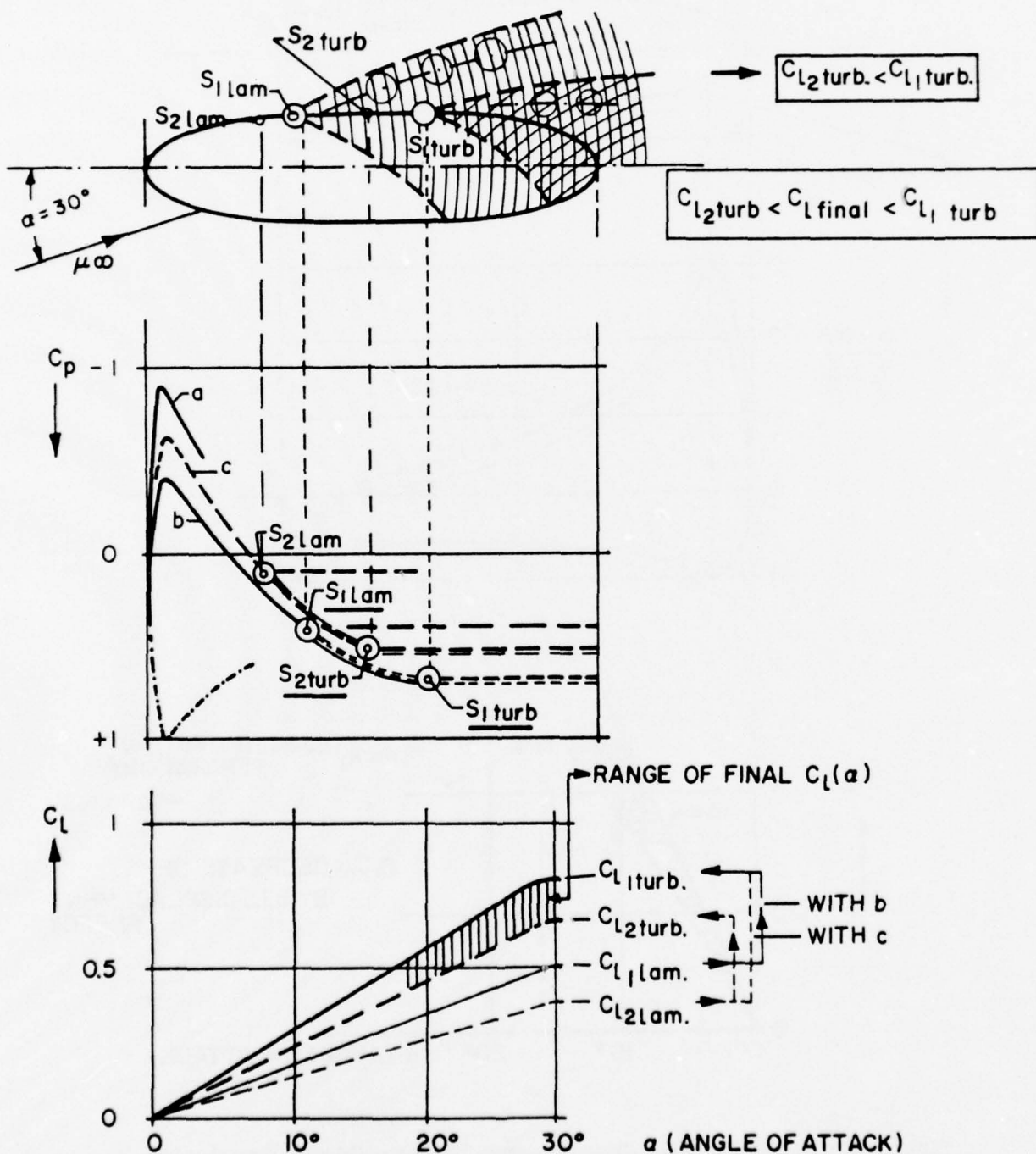Decreasing).

Figure 2. Real Flow, Realistic High Re-Number (10^6).
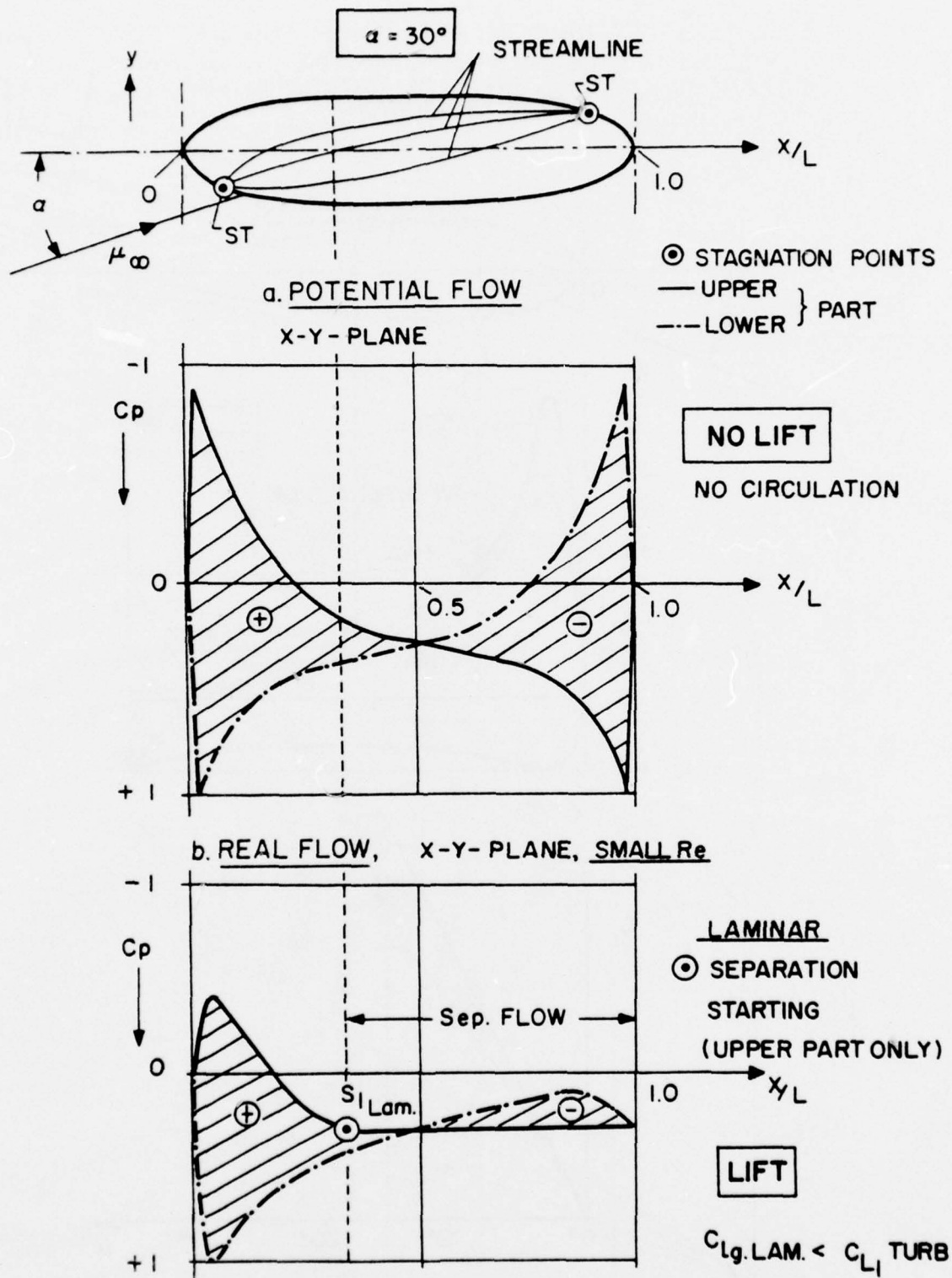
Figure 3. Flow Separation in 3 Dimensions Displacement + Induction Effects of Vortex Formations at an Axisymmetrical Lifting Body.

39

Figure 4. Flow Separation Displacement Effect (Strong Circulation Decreasing).

THEORETICAL ASPECTS ON COMPUTING 3-D VISCOUS FLOW AT HIGH REYNOLDS NUMBERS

by

E. Elsholz and W. Haase[+])

I. Introduction

For many purposes, the flow field induced by a vehicle under free-flight conditions is of great interest. The principle phenomena are described by potential flow- and boundary-layer-theory though both of them are valid only within restricted areas of the whole field. Moreover, detached flow becomes a severe problem.

Complete results of the viscous flow may be obtained from the Navier-Stokes-equations. Though there is much experience of several authors, certain numerical difficulties arise from the viscous equations itself, especially when calculating at high Reynolds-numbers.

II. Formulation of the Problem

The incompressible, laminar, steay state 3-D flow past a body of arbitrary shape is to be calculated from the Navier-Stokes equations using a finite difference method.

Assume a rectangular computational domain as indicated. When formulating equations, all quantities used are non-dimensionalized by the free stream quantities and a reference length according to the body's geometry. The body is situated inside the computational

---
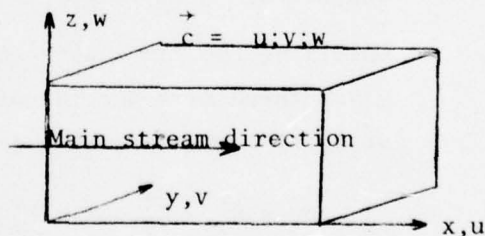
[+]) Wissenschaftliche Mitarbeiter bei Prof. Walz, Emmendingen
   c/o Technische Universität Berlin
   Institut für Thermo-Fluiddynamik

domain and its shape may be given by a certain number of gridpoints that have been previously defined to be located on the body's surface.

III. Basic Equations and Boundary Conditions

Eliminating the pressure gradients from the Navier-Stokes-equations yields into the vorticity-transport equ.s

$$\frac{\Delta\xi^x}{R_e} = \vec{\nabla}(c\cdot\xi^x) - \nabla u\cdot\vec{\xi}$$

$$\frac{\Delta\xi^y}{R_e} = \vec{\nabla}(c\cdot\xi^y) - \nabla v\cdot\vec{\xi} \qquad\qquad (1)$$

$$\frac{\Delta\xi^z}{R_e} = \vec{\nabla}(c\cdot\xi^z) - \nabla w\cdot\vec{\xi}$$

wherein the rotational vector is defined as

$$\vec{\xi} = \{\xi^x;\ \xi^y;\ \xi^z\} \qquad \begin{aligned} \xi^x &= w_y - v_z \\ \xi^y &= u_z - w_x \\ \xi^z &= v_x - u_y \end{aligned} \qquad (2)$$

(Superscripts denote the component of a vector, subscripts indicate partial differentiation with respect to the direction indicated. Δ is the Laplacian operator and the $\vec{\nabla}$ Lagrangian.) Combining the continuity-equ. $\nabla c - 0$ and the rotational vector gives three more partial differential equations governing the velocity components (see also [1]).

$$\Delta u = \xi^y_z - \xi^z_y;\quad \Delta v = \xi^z_x - \xi^x_z;\quad \Delta w = \xi^x_y - \xi^y_x \qquad (3)$$

The equation for the pressure coefficient $c_p = (p-p_\infty)/p_\infty$

$$\Delta c_p = -[u^2_x + v^2_y + w^2_z + 2(w_y v_z + u_z w_x + v_x u_y)] - \frac{4}{3Re}\ \Delta(\vec{\nabla c}) \qquad (4)$$

The last term on the right should not be neglected but indeed turns out to be important for proper results [2].

42

The outer boundry conditions are taken from the free stream
quantities or from symmetry conditions, respectively. At the
outflow boundary downstream the body, there will be used no
specific B.C. but an extrapolating routine [3].
According to adhesive effects at the surface of the body,
there are additional "inner" boundary conditions, i.e. $\vec{c} = 0$.

IV. Difference Scheme

Some fundamental problems of differential approximation may
be discussed using the model equation

$$-A \cdot f_x + B \cdot f_{xx} = 0 \qquad\qquad 0 \le x \le 1 \qquad\qquad (5)$$

$$\text{B. C.: } f(x = 0) = 0; \; f(x = 1) = 1$$

wherein A,B are constant (B > 0).

The exact solution is $\;f(x) = (e^{A x / B} - 1)/(e^{A / B} - 1)$

Assume a constant step-size $\;\Delta x = x_i - x_{i-1} = const.$

Then write
$$f_1 = f(x_{i-1})$$
$$f_2 = f(x_i)$$
$$f_3 = f(x_{i+1}).$$

Introducing second order centered differencing

$$f_x = \frac{f_3 - f_1}{2 \Delta x} + 0 \, (\Delta x^2)$$

$$f_{xx} = \frac{f_1 - 2f_2 + f_3}{\Delta x^2} + 0 \, (\Delta x^2) \qquad\qquad (6)$$

yields into

$$- (f_3 - f_1) + \frac{1}{Q} (f_1 - 2f_2 + f_3) + 0 \, (\Delta x^2) = 0; \; Q = \frac{A \Delta x}{2B} \qquad (7)$$

Now the quantity Q corresponds to half of the local "cell"-
Reynolds-number. Direct dolution by a Gauss-algorithm shows
the problem : If $|Q| < 1$, qualitatively correct viscous solutions
are obtained while for $|Q| > 1$ severe oscillations arise [4].

43

Moreover, iterative procedures fail when $|Q|>1$ as the main diagonal of the matrix system is no longer dominant.

However, first order upwind differencing avoids both of the difficulties. Replacing the first derivation streamwise by

$$A > 0 : f_x = \frac{f_2 - f_1}{\Delta x} + 0 \ (\Delta x)$$

$$A < 0 : f_x = \frac{f_3 - f_2}{\Delta x} + 0 \ (\Delta x) \tag{8}$$

gives

$$A > 0 : -2 \ (f_2 - f_1) + \frac{1}{Q} \ (f_1 - 2f_2 + f_3) + 0 \ (\Delta x) = 0$$

$$A < 0 : -2 \ (f_3 - f_2) + \frac{1}{Q} \ (f_1 - 2f_2 + f_3) + 0 \ (\Delta x) = 0 \tag{9}$$

This formulation is interesting also for another reason: a disturbation will go downstream with the local flow component which seems to be reasonable from the physical point of view [2].

When $A > 0$ equ. (9) leads to

$$(2 + \frac{1}{Q}) \ f_1 - 2 \ (1 + \frac{1}{Q}) \ f_2 + \frac{1}{Q} \ f_3 + 0 \ (\Delta x) = 0 \tag{10}$$

It becomes obvious that the main diagonal is dominant even when $0 \gg 1$. Furthermore, let 0 tend to infinity, the formula gives $f_2 \to f_1$, that is, oscillations do not occur.

On the other hand, this method produces explicit artificial viscosity [5]. From Taylor's expansion we get $\frac{f_2 - f_1}{\Delta x} = f_x - \frac{\Delta x}{2} f_{xx} \pm \cdots$

Thus, the truncation error changes the quantity B into $B + \frac{1}{2} A\Delta x$.

Indeed, an optimum differential approximation should be of extremely high order. Investigating this, oscillations become the basic problem again. Recent test calculations in order to eliminate oscillations when solving the model equation have shown that the approximation should reach the order of some $0(\Delta x^{100})$ which depends on the value of 0. So up to the present date this way of solution seems to be rather unrealistic. In other words, as long as it is impossible to use extremely high order approximation the basic problem of oscillation cannot be solved directly.

However, an indirect solution becomes possible from iterative damping characteristics. Thus, the problem is reduced to construct

44

a stable and convergent approximation that avoids explicit numerical viscosity. Due to this aim, the principle idea is to modify the first derivative as follows

$$f_x = \frac{f_3 - f_2 + f_2 - f_1}{2 \Delta x} = \frac{1}{2} \left[\frac{f_3 - f_1}{\Delta x} + \frac{f_2 - f_1}{\Delta x} \right] + 0 \, (\Delta x^2) \qquad (11)$$

Referring to the local flow direction, one of the values may be taken from previous iteration.

$$A > 0 \quad f_x = \frac{1}{2} \left[\frac{f_3 - \bar{f}_2}{\Delta x} + \frac{f_2 - p_1}{\underline{\Delta x}} \right]$$

$$A < 0 \quad f_x = \frac{1}{2} \left[\frac{f_3 - f_2}{\Delta x} + \frac{f_2 - f_1}{\Delta x} \right]$$

$$(12)$$

A scheme like this has the physical property like the first order upwind method discussed above. If the method converges f_2 tends to $\bar{f}_2$, and the second order centered approximation will be reached in the end. In order to damp down the oscillations, successive over/under-relaxation becomes necessary. According to high Reynolds-number calculation, the relaxation factor ω must be less than unity (under-relaxation). Finally, controlling ω turns out to be a delicate problem as oscillations only vanish when ω is kept small enough. This must be ensured by an automatic routine during calculations.

V. Method of Solution for 3-D Problem

Rewriting equ.(12) with respect to the conservative form of the vorticity-transport equ.s (1) leads to a convective term like

$$u > 0 \quad (u\xi^x)_x = \frac{1}{2} \left[\frac{u_3 \xi_3 - u_2 \bar{\xi}_2}{\Delta x} + \frac{u_2 \xi_2 - u_1 \xi_1}{\Delta x} \right]$$

$$u < 0 \qquad = \frac{1}{2} \left[\frac{u_3 \xi_3 - u_2 \xi_2}{\Delta x} + \frac{u_2 \xi_2 - u_1 \xi_1}{\Delta x} \right].$$

$$(13)$$

The corresponding three dimensional approximation results from superposing the evaluated formulae applied to each of the axis directions. This may be done successively within the program-system.

When initial values $\vec{c}$, ξ, c_p are set calculations start solving
equ.(1). Reaching some iterative limit one may compute equ.(3).
As both sets of equations are strongly coupled this procedure
must be repeated until the final accuracy will be obtained. Then
the pressure equ.(4) can be solved using the calculated flow field
data.

VI. References

1) W. Schönauer : Numerical Experiments with a Difference Model
       for the Navier-Stokes Equations (Turbulence Model)
       in: High-Speed Computing in Fluid Dynamics
            The Physics of Fluids Suppl.II, 1969, pp 228-232.

2) P. J. Roache : Computational Fluid Dynamics
       Hermon Publishers, Albuquerque, N.M., 87108, 1972.

3) R. Peyret/H. Viviand : Numerical Solution of the Navier-Stokes
       Equations for Compressible Fluids
       in: AGARD Lecture Series No. 73, 1975.

4) S. I. Cheng : Accuracy of Difference Formulation of Navier-Stokes Equ.
       in: High-Speed Computing in Fluid Dynamics/The Phys.of Fluids
       Suppl.II, 1969,pp 234-241.

5) P. J. Roache : On Artificial Viscosity
       in: Journal of Computat.Physics 10, 1972, pp 169-184.

SOME NEW RESULTS ON CALCULATING THREE-DIMENSIONAL
VISCOUS FLOWS

by

W. Haase and E. Elsholz [+])

This paper presents some new results calculated from the three-dimensional Navier-Stokes-equations on laminar steady state flow. The fluid may be homogeneous and incompressible.

Assume a body located inside of a 3-D physically rectangular domain which should be equivalent with a cartesian coordinate system. Uding this type of domain the question arises, how to realize an arbitrarily shaped body in a cartesian coordinate system. This problem results in variable step sizes in each of the coordinate directions, in order to get the body's shape as close to reality as possible.

There exist three potentialities managing this:

1) Step sizes are generated in such mode that no gridpoint is located on the body's surface.

2) Step sizes are adjusted in this way that all gridpoints are located on the surface.

3) Combination of method 1) and 2).

These facts indeed allow the construction of arbitrarily shaped bodies in the best manner. On the other hand one important limitation must be observed namely keeping step size ratios of two neighboring step sizes within values of 0.5 and 2.0 - due to numerical calculations.

[+]) Wissenschaftliche Mitarbeiter bei Prof. Dr.-Ing. A. Walz, Emmendingen, c/o Technische Universitat Berlin, Institut für Thermo- und Fluiddynamik

It can be realized that these limits are making further trouble because it should be possible to insert or remove mesh lines where-ever it is necessary. While this results in deviations from the original contour (if one tries to use only method 2) we profit by a combination of method 1) and 2). Therefore, in our present calculations all problems of this nature become trivial more or less. An important - nontrivial - job to do was the calculation of the pressure distribution by solving the Poisson equation for the pressure coefficient. There are no numberical stability problems as mentioned by RIMON/CHENG/1/ and other authors. Calculations had been done using a complete program system for solving the compressible Navier-Stokes-equations by Mr. Elsholz. The dashed line in figure 1a represent the computed result by RIMON/CHENG who got their pressure distribution by integration along the body's equator. Solving the Poisson pressure equation however yields in pressure information within the whole computational domain.

Next figure (1b) deals with the flowfield configuration post a sphere. The Reynolds number based on the sphere diameter is 133. While the upper part of this figure shows the photograph of this flowproblem made by TANEDA the lower part gives a look at our computed results. Because of symmetry we calculated only half of the sphere and used 51 times 21 times 41 grid points in the x, y, z direction of the computational domain. Wake length, separation point and location of the vortex center compare favourably with the experiment.

To compute a true three-dimensional flow field together with these famous but unfortunately critical high Reynolds numbers we first calculated flow past a spheroid with an axis ratio of 3:1 under an angle of attack of 30 degrees /2/. Calculations turned out to be numerically stable although we had to handle two outflow boundaries on the top and on the right hand side of the domain. Encouraged by these results (and Professor Walz) we took the change to compute the flow field past a slender body of revolution with and without an additional wing which was investigated by

GROSCHE /3/ by means of a directional probe in the 3 m wind tunnel of the AVA Göttingen/Germany of the DFVLR. Because of a small free stream Mach number of about 0.12 we could use our incompressible program system in a perfect way.

The body is shown in Figure 2. It has a total length of 15 diameters. The nose profile has nearly the same form used by AGARD Calibration Model B/4/. Span of the airfoil is four times the body diameter, his thickness has an amount of 20% of the diameter. For our computations we chose two test cases, a first one without and a second one with this additional airfoil. Morevoer we used an angle of attack of 15 degrees and a Reynolds number of $7 \cdot 5 \cdot 10^6$ based on the length of the slender body of revolution.

Unfortunately we had an extreme lack of time because of computer failure, therefore we are very sorry to say that we are not able to present plotted results of the body/wing configuration, furthermore the velocity plots of Figures 4 and 6[+]) may be also taken as partly finished articles.

All figures from number 3 to 6 represent vector plots of the velocity components normal to the main axis (x-axis) of the body at a distance of $x/D = 11$ and $x/D = 13$ from the leading edge (D = diameter). Upper figures (3 and 5) always give a look at the measurement /3/ while the lower ones are showing our calculations. The centers of these trailing vortices do not have exactly the same locations the measured have. But if the reader considers again, that results are taken from the running iteration comparison is not too bad in truth.

"The technique of obtaining numerical solutions of the fluid-dynamical equations with quantitative accuracy is not trivial, even with the help of a high speed computing machine" (Rimon/ Cheng)

- but it denotes a practicable way.

49

/1/ RIMON, Y.   Numerical Solution of a Uniform Flow over a
    CHENG, S.I.   Sphere at Intermediate Reynolds Numbers,
                       The Physics of Fluids, 12, No. 5, (1969),
                       pp. 949-959

/2/ ELSHOLZ, E.   Calculation of Three-Dimensional Viscous
    HAASE, W.   Flow Past a Body of Arbitrary Shape,
                       Proceedings of the Gamm-Conference on
                       Numerical Methods in Fluid Mechanics,
                       DFVLR, Köln, 1975, pp. 29-36.

/3/ GROSCHE, F.R.   Windkanaluntersuchungen des Wirbel-systems
                       an einem angestellten schlanken Rotation-
                       skorper ohne und mit Tragflugel.
                       Z. Flugwiss. 18, Heft 6, (1970)

/4/ AGARD   AGARD Wind Tunnel Calibration Models,
                       Specification 2 (1975)
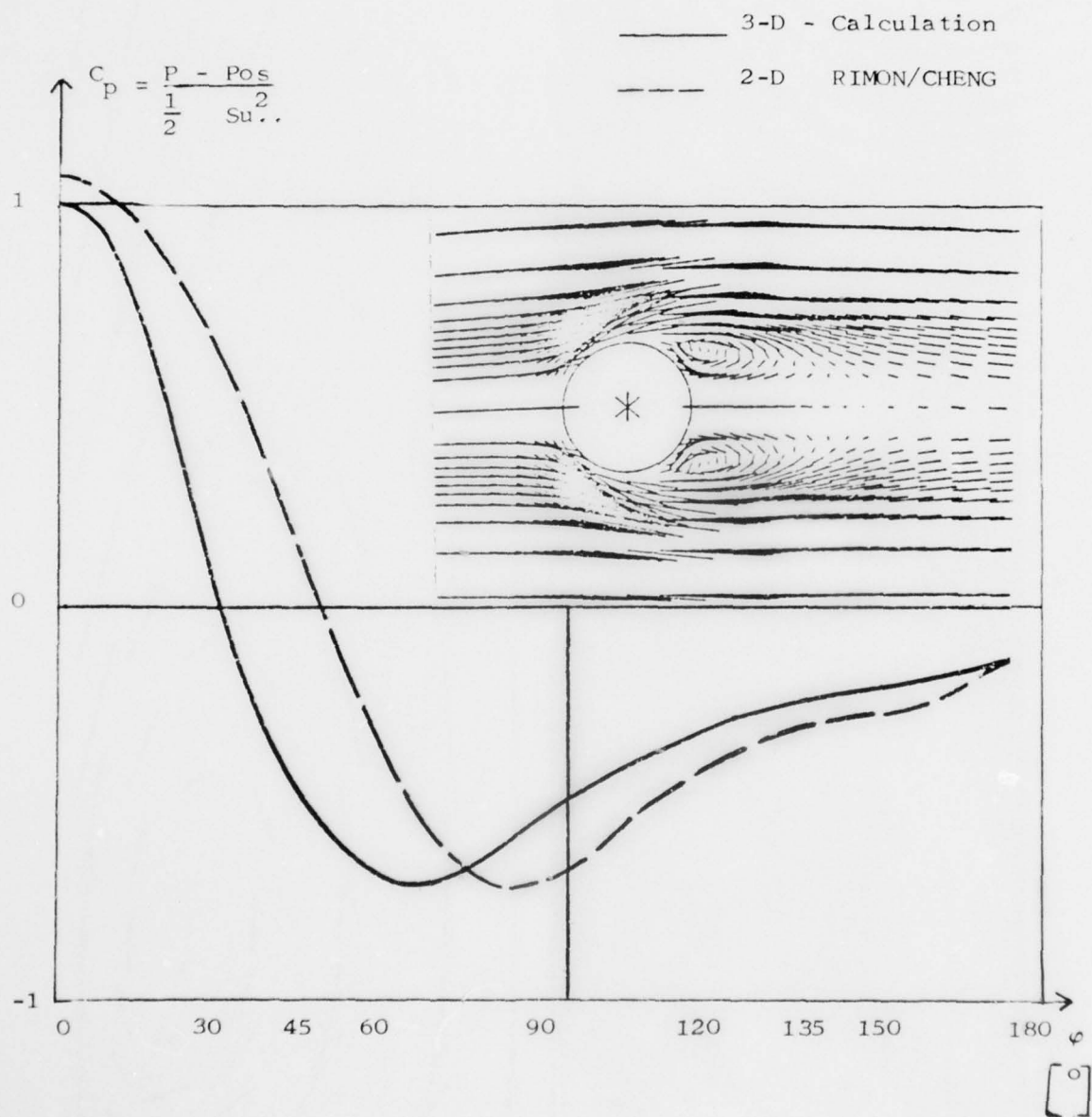
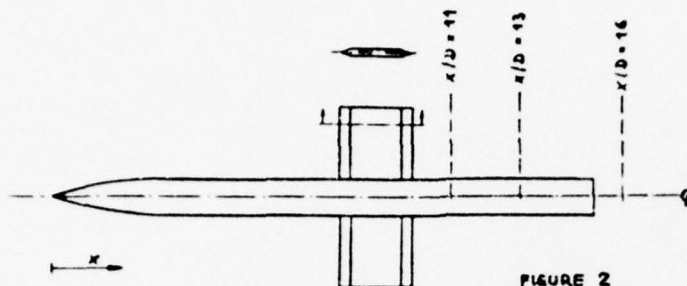PRESSURE - COEFFICIENT   SPHERE: Re 200
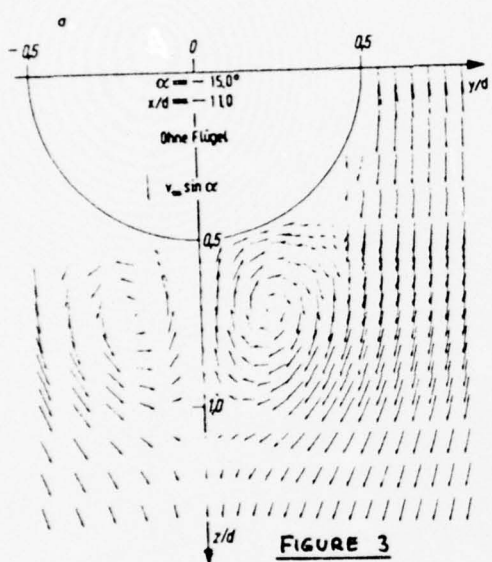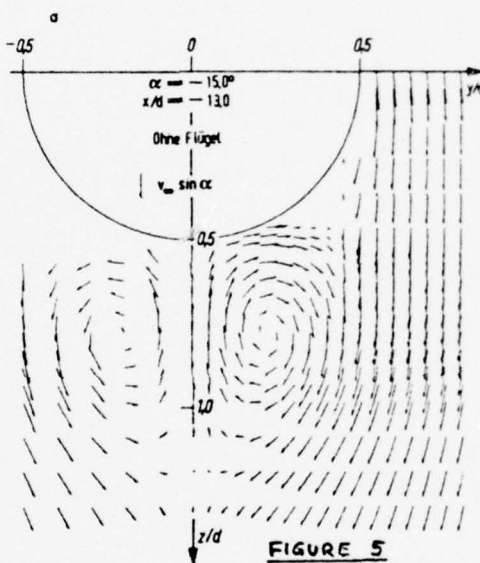
Figure 1a

51

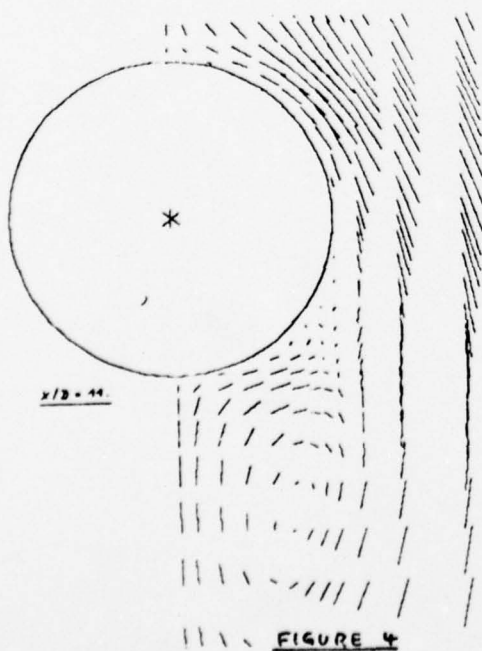$R = 133$
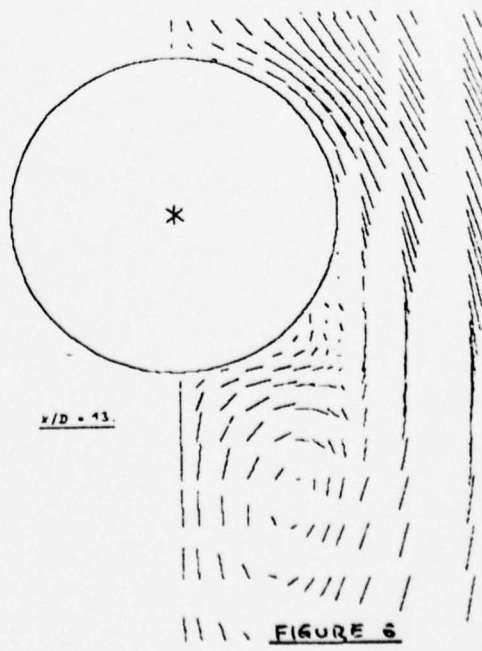
52
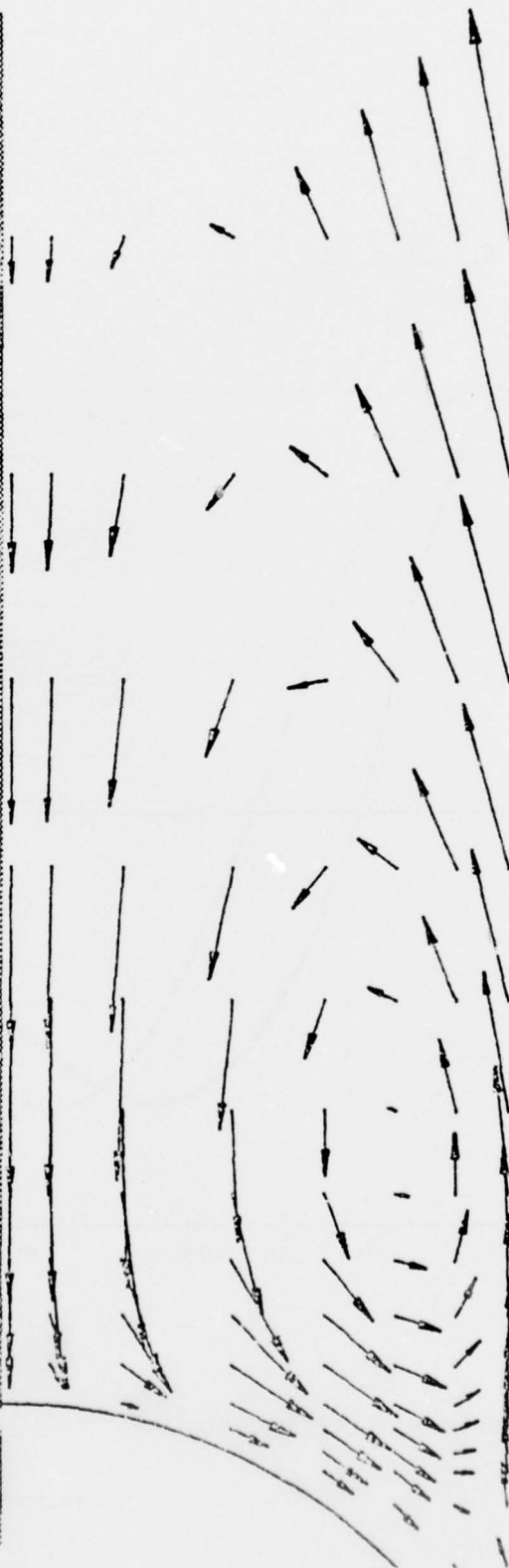
FIGURE 2

FIGURE 3

FIGURE 5

FIGURE 4

FIGURE 6

53

RESULTS OF A CALCULATION METHOD FOR THREE-DIMENSIONAL, COMPRESSIBLE, TURBULENT BOUNDARY LAYERS

by

H. W. Stock
Dornier GMBH
Friedrichshafen, Germany

ABSTRACT

The integral method proposed by D.F. Myring [1] extended by P.D. Smith [2] to adiabatic compressible flows has been used for the present boundary layer calculations. The calculated results will be compared with available experimental data.

a. The East and Hoxey test case: The boundary flow along a flat plate, on which a circular cylinder is mounted vertically.

b. The Hall and Dickens test case: The boundary layer flow along the insulated side wall of a supersonic nozzle, which produces crosswise pressure gradients.

c. The Johnston test case: The boundary layer development on a flat plate, the potential flow is given by a two-dimensional perpendicularly impinging jet.

d. The Berg and Elsenaar test case: The boundary layer flow along a swept flat plate with an imposed pressure gradient which leads to separation. The experiment tries to simulate flow conditions on an infinite swept wing.

The method has been extended by incorporating the lag entrainment method proposed by J.E. Green et al [3]. The corresponding changes will be discussed. In connection with test case d. the sensitivity of the method to perturbations in the potential flow data for boundary layers

near separation will be shown. Furthermore the importance of the empirical correlation of the form parameters H_1-$\bar{H}$ will be demonstrated using test case d. Finally boundary layer calculations will be presented for transonic wings where the three-dimensional potential flow data were obtained by solving the transonic potential equation for small perturbations with a relaxation technique. The results on a finite rectangular and a tapered wing with varying sweep of the leading and trailing edge will be shown.

1. INTRODUCTION

The aim of the present work is to develop for calculating compressible, turbulent boundary layers a program, which should serve together with a program for transonic potential flow data in the design procedure for three-dimensional transonic wings. Via iterative calculations - potential flow and boundary layer flow - pressure distributions on wings including viscous effects will be calculated for attached flows.

2. CALCULATION METHOD

2.1 Integral Method (D.F. Myring[1], P.D. Smith [2])

The boundary layer calculation is based on the integral method developed by D.F. Myring[1] which has been extended to compressible flows by P.D. Smith[2]. Only a brief description of the method will be given here, for detailed information see Ref. 1, 2.

The integral equations for three-dimensional boundary layers are written in non-orthogonal curvilinear corrdinates. Only adiabatic flows are considered. For the solution of the problem the x and y momentum equations and the entrainment equation are used. The three-dimensional boundary layer velocity profile is decomposed in a profile in the direction of the potential flow, X, (streamwise direction) and orthogonal to X in a profile in the direction of the secondary flow, Y, (cross-flow direction). Empirical relations (Mayer-[4] or Johnston-[5] profiles) allow the calculation of the cross-flow profile as a function of the streamwise profile. The integral quantities which appear in the X, Y coordinate system, can be evaluated easily from the

streamwise and cross-flow profiles. The choice of the nonorthogonal
curvilinear corrdinate system x,y, in which the boundary layer dev-
elopment will be calculated, determines the functional relation between
X,Y and x,y. The integral quantities in the x,y system can be computed
from those in the X,Y system. For the solution of the resulting system
of three partial differential equations the following empirical relations
are used:

- The velocity profile in the streamwise direction can be repre-
  sented by power law profiles
- The Ludwieg-Tillmann equation is used for the calculation of
  the skin friction
- The influences of compressibility are taken into account by Eckert's
  reference temperature concept
- For the calculation of the entrainment coefficient the formulation
  of Green[6] is used.

2.2   Lag Entrainment Method (Green et al [3])

The lag entrainment method of Green et al.[3] has been used to ameliorate
the calculation procedure. The original version of Myring [1] uses an
expression, developed by Head [7], for the entrainment coefficient F
which is correlated to the shape parameter $\bar{H}$. This correlation is based
on measurements in equilibrium boundary layers. P.D. Smith [2] has used
an expression for $F = F(\bar{H})$ as proposed by Green [6] which is valid for
compressible flows. Both Head's and Green's correlation should be
applied only in the case of equilibrium boundary layers. The lag
entrainment method however calculates the entrainment coefficient F
via a differential equation, where the change in F is set proportional
to the deviation of the actual boundary layer from that in an equilib-
rium state. Hence Green's et al.[3] method should yield results which
are more reliable.

2.3   Boundary Conditions

Myring [1] has shown for the incompressible case that the resulting
three differential equations are of hyperbolic nature. This situation
is not changed by the introduction of compressibility. Hence, the two
outmost characteristic directions define the domain of influence and

57

dependence. It may therefore be deduced that boundary conditions are needed along boundaries across which characteristics are entering the region of integration. For the three-dimensional boundary layer this is equivalent to saying that boundary conditions are needed along boundaries across which boundary layer fluid is entering the integration region. It also follows that boundary conditions need not to be specified along boundaries across which fluid is leaving the integration area.

The actual program will be used for calculations where no boundary conditions are available. Hence, the present version is such that errors may be introduced along parts of the boundaries and propagate along characteristic lines into the calculation domain.

3.   COMPARISON WITH MEASUREMENTS

3.1   East and Hoxey's Test Case

East and Hoxey [8] measured the boundary layer development in the law speed regime along an unswept flat plate on which a cylinder was mounted vertically, see Fig. 1. The region upstream of the separation line on one side of the symmetry plane was investigated. For the calculation a cartesian coordinate system was used. Fig. 2 shows the computed and measured boundary layer quantities for different y-stations. The experiment indicates separation for $x \simeq 1.0$ in the symmetry plane, none of the calculation procedures predicts this behavior.

3.2   Johnston's Test Case

Johnston [5] investigated the three-dimensional boundary layer in incompressible flow on the roof of a test section in which a pressure distribution was produced by a jet impinging against the back wall of the test section. The pressure distribution was not measured in sufficient detail for a boundary layer calculation, such that the external flow data were obtained from a potential flow calculation [9] for vertically impinging jets. For the boundary layer calculation a cartesian coordinate system was used. The results are shown in Fig. 4.

3.3   Hall and Dicken's Test Case

Hall and Dickens [10] measured the boundary layer development along the
insulated side wall of a supersonic nozzle. The measurements were made
along three streamlines denoted by A, B, and C, Fig. 5, which also
shows the nozzle geometry and the Mach number distribution along stream-
line B. A nonorthogonal coordinate system was used in the calculation,
in which the y-direction was identical to that shown in Fig. 5 and the
x-direction followed the indicated streamlines. Fig. 6 shows the
results along streamline B.

The change in sign of the curvature of the streamlines A, B, and C
indicates a change in sign of the pressure gradient in the y-direction.
In such cases the cross-flow profiles are of the "cross-over" type,
i.e., the cross-flow velocity changes sign within the boundary layer.
Such profiles can not be represented by a quadratic correlation, such
as Mager or Johnston cross-flow profiles. Nevertheless the computed
results are in good agreement with the measurements.

3.4   Berg and Elsenaar's Test Case

The experiment of Berg and Elsenaar [11] is of special importance, as
out of the available measurements of three-dimensional boundary layers
this experiment simulates the flow conditions on swept wings. Berg and
Elsenaar probed the turbulent boundary layer on a swept flat plate
(35° sweep) in incompressible flow. The tunnel wall was formed such
that the adverse pressure gradient was sufficient to separate the
boundary layer. Furthermore, care was taken to achieve infinite swept
wing conditions by designing the contour of the side plates. In Fig. 7
the potential flow data are shown for different interpretations of the
flow quantities. Curve 1 corresponds to the measured quantities U_e and
α , curve 2 was evaluated from measured U_e and the infinite swept wing
condition and curve 3 was deduced from the wall pressure data and the
infinite swept wing condition. The shaded region indicates the area
where separation was observed in the experiment. The calculations were
performed in a nonorthogonal corrdinate system, where the x-direction
was identical with the tunnel axis and the y-direction was parallel to

the leading edge of the plate. All y-derivatives were identical to zero (infinite swept wing concept). Fig. 8 shows the results based on external flow data corresponding to curve 3. Included for comparison are the results of another integral method proposed by Michael and Cousteix [12]. All calculations do not predict separation.

Fig. 9 and 10 show the results for Mager- and Johnston-profiles for the different external flow data. Fig. 9 gives the results of the lag entrainment method using Mager profiles. For the wall pressure data (curve 3) none of the calculations predicts separation. The results including lag entrainment lie closer to the results of Michel and Cousteix [12], who used a more elaborate integral method, Fig. 9. For the external flow data, corresponding to the measured values of U_e and (curve 1), the present calculations predict separation for both Mager- and Johnston-profiles, where the use of Johnston profiles tends to indicate separation too early. The results in Figs. 9 and 10 in total indicate how sensitive the present calculation method reacts on relative small variations in the external flow field, if the boundary layer is close to separation. Fig. 11 compares the calculated entrainment coefficient F with the measurements using Mager profiles in the original version of the P.D. Smith method and with the lag entrainment method included. As can be seen the agreement using lag entrainment is by far better.

The power law profiles used for the description of the velocity distribution in the boundary layer in the direction of the external flow do not represent the conditions in a boundary layer which is close to separation. The momentum loss in the flow close to the wall can not be described correctly for strong adverse pressure gradients. Hence, the relation between the shape parameters H_1 and $\bar{H}$ in the P.D. Smith method which is based on power law profiles is believed to be one of the main reasons for the unsatisfactory results.

60

The dominant terms in the entrainment equation for small crossflow effects are

$$\theta_{11} \frac{d\overline{H}}{dx} = \frac{d\overline{H}}{dH_1} \ [F-H_1 \left\{ \frac{C_f}{2} - (\overline{H} + 1) \ (1 + .2 \ M^2) \ \frac{\theta_{11}}{U_e} \ \frac{dU_e}{dx} \right\} \ ] \qquad (1)$$

It is obvious from equation (1) that the H_1-$\overline{H}$ correlation governs the change of the form parameter $\overline{H}$.

To demonstrate the influence of the H_1-$\overline{H}$ correlation, three different correlations have been used to calculate the Berg and Elsenaar test case.

$$H_1 \ (1) = 2 \ \overline{H}/(\overline{H}-1)$$
$$\frac{d\overline{H}}{dH_1} \ (1) = - (\overline{H}-1)^2/2 \qquad\qquad (2)$$

$$H_1 \ (2) = 3.15 + 1.72/(\overline{H}-1) - 0.01 \ (\overline{H}-1)^2$$
$$\frac{d\overline{H}}{dH_1} \ (2) = - (\overline{H}-1)^2/[1.72 + 0.02 \ (\overline{H}-1)^3] \qquad\qquad (3)$$

$$H_1 \ (3) = [H_1 \ (1) + H_1 \ (2)]/2$$
$$\frac{d\overline{H}}{dH_1} \ (3) = [\frac{d\overline{H}}{dH_1} \ (1) + \frac{d\overline{H}}{dH_1} \ (2)]/2 \qquad\qquad (4)$$

The different correlations are shown in Fig. 12. Equation (2) results from power law profiles, which can also be used for adiabatic, compressible flows[13]. Equation (3) was proposed by Green[3]. Equation (4) represents the mean value between Equations (2) and (4). Fig. 13 gives the results obtained for Mager profiles and wall pressure data. It is seen clearly that a more elaborate correlation for H_1-$\overline{H}$ is needed in order to obtain more reliable results. A one parameter profile family like the power law profiles fails to describe a reliable H_1-$\overline{H}$ relationship, possibly a two parameter profile family [14, 15] may improve the situation. Fig. 14 shows the results for the skin friction coefficient calculated for the different potential flow data using Mager and Johnston profiles, with or without lag entrainment and using the different H_1-$\overline{H}$ relationships.

4.   CALCULATIONS OF THE BOUNDARY LAYER DEVELOPMENT ON
      WINGS IN THE TRANSONIC FLOW REGIME

4.1   Finite Rectangular Wing (NACA 63A006)

The pressure distribution on the wing of the wing-body configuration[16]
was calculated with a relaxation method [17, 18] for an angle of attach
of 2° and a Mach number of 0.9. Fig. 16 shows the pressure distribution
in the wing section close to the fuselage (wing section 1) close to
the tip (wing section 9) and in the middle of the Wing (wing section 5).

4.1.1   Initial Conditions

The boundary layer calculation was done in a cartesian coordinate system.
The y-stations correspond to the nine wing sections. As initial condi-
tions laminar boundary layer quantities were used which would exist in
the stagnation line of an unswept cylinder, the radius of which is equal
to the nose radius of the wing. In the vicinity of the stagnation line
the boundary layer thicknesses do not change. Consequently, the calcula-
tion can be started with the stagnation quantities close to the leading
edge. Two different calculations were done starting from 0.04% chord
and 1% chord. No difference did show up. Fig. 16 shows the boundary
layer development on the upper surface in the 5th wing section starting
from 1% chord for different initial conditions. The continuous line
gives the results for the initial conditions obtained from the stagna-
tion line quantities on the unswept cylinder; the dashed line shows the
calculations for 10 times and the last curve corresponds to 100 times
these initial conditions. As can be seen, the calculations are rela-
tively insensitive to the perturbations in the initial conditions. The
differences decay from 1,000% and 10,000% at the leading edge to 2% and
15% respectively at the trailing edge.

4.1.2   Results

Fig. 16 shows the pressure distribution and boundary layer quantities
on the upper and lower surface in the wing sections 1, 5, and 9. The
calculations were started at 1% chord and the initial conditions were
those on the cylinder. The results show qualitatively the expected
behaviour of the boundary layer development. In the region of the

pressure rise on the upper surface between 50% and 60% chord the boundary layer grows rapidly ($\theta_{11}, \delta^*, \bar{H}$) and the skin friction C_f decreases. A similar behaviour is seen close to the trailing edge.

4.2 Calculations of the Boundary Layer Development on a Tapered Wing with Fuselage

The plan form of the wing is shown in Fig. 19. A nonorthogonal coordinate system was used, such that the calculation proceeds along percentage lines. The Mach number was 0.835 and the angle of attack 0.5°. The calculation was considered as a test case, to see how the data transport from the potential flow program and the automatic generation of the coordinate system worked out. The pressure distribution shown in Fig. 17 was obtained with a rather crude grid and the solution was not fully converged, but good enough to make the first trial with the boundary layer program. As initial conditions the stagnation line boundary layer quantities on swept cylinders were used. Fig. 18 gives an idea of the displacement surface on the upper and lower surface and Fig. 19 shows the potential and limiting streamline inclination distribution. The displacement thickness δ^* of the three-dimensional boundary layer can get negative (see Fig. 18 in the first wing section) as δ^* is calculated from

$$\frac{\partial}{\partial x} (f_1 \rho_e u_1 \delta^*) + \frac{\partial}{\partial y} (f_2 \rho_e v_1 \delta^*) = \frac{\partial}{\partial x} (f_1 \rho_e U_e \Delta_1) + \frac{\partial}{\partial y} (f_2 \rho_e U_e \Delta_2) \qquad (5)$$

where f_1 and f_2 are functions of the components of the metric tensor, u_1 and v_1 are the components of U_e and Δ_1, Δ_2 the displacement thicknesses in the x- and y- direction respectively.

5. CONCLUSIONS

Calculating the different test cases an advantage of this method gets obvious, without a change to the program the boundary layer development was calculated in different coordinate systems. The results as compared with measurements show a satisfactory agreement. The inclusion of the lag entrainment method does improve the predictions. It is seen that the present method is rather stable, i.e., perturbation in the initial conditions decay rapidly.

LIST OF SYMBOLS

C_f Skin friction coefficient

F Entrainment coefficient

f_1, f_2 Equation 5

$\overline{H}$ Form parameter, $\overline{H} = \dfrac{1}{\theta_{11}} \int \dfrac{\rho}{\rho_e} \left(1 - \dfrac{u}{u_e}\right)$

H_1 Form parameter, $H_1 = (\delta - \delta_1{*})/\theta_{11}$

M Mach number

u Velocity component in the external flow direction

x, y, z Coordinates

α Angle between the projection of the external flow direction direction onto the surface and the chosen x-direction

β Angle between the projection of the external flow direction onto the surface and the limiting streamline

δ Boundary layer thickness

δ^* Displacement thickness of the three-dimensional boundary layer

δ_1^* Displacement thickness corresponding to the velocity profile in the external flow direction

Δ_1, Δ_2 Displacement thicknesses defined in the chosen x and y coordinate system

θ_{11} Momentum thickness corresponding to the velocity profile in the external flow direction

ρ Density

SUBSCRIPTS

Ref   Reference quantitiy

e Outer edge of the boundary layer

REFERENCES

1. Myring, D.F., An Integral Prediction Method for Three-Dimensional Turbulent Boundary Layers in Incompressible Flow, R.A.E. TP. 70147, 1970.

2. P.D. Smith, An Integral Prediction Method for Three-Dimensional Compressible, Turbulent Boundary Layers, ARC, R+M, Nr. 3739, 1974.

3. Green, J.E., D.J. Weeks, and J.W.F. Brooman, Prediction of Turbulent Boundary Layers and Wakes in Compressible Flow by a Lag-Entrainment Method, R.A.E. TR 72231, 1973.

4. Mager, A., Generalisation of Boundary-Layer Momentum Integral Equations to Three-Dimensional Flows, Including Those of Rotating Systems, NACA Rep. 1067, 1952.

5. Johnston, J.P., Three-Dimensional Turbulent Boundary Layer, MIT Gas Turbine Lab. Rpt. 39, 1957.

6. Green, J.E., Application of Head's Entrainment Method to the Prediction of Turbulent Boundary Layers and Wakes in Compressible Flows, R.A.E. TR 72079, 1972.

7. Head, M.R., Entrainment in the Turbulent Boundary Layer, ARC R+M, Nr. 3152, 1958.

8. East, L.F. and R.P. Hoxey, Low Speed Three-Dimensional Turbulent Boundary Layer Data. Part I, RAE TR 69041, 1969.

9. Pai, S., Fluid Dynamics of Jets, D. Van Nostrand Co., Inc., New York, 1954.

10. Hall, M.G. and Dickens, H.B., Measurements in a Three-Dimensional Turbulent Boundary Layer in Supersonic Flow. ARC, R+M, Nr. 3537, 1966.

11. Van Den Berg, B. and Elsenaar, A., Measurement in a Three-Dimensional Incompressible Turbulent Boundary Layer in an Adverse Pressure Gradient Under Infinite Swept Wing Conditions, NLR TR 72092 U, 1972.

12. Michel, R. and Cousteix, J., Theoretical Analysis of Three-Dimensional Turbulent Boundary Layers, Euromech 60, Trondheim 1975, ONERA TP Nr. 1975-43.

13. Spence, D.A., The Growth of Compressible Turbulent Boundary Layers on Isothermal and Adiabatic Walls, ARC, R+M, Nr. 3191, 1961.

14. Coles, D., The Law of the Wake in the Turbulent Boundary Layer, J. Fluid. Mech., Vol. 1, pp. 191-226, 1956.

15. Thompson, B.G.J., A New Two Parameter Family of Mean Velocity Profiles for Incompressible, Turbulent Boundary Layers on Smooth Walls, ARC, R+M, Nr. 3463, 1967.

16. Klunker, E.B. and Newman, P.A., Computation of Transonic Flow About Lifting Wing-Cylinder Combinations, J. Aircraft, Vol. 11, Nr. 4, 1974.

17. Rohlfs, S. and Vanino, R., A Relaxation Method for Two- and Three-Dimensional Transonic Flows, Euromech 40, Saltjöbaden, 1973.

18. Schmidt, W. and Vanino, R., The ANalysis of Arbitrary Wing-Body Combinations in Transonic Flow Using a Relaxation Method, Symposium Transsonicum II, Göttingen, 1975, Springer Verlag, Berlin Heidelberg New York, 1976.
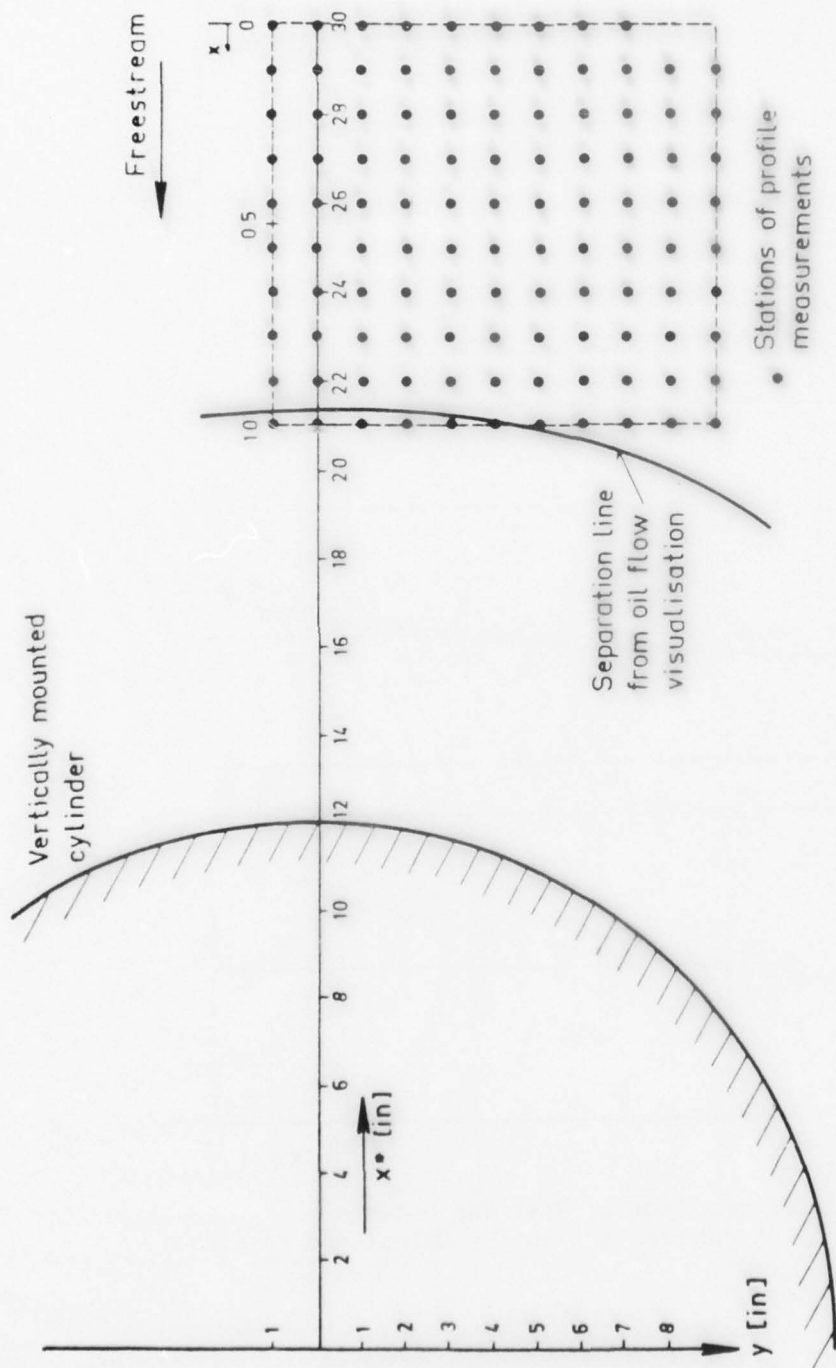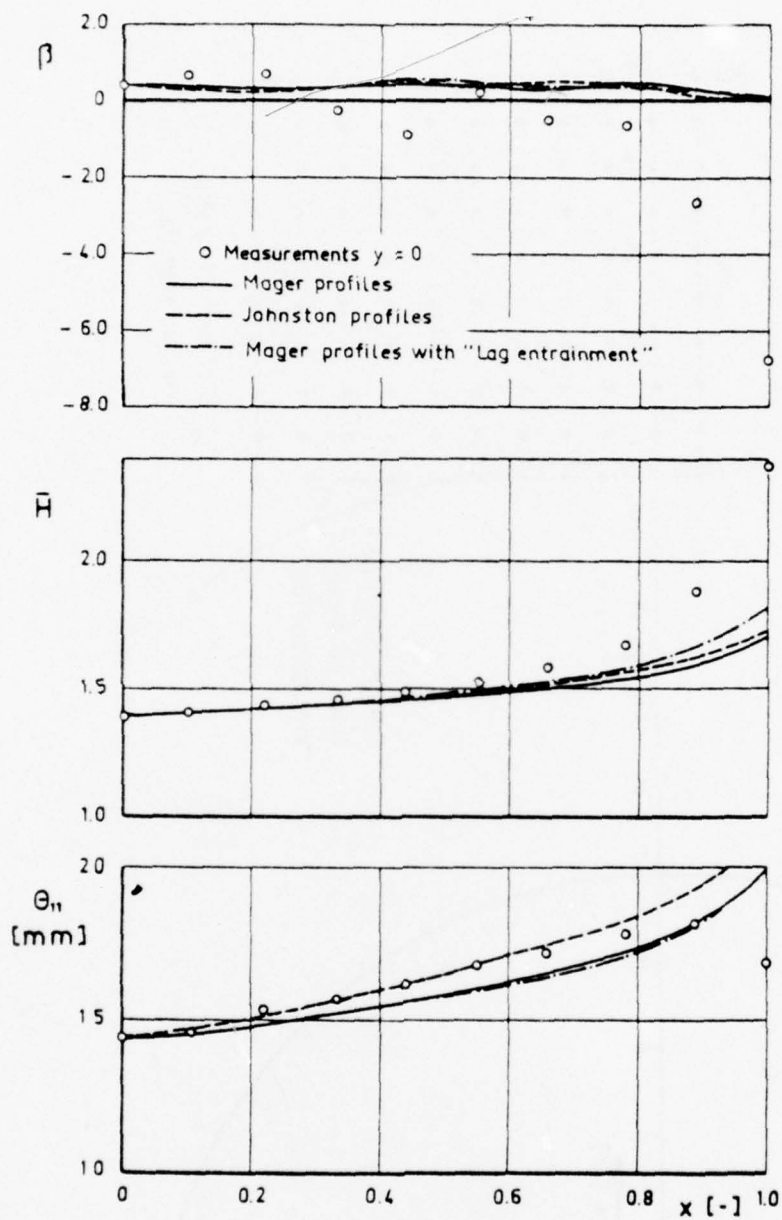
Fig. 1. Layout of East and Hoxey's Experiment.

Fig. 2. Comparison of East and Hoxey's
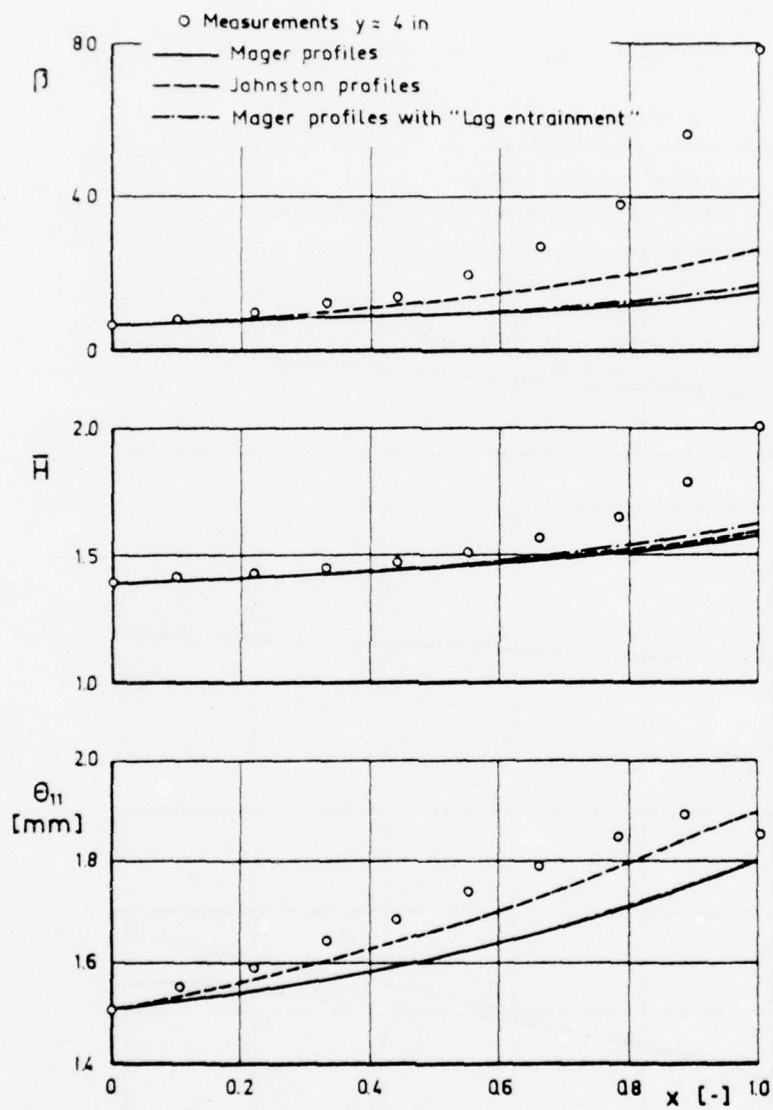Measurements with the Calculated Results.
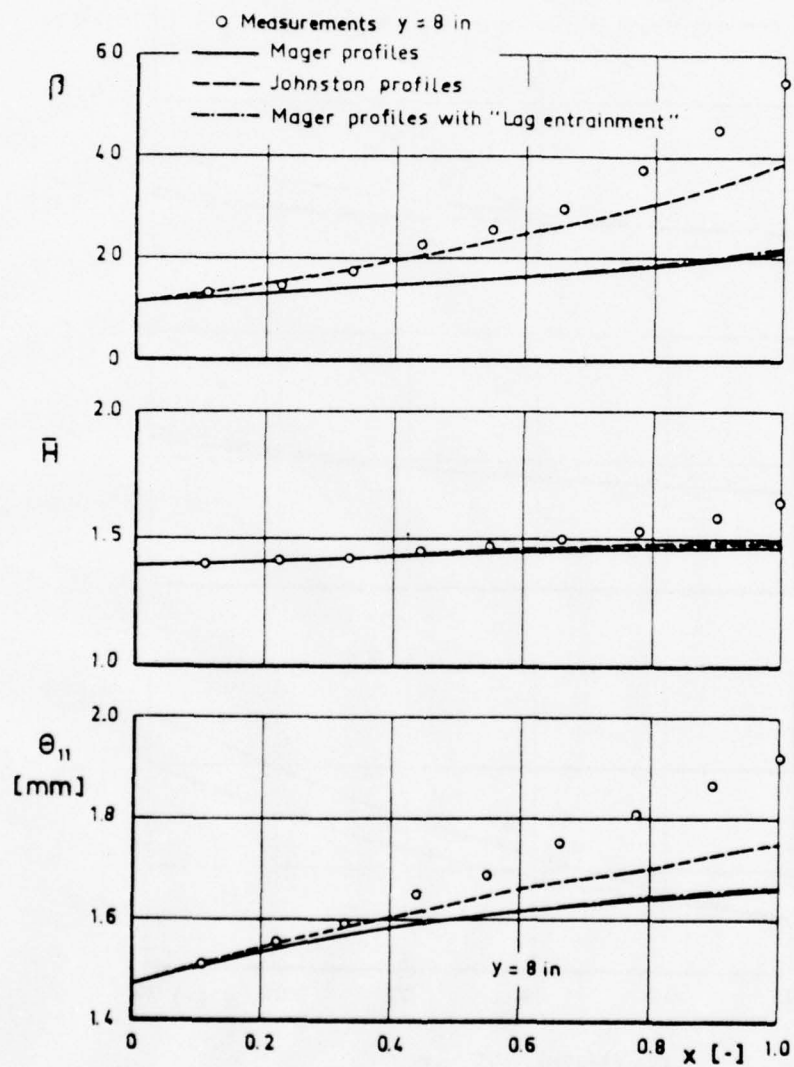
68

Fig. 2.   Continued.
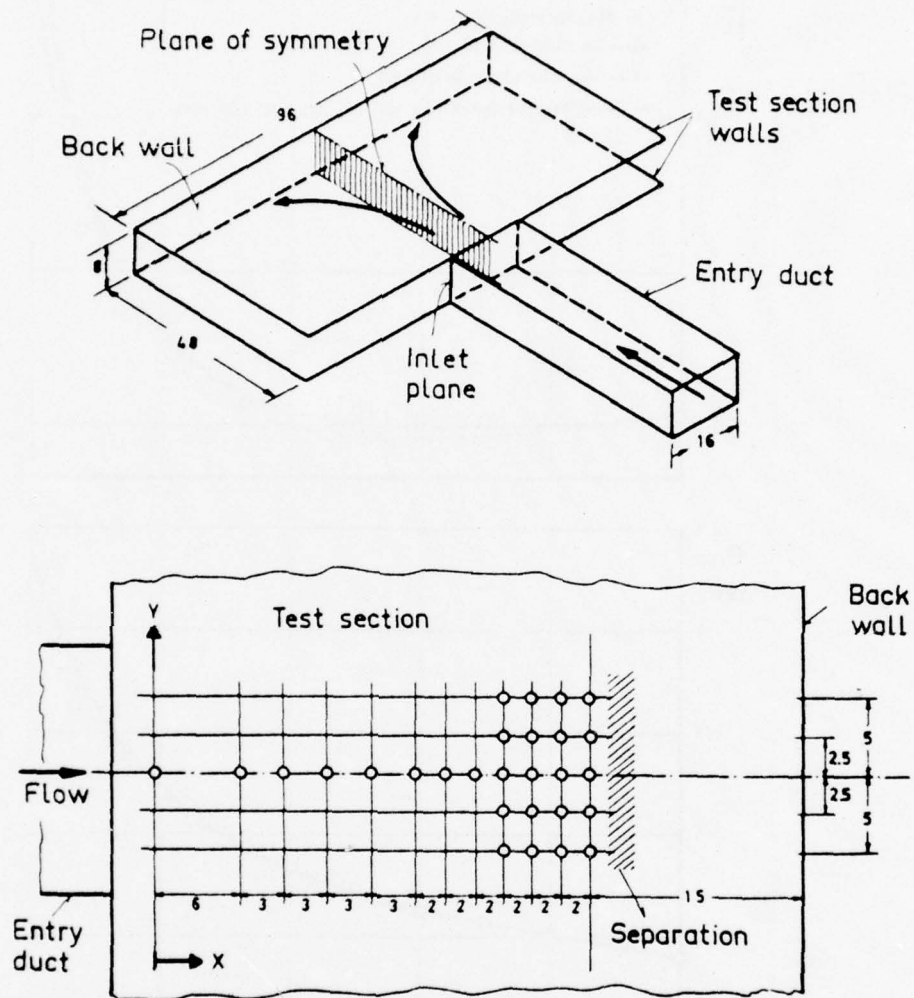
Fig. 2. Continued.

Fig. 3. Layout of Johnston's Impinging
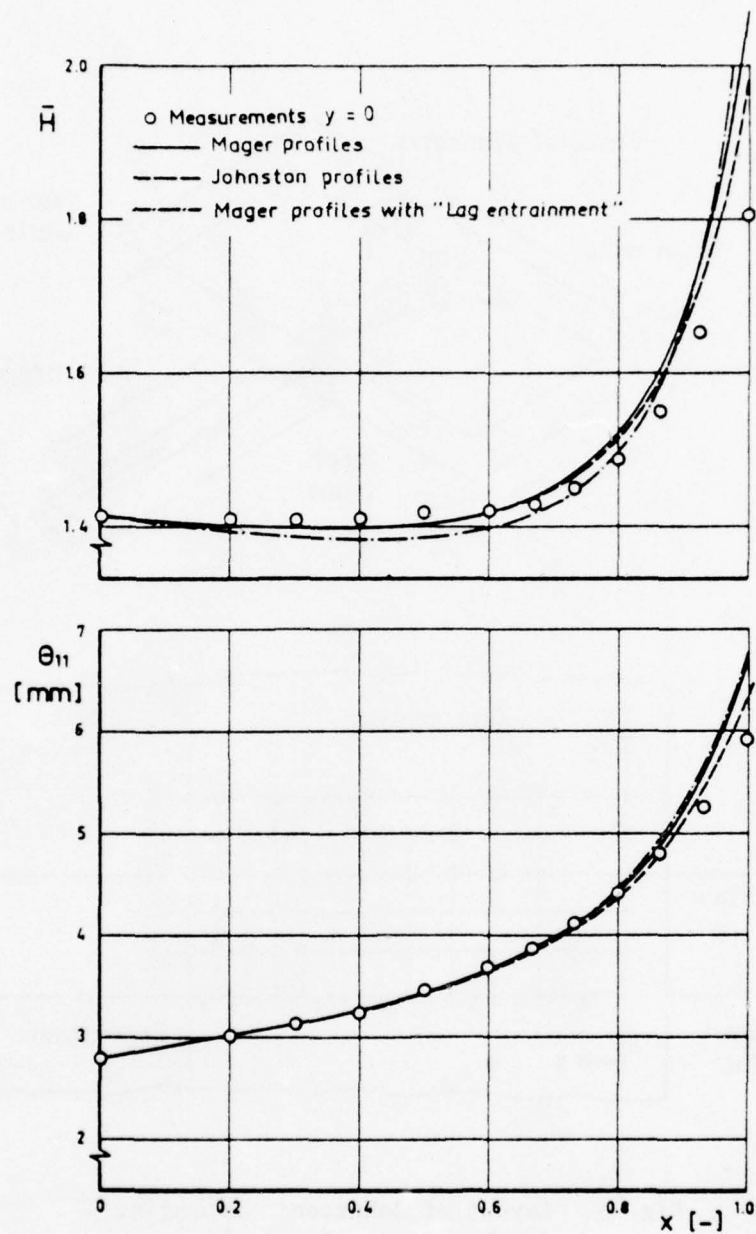Jet Experiment (in Inch).

71

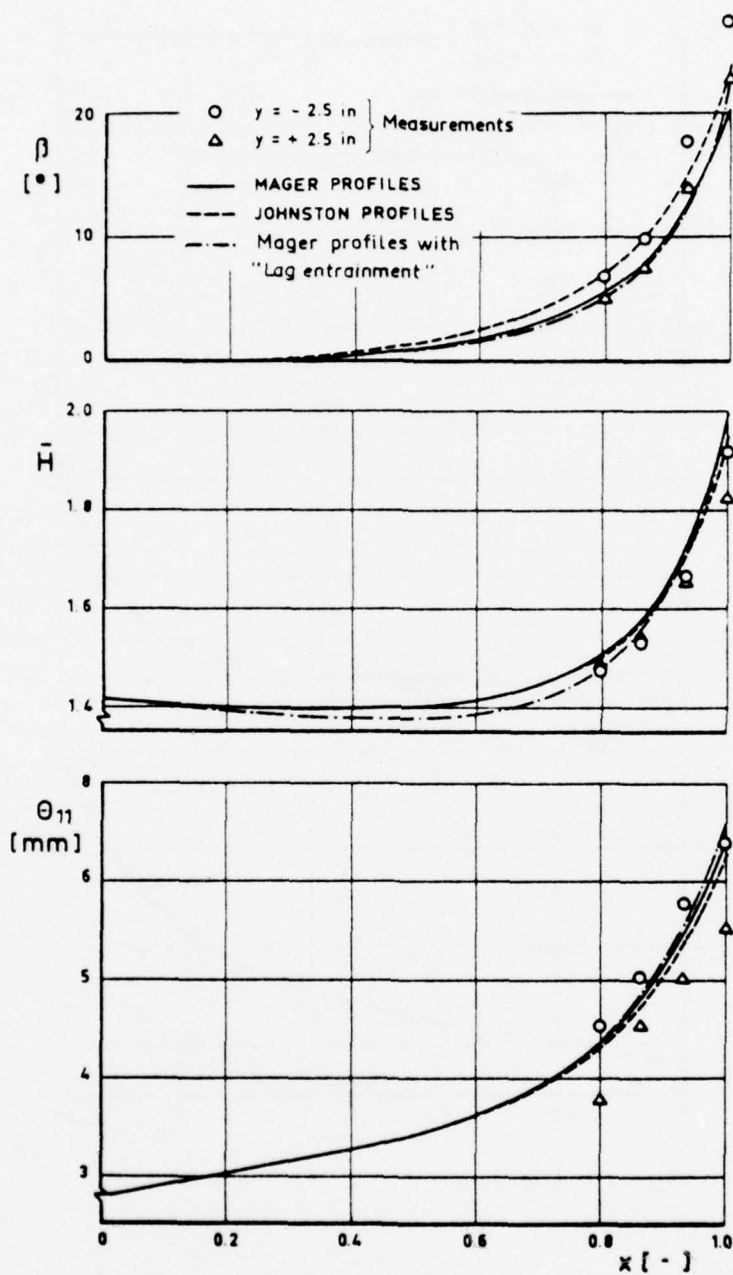Fig. 4. Comparison of Johnston's Measurements
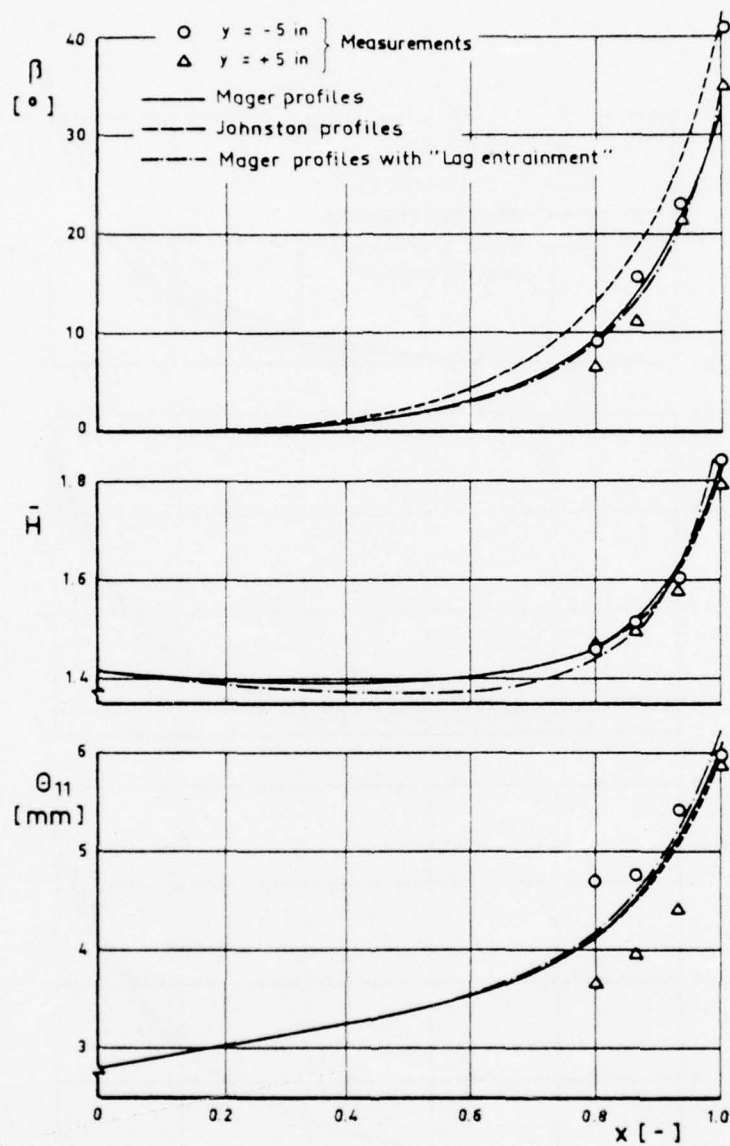With the Calculated Results.
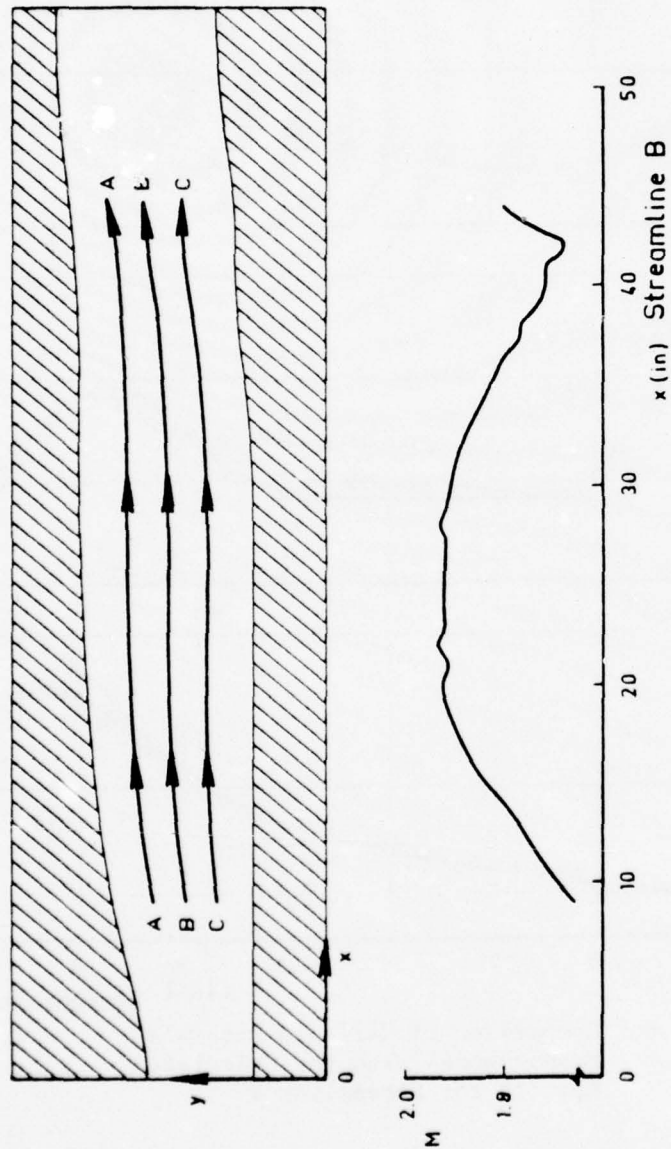
Fig. 4. Continued.

73

Fig. 4. Continued.

Fig. 5. The Contour of the Supersonic Nozzle, the Streamlines of the External Flow and the Mach Number Distribution Along Streamline B of Hall and Dicken's Experiment.

75

β
[°]

○ Measurements
—— Mager profiles
——— Johnston profiles
—·—· Mager profiles with "Lag entrainment"

2.0
1.5
1.0
5
0
- 5
-1.0

H̄

1.5

1.4

1.3

Θ₁₁
[mm]

2

1

0

10   15   20   25   30   35   40   45
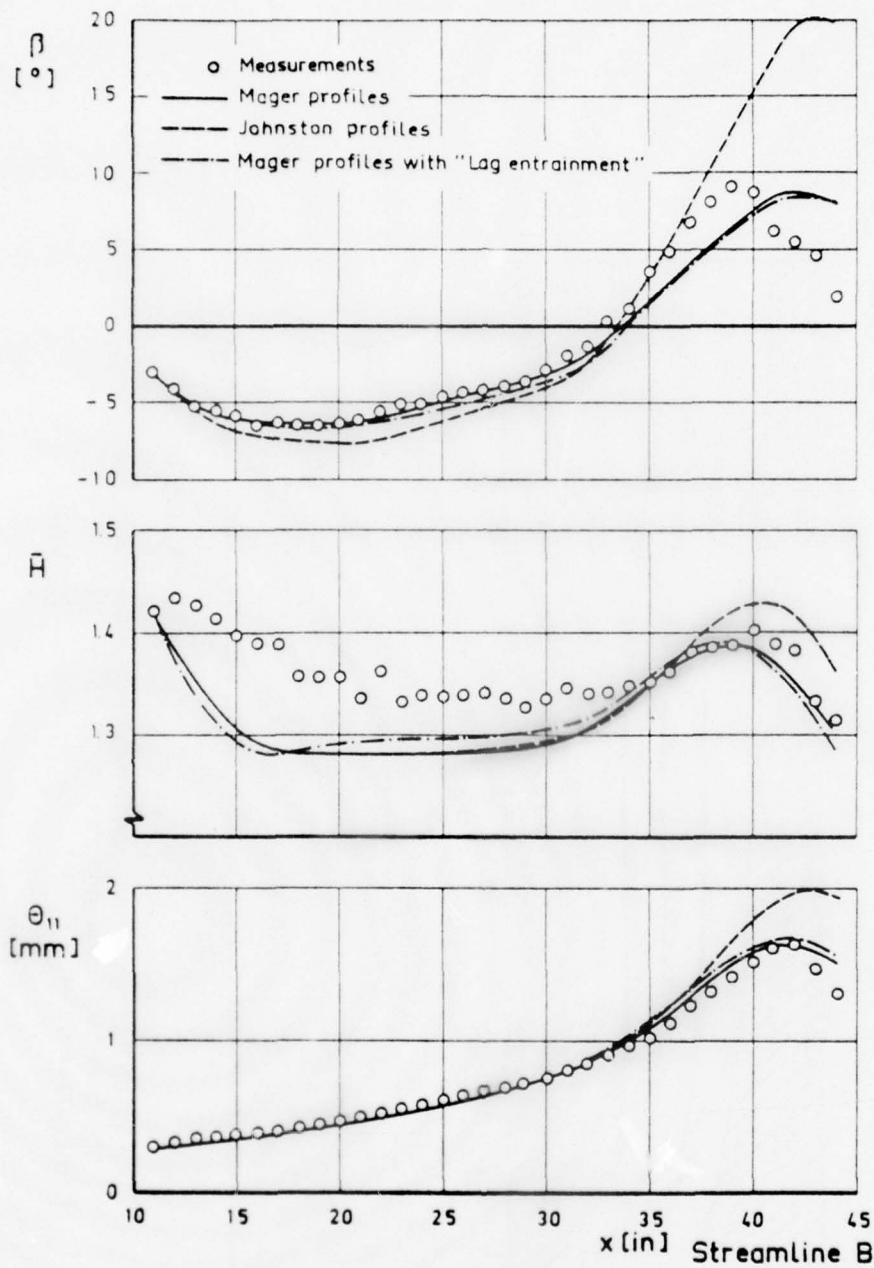x [in]   Streamline B

Fig. 6.   Comparison of Hall and Dicken's
Measurements With the Calculated
Results for Streamline B.
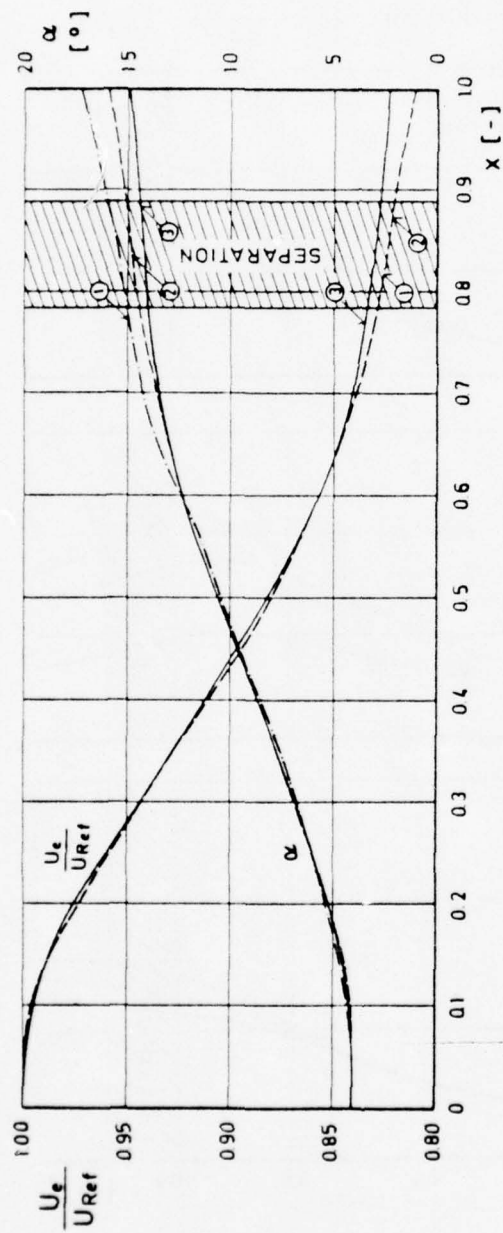
Fig. 7.   Potential Flow Data of Berg and Elsenaar's
           Experiment.

           (1) Measured U_e and α
           (2) Measured U_e and Infinite Swept Wing Conditions
           (3) Measured Wall Pressure and Infinite Swept Wing Conditions
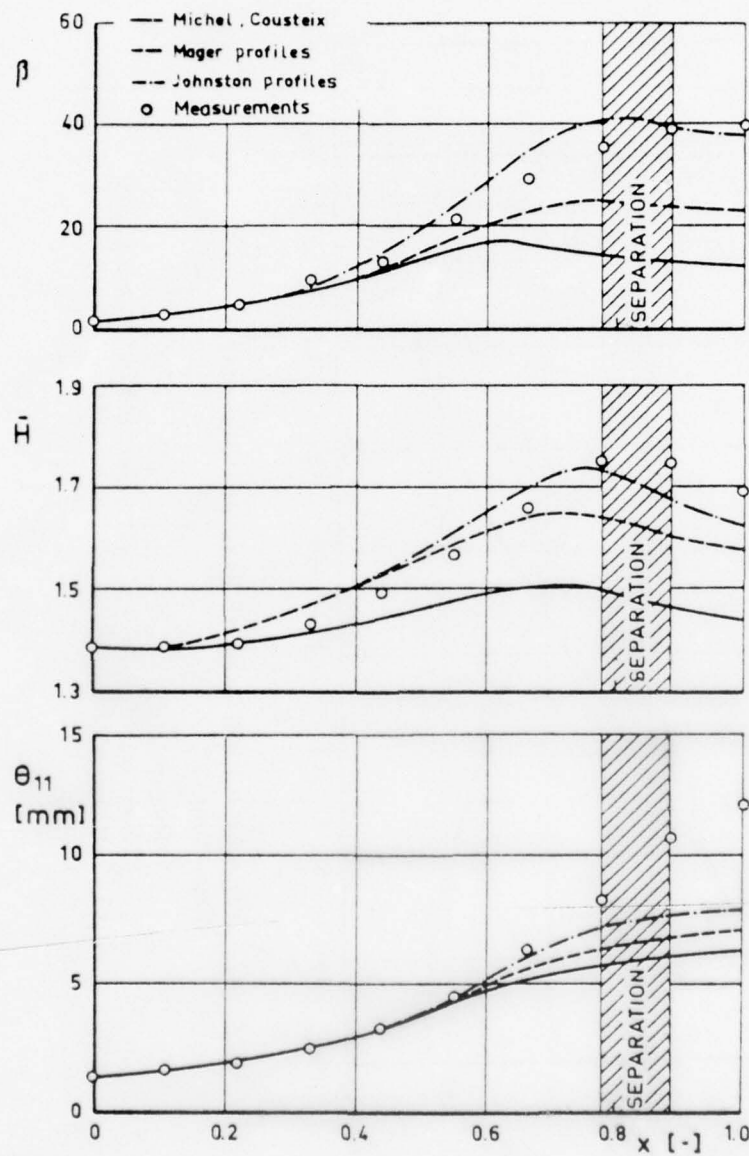
Fig. 8. Comparison of Berg and Elsenaar's
Measurements With Different Calculation
Methods Using Wall Pressure Data.
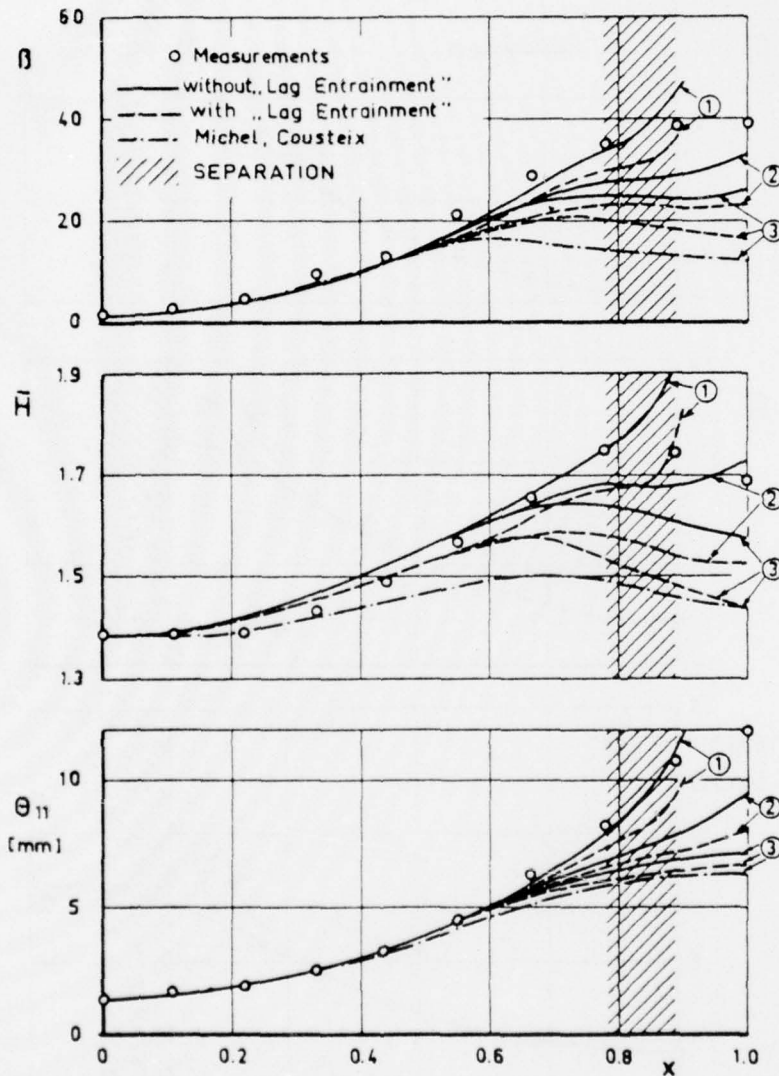
Fig. 9. Results for the Different Potential
Flow Data Using Mager Profiles and
Different Calculation Methods (Berg
and Elsenaar).

79
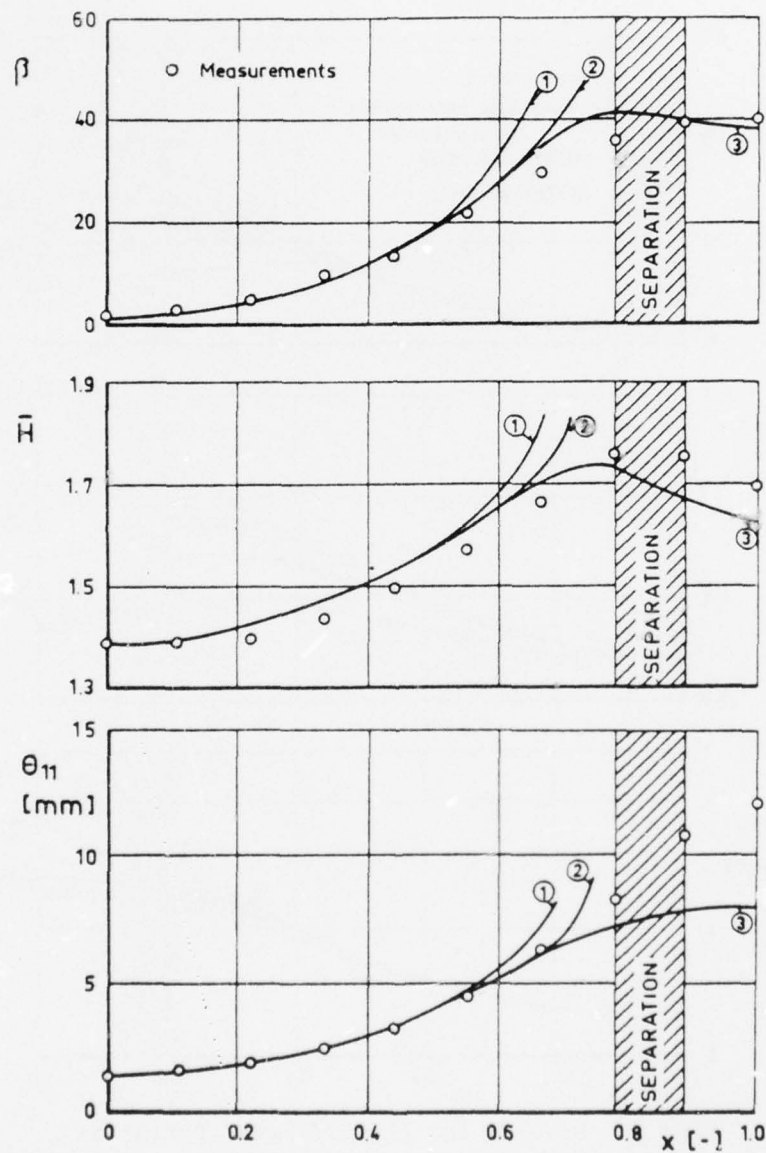
Fig. 10. Results for the Different Potential
Flow Data Using Johnston Profiles
(Berg and Elsenaar).
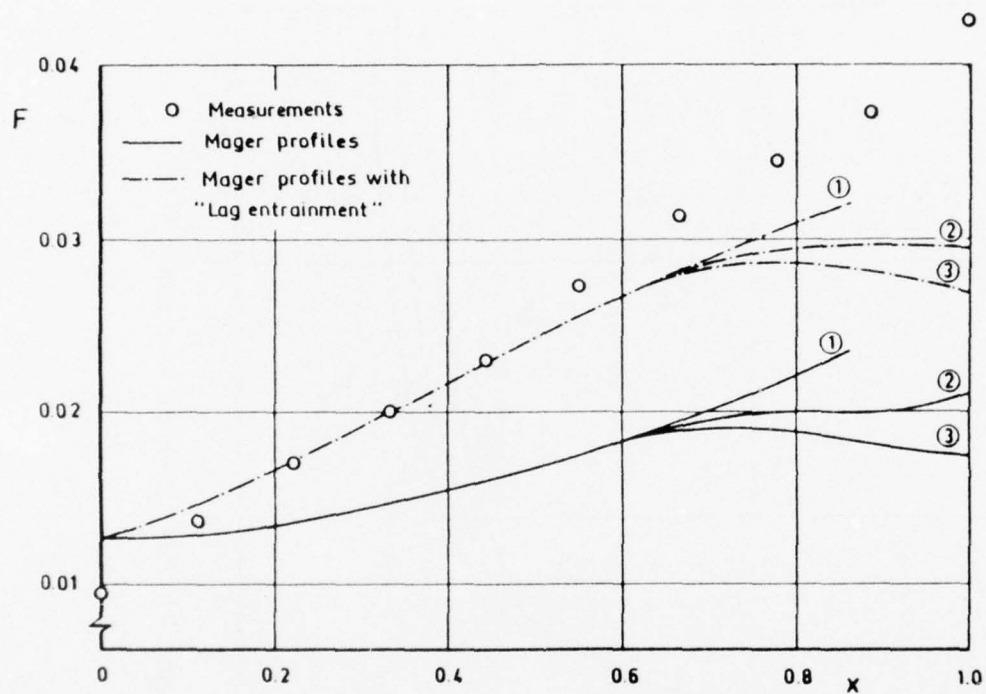
Fig. 11. Entrainment Coefficient F for the Different Potential Flow Data (Berg and Elsenaar).

81
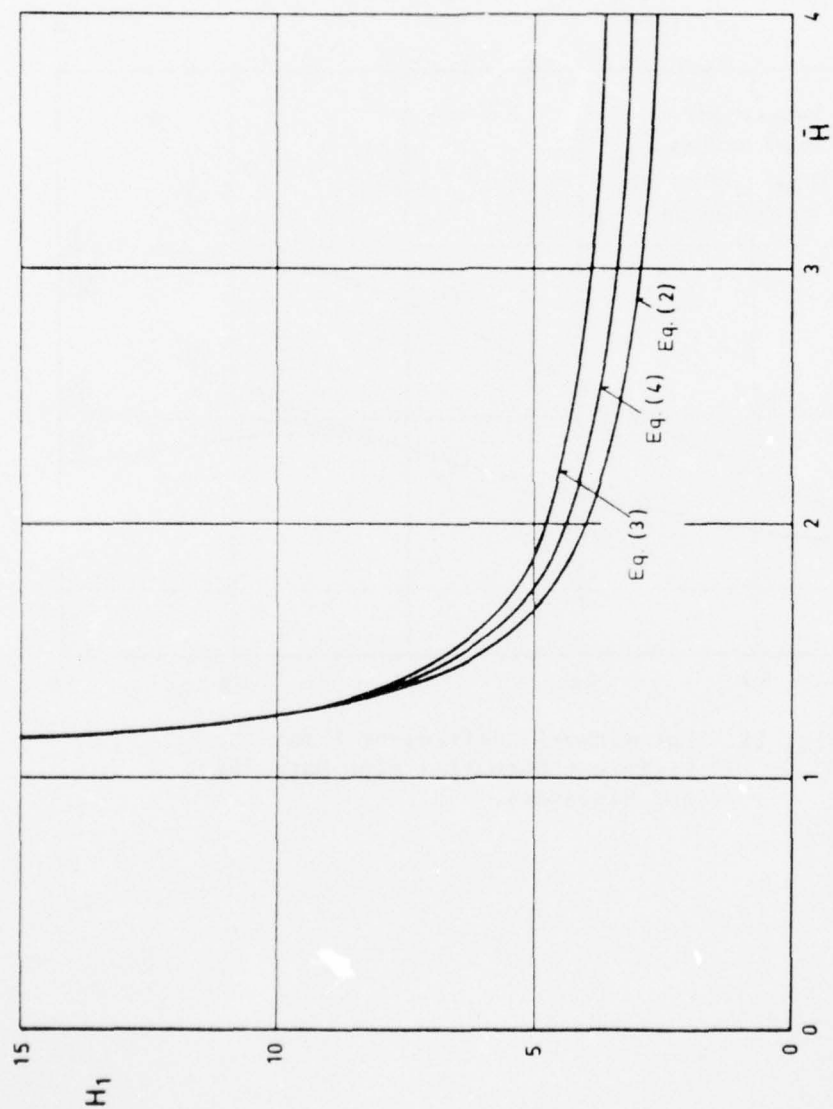
Fig. 12. Empirical Correlations for the Form Parameters $H_1 - \bar{H}$
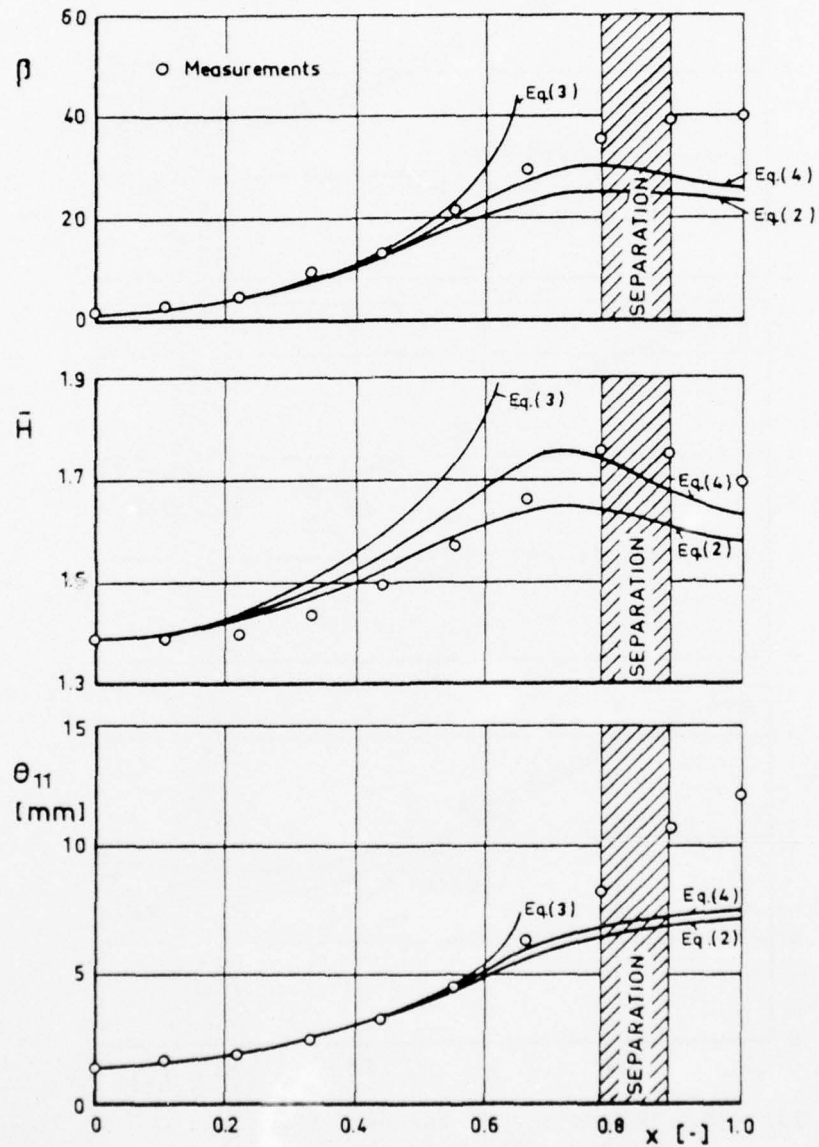
Fig. 13. Results for the Different H_1-$\bar{H}$ Correlations Using Mager Profiles and Wall Pressure Data (Berg and Elsenaar).

83
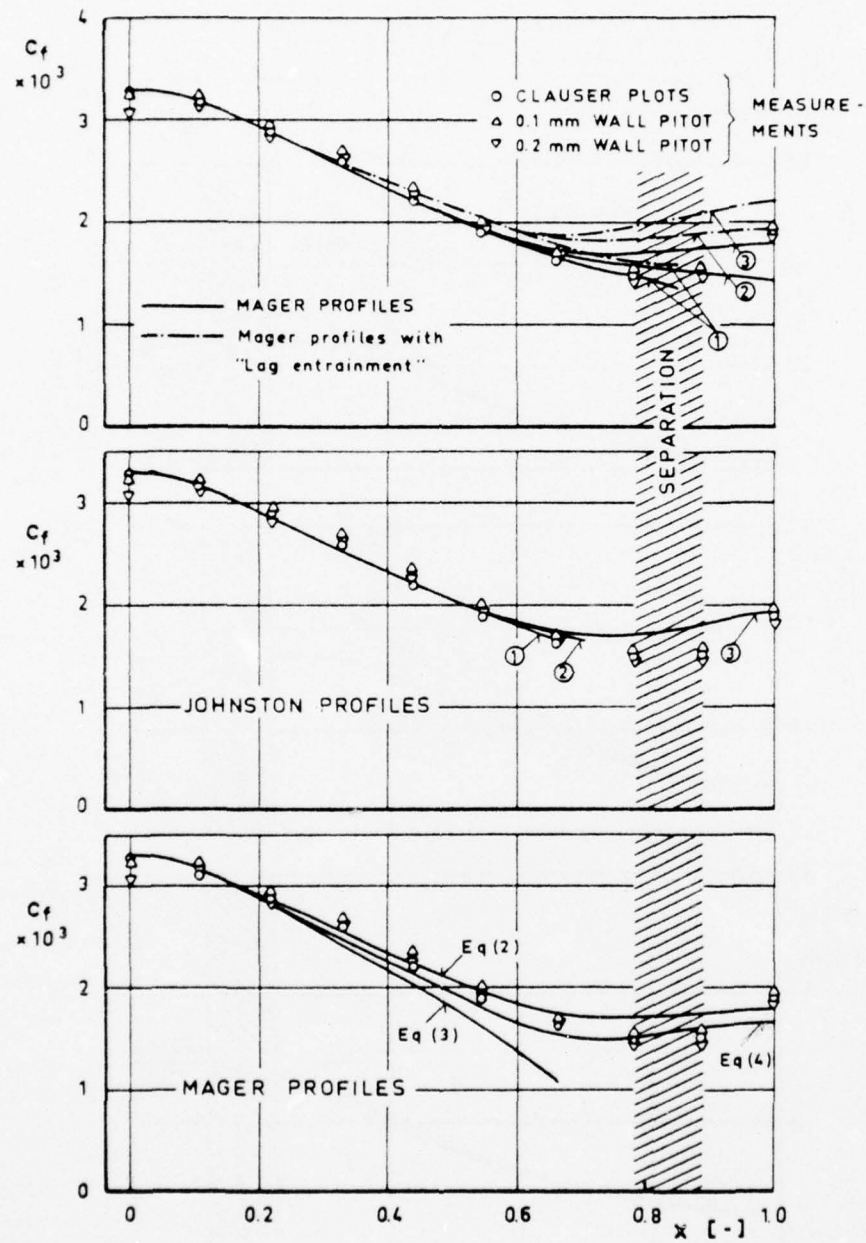
Fig. 14. Comparison of the Skin Friction
Measurements with the Calculated
Results.
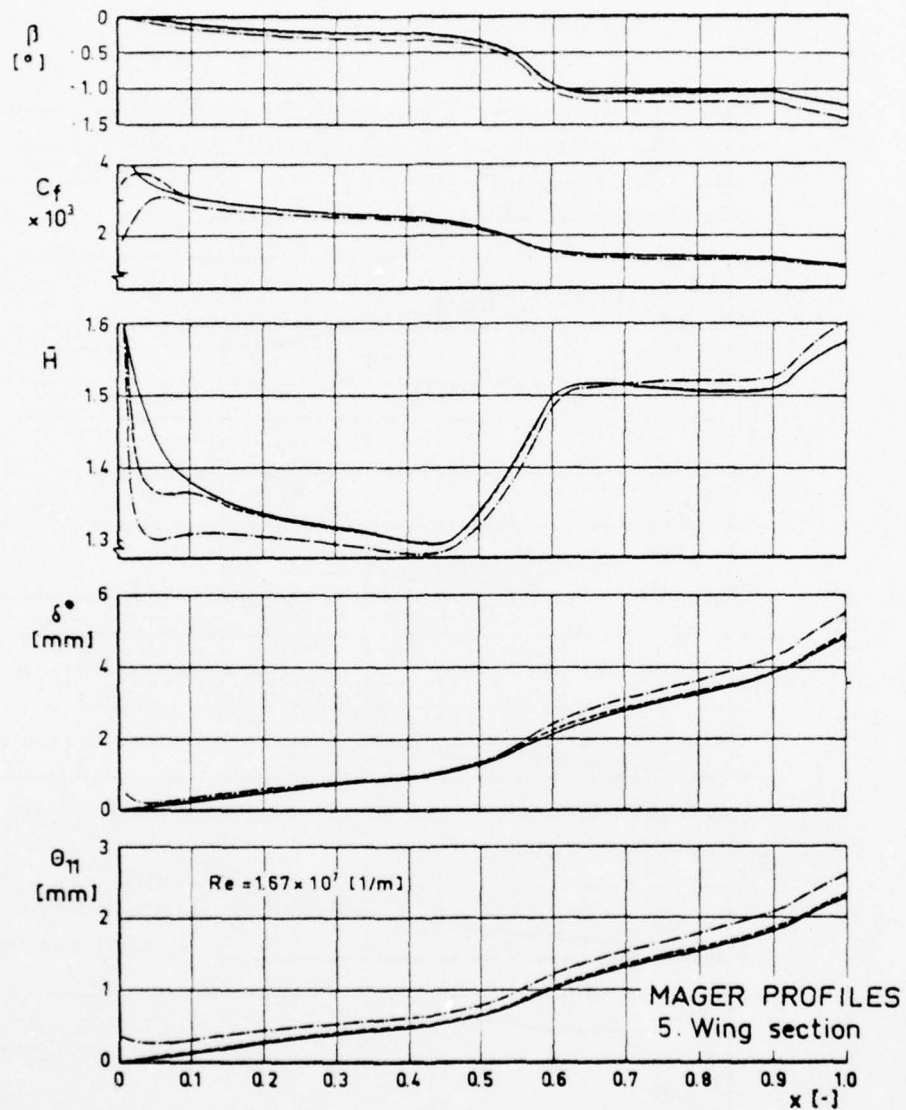
Fig. 15. Influence of the Initial Conditions
on the Boundary Layer Development on
the Upper Surface of a Finite Rectangular
Wing (NACA 63 A 006) for an Angle of
Attack of 2° and $M = 0.9$.

85
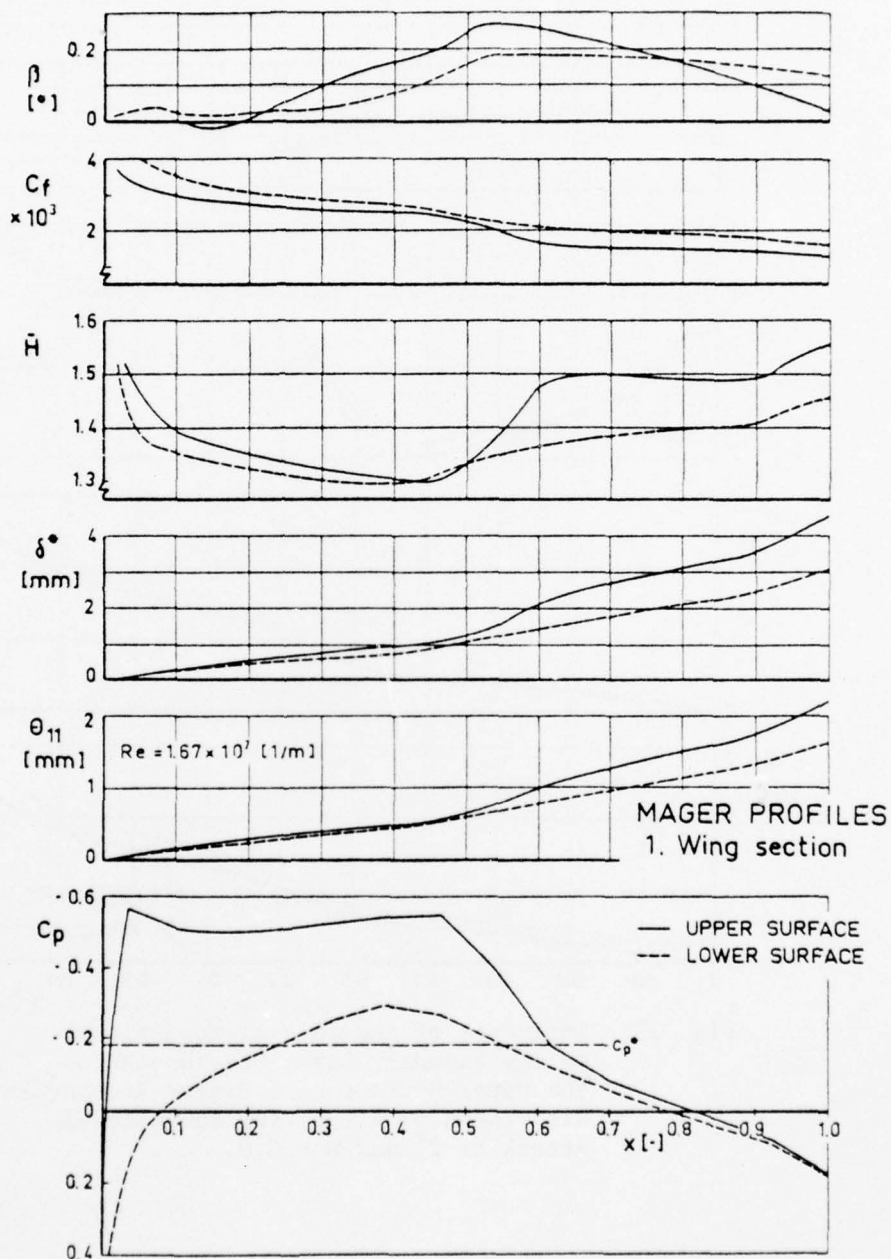
Fig. 16. Boundary Layer Development on a Finite
Rectangular Wing (NACA 63 A 006) for an
Angle of Attack of 2° and M = 0.9.
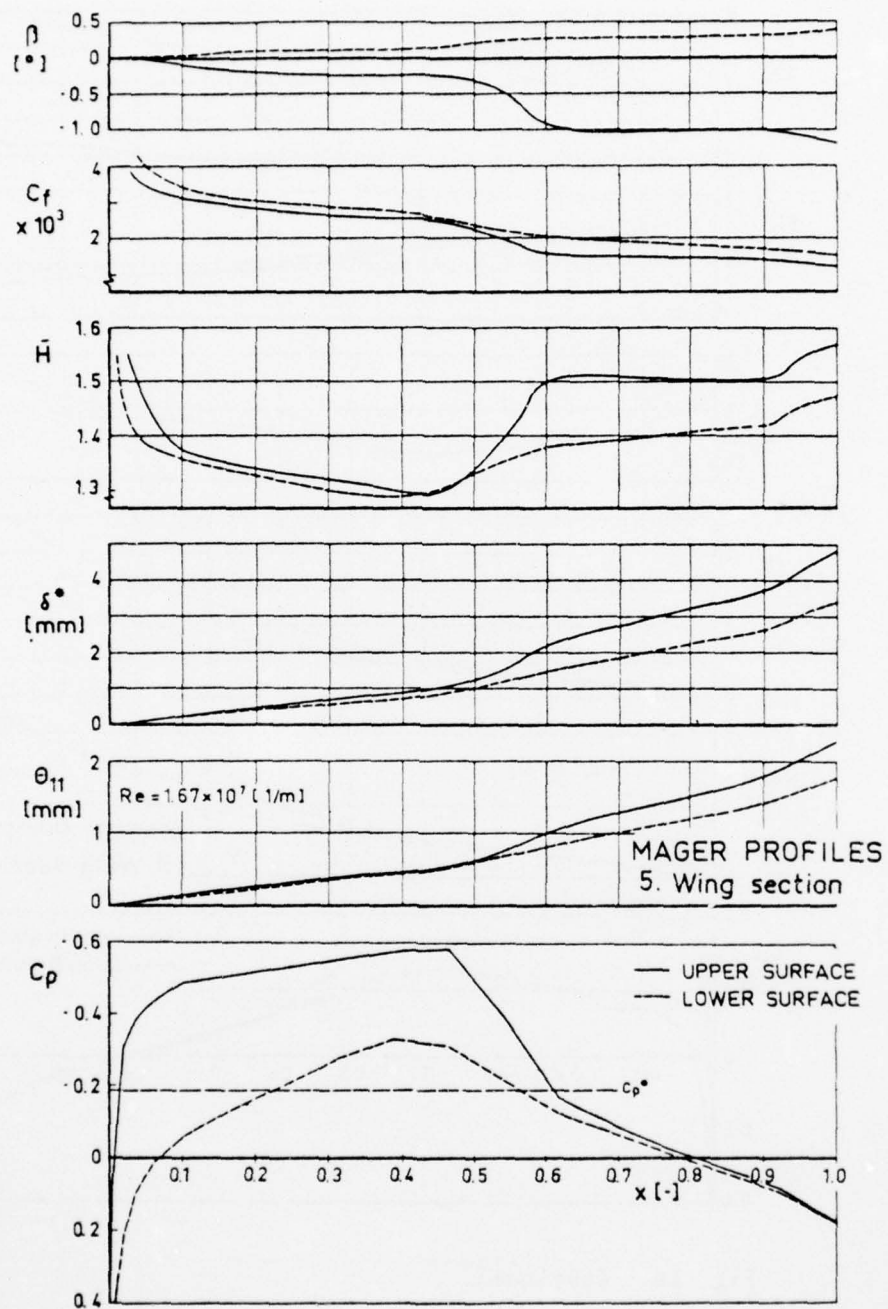
Fig. 16. Continued.
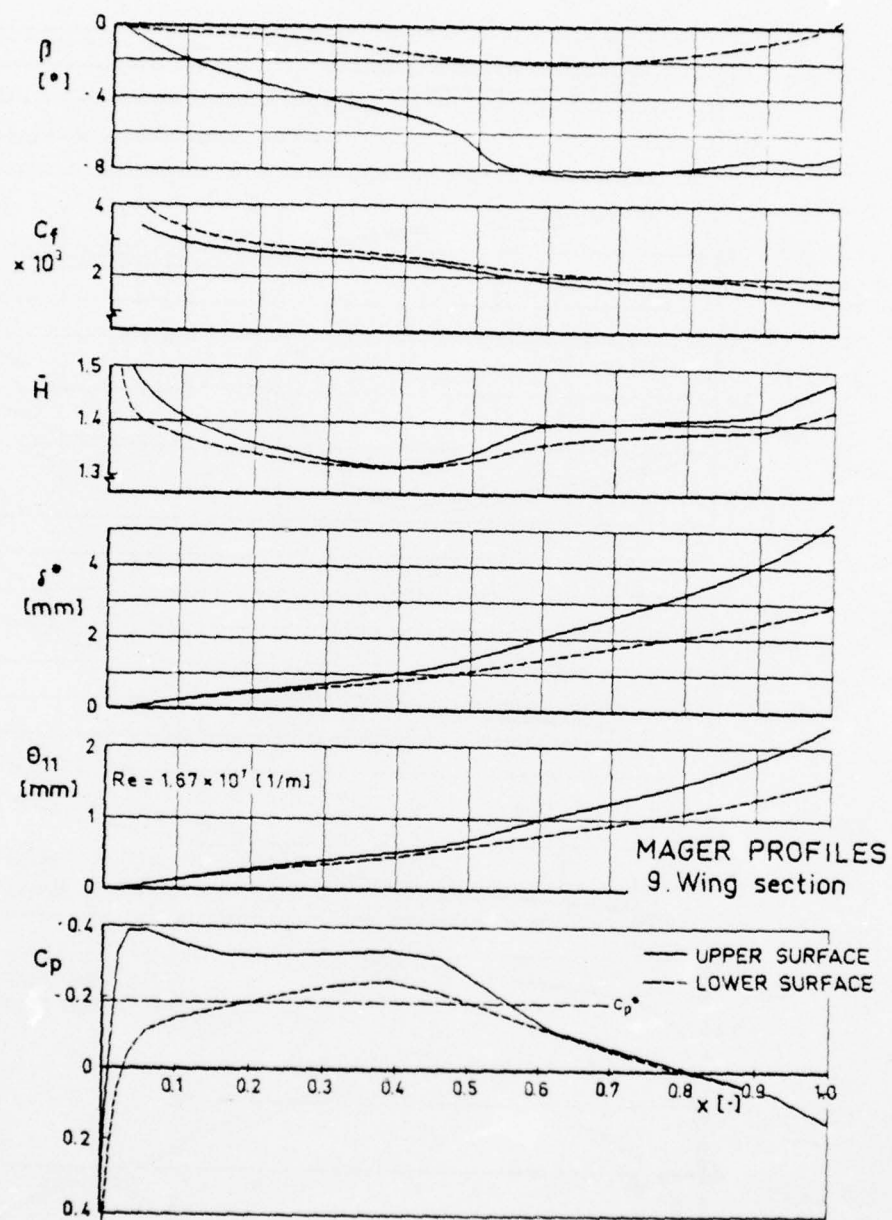
Fig. 16. Continued.
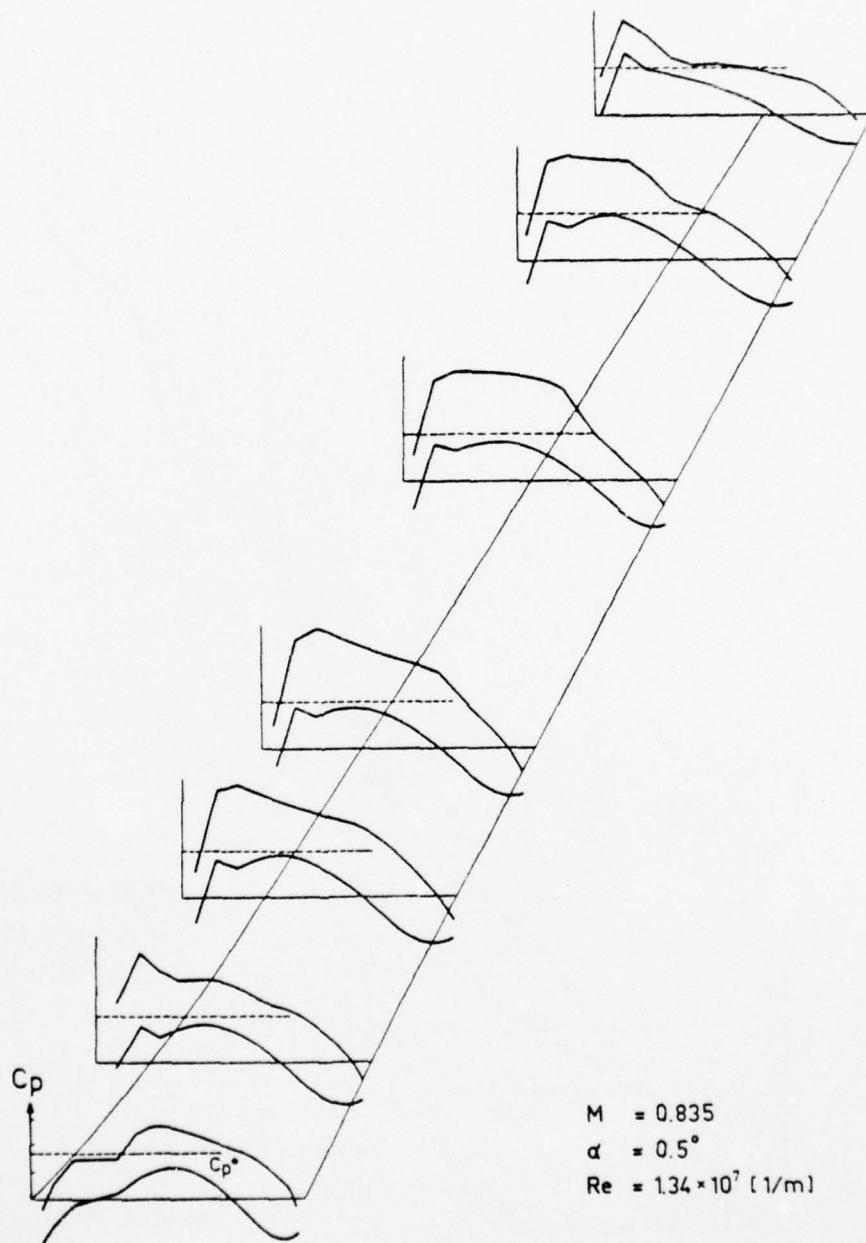
Fig. 17. Pressure Distribution on the
Supercritical Wing (SKF, Alpha Jet).

$M = 0.835$
$\alpha = 0.5°$
$Re = 1.34 \times 10^7 \; [1/m]$

MAGER PROFILES
——— UPPER SIDE
----- LOWER SIDE

$M = 0.835$
$\alpha = 0.5°$
$Re = 1.34 \times 10^7 \ [1/m]$
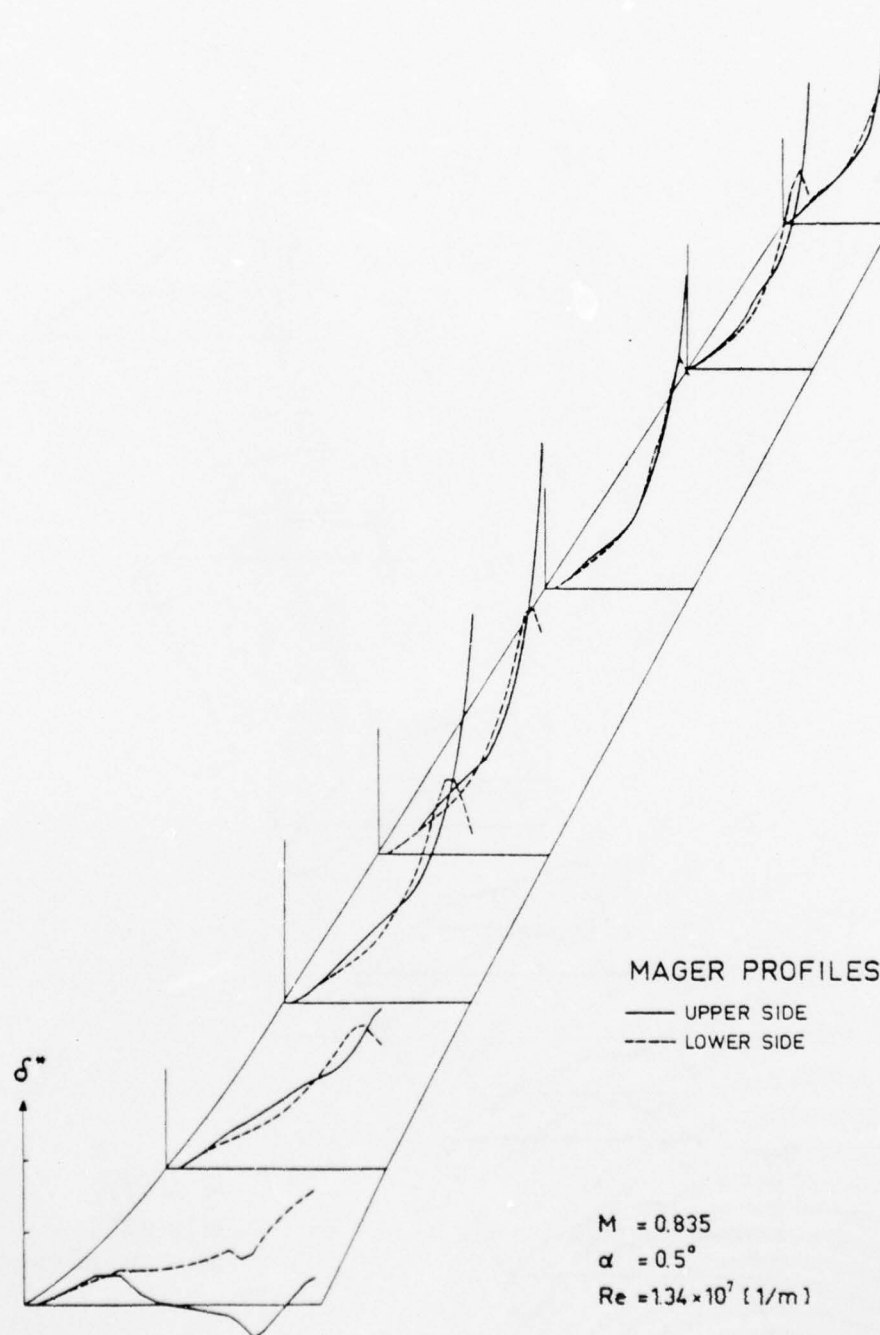
Fig. 18. Displacement Thckness Distribution
On the Supercritical Wing (SKF, Alpha Jet).
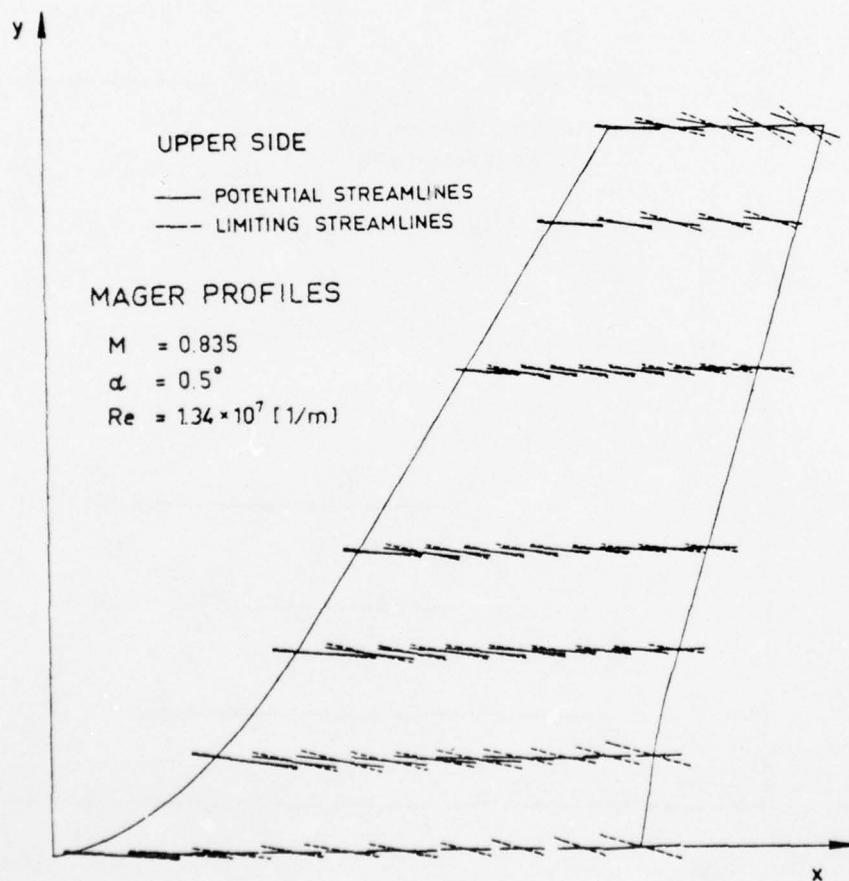
Fig. 19. Potential and Limiting Steamline
Inclination on the Supercritical
Wing (SKF, Alpha Jet).

LOWER SIDE

POTENTIAL STREAMLINES
LIMITING STREAMLINES.

MAGER PROFILES

$M = 0.835$
$\alpha = 0.5°$
$Re = 1.34 \times 10^7 \, [1/m]$
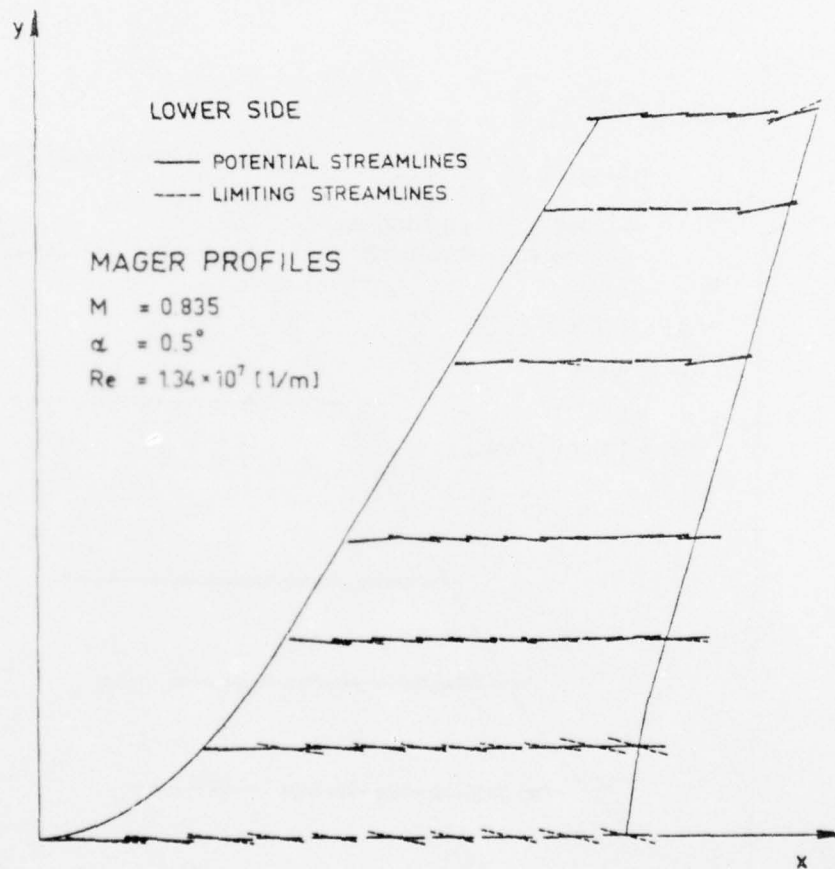
Fig. 19. Continued.

FLOW FIELD MEASUREMENTS IN AN ASYMMETRIC AXIAL CORNER AT M = 12.5

James R. Cooper[*] and Wilbur L. Hankey, Jr.[**]
Air Force Flight Dynamics Laboratory
Wright-Patterson AFB, Ohio

Abstract

A detailed study of shockwave boundary layer interaction and interference heating of an axial corner typical of vehicle junctions has been made. Extensive impact pressure profiles were obtained in addition to static pressure information and oil flow studies. Measurements revealed two large vorticies within the boundary layer responsible for high local heating. A complex inviscid shock pattern dominated by a triple point structure was also determined. A theoretical reconstruction of the flow was accomplished using conical flow relationships to calculate the conically symmetric inviscid supersonic flow.

Nomenclature

M	Mach number
p	Static pressure
P_1	Impact pressure
r, θ, ϕ	Spherical coordinate system
R	Flow reattachment location
S	Flow separation location
u, v, w	Velocity components parallel to x, y, and z axis

[*]First Lieutenant, USAF, Hypersonic Research Laboratory

[**]Senior Scientist, Hypersonic Research Laboratory, Member AIAA
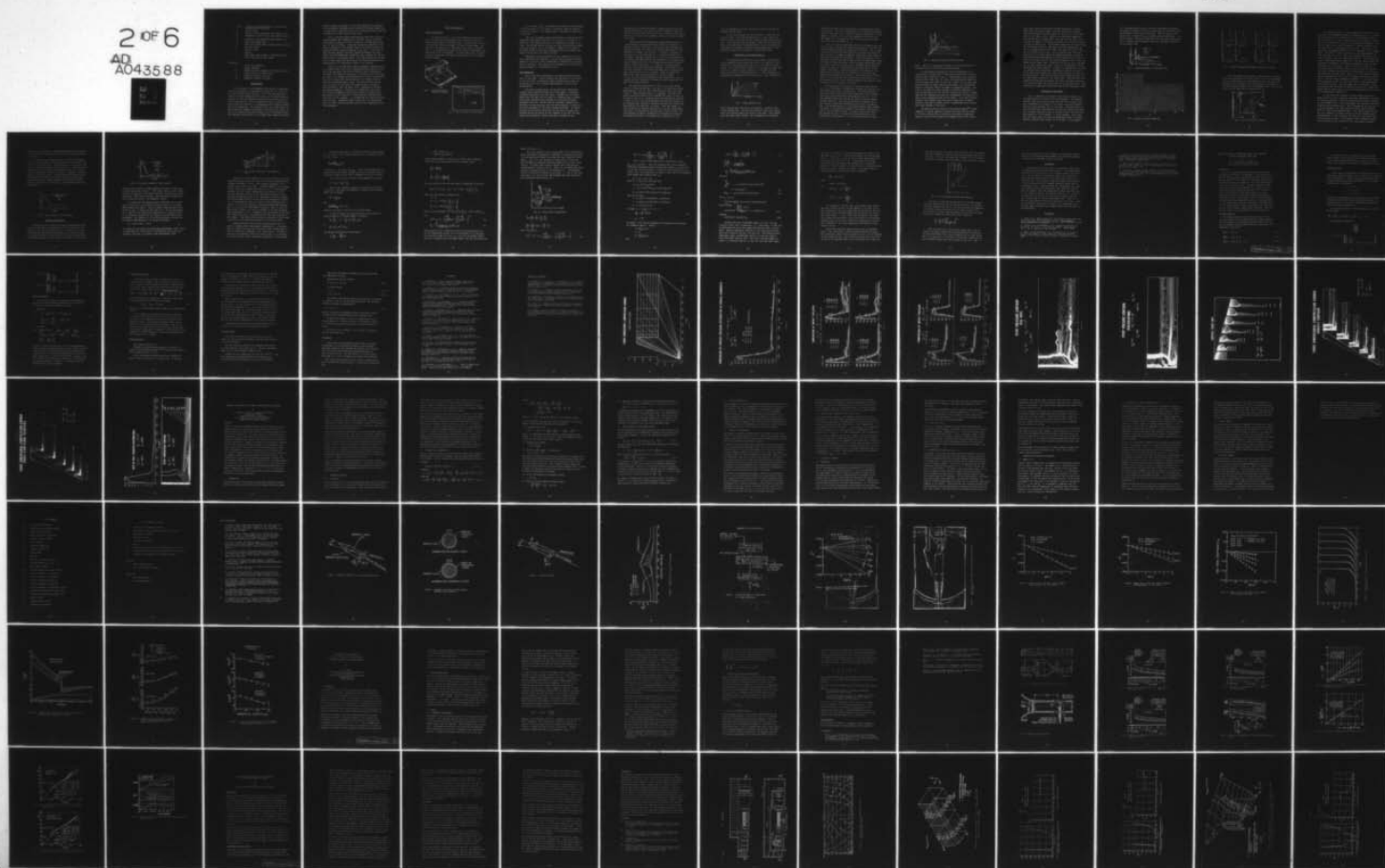
x,y,z	Cartesian coordinates where x is in the free stream velocity direction
V	Flow velocity
Y	Conical y value normalized with respect to x
Y_d	Normalized y value of plate bow shock location
Z	Conical z value normalized with respect to x
α	Body flow turning angle
δ	Body flow turning angle including viscous effects
θ	Bow shock angle
ξ	Pressure ratio
ρ	Density
σ	Shock angle with respect to spherical surface
ω	Cross flow angle on unit sphere

Subscripts

c	Cross flow component
n	Normal component
r	Radial direction component in spherical system
T	Values related to triple point
θ	Component parallel to θ axis
ϕ	Component parallel to ϕ axis

Introduction

In the design of an aerodynamic body subject to hypersonic flow it is important to understand the nature of the flow field that will develop around the body. One of the most important reasons for understanding the flow is due to its high heating potential, not only in stagnation regions, but near flow interference regions as well. Often in hypersonic flow bow shocks generated by various portions of a configuration will trigger boundary layer flow separation. The separated flow, after negotiating the adverse pressure gradient presented by the shock, will attach itself to the surface and cause heating rates at reattachment which can sometimes exceed those at the leading edge stagnation regions.

94

Without adequate knowledge of this three-dimensional separation and reattachment phenomena and its associated heating capability, a design may not properly account for the higher heating rates and subsequent structural failure could occur.

One of the more common configurations that cause shock induced boundary layer separation is the axial corner, typically occurring on a vehicle at such locations as the wing-body, body-tail or inlet junctions. Strong bow shocks are generated by the surface impinges on the boundary layer of the second surface imposing an adverse pressure gradient on the flow. As a result of this pressure gradient, multiple separation bubbles can occur which, in three-dimensional separation, will scavenge off the low energy flow of the boundary layer. The reattaching flow then consists of high energy air which causes the elevated heating rates experienced in the reattachment region of the surface.

Because of the bow shock induced separation characteristics of an axial corner, the corner configuration was selected to generate the hypersonic flow field studied in this investigation. To enhance the separation features of the axial corner the boundary layer to be separated was developed on a surface aligned with the flow to insure that the bow shock of the surface would be weak and the boundary layer large. The second surface was inclined so that the flow would be compressed and a strong bow shock generated. Thus the axial corner configuration selected was highly asymmetric, consisting of a wedge and a flat plate. Data from the asymmetric axial corner, which is presented here, was acquired for the purpose of satisfying the following basic objectives of this program: (1) determining the flow field structure in a highly asymmetric axial corner, and (2) associating areas of local elevated heating rates with the accompanying flow field phenomena.

Model and Apparatus

Model and Facility

As indicated in Fig. 1 the shock interference corner flow
model used for this study consists of a flat plate with a 15°
wedge located along its right-hand side. The flat plate is 16 in.
long and 8 in. wide with a sharp, 20° bevel, leading edge. The
surface of the plate aft of the leading edge strip, as shown in
Fig. 2, is a removable instrumented steel insert containing static
pressure ports in 43 locations. A recessed base plate, to which
the insert is secured, provides an access path for the necessary
pressure tubing.
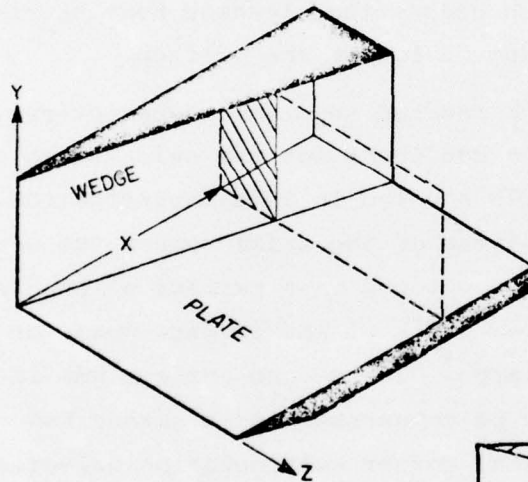
Fig. 1 Corner Flow Model &
Coordinate System

2 INCHES
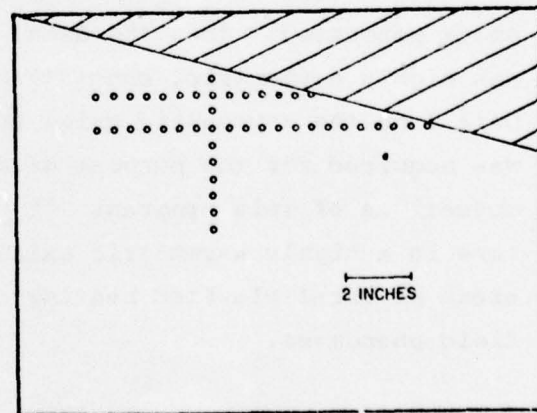
Fig. 2 Plate Pressure Instrumentation

A 6 in. high, 16 in. long wedge shock generator is positioned on the flat plate at a 15° angle of incidence using two brackets to hold it in place. The leading edge of the wedge is sharp with a 20° bevel.

The plate and wedge assembly were mounted in the ARL 20-inch Hypersonic Wind Tunnel facility with the plate at 0° angle of attack and the wedge presenting a 15° compression surface to the flow. The 20-inch HWT has an open flow test section with a usable flow core of about 10 in. in diameter. Support of the model is provided through a sting mount arrangement which can retract the model from the flow for tunnel starting.

Throughout the investigation the flow conditions in the 20-inch tunnel were held constant. All data were gathered at a Mach number of 12.5 with a total temperature of 1800^OR and a total pressure of 1200 psia. The flow was fully laminar with a free stream Reynolds number of 0.93 million per foot.

Instrumentation

Data on the flow conditions in the axial corner were gathered in three ways. Static pressure was recorded at 43 locations on the flat plate, an extensive impact pressure survey was conducted and an oil flow technique was employed to aid in flow visualization.

The static pressure ports on the plate were connected by pressure lines, passing through the sting support, to pressure transducers mounted in the test cabin. Signals from the transducers were fed from the test cabin to an Ambilog data recording system where pressures were recorded at one second intervals throughout each run. Because only 25 transducer channels were available for any given run, two runs were required to record all 43 static pressures for the given running conditions. To insure uniform flow conditions two ports from the first run were also recorded during the second run and compared to see that the same values were indicated. Before each day of running all the

97

transducers were calibrated against a known pressure source and again checked against the source after the running was complete. The two-run series was rerun several times to check on the repeatability of the tunnel flow conditions as well as the data acquisition system.

Impact pressure information was acquired through the use of a tunnel mounted, computer controlled probe system capable of movement along all three axes. An extensive survey program was conducted in which the corner flow structure was probed in three different y-z planes. For a given x location, a constant y value was fed to the probe and the z value was stepped in 0.1 increments. The probe traveled 12 in. in the -z direction until it contacted the wedge surface then returned to its original location to complete each run. The average time per run was about 90 seconds. After each run the y location of the probe was increased 0.1 in. and the procedure repeated. In this way the entire flow structure of the corner was mapped with a matrix of impact pressures with a 0.1 in. spacing. Three y-z planes were mapped, but only the data attained at the last station, x = 12.5 in., were used extensively in this study due to the increased relative fineness of the matrix at that station with respect to the flow structure.

The probe was constructed of .093 in. I.D. steel tubing filed to a sharp leading edge. The face of the probe was aligned approximately 7° off the free stream direction toward the wedge surface to keep alignment errors to a minimum. Lag time in the probe system was accounted for by allowing the probe to "rest" at the end of each 0.1 in. movement before the pressure was recorded. A check to see if this was an adequate precaution was carried out by comparing data recorded as the probe went into the corner with data taken as the probe left the corner. With this method, if the lag time is not properly accounted for, pressure discontinuities tend to be displaced in the direction of probe travel. Lag time problems are easily determined by overlaying data recorded in opposite directions. No problems were encountered in this

test and subsequent data were recorded in only one direction to minimize running times.

To aid in visualizing the flow structure, several oil flow runs were made. After some experimentation, it was found that discrete oil dots provided the most clearly defined surface structure. Flow separation and reattachment lines could be identified from the flow pattern by observing whether the oil flow lines were converging or diverging. Convergence was interpreted as a flow separation region and divergence as a reattachment line.

Discussion of the Inviscid Model

To accomplish the objectives of this study, reconstruction of the asymmetric axial corner flow field, it is useful to first consider the entirely inviscid case for the 15° wedge-flat plate corner. For reconstruction purposes it is possible to assume that the flow is conical in nature, which is to say that the flow structure grows in a linear manner with x . This assumption was qualitatively confirmed in the oil flow tests. Fig. 3 depicts the
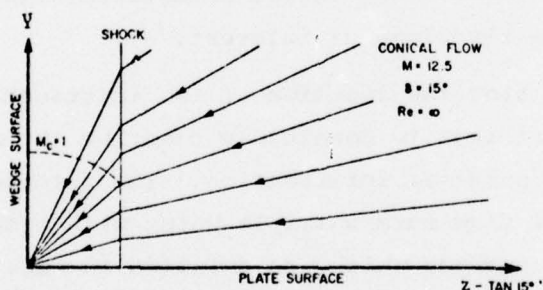

Fig. 3   Ideal Inviscid Flow

ideal inviscid flow structure in an arbitrary -z plane of the corner configuration. In the free stream the "cross flow streamlines" are directed toward the x-axis of the model. Upon encountering the wedge shock, however, the "streamlines" are adjusted

such that the flow is in the direction of the wedge-plate inter-
section line. This line, toward which all the "cross flow stream-
lines" finally converge, is termed a vortical singularity. In the
immediate vicinity of the vortical singularity the cross flow
Mach number, M_c, is subsonic so that there exists in the flow a
cross flow sonic line where $M_c = 1$.

Now, if a viscous displacement effect is allowed on the flat
plate so that it appears as a compression surface to the flow, the
resulting inviscid structure becomes more realistic. Fig. 4 illus-
trates the new inviscid model which now represents the inviscid
flow structure of a highly asymmetric double wedge axial corner in
which two bow shocks are now present. The plate develops a con-
siderable boundary layer and a weak shock is introduced which shall
be termed the plate bow shock. Given a nominal compression thick-
ness seen by the free stream flow for the wedge and the plate, a
location as well as a strength can be associated with each bow
shock in this model. Using the location of the shocks, it is a
simple matter to find a set of coordinates in the cross flow
plane which represent the location of the intersection of the bow
shocks. For convenience the coordinates are represented as Z_T
and Y_T which are the z and y values normalized with respect to the
x location of the z-y plane of interest.

In conical flow the location of two intersecting shocks,
(Z_T, Y_T), is sufficient to completely describe the resulting flow
field around the point of intersection. The intersecting bow
shocks in conical flow form a triple point with a third embedded
shock and a slip surface which are detailed in Fig. 4. Is is
this embedded shock which sets up the adverse pressure gradient
causing separation. Flow passing through the wedge bow shock
will acquire a new value of pressure p_4 and cross flow angle ω_4.
Due to the characteristics of a slip surface which cannot support
a pressure or flow direction mismatch the values of pressure, p_4
and p_3, and flow angle, ω_4 and ω_3, must be identically equal.
An iteration process is required to simultaneously solve the
appropriate relationships for the flow values around the triple
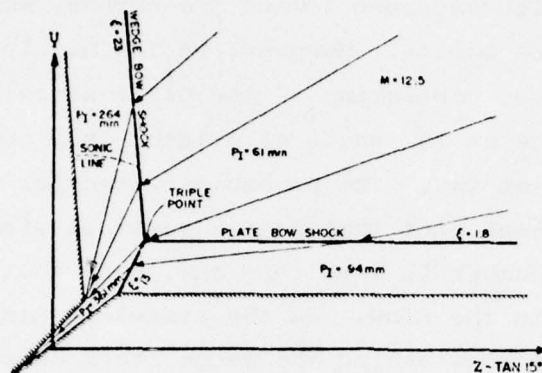
Fig. 4   Inviscid Flow With Viscous Effects

point. The set of equations necessary for this process will be
developed fully in the section on data analysis.

By simultaneously solving the shock relationships for a
triple point, a Gonar-like[1] solution was found which is repre-
sented by the structure of Fig. 4. Examination of the resultant
inviscid model shows that the "cross flow streamlines" again are
directed toward the x-axis in the free stream. As the cross flow
passes through the wedge and plate bow shocks, the "streamlines"
acquire a direction toward two separate singularity points. The
flow of the wedge bow shock realizes a vortical singularity in
the inviscid model, but the flow of the plate bow shock is turned
again by the embedded shock and the "streamlines" are turned to a
new vortical singularity deep in the corner. It is this inviscid
finger of high energy cross flow, with a high value of impact
pressure, that will be shown to have a significant effect in the
high local heating of the plate.

Information given in earlier corner flow studies[2,3] using
symmetric or nearly symmetric corners noted that the bow shocks
of the two surfaces did not intersect directly but formed two
separate triple points joined by a diagonal shock in the corner.

101

Each triple point generated an embedded shock which extended toward the body surface where it caused the flow to separate. Slip surfaces which extended toward the corner, were also generated at the triple points. However, in the highly asymmetric case modeled above, consisting of the plate at zero angle of attack and the wedge at 15° angle of attack, only one triple point is found instead of two. The probable reason for this arises from the previously noted fact that near a vortical singularity the cross flow Mach number is less than one, such that a sonic line ($M_c = 1$) exists in the flow. In the symmetric case the sonic line in the cross flow behind the wedge shock exists inboard of the shock intersection whereas the shock intersection occurs inboard of the sonic line for the highly asymmetric case. Since imbedded shocks cannot exist in subsonic cross flow, the conditions for a second triple point cannot be met in the asymmetric corner. The wedge bow shock, however, is capable of curving near the point of the bow shock interaction, negating the need for a second triple point and allowing the corner flow structure to exist with one triple point. Note that the sonic line, indicated in Fig. 4, is located well outboard of the triple point. From the above discussion the wedge bow shock below the sonic line can be expected to be curved to meet the triple point at the required slope. This conclusion is supported by data discussed in the following section.

Discussion of Test Data

Fig. 5 summarizes the salient flow features deduced from the experimental test data of this investigation. The primary inviscid flow field structure was obtained from the impact pressure information and coupled to the viscous structure obtained from the static pressure and oil flow data. Discontinuities in the flow field were identified by plotting any large discontinuities in impact pressure values in a field of more than 1500 readings taken at x = 12.5 inches. Of these readings, those taken near the triple point location are presented in Fig. 6 in their relative locations with respect to the corner. As an example,

102

for the wedge shock location a line was established separating
the impact pressures of the free stream value of 61 mm from those
reading about 250 mm behind the shock. Thus the location of a
shock with a strength of p_2/p_1 equaling 23 was established. In a
similar manner, the entire flow field structure was reconstructed.
Fig. 7 presents impact pressure profiles at several Z locations
in the corner flow.

Fig. 5 Salient Features of Flow Structure

Fig. 6 Impact Pressure Readings

103
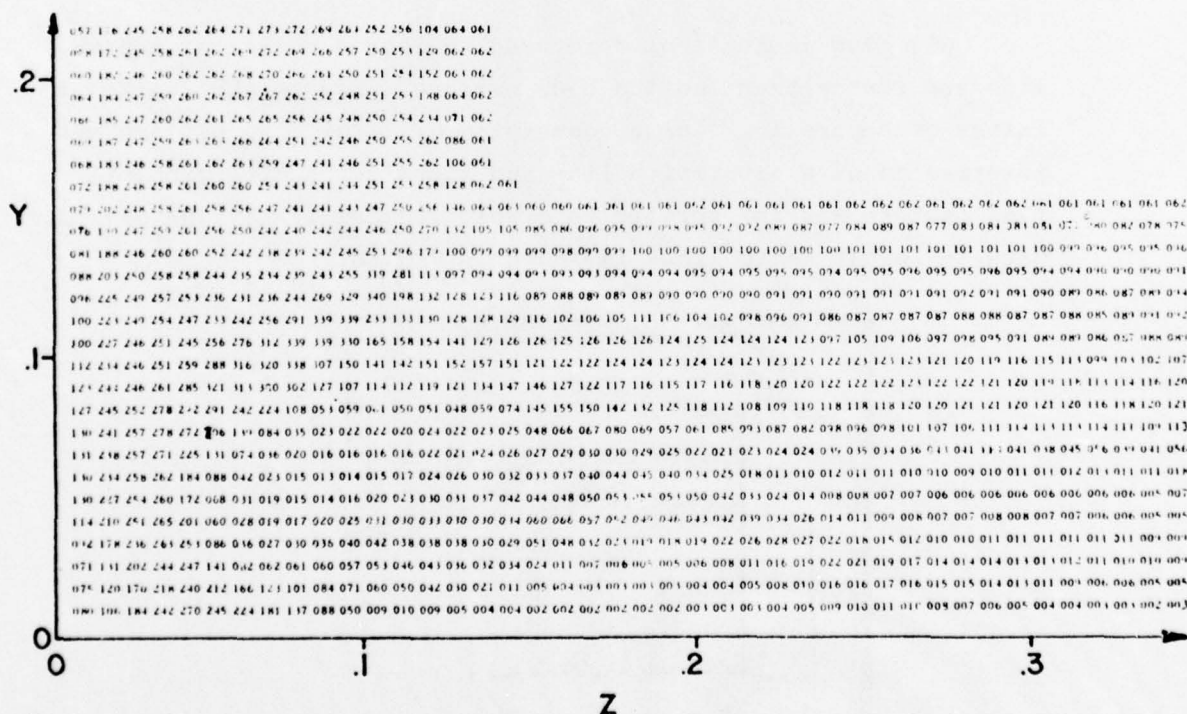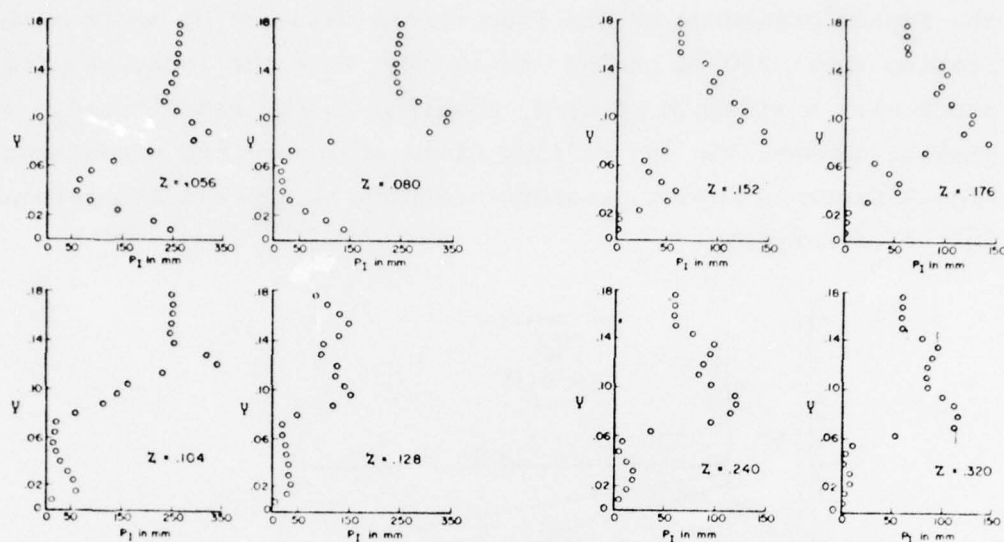
Fig. 7   Impact Pressure Profiles at Various Z Values

Oil flow indications were used to locate points of separation and reattachment on the body surface. Due to the characteristics of separating flow a converging oil flow line pattern was interpreted as a separation line and likewise, a diverging oil flow pattern was interpreted as a reattachment line. The oil flow used to locate these lines is shown in Fig. 8.

Fig. 8   Oil Flow on Plate Surface

The salient features of this asymmetric corner flow, as indicated by the experimental data and summarized in Fig. 5, include one triple point at the intersection of the wedge bow shock and the plate bow shock. This triple point is very similar to either one of the triple points shown in the Charwat and Redekopp[2] symmetric corner flow in that it generates a similar embedded shock and slip surface. The embedded shock of Fig. 5 provides an adverse pressure gradient which is felt far upstream in the boundary layer. The effect is first observed on a line approximately 45° from the x-axis or at $Z = 1$ where the boundary layer cross flow first separates. This line has been termed S_1. An important feature of three-dimensional separation is the fact that, unlike two-dimensional separation, the dividing streamline is not the same streamline that reattaches. Due to the open end feature of a three-dimensional separation bubble, flow entering the bubble is constantly scavenged away and must be replenished by a portion of the separation boundary layer. Hence, it is the uppermost higher energy streamline of this layer of scavenged flow that reattaches and not the low energy separating streamline. It is this feature which primarily accounts for the high value of three-dimensional interference heating. The more energy that is available in the reattaching flow the higher the heating rate will be. Within the bubble reverse flow occurs in the cross flow plane much as it does in two-dimensional separations.

As the cross flow continues it gains enough energy from upper layers of flow to reattach, but almost immediately is forced to separate again due to the continuing adverse pressure gradient of the embedded shock. This reattachment and separation have been termed R_1 and S_2 respectively. The thickening of the flow due to S_1 and S_2 generates two weak separation shocks which intersect with the triple point embedded shock. The second separation bubble at S_2 appears to scavenge nearly all of the remaining plate boundary layer to such an extent that near R_2 no detectable viscous layer was present. On the wedge a small separation bubble (S_3) is present in the corner with the reattaching streamline

105

striking the plate near R_2. This small buble was felt necessary
to round off the corner and was not felt to be a dominant feature
of the flow.

At the mutual reattachment point, R_2, where the boundary
layer is extremely thin, an inviscid finger extends down from the
region of the triple point. As was expected, the heating in this
region is extremely high as indicated in Fig. 9. The heating data
is taken from tests conducted by Lockheed for an FDL[4] program
using the same model tested in this study. Temperature sensitive
paint was used in the test. The wall pressures indicated in Fig.
10 support the foregoing data in attesting to the high energy
level present at R_2. Impact pressures of 270 mm were recorded
within 0.1 inches of the surface at R_2 compared with 61 mm in the
free stream.
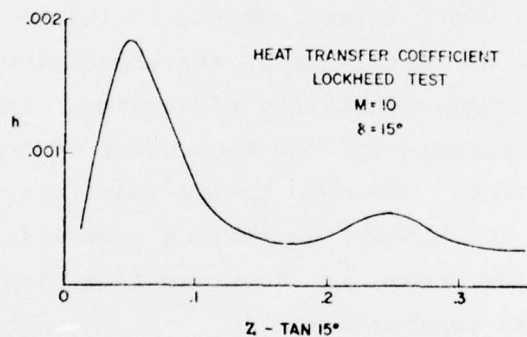
Fig. 9   Heat Transfer on Plate Surface

Analytic Calculations

Calculations were carried out using the experimental obser-
vations to establish the credibility of the test data and, con-
sequently, the flow field model of Fig. 5. Working in the cross
flow plane and starting with experimental free stream conditions,
a conically symmetric inviscid supersonic flow was computed based
upon measured locations of the surface bow shocks. The bow shock
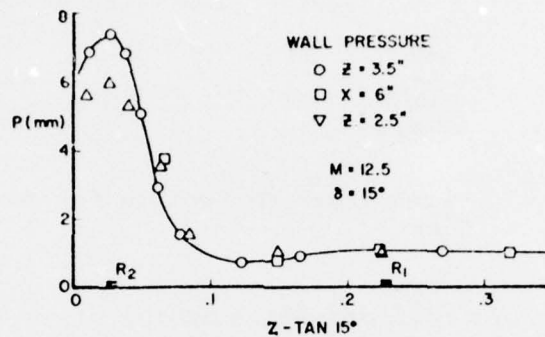
Fig. 10   Pressure Readings on Plate Surface

locations were chosen as a known parameter because of their well
defined experimental location. Other known values used for calcu-
lations, in addition to bow shock locations, included free stream
conditions, triple point location, plate bow shock strength, and
the location and slope of the separation shocks.

In calculating the boundary layer displacement it is neces-
sary to account for the slightly nonconical nature of the shock
and boundary layer growth. Using a tangent wedge approach illus-
trated in Fig. 11, where the body angle is α, the bow shock angle
is θ, and the total compression angle seen by a conical flow is
δ, an effective location for the origin of the bow shock can be
determined. The distance Y_d of the bow shock above the axis can
be measured experimentally. The resulting equality

$$Y_d = \tan \theta + \tan \delta - \tan \alpha \qquad\qquad (1)$$

is solved for the effective leading edge displacment, $\tan \delta - \tan \alpha$,
by iterating on δ, which gives a resulting θ for given flow con-
ditions, until the Y_d is equal to the experimental value.

107
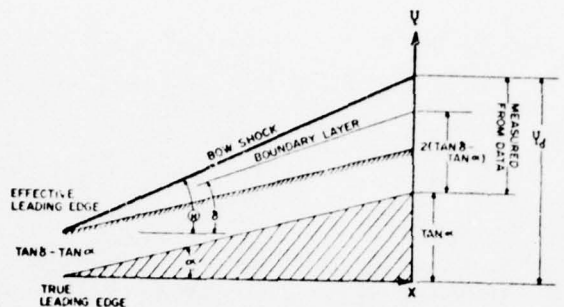
Fig. 11   First Order Correction for Nonconical
Flow

Carrying out this procedure on the plate results in a total
compression angle seen by the flow of 2.1° with a normalized dis-
placement thickness of 0.073. The required adjustment to the
leading edge location is 0.0367. A similar analysis of the wedge
surface results in a compression angle of 15.7°, a displacement
thickness of 0.026, and a leading edge correction of 0.01 31 .
Thus any measured location in the flow must be adjusted by de-
creasing the measured value by the appropriate effective leading
edge displacement before it can be used for calculation purposes,
i.e. all measurements along the Z axis (z axis normalized with
respect to x) must be reduced by the wedge leading edge displace-
ment, 0.01 31, and all measurements along the Y axis (y axis nor-
malized with respect to x) must be reduced by the plate leading
edge displacement, 0.0367. Henceforth all coordinates in the flow
field which are used for calculations will have been adjusted in
this manner. This minor correction may be viewed as a first order
correction for the nonconical behavior of the viscous layer.

Having determined the bow shock locations with their re-
spective boundary layer displacement thicknesses, it is now pos-
sible to follow the shocks into the corner until intersection oc-
curs to locate the coordinates of the triple point. In order to
calculate the conditions around the triple point it is necessary
to develop conical shock relationships applicable to the problem.

Consider a shock wave in conical flow with an inward normal $\underline{n}$. The slope of the shock wave projection on a spherical surface is $\tan \sigma$, where

$$\left(\frac{d\phi}{\sin\phi\,d\theta}\right)_{shock} = \tan \sigma$$

Therefore $\underline{n} = -\cos\sigma\,\underline{u}_\phi + \sin\sigma\,\underline{u}_\theta$. Since the shock wave must be generated by radial lines through the apex it is apparent that the shock wave normal does not have a component in the $\underline{u}_r$ direction.

The velocity vector does have three components in general

$$\underline{V} = u\,\underline{u}_r + v\,\underline{u}_\phi + w\,\underline{u}_\theta$$

The last two components produce the velocity in the cross-flow plane. From these two components a conical cross-flow Mach number may de defined.

$$M_c^2 = \frac{v^2 + w^2}{c^2}$$

and

$$\left(\frac{d\phi}{\sin\phi\,d\theta}\right)_\Psi = \frac{v}{w} \equiv \tan \omega$$

where ω is the angle of flow in the cross-flow plane.

To find the change in properties across a shock wave the normal component of the Mach number is required.

$$M_n = \frac{\underline{V}_1}{c_1} \cdot \underline{n} = -\frac{V_1}{c_1}\cos\sigma + \frac{w_1}{c_1}\sin\sigma$$

or

$$M_n^2 = M_{c_1}^2 \sin^2 (\sigma - \omega_1)$$

The pressure ratio across a shock wave is

$$\xi = \frac{p_2}{p_1} = \frac{7M_n^2 - 1}{6}$$

or

$$\xi = \frac{7M_{c_1}^2 \sin^2(\sigma - \omega_1) - 1}{6}$$

Using Rankine-Hugoniot relations the density and temperature ratios are easily determined from the pressure ratio.

$$\frac{P_2}{P_1} = \frac{6\xi + 1}{\xi + 6}$$

$$\frac{T_2}{T_1} = \frac{c_2^2}{c_1^2} = \xi \left(\frac{\xi + 6}{6\xi + 1} \right)$$

Now the velocity after the shock may be determined vectorially.

$$\underline{V}_2 = \underline{V}_1 + \underline{n} \, (V_{n_2} - V_{n_1}) = \underline{V}_1 + \underline{n} \, (\underline{V}_1 \cdot \underline{n}) \left(\frac{\rho_1}{\rho_2} - 1 \right)$$

where the new velocity components are

$$u_2 = u_1$$
$$v_2 = v_1 - \cos\sigma \, M_n \, c_1 \left(\frac{\rho_1}{\rho_2} - 1 \right)$$
$$w_2 = w_1 + \sin\sigma \, M_n c_1 \left(\frac{\rho_1}{\rho_2} - 1 \right)$$

Thus, the relationships for $\tan\omega_2$ and $M_{c_2}^2$ in terms of ξ and M_{c_1}

are

$$\tan^2(\omega_2 - \omega_1) = \left[\frac{7M_{c_1}^2}{6\xi + 1} - 1 \right] \left[\frac{1.4M_{c_1}^2}{\xi - 1} - 1 \right]^{-2} \quad (2)$$

$$M_{c_2}^2 = \frac{M_{c_1}^2 (6\xi + 1) - 5 (\xi^2 - 1)}{\xi(\xi + 6)} \quad (3)$$

These equations are as expected since they become identical to the two-dimensional oblique shock relationships[5] by replacing the shock wave angle (θ) by $\sigma - \omega_1$, the free stream Mach number (M_1) by the conical cross flow Mach number (M_c) and the deflection

110

angle (δ) by $\omega_2 - \omega_1$.

Since the location of the triple point in the flow field is known, sufficient information is available to completely describe the flow properties behind the shocks and their respective shock angles. Fig. 12 is the calculated triple point for the flow field showing the regional numbering scheme used in these calculations. To obtain these results observe that conditions are assumed known in regions 1 and 2. Shock 1-4, the wedge bow shock, produces a pressure p_4 and a flow direction ω_4 . The embedded shock 2-3 produces a pressure p_3 and angle $_3$. Due to the characteristics of a slip surface the pressures and flow directions must identically match across 3-4.
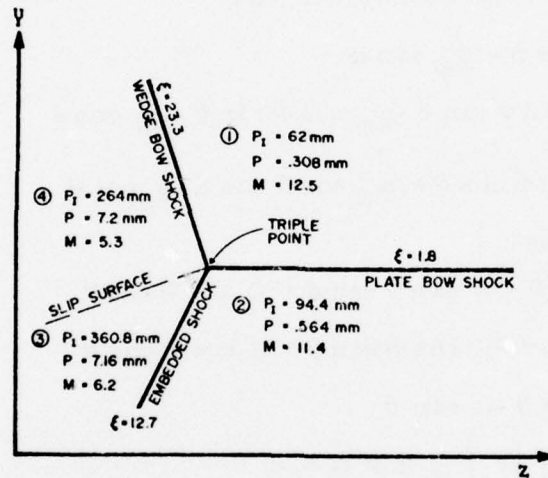

Fig. 12   Triple Point Calculations

$$\xi_4 = \frac{P_4}{P_1} = \frac{P_3}{P_1} = \frac{P_3}{P_2} \frac{P_2}{P_1}$$

$$\frac{P_3}{P_2} = \frac{\xi_4}{\xi_2} \quad \text{where} \quad \frac{P_2}{P_1} = \xi_2$$

Thus, from before

$$\tan^2 (\omega_4 - \omega_1) = \left[\frac{7M_{c_1}^2}{6\xi_4 + 1} - 1 \right] \left[\frac{1.4M_{c_1}^2}{\xi_4 - 1} - 1 \right] \tag{4}$$

111

$$\tan^2 (\omega_3 - \omega_2) = \left[\frac{7M_{c_2}^2}{6 \dfrac{\xi 4}{\xi 2} + 1} - 1 \right] \left[\frac{1.4 M_{c_2}^2}{\dfrac{\xi 4}{\xi 2} - 1} - 1 \right]^{-2} \tag{5}$$

Solve for ξ_4 by equating $\omega_3 = \omega_4$ for known values of M_{c_1}, M_{c_2}, ω_1, ω_2 and ξ_2. Only two solutions will result which are physically significant when nondecreasing entropy is required as is the case in this problem. To carry out this solution for the corner flow, flow properties in regions 1 and 2 must be determined. Both regions have uniform flow, i.e.

$$\underline{V} = A \underline{i} + B \underline{j} + C \underline{k}$$

where A, B, and C are constants and

$$\underline{i} = \underline{u}_r \cos\phi - \underline{u}_\phi \sin\phi$$

$$\underline{j} = -\underline{u}_r \sin\phi \sin\theta - \underline{u}_\phi \cos\phi \sin\theta - \underline{u}_\theta \cos\theta$$

$$\underline{k} = \underline{u}_r \sin\phi \cos\theta + \underline{u}_\phi \cos\theta \cos\theta - \underline{u}_\theta \cos\theta$$

Then for the case

$$u = A \cos\phi - B \sin\phi \sin\theta + C \sin\phi \cos\theta$$

$$v = -A \sin\phi - B \cos\phi \sin\theta + C \cos\phi \cos\theta$$

$$w = -B \cos\theta - C \sin\theta$$

In region 1, $A = \left| V_1 \right|$, $B = C = 0$

$$M_{c_1}^2 = M_1^2 \sin^2\phi \tag{6}$$

$$\omega_1 = 90^\circ$$

In region 2, the flow has undergone an oblique shock generated by a wedge at angle δ. Hence,

$$A = \left| V_2 \right| \cos\delta$$

$$B = 0$$

$$C = \left| V_2 \right| \sin\delta$$

and

$$\tan^2 \delta = \left[\frac{7M_1^2}{6\xi_2+1} - 1 \right] \left[\frac{1.4M_1^2}{\xi_2-1} - 1 \right]^{-2} \tag{7}$$

$$\left| \frac{V_2}{V_1} \right|^2 = 1 - \frac{5(\xi_2^2-1)}{M_1^2(6\xi_2+1)}$$

$$M_2^2 = \frac{M_1^2(6\xi_2+1) - 5\xi(\xi_2^2-1)}{\xi_2(\xi_2+6)} \tag{8}$$

Therefore

$$\frac{M_{c_2}^2}{M_2^2} = (-\cos\delta\sin\phi + \sin\delta\cos\phi\cos\theta)^2$$
$$+ (-\sin\delta\sin\theta)^2 \tag{9}$$

$$\tan\omega_2 = -\cos\delta\sin\phi + \sin\delta\cos\phi\cos\theta \tag{10}$$

Also $u_1 = u_2$ or

$$\left| V_1 \right| \cos\phi = \left| V_2 \right| (\cos\delta\cos\phi + \sin\delta\sin\phi\cos\theta)$$

which becomes

$$\tan\phi\cos\theta = \frac{\left| \dfrac{V_2}{V_2} \right| - \cos\delta}{\sin\delta} = \text{constant} \equiv Y_T \tag{11}$$

likewise

$$\tan\phi\sin\theta = \text{constant} \equiv Z_T \tag{12}$$

Now with the free stream Mach number, M - 12.5, and the corrected triple point coordinates, Y_T = .1053 and Z_T = .3769, the corresponding plate bow shock angle and pressure ratio is determined. Angular components (θ and ϕ) of the triple point coordinates can be gained from Eqs. (11) and (12). The effective plate compression angle is determined from Eq. (7) and the region 2 cross flow angle from Eq. (10). The cross flow Mach number in region 1 is obtained from Eq. (6) and the cross flow Mach number

in region 2 is from Eq. (9) after determining the region 2 flow
Mach number in Eq. (8). With this information and the knowledge
that $\omega_1 = 90^{\circ}$, Eqs. (4) and (5) can be solved simultaneously by
iterating on ξ_4 until $\omega_3 = \omega_4$. Displaying the solutions
graphically aids in choosing the solution that is physically
practical. Fig. 12 displays the results for the calculated triple
point flow field. Finally, the slopes of the discontinuities
(dY/dZ) around the triple point can be determined.

$$\frac{dY}{dZ} = \tan (\Gamma - \theta)$$

where

$$\tan \Gamma = \tan \sigma \sec \phi$$

and

$$\sin^2(\sigma_4 - \omega_1) = \frac{6\xi_{4+1}}{7M_{c_1}^2}$$

$$\sin^2(\sigma_3 - \omega_2) = \frac{6\frac{\xi_4}{\xi_2} + 1}{7M_{c_2}^2}$$

The separation shock locations and boundary layer thicken-
ings were verified in much the same manner as the triple point.
The coordinates of the first separation shock origin at the boun-
dary layer surface were determined from the data as was the pre-
sure ratio across the shock. With this information, the condi-
tions behind the shock and the cross flow slope of the thickened
boundary layer can be found. Using this information as the ini-
tial condition for the second separation shock solution yields
similar results.

Since both separation shocks interact with the embedded
shock of the triple point, typical shock interaction solutions
were calculated, again using the presented data to aid in choosing
the most practical case. Fig. 13 gives the results of the inter-
actions on the embedded shock and the associated flow conditions.

114

The region between the triple point slip surface and the embedded shock is a supersonic inviscid finger which extends toward R_2 on the plate. This jet, much like that of Edney's[6] type IV shock interaction, supports the high heating in this region of the plate.
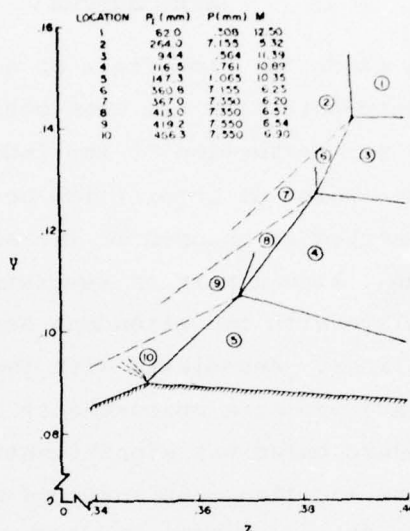
Fig. 13   Flow Calculations Near Embedded Shock

In order to establish the credibility of the data through the above calculations, the calculated locations of discontinuities were compared with those of the data along with a comparison of calculated impact pressures with the impact pressure data. From the static pressure and Mach number in each region an impact pressure was calculated using normal shock relations.

$$\frac{P_{I_1}}{P_1} = \left(\frac{6M_1^2}{5}\right)^{7/2}\left(\frac{6}{7M_1^2 - 1}\right)^{5/2}$$

With the exception of the inviscid finger region near the corner, all impact pressures and flow discontinuity locations of the data were within 10% of those calculated for the same region. Due to the small size of the finger, calculations resulted in impact pressures higher than those recorded in the test.   This

115

error was partially due to the tendency of the pressure probe to smear out very localized high pressure cells and, thus, indicate a lower pressure than may actually be present.

Conclusions

In this study the flow field of an asymmetric axial corner in laminar hypersonic flow has been measured. These measurements permitted the reconstruction of the induced inviscid flow structure. Only one point of interaction between the surface bow shocks was observed as opposed to two such triple points in the symmetric case. Also a pair of separation bubbles was observed on the flat plate with two attendant separation shocks and two reattachment lines. Associated with the reattachment lines, surface heating and pressure measurements have shown two peaks of which the inboard value was significantly higher than that found at the outboard location. An inviscid supersonic jet, similar to the Edney type IV, was detected and found to impinge upon the plate surface near the second reattachment point. This jet resulted in high impact pressures and heating at this point. Analytic calculations carried out to support the experimental data, produced impact pressures which compared quite favorably with the recorded values.

References

1. Gonar, A.L., "Exact Solution of the Problem of Supersonic Flow of Gas Past Some Three-Dimensional Bodies," PMM (Journal of Applied Mathematics & Mechanics), Vol. 28, No. 5, 1964, pp. 974-976

2. Charwat, A.F. and Redekopp, L.B., "Supersonic Interference Flow Along the Corner of Intersecting Wedges," AIAA Journal, Vol. 5, No. 3, March 1967, pp. 480-488.

3. West, J.E. and Korkegi, R.H., "Interaction in the Corner of Intersecting Wedges at a Mach Number of 3 and High Reynolds Numbers," ARL 71-0241, Aerospace Research Laboratories, October 1971.

4. Schultz, H.D. and Baker, R.C., "Pressure and Heat Transfer
Measurements in Regions of Three-Dimensional Shockwave-Boundary
Layer Interactions," Lockheed Missiles & Space Co., Sunnyvale,
Calif., LMSC-D157341, March 1972.

5. Ames Research Staff, "Equations, Tables, and Charts for Com-
pressible Flow," NACA Rept. 1135, Ames Aeronautical Laboratory,
Moffett Field, Calif., 1953.

6. Edney, B.E., "Anomalous Heat Transfer and Pressure Distribu-
tions on Blunt Bodies at Hypersonic Speeds in the Presence of an
Impinging Shock," FFA Rept. 115, The Aeronautical Rsch. Institute
of Sweden, February 1968.

NUMERICAL SOLUTION OF COMPRESSIBLE NAVIER-STOKES EQUATIONS
FOR THREE-DIMENSIONAL CORNER FLOW

by

J. S. Shang and W. L. Hankey Jr.
Air Force Flight Dynamics Laboratory
Wright-Patterson Air Force Base, Ohio

Introduction

There is little doubt that numerical analysis has added a
new dimension to research in aerodynamics. Recent progress in
numerical analysis provides new insight into both theoretical[1,2,3]
and experimental[4,5,6] investigations. The present analysis demon-
strated the feasibility to numerically investigate three-dimen-
sional axial corner flow fields. An explicit numerican scheme
was selected over an implicit method[7] due to recent success in
computing flow fields containing shock waves.[4,5,6] In order to
instill some confidence in the present approach, the three-
dimensional code was first checked by comparing degenerate two-
dimensional analytic and experimental flows. A three-dimensional
calculation was then accomplished for an axial corner generating
by a 10° wedge and flat plate at the hypersonic Mach number of 12.5.
The corresponding Reynolds number based upon the free stream prop-
erty was 0.92×10^{6} which insured laminar conditions. This case
was then compared with experiment[8] to establish credibility.

Governing Equations

The governing equations of the present analysis are the
unsteady, compressible three-dimensional Navier-Stokes equations.
The time dependency of the governing equations permits the solu-
tions to progress naturally from an arbitrary initial guess to an
asympototic steady state.[9]

$$\frac{\delta\rho}{\delta t} + \nabla \cdot (\rho\bar{u}) = 0 \tag{1}$$

$$\frac{\delta\rho\bar{u}}{\delta t} + \nabla \cdot (\rho\bar{u}\,\bar{u} - \bar{\bar{\tau}}) = 0 \tag{2}$$

$$\frac{\delta\rho e}{\delta t} + \nabla \cdot (\rho e\bar{u} + \bar{q} - \bar{u} \cdot \bar{\bar{\tau}}) = 0 \tag{3}$$

The equation of state, Sutherland's viscosity low and Prandtl number (0.73) formally close the system of equations. The associated boundary conditions for the problems consiered differ widely and will be delineated in a subsequential section.

Coordinate System

A major difficulty encountered in analyzing practical three-dimensional aerodynamic problems is the accomodation of complicated body configurations. A general coordinate transformation was successfully demonstrated by Knight and Hankey[10]. The coordinate transformation is introduced as

$$\xi = \xi \ (x)$$
$$\eta = \eta \ (x, y, z) \tag{4}$$
$$\zeta = \zeta \ (x, y, z)$$

In order to achieve appropriate grid-spacing to resolve significant features of this flow field at high Reynolds numbers, the coordinate normal to the surface is stretched exponentially to yield a cell Reynolds number near 2.

The governing equations in the transformed space yields the following form

$$\frac{\delta \bar{U}}{\delta t} + \xi_x \frac{\delta F}{\delta \xi} \ \sum_i \ \eta_{xi} \frac{\delta G}{\delta \eta} + \sum_i \ \zeta_{xi} \frac{\delta H}{\delta \zeta} = 0; \quad i \quad 1,2,3 \tag{5}$$

The dependent variables are

$$\bar{U} = \begin{Bmatrix} \rho \\ \rho u \\ \rho v \\ \rho w \\ \rho e \end{Bmatrix} \tag{6}$$

$$F = G_1 = H_1 = \begin{Bmatrix} \rho u \\ \rho u u - \tau_{xx} \\ \rho u v - \tau_{xy} \\ \rho u w - \tau_{xz} \\ \rho u e + q_x - (u.\tau_{xx} + u.\tau_{xy} + w.\tau_{xz}) \end{Bmatrix} \tag{7}$$

120

$$G_2 = H_2 = \begin{Bmatrix} \rho v \\ \rho v u - \tau_{xy} \\ \rho v v - \tau_{yy} \\ \rho v w - \tau_{yz} \\ \rho v e + q_y - (u.\tau_{xy} + v.\tau_{yy} + w.\tau_{yz}) \end{Bmatrix} \qquad (8)$$

$$G_3 = H_3 + \begin{Bmatrix} \rho w \\ \rho w u - \tau_{xz} \\ \rho w v - \tau_{yz} \\ \rho w w - \tau_{zz} \\ \rho w e + q_z - (u.\tau_{xz} + v.\tau_{yz} + w.\tau_{zz}) \end{Bmatrix} \qquad (9)$$

Numerical Procedure

The system of equations is solved by a two-step predictor and corrector scheme originated by MacCormack.[11] The predictor and corrector equations are defined as follows

Predictor:

$$\bar{U}^{n+1*} = \bar{U}^n - \frac{\Delta t}{\Delta \xi} \xi_x (F_{i+1}^n - F_i^n - \frac{\Delta t}{\Delta \eta} \sum_m \eta_{xm}$$

$$(G_{m,J+1}^n - G_{m,j}^n) - \frac{\Delta t}{\Delta \zeta} \sum_m \zeta_{xm}$$

$$(H_{m,k+1}^n - H_{m,k}^n) \qquad (10)$$

Corrector:

$$\bar{U}^{n+1} = \frac{1}{2} \left\{ \bar{\bar{U}}^{n+1*} + \bar{\bar{U}}^n - (\frac{\Delta t}{\Delta \zeta}) \xi_{xm} F_{mi}^{n+1*} - F_{mi-1}^{n+1*} \right.$$

$$-(\frac{\Delta t}{\Delta \eta}) \sum_m \eta_{x_m} (Gm_i^{n+1*} - Gm_{i-1}^{n+1*}) - (\frac{\Delta t}{\Delta \zeta}) \sum_m \zeta_{x_m} \qquad (11)$$

$$\left. (H_{m_K}^{n+1*} - H_{m_{K-1}}^{n+1*}) \right\}$$

The stress and heat flux terms in F, G and H are approximated by central, forward and backward differing in such a manner that after a complete cycle of the predictor and corrector operations the second derivations are effectively approximated by a central differing scheme (and are accurate to second order). Equations (10), (11), are split into three groups of operators; each aligned with a transformed coordinate. Therefore, an alternating direction procedure can be easily implemented.

121

Stability and Accuracy

The present numerical scheme is second order accurate in space and time. Although to date no completely satisfactory stability analysis has been performed for the finit difference form of the Navier-Stokes equation[4], the Courant-Friedrich-Lewy condition for the inviscid domain serves as a useful indicator.[12]

$$\Delta t_{CFL} = \min \left\{ \left[\frac{|u|}{\Delta x} + \frac{|v|}{\Delta y} + \frac{|w|}{\Delta z} + C\sqrt{\frac{1}{\Delta x^2} + \frac{1}{\Delta y^2} + \frac{1}{\Delta z^2}} \right] \right\}^{-1} \qquad (12)$$

For the present viscous computations, an empirical formula suggested by Tannehill, et al[13] seems to be adequate.

$$\Delta t_{CFL} \leq \Delta t_{CFL} / (1+2/R_{e\nabla}) \qquad (13)$$

where $R_{e\nabla}$ is the minimum mest Reynolds number of the computational domain.

Flows containing strong shock waves often cause numerical oscillations. The large truncation errors in the early transitory stage of the computation also may cause divergence of the numerical solution. Three numerical smoothing schemes are incorporated into the present numerical procedure. Both the convective volocity modification and the fourth-order pressure damping suggested by MacCormack[4] are adopted. Additional normal stress damping due to McRae[14] designed to counteract the abnormal transitory behavior is also included.

Numerican Results

Two dimensional check cases:

Although the three-dimensional code was an extension of a successful two-dimensional program[5,6,10] verification was required before attempting a full 3-D case.

First, flow between two parallel plates was simulated for which an analytic solution exists (Couette flow). A comparison

122

was selected for flow between a fixed and moving plate (1100 fps), each at a terperature of 200°R, and 126.5°R respectively and separated bt a dustabce if 0.175 ft. To simplify the analysis a linear viscosity relationship with temperature was utilized.

Two cases were calculated for flow along the x-axis and also for flow aligned with the z-axis. In both cases all three directional operators were active during the calculations. The maximum deviation between the numerical and analystic results is less than two percent.

Next a comparison with a previous two-dimensional Navier-Stokes solution[15] was accomplished for which experimental verification existed. The case selected was for shock impingement on a flat plate laminar boundary layer. The case considered was for a free stream Mach number of 2, a Reynolds number of 2.96×10^5 and an incident shock angle of 32.58°. Acceptable agreement between the two and three dimensional codes were achieved. (Not shown.) The small discrepancy between the codes is attributed to differences in the grid and implementation of the boundary conditions.

Confirmation of the code having been demonstrated one can now proceed to investigate a three-dimensional problem.

3 D Axial Corner

The complex flow structure in the vicinity of an axial corner, for which detailed experimentsl flow field data existed,[8] was next investigated.

The axial corner was formed by the orthogonal intersection of a 100° wedge and a flat plate (Fig. 1). The free stream Mach number was 12.5 and the Reynolds number was 10^6.

Although inviscid computations exist for this case[16,17], one must compare with the experiment[8] due to the strong viscous-inviscid interaction which persists at these test conditions.

The initial and boundary conditions for axial corner flow are summarized as follows:

Upstream and initial conditions

$$\bar{U} (t_i, o, y, z) = \bar{U}_w \qquad\qquad (14)$$

At corner surface;

$$\bar{u} = 0 \qquad\qquad (15)$$

$$T = T_w \simeq 0.4 \, To \qquad\qquad (16)$$

The boundary conditions for density at the surface is obtained by solving $\bar{n} \cdot \nabla p = 0$ and the equation of state. The far-field boundary conditions are prescribed as

$$\bar{n} \cdot \nabla U = 0 \qquad\qquad (17)$$

where $\bar{n}$ is normal to the boundary surface, which merely reflects the returning to two-dimensional flow far from the corner.

The downstream boundary condition is approximated by a no-change condition in a conical direction. This boundary condition is a low-order approximation and should have little upstream influence.

Priliminary results (Figures 2-10) are shown for comparison with the wind tunnel data.

Conclusions

A three dimension-time dependent Navier-Stokes code employing MacCormack's finite difference scheme has been developed. Successful comparisons were performed for analytic cases (Couette flow) and for two dimensional shock-boundary interaction to first validate the code. The flow field for a 3-D axial corner, Mach number 12.5, was then computed and compared with experiment.

This investigation demonstrated that numerical methods may be used to determine the general features of complex three-dimensional flows.

REFERENCES

1. Stewartson, K. "Bulti-Structured Boundary Layers on Flat Plates and Related Bodies," "Advances in Applied Mechanics." Vol. 14, pp. 145-239 Academic Press, 1974.

2. Burggraf, O.R. "Asympotitic Theory of Separation and Reattachment of a Laminar Layer on a Compression Ramp." "Flow Separation" AGARD Conference Pre-print No. 168, pp. 10-1 - 10.J May, 1975.

3. Brilliant, H. M. and Adamson, T. E., Jr., "Shock Wave Boundary-Layer Interactions Laminar Transonic Flow" AIAAJ, No 12, No. 3, pp. 232-329, March, 1974.

4. MacCormack, R. W. and Baldwin, B. S. "A Numerical Method for Solving the Navier-Stokes Equations with Application to Shock Boundary Layer Interactions." AIAA Paper 75-1, AIAA 13th Aerospace Sciences Meeting, January 1975.

5. Shang, J. S. and Hankey, W. L., Jr., "Numerical Solutions of the Navier-Stokes Equations for Supersonic Turbulent Flow over a Compression Ramp" AIAA Paper 75-4, AIAA 13th Aerospace Science Meeting, January, 1975.

6. Shang, J. S., and Hankey, W. L., Jr., and Law, C. H., "Numerical Simulation of Shock Wave-Turvulent Boundary Layer Interaction" AIAA Paper 76-95 to be presented at AIAA 14th Aerospace Science Meeting, January 1976.

7. Briley, W. R., and McDonald, H. "Solutions of the Three-Dimensional Compressible Navier-Stokes Equations by an Implicit Technique", Lecture Notes in Physics, Vol. 35, Springer-Verlag, pp. 105-110.

8. Cooper, J. R., and Hankey, W. L., Jr., "Flow Field Measurements in an Asymmetric Axial Corner at M = 12.5" AIAAJ Vol. 12, No. 10, 1357, October, 1974, pp. 1353-1357.

9. Crocco, L., "A Suggestion for the Numerical Solution of the Navier-Stokes Equations" AIAAJ Vol. 3, No. 10, October, 1975, p. 1862.

10. Knight, D. D. and Hankdy, W. L., Jr., "Numerical Simulations of Non-Chemically Reacting Radial Supersonic Diffusion Laser", AIAA Paper 76-60 to be presented at AIAA 14th Aerospace Science Meeting, January 1976.

11. MacCormack, R. W. "Numerical Solutions of the Interactions of a Shock Wave with a Laminar Boundary Layer" Lecture Notes in Physics, Vol. 8, Springer-Verlag, 1971, p. 151.

12. MacCormack, R. W. and Warming, R. F., 'Survey of Computational Methods for Three-Dimensional Supersonic Inviscid Flows with Shock." Paper reprinted from Lecture Series No. 64 AGARD.

References, Continued

13. Tannehill, J. C., Holst, T. L. and Rakich, J. V., "Numerical Computations of Two-Dimensional Viscous Blunt Body Flows with an Impinging Shock", AIAA Paper 75-154, AIAA 13th Aerospace Science Meeting, January, 1975.

14. McRae, D. S. "A Numerical Study of Supersonic Viscous Cone Flow at High Angle of Attack", AIAA Paper 76-97 to be presented at AIAA 14th Aerospace Science Meeting, January, 1976.

15. Hakkinen, R. J., Greber, L., Trulling, L. and Abarbanel, S. S., "The Interactions of an Oblique Shock Wave with a Laminar Boundary Layer", NASA Memo 2-18-19, 1959.

16. Kutler, P., "Numerical Solution for the Inviscid Supersonic Flow in the Corner Formed by Two Interacting Wedges", AIAA Paper 73-677, 1973.

17. Shankar, V. and D. A. Anderson, "Numerical Solutions for Inviscid Supersonic Corner Flows", Final Report ISU-ERI-AMES-74090 Engineering Research Institute, Iowa State University, Ames, Iowa, May, 1974.

THREE DIMENSIONAL COMPRESSION CORNER

GRID-POINT SYSTEM
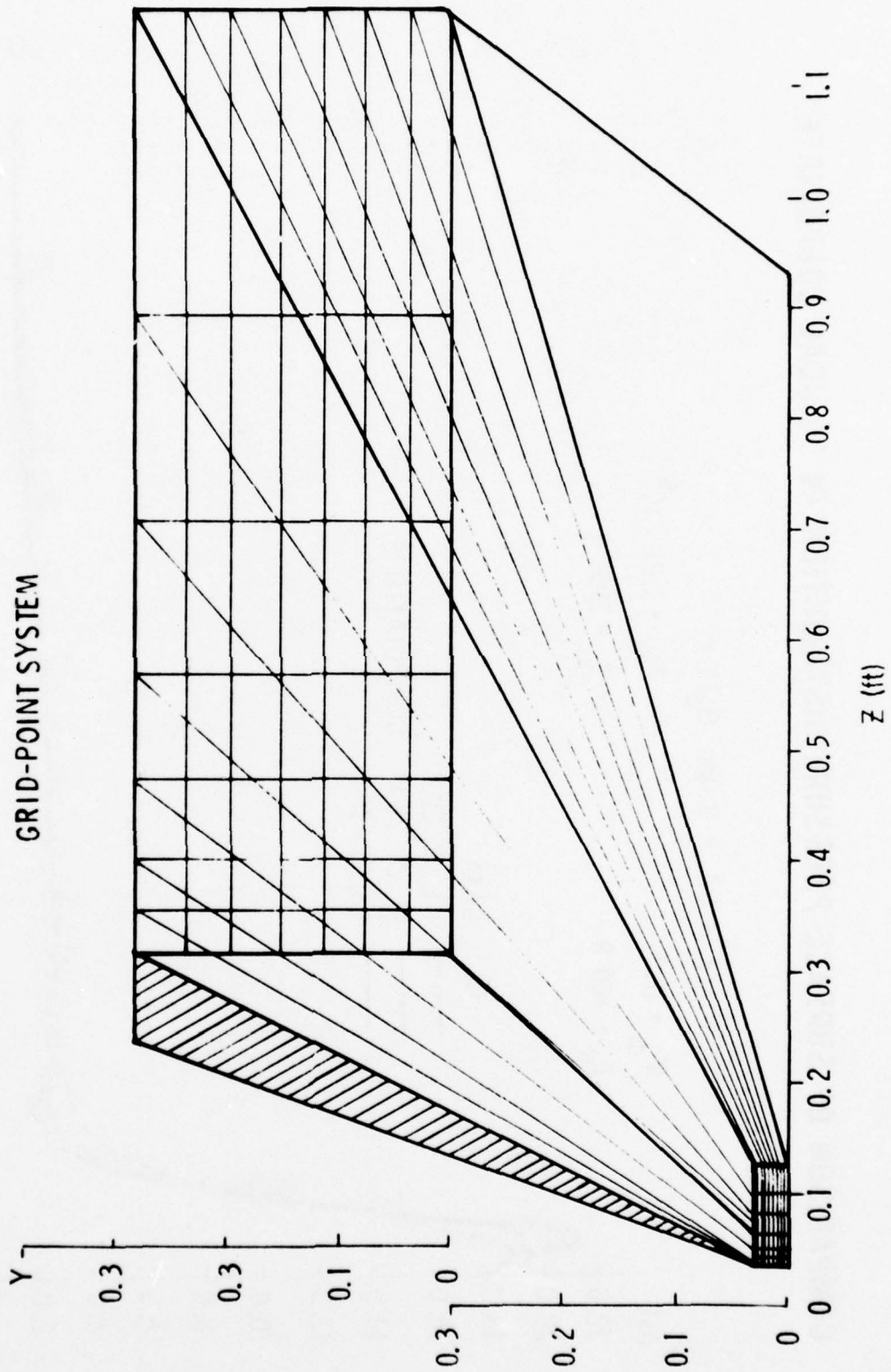
Figure 1.

COMPARISON OF SURFACE PRESSURE DISTRIBUTION IN CONICAL COORDINATE

$$\bar{z} = (z + X \tan \theta_w) / X$$

$M_\infty = 12.5$ $\quad R_{e_L} = 1.21 \times 10^6$

$T_w = 660\ R$ $\quad T_0 = 1800°\ R$

⊙ DATA

--- (8, 12, 20)

—·— (8, 20, 28) COMPUTATIONS

——— (8, 32, 36)

P_{psf}

22.0 20.0 18.0 16.0 14.0 12.0 10.0 8.0 6.0 4.0 2.0 0

$\bar{z}$

0.30 0.40 0.50 0.60 0.70 0.80 0.90 1.00 1.10
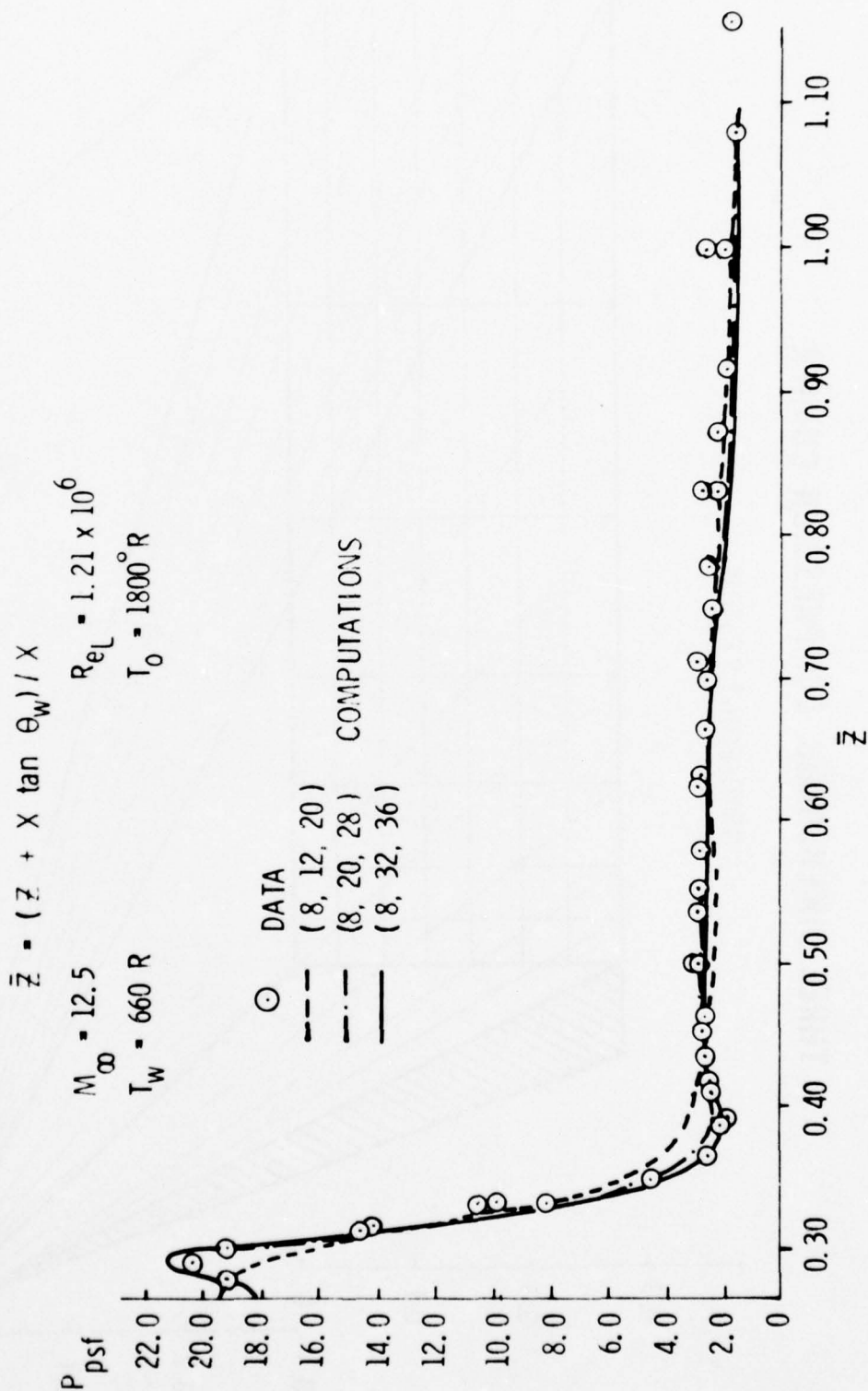
Figure 2.

Figure 3.

COMPARISON OF IMPACT PRESSURE

Figure 4.

130
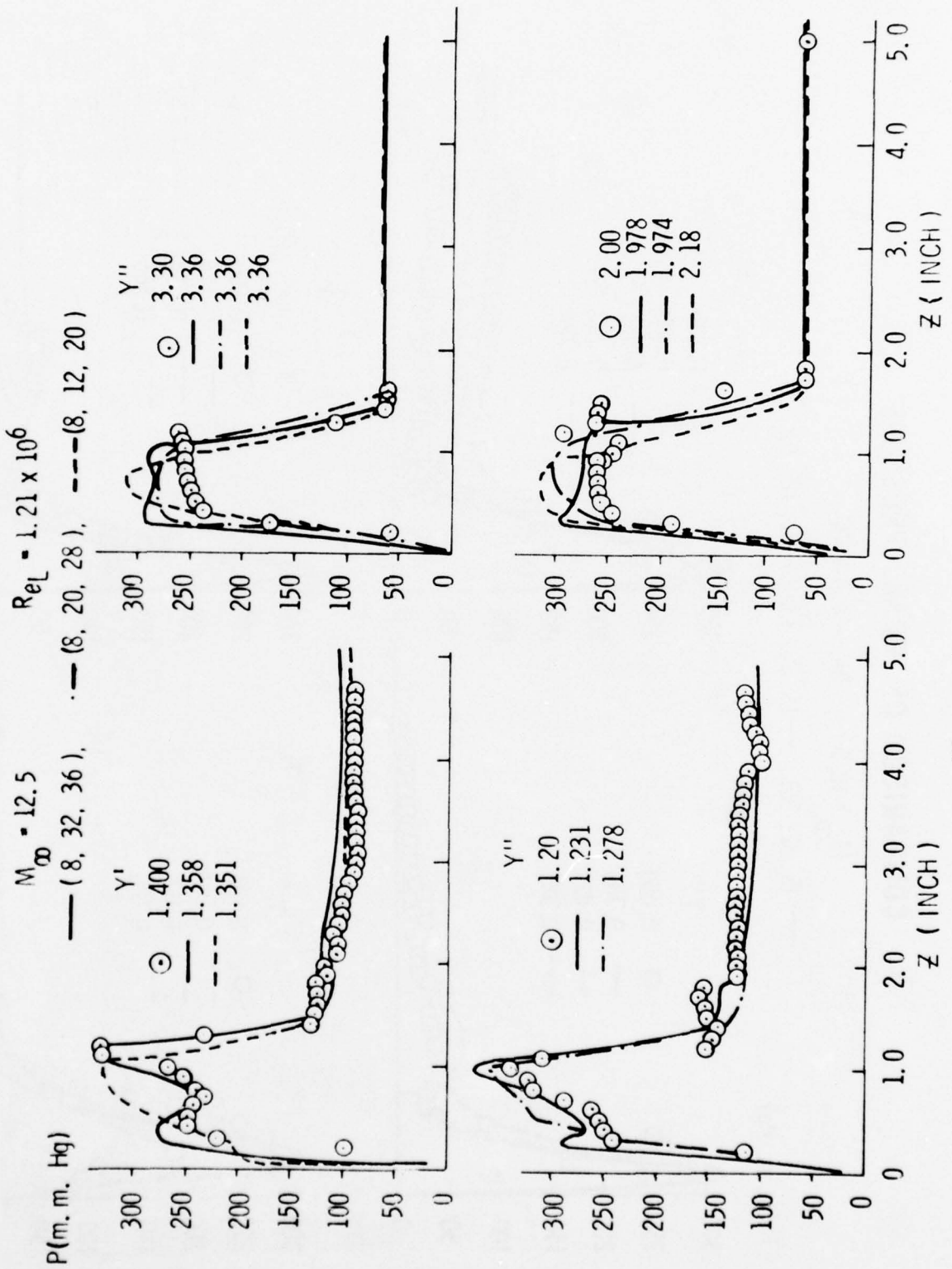
PITOT PRESSURE CONTOUR
(Exp. data)

$M_\infty = 12.5$ $Re_L = 1.21 \times 10^6$ $\theta_W = 15°$

$T_W = 660°R$ 1355 PTS
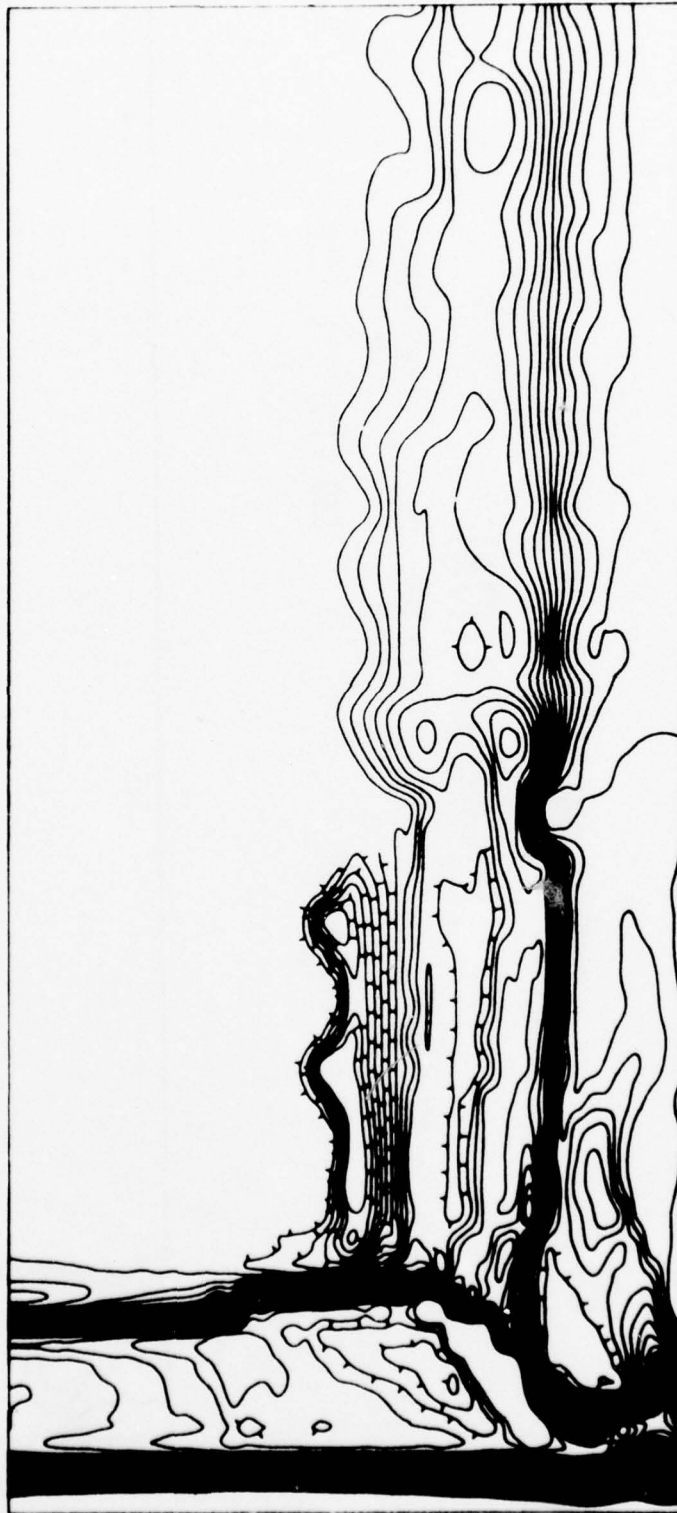
Figure 5.

PITOT PRESURE CONTOUR
(CALCULATION)

$M_\infty = 12.5$ $Re_L = 1.21 \times 10^6$ $\theta_W = 15°$

$T_W = 660°$ 560 PTS
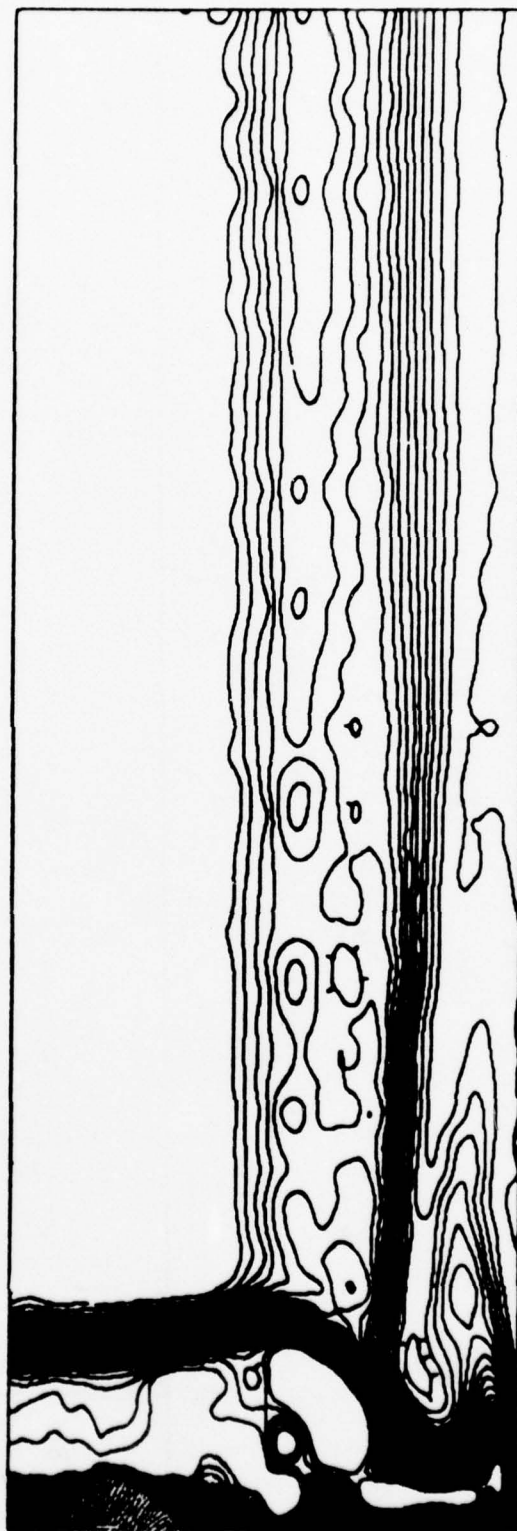
Figure 6.

SURFACE FORCE MAP

$M_\infty = 12.5$ $Re_L = 1.21 \times 10^6$

$T_W = 660°R$ $\theta_W = 15°$

Figure 7.

133
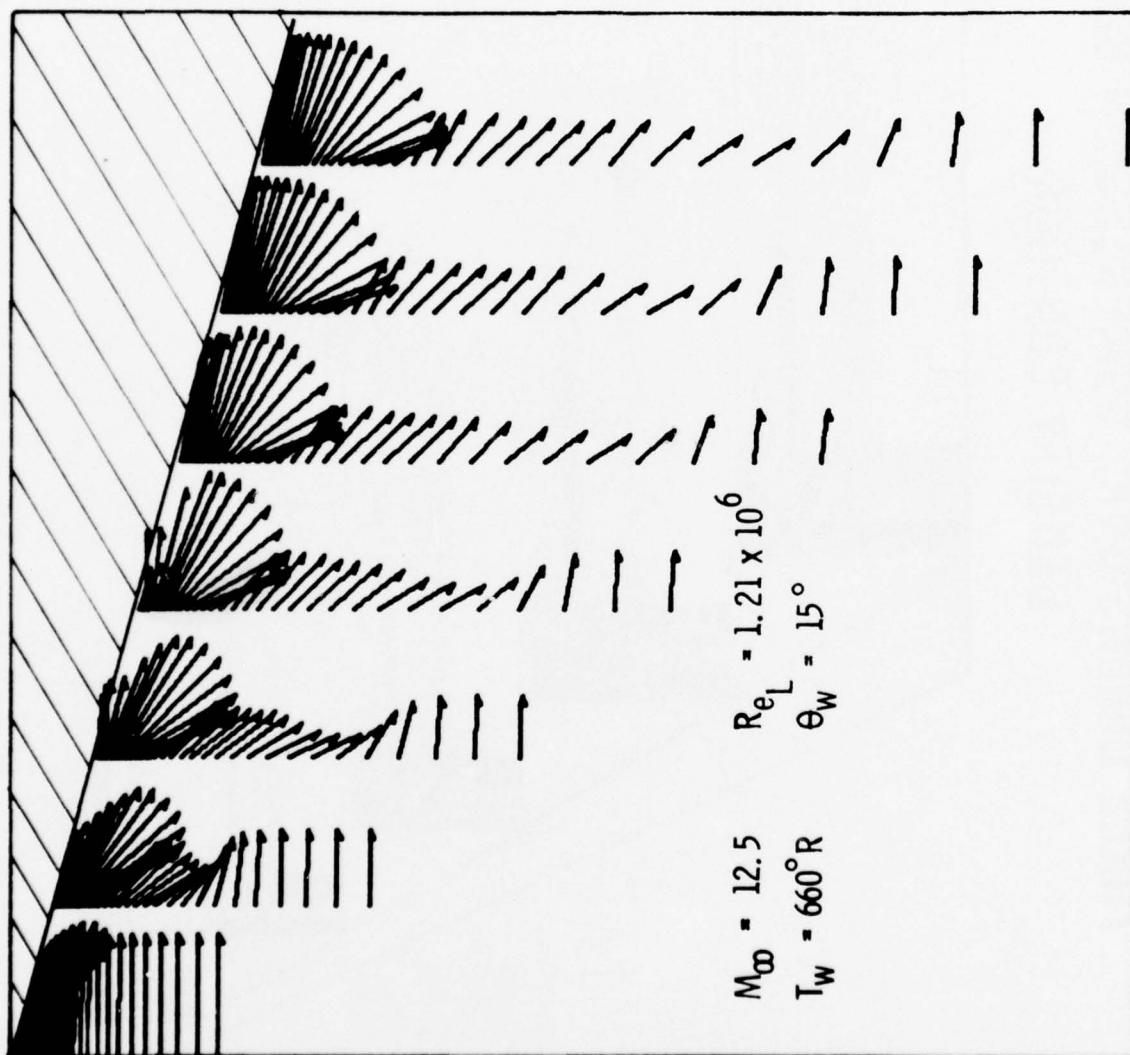
THREE DIMENSIONAL COMPRESSION CORNER
DENSITY CONTOUR

MACH NO = 12.50

$R_{e_l} = 1.21 \times 10^6$

$\theta_W = 15°$

$T_W = 660°R$
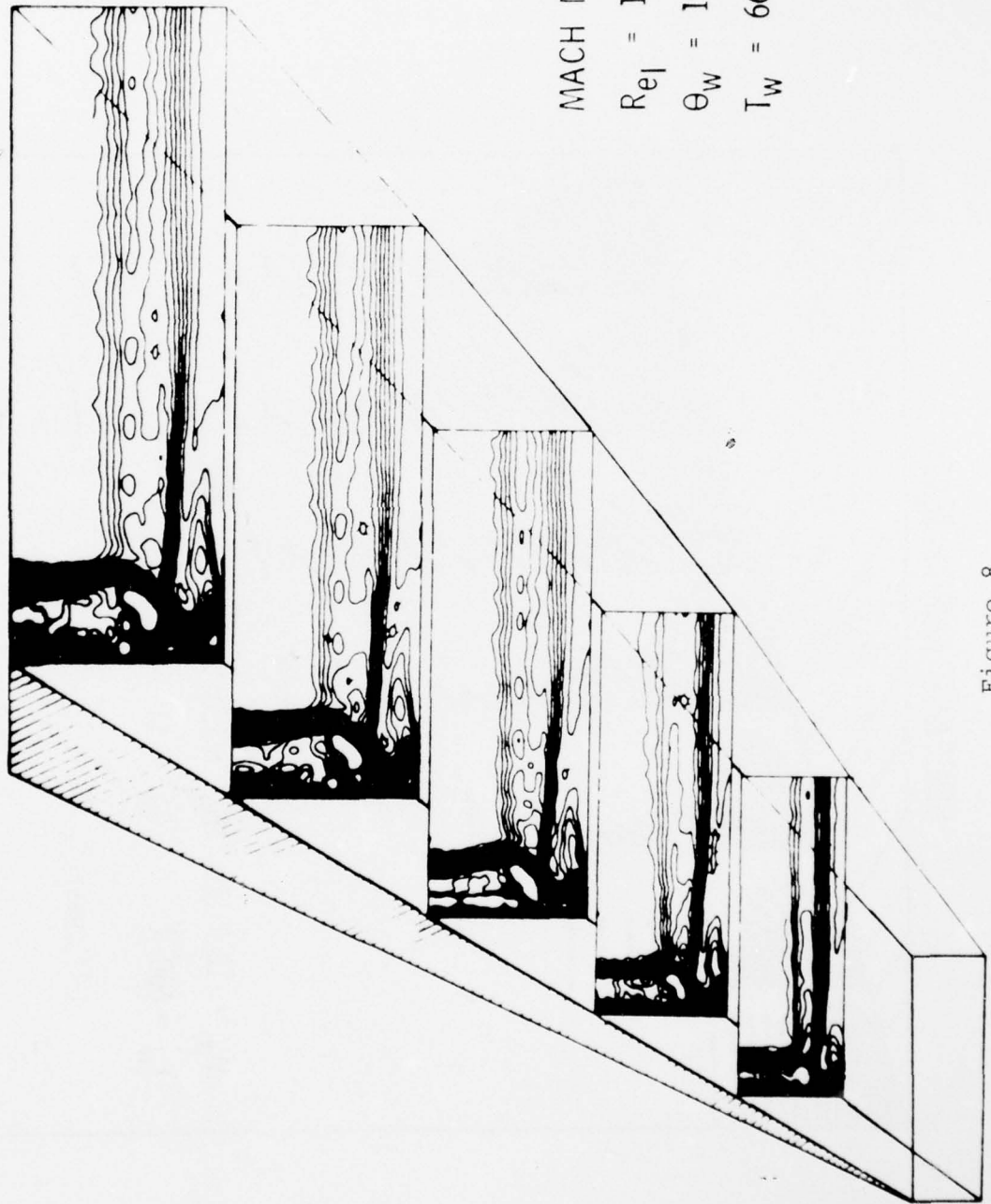
Figure 8.

THREE DIMENSIONAL COMPRESSION CORNER
CROSS FLOW PLANE VELOCITIES

MACH NO = 12.5

$R_{e_l} = 1.21 \times 10^6$

$\theta_w = 15°$

$T_w = 660°R$

Figure 9.

RATE OF HEAT TRANSFER DISTRIBUTIONS

$M_\infty = 12.5$ $Re_L = 1.21 \times 10^6$

$T_w = 660°R$ $T_0 = 1800°R$

Q/Q_{2D}

18.0
16.0
14.0
12.0
10.0
8.0
6.0
4.0
2.0
0

0   1.0   2.0   3.0   4.0   5.0   6.0   7.0   8.0   9.0   10.0

Z (INCH)

TOTAL TEMPERATURE CONTOUR

$M_\infty = 12.5$ $Re_L = 1.21 \times 10^6$

$T_w = 660°R$ $T_0 = 1800°R$

$T_0 °R$
1800
1700
1600
1400
1200
1000
900
800

Figure 10.

136

BOUNDARY LAYER STUDIES ON A YAWED, SPINNING BODY OF REVOLUTION

by

W. Sturek, R. Reklis, L. Kayser and K. Opalka
Wind Tunnels Branch
Exterior Ballistics Laboratory
U.S. Army Ballistic Research Laboratories
Aberdeen Proving Ground, Maryland

ABSTRACT:

Studies of the three dimensional boundary layer development over yawed, spinning bodies of revolution are being carried out at the Ballistic Research Laboratories due to Army interest in determining Magnus effects for artillery projectiles. This paper describes a combined theoretical-experimental research effort with the overall objective of developing a method for computing Magnus effects that could be used in the design of artillery projectiles. Numerical techniques are described for computing: (1) the three dimensional turbulent boundary layer development over a yawed, spinning body of revolution; (2) the three dimensional boundary layer displacement surface for an arb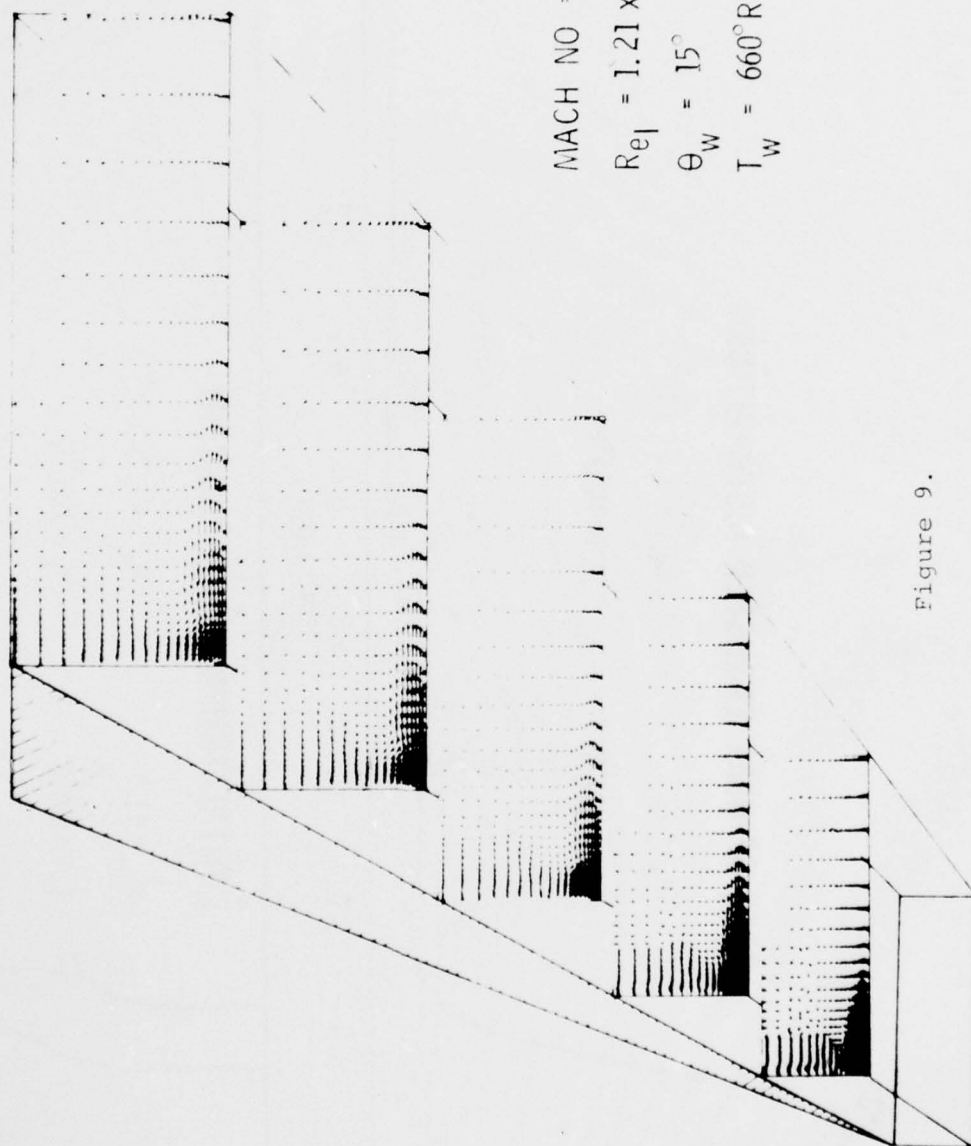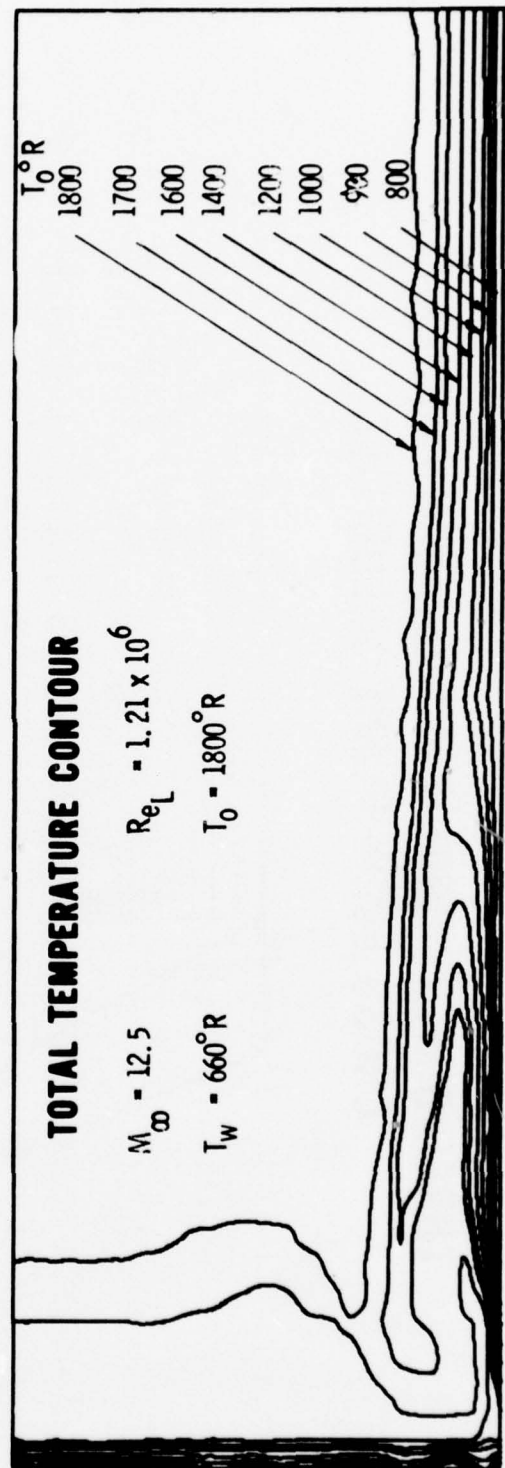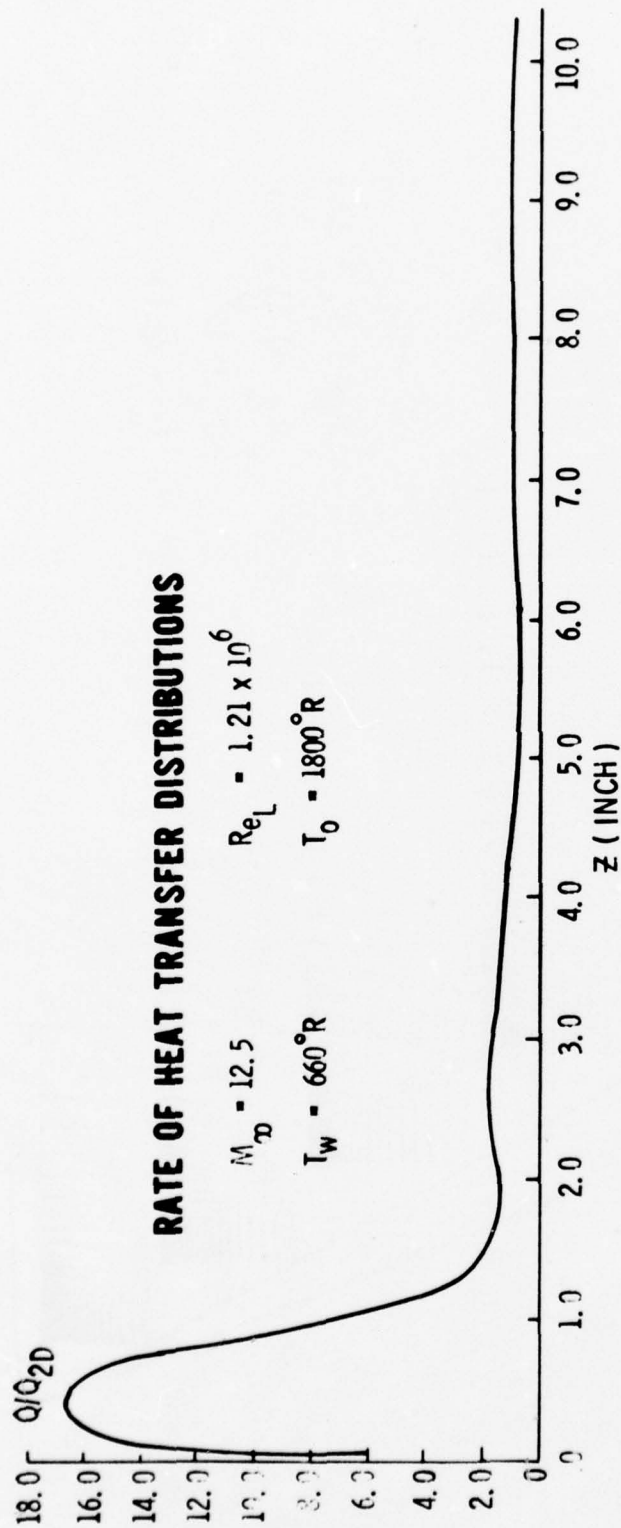itrary body of revolution; and (3) the three dimensional inviscid flow field over a yawed, pointed body of completely general configuration with no plane of symmetry. The computations are compared to experimental measurements of Magnus force and turbulent boundary layer profile characteristics. Two body geometries are considered: (1) a 10° half angle cone; and (2) a six caliber long secant-ogive-cylinder model closely approximating the M549 projectile shape. Comparisons are shown for M = 2, 3; $\alpha = 2^o$, 4.2^o; and spin rates up to 30,000 RPM. The agreement between theory and experiment is considered to be exceptionally good.

1.   INTRODUCTION

Recent Army interest in achieving increased range and greater payload capacity in artillery projectiles has led to designs with long, slender

ogives, increased projectile length, and bottailed afterbodies. These designs have resulted in decreased drag with a resulting increase in range; however, the aerodynamic stability of these shapes is less than more conventional designs. This means that these new shapes are more susceptible to a Magnus induced instability.

As shown in Figure 1, the Magnus force is a side force that occurs on a spinning projectile in flight at angle of attack. Magnus is a small force, it is typically 1/10 to 1/100 of the normal force; however, its effect is important because the Magnus moment acts to undamp the projectile throughout its flight. Thus, it is desirable to minimize the Magnus moment in order for the projectile to fly at a small average angle of attack and achieve the greatest range capability.

Magnus has been modeled theoretically as resulting from spin induced distortion of the boundary layer. This effect is illustrated schematically in Figure 2 where a cross-sectional view of a body of revolution is shown. The body is at angle of attack as indicated by the cross flow velocity. In the view where there is no surface spin, the profile of the edge of the boundary layer is symmetric with respect to the plane of the angle of attack. In the view where the surface is spinning, the profile of the boundary layer is asymmetric with respect to the plane of the angle of attack--thus, the inviscid pressure distribution (which responds to the aerodynamic shape composed of the model plus boundary layer displacement surface) is asymmetric and yields a net side force.

The U.S. Army Ballistic Research Laboratories have placed increased emphasis on research into the Magnus effect. In this paper, recent results will be discussed of a combined theoretical-experimental research effort to develop a method for computing Magnus effects for use in artillery projectile design.

2. THEORETICAL APPROACH

2.1 Background

Since the Magnus effect is a viscous phenomena, computation of the boundary layer development is the foundation for computations of the Magnus force. The boundary layer we are considering is fully three dimensional with the

added complication of the interaction of surface spin with the cross flow velocity. The inviscid flow also requires special attention since, in order to compute the Magnus force, the inviscid flow computation technique must be able to compute the three-dimensional flow over a body plus boundary layer displacement surface with no plane of symmetry.

The starting point for this theoretical effort was chosen to be the laminar boundary layer development over a yawed, 10° half angle cone in supersonic flow since convenient simplification is obtained in the equations of motion. The initial theoretical effort was carried out under contract with the University of California at Davis with Prof. H.A. Dwyer[1,2] as principal investigator. In order to follow up on the success of the work under this contract, Prof. Dwyer was engaged through the Army's Scientific Services program to extend the capabilities of the numerical technique to include effects of longitudinal pressure gradient and turbulence in order that computations of turbulent boundary layer development over arbitrary bodies of revolution closely approximating an artillery projectile shape could be accomplished. All of the numerical computations and some of the reprogramming required to enable computations to be made for an arbitrary body of revolution have been carried out as an in-house research task.

2.2 Boundary Layer Computations

The basic equations defining the three dimensional compressible, turbulent boundary layer flow over an axisymmetric body of revolution described by the relation $r = r(x)$ are listed below[3] (see coordinate system in Figure 3):

Continuity

$$\frac{\partial}{\partial x} (r\bar{\rho}\bar{u}) + \frac{\partial}{\partial y} (r\bar{\rho}\hat{v}) + \frac{\partial}{\partial \phi} (\bar{\rho}\bar{w}) = 0 \qquad (2.2.1)$$

x-Momentum

$$\bar{\rho} \left[\bar{u}\, \frac{\partial \bar{u}}{\partial x} + \hat{v}\, \frac{\partial \bar{u}}{\partial y} + \frac{\bar{w}}{r}\, \frac{\partial \bar{u}}{\partial \phi} - \frac{\bar{w}^2}{r}\, \frac{\partial r}{\partial x} = - \frac{\partial \bar{p}_e}{\partial x} + \frac{\partial}{\partial y} \left[\mu\, \frac{\partial \bar{u}}{\partial y} - \overline{\rho u'v'} \right] \qquad (2.2.2)$$

ϕ-Momentum

$$\bar{\rho} \left[\bar{u}\, \frac{\partial \bar{w}}{\partial x} + \hat{v}\, \frac{\partial \bar{w}}{\partial y} + \frac{\bar{w}}{r}\, \frac{\partial \bar{w}}{\partial \phi} + \frac{\bar{u}\bar{w}}{r}\, \frac{\partial r}{\partial x} = - \frac{1}{r}\, \frac{\partial \bar{p}e}{\partial \phi} + \frac{\partial}{\partial y} \left[\mu\, \frac{\partial \bar{w}}{\partial y} - \overline{\rho v'w'} \right] \qquad (2.2.3)$$

139

Energy

$$\bar{\rho} \left[\bar{u} \frac{\partial \bar{h}}{\partial x} + \hat{v} \frac{\partial \bar{h}}{\partial y} + \frac{\bar{w}}{r} \frac{\partial \bar{h}}{\partial \phi} \right] = \bar{u} \frac{\partial \bar{P}_e}{\partial x} + \frac{\bar{w}}{r} \frac{\partial \bar{P}_e}{\partial \phi}$$

$$+ \mu \left[\left(\frac{\partial \bar{u}}{\partial y} \right)^2 + \left(\frac{\partial \bar{w}}{\partial y} \right)^2 \right] - \overline{\rho u'v'} \frac{\partial \bar{u}}{\partial y} - \overline{\rho v'w'} \frac{\partial \bar{w}}{\partial y} \qquad (2.2.4)$$

$$+ \frac{\partial}{\partial y} \left[\frac{\mu}{Pr} \frac{\partial \bar{h}}{\partial y} - \overline{\rho v'h'} \right]$$

where $v = v + \dfrac{\overline{\rho' v'}}{\bar{\rho}}$ and the bar indicates a time averaged quantity.

In order to obtain closure for this system of equations, the following models of the turbulence terms have been introduced[4]:

(1) Turbulent shear stress

$$- \overline{\rho u'v'} = - \overline{\rho v'w'} = \bar{\rho} \ell^2 \left[\left(\frac{\partial \bar{u}}{\partial y} \right)^2 + \left(\frac{\partial \bar{w}}{\partial y} \right)^2 \right] = \varepsilon \left[\left(\frac{\partial \bar{u}}{\partial y} \right)^2 + \left(\frac{\partial \bar{w}}{\partial y} \right)^2 \right]^{\frac{1}{2}}$$

where ε is introduced as the turbulent eddy viscosity and the mixing length, $\ell = .09 \, \delta \tanh [(.4/.09) \, (y/\delta)]$. Van Driest damping is used to account for the effect of the laminar sublayer.

(2) Turbulent heat transfer

$$- \overline{\rho v'h'} = \frac{k_t}{c_p} \frac{\partial \bar{h}}{\partial y}$$

The turbulent Prandtl number is introduced as

$$Pr_t = c_p \varepsilon / k_t = 0.90$$

The numerical technique used to solve these equations is an implicit technique that takes into consideration the change in direction of the crossflow velocity that occurs on the side of the model where the inviscid crossflow opposes surface spin. This technique correctly models the crossflow convection process occurring within the boundary layer. In order to improve the speed and accuracy of the numerical solution, several coordinate transformations are employed:

(1) Mangler transformation of axisymmetric growth,

$$\xi \quad \int_o^x r^2 dx;$$

(2) Blasius type transformation of normal growth,

$$\eta = \left(\frac{P_\infty}{P_e} \right)^{\frac{1}{2}} \left(\frac{\rho_\infty u_\infty}{2\mu_\infty \xi} \right)^{\frac{1}{2}} \int_o^y \frac{\rho}{\rho_\infty} \quad rdy; \quad \text{and}$$

(3) coordinate stretching to allow closer grid spacing near the wall[5]

$n_j = 100$ (1.5 exp [(j-1)(1/60)(1/.05)] - 1)/(1.5 exp (1/.05) - 1)

where j = 1, 2, 3 61

In computing the boundary layer development, the effect of turbulence is turned on gradually over three longitudinal steps. The computation grid in the azimuthal plane is in 10° increments. Three iterations are performed at each station for turbulent computations. For comparison with experiment, the location of boundary layer transition is fixed at the location of the boundary layer trip on the experimental model.

2.3   Three Dimensional Displacement Surface

The three dimensional displacement surface is not merely the vector sum of the longitudinal and circumferential components of the boundary-layer displacement thicknesses. Instead, the differential equation derived by Moore[6]:

$$\frac{\partial}{\partial x} [\rho_e u_e r (\delta^*_{3D} - \delta^*_x)] + \frac{\partial}{\partial \phi} [\rho_e w_e (\delta^*_{3D} - \delta^*_\phi)] = 0 \qquad (2.3.1)$$

must be solved for δ^*_{3D}, the three dimensional boundary layer displacement thickness where

$$\delta^*_x = \int_o^\delta (1 - \frac{\rho u}{\rho_e u_e}) \, dy \text{ and } \delta^*_\phi = \int_o^\delta (1 - \frac{\rho w}{\rho_e w_e}) \, dy$$

Dwyer[3] has shown that equation (2.3.1) is of the general form

$$P \frac{\partial \delta^*_{3D}}{\partial x} + Q \frac{\partial \delta^*_{3D}}{\partial \phi} = R_1 \delta^*_{3D} + R_2 \qquad (2.3.2)$$

The singularity in δ^*_{3D} and δ^*_x at x = 0 can be avoided by starting the computations at a small, finite value of x and computing approximate starting conditions. Equation 2.3.2 can then be solved as an ordinary differential equation, providing the differencing in the circumferential direction is carried out from $\phi = 0$ to 180° and from $\phi = 0$ to -180° in order to obey the zone of influence defined by $\frac{dx}{d\phi} = r \frac{u_e}{w_e}$.

An example of computed values of δ^*_{3D} for the cone model are shown in Figure 4. It is seen that the laminar boundary layer is affected much more strongly by surface spin than the turbulent boundary layer.

141

2.4 Inviscid Computations

The development of a numerical technique for computing the three dimensional inviscid flow field over a yawed, pointed, body in supersonic flow was a very important step in the development of a capability for computing Magnus effects[7]. The program uses MacCormack's[8] "shock capturing" numerical technique. This is a second order accurate scheme that uses a predictor-corrector technique to solve the equations of motion in an implicit marching scheme. The unique feature of the program developed by Sanders for the Magnus problem is that the flow field is computed about an axisymmetric model plus displacement surface which, due to the distortion of the boundary layer by surface spin, has no plane of symmetry.

2.5 Sequence of Computations

The sequence of computations which must be run in order to compute Magnus effects is indicated in Figures 5a and 5b. Each block indicates a separate computer program along with its required input information and the output. The two main programs are outlined in asterisks.

In order to start the boundary layer computation for the spinning model, initial profile data are generated for the limiting case of the laminar boundary layer at the tip of a non-spinning cone. These data, along with the outer boundary condition of the inviscid flow, enable the marching technique to begin for specific conditions of Mach number, angle of attack, wall temperature, spin rate, and free stream properties. The output of this program consists of wall shear and centrifugal pressure gradient contributions to the Magnus effect (these will be discussed in more detail in section 2.6) and the longitudinal and circumferential components of the boundary layer displacement surface as functions of longitudinal and azimuthal position over the entire surface of the model.

The output of the boundary layer program is input to the program which solves for the three dimensional boundary layer displacement thickness, δ^*_{3D}. Input data for this program are in the surface coordinate system used for the boundary layer computations. The output of this program is transformed into a cylindrical coordinate system in order to facilitate computation of the inviscid flow. The output consists of the surface coordinates of the model plus δ^*_{3D} as well as the local derivatives of the surface coordinate in the axial and azimuthal directions.

142

The final step is the computation of the inviscid flow over the newly defined body which is of completely arbitrary configuration with no plane of symmetry. The starting conditions consist of the inviscid flow field for the asymptotic cone tip of the original model. Pitch and yaw plane force and moment aerodynamic coefficients are the final outputs obtained.

2.6 Boundary Layer Components of the Magnus Effect

Due to spin induced asymmetry in the computed velocity profiles, three contributions to the Magnus effect are generated within and at the surface of the spinning model which are independent of the boundary layer displacement effect sensed by the outer inviscid flow. These components are: (1) longitudinal velocity wall shear, $\tau_x = \mu (\partial u/\partial y)_{y+0}$; (2) circumferential velocity wall shear, $\tau_\phi = \mu (\partial w/\partial y)_{y=0}$; and (3) centrifugal pressure gradient, $\Delta p = \int_o^y \rho \frac{w^2}{r} dy$. For a non-spinning model, the net contribution of each of these components would be zero. However, due to the asymmetry induced by surface spin, a small contribution to a side force is obtained. The relative magnitude of these components of the Magnus force is shown in Figure 6. These computations are for a 10° half angle cone model. Figure 6 shows a comparison between laminar and turbulent boundary layer. The contributions of τ_ϕ and Δp oppose and are of comparable magnitude, while the contribution of τ_x is minimal. The arithmetic sum of the three components is indicated by $C_{YBL} = \tau_x + \tau_\phi + \Delta p$.

3. EXPERIMENTAL STUDIES

3.1 Background

Experimental studies are being carried out to provide data that will be useful in evaluating and help guide the development of the theoretical effort. The experimental studies consist of: (1) strain-gage balance force measurements; (2) optical studies of the effects of spin and yaw on boundary layer transition; (3) detailed profile measurements of the boundary layer on a yawed, spinning body of revolution; and (4) wall static pressure measurements on a yawed body of revolution. Experimental data have been obtained for three model configurations: (1) 10° half angle cone; (2) seven caliber tangent-ogive-cylinder model with a one caliber ogive; and (3) six caliber secant-ogive-cylinder model closely approximating

143

the M549 projectile shape. In this paper only those experimental measurements which will be compared to the theoretical computations will be discussed.

The experimental measurements have been carried out using Supersonic Tunnel No. 1 of the Ballistic Research Laboratories[9]. This is a continuous flow, closed return facility with a symmetric, flexible plate nozzle. Measurements have been made for M = 2, 3, and 4 over a Reynolds number range of 4.1 to 8.9×10^6 based on model length.

3.2 Force Measurements

Measurements of Magnus and normal force have been obtained using the strain-gage balance technique. The models are free to rotate on internally mounted ball bearings. High pressure air is forced into an inner cavity through the hollow support strut. As the air exhausts through a single row of turbine nozzles, the model is spun up to speeds as high as 40,000 RPM. The measurements are obtained while holding the model at a fixed angle of attack. Data from the strain-gage balance are recorded automatically on magnetic tape at fixed intervals of time as the model coasts down to zero spin.

3.3 Boundary Layer Profile Measurements

Measurements of the total head pressure through the boundary layer on the secant-ogive-cylinder model have been made using a specially constructed probe drive mechanism that drives the probe through a plane perpendicular to the model axis. A picture of the model with this probe drive mechanism in place is shown in Figure 7. Measurements have been obtained for three longitudinal stations on the model at M = 3, $\alpha = 2^o$ and 4°, and for spin rates of 0 and 20,000 RPM. The model RPM was held constant within $\pm$ 50 RPM using an automatic control for the air supply to the driving turbine. These measurements were obtained for azimuthal stations completely about the azimuthal plane at 30° increments. The total head probe has a flattened, rectangular opening .0076x.254cm with a lip thickness of .0025cm. The probe was oriented perpendicular to the model axis to measure the longitudinal component of the velocity. Velocity profiles were calculated from the total head measurements using the Rayleigh pitot formula and calculated values of wall static pressure. The static pressure was assumed constant through the

the boundary layer and was equal to the wall static pressure. The total temperature was assumed to vary according to the linear Crocco temperature-velocity relationship. The adiabatic wall temperature was computed using a recovery factor of 0.88.

The surveys through the boundary layer were obtained by starting at a position well beyond the boundary layer and taking data as the probe is driven toward the model surface. Contact with the model surface was indicated by the closing of an electrical ground circuit. While the model was spinning, the probe was driven close to, but not touching, the model surface ($y \sim 0.02$cm).

A measurement of the wall shear stress was obtained for the non-spinning model using the Preston tube technique. The Preston tube is a circular total head probe mounted flush with the model surface and sized to lie within the logarithmic portion of the law of the wall velocity profile. The wall shear stress was computed from the measured total pressure and the computed wall static pressure using the calibration relations given in reference 10.

These measurements were obtained for a tripped turbulent boundary layer. The trip consisted of three machined rings .152cm. thick with small diamond shaped protuberances.

4.   COMPARISON OF THEORY WITH EXPERIMENT

4.1   Magnus Force

Computed values of Magnus force are compared to the experimental measurements in Figures 8, 9, and 10. The Magnus force is shown plotted as a function of the nondimensional spin rate. Results for the cone model are shown in Figures 8 and 9. The agreement for M = 2 is exceptionally good; however, the agreement for M = 3 is also considered to be quite encouraging. The agreement indicated in Figure 10 for the secant-ogive-cylinder model is also considered to be remarkably good. The total computed Magnus force shown here is the arithmetic sum of the contributions due to τ_x, τ_ϕ, Δp, and δ^*_{3D}. It is worthwhile to emphasize that this marks the first time that computations of the Magnus effect have been carried out in a conceptually "exact" manner for the turbulent boundary layer on a realistic projectile configuration.

145

4.2   Boundary Layer Profile Characteristics

Computed and experimental velocity profiles are compared in Figure 11 for the longitudinal station closest to the model base. The comparison is considered to be very good although the computed profile is less full at $\phi = 0$ and more full at $\phi = 180^O$ than the experimental data. The agreement for these three dimensional profiles is actually comparable to that obtained for supersonic two dimensional flow measurements. The wall static pressure input to the boundary layer computation as a boundary condition is shown in Figure 12 for four azimuthal stations. On the ogive portion of the model, the longitudinal and circumferential velocities experience a favorable pressure gradient. As the base of the model is approached on the cylinder portion, the longitudinal velocity component encounters a mild adverse pressure gradient; and the circumferential velocity component must negotiate first a favorable and then an adverse pressure gradient.

Values for the longitudinal component of the boundary layer displacement thickness are compared in Figure 13. Values are shown for three longitudinal stations for $M = 3$ and $\alpha = 2^O$. These plots indicate excellent agreement between theory and experiment at $Z/D = 4.44$; however, the agreement is less satisfactory at the last station, $Z/D = 5.56$. This plot indicates significant disagreement between theory and experiment for the boundary layer growth rate. This is not surprising since the turbulence model did not provide for any adjustment as a function of pressure gradient. Since there has been some experimental evidence that the ratio $\overline{v'w'}/\overline{u'v'}$ does not remain a constant = 1 through the boundary layer, a computation was run in which the ratio $\overline{v'w'}/\overline{u'v'}$ was fixed at 0.3. The results of this computation are shown in Figure 13 as a dashed line. It is interesting to see the significant effect that this modification has on the longitudinal displacement thickness. It is also apparent that this modification does not yield a physically reasonable azimuthal distribution for δ_x^*.

Computed and measured values for skin friction coefficient are shown in Figure 14. The skin friction coefficient is referenced to free stream static properties upstream of the model rather than the more conventional

approach of using local properties at the edge of the boundary layer. The agreement indicated is within ±10%. This is considered quite good since the Preston tube is expected to yield an accuracy of ±10% for two dimensional flat plate boundary layer flow. The use of the Preston tube here to obtain measurements in a three dimensional boundary layer flow using two dimensional calibration data must be regarded as speculative and mainly of qualitative interest.

4.3   Summary Comments

The general impression obtained in comparing the computations to experimental data is that the numerical techniques are working quite well and yielding very impressive agreement with experimental data. The results for Magnus force are considered extremely encouraging. The comparisons with detailed profile characteristics reveal minor differences that should yield to further numerical studies using more sophisticated models for the turbulent transport properties. Other refinements in the boundary layer computation such as a correction for transverse curvature and inclusion of boundary region effects should be incorporated. However, it is felt that the numerical techniques now available are capable of yielding computations of Magnus effects that would be useful for engineering design purposes.

5.   CONCLUDING REMARKS

A combined theoretical-experimental study of the Magnus effects on yawed, spinning projectiles has been discussed. The overall objective of this effort is to develop a method for computing Magnus effects that could be used in the design of artillery projectiles. Numerical techniques have been developed for computing: (1) the three dimensional turbulent boundary layer development over a yawed, spinning body of revolution; (2) the three dimensional boundary-layer displacement surface for an arbitrary body of revolution; and (3) the three dimensional inviscid flow field over a yawed, pointed body of completely general configuration with no plane of symmetry. The computations have been compared to experimental measurements of Magnus force and turbulent boundary layer profile characteristics. The agreement between the theory and experiment is considered to be exceptionally good. It is concluded that the overall

147

objective of this research effort has been successfully accomplished. However, further effort to refine the computation capability now available and obtain more comprehensive comparisons with experimental data should be carried out. It is further emphasized that effects due to nose bluntness and protuberances such as rotating bands must be examined before the computation capability can be considered to have the full capability desired for artillery projectile design studies.

LIST OF SYMBOLS

c_f skin friction coefficient

c_p specific heat at constant pressure

C_n normal force coefficient

C_y Magnus (side) force coefficient

D diameter of base of model

h static enthalpy

k molecular conductivity

k_t turbulent conductivity

ℓ mixing length

p pressure

P spin rate, radians per second

P_r molecular Prandtl no., $c_p \mu/k = .71$

r local radius of model

Re_ℓ Reynolds number based on model length

u velocity component in x direction

v velocity component in y direction

V velocity along model trajectory

w velocity component in ϕ direction

x surface coordinate in longitudinal direction

y, Y coordinate perpendicular to local surface

z cylindrical coordinate along model axis

α angle of attack

ϵ turbulent eddy viscosity

δ boundary layer thickness

δ^* boundary layer displacement thickness

Δp centrifugal pressure gradient contribution to side force

η transformed y coordinate

μ molecular viscosity

ξ transformed x coordinate

ρ density

τ_x longitudinal velocity wall shear contribution to side force

τ_ϕ circumferential velocity wall shear contribution to side force

ϕ coordinate in circumferential (azimuthal) direction

Subscripts

e   edge of boundary layer

∞ free stream reference condition

Superscripts

'   fluctuating quantity

–   time averaged quantity

LIST OF REFERENCES

1.   H.A. Dwyer, "Three Dimensional Flow Studies Over a Spinning Cone at Angle of Attach," BRL Contract Report No. 137, U.S. Army Ballistic Research Laboratories, Aberdeen Proving Ground, Maryland, February 1974, AD774795.

2.   H.A. Dwyer and B.R. Sanders, "Magnus Forces on Spinning Supersonic Cones. Part I: The Boundary Layer," BRL Contract Report No. 248, U.S. Army Ballistic Research Laboratories, Aberdeen Proving Ground, Maryland, July 1975. AD A013518.

3.   H.A. Dwyer, "Methods for Computing Magnus Effects on Artillery Projectiles," BRL Contract Report, to be published, U.S. Army Ballistic Research Laboratories, Aberdeen Proving Ground, Maryland.

4.   T.C. Lin and S.G. Rubin, "A Two-Layer Model for Coupled Three Dimensional Viscous and Inviscid Flow Calculations," AIAA Paper No. 75-853, 8th Fluid and Plasma Dynamics Conference, Hartford, Connecticut, June 1975.

5.   F.G. Blottner, "Variable Grid Scheme Applied to Turbulent Boundary Layers," Journal of Computer Methods in Applied Mechanics and Engineering, 1975.

6.   F.N. Moore, "Displacement Effect of a Three-Dimensional Boundary Layer," NACA TN 2722, June 1952.

7.   B.R. Sanders, "Three-Dimensional, Steady, Inviscid Flow Field Calculations with Application to the Magnus Problem," PhD Dissertation, University of California, Davis, California, May 1974.

8.   R.W. MacCormack, "Numerical Solution of the Interaction of a Shock Wave With a Laminar Boundary Layer," Proceeding of the International Conference on Numerical Methods in Fluid Dynamics, Lecture Notes in Physics, Vol. 8, Maurice Nolt, ed., Springer-Verlag, 1971.

9.   J.C. McMullen, "Wind Tunnel Testing Facilities at the Ballistic Research Laboratories," BRL Memorandum Report No. 1292, U.S. Army Ballistic Research Laboratories, Aberdeen Proving Ground, Maryland, July 1960. AD 244180.

10. P. Bradshaw and K. Unsworth, "A Note on Preston Tube Calibrations in Compressible Flow," IC Aero Report 73-07, Imperial College of Science and Technology, London, Great Britain, September 1973.
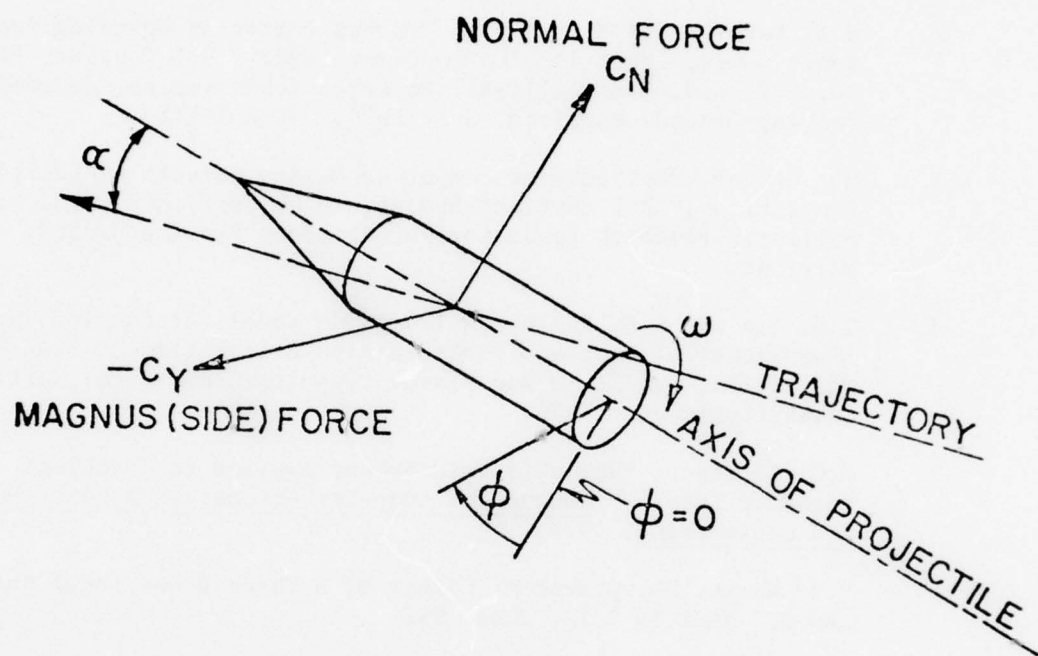
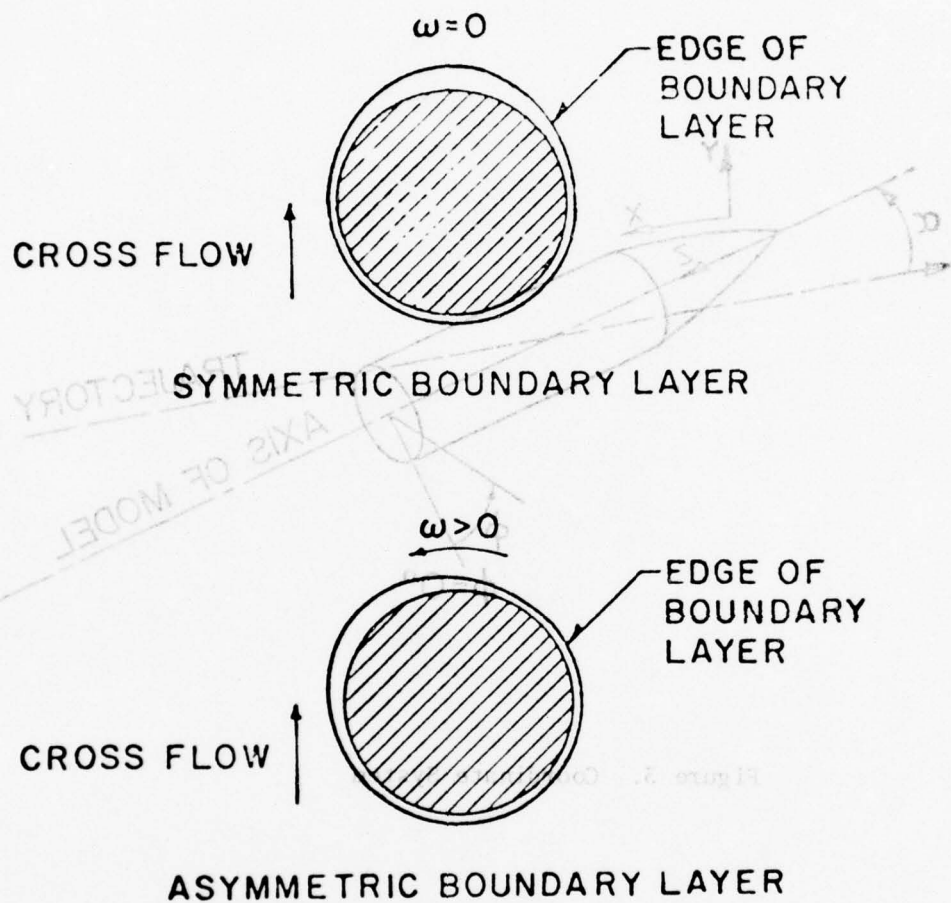Figure 1. Magnus and Normal Fo-ces on Spinning Projectile

Figure 2. Schematic Illustration of Spin Induced
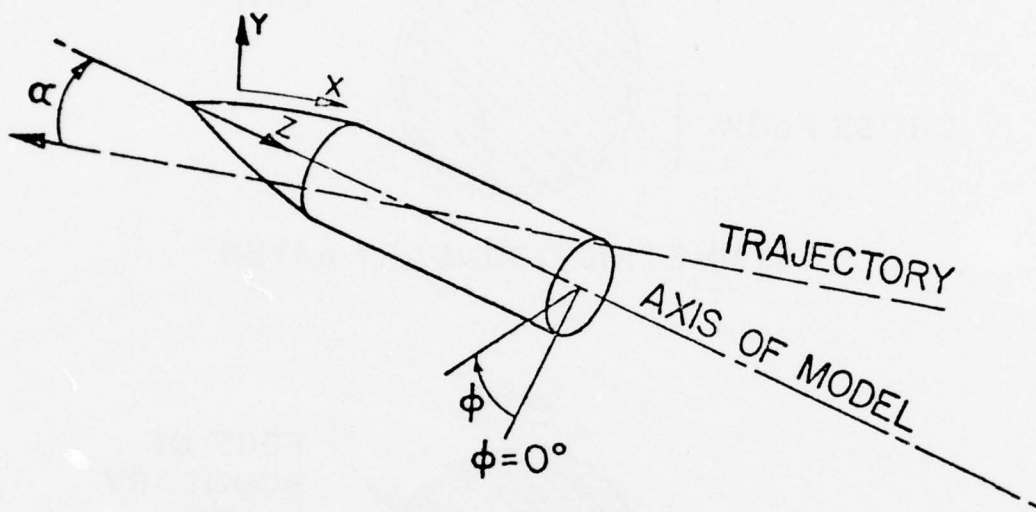Boundary Layer Distortion
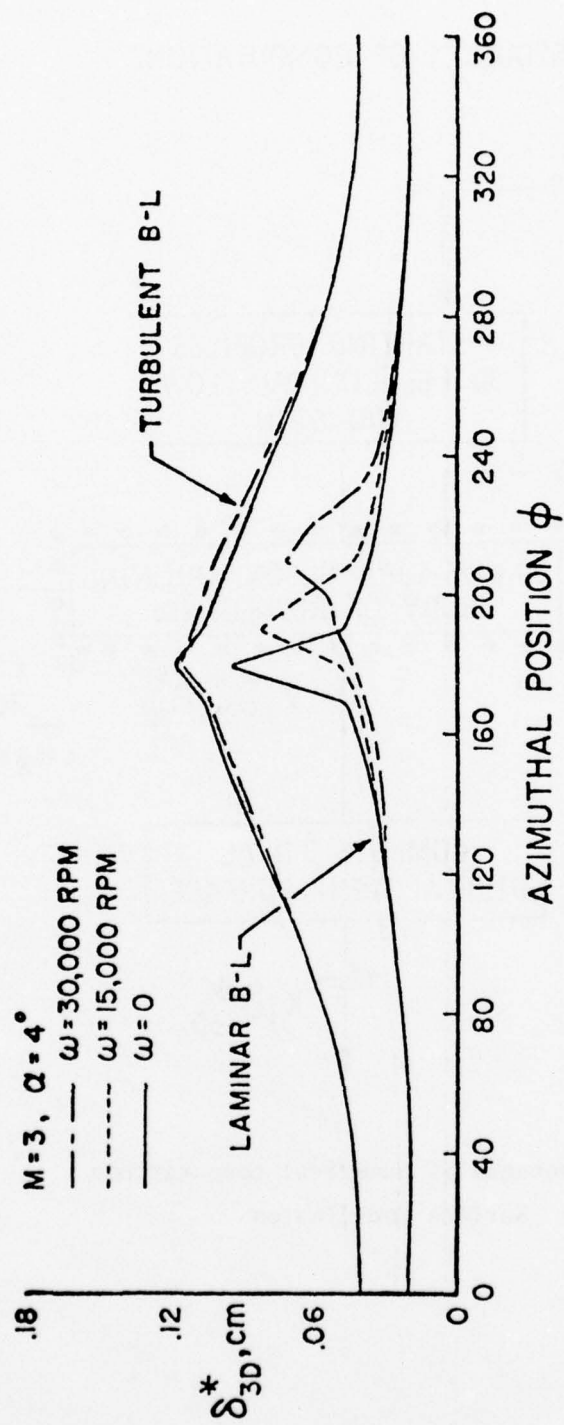
Figure 3. Coordinate System

Figure 4. Computations of δ_{3D}^* for 10^0 Cone Model

SEQUENCE OF COMPUTATIONS

APPROX PROFILES
3 D INVISCID FLOW
u, w, T, p

STARTING PROFILES
3D LBL CONICAL FLOW
W/O SPIN

3 D INVISCID FLOW

3D LAM-TURB BL ON SPINNING
BODY OF REVOLUTION

$x, \delta_x^*, \delta_\phi^*$

BL CONTRIBUTIONS
TO MAGNUS
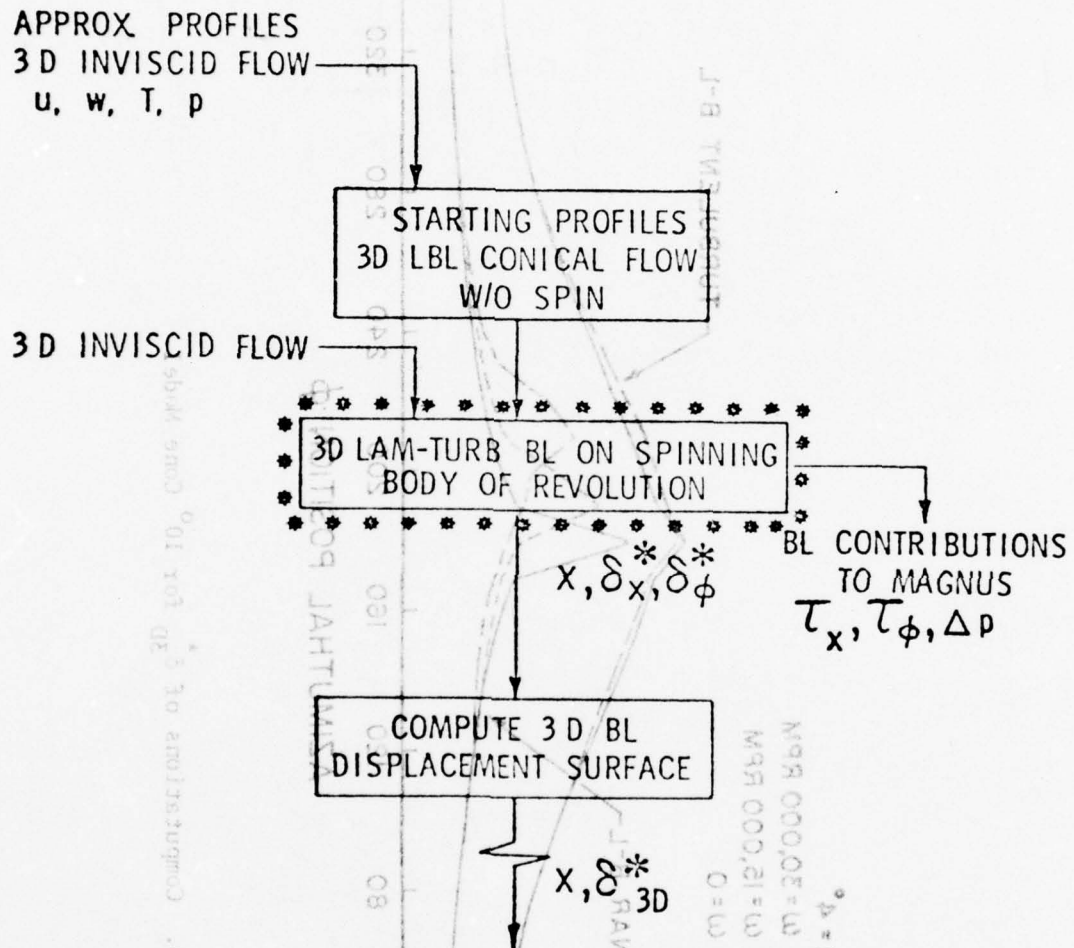$\tau_x, \tau_\phi, \Delta p$

COMPUTE 3 D BL
DISPLACEMENT SURFACE

x, δ^*_{3D}

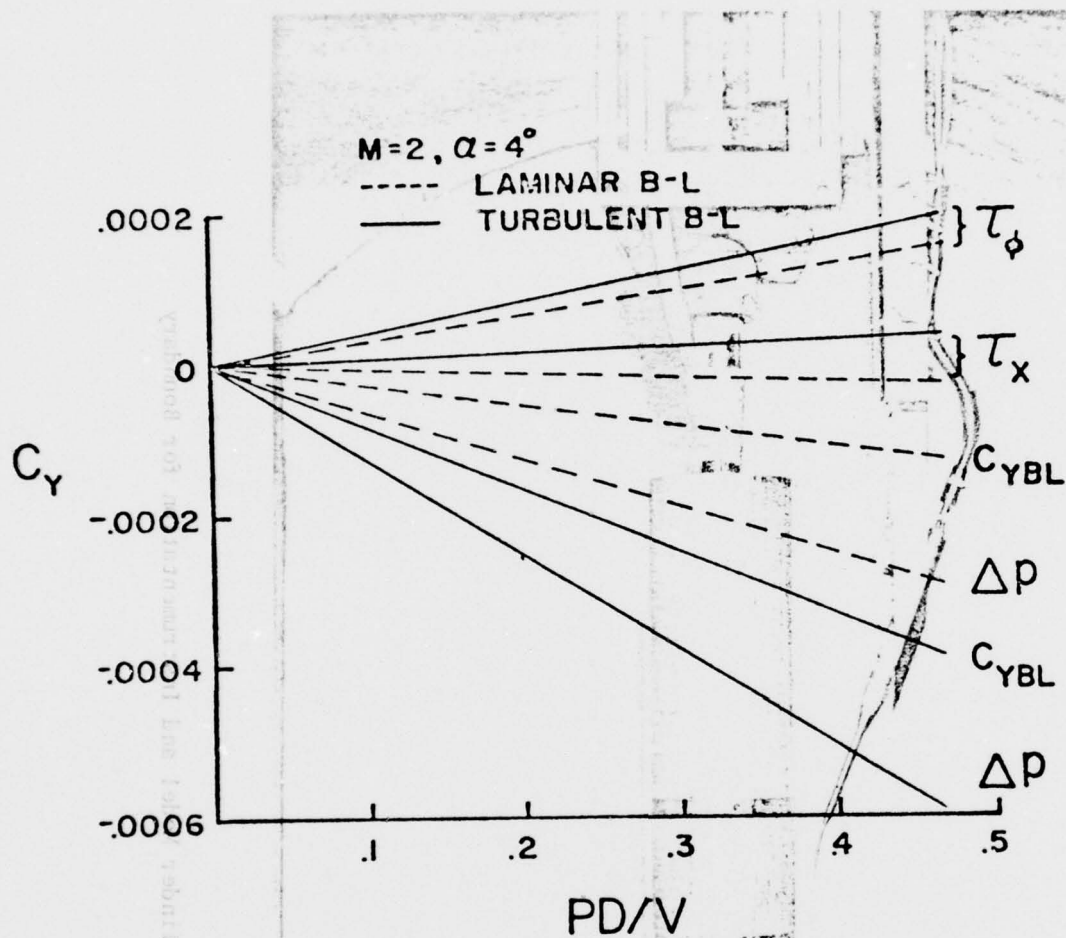Figure 5. Sequence of Numerical Computations

a) Surface Coordinates

Figure 6. Boundary Layer Contributions to the Magnus Effect:
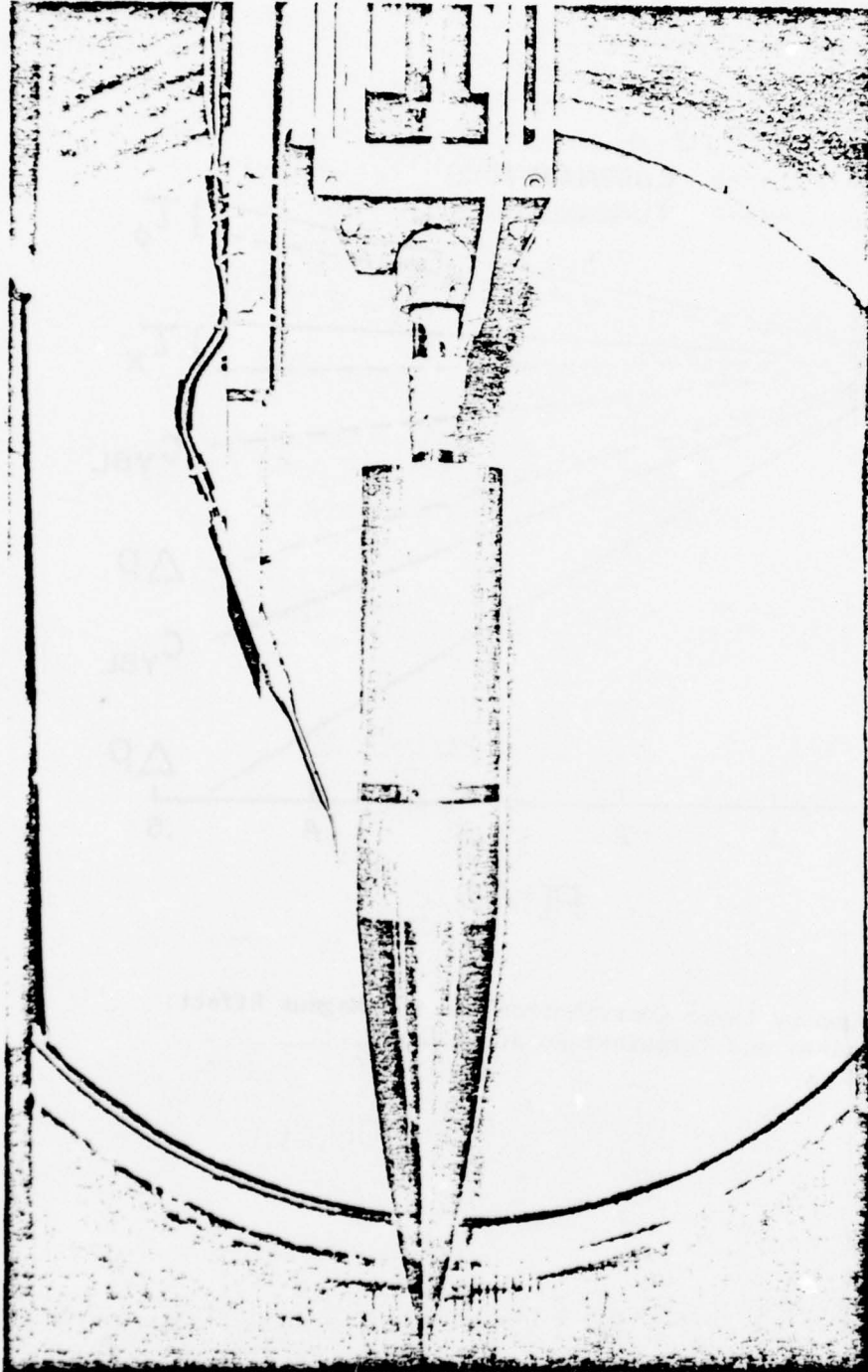Laminar and Turbulent Boundary Layer

Figure 7. Secant-Ogive-Cylinder Model and Instrumentation for Boundary
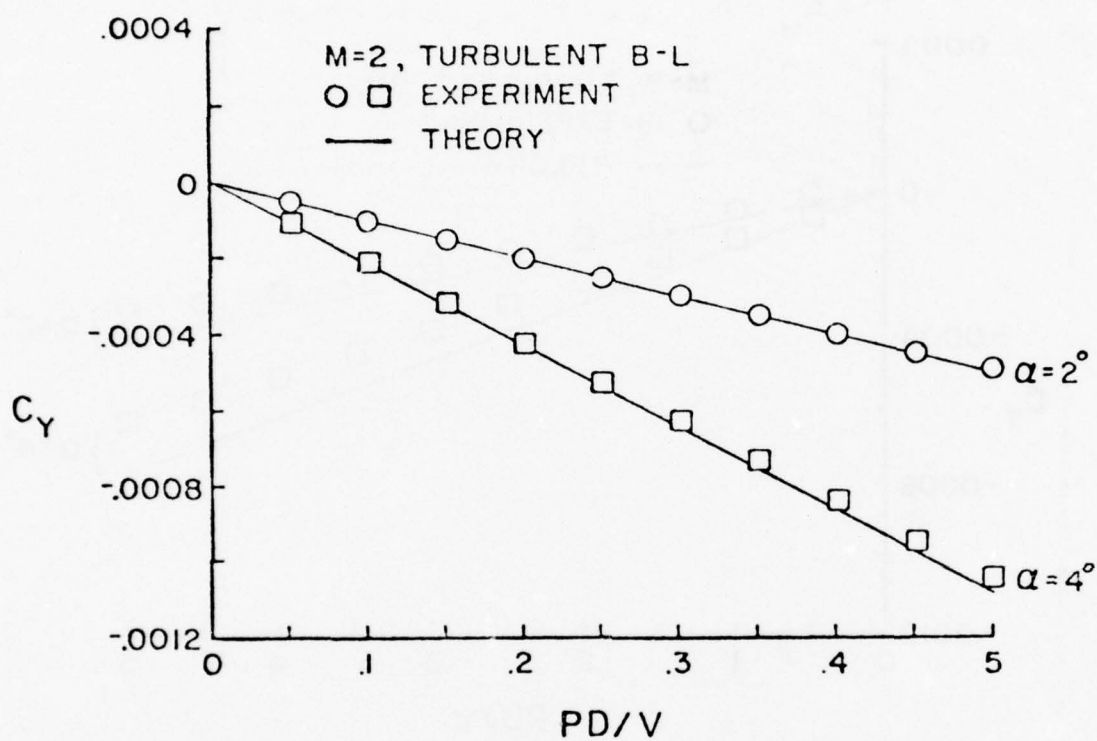Layer Surveys

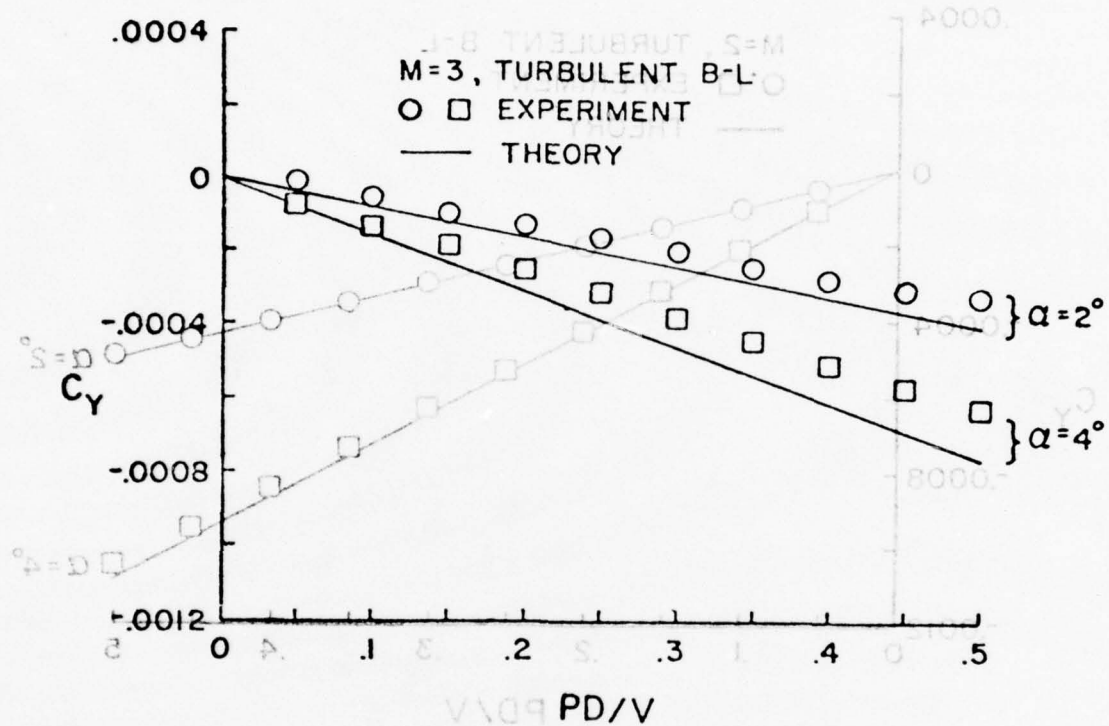Figure 8. Magnus Force vs Spin Rate, Theory Compared with Experiment, 10° Cone Model, M = 2

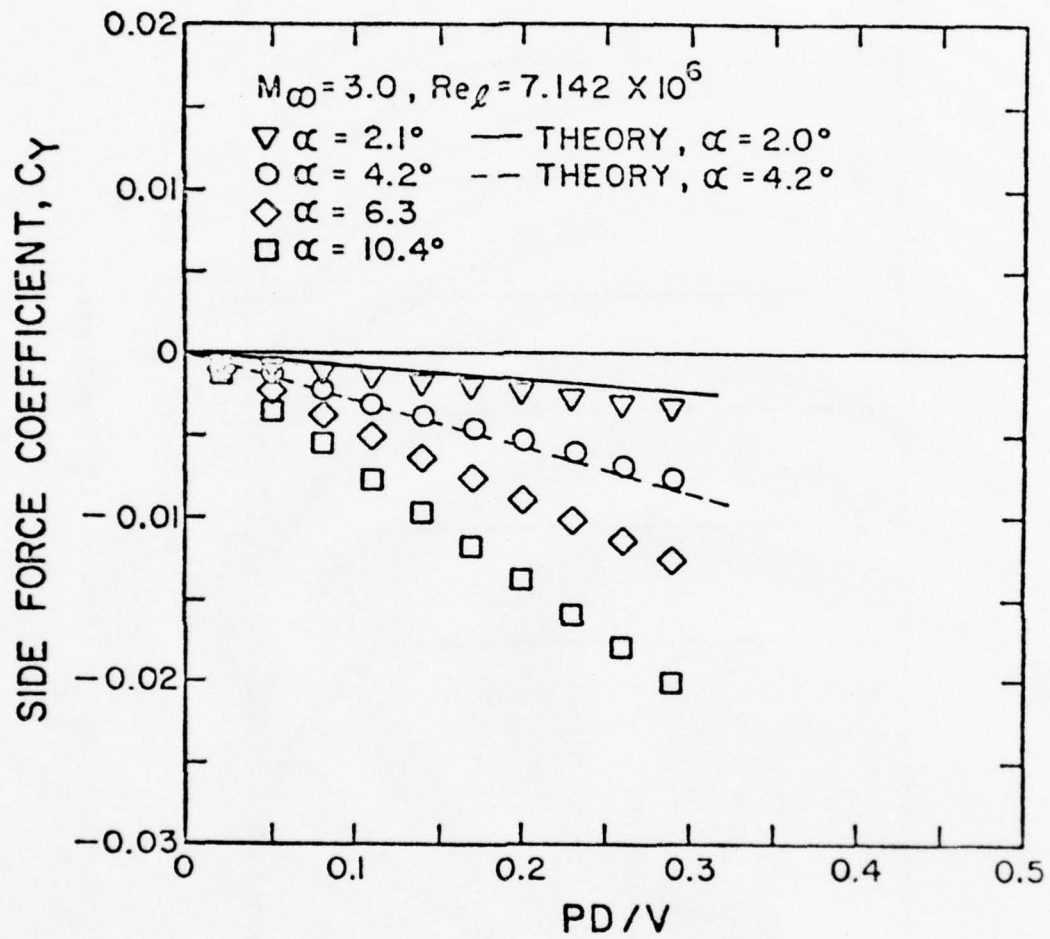Figure 9. Magnus Force vs Spin Rate, Theory Compared with Experiment, 10° Cone Model, M = 3

Figure 10. Magnus Force vs Spin Rate, Theory Compared
with Experiment, SOC Model, M = 3
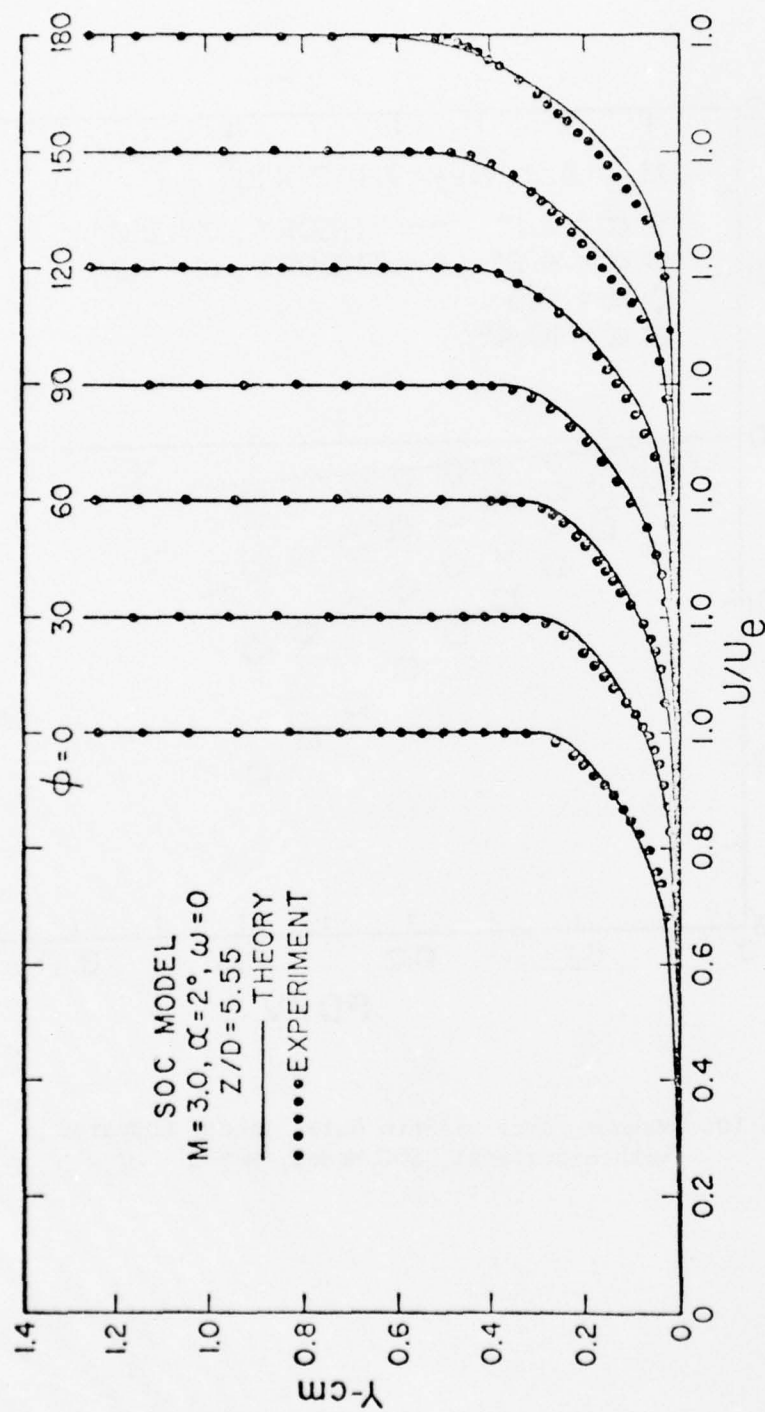
Figure 11. Velocity Profiles, Theory Compared with Experiment, SOC Model, $M = 3$, $\alpha = 2^o$
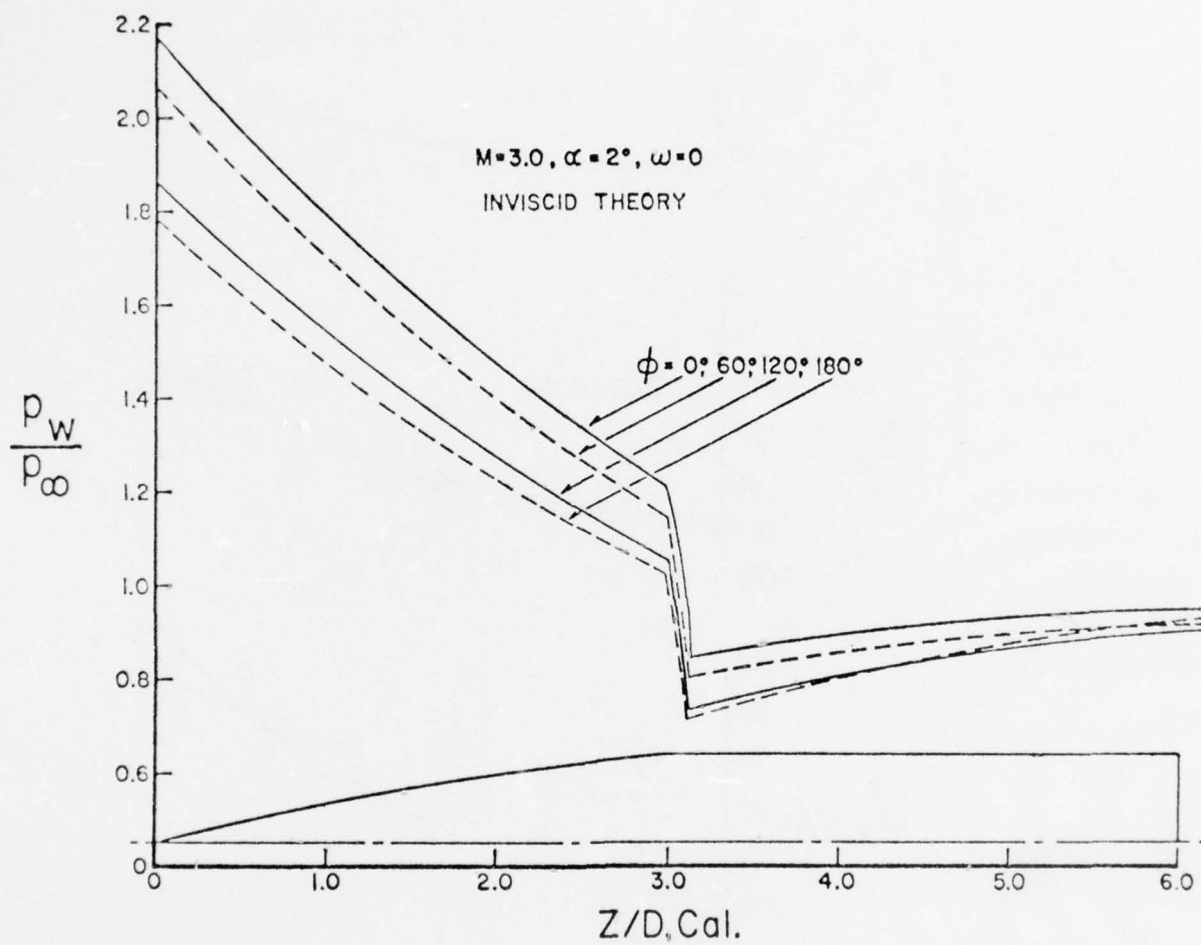
Figure 12. Computed Wall Static Pressure Distribution Used for
Boundary Layer Computation, SOC Model

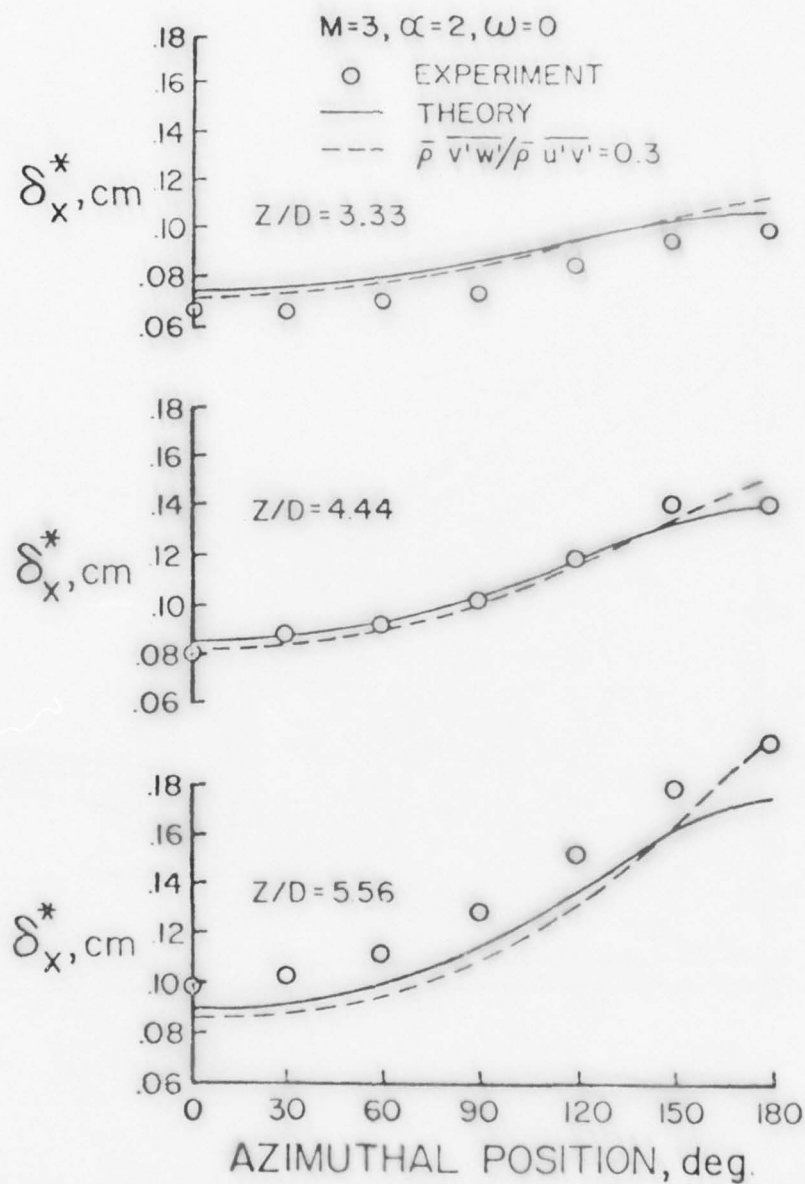Figure 13. Boundary Layer Displacement Thickness, δ_x^*, Theory Compared with Experiment, SOC Model, $M = 3$, $\alpha = 2^\circ$
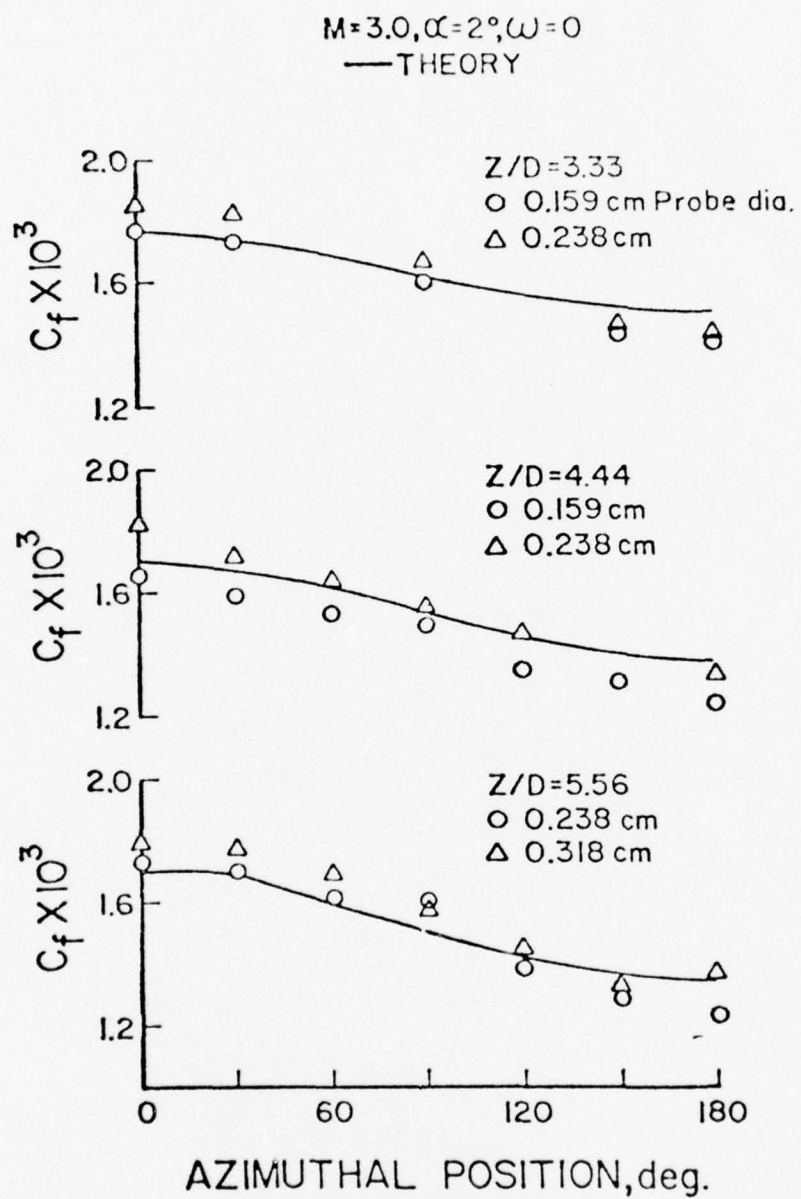
164

Figure 14. Skin Friction Coefficient, Theory Compared
with Experiment, SOC Model, $M = 3$, $\alpha = 2°$

MEASUREMENTS OF INCOMPRESSIBLE
VELOCITY FLUCTUATIONS AND THEIR EFFECT
ON TURBULENT BOUNDARY LAYER CHARACTERISTICS

by

H.U. Meier
Deutsche Forschungs- und Versuchsanstalt
für Luft- und Raumfahrt E.V.
Aerodynamische Versuchsanstalt Göttingen
Bunsenstrasse 10
D-3400 Göttingen

1. Introduction

The influence of the wind tunnel turbulence on experimental results
is a well-known phenomenon. However, the effect of grid-generated
turbulence levels in the range of $0.1\% \leq Tu \leq 1.\%$ is not investigated
experimentally. At the previous DEA meeting in 1975 a current investi-
gation in the DFVLR-AVA, being concerned with the influence of such low
free stream turbulence on the development on a turbulent boundary layer,
was described briefly [1]. Solving calibration problems of hot wires,
applied to flows of extremely low turbulence, extensive measurements of
velocity flucturations in a subsonic wind tunnel flow were carried out.

The decay of turbulence intensity and the deviation from isotropic
turbulence was studied. Isotropic turbulence is the simplest type
of turbulence, since no preference for any specific direction of the
fluctuating velocities occurs ($u' = v' = w'$). Thus a minimum number
of quantities and relations are required to describe its structure and
behaviour. Even when no actual turbulent flow shows true isotropy the

167

turbulence is often isotropic to a sufficient degree of approximation. Then simple theoretical hypothesis can be applied for the further analysis of the experimental data.

In order to be able to study the influence of variable free stream turbulence levels on the boundary layer development, velocity profiles in side-wall boundary layers were measured for different distances and approximately zero pressure gradient in flow direction.

2. Experimental Set-up

The low turbulence tunnel of the DFVLR-AVA was described in detail in Ref. [1]. For convenience and better understanding the sketch of the tunnel and the test section are given again in this paper (compare Figs. 1 and 2). The velocity flucturations in x-direction (flow direction) were measured with a single hot wire, and in y- and z-direction with X-hot wires. The hot wire probes were connected to a constant temperature anemometer unit from Thermosystem Inc. (TSI). The output was obtained from a RMS-voltmeter (TSI) which enabled measurements of true RMS-values $(\overline{u'^2})^{\frac{1}{2}}$, $(\overline{v'^2})^{\frac{1}{2}}$, $(\overline{w'^2})^{\frac{1}{2}}$ of the fluctuating velocity components u', v', and w'. All turbulence measurements were carried out with a low pass filter with a maximum frequency of 2 kHz. The calibration procedure of the hot wires is given in Ref. [1] .

3. Results

3.1 Turbulence Measurements

The turbulence level in the wind tunnel was investigated with and without grids. Due to the fact that the grids were installed at the end of the nozzle exit the decay of grid generated turbulence in a rectangular channel could be simulated. Three different grid sizes were used. The geometry was varied in such a way that the difference (M-d) between meshsize M and the wire diameter d was approximately constant. In Fig. 3 the measured turbulence levels in the wind

168

tunnel with and without grids for different distances from the leading edge are shown. The pressure gradient in flow direction at $U_\infty \approx 30$ m/s was approximately zero. The black symbols are indicating measurements with a single hot wire probe while the open symbolds are representing results from a X-hot wire probe. The results of the single wire probe are slightly higher compared with those of the X-probe, but they are in the range of the expected accuracy.

In order to be able to proof the existence of quasi isotropic turbulence in the investigated tunnel flow, the v' and w' fluctuating velocity components were measured with X-hot wires. The results of these tubulence measurements are shown in Figs. 4 and 5. The decay of the fluctuating velocity components v', w' in y- and z-direction with increasing distance from the leading edge is similar to that of the u' -velocity component. However, as shown in Fig. 6, the measurements indicated that the ratio of the longitudinal to lateral turbulent intensities is consistently larger than 1.1 for distances $x_{LE} \leq 1500$ mm. This result is qualitatively in agreement with published results of anisotropic grid turbulence. UBEROI [2] found by measurements of turbulence behind a square-mesh biplane grid made of round rods that the RMS turbulent velocity fluucturations are characterized by

$$\left(\overline{v'^2}\right)^{\frac{1}{2}} = \left(\overline{w'^2}\right)^{\frac{1}{2}} = \frac{\left(\overline{u'^2}\right)^{\frac{1}{2}}}{1.18} \quad .$$

However, in our experiment the $\left(\overline{v'^2}\right)^{\frac{1}{2}}$ -component is smaller than the $\left(\overline{w'^2}\right)^{\frac{1}{2}}$ -component. This result can be explained by the special geometry of the wind tunnel test section where the dimension in z-direction is about five times of that in y-direction. (The measurements of UBEROI were made in an axisymmetric nozzle.) As

169

indicated in Fig. 6 the tunnel turbulence has become isotropic*)
by a distance of $x_{LE} \sim 2,000$ mm only for the small grids 1 and 2.
The turbulence generated by the largest investigated grid (3) is
even for this long distance not isotropic. This result is not in
agreement with experiments carried out by PORTFORS and KEFFER [3]
who found already isotropic turbulence at a distance from the
leading edge of about 30 mesh lengths [30 M $\hat{=}$ ($x_{LE} \sim 600$ mm)].
Clearly, the experimental verification of a condition of isotropy
depends upon the accuracy to which the three components of turbulent
intensity can be determined. In Ref. [3] it is demonstrated
that the experimental results depend strongly on the applied
measuring technique and data reduction procedure. However, the
authors of Ref. [3] found that for distances $x_G/M \stackrel{<}{=} 20$ (x_G distance
from the grid) the ratios of the longitudinal to lateral compo-
nents $(\overline{u'^2})^{\frac{1}{2}} / (\overline{w'^2})^{\frac{1}{2}}$ is greater than unity, while the RMS values
of the velocity fluctuations $(\overline{u'^2})^{\frac{1}{2}} / (\overline{v'^2})^{\frac{1}{2}}$ are considerably
smaller than unity. This was not found by UBEROI and in the here
described experiments.

If simple theoretical relations for the decay of the turbulence
intensity u'/U_∞ shall be applied, the distance from the virtual
origin, at which $U_\infty /u' = 0$, to the grid has to be known.

In order to find this virtual origin it was assumed - following
ROTTA [4] - that the decay of the RMS-values of the measured
longitudinal velocity fluctuations $(\overline{u'^2})^{\frac{1}{2}}$ is proportional to
$(x_{LE})^{-n}$. (For our test conditions $x_G \sim x_{LE}$.) COMTE-BELLOT and
CORRSIN [5] found values for n in the range of n = 1.2 and n =
1.3. In Fig. 7 the calculated values of $(\overline{u'^2})^{-(2/n)}$, (n = 1.3),
for the three different investigated grids are plotted versus
the distance from the leading edge. x_{LE}: The points were approxi-
mated by straight lines and the distance x_{vo} from the grid to
the virtual origin was found to be $x_{vo} \sim 250$ mm. The slope of the

---

*) Actually, true isotropy requires more than equality of the
intensity components. Their energy spectra must be related
through the isotropic expressions over the complete wave-
number range of turbulence. This was not proofed in the
experiment.

straight lines in Fig. 7 indicated that the measured turbulence data for the different grids could be correlated multiplying the distance $(x_{LE} - x_{vo})$ with the grid-parameter M/d. The result is shown in Fig. 8. The decay of turbulence intensity of all three grids can be correlated and described by the relation

$$\left(\frac{U_\infty}{u'}\right)^{2/n} = 0.133 \ [(x_{LE} - x_{vo}) \ \frac{M}{d}] \ .$$

3.2   Boundary Layer Mean Flow Measurements

Knowing the turbulence intensities of the wind tunnel, boundary layer measurements were made with and without grids. The transition from laminar to turbulent boundary layer flow was fixed installing an artificial roughness at x_{LE} = 50 mm. In Fig. 9 and 10 the measured velocity profiles U/u_τ without and with grids are plotted versus the dimensionless wall distance Y* (u_τ is the shear stress velocity). The boundary layer velocity profiles at very low turbulence levels in the free stream show in the outer part a large "overshoot" of the velocity ratio U/u_τ above the logarithmic line

$$\pi = \frac{\kappa}{2} \ \Delta \ \frac{U}{u_\tau} \qquad .$$

(κ = 0.4, the von Kármán constant).

At low turbulence levels π is seen to have approximately the same value that COLES found for the flat plate ($\pi \sim 0.5$). The influence of the free stream turbulence on the wake component is clearly indicated by the velocity profiles in Fig. 10. The velocity overshoot decreases if the turbulence intensity is increased by very small amounts ($\Delta Tu_1 \sim 0.4\%$). It becomes clear from a further analysis of the measured boundary layer profiles that the main change will occur in the wake region of the profile. The boundary layer thickness increases considerably with increasing turbulence intensity.

171

The local skin friction coefficient calculated from the measured profiles - using the law of the wall, or Ludwieg/Tillmann formula - remains approximately constant. This can be seen too from the development of the momentum thicknesses δ_2 with increasing distances x_{LE} (compare Fig. 11). The boundary layer measurements with grid generated free stream turbulence lead to higher integral values δ_2, where

$$\delta_2 = \int_{y=0}^{y=\delta} \frac{U}{U_\infty} \left(1 - \frac{U}{U_\infty}\right) dy \quad .$$

On the other hand the slope $d\delta_2/dx$ is equal to that of the low turbulence case. The reason for the high values of δ_2 is based on two facts:

Due to the location of the grid close to the leading edge (compare Fig. 2)

   -the turbulence intensity is extremely high when the boundary layer starts to grow

   -and due to the wake of one rod, the boundary layer starts with a final amount of momentum loss, which appears as an additive constant for all distances.

The results of these measurements imploy that these two effects should be separated. In the meantime measurements are carried out where the grids are located about 500 mm upstream of the leading in the tunnel nozzle. Now the boundary layer can be studied at low, grid generated turbulence intensity and very small changes of the turbulence intensity Tu in x-direction.

Acknowledgement:

4. References

1.   Meier, H. U., The influence of low free stream turbulence on the development of the turbulent boundary layer at zero pressure gradient - Preliminary Results - In: Boundary Layer Effects 4th US-FRG Meeting BMV$_g$-FBWT 75-21, 1975.

2.	Uberoni, M.S., Small exisymmetric contraction of grid turbulence, J. Fluid Mech., Vol. 24, Part 3, pp. 539-543, 1966.

3.	Portfors, E. A. and Keffer, J. F., Isotropy in initial period grid turbulence, Phys. Fluids, Vol. 12, pp. 1519-1521, 1969.

4.	Rotta, J. C., Turbulente Strömungen, B. G. Teubner Verlag, Stuttgart, 1971.

5.	Comte-Bellot, G., The use of a contraction to improve the isotropy of grid-generated turbulence, J. Fluid Mech., Vol. 25, pp. 657-682, 1966.

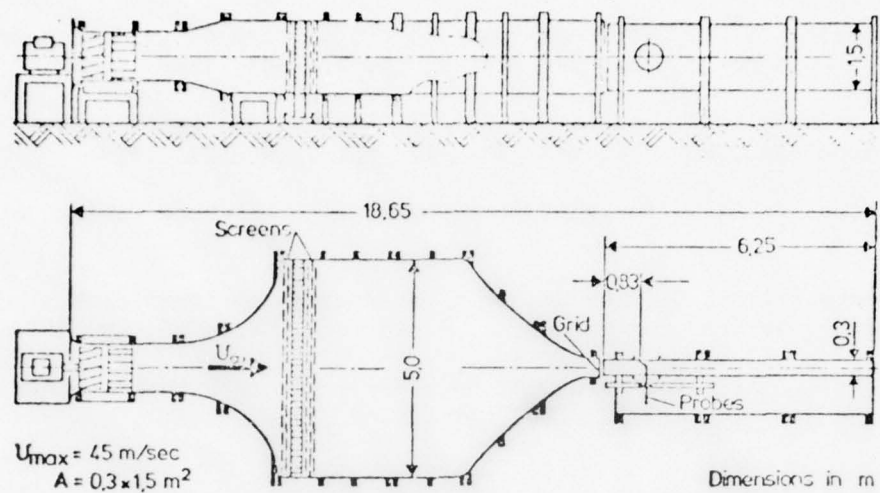6.	Coles, D. E., The turbulent boundary layer in a compressible fluid, Rand Report R 403-PR, 1962, ARC 24-497, 1963.
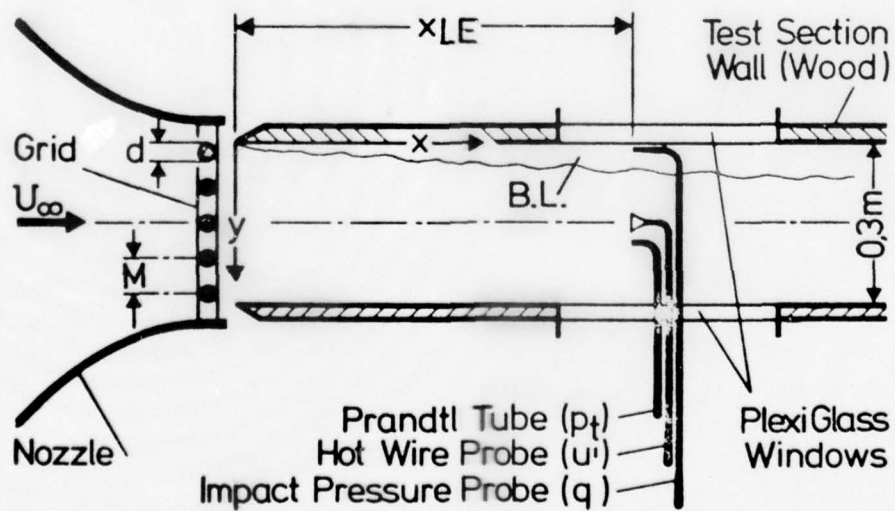
Fig. 1   Low Turbulence Wind Tunnel of the DFVLR-AVA

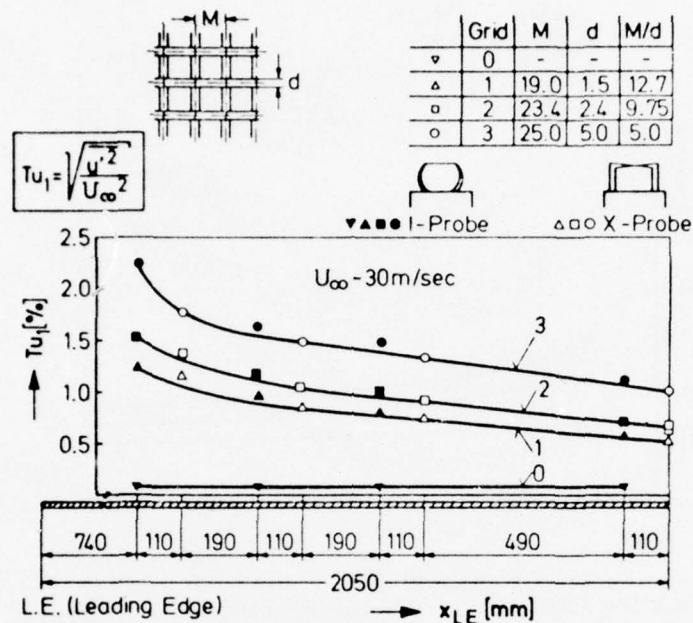Fig. 2   Sketch of the Test Section

174

Grid	M	d	M/d
0	-	-	-
1	19.0	1.5	12.7
2	23.4	2.4	9.75
3	25.0	5.0	5.0

$$Tu_1 = \sqrt{\frac{\overline{u'^2}}{U_\infty^2}}$$

▼▲■● I-Probe △□○ X-Probe

$U_\infty - 30\,m/sec$

Fig. 3 Decay of the Turbulence Level - $Tu_1 = \sqrt{\overline{u'^2}/U_\infty^2}$ Downstream of Grids

Grid	M	d	M/d
1	19.0	1.5	12.7
2	23.4	2.4	9.75
3	25.0	5.0	5.0

$$Tu_2 = \sqrt{\frac{\overline{v'^2}}{U_\infty^2}}$$
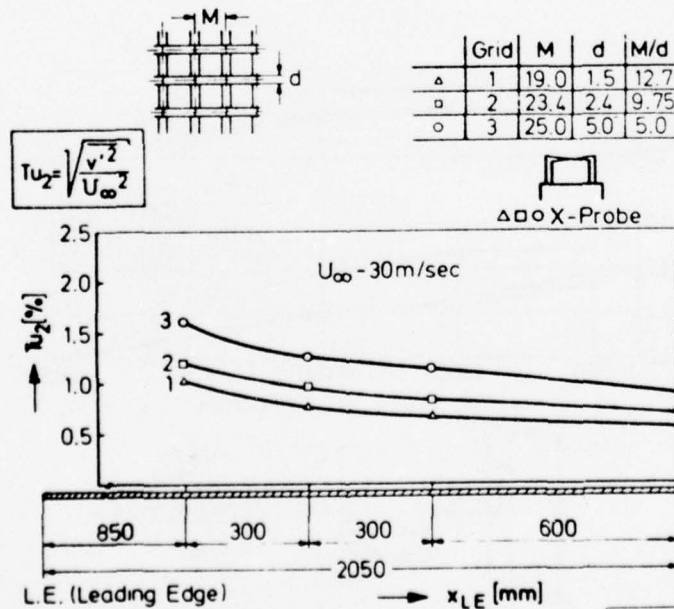
△□○ X-Probe

$U_\infty - 30\,m/sec$

Fig. 4 Decay of the Turbulence Level $Tu_2 = \sqrt{\overline{v'^2}/U_\infty^2}$ Downstream of Grids
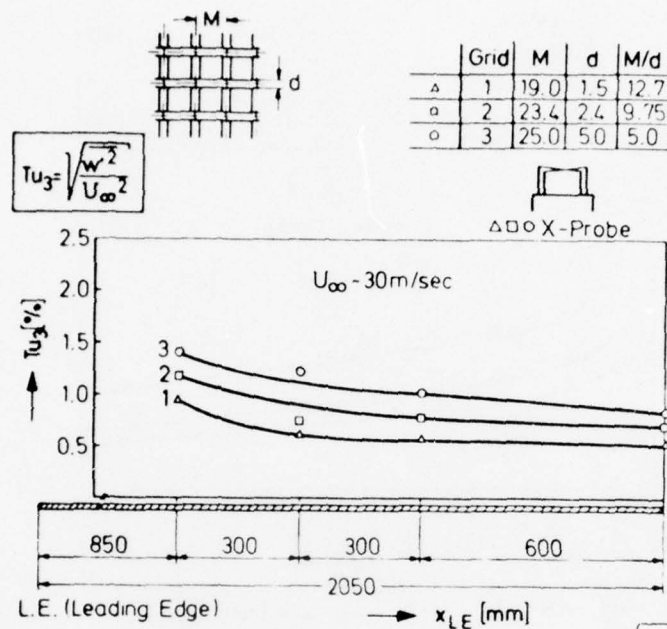
175

Fig. 5   Decay of the Turbulence Level $Tu_3 = \sqrt{\overline{w'^2}/U_\infty^2}$
Downstream of Grids
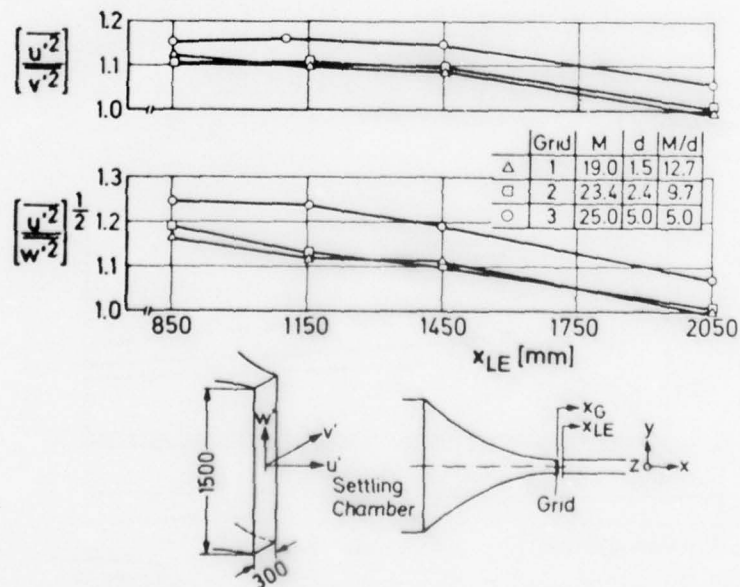
Fig. 6   Decay of the Longitudinal to Lateral Turbulent Intensity
Ratios

176
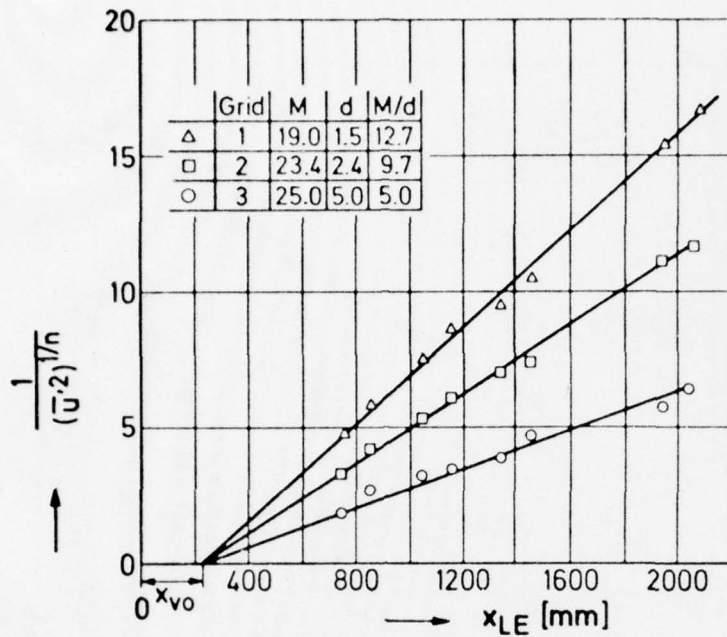
Fig. 7   Evaluation of the Virtual Origin x_{vo} of Turbulence for Different Grids (n=1.3)
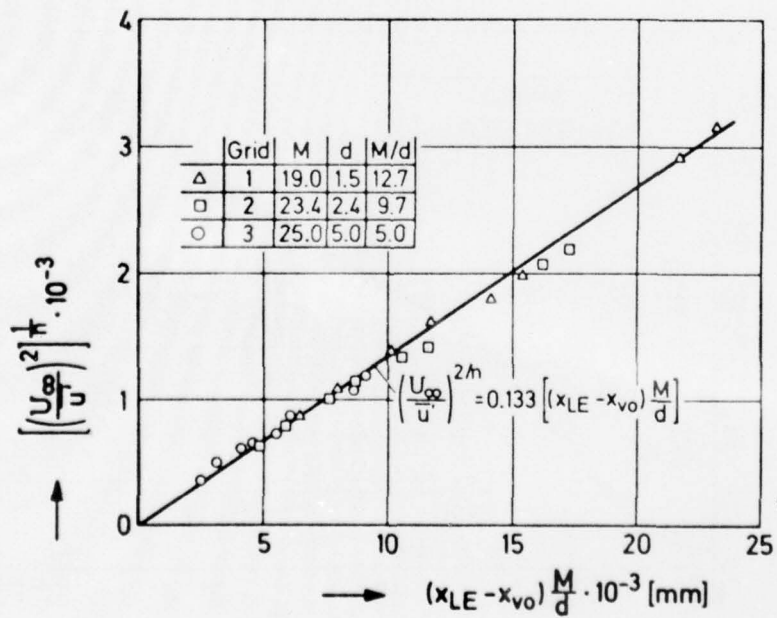
Fig. 8   Decay of Tu_1 Downstream of Different Grids (n=1.3)

177

Fig. 9   Mean Boundary Layer Velocity Profiles for the Free
Stream Turbulence Level $Tu_1 = 0,06\%$ and Different
Distances x_{LE}

Fig. 10   Mean Boundary Layer Velocity Profiles for Different
Free Stream Turbulence Levels and Distances x_{LE}

178

Fig. 11 Momentum Thicknesses δ_2 for Different Turbulence Levels and Distances x_t

179

THREE DIMENSIONAL BOUNDARY LAYER MEASUREMENT
ON THE DOUBLE MODEL OF A SHIP

by

J. Kux
Institut für Schiffbau der Universität Hamburg

INTRODUCTION

Methods for the prediction of ship resistance are still far from being
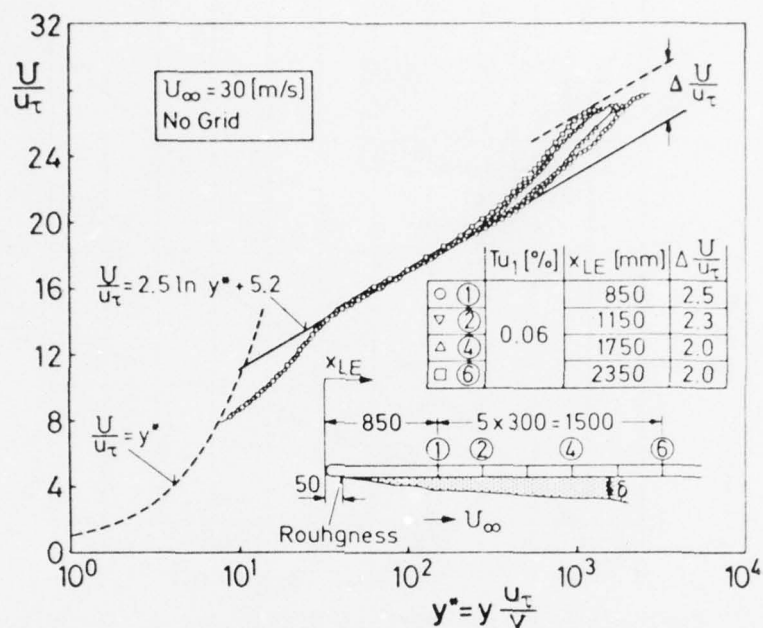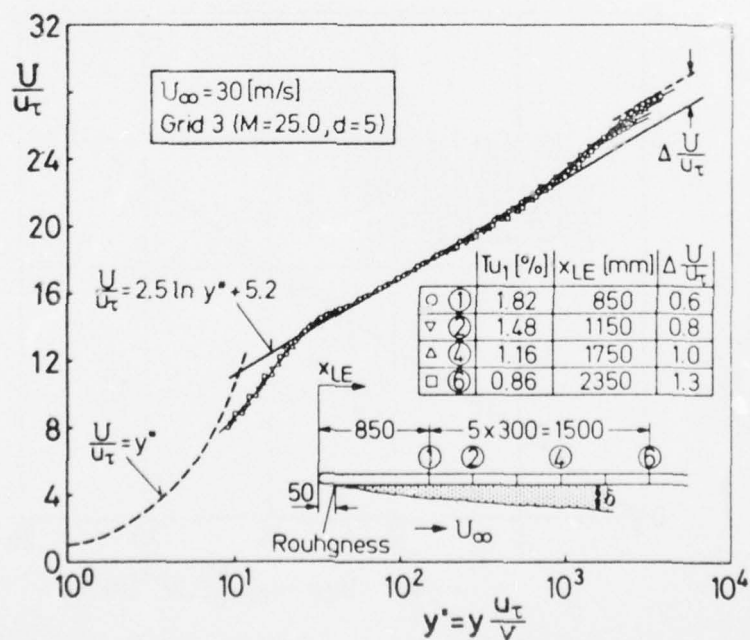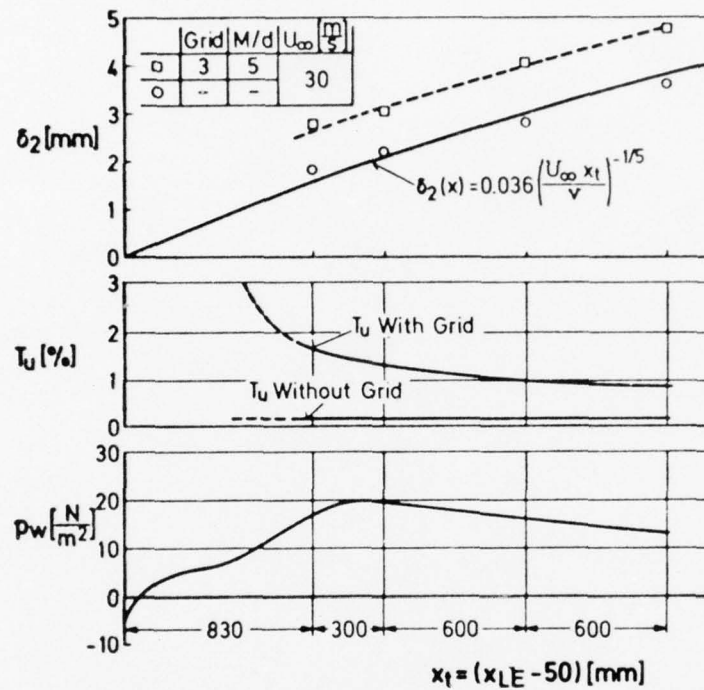satisfactory. In order to improve the prediction of the viscous part
of ship resistance a systematic investigation of the three-dimensional
boundary layer on a ship hull was started at the Institut für Schiffbau.
The scope was to obtain experimental data from model measurements and
to test different methods of boundary layer calculation. Severe reductions
of the funds lead to basic changes in the research program: The activity
of the whole basic hydrodynamics group - including the mentioned program
on boundary layers-was stopped. This group was composed by Prof. K.
Wieghardt, Mr. H.-P. Hoffman, who made the pressure probe investigations,
Mr. M. Scheinpflug, in charge of the development of the laser velocimeter,
and myself.

While a great deal of research activity is at present inverted into a
better modeling of the third-order correlation and similar terms in the
transport-equations for the Reynolds-stresses, it may be allowed to ask
what a degree of sophistication is really necessary for a prediction
method to conform certain accuracy requirements for the predicted values.
Here, limitations and power of two very simple calculation methods will
be made evident.

EXPERIMENTAL INVESTIGATIONS

The results of pressure probe measurements on a ship hull double model
in a wind tunnel are presented together with some calculations of the
outer flow and the boundary layer in two dimensional approximation. The

181

model investigated, Figure 2, is a double model (length 2.74m) of the under water hull of a modern cargo liner (C_B = 0.85, B/T = 2.7, L/B = 6.6) with a parabolical bow. It was fitted with about 230 pressure taps which allowed to chart the pressure distribution over the surface with a certain precision. The wind tunnel, Figure 7, is a Göttingen type tunnel with a slotted wall test section. No forces or moments were registrated and three different speeds were chosen corresponding to Reynolds numbers (characteristic length is the model length) $6.8 \cdot 10^6$, $4.8 \cdot 10^6$, and $2.8 \cdot 10^6$, the model aligned so as to ensure zero angle of attack.

The boundary layer was investigated at various stations with pressure probes. A static pressure probe, a Pitot tube and a three-hole probe were traversed through the boundary layer in a direction always normal to the hull surface. A five-hole probe was also used, its results being in full agreement with those of the three-hole probe as regarding to the flow angle in a tangential plane. The data on the flow angle toward or away from the hull surface in the regions with a thick layer have not yet been analyzed. Care was taken to correct the static-pressure-probe response for the flow angle. Wall shear stresses were measured by the Preston-tube-method and were also calculated by the Ludwieg-Tillman formula in spite of three dimensionality and pressure gradients of the flow. On line processing of the data was used ensuring that results were available immediately after the measurement. Turbulence intensity or shear-stress distribution were not measured. By means of an appropriate strip it was ensured, that the boundary layer was fully turbulent. This was checked by measuring spectra of the turbulence at equal relative depth in the layer at different stations.

As results a few selected velocity profiles will be presented. Figures 3 and 6 show the stations on the hull indicating the varying thickness of the boundary layer. Typical profiles for the station labeled number 18 are shown in Figures 4 and 5. It is seen that at station 18, 1.72 m from the bow, there is still negligible cross flow in the boundary layer and this is true for each position on the girth. Things have changed at station 26 which is at 2.509 m from the bow (Figure 6). Here we see that the cross flow profiles may not be approximated by the usual formulae (Figure 7) nor does the polar plot resemble the Johnston triangle any

more (Figure 8). The girthwise variation of the cross flow becomes evident and may be put in relation to the girthwise pressure distribution shown in the inset.

If one tries to apply the well known methods from two dimensional layers to these profiles, one would first of all ask if the logarithmic law of the wall remains valid. Not taking into consideration the cross flow angle, i.e., considering the velocity vectors of the profile as if they were co-planar, the results are as shown in Figure 9. With the exception of the profile at the point labeled as number 182 the plot may be considered as acceptable. It may not bear a deeper physical sense but it is nevertheless surprising that a change of the constant C to a value of -3.8 allows to fit the profile quite well.

CALCULATIONS

As shown in Figure 10 the potential calculation [1] (using over 400 elements for a quarter of the double model) leads to a complicated pattern of lines of constant pressure on the hull surface. At a first sight the agreement seems to be extremely good. In fact, differences are large only in the stern region. Yet, there are also slight differences in the bow region which are difficult to explain. Integration over the model surface should of course give zero pressure force for potential flow, but unfortunately, it does not. Apparently, our computation method should be improved. Also the integration over the experimental pressure distribution did not yield a satisfactory result.

The most primitive way to treat a boundary layer is to consider it as a flat plate boundary layer. Here the so called Schoenherr-line was chosen as friction law [3] [4]. The arc length of the outer flow streamline was taken as the distance on which Re-number is based. Five stream lines (compare Figure 2) were constructed manually on the hull surface on the basis of the calculated directional field of the outer flow.

A much higher degree of complexity in calculation effort is required if one of the usual calculation methods is to be applied. The simplest choice is to use a two-dimensional integral method. Here the method of Rotta [2] was chosen and the calculation performed along the same streamlines taking now the pressure gradient into account but still neglecting streamline-

divergence and curvature influence. The calculated and the measured pressure distribution on such a streamline are compared in Figure 11. The calculations have not yet been repeated with the measured pressure distribution.

Figures 12 to 16 show a comparison of the calculated values for the skin friction coefficient, and integral parameters with experimental results. The skin-friction coefficient was obtained by different methods: It was measured with a Preston tube, it was determined by fitting the law of the wall (with the usual values of the constants) and it was derived from the momentum loss thickness by the Ludwieg-Tillmann-formula. The friction coefficients derived here are all related to the incident velocity and not as usual to the local velocity at the boundary layer edge. Integral parameters were calculated from velocity profiles neglecting curvature.

At hull station 18 both flat plate and two dimensional calculation give values which are of the right order of magnitude, though a bit low. The same is true for the integral parameters. Of course, these simple methods are not able to reproduce the details of the girthwise distribution of these parameters.

Even at frame 26, where there are enormous cross-flow angles, the mean value of the skin friction coefficient is still well predicted by these very simple methods. Here, two displacement thicknesses, four momentum loss thicknesses and two energy loss thicknesses are presented. It was not possible to compute the real displacement thickness (one component) nor the real momentum loss thickness (a two component magnitude) because of the lack of streamwise information.

The limitations of the rather simple calculation methods are clearly visible, but also their power is demonstrated. A most striking result is the very good prediction of separation by the two dimensional method on streamline 4 and only on this streamline. In the experiment, a rather small region of separated flow could be seen.. Only streamline 4 crosses this domain of separated flow and the point of separation predicted seems to be quite accurate.

184

CONCLUSIONS

The development of highly sophisticated calculation methods for three dimensional boundary layers will, of course, be necessary for a thorough understanding of the flow itself. Yet, so far it seems that the viscous pressure drag is the component of total resistance where the geometrical influence predominates, while it seems to be easy to predict the skin friction approximately ignoring the influence of geometry. To obtain a realistic picture of the pressure distribution also at the stern of the body the wake has to be included somehow in the calculation procedure. It is this wake which in conjunction with body geometry determines the pressure field in the stern region and prescribes flow separation. Boundary layer calculation will serve as a step in an iterative process to find the right flow pattern around the combination of body and simulated wake yielding the pressure distribution in accordance with reality. But at present we think that the most urgent need is for more experimental evidence on what is really happening in the stern region and to compare results from various body forms. Only such basic experimental information will lead us to more reliable calculation procedures.

REFERENCES

[1]   Hess, J.L.; Smith, A.M.O.:
      Calculation of Potential Flow about Arbitrary Bodies, in Progress
      in Aeronautical Sciences, Vol. 8, Küchemann, D., editor, (1967),
      S. 1-138.

[2]   Rotta, J.-C.:
      Fortran IV-Rechenprogramm für Grenzschichten bei kompressiblen
      ebenen und achsensymmetrischen Strömungen, Deutsche Luft- und
      Raumfahrt, Forschungsbericht 71-51 (1971).

[3]   Wieghardt, K.:
      Über den Reibungswiderstand der Platte, Institut fur Schiffbau,
      Bericht Nr. 291.

[4]   Winter, K.G.; Gaudet, L.:
      Turbulent Boundary-Layer Studies at High Reynolds Numbers at Mach
      Numbers between 0.2 and 2.8 R.&M. No. 3712 (1973), Aeronautical
      Research Council, Reports and Memoranda, London.

Figure 1

I f S — Windkanal

Schnitt A - B

Schnitt C - D
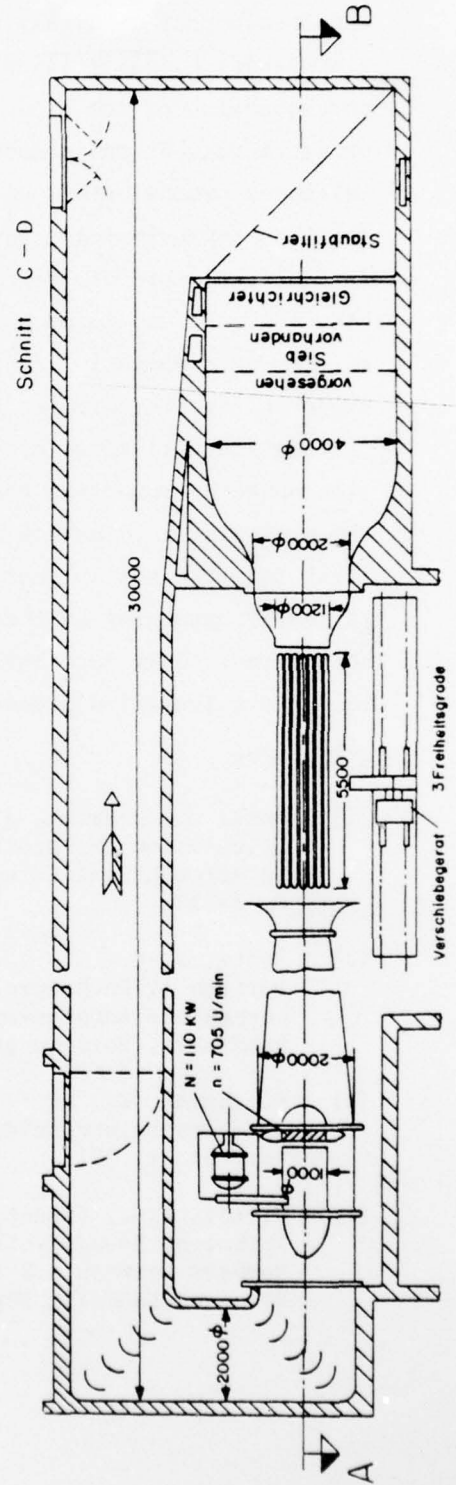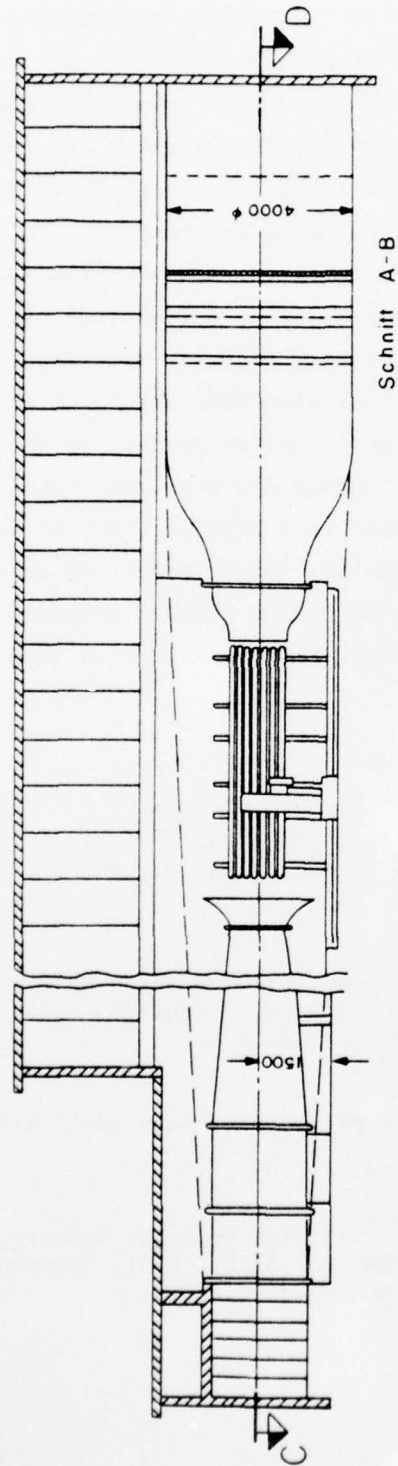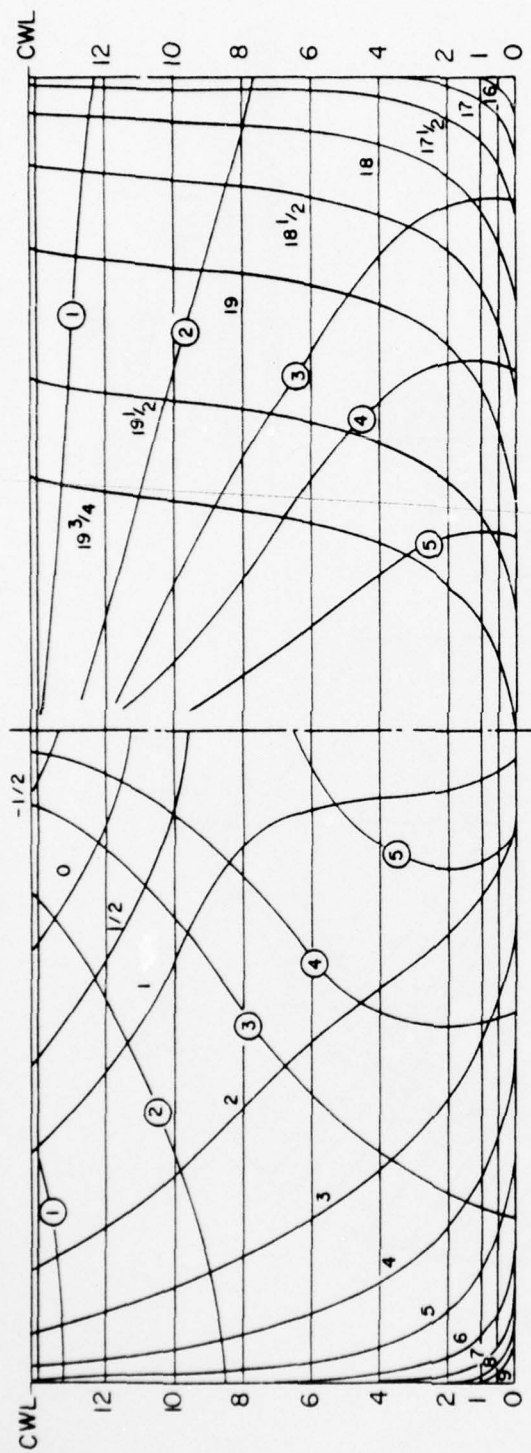
Figure 2. Body Plan of Model with Double-Hull Streamlines
Derived from Pot. Theory.

187

Figure 3. Boundary Layer Thickness δ ($P_{tot} = 0.99 P_{tot}|_e$) Around Girth of Model ($x = 1720mm$, $x = 2000mm$).

Figure 4

STATION 126   RE = 68 × 10⁵

(DELTA = 24.00MM   Q0 = 39.57 M/SEC)

POLAR PLOT OF THE MEAN VELOCITY PROFILE

PROFILE EXPRESSED IN TERMS OF STREAMWISE AND CROSSFLOW COMPONENTS
O = CROSSFLOW PROFILE   X = STREAMWISE PROFILE

189

Figure 5

STATION 129   RE = 6.8 × 10^6 Q0 = 41.41 M/SEC

(DELTA = 40-50MM)

CWL

KEEL

POLAR PLOT OF THE MEAN VELOCITY PROFILE

V/Q0

U/Q0

0.00 0.10 0.20 0.30 0.40 0.50 0.60 0.70 0.80 0.90 1.00

0.10 0.00 -0.00 -0.20 -0.30

Z(MM)

56.00 48.00 40.00 32.00 24.00 16.00 8.00 0.00

-0.30 -0.10 0.10 0.30 0.50 0.70 0.90 1.10

U/Q0, V/Q0

PROFILE EXPRESSED IN TERMS OF STREAMWISE AND CROSSFLOW COMPONENTS

o = CROSSFLOW PROFILE   x = STREAMWISE PROFILE

190

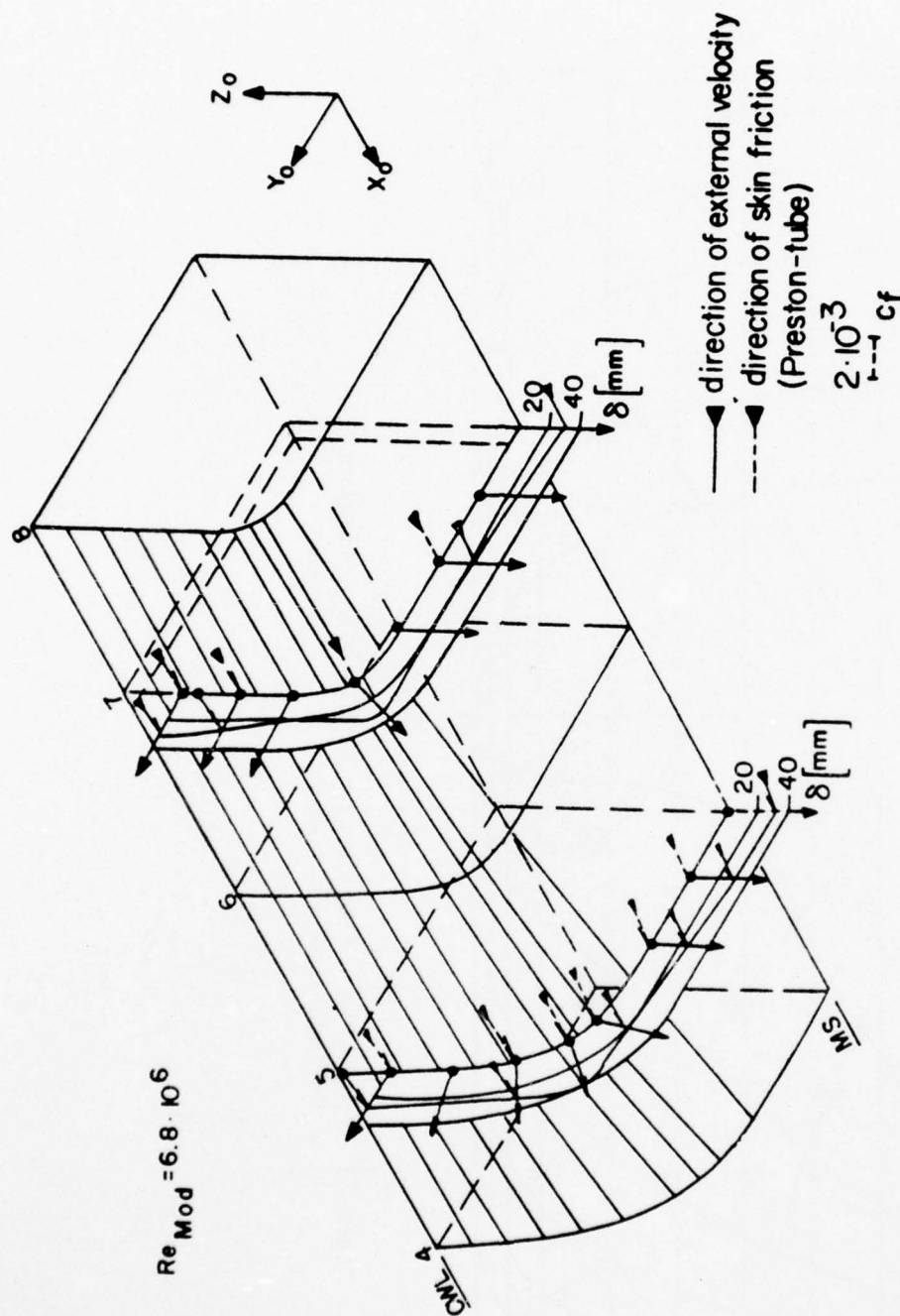Figure 6. Boundary Layer Thickness δ ($P_{tot} = 0.99P_{tot}|_e$) Around Girth of Model ($x = 2,509$mm) (E1, E2 planes of measurement in the wake)
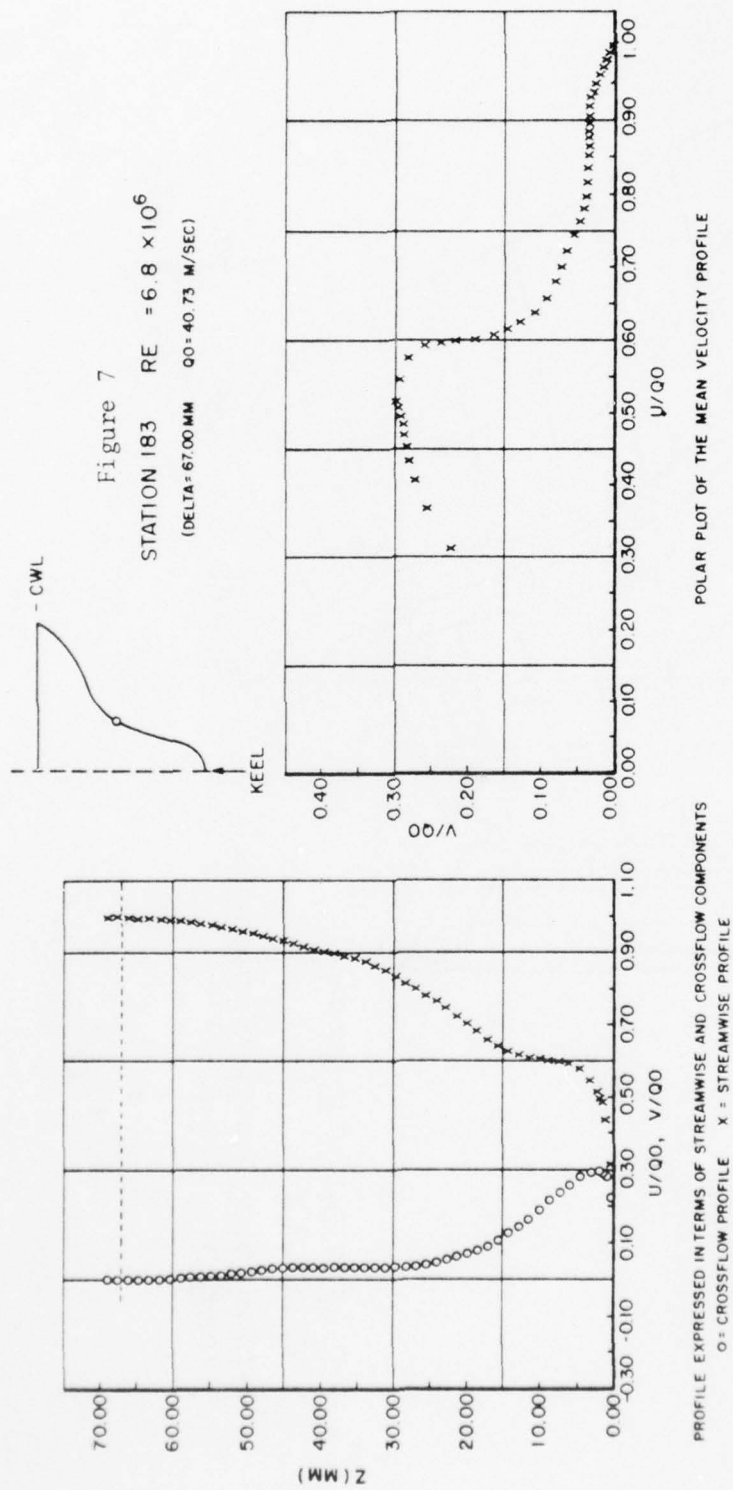
Figure 7

STATION 183   RE = 6.8 ×10⁶   Q0 = 40.73 M/SEC

(DELTA = 67.00 MM)

POLAR PLOT OF THE MEAN VELOCITY PROFILE

PROFILE EXPRESSED IN TERMS OF STREAMWISE AND CROSSFLOW COMPONENTS

O = CROSSFLOW PROFILE   X = STREAMWISE PROFILE

STREAMWISE PROFILE

Figure 8

193
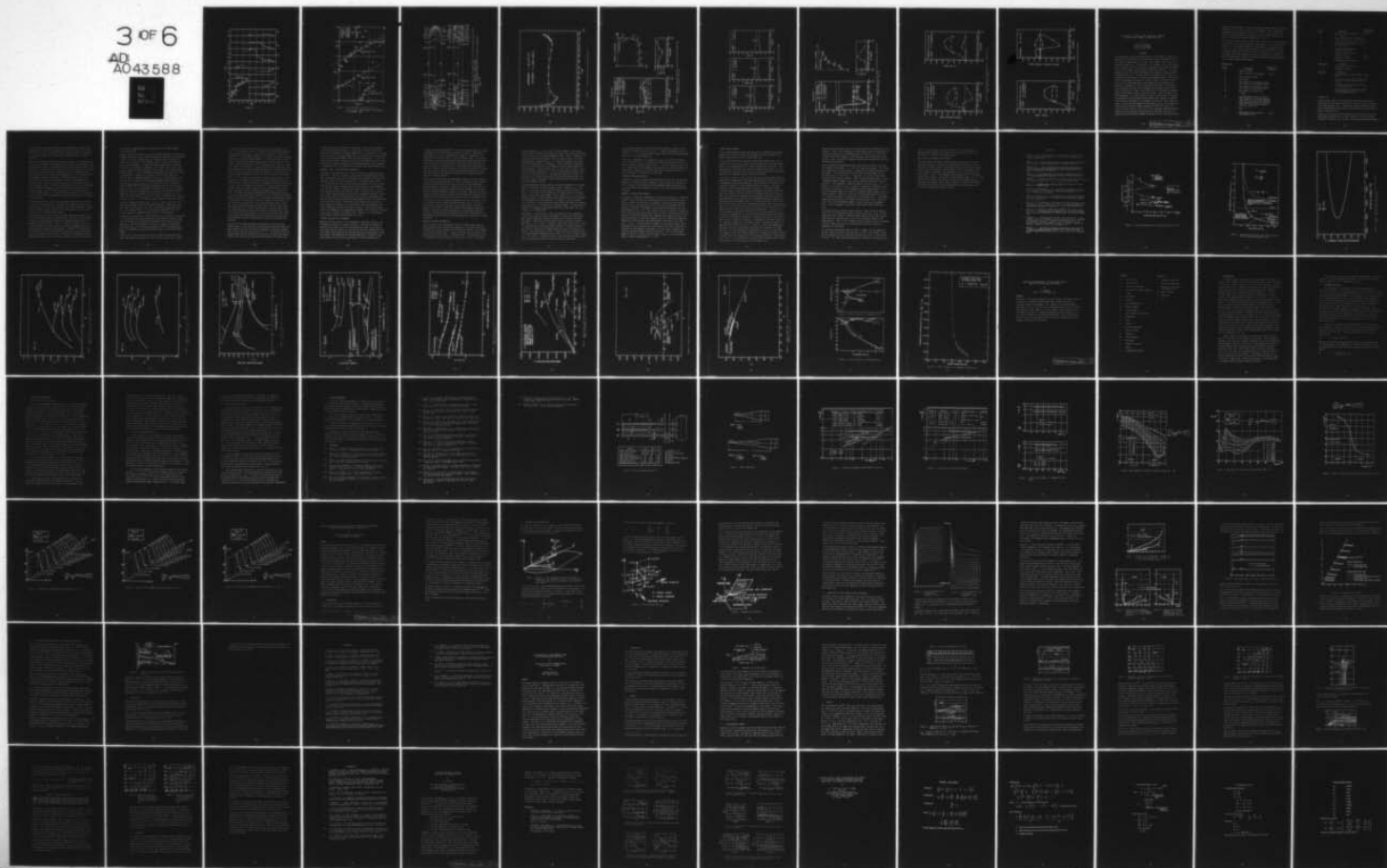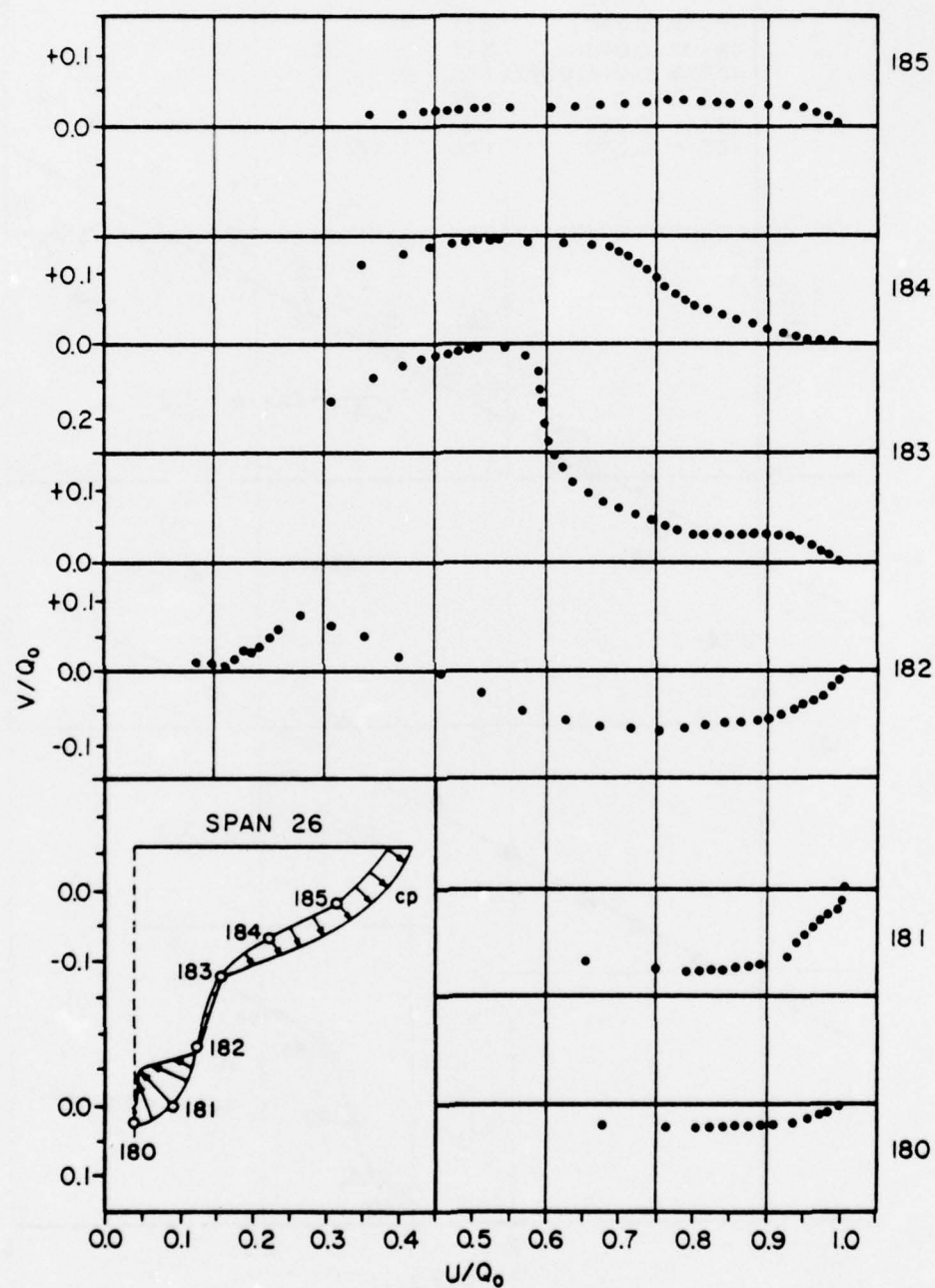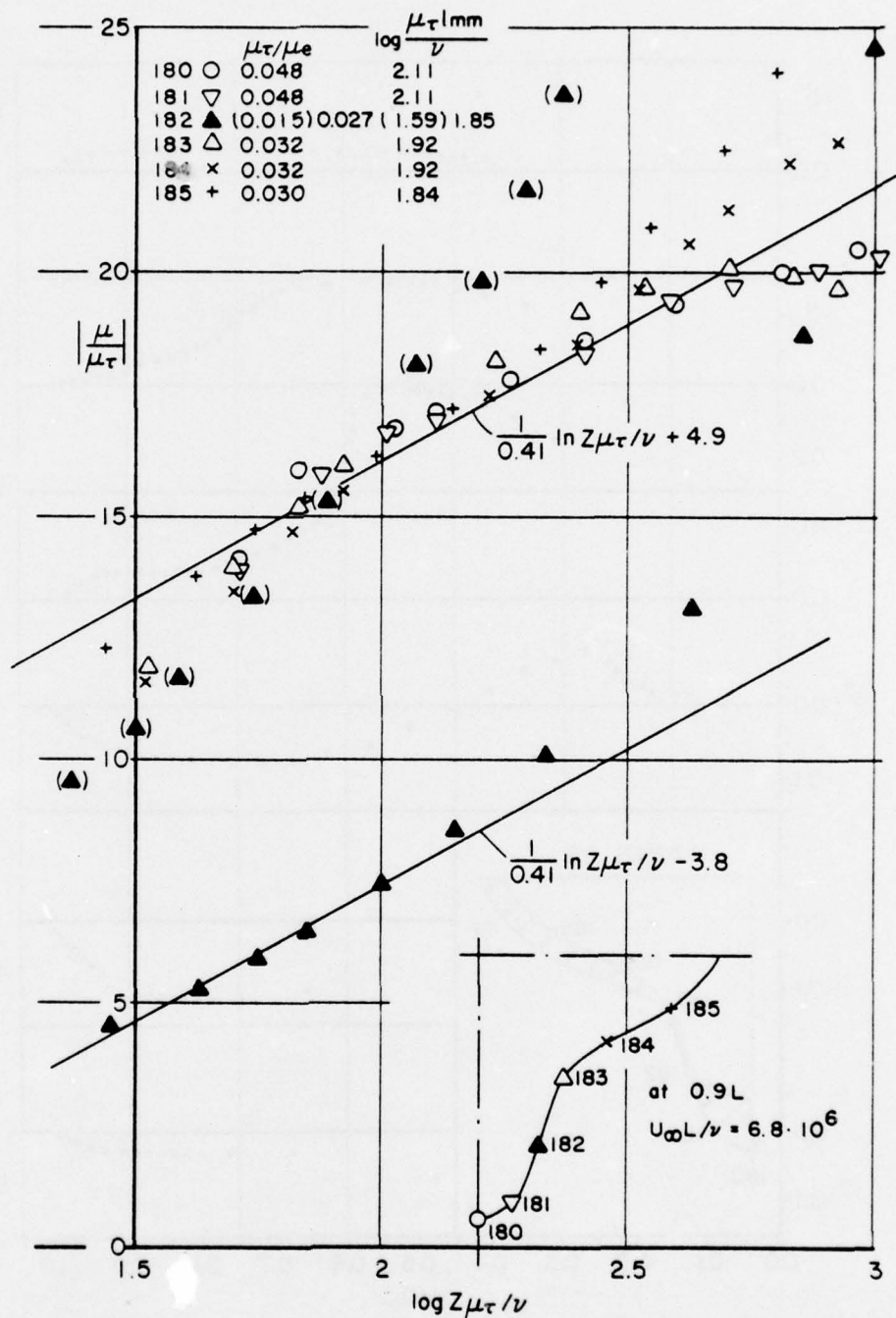
Figure 9. Law of the Wall: $\dfrac{u}{u_\tau} = \dfrac{1}{\kappa} \ln zu_\tau/\nu + c$; $\kappa = 0.41$, $c = 4.9$. Double Model in Wind Tunnel, H.P. Hoffmann, 1976.

194
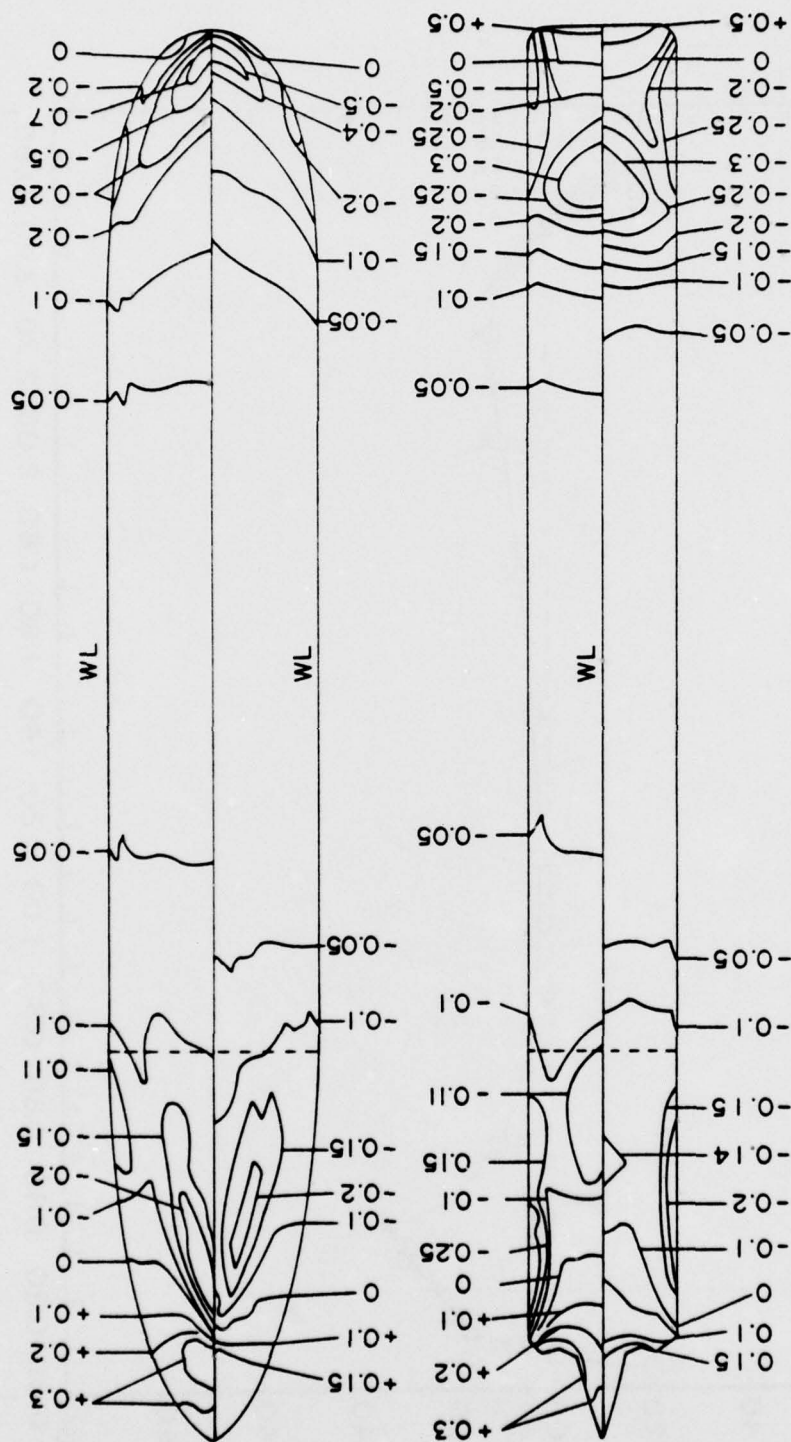
Figure 10. Pressure Distribution (c_p) on a Double Model (L=2.74m) of a Cargo Ship (C_B=0.85)

Upper Half: Theoretical (HESS & SMITH)
Lower Half: Experimental (Double-Hull in Wind Tunnel IFS Hamburg,
R_N=6.8·10[6]
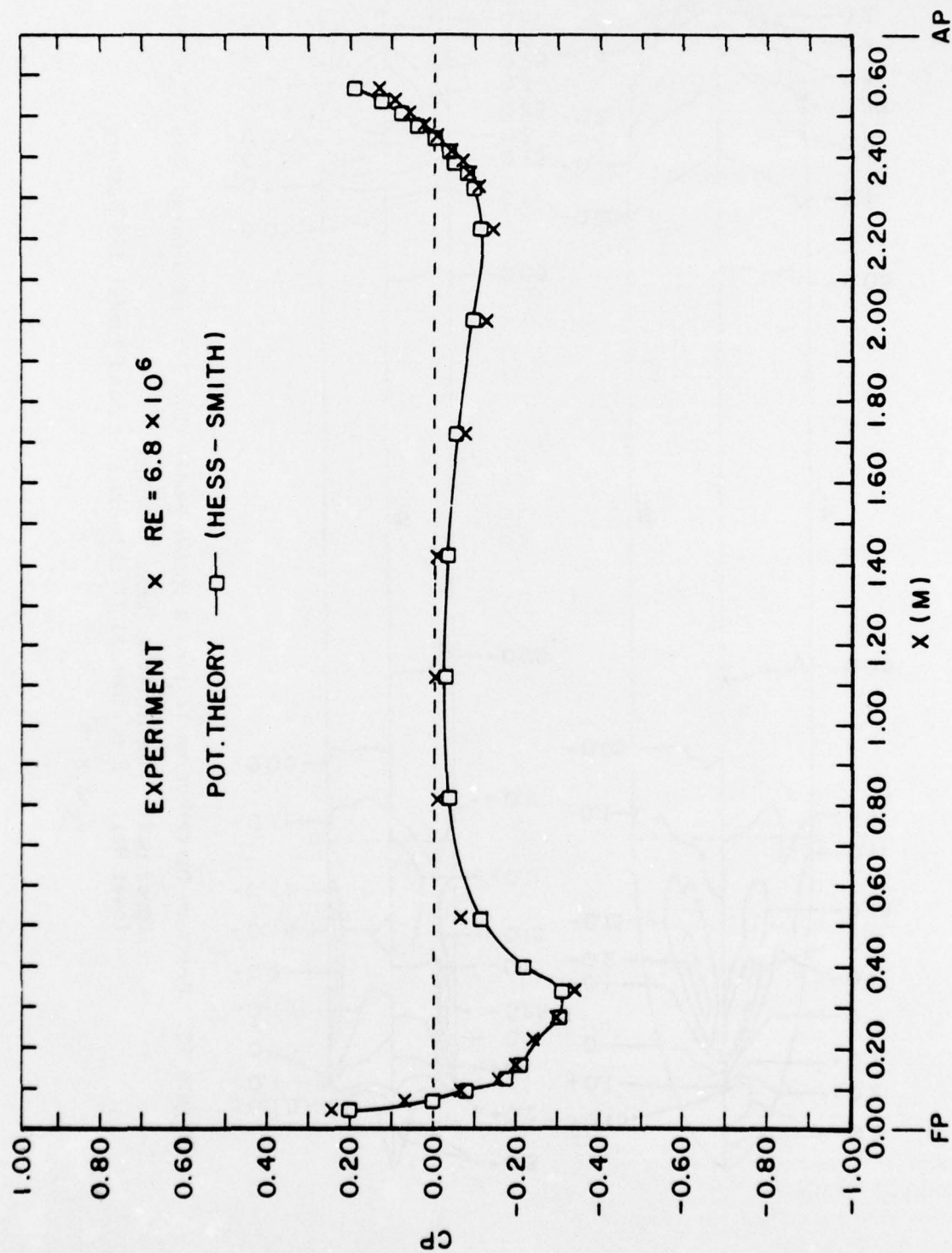
Figure 11. Pressure Distribution Along Streamline No. 2.
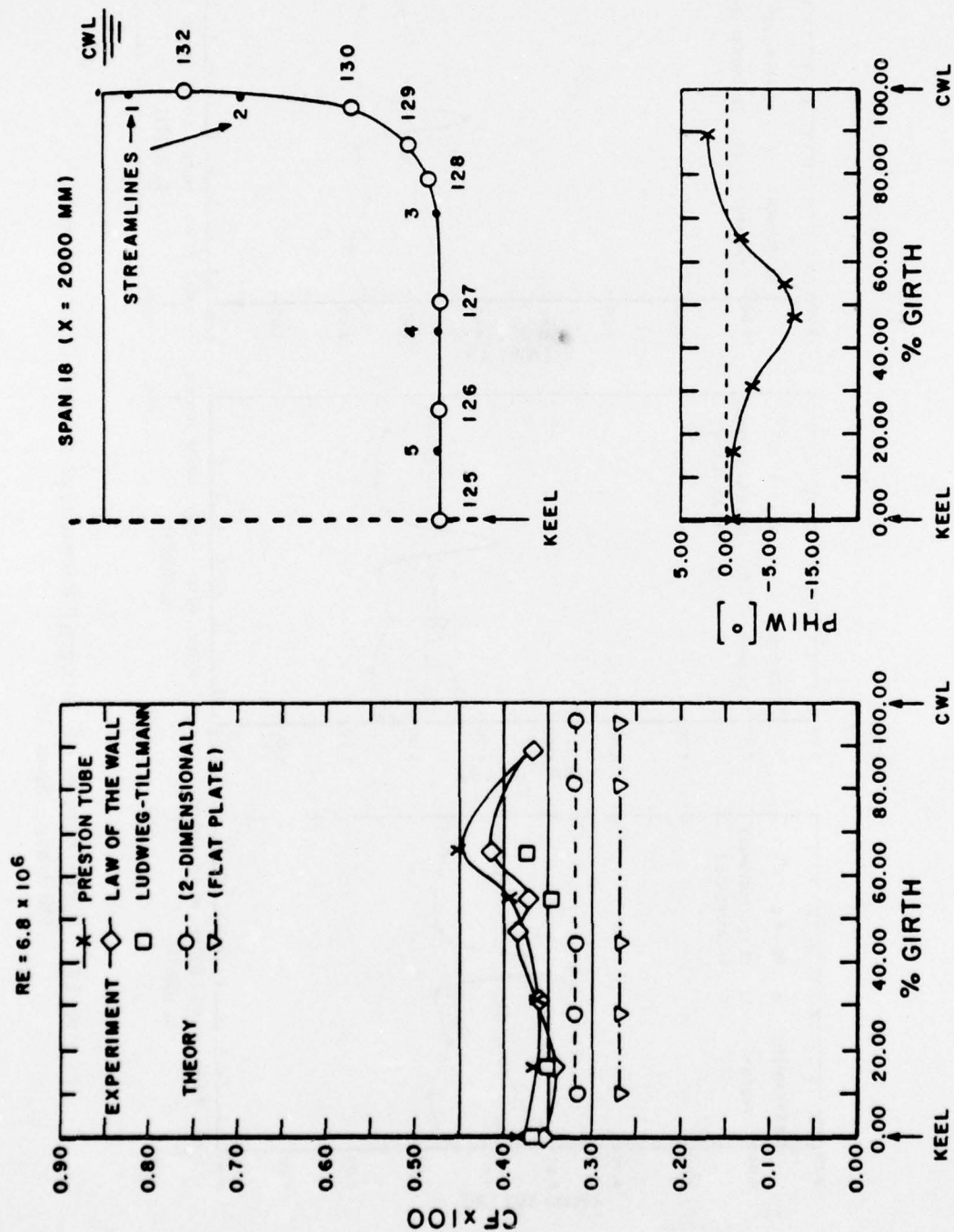
Figure 12. Magnitude and Direction of Skin Friction Vector Around Girth of Model (Midship, Span 18).

197
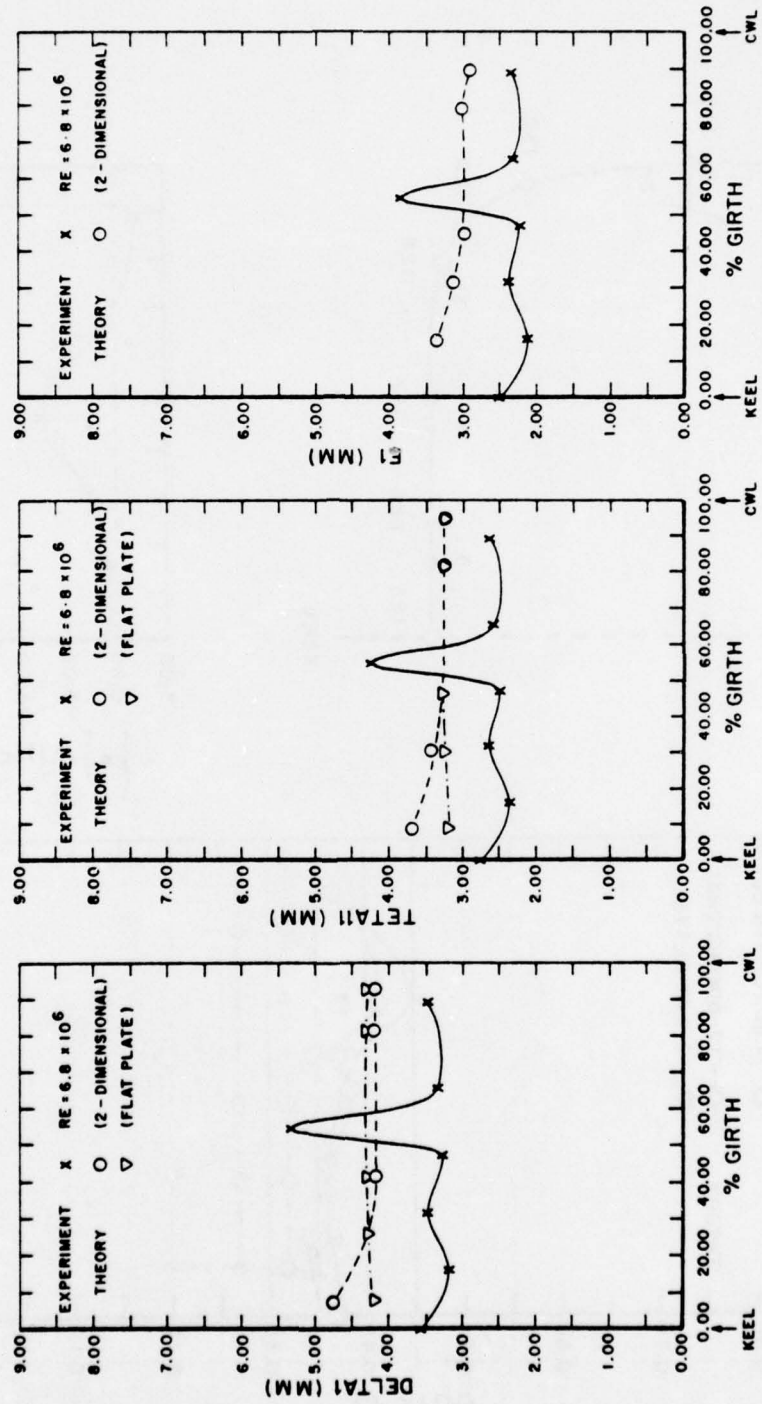
Figure 13. Distribution of Integral-Parameters Around Girth of Model (Midship, Span 18).

198
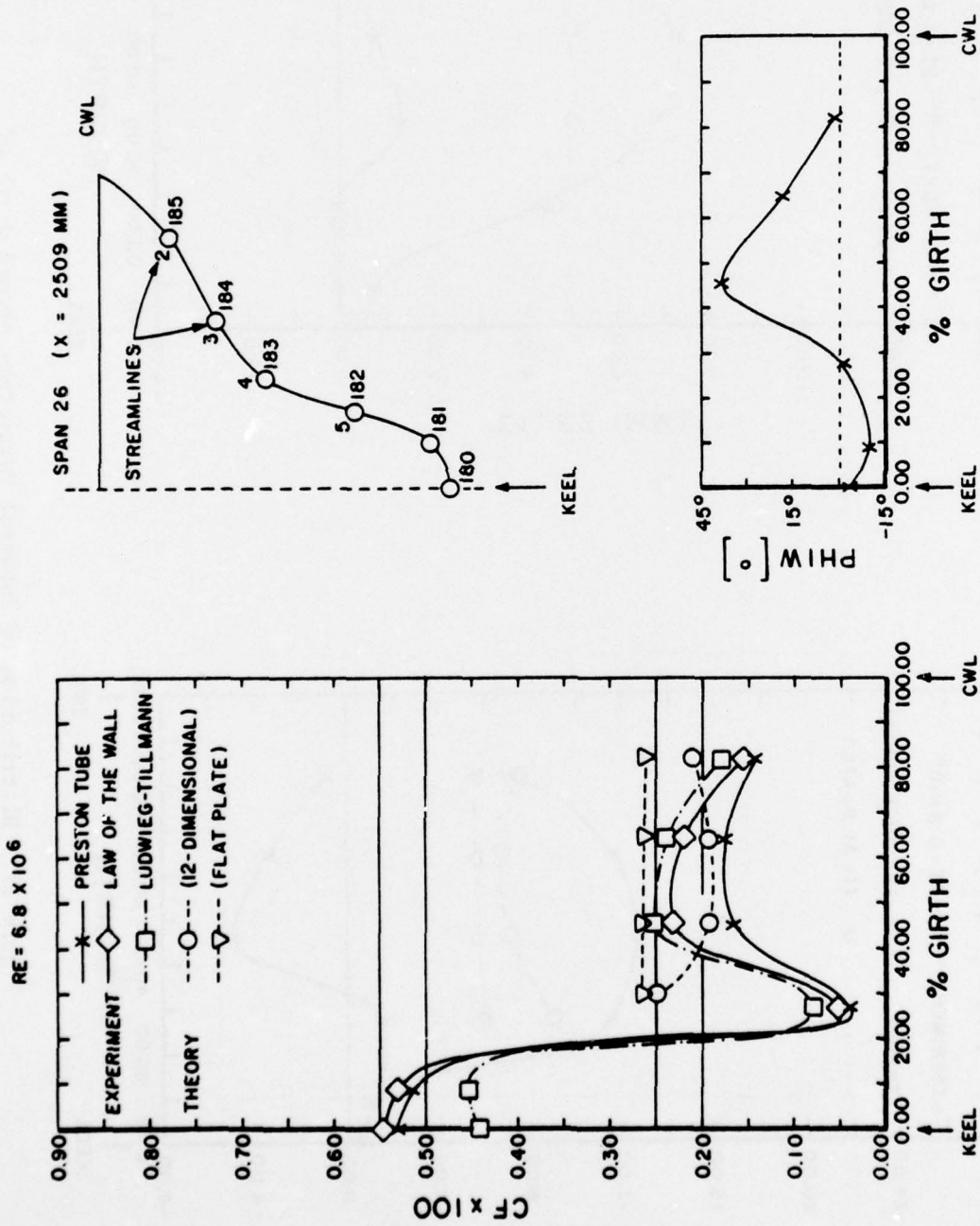
Figure 14. Magnitude and Direction of Skin Friction Vector Around Girth of Model (Afterbody, Span 26).

199
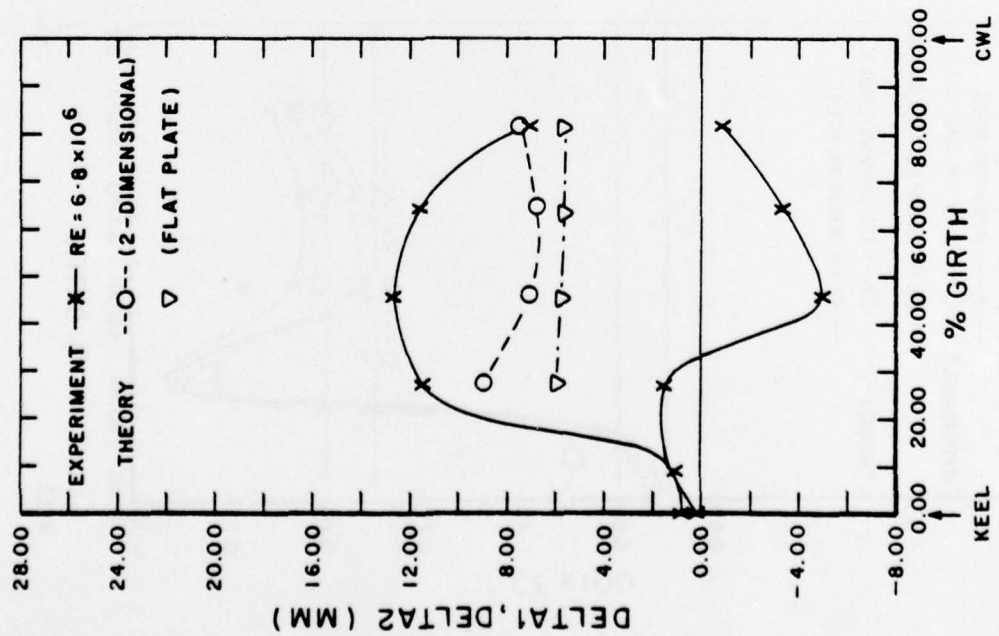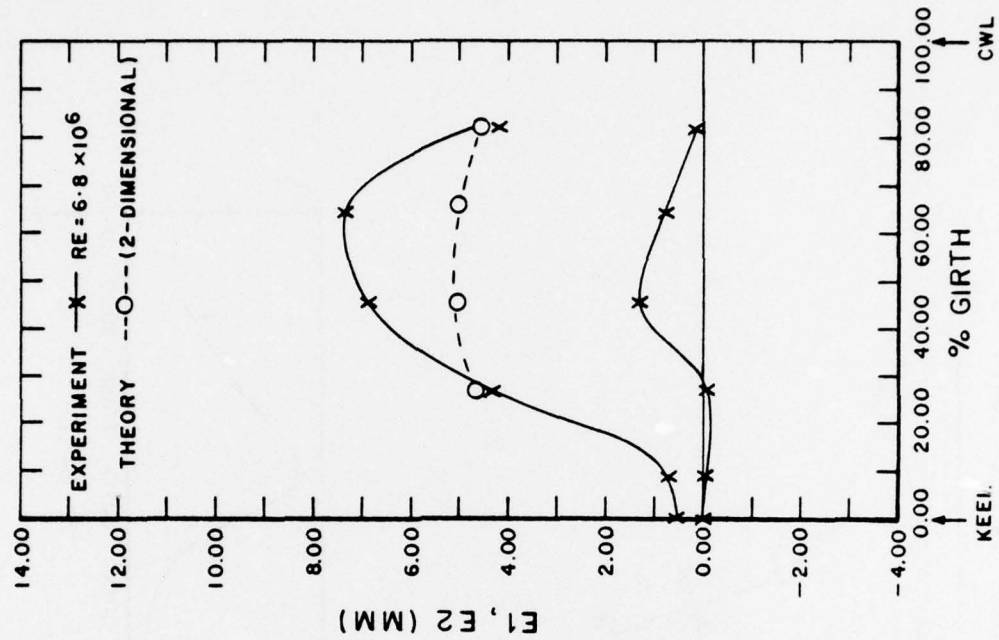
Figure 15. Distribution of Integral-Parameters Around Girth of Model (Afterbody, Span 26).

200
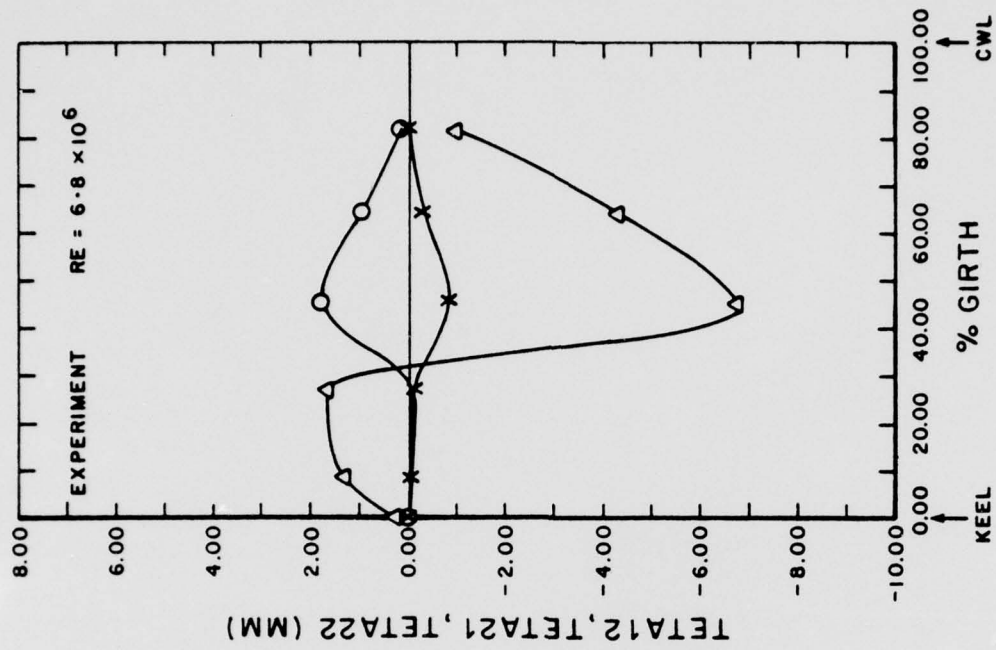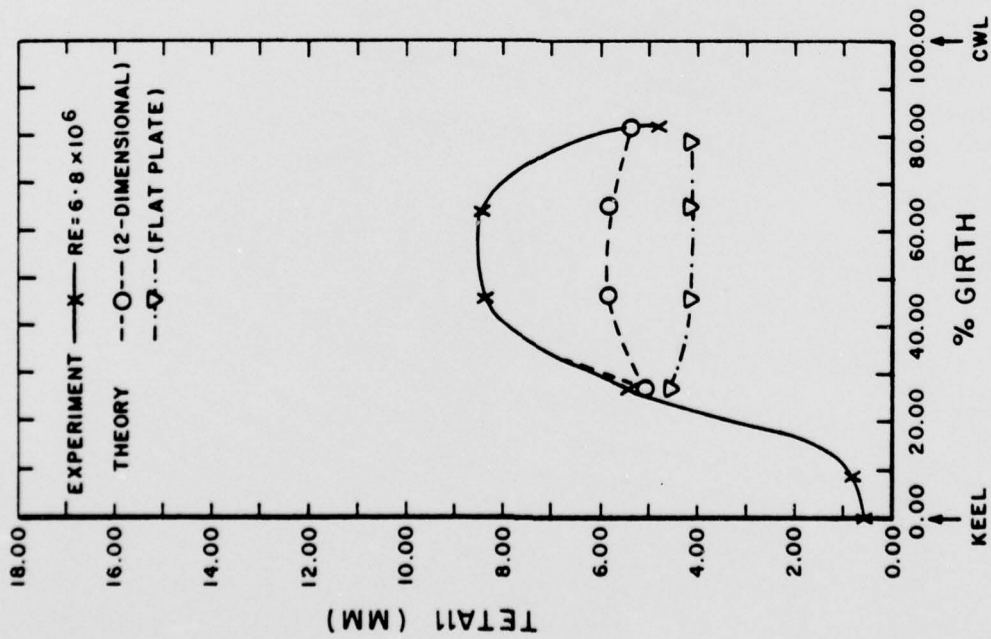
Figure 16. Distribution of Integral-Parameters Around Girth of Model (Afterbody, Span 26).

201

EFFECT OF WALL COOLING ON THE STABILITY OF LAMINAR
BOUNDARY LAYERS FORMED IN SHOCK TUBE FLOWS

by

Louis I. Boehman
University of Dayton
Dayton, Ohio 45469

ABSTRACT

A distinguishing feature of boundary layers in shock tubes is that in the
boundary layer flow induced by a normal shock, the wall temperature (T_w) is
less than the termperature at the edge of the boundary layer (T_e) for all
shock Mach numbers (M_s). The cooling of the boundary layer in this type of
flow is such that the ordinary types of disturbances considered in boundary
layer stability theory are essentially completely damped out. This fact
prompted a search for other disturbances that might be unstable in highly
cooled boundary layers. Two new classes of disturbances have been dis-
covered which are unstable in highly cooled boundary layers. Both classes
of these disturbances originate in the free stream in the form of sonic
or near sonic disturbances which carry energy into the boundary layer.
One class corresponds to sonic disturbances which travel slower than the
free stream and the other class correspond to disturbances which travel
faster than the free stream. This latter class of disturbances represent
acoustic disturbances present in the free stream. With the former class
of disturbances, it is now possible to remove a paradox that has existed
with respect to linear stability theory predictions compared to measured
transition Reynolds numbers. The paradox has been that linear stability
theory critical Reynolds numbers for flows with $T_w/T_e < 1$ have exceeded mea-
sured transition Reynolds numbers whereas for flows with $T_w/T_e > 1$ the
critical Reynolds numbers have been less than measured transition Reynolds
numbers and have generally showed qualitative agreement with trends in
measured transition Reynolds number variations with wall cooling, pressure

gradient, and Mach number. The critical Reynolds number-amplification rate
characteristics of the former class of disturbances lead to qualitative
agreement between predicted values of the onset of transition with the
Boison's recent measurements of transition in shock tube boundary layer
flows in the range of shock Mach numbers of 3 to 4.5.

The stability characteristics of these newly discovered unstable disturbances
are presented for shock Mach numbers in the range of 1.5 to 4.5 which cor-
responds to a Mach number range for the flow behind the moving shock of
0.6 to 1.76. Some important implications of these disturbances in terms
of using boundary layer cooling as a means of boundary layer control are
discussed. Particular emphasis is given to the potential of using this
form of boundary layer control on subsonic aircraft to achieve drag reduc-
tion and hence improved fuel economy.

NOMENCLATURE

Symbol	Definition	Characteristic Measure
a	-Speed of sound	
c	-Phase velocity of disturbance	U_∞^*, U_2^*
ℓ	-Characteristic length	
M	-Mach number	
M_e	-Mach number of flow behind a shock wave-shock fixed coordinate system	
M_2	-Mach number of flow behind a shock wave-lab-fixed coordinate system	
M_s	-Mach number of moving shock $= U_s^*/a_1^*$	
R_x	-Reynolds number: Based on distance from leading edge in steady boundary layer flows, $R_x = U_\infty^* x^*/\nu_\infty^*$; Based on total distance particle has traveled relative to wall in shock induced flows, $R_x = U_2^* x^*/\nu_2^*$	
R	$-\sqrt{R_x}$	
T	-Temperature based on absolute thermodynamic scale	T_∞^*, T_e^*

204

Symbol	Definition	Characteristic Measure
U	-Mean flow velocity component in x^* direction	U_∞^*, U_2^*
U_∞^*	-Free stream, mean flow velocity in steady boundary layer, x^* direction	
U_2^*	-Velocity of mean flow in free stream behind moving shock wave $U_2^* = \|U_s^*\| - \|U_e^*\|$	
α	-Disturbance wave number in streamwise direction	ℓ^{-1}
δ	-Boundary layer thickness	
μ	-Dynamic viscosity	μ_∞^*, μ_e^*
ν	-Kinematic viscosity	ν_∞^*, ν_e^*
Ψ	-Disturbance stream function	

Superscripts	Definition
$(\ )'$	-Derivative with respect to y
$(\ )^*$	-Dimensional quantity

Subscripts	Definition
∞	-Free stream value (steady boundary layer flow)
e	-Free stream values based on flow behind shock wave, shock-fixed coordinate system
1	-Undisturbed flow conditions in front of moving shock wave
2	-Flow conditions in free stream of mean flow behind moving shock wave, lab-fixed coordinate system

INTRODUCTION

During the past decade, great strides have been made toward a better understanding of the causes and nature of transition in wind tunnel and free-flight boundary layers. The greatest analytical progress toward a better understanding of transition has been through the linear stability theory of parallel flows.

The work of Les Mack at JPL has provided the new discoveries that have gained added importance for the linear stability as a tool for understanding of transition. His discovery of multiple mode, multiple families

of solutions to the compressible flow small disturbance equations and his demonstration of the physical importance of these new types of solutions, has made it possible to formulate a quasi-theoretical model of transition for supersonic flows based on the linear stability theory of parallel flows[1].

Mack's quasi-theoretical model includes two mechanisms for relating the influence of environmental disturbances on the response of the boundary layer. One mechanism is that of the forced oscillation of the boundary layer. One mechanism is that of the forced oscillation of the boundary layer caused by discrete free stream pressure disturbances (acoustic radiation) and the other mechanism is the response of the boundary layer to a spectrum of free environmental pressure disturbances. Within the context of these two mechanisms he has been able to study the effect of Mach number, unit Reynolds number, and wall cooling on transition in wind tunnel and free-flight boundary layers. He has had a good degree of success in explaining how environmental disturbances can affect transition as Mach number, unit Reynolds number, and wall cooling are changed. The accuracy of Mack's transition model appears to be limited for the most part by the accuracy to which the nature of the environmental disturbances themselves are known in a given facility.

In order to apply Mack's model to the problem of predicting the location of the onset of transition to a supersonic flow situation one must have available the basic results of a parallel flow, small disturbance stability analysis, namely, neutral stability curves and amplification rate versus frequency for a range of Reynolds numbers.

The great deal of progress that has been made toward understanding transition in wind-tunnel and free-flight boundary layers has not been matched by progress in understanding transition in laminar boundary layers induced by a moving shock wave. This is in spite of the fact that a considerable amount of data on transition in shock-tube boundary layers has been generated during the past two decades. Morkovin[2] has summarized the nuances and contradictory observations that have been made concerning transition in shock-tube facilities. In Reference 2, Morkovin provided a companion document to his earlier work in which he provided an assessment

of the level of understanding of wind-tunnel and free-flight boundary layer transition[3].

Recently, Boison[4] conducted a series of careful experiments on shock tube boundary layer transition in order to examine the influence of environmental factors such as wall vibration and free stream acoustic disturbances on transition in addition to the influence of wall cooling, unit Reynolds number, and Mach number. In these experiments extraordinary precautions were taken to eliminate wall roughness as a possible cause of early transition in addition to the influence of wall cooling, unit Reynolds number, and Mach number. In these experiments extraordinary precuations were taken to eliminate wall roughness as a possible cause of early transition. Boison's data at a Reynolds number per foot of 5×10^5 showed that as the wall cooling is increased (by increasing shock Mach number therefore decreasing T_{wall}/T_{edge}) from T_w/T_e of 0.45 down to 0.06, the transition Reynolds number first increased then decreased (reversal) then increased again (re-reversal), then decreased, increased again, and so on; showing a number of transition reversals and re-reversals. The transition Reynolds number was found to be extremely sensitive to small changes in cooling especially at the smaller T_w/T_e ratios. Figure 1 shows Boison's transition results for $R_e/ft = 5 \times 10^5$ along with that of several other investigators.

The first transition reversal loop $.17 < T_w/T_e < .36$ seems to be fairly well established although more results would be desirable to definitely show that only one loop exists in this wall cooling range rather than perhaps tow. Also shown in Figure 1 is a calculation of Reshotko[5] for the cooling required for complete stabilization of 2-D disturbances.

It should be noted that this result by Reshotko is not based on a completely valid solution of the stability equations as determined by Mack (see page 14.1 of Reference 6) but should be approximately true since the stability function v_o (defined in Reference 6) contains no zeros in the boundary layer where $T_w/T_e = 0.38$ so that according to Mack[6] no unstable first-mode, 2-D disturbances are possible except possibly at very high Reynolds numbers.

Efforts to use stability theory as a guide to understanding transition in shock tube boundary layers have not been usccessful partly due, no doubt,

to the fact that only one stability analysis has been performed using velocity and temperature profiles characteristic of compressible boundary layers behind a moving shock. This analysis performed by Ostrach and Thornton[7] in 1962 produced minimum critical numbers that greatly <u>exceeded</u> the measured transition Reynolds numbers -- the deviation increasing by orders of magnitude with more cooling (higher shock Mach numbers). Their analysis was based on the Dunn-Lin[8] asymptotic approach and did not take into account 3-D disturbances. Ostrach and Thornton concluded that shock tube transition did not occur through amplification of Tollmien-Schlichting waves but rather was caused by finite disturbances in the form of the inherently large environmental disturbances that are present in shock tubes.

Mack's [9,10] discovery of the existence of multiple mode, multiple family solutions to the parallel flow linear stability equations for the case where the wall is supersonic relative to the phase velocity of a disturbance $(c_r/a_w > 1)$ led to the suggestion by Morkovin[2] that the Ostrach-Thornton analysis ought to be redone using the full set of parallel flow, linear stability equations and direct numerical integration in the fashion of Mack. Since Mack had shown that depending on the amount of wall cooling (T_w/T_e) 2-D first mode unstable disturbances could be stabilized and second mode 2-D disturbances destabilized, it was thought that perhaps the intricate cooling effects on transition in shock tube boundary layers could be correlated with the stabilization of first mode disturbances over certain T_w/T_e ranges and destabilization of higher modes over other T_w/T_e ranges. This suggestion was put forth by Morkovin prior to Boison's work. When Boison discovered the existence of the multiple transition reversal loops in his shock tube transition data he also saw the possibility that these loops might be explained through a stability analysis of the shock tube laminar boundary layer which recognized the existence of multiple mode solutions.

In early 1972, an effort was begun by the author to redo the Ostrach-Thornton analysis using University of Dayton Research Institute (UDRI) computer programs that had successfully been applied to supersonic boundary layer stability problems for flat plates [11,12]. This initial effort was disappointing insofar as higher mode solutions for the shock tube laminar boundary layer could not be found and the first mode 2-D solutions only

confirmed the results of Ostrach and Thornton. In this initial effort, it
was found that the higher modes are associated with large values of the
product of wave number and Reynolds number which is characteristic of higher
modes in low free-stream Mach number which is characteristic of higher modes
in low free-stream Mach number flows with high cooling rates. It was also
found that much smaller integration step sizes were required to successfully
integrate the stability equations for shock-tube boundary layers compared
to integration step sizes required for insulated wind tunnel boundary layers.

SUBSONIC, SONIC, AND SUPERSONIC DISTURBANCES

In Figure 2 are shown three curves of phase velocities versus shock Mach
number (M_s). The curve labeled c_r (M_w=1) shows tha minimum phase velocity
that a disturbance must have in order that the disturbance be moving super-
sonically relative to the flow at the wall. The second curve, labeled
$c_r = 1+1/M_2$ shows the phase velocity that a disturbance must have in order
that the free stream is moving sonically with respect to the disturbance,
i.e., the free stream is moving in the upstream direction at M = 1 relative
to an observer moving at the velocity $1+1/M_2$. The third curve, labeled
$c_o = 1-1/M_2$, shows the phase velocity that a disturbance must have in order
that the free stream is moving sonically with respect to disturbance but
with the relative velocity between the disturbance and the free stream being
in the direction of flow. These three curves together form a region in
which subsonic disturbances exist for which the local Mach number of the
flow is supersonic relative to the phase velocity. This region of phase
velocities encompasses the higher mode disturbances that can exist (according
to the inviscid theory) are subsonic ones. Above M_s = 3.5 both subsonic
and supersonic multiple mode solutions can exist.

INCOMING AND OUTGOING DISTURBANCES

Whenever the phase velocity of a disturbance is supersonic, that is, the
disturbance is moving at a velocity relative to the free stream which is
greater than or equal to the free stream speed of sound, ($c_r \leq 1-1/M_2$) or
$c_r \geq 1+1/M_2$), the two solutions to the inviscid stability equations for the
free-stream represent Mach lines eminating from a point disturbance in the
free-stream. One characteristic solution represents a reflected or out-
going sound wave and the other characteristic solution represents an

incident or incoming sound wave[6]. For neutral outgoing Mach waves, energy is transported in the direction of increasing y, that is, into the free stream whereas for neutral incoming waves, energy is transported in the direction of decreasing y, that is, into the boundary layer. For subsonic disturbances, the inviscid free-stream solutions no longer represent sound waves, but represent two exponentially varying pressure fields caused by inviscid flow over a moving wavy wall. The solution whose characteristic value has a negative real part represents the pressure field over the moving wavy wall (outgoing solution) and the solution whose characteristic value has a positive real part represents the pressure field under the moving wavy wall (incoming solution).

In the viscous theory two of the independent solutions are almost identical to the inviscid solutions except for a small viscous decay term. Ordinarily in stability theory the inviscid solution (or the viscous counterpart) whose characteristic value has a positive real part is not used since this solution increases exponentially upwards from the boundary layer and thus does not satisfy the boundary conditions at infinity. However this solution along with the other solution can be used to determine the response of the boundary layer to disturbances which originate outside of the boundary layer.

In the present analysis incoming disturbances have been considered as well as disturbances which originate inside the boundary layer. As weill be shown in the next section, the wall cooling associated with shock tube boundary layers flows is sufficient to effectively completely damp out all subsonic, outgoing, first-mode disturbances. Corresponding higher mode solutions, some of which can be amplified are of such a high frequency (in the megahertz range) that they are not considered to be important in causing transaction.

SUBSONIC, OUTGOING DISTURBANCES

As was mentioned in the Introduction, the first efforts showed that very small integration step sizes would be required to successfully numerically integrate the stability equations for the shock-tube boundary layer compared to wind tunnel boundary layers. Figure 3 shows the neutral stability curve which was obtained for the M_s = 1.5 boundary layer. One hundred and thirty-six integration steps were required to obtain these results. The minimum

critical Reynolds, R_c, is seen to be 13,180 and compares to the Ostrach-Thornton value of 14,000 for the same value of M_s. The present calculations as well as those of Ostrach and Thornton were for 2-D waves. Subsequent calculations for oblique disturbances, shown in Figures 4 and 5 for several Reynolds numbers, showed that M_s = 1.5, oblique disturbances were always more highly damped than 2-D disturbances. Similar calculations performed for M_s = 3.0 also show that 3-D disturbances are more highly damped than 2-D disturbances. Typical results at M_s = 3.0 are shown in Figures 6 and 7. The results shown in Figures 4 to 7 are for disturbances belonging to the c_o family (or conventional family). No higher mode amplified solutions for this family of solutions are possible for shock tube boundary layers since the wall cooling is sufficient to remove the generalized inflection point from these boundary layers[6].

First and higher-mode outgoing subsonic solutions belonging to the "regular" family of solutions (solutions which have a phase velocity of c_r = $1+1/M_2$ when α = 0 and which are always amplified when c_r becomes less than or equal to 1) have also been investigated. The regular family of solutions persist to low subsonic Mach numbers, since, except at M = 0, it is always possible to find a c_r large enough so that a supersonic relative flow region exists somewhere in the boundary layer. In Figure 2, the curve labeled c_r = $1+1/M_2$ ($\hat{M}_w$ = 1) shows the phase velocity which this family of solutions starts out at (α= 0) as a function of shock Mach number. For this family of solutions to have amplified or neutral solutions c_r must become less than or equal to 1, respectively[6].

From Figure 2 it is seen that in shock tube boundary layers a supersonic relative flow region for subsonic disturbances can only exist when $M_s \geq 1.8$. Thus, regular, amplified, subsonic solutions are not possible below this Mach number. Some typical regular family solutions are shown in Figures 8 and 9 for M_s = 1.5, 2, and 4. In Figure 8, the dispersion relation c_r versus α is shown for both fiscous and inviscid solutions. As shown in Figure 9, the viscous solutions are all damped whereas the inviscid solutions are all neutral. The only exception is at M_s = 4 where the inviscid solutions show a very small amount of amplification for α>3.5. For α>3.5, the phase velocity, c_r, is less than one. According to Mack, a necessary condition for an amplified inviscid regular solution to exist is that c_r be less than 1.

211

Calculations performed to date indicate that an amplified regular viscous solution can likewise only exist if $c_r < 1$. In Mack's terminology, the solution for $c_r = 1$ is called the regular neutral solution and the corresponding value of α is given the symbol α_{11}.

The viscous counterpart to α_{11} denoted by $(\alpha_{11})_v$ has not been determined since the value of $(\alpha_{11})_v$ is so high that smaller step sizes than even 0.02 would be needed to reach a condition of $c_r = 1$ for the regular viscous solution. Additionally, the frequency associated with this solution would be in the megahertz range which is outside the range of frequencies that are usually considered to be important in transition.

SUPERSONIC OUTGOING SOLUTIONS

In reference 6, Mack has shown that with sufficient wall cooling, amplified, supersonic, outgoing solutions belonging to the c_o family of solutions can exist. However, these solutions have wave numbers which are greater than α_{11} so that again, high frequency solutions be the only possible amplified solutions.

SUMMARY OF OUTGOING WAVE RESULTS

The results of stability computations for outgoing disturbances in shock tube boundary layers encompassing two-dimensional and three-dimensional disturbances, subsonic and supersonic disturbances, and multiple mode solutions of both subsonic and regular families has not yielded solutions which can explain or correlate with boundary layer transition measurements in shock tube boundary layers. Since these outgoing solutions represent disturbances which originate within the boundary layer, one must conclude that within the context of a small disturbance linear boundary layer stability theory, outgoing disturbances in shock tube boundary layers are effectively completely damped out for the range of shock Mach numbers considered in this study ($M_s = 1.5$ to 4). One would have to further conclude, again subject to the limitations on the validity of the linear theory, that were it possible to eliminate all environmental disturbances in a shock tube, extremely high transition Reynolds numbers should be attainable. Even at a shock Mach number as low as 1.5, linear stability theory predicts a critical Reynolds number as high as approximately 1.7×10^8.

INCOMING WAVE SOLUTIONS

Neutral incoming wave solutions have been used in conjunction with neutral outgoing wave solutions by Mack to determine the forced response of the laminar boundary layer to free stream sound waves.

A similar approach has been applied to shock tube boundary layers in the present work. To date no evidence has been found that the forced response analysis can explain transition in shock tube boundary layer flows. Wall cooling has the same effect for shock tube boundary layer flows as it has for supersonic wind tunnel flows, that is, wall cooling tends to weaken the response of the boundary layer to forced oscillations.

A new type of solution to the stability equations was discovered during the course of the outgoing wave study and which shows some promise of providing a mechanism for explaining transition. These solutions are related to the solutions obtained in a forced response analysis insofar as the neutral solutions of the new type represent a special class of forced response solutions, namely, those forced response solutions for which no reflected wave is necessary in order to satisfy the boundary conditions at the wall. These new solutions are incoming wave eigensolutions and were originally discovered when it was noted that certain damped supersonic incoming wave eigensolutions would abruptly end in a c_r versus α plot unless one allowed the sign of the real part of the characteristic value of the viscous counterpart to the inviscid free-stream solution to switch from negative to positive. Figures 10 and 11 show some of these new eigensolutions. In Figure 10, as α is decreased at constant R, the real part of the characteristic value of the viscous counterpart to the inviscid solution changes sign from negative to positive at the points labeled as a "transitional" region. For α greater than α at this "transitional region," the amplitude of the waves decrease as y increases whereas for α less than α at this "transitional region," the amplitude of the waves increases as y increases. These new incoming wave eigensolutions must be interpreted differently than outgoing wave eigensolutions. For the incoming wave eigensolutions, positive c_i means that the strength of the free-stream disturbance is growing in time while negative c_i implies that the strength of the free-stream disturbance is decreasing in time. Thus, c_i is an attribute of the free-stream disturbance and is not by itself related to the instability of the boundary layer.

There are finite Reynolds stresses associated with these incoming wave eigen-solutions. Thus, these incoming wave eigensolutions provide a mechanism for energy redistribution in the boundary layer. Since there is a net energy transport from the disturbance to the mean flow, these incoming wave eigen-solutions offer a potentially important mechanism for changing the character of the mean flow profile.

These incoming wave eigensolutions have been found to exist for both types of supersonic disturbances, i.e., for $c_r \leq 1-1/M_2$ and $c_r \leq 1+1/M_2$. For incoming wave eigensolutions with $c_r \leq 1-1/M_2$, an especially interesting phenomena has been found. Two separate families of solutions have been found to exist. One family has its origin at $c_r = 1-1/M_2$ and $\alpha = 0$ while the other family originates from subsonic solutions. Above a certain Reynolds number, labeled "changeover Reynolds number" (R_{ch}), the two families switch their relative positions. This phenomena is shown in Figures 12 and 13 for $M_s = 3.25$. In Figure 14, the variation of R_{ch} is shown as a function os shock Mach number. The physical importance of this changeover Reynolds number appears to be that for Reynolds numbers less than the changeover Reynolds number the forced response analysis shows that a relatively strong reflected wave is present, i.e., significant energy is carried out of the boundary layer. For Reynolds numbers greater than R_{ch}, the strength of the reflected wave is relatively weak. Thus, when the Reynolds number is greater than R_{ch}, the boundary layer is more susceptable to mean flow profile modification than when $R < R_{ch}$.

The variation of R_{ch} versus M_s shown in Figure 14 does follow the general trend of the first transition reversal observed by Boison. Thus, it would appear that this "changeover Reynolds number" might have the same physical significance for incoming waves as the critical Reynolds number has for outgoing waves. That is, the "changeover Reynolds number" seems to represent a Reynolds number which must be reached before significant transition mechanisms can take effect.

The transition measurements shown in Figure 1 suggest that the changeover Reynolds number associated with supersonic and sonic waves having $c_r \leq 1/M_2$ may be responsible for the transition reversal which occurs in the vicinity of Tw/Te $\simeq$ .35. Some other mechanism must be responsible for transition for

214

Tw/Te>.35. One possibility is that there may be a similar changeover Reynolds number phenomena associated with waves having $c_r \leq 1+1/M_2$. This possibility is currently being investigated.

WALL COOLING FOR BOUNDARY LAYER CONTROL

The strong stabilizing effect of wall cooling on outgoing waves suggests that wall cooling is a potentially useful method for delaying the onset of transition on flight vehicles. The results presented in this paper suggest further that wall cooling is very effective in stabilizing boundary layers in the subsonic flow regime. The same amount of wall cooling associated with the $M_s = 1.5$ ($M_2 = .603$) boundary layer when applied to a steady flow boundary layer with $M = .603$ yields a critical Reynolds number R_x of 1.4×10^8 which is only slightly less than the critical Reynolds number of the $M_s = 1.5$ shock tube wall boundary layer. Work in progress is being directed toward quantifying the effect that wall cooling can have on delaying transition and thus reducing drag on subsonic aircraft.

REFERENCES

1. Mack, L. M., "On the Application of Linear Stability Theory to the Problem of Supersonic Boundary-Layer Transition," AIAA preprint No. 74-134, February 1974.

2. Morkovin, M. V., Lessons from Transition of Shock-Tube Boundary Layers, AFOSR Scientific Report AFOSR-TR-72-0057, November 1971.

3. Morkovin, M. V., Critical Evaluation of Transition from Laminar to Turbulent Shear Layers with Emphasis on Hypersonically Traveling Bodies, AFFDL-TR-68-149, March 1969.

4. Boison, J.C., Investigation of Test Facility Environmental Factors Affecting Boundary Layer Transition, AFFDL-TR-73-106, September 1973.

5. Reshotko, E., "Transition Reversal and Tollmien-Schlichting Instability," The Physics of Fluids, Vol. 6, No. 1, pp. 335-342, March 1963.

6. Mack, L. M., Boundary-Layer Stability Theory, JPL Report No. 900-277 Revision A, November 1969.

7. Ostrach, S. and Thornton, P. R., "Stability of Compressible Boundary Layers Induced by a Moving Wave," Journal of the Aerospace Sciences, Vol. 29, March 1962, pp. 289-296.

8. Dunn, D. W. and Lin, C. C., "On the Stability of the Laminar Boundary Layer in a Compressible Fluid," Journal of the Aeronautical Sciences, July 1955, pp. 455-477.

9. Mack, L. M., "The Stability of the Compressible Laminar Boundary Layer According to a Direct Numerical Solution," in Recent Developments in Boundary Layer Research, AGARDograph 97, Part I, pp. 329-362, 1965.

10. Mack, L. M., "Progress in Compressible Boundary Layer Stability Computations," in Proceedings of the Boundary Layer Transition Workshop, Vol. 4, Aerospace Corp. Report No. TOR-0172, pp. 1-1 to 1-35, December 1971.

11. Boehman, L. I., "Recalculation of Brown's Stability Results." Paper presented at the 1971 Boundary Layer Transition Specialist's Workshop, San Bernadino, California. Published in Proceedings of the 1971 Boundary Layer Transition Workshop, Volume 4, Aerospace Corporation, Report No. TOR-0172 (S 2816-16)-5, December 1971.

12. Boehman, L. I., The Effect of Boundary Layer Growth on the Stability of Supersonic Boundary Layers, AFFDL-TR-73-69, Air Force Flight Dynamics Laboratory, Wright-Patterson Air Force Base, Ohio, September 1973.

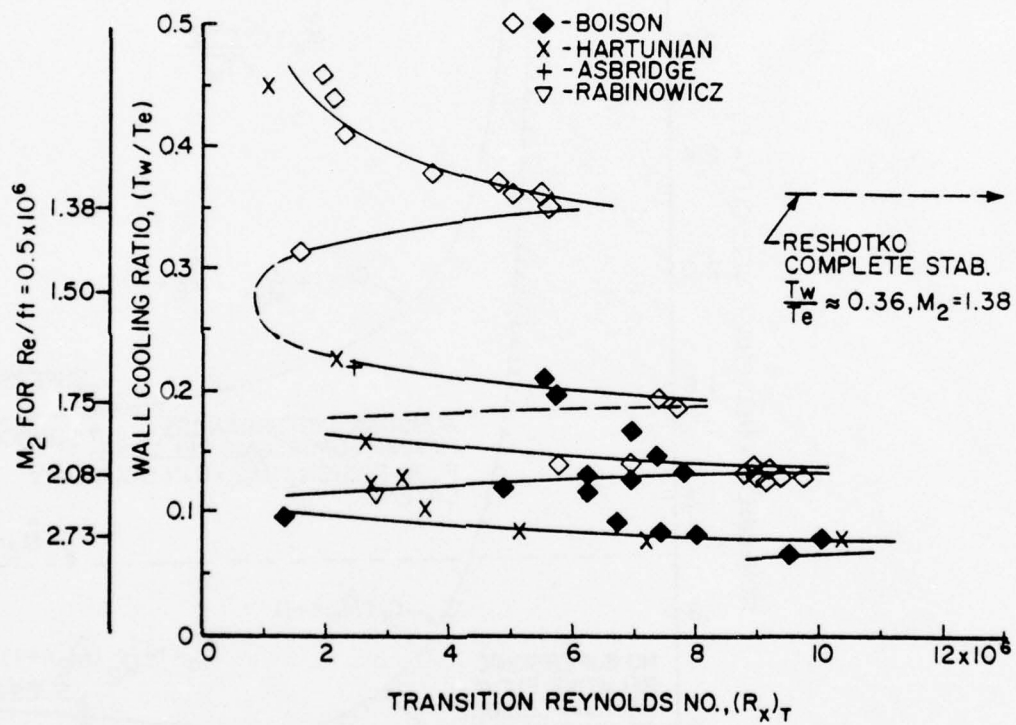Figure 1. Transition Reynolds No. Correlation, Re/ft-0.5 x 10^{6}.
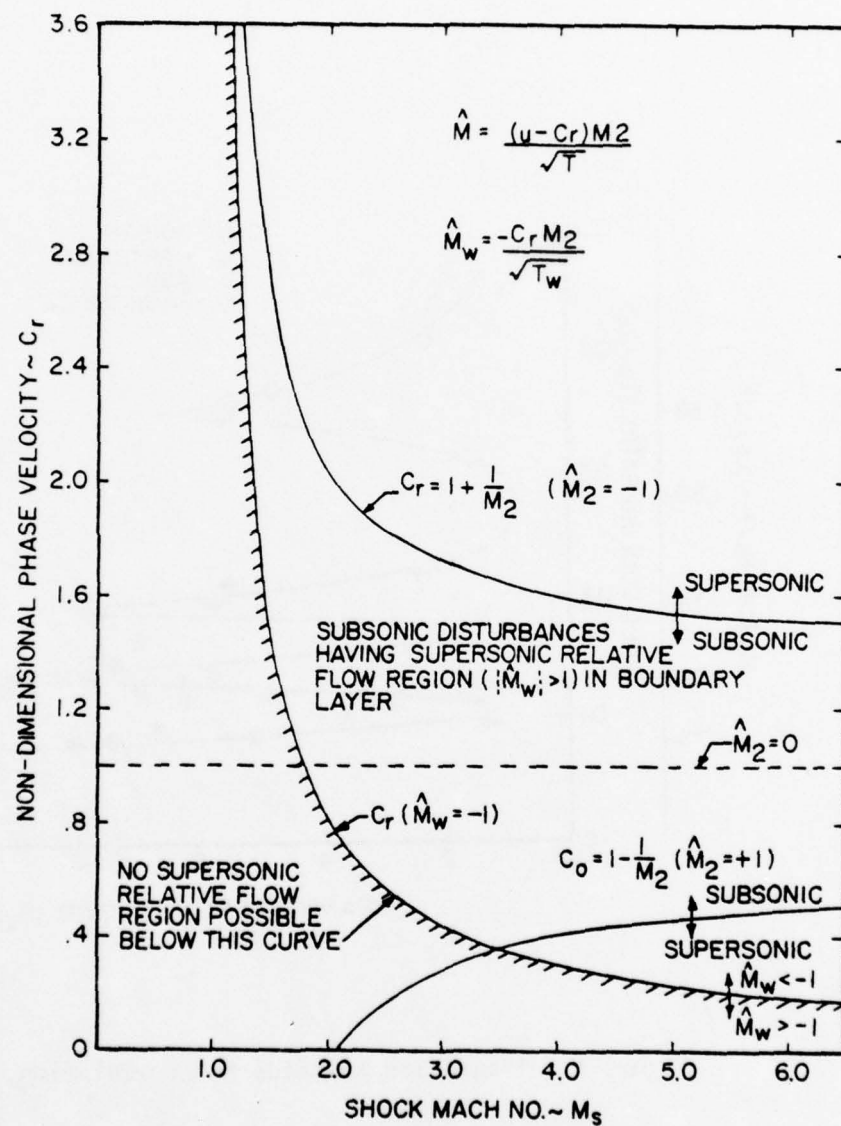
Figure 2. Supersonic and Subsonic Wave Phase Velocities for the Shock-Tube Boundary Layer.

218
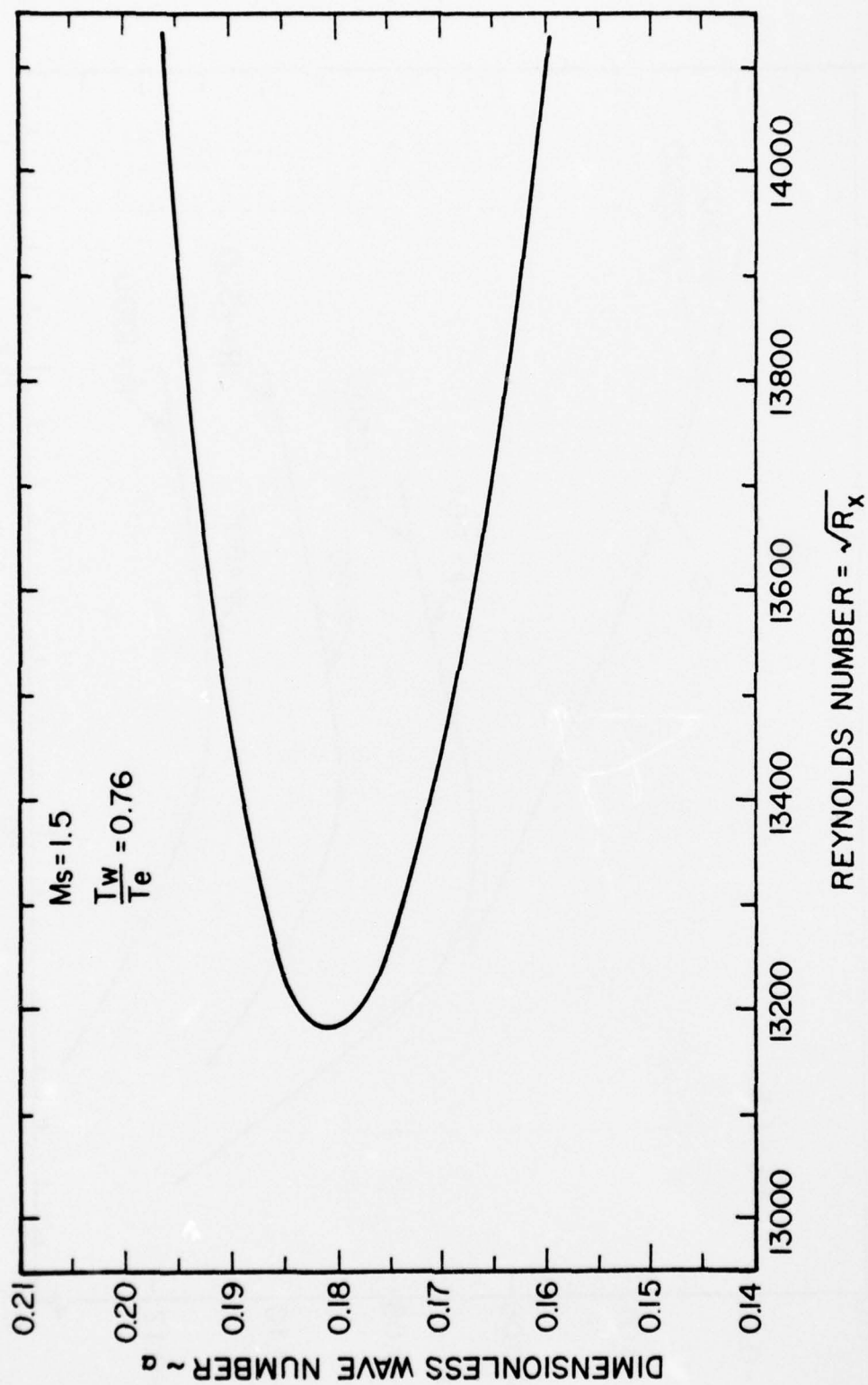
Figure 3. Neutral Stability Curve for M_S = 1.5 Shock-Tube Boundary-Layer -- Two-Demensional Disturbances.
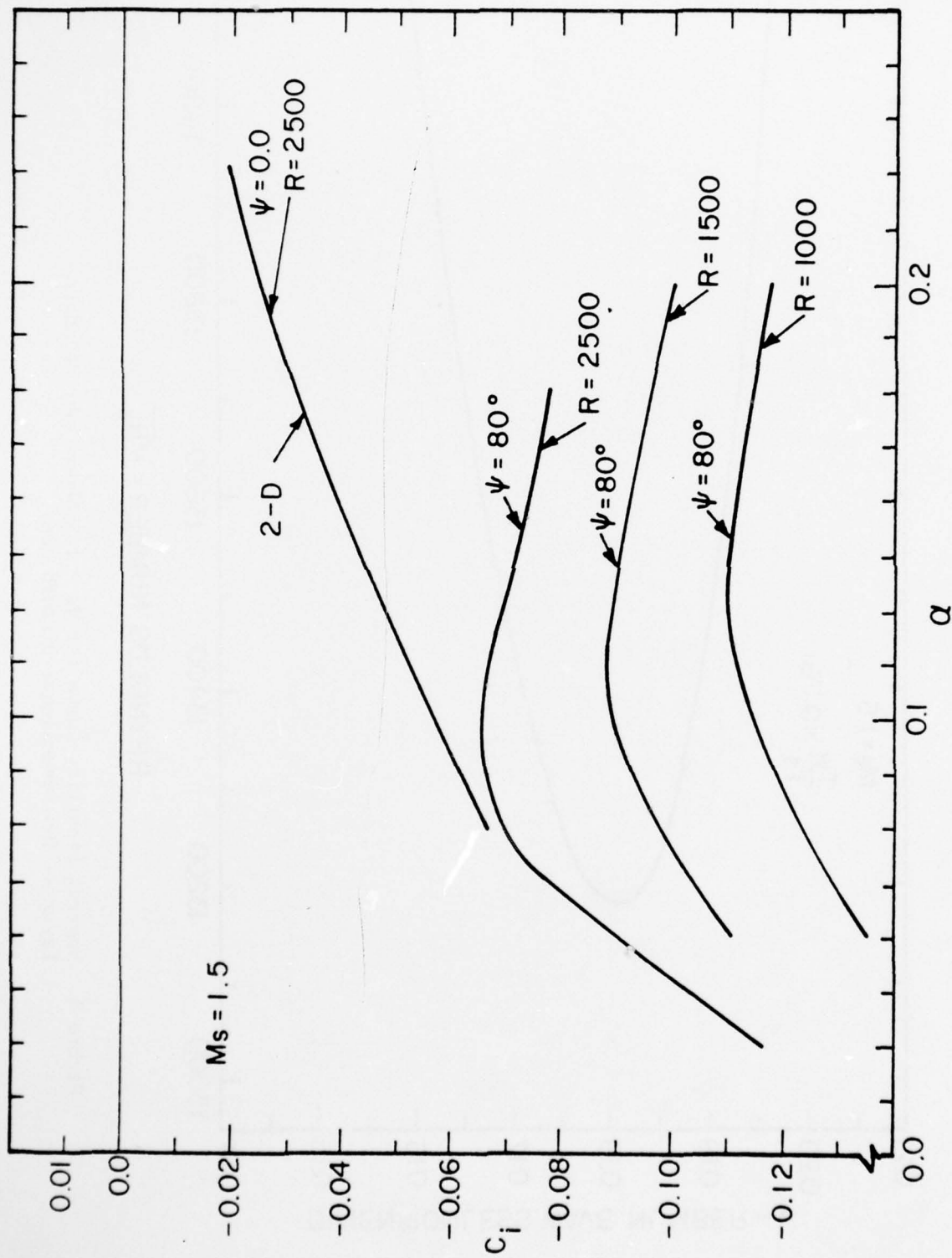
Figure 4. Effect of Wave No. (α) on Amplification (c_i) for Varying Reynolds Number (R). Wave Angle; $\psi = 800$, $M_s = 1.5$.
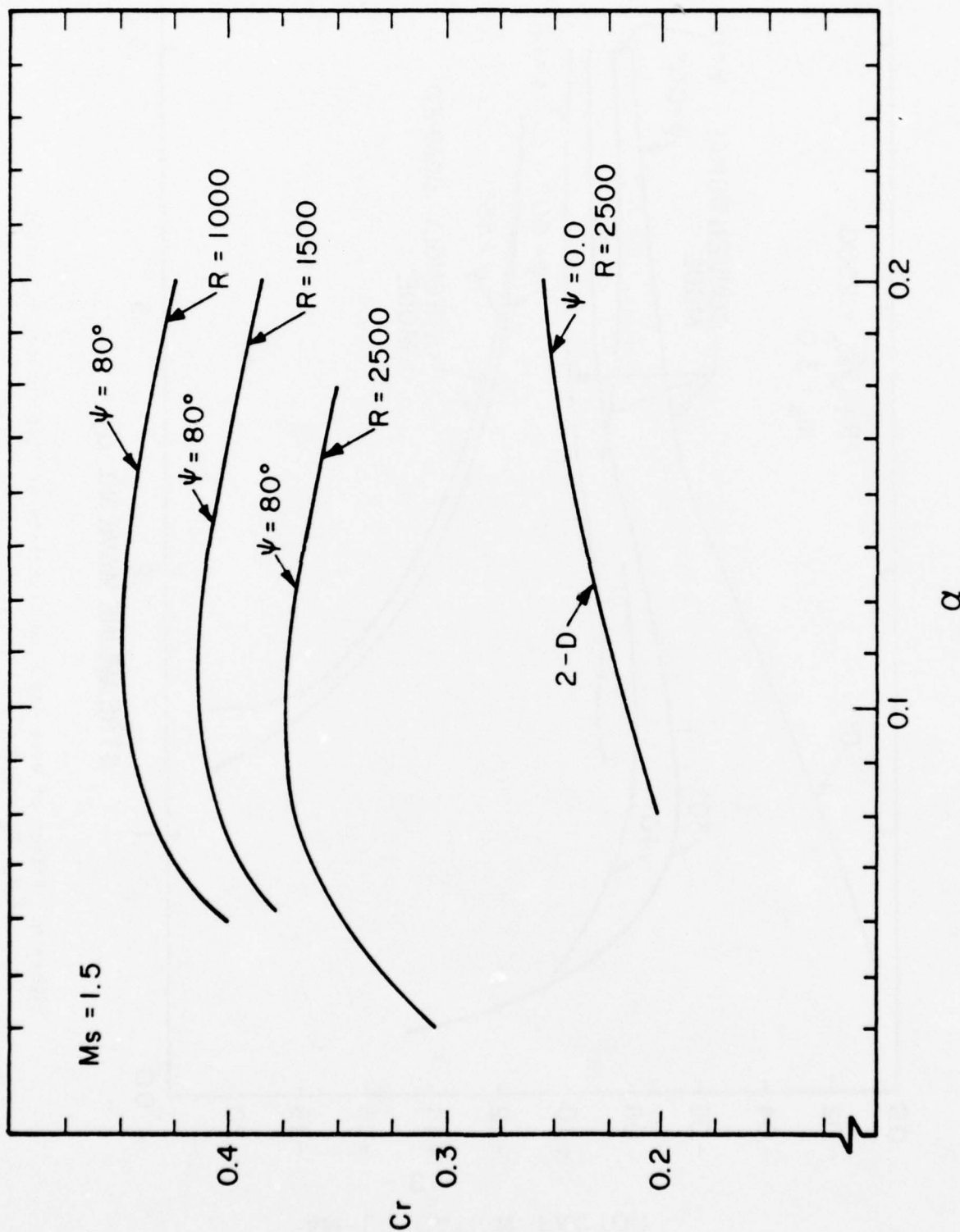
Figure 5. Effect of Wave No. (α) on Phase Velocity (C_r for Varying Reynolds Numbers (R). Wave Angle; $\psi = 80^\circ$, $M_s = 1.5$.
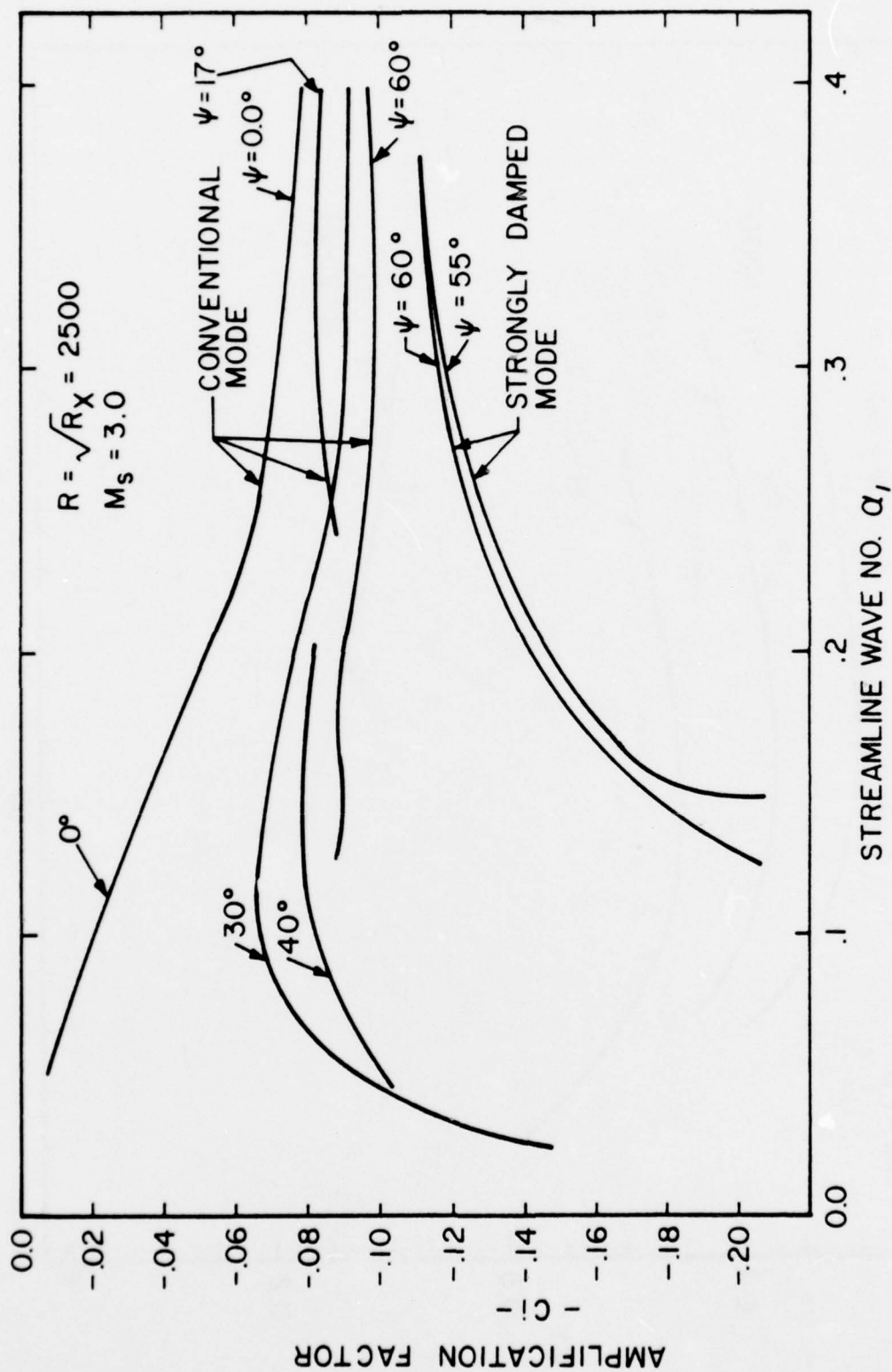
Figure 6. Effect of Wave Angle on Stability of Disturbances c_i versus α_1, $M_s = 3.0$.
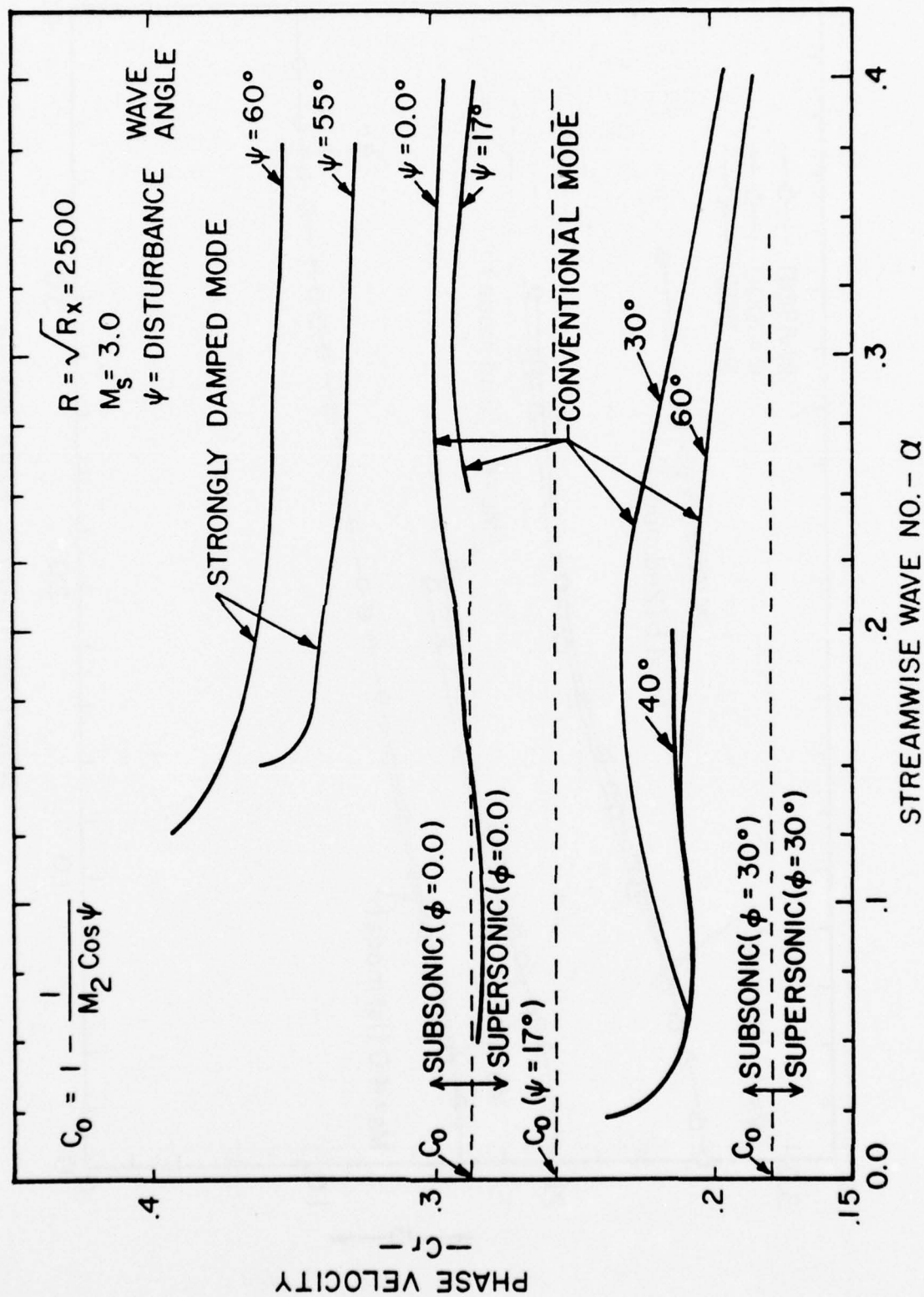
Figure 7. Effect of Wave Angle of Dispersion, c_r versus $\check{\alpha}_1$ for $M_s = 3.0$.
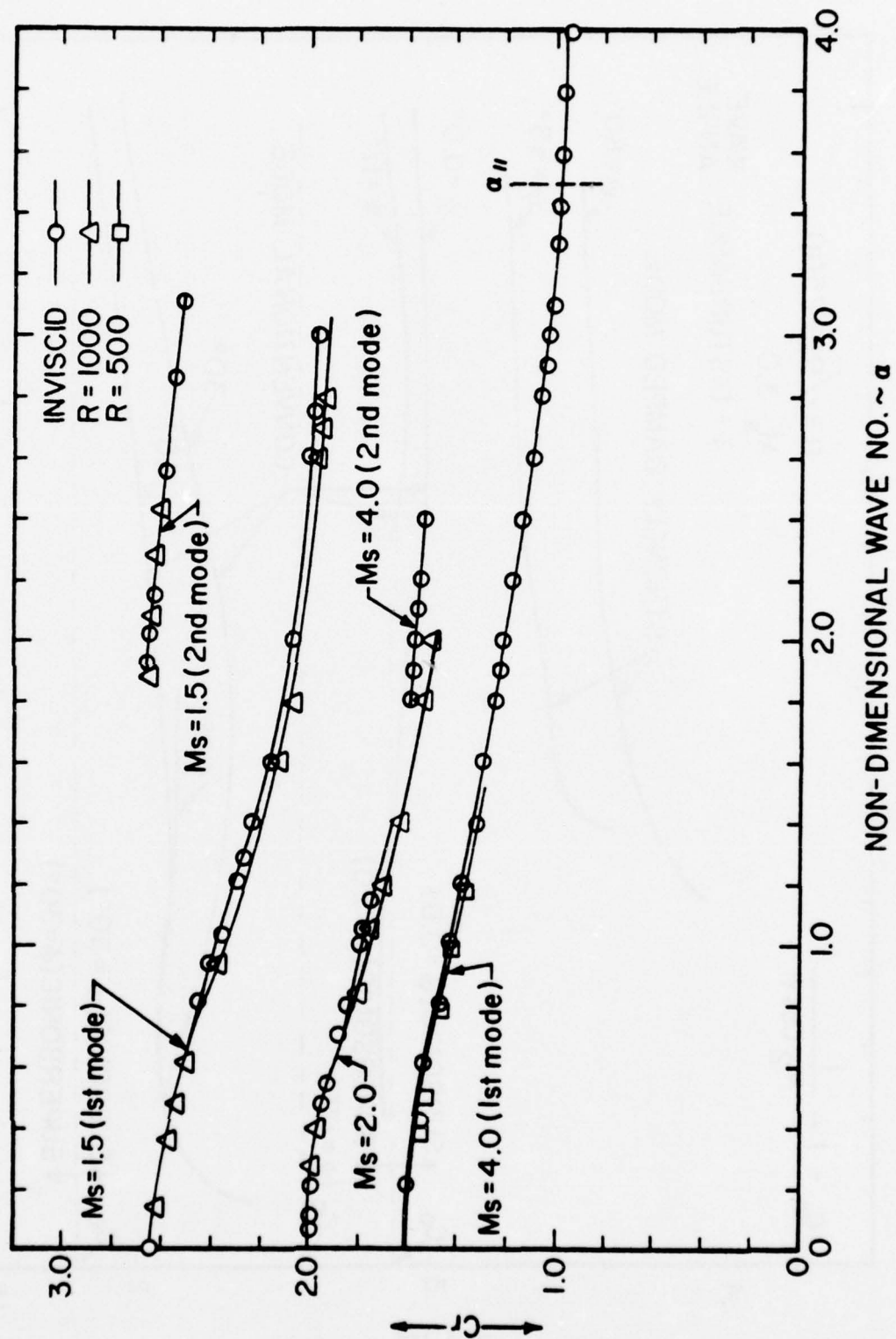
Figure 8. Phase Velocity as a Function of α for First and Second Mode Regular Subsonic Disturbances.
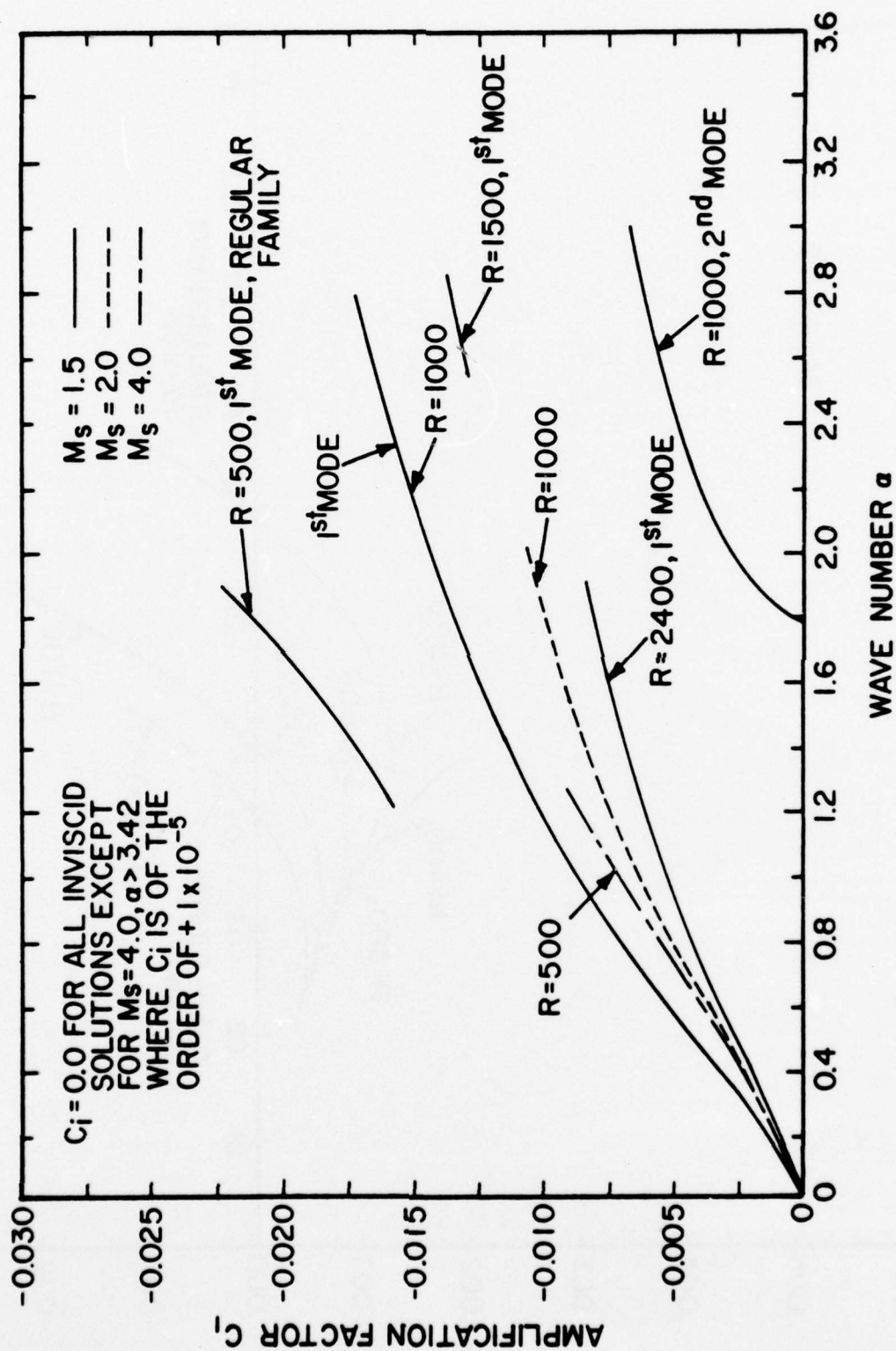
Figure 9. Amplification Factor Versus Wave Number for Subsonic Regular Family of Solutions, M_s = 1.5, 2, and 4.
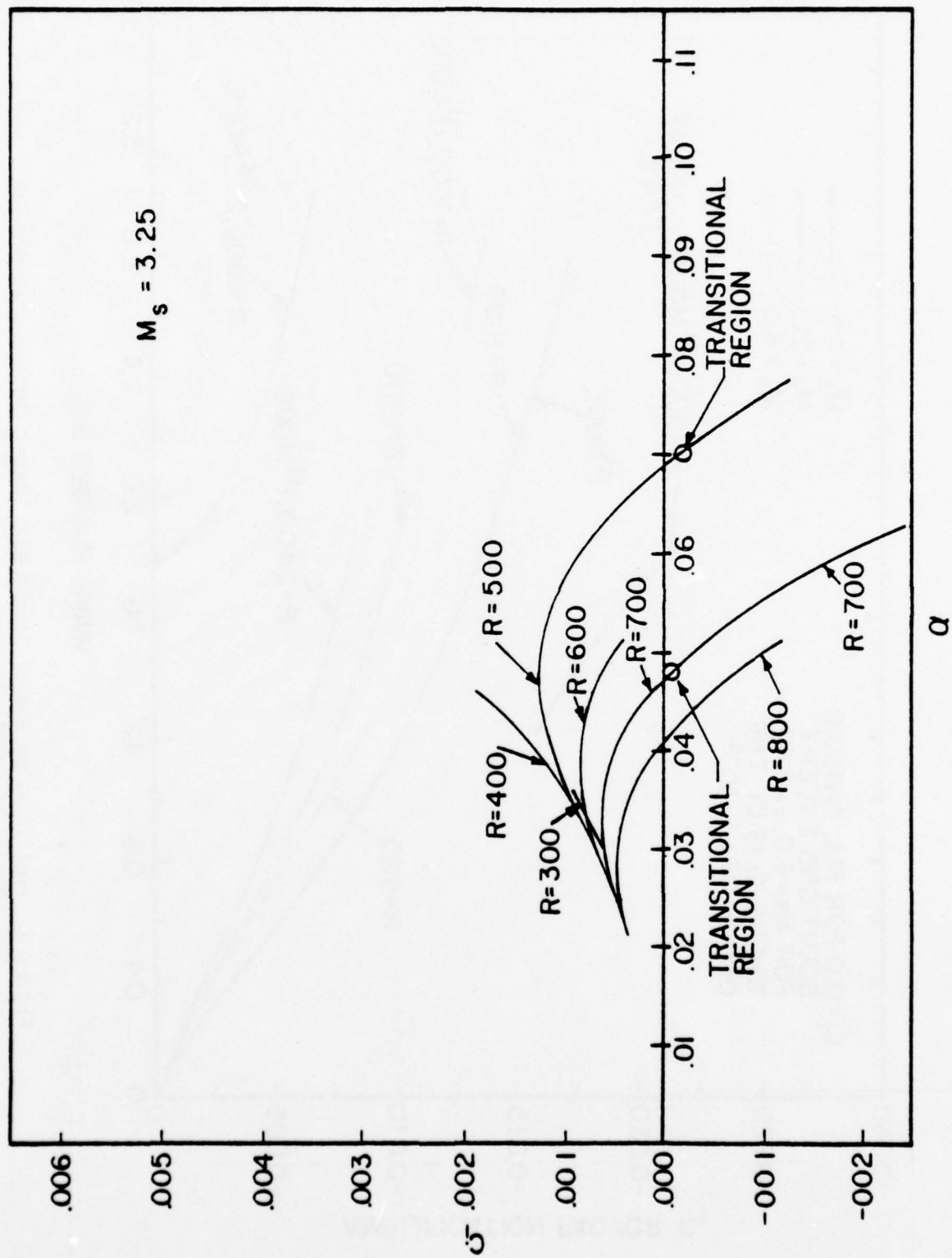
Figure 10. Effect of Wave Number (α) on Amplification (c_i), $M_s = 3.25$.
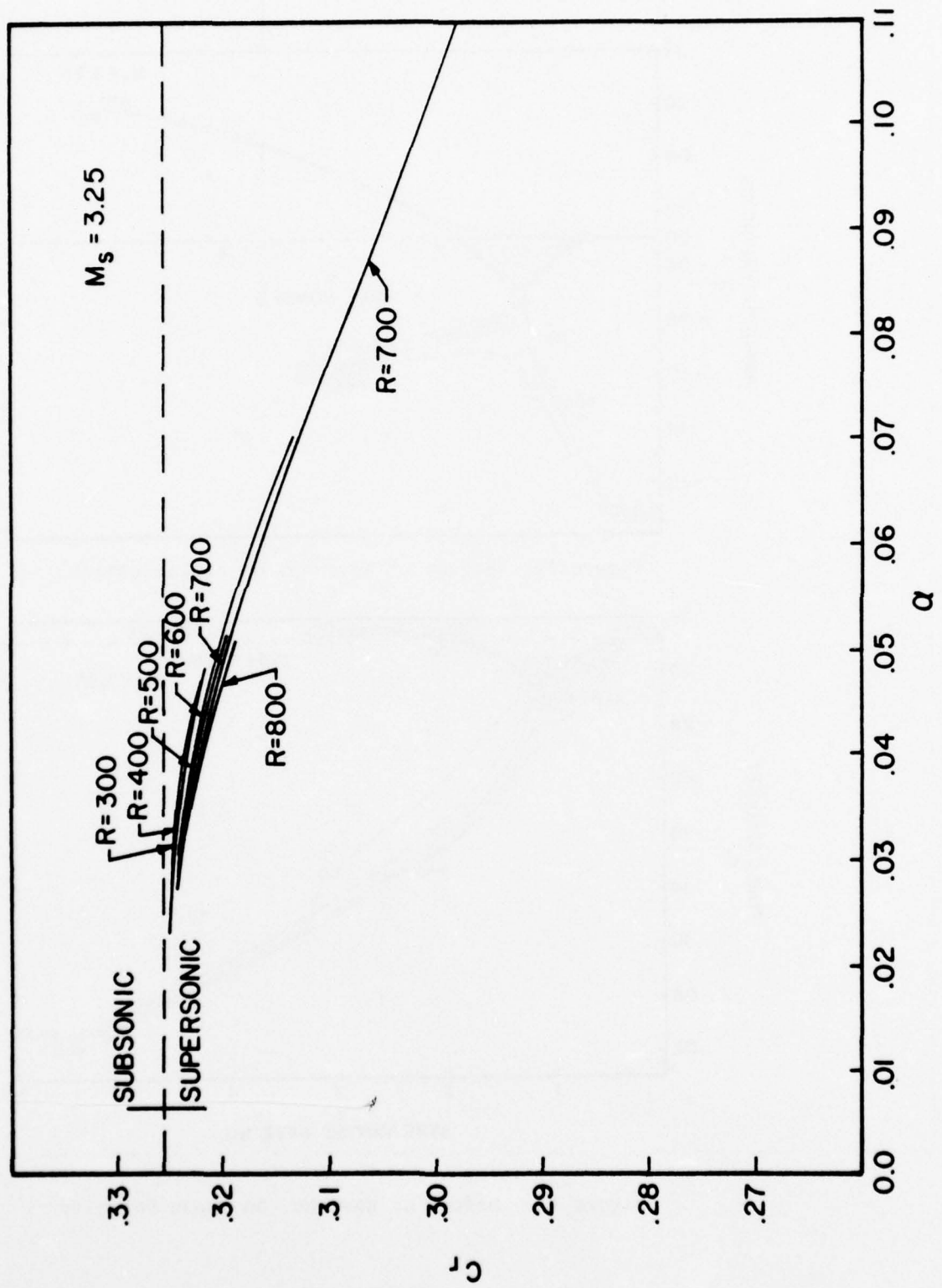
Figure 11. Effect of Wave Number (χ) on Phase Velocity (c_r) for Varying Reynolds Number ($R = R_x$), $M_s = 3.25$.
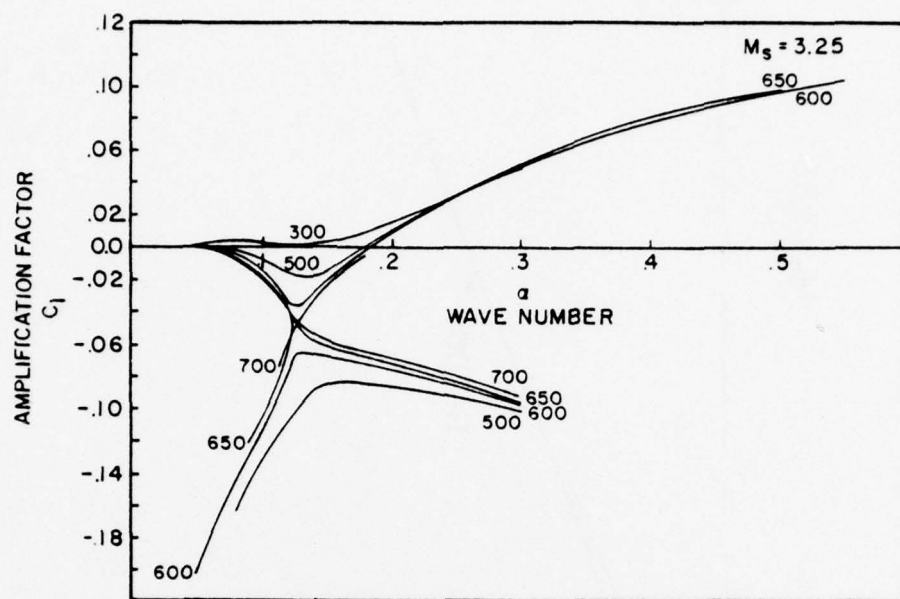
Figure 12.   Effect of Wave No. on Amplification.
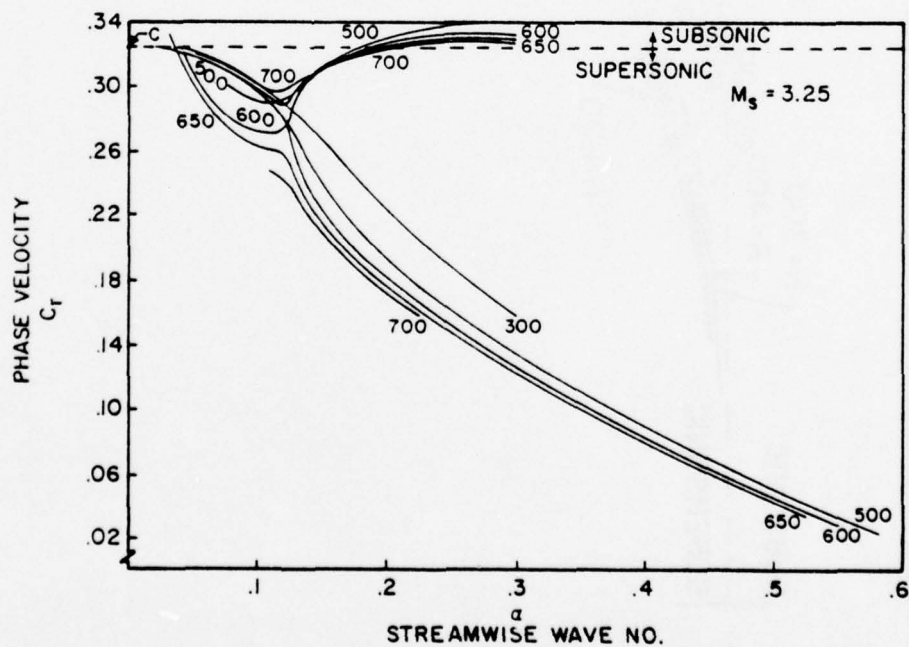
Figure 13.   Effect of Wave No. on Phase Velocity

228
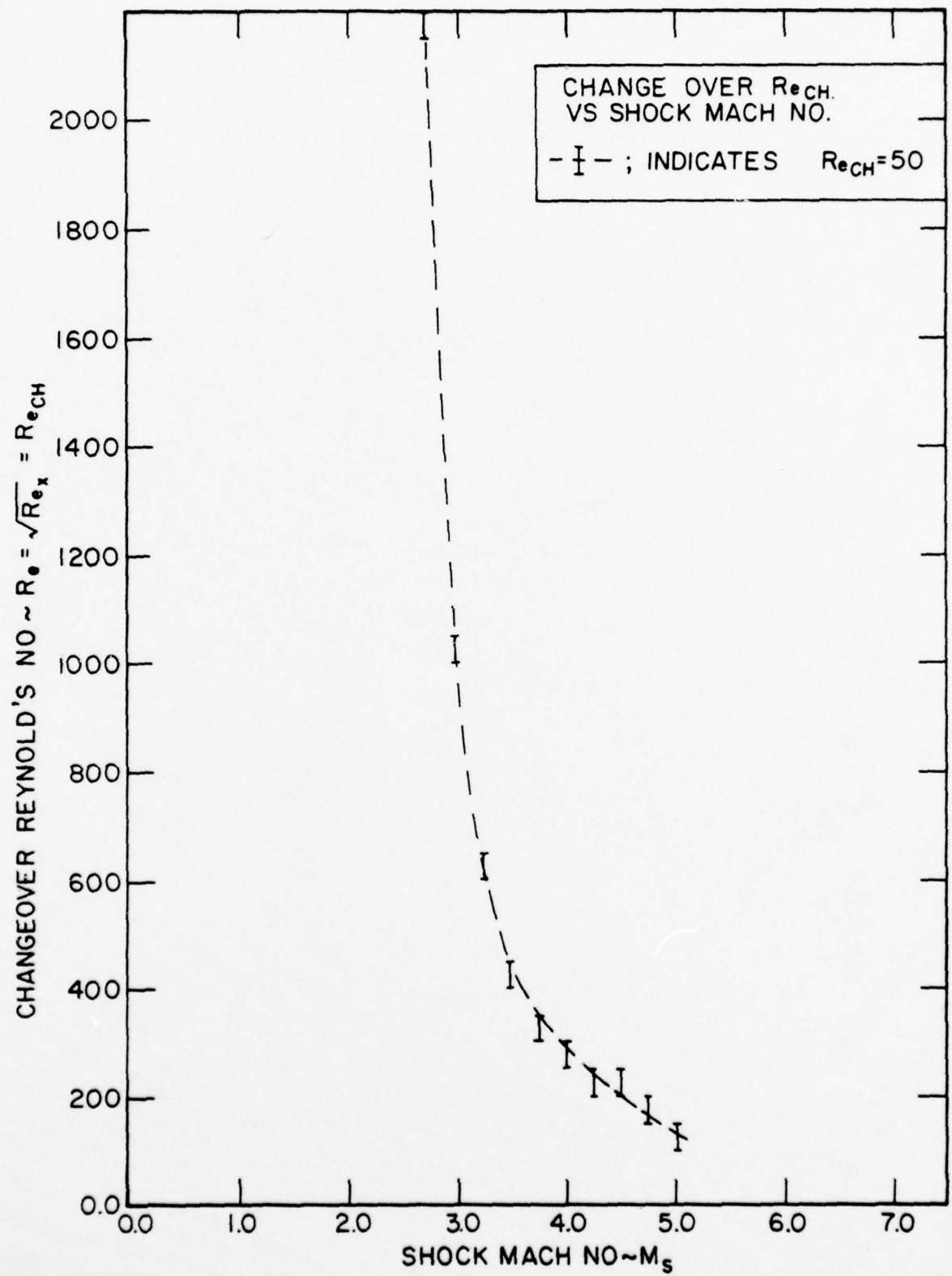
Figure 14.   Effect of Mach No. on "Changeover" Reynolds No.

TRANSITION MEASUREMENTS ON A 5° HALF-ANGLE CONE AT MACH 5 IN A LUDWIEG-TUBE WIND-TUNNEL

by

P. Krogmann
DFVLR - AVA Göttingen, FRG

ABSTRACT:

Transition of the laminar boundary layer on a sharp 5° half-angle cone was observed in the DFVLR-AVA Ludwieg-Tube Tunnel at Mach 5 by means of local heat transfer measurements. In a range of unit Reynolds numbers from Re/cm = 10^5 to $5 \cdot 10^5$ the results obtained did not show the so-called 'Unit Reynolds number effect', as it was found in several other facilities. A variation of the wall to stagnation temperature ratio from T_w/T_0 = 0.5 to 0.9 had no effect on transition Reynolds number. Small variations of angle of attack strongly affected the location of transition on the most windward and leeward cone generator.

NOTATION:

c_p	specific heat
c_r	phase velocity
d	diameter of the model
h	characteristic tunnel dimension
l	length
Ma	Mach number
p	pressure
$\dot{q}$	heat transfer rate
Re	Reynolds number
St	Stanton number
s	wall thickness of the model
T	temperature
t	time
U	velocity
x	distance along cone
α	angle of attack
β	frequency
Θ	cone half-angle
λ	wavelength
ν	kinematic viscosity
ρ	density
φ	circumferential angle

SUBSCRIPTS:

o	stagnation conditions
∞	free stream conditions
e	conditions at the edge of the boundary layer
M	model material
tr	transition
w	wall

1.   INTRODUCTION:

This paper presents some results of an experimental investigation intended to get information about local heat transfer and transition behaviour on simple body shapes in supersonic flow. It is well-known that transition of the boundary layer is affected by various factors, and often experimental transition results from different investigations have been compared neglecting those factors involved within the experiments. Transition Reynolds number varies considerably with local Mach number, pressure gradient, nose blunting, and wall-roughness, [1], [2], [3]. One of the most serious (and mysterious) problems in transition measurements in wind-tunnels is the effect of stagnation pressure and temperature level, according to which the transition Reynolds number increases and with unit Reynolds number. Beside the unit Reynolds number effect PATE et al. [4], [5], [6], [7], observed an influence of the size of the test section on transition Reynolds number. Experiments of LAUFER [8] showed that the turbulent boundary layer along the tunnel walls is the source of aerodynamic noise. Generally the unit Reynolds number effect is related to this noise radiated from the turbulent boundary layer, and in Reference [4] it was mentioned that the intensity of the pressure fluctuations was proportional to the size of the test section. However, transition measurements in an aeroballistic range, where disturbances associated with wind-tunnel flows should not be present, showed a unit Reynolds number effect even stronger than in wind-tunnels, [9], [10].

Another difficulty encountered in experimental transition investigations is the effect of the temperature ratio T_w/T_0. The experiments of References [2], [11], [12], showed no influence of T_w/T_0 on the transition Reynolds number, whereas in [13] and [14] transition Reynolds number decreased moderately with increasing T_w/T_0, and an opposite trend was observed in [15], [16]. Much stronger effects occured in References [17], [18], [19], where at low temperature ratios a 'transition reversal' or even a 're-reversal' was observed. In References [19] and [20] it was also shown that transition is sensitive to small variations in angle of attack in a manner that transition was promoted on the leeward side of a slender cone and delayed on the windward side.

233

In the present investigation the location of transition was detected by means of local heat transfer measurements at different unit Reynolds numbers, temperature ratios, and angles of attack.

2.   EXPERIMENTAL DETAILS:

The experiments were carried out in the DFVLR-AVA Ludwieg Tube facility at Göttingen. This facility, shown as a sketch in Figure 1, consists of three test-legs for mach numbers from Ma = 3 to $\approx$ 12, and is capable of relatively high Reynolds numbers. The measurements were made mainly at a free stream Mach number of Ma_∞ = 5 on 5° half-angle cones and partly at Ma_∞ = 6.8 on a 10° half-angle cone in tunnel B, which has axisymmetric, contoured nozzles with an exit diameter of 0.5 m. Further information on the facility may be taken from Figure 1 or from Reference [2]. The variation of unit Reynolds number was accomplished by varying stagnation pressure and/or stagnation temperature, and the model was at room-temperature. The models used were electro-formed cones, made of nickel. They were equipped with thermocouples along a conical ray and had a final surface finish of approximately 1 μm. The main dimensions of the models are shown in Figure 2.

For the local heat transfer rate measurements the so-called 'thin skin technique' was applied. The thin skin (s$\approx$0.2 mm) of the model, when exposed to the flow, is used as a calorimeter, and the local temperature rise with time is measured. From this one obtains for the local heat transfer rate,

(1) $\dot{q} = \rho_M \, c_{pM} \, s \, (dT/dt)$

where ρ_M is the density and c_{pM} the specific heat of the model material. In the following the heat transfer rates obtained from Equation (1) were non-dimensionalized with free stream and stagnation conditions to Stanton numbers

(2) $St = \dfrac{\dot{q}}{\rho_\infty U_\infty \, c_p \, (T_0 - T_w)}$

234

3. RESULTS AND DISCUSSIONS:

3.1 Effect of Unit Reynolds Number

Heat transfer measurements have proven to be one of the best methods
to detect transition on models in supersonic flow. Due to the change of
the boundary layer profile at transition the skin friction increases con-
siderably and, therefore, the local heat transfer rate. In this paper
the start and the end of transition are defined as the location of the
minimum and maximum in the heat transfer distribution, and the corresponding
transition Reynolds number is based on the distance from the tip of the
model. In Figure 3 the transition results obtained on the two 5° half-
angle cones $_1$ = 17 cm (Symb. ◑ ○) and $_1$ = 52 cm (Symb. ▲ △) are compared
with results from other facilities. In the range of unit Reynolds number,
based on local flow properties at the edge of the boundary layer, from
$(U/\nu)_e = 10^5$ to $5 \cdot 10^5$ cm^{-1} the transition Reynolds numbers of the present
investigation are independent of unit Reynolds number. Results from
other facilities show an increase of transition Reynolds number with in-
creasing unit Reynolds number. This figure also exhibits the effect of
tunnel size on transition. For identical edge Mach number unit Reynolds
number, and the same method of transition detection the transition Reynolds
number is much higher in a 40 x 40in tunnel (Symb. ▧) than in a 12 x 12in
tunnel (Symb. ▽). The upper left curve in Figure 3 denotes an estimate
of transition Reynolds numbers on a slender cone after two-dimensional
measurements in a very large tunnel (16 x 16 ft).

The effect of Reynolds number as well as the effect of different
tunnel size generally is related to free stream disturbances which are
radiated from the turbulent boundary layer on the tunnel walls. This is
a plausible explanation for the different results, but it is not an
explanation for the strong Reynolds number effect in POTTER's data [9],
obtained in an aeroballistic range. Later measurements made in the same
facility [10] once again confirmed this trend. Even an artificial sound
field of 130 dB (800 Hz) had no effect on transition Reynolds number.

IN the following Figure 4 an attempt was made to correlate in a
simple manner transition results from different facilities. The only
similarity parameters for wind tunnel flows are the Mach number, unit

Reynolds number and a characteristic dimension. Thus, for a constant free-stream Mach number the transition Reynolds number should depend only on the Reynolds number based on local flow conditions and a characteristic tunnel dimension. Figure 4 shows the transition results of the foregoing Figure 3 plotted against 'tunnel Reynolds number' based on test-section diameter or width. The Reynolds number ranges are denoted only by two symbols, and it is seen that the results from the 12 x 12in tunnel and 40 x 40in tunnel now collapse on one curve. Even the estimate of transition Reynolds number in a 16 x 16 ft. tunnel fits good to the other results. For the high tunnel Reynolds numbers the results of [7] are of the same order of magnitude as those obtained in the present experiments, and the unit Reynolds number effect obviously vanishes at still higher Reynolds numbers. Due to these facts it is concluded that the present data more or less represents the limiting value of transition Reynolds number.

3.2   Effect of Temperature Ratio T_w/T_0

Various trends of transition behaviour at different temperature ratios have been mentioned already in the introduction. Some of the discrepancies in the transition results at different temperature ratios certainly have to be attributed to a unit Reynolds number effect, because the experiments were not performed at constant Reynolds number. RESHOTOKO [22] proposed to use stability theory as a guide to the evaluation of transition data. Among others the dominating parameter in stability theory is the dimensionless frequency $\beta\nu/U^2$ or wavelength $\lambda U/c_r$. After RESHOTKO the transition Reynolds number should vary with U^2/ν. In most wind-tunnels a variation of free stream Reynolds number can be achieved only by varying the pressure level at constant stagnation temperature (therefore, U = const.). Therefore, U/ν and U^2/ν are varied in the same way, and the effects of these two parameters cannot be studied independently.

In the present experiments the unit Reynolds number was held constant at $(U/\nu)_e = 1.8 \times 10^5$ cm^{-1} by varying the stagnation pressure according to the stagnation temperature level. By this the temperature ratio was varied from $T_w/T_0 = 0.5$ to 0.9, and the corresponding variation in free stream velocity was about 21%. Figure 5 shows the transition Reynolds numbers obtained plotted against temperature ratio. In the whole range

236

of T_w/T_0 the transition Reynolds number is unaffected. In addition, a variation of unit Reynolds number by changing stagnation temperature at constant pressure level had no effect on transition, Figure 5b.

3.3 Effect of Angle of Attack

The flow field on a cone at zero incidence is in first approximation two-dimensional and can be described by flat plate flow, if an appropriate transofrmation is applied. However, at angle of attack the flow field becomes three-dimensional and correspondingly complicated. Due to cross-flow components and pressure gradients the flow tends to separate. At separation skin friction and heat transfer have a minimum. Thus, the separation point can be easily detected by local heat transfer measurements. Figure 6 contains the Stanton numbers in the symmetry plane of a 10° half-angle cone at angle of attack ($Ma_\infty = 6.8$). In this case the flow is fully laminar along the cone, and the increasing heat transfer for $\alpha > 10^O$ at the downstream measuring stations indicates flow separation. For higher Reynolds number at Mach 5 the flow along the 5° half-angle cone at zero incidence is still laminar, but at α 1^O the heat transfer starts to increase at the aft measuring station on the most leeward ray, Figure 7. This is due to boundary layer transition, and the transition location rapidly moves upstream with increasing angle of attack. Effects of separation on the heat transfer become evident at $\alpha > 5^O$ where the Stanton numbers again increase.

The rapid movement of transition location with angle of attack is illustrated in Figure 8. Here the transition location relative to that at $\alpha = 0^O$ the transition location has moved upstream approximately 60% on the most leeward ray and 40% on the windward ray. For $\alpha > 3^O$ the position of transition on the leeward side becomes fixed at a distance from the tip of about one-fourth of the initialposition at $\alpha = 0^O$.

The following figures show the heat transfer distributions for three constant angles of attack. The Stanton numbers are normalized with those of the most windward ray. At $\alpha = 5^O$, Figure 9 the high heating rates on the leeward portion of the model exclusively are due to boundary layer transition, but at $\alpha = 10^O$ and 15°, Figures 10 and 11 the effects of transition and separation are mixed and cannot be distinguished independently.

237

4. CONCLUDING REMARKS:

Local heat transfer measurements on slender cones were carried out in the DFVLR-AVA Ludwieg-Tube wind-tunnel. Boundary layer transition was detected from heat transfer distribution, and transition behaviour was investigated for different unit Reynolds numbers, temperature ratios T_w/T_0 and different angles of attack.

The results obtained did not show a unit Reynolds number effect. In a range of unit Reynolds numbers from Re/cm = 10^5 to $5 \cdot 10^5$ the transition Reynolds numbers were independent of unit Reynolds numbers.

Neither a variation of the temperature ratio from T_w/T_0 = 0.5 to 0.9 at constant unit Reynolds number nor a variation of T_w/T_0 at constant stagnation pressure had an effect on transition.

Experiments at angle of attack have shown that transition is extremely sensitive to small variations of angle of attack. On the most leeward ray the transition location moved upstream, such that for $\alpha = 3^o$ the transition distance was approximately constant at about one-fourth of that found for $\alpha = 0^o$.

5. REFERENCES:

[1] Potter, J.L. and Whitfield, J.D., Boundary Layer Transition under Hypersonic Conditions. AGARDograph 97, Part III, May 1965.

[2] Sanator, R.J., DeCarlo, J.P., and Torillo, D.F., Hypersonic Boundary Layer Transition Data for a Cold-Wall Slender Cone. AIAA Journ. Vol. 3, No. 4, 1965, pp. 758-760.

[3] Michel, R., Factors Affecting Boundary Layer Transition at Hypersonic Speeds. RAE Library Translation No. 1073, 1964.

[4] Pate, S.R. and Schueler, C.J., Radiated Aerodynamic Noise Effects on Boundary Layer Transition in Supersonic and Hypersonic Wind Tunnels. AIAA Journ. Vol. 7, No. 3, 1969, pp. 450-457.

[5] Pate, S.R. and Brown, M.D., Acoustic Measurements in Supersonic Transitional Boundary Layers. AEDC TR-69-182, 1969.

[6] Pate, S.R., Supersonic Boundary Layer Transition: Effects of Roughness and Free Stream Disturbances. AIAA Journ. Vol. 9, No. 5, 1971, pp. 797-803.

[7] Pate, S.R., Measurements and Correlation of Transition Reynolds
Numbers on Sharp Slender Cones at High Speeds. AIAA Journ. Vol. 9,
No. 6, 1971, pp. 1082-1090.

[8] Laufer, J., Aerodynamic Noise in Supersonic Wind Tunnels. Journ.
of the Aerosp. Sc., Vol. 28, No. 9, 1961, pp. 685-692.

[9] Potter, J.L., Observations on the Influence of Ambient Pressure on
Boundary Layer Transition. AIAA Journ. Vol. 6, No. 10, 1968,
pp. 1907-1911.

[10] Potter, J.L., Boundary Layer Transition on Supersonic Cones in an
Aeroballistic Range. AIAA Journ. Vol. 13, No. 3, 1975, pp. 270-277.

[11] Softley, E.J., Graber, B.C., and Zempel, R.E., Experimental Observa-
tion of Transition of the Hypersonic Boundary Layer. AIAA Journ.
Vol. 7, No. 2, 1969, pp. 257-263.

[12] Maddalon, D.V. and Henderson, A. Jr., Boundary Layer Transition on
Sharp Cones at Hypersonic Mach Numbers. AIAA Journ. Vol. 6, No. 3,
1968, pp. 424-431.

[13] Cary, A.M., Turbulent Boundary Layer Heat Transfer and Transition
Measurements for Cold-Wall Conditions at Mach 6. AIAA Journ.
Vol. 6, No. 5, 1968, pp. 958-959.

[14] Maddalon, D.V., Effect of Varying Wall Temperature and Total
Temperature on Transition Reynolds Number at Mach 6. AIAA Journ.
Vol. 7, No. 12, 1969, pp. 2355-2357.

[15] Deem, R.E. and Murphy, J.S., Flat Plate Boundary Layer Transition at
Hypersonic Speeds. AIAA paper 65-128, 1965.

[16] Stetson, K.F. and Rushton, G.H., Shock Tunnel Investigation of
Boundary Layer Transition at M = 5.5. AIAA Journ. Vol. 5, No. 5,
1967, pp. 899-906.

[17] Sheets, N.W., Free-Flight Boundary Layer at Transition Investigation
at Hypersonic Speeds. AIAA paper 65-127, 1965.

[18] Richards, B.E. and Stollery, J.L., Further Experiments on Transition
Reversal at Hypersonic Speeds. AIAA Journ. Vol. 4, No. 12, 1966,
pp. 2224-2226.

[19] Wisniewski, R.J. and Jack, J.R., Recent Studies on the Effect of
Cooling on Boundary Layer Transition at Mach 4. Journ. Aerosp. Sc.
Vol. 28, No. 3, 1961, pp. 250-251.

[20] Dicristina, V., Three-Dimensional Boundary Layer Transition on a
Sharp 8° Cone at Mach 10. AIAA Journ. Vol. 8, No. 5, 1970,
pp. 852-856.

[21] Ludwieg, H., Hottner, Th., and Grauer-Carstensen, H., Der Rohr-
     windkanal der Aerodynamischen Versuchsanstalt Gottingen. Jahrbuch
     1969 der DGLR, 1970, S. 52 - 58.

[22] Stability Theory as a Guide to the Evaluation of Transition Data
     AIAA Journ. Vol. 7, No. 6, 1969, pp. 1086-1091.
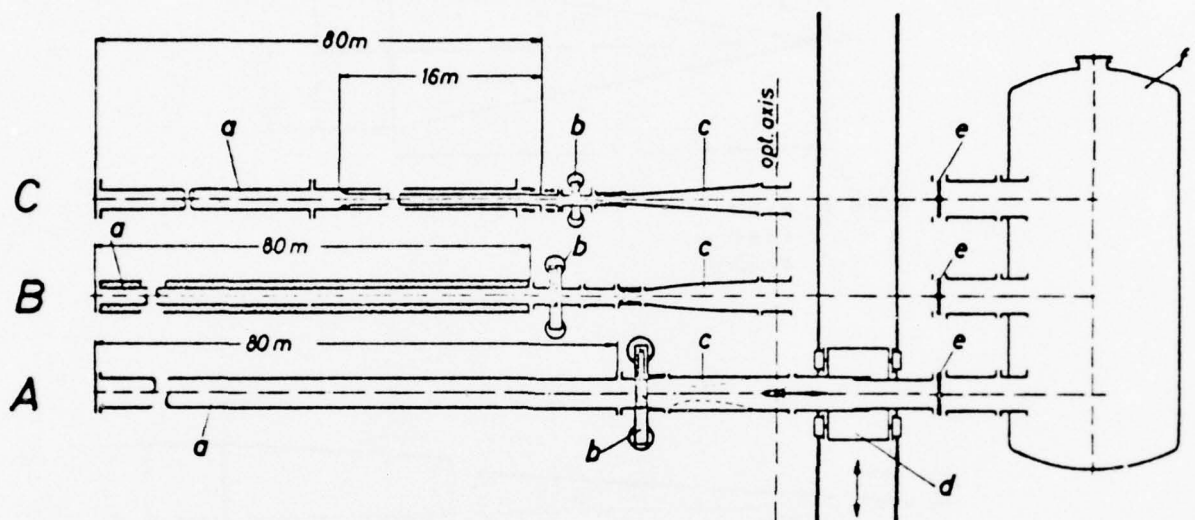
Tunnel	Ⓐ	Ⓑ	Ⓒ
Mach Number Range	2.8 ÷ 4.5	5 ÷ 6.9	9 ÷ 11.7
Test - Section [m]	0.5 x 0.5	0.5 ∅	0.5 ∅
Max. Supply Pressure [at]	15	40	150
Max. Supply Temperature [°C]	20	500	850
Running Time [sec]	≈ 0.4	≈ 0.3	≈ 0.3
Max. Re-Number x10⁻⁶ [m⁻¹]	80 ÷ 50	50 ÷ 18	12 ÷ 6

ⓐ Supply - Tube
ⓑ Fast - Acting Valve
ⓒ Nozzle
ⓓ Movable Model - Support
ⓔ Valve
ⓕ Vacuum Tank

Figure 1. Sketch of Ludwieg Tube Facility.

241
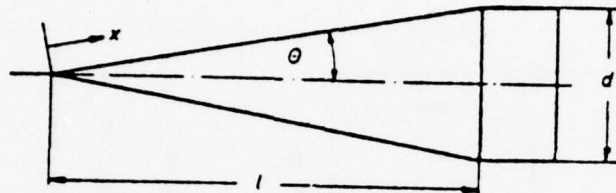
Model I: θ = 10°
l = 8.5 cm
d = 3.0 cm
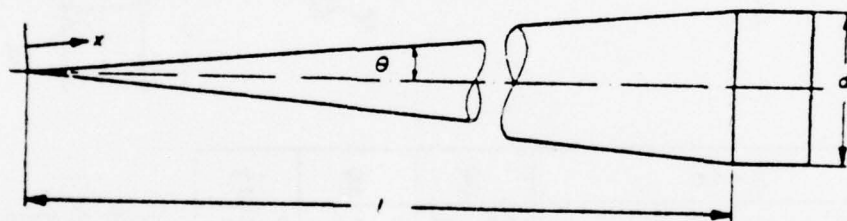
Model IIa: θ = 5°
l = 17.15 cm
d = 3.0 cm

Model IIb: θ = 5°
l = 51.4 cm
d = 9.0 cm

Figure 2. Modell Dimensions.
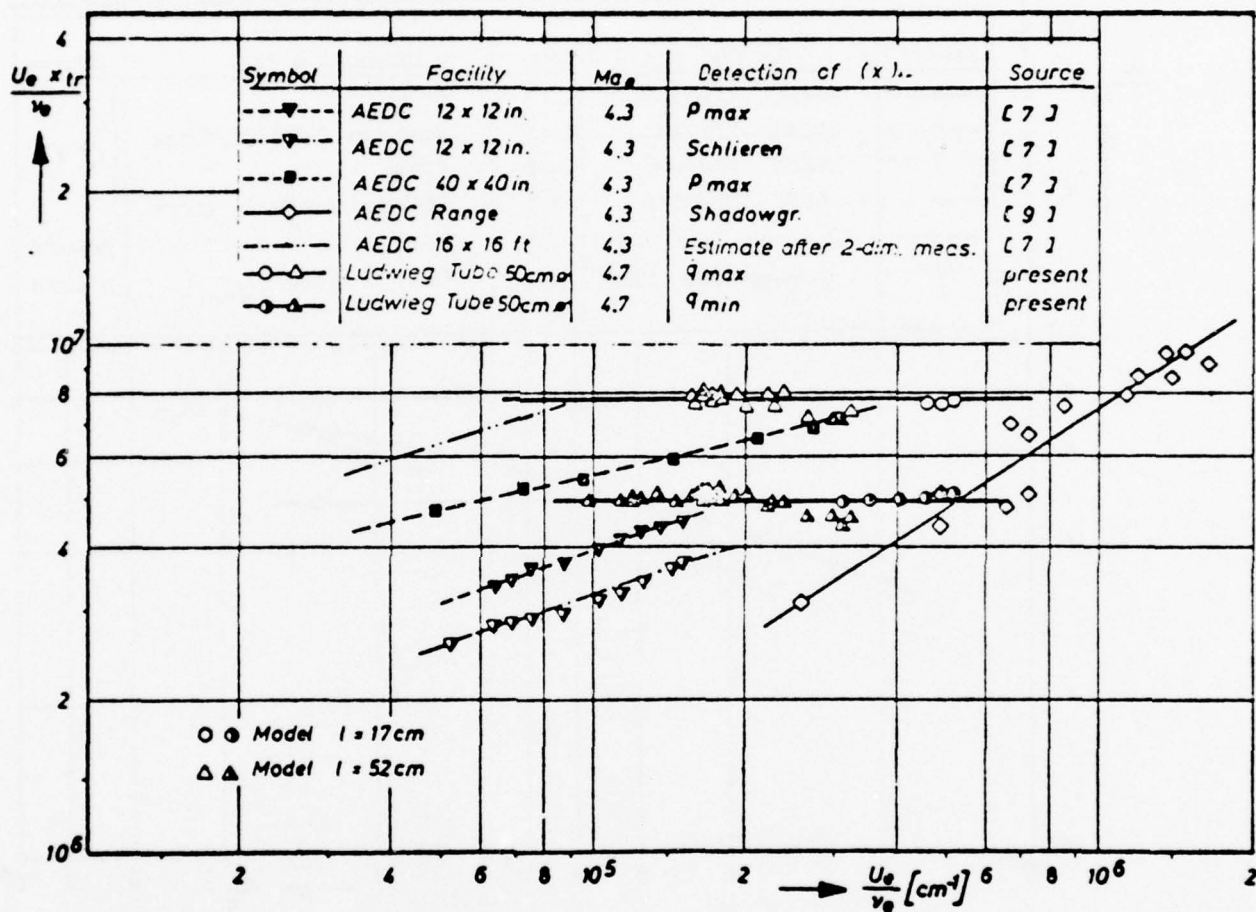
Figure 3.   Transition Re-Numbers from Different Facilities.

Symbol	Facility	Ma_e	Detection of $(x)_{tr}$	Source
---▽---	AEDC 12 x 12 in.	4,3	P_{max}	
---▽-·-	AEDC 12 x 12 in.	4,3	Schlieren $\cong 0,82(x)P_{max}$	[7]
---□---	AEDC 40 x 40 in.	4,3	P_{max}	
---·-·	AEDC 16 x 16 ft.	4,3	Estimate after 2-dim. meas.	
─○─	Ludwieg Tube 50cm²	4,7	$\dot{q}_{max}$	present
─●─	Ludwieg Tube 50cm²	4,7	$\dot{q}_{min} = 0,625(x)_{\dot{q}_{max}}$	present
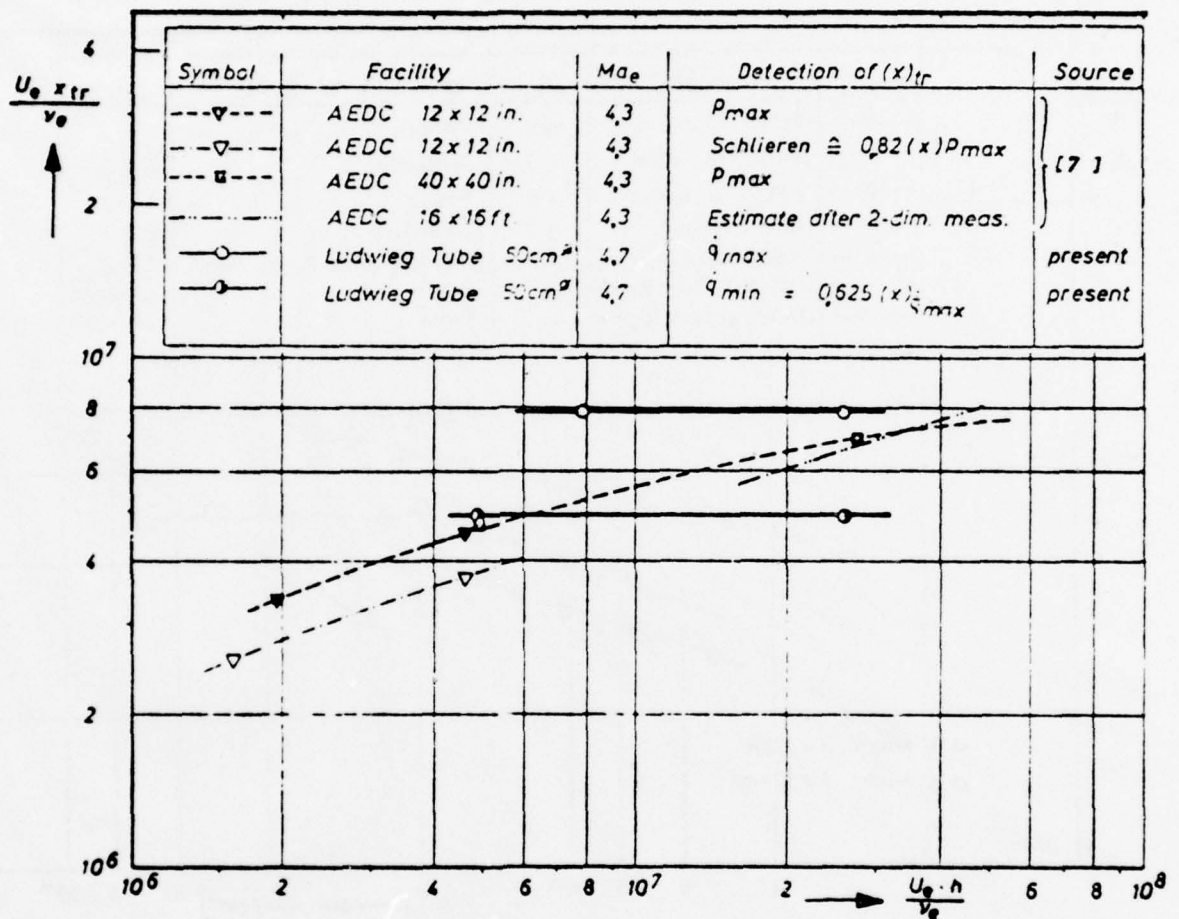
Figure 4. Correlation of Transition Re-Numbers

244
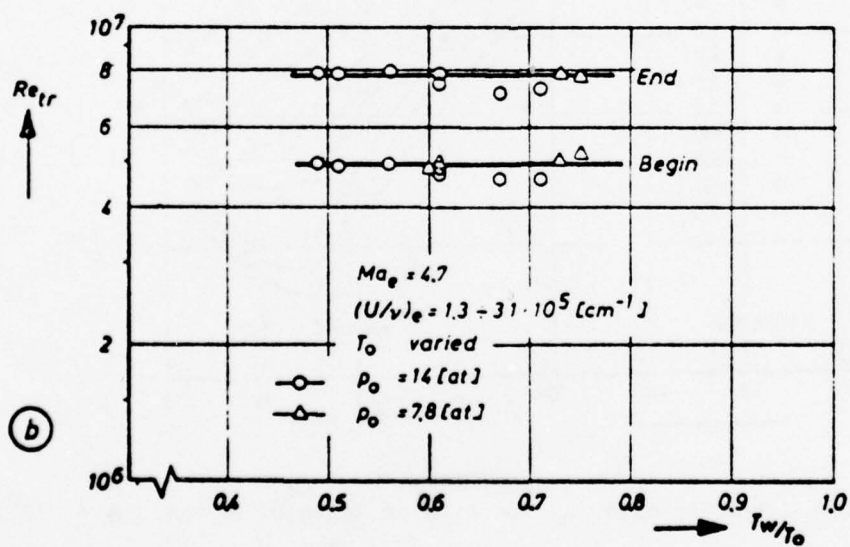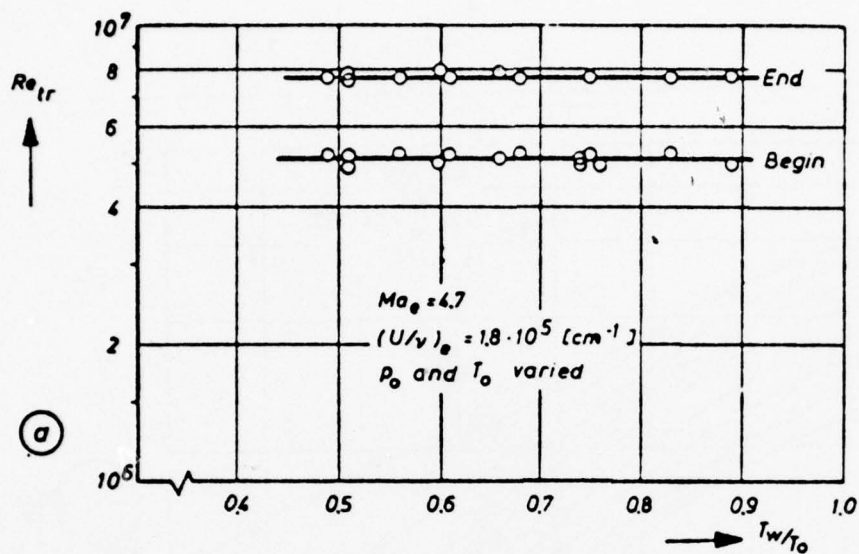
Figure 5. Transition Re-numbers vs. Temperature Ratio T_w/T_0.
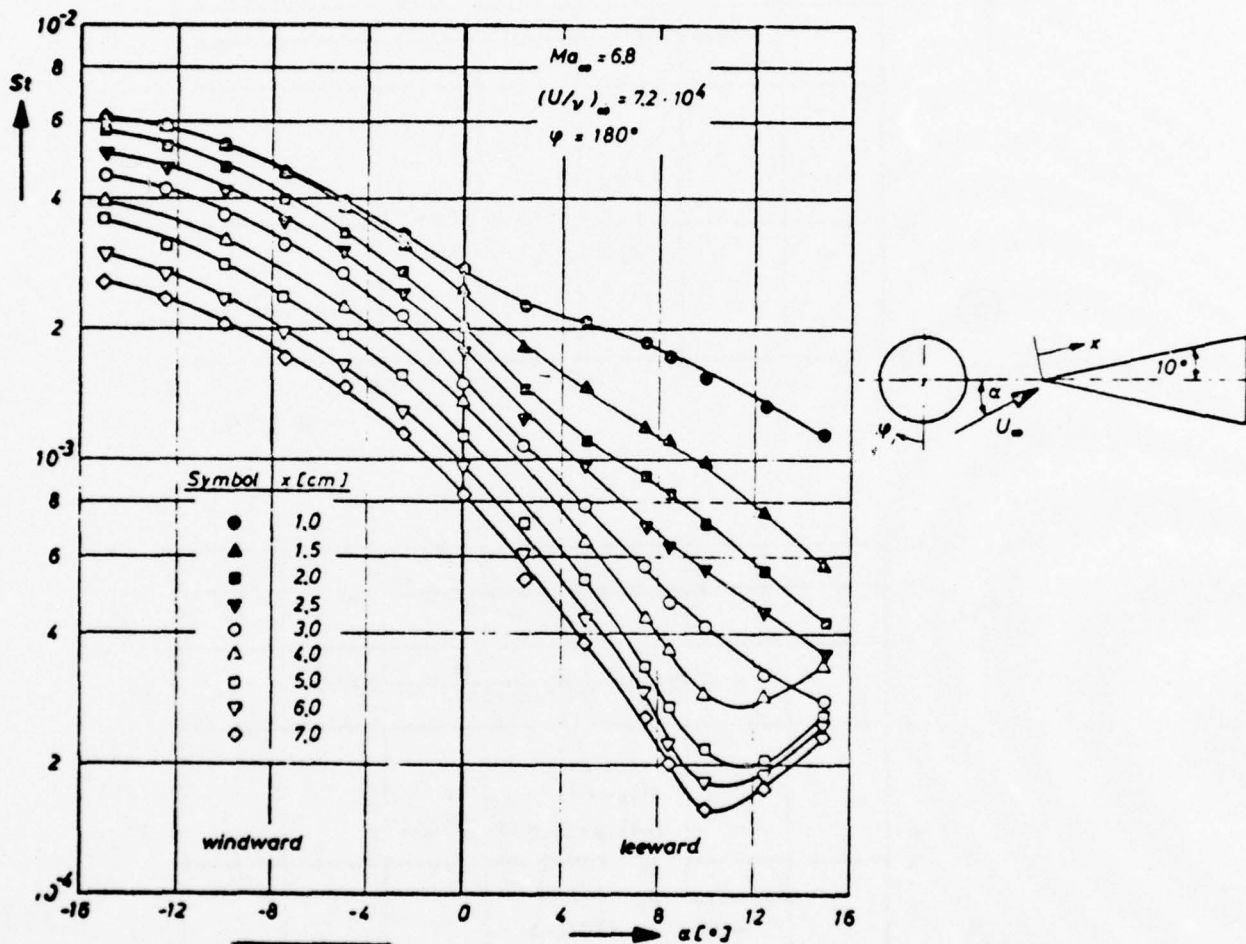
Figure 6. Heat Transfer as Function of Angle of Attack ($\Theta = 10^{O}$).
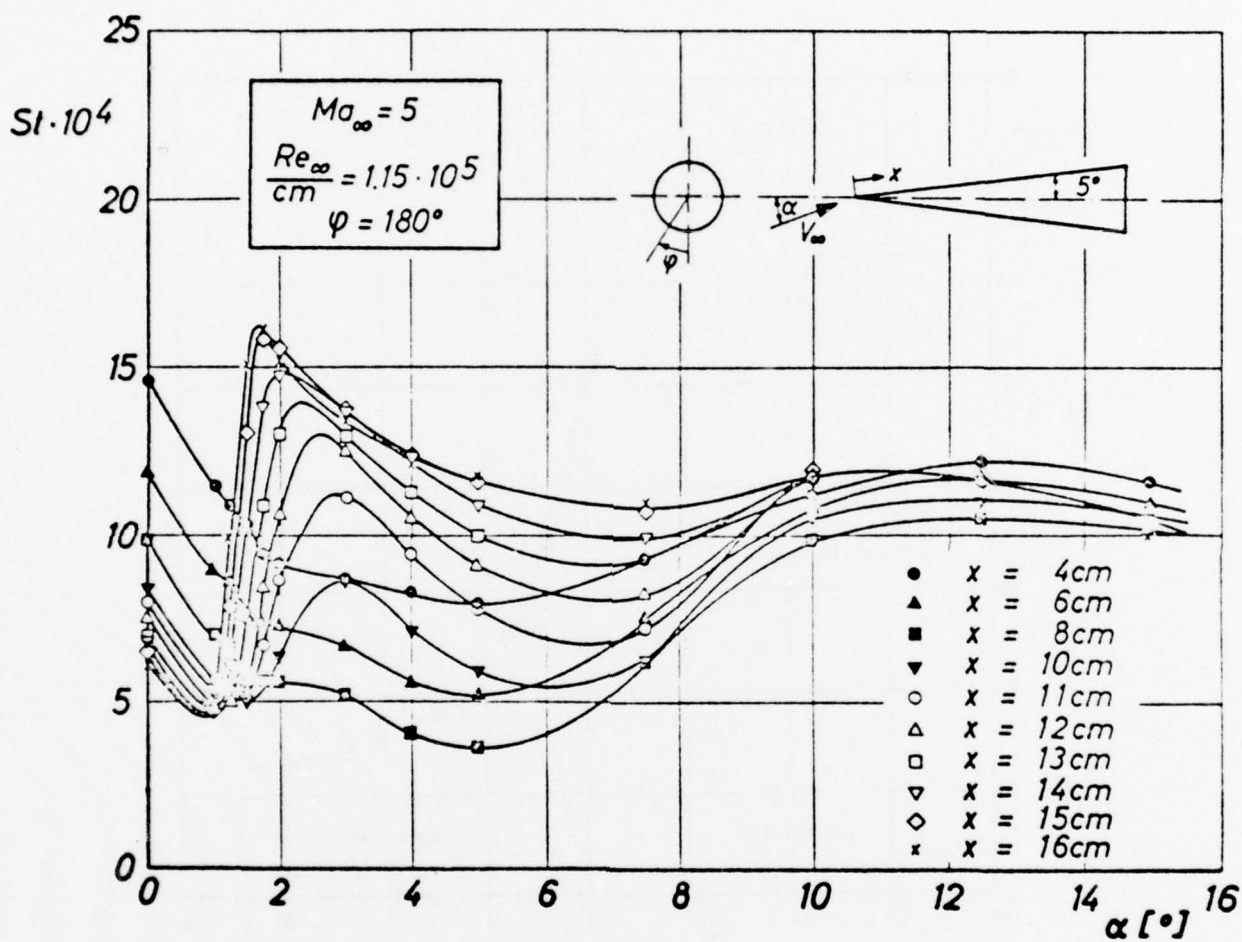
Figure 7. Heat Transfer as Function of Angle of Attach ($\Theta = 5^O$).
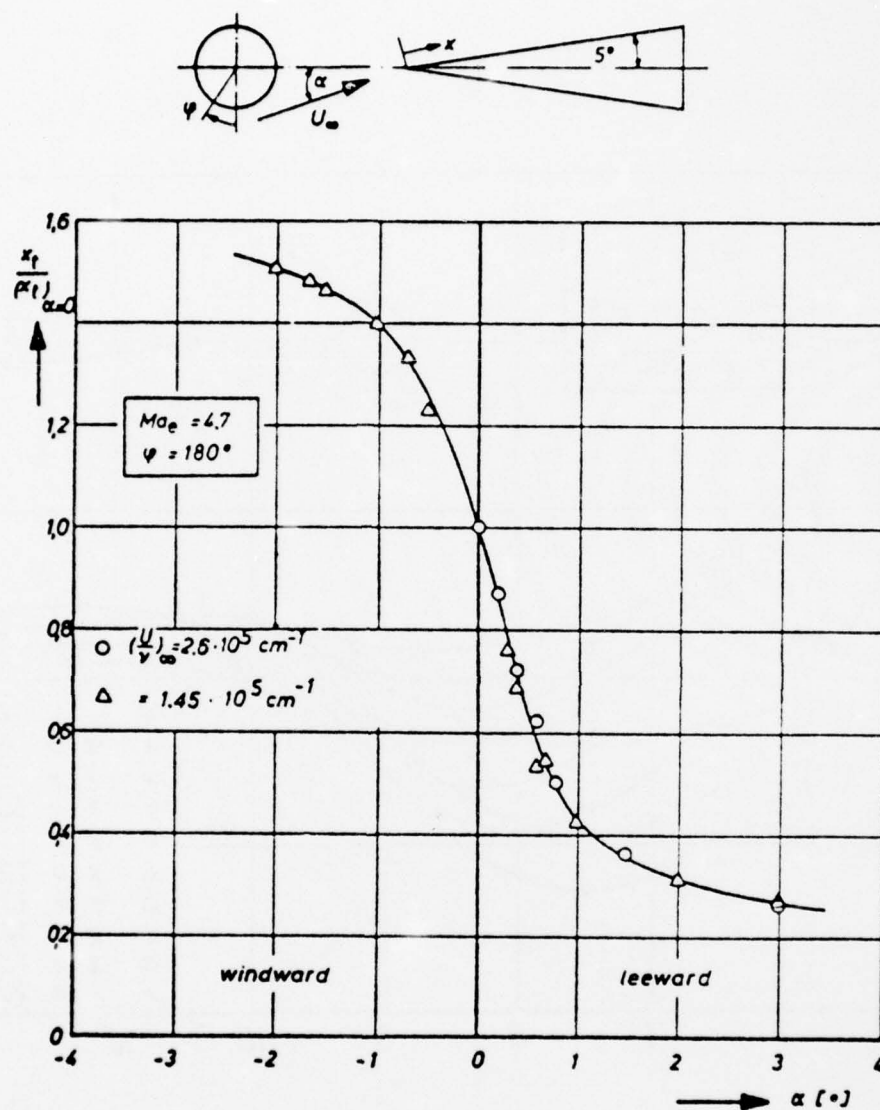
Figure 8. Effect of Angle of Attack on the Location of Transition.
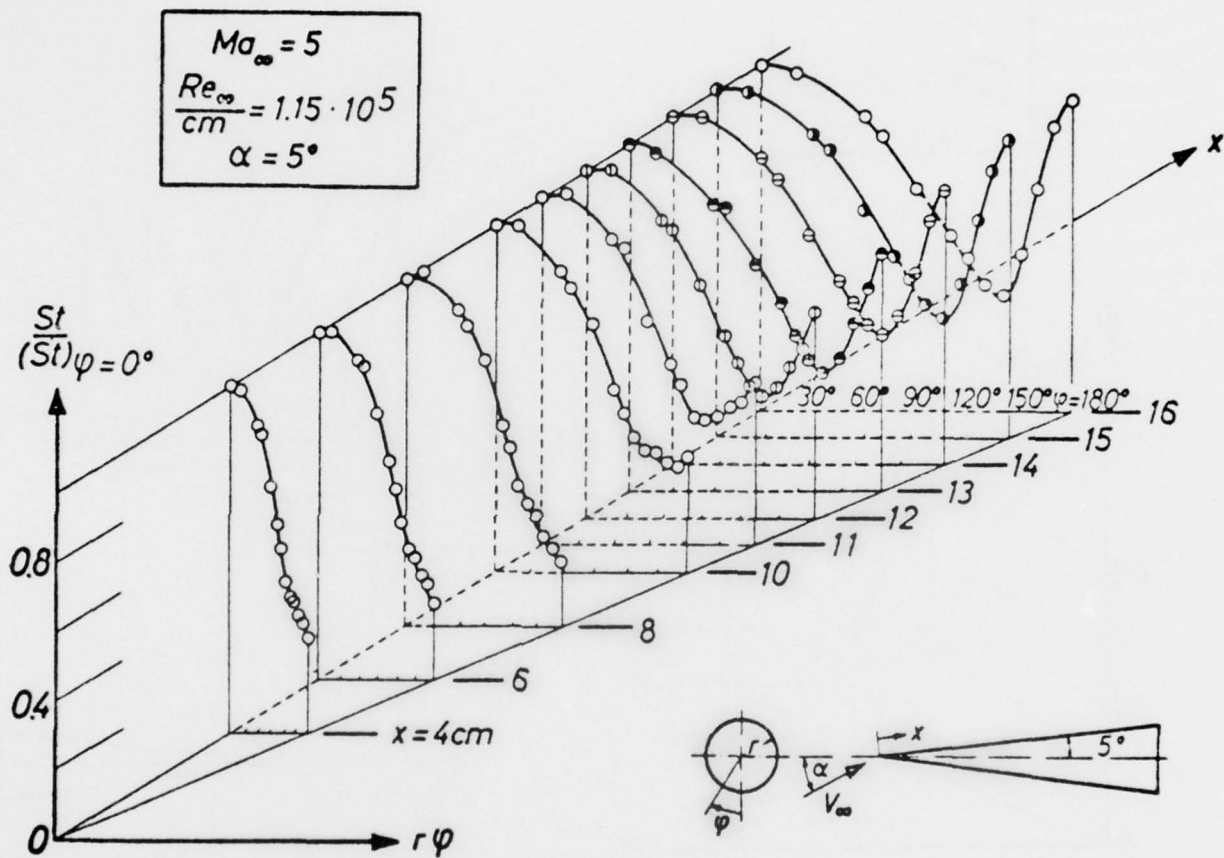
Figure 9.   Variation of Circumferential Heat Transfer ($\alpha = 5^{\circ}$).
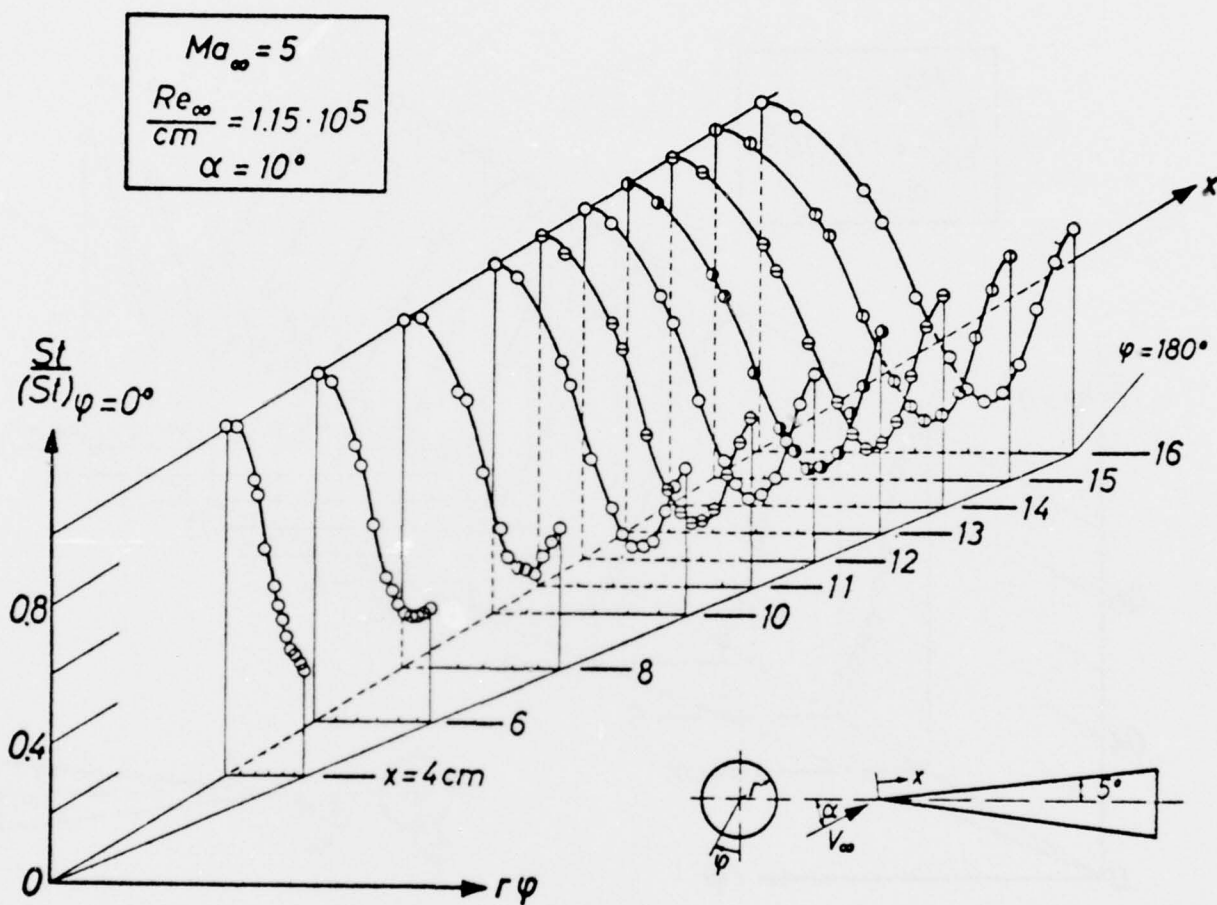
Figure 10. Variation of Circumferential Heat Transfer ($\alpha = 10^\circ$).
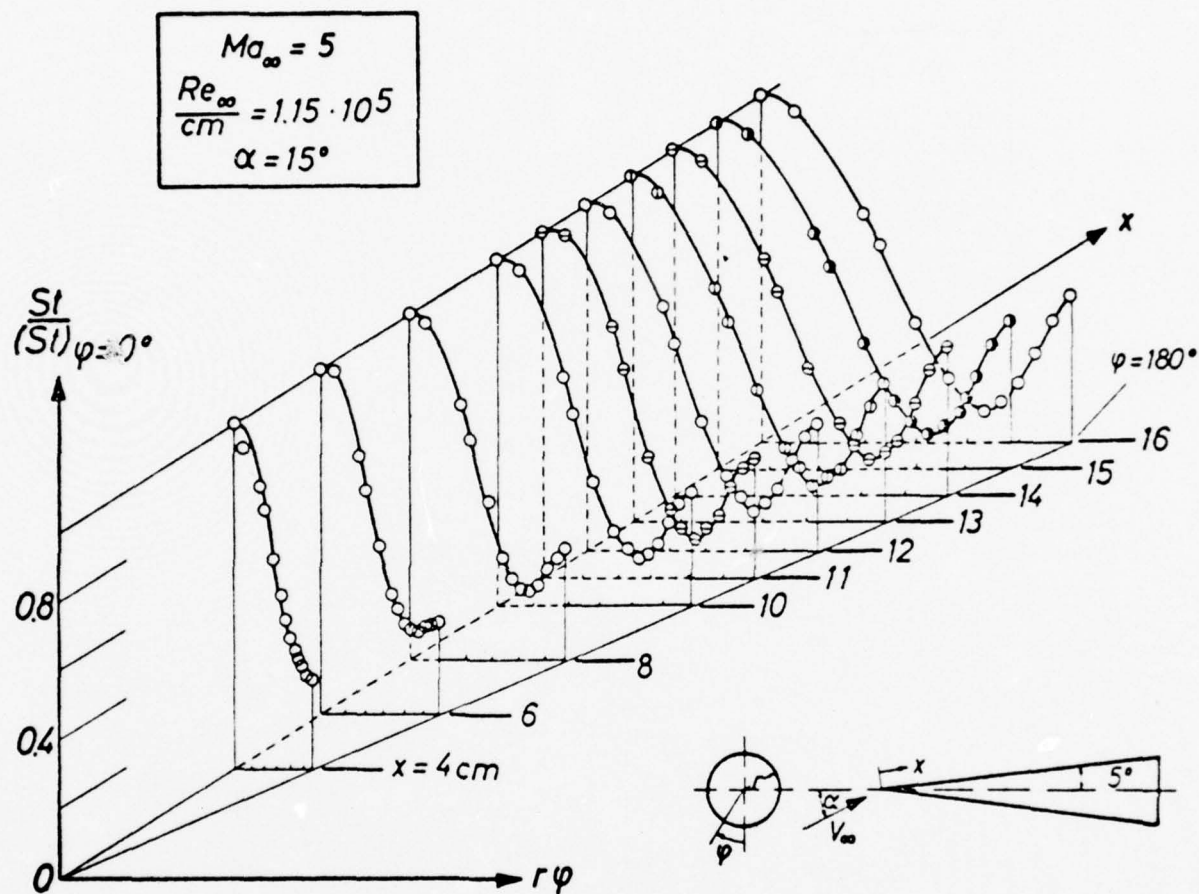
Figure 11. Variation of Circumferential Heat Transfer ($\alpha = 15^{\circ}$).

251

SOME INVESTIGATIONS FOR THE EVALUATION OF STABILITY AND TRANSITION
CRITERIA FOR BOUNDARY LAYERS ON SWEPT WINGS *

by

Ernst H. Hirschel and Vera Jawtusch
DFVLR, Köln, W. Germany

SUMMARY

The investigations consist of three parts: (a) calculation of the quasi two-
dimensional boundary layer on infinite swept wings, (b) calculation of the
laminar three-dimensional boundary layer on finite swept wings, (c) appli-
cation of currently known stability and transition criteria to the calculated
boundary layers. Part (a) of the investigations is being made in order to
study how good the infinite swept wing approximation in different sections
of the wing is compared with the exact three-dimensional solution. Part
(b) deals with the problems of arranging the coordinate system on the wings
surface, the presentation of the metric tensor, the interpolation of the
external boundary condition field, the formulation of the boundary layer
equations with respect to curvature effects, and finally the calculation of
the boundary layer. In part (c) stability and transition criteria are
applied to the boundary layers calculated in (a) and (b) in order to as-
certain the value of these criteria. Some experimental data are available,
more will become available in near future from work of members in the
Eurovisc Working Party on Transition in Boundary Layers. The investiga-
tions are in different stages. This paper contains the discussion of
details of the investigation concerning the boundary layer calculations,
some results of these calculations, and some comments on the current state
of the work to part (c).

1.   INTRODUCTION

At the DFVLR in Porz-Wahn, near Köln (Cologne), work on the numberical
integration of the equations of three-dimensional boundary layers has

started late in 1967. Several papers by Krause, Hirschel, and Bothmann between 1967 and 1970 dealt with numberical stability[1], the development of an implicite finite-difference method[2], and since no inviscid flow-field data from three-dimensional bodies were available at that time, with problems like suction, injection, tangential injection, wake simulation, hot spot, aerodynamic boundary layer fence and so on in three-dimensional boundary layers on flat configurations[3, 4, 5]. This work was interrupted for some time, but continued 1972 in two different directions. One direction is the problem of turbulence in three-dimensional boundary layers, with respect to the mathematical formulation, especially the fourth order Mehrstellen-integration method[6,7], and the other the problem of transition from laminar to turbulent state in three-dimensional boundary layers, especially on swept wings. Here first in cooperation with the RAE known stability and transition criteria were applied in a parametrical study to calculated quasi two-dimensional boundary layers (infinite swept wing case)[8,9], and then a broader approach to the problem was made.

At present the following problems are studied: (1) boundary layer equations in nonorthogonal coordinate systems with respect to strongly curved surfaces (leading edge, fuselage-wing intersection, etc.), (2) calculation of (laminar) boundary layers on infinite and finite swept wings with and without surface curvature with regard to the calculated velocity profiles which are to be used in stability analysis, (3) linear stability in three-dimensional boundary layers, (4) application of known stability and transition criteria to boundary layers on finite swept wings and comparison with experiments, (5) calculation of the mean flow properties in transition regions.

The work on items 3, 4, and 5 is coordinated with the work of members of the Eurovisc Working Party on Transition in Boundary Layers[10, 11], which has working connection with the US Transition Study Group with its chairman E. Reshotko.

In the following some results and experiences are discussed from items 2 and 4.

2. BOUNDARY LAYER CALCULATIONS

The numerical method[2] has been adapted to the calculation of laminar boundary layers on finite swept wings. The first studies have been made for an untapered swept wing, Figure 1, for which panel method calculations of the inviscid flow field were available[12].
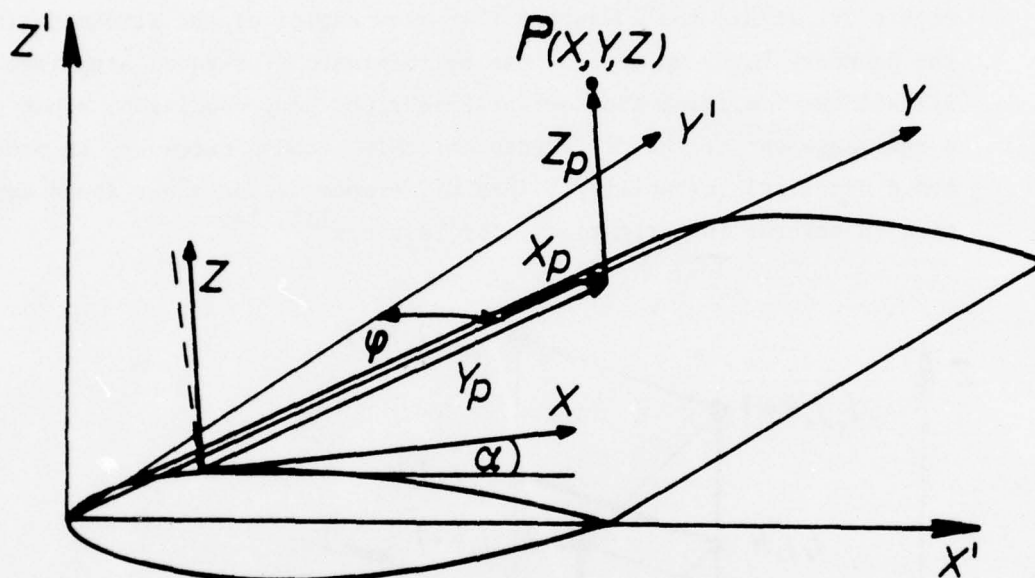
Figure 1. Schematic of the coordinate system on an untapered swept wing. The coordinates x and y lie in the surface, and are nonorthogonal, the coordinate z is orthogonal to the surface.

It was decided to use a body oriented nonorthogonal coordinate system since a streamline oriented system has to be recalculated for each solution. The metric tensor for the system sketched in Figure 1 is very simple if the boundary layer thickness can be considered as small compared to the local radius of curvature of the surface:

$$(2.1) \qquad G = \begin{vmatrix} 1 & \cos\alpha(x)\sin\varphi & 0 \\ \cos\alpha(x)\sin\varphi & 1 & 0 \\ 0 & 0 & 1 \end{vmatrix}$$

255

If one choses to calculate in the wing planform it reduces to

$$(2.2) \qquad G = \begin{vmatrix} 1 & \sin\varphi & 0 \\ \sin\varphi & 1 & 0 \\ 0 & 0 & 1 \end{vmatrix}$$

The finite-difference molecule used is the step-scheme suggested in[1], Figure 2. It has the advantage that skew angles of the stream-surfaces in the boundary layer up to 135° can be tolerated (for equal stepsizes Δx and Δy) without violating the Courant-Friedrichs-Levy condition, since otherwise a rearrangement of the difference molecule becomes necessary in order to avoid numerical instability. This difference molecule has found application in several investigations, for instance[13, 14].

Figure 2. Finite difference molecule.

In the present case the calculation sweeps parallel to the leading edge from the inner to the outer wing portion. The sweep procedure advances in chord direction, starting at the leading edge.

Initial conditions are being specified at the leading edge and the symmetry line. In both cases the same approach-differenciating the momentum equation for the direction normal to the line - is used. The symmetry line approach has been used in the first calculations only, since the results for this area, together with difficulties concerning the convergence of the solution, show that this appraach is doubtful. Here results from item 1 in the introduction will show how the boundary layer should be treated in such areas where strong lateral curvature exists as along almost the whole summetry line. The approach used for the results contained in this paper is shown in Figure 3. Again the leading edge solution (in the present case for a symmetric profile at small or zero angle of attack) has to be found. Then at a suitable spanwise station the quasi two-dimensional infinite swept wing approach is being applied in direction parallel to the x'-axis-not in direction normal to the leading edge, as normally done. This solution together with the leading edge solution will form the initial condition for the three-dimensional area. The error introduced by this approach
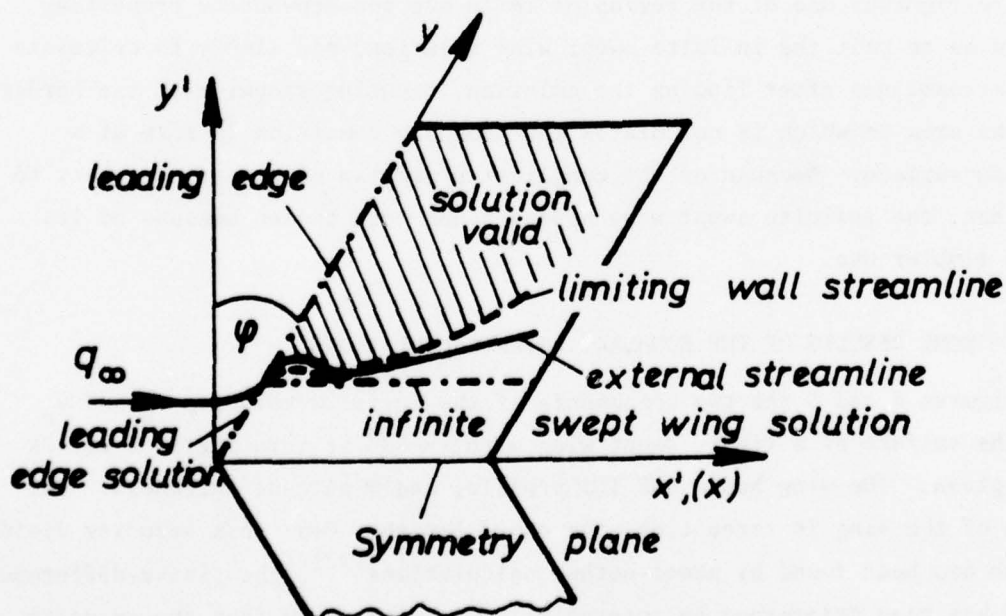

Figure 3.   Schematic of flow field.

concerns the region between the spanwise station, where the infinite swept wing solution has been found, and that streamline in the boundary layer originating from the intersection of the spanwise station with the leading edge, that lies at largest distance from the spanwise station. In Figure 3 this is first the external streamline and later the limiting wall-stream line because of the point of inflexion in the external streamline. It is possible that streamlines between these lines can become important, especially near the point of inflexion of the external streamline. Nevertheless, this will be a minor effect only.

In the foregoing discussion the region of influence and dependence properties of three-dimensional boundary layers have been brought into use in connection with the initial solution problem. These properties, which are due to the fact that approximately the streamlines are characterictics (for practical purposes the projections of the streamlines into the overflowed surface are used) have been discussed first by Mager[15] and Raetz[16]. The Courant-Friedrichs-Levy condition reflects this fact in connection with the domain of dependence of the difference-molecule, which has to include the domain of dependence of the differential equation, otherwise no numerical stability can be ensured, even for implicit formulation[1, 2].

A more rigorous use of the region of influence and dependence properties would be to omit the infinite swept wing solution, and simply to calculate the streamlines after finding the solution, creating stepwise at the border of the area in which is calculated the boundary condition in form of a stream surface. Because of the complicated program structure necessary to do that, the infinite swept wing approach has been chosen because of its much simpler use.

3.   SOME RESULTS OF THE BOUNDARY LAYER CALCULATIONS

In Figures 4 and 5 the two components of the inviscid velocity u_e and v_e at the surface of a finite swept wing with $\varphi = 30^o$ at zero angle of attack are given. The wing has a RAE 101 profile, and 9 percent thickness. The span of the wing is three times the chord length. From this velocity field, which has been found by panel-method calculations[12], the finite-difference grid has been determined by interpolation in such a way that the velocity
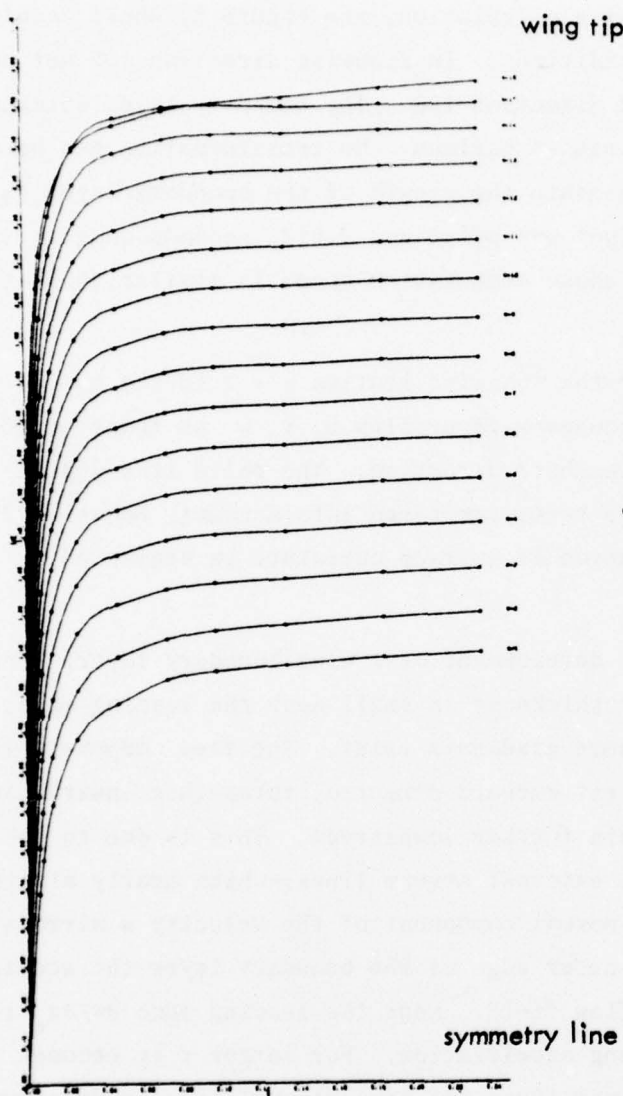
Figure 4.   Velocity component $u_e(x)$
at different
stations y = const
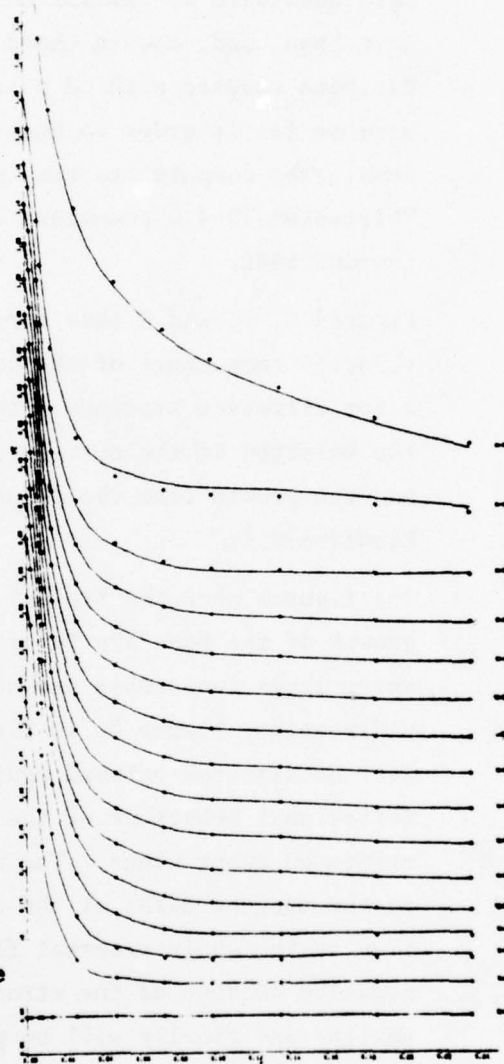
Figure 5.   Velocity component $v_e(x)$
at different
stations y = const

increments Δu_e and Δv_e are bounded, and the resulting Δx and Δy, too.
Figure 5 shows very large gradients of v_e in y-direction near the line of
symmetry (N = 1), which gave rise to the problems already mentioned in
chapter 2.

The present boundary layer results have been found in the area $0 \leq x \leq 0.257$,
and $0.046 \leq y \leq 1.63$. x = 0 represents the leading edge, and y = 0.046 the

location of infinite swept wing calculation, see Figure 3, whose results have been used as initial conditions. In spanwise direction 105 net points have been used, and in chord direction 150. The boundary layer thickness has been covered with 38 points at maximum. No transformation has been used so far in order to compensate the growth of the boundary layer thickness. The computation time per net point was 0.012 seconds on a Telefunken TR 440 computer, whose computation speed is similar to that of the CDC 6400.

Figures 6, 7, and 8 show for the spanwise station y = 1.10 the three velocity components of the boundary-layer flow u, v, w as function of z for different stations x in chord direction. The solid line depicts the solution if the curvature terms are taken into account, Equation 2.1, and the broken line the solution if surface curvature is neglected, Equation 2.2.

The figures show the typical development of a wing boundary layer. The growth of the boundary layer thickness is small near the leading edge, where large favourable pressure gradients exist. The flow component in y-direction, Figure 7, is first outward directed, turns then inward, and will be directed outward again further downstream. This is due to the inflexional behaviour of the external stream lines, which nearly always exists on swept wings. The normal component of the velocity w mirrors in the tangent $\partial w/\partial z$ at the outer edge of the boundary layer the acceleration of the whole external flow field. Near the leading edge $\partial w/\partial z_e$ is negative because of the strong acceleration. For larger x it becomes smaller and finally will be positive when the external flow is decelerated.

The solution shows appreciable differences especially in the spanwise velocity component, if the curvature of the wing surface is neglected. This is of importance if the stability of the flow is to be considered, regardless of the uncertainty of the criteria available today. An analysis of boundary layer parameters and shape functions calculated from these profiles is under way.
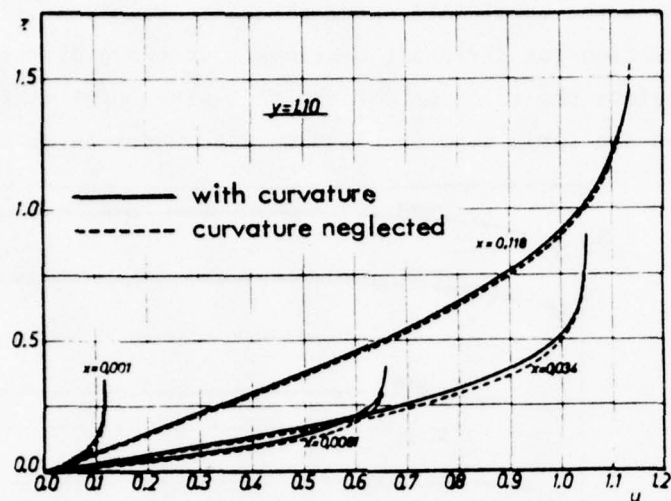
Figure 6. Profiles of the tangential component u(z)
of the velocity in the boundary layer at
y = 1.1, and different stations x.
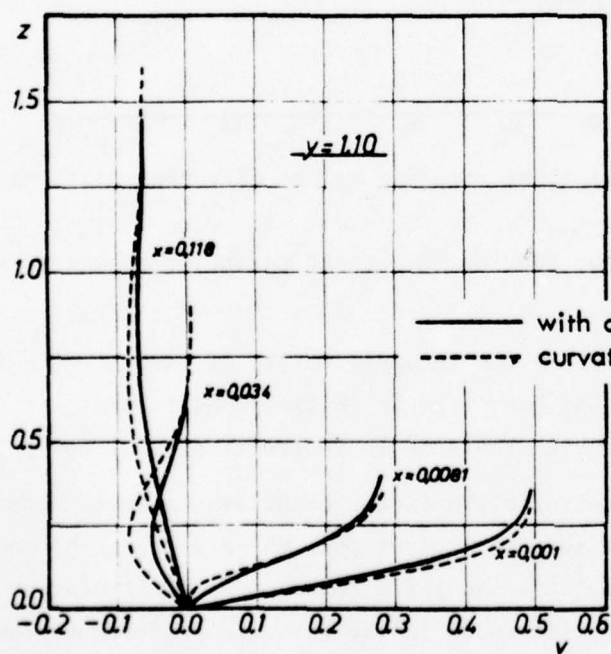
Figure 7. Profiles of the tangential
component v(z) in the boundary
layer at y = 1.1, and different
stations x.
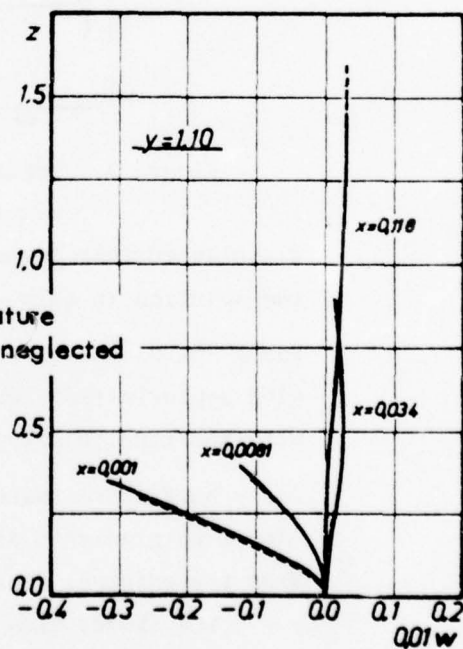
Figure 8. Profiles of the normal
component w(z) in the
boundary layer at y=1.1,
and different stations x.

In Figure 9 the total wall shear stress τ_w is given as function of the span-wise direction for different stations x in chord direction. The broken line again depicts the solution for the flat wing. The differences between the solutions are large near the leading edge, where large curvature exists, and
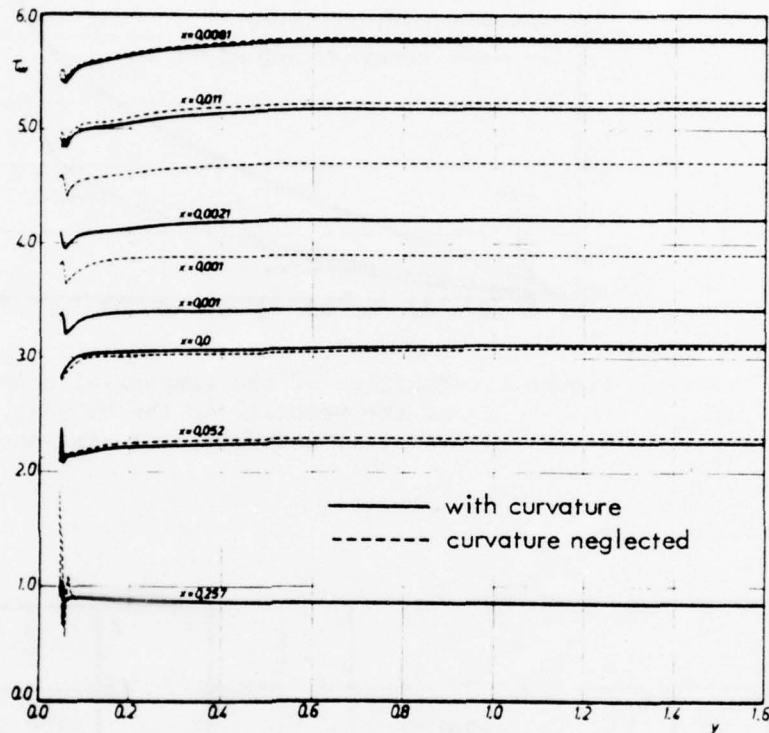
Figure 9. Total wall shear stress $\tau_w(y)$ at different stations x.

diminish further downstream, showing the strong parabolic behaviour of the solution in this way.

For y $\simeq$ 0.05 the curves exhibit the incompatibility of the infinite swept wing approximation, which has been used as initial condition at y = 0.046, with the true solution. Large gradients in y-direction exist for y $\lesssim$ 0.1.

For y >0.8 approximately infinite swept wing conditions seem to appear. Almost no gradients are present in y-direction, which also can be seen from the external flow data[12]. An infinite swept wing calculation at y = 0.964 showed also few differences in the velocity profiles to those of the finite wing calculation. This is also true for the leading edge

area since the leading edge solution for the finite wing has been used as initial data for the infinite swept wing calculation.

Figure 10 shows both the external and the limiting wall streamlines on the wing for the different cases calculated. Since the external streamlines have an only weak inflexional behaviour the crossover of the limiting wall
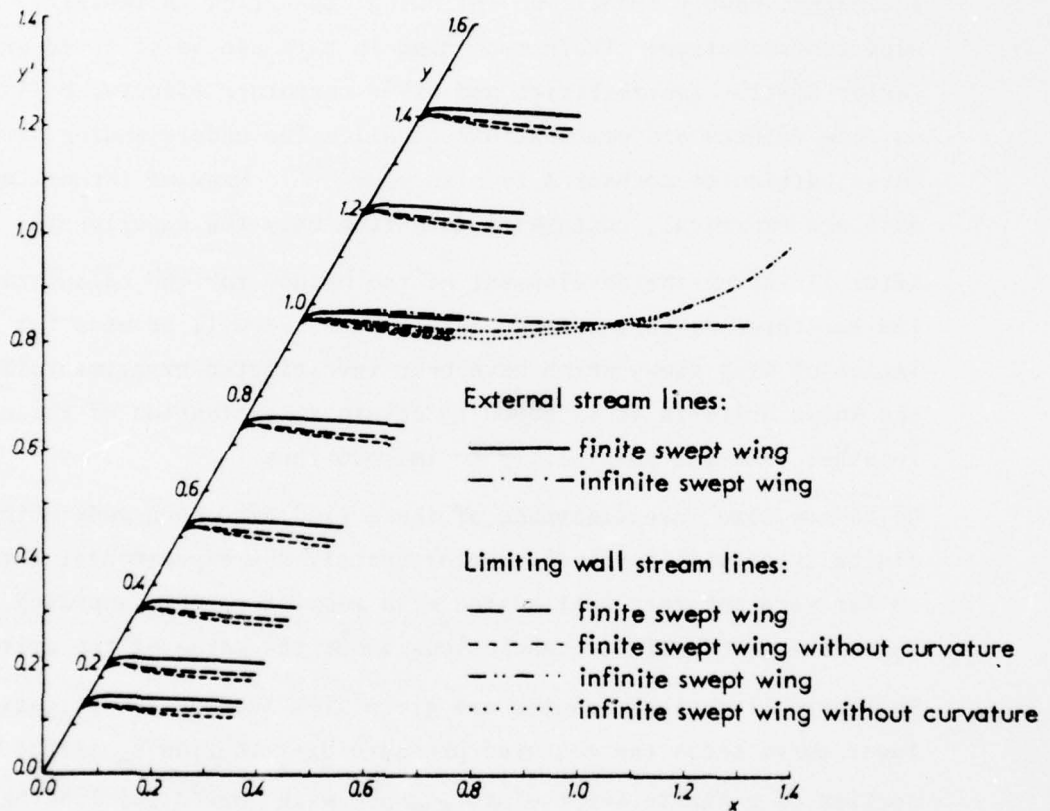
Figure 10. Streamlines on the wing.

stream lines takes place far downstream of the leading edge. The location of the calculated limiting wall streamlines is relatively strong affected if wall curvature is neglected in the boundary layer calculation. The infinite swept wing approximation gives a slightly changed location of the external streamline showing that the gradients of the external flow in y-direction have not completely vanished at $y = 0.964$.

4. APPLICATION OF KNOWN STABILITY AND TRANSITION CRITERIA

The transition laminar-turbulent in three-dimensional boundary layers,
especially on wings is poorly understood today. M. G. Hall[17] gave an
overlook over existing criteria which have been put to use in parametrical
studies such as[8] and[18]. One problem is that other transition mechanism
exist beside the classical Tollmien-Schlichting instability with transition
following, namely transition following cross-flow instability, and leading
edge contamination. These mechanism in turn can be affected and changed by
Taylor-Görtler instabilities and other curvature effects, by laminarisation,
surface effects and combinations of all. The understanding of most of
these particular mechanism is also poor[10]. Many of the criteria avail-
able are empirical, containing data from only few experiments.

After finishing the development of the method for the calculation of
laminar three-dimensional boundary layers, it will be used for the calcu-
lation of wing flows which have been investigated experimentally. Applying
the known criteria it is hoped to obtain an evaluation of these criteria
together with the possibility to improve them.

Up to now some investigations of these kind have been made using the in-
finite swept wing approach. Unfortunately the experimental data available
so far were not very well suited with respect to this approach. The re-
sults allow no definite conclusions about the value of the criteria.

In Figure 11 typical results are given from such an investigation. The
lower curve shows the measured pressure distribution c_p (x^*/c) in one cross
section of a finite swept wing $(\varphi \approx 55^o)$ with curved (!) leading edge[19].
The upper curve shows the measured wall shear stress c_f (x^*/c) at the same
station exhibiting clearly the transition region. Using the pressure dis-
tribution on infinite swept wing calculation has been made and the criteria
discussed in References 17, 8, and 18, have been applied.

Results: (a) Leading edge contamination is possible with $R_\Theta \approx 150 > R_{\Theta crit}$ = 100.
(b) Relaminarisation is possible for $x^*/c < 0.025$. (c) No cross-flow
instability seems to be existent since $X_{max} \approx 36 < X_{crit}$ = 120 ± 20. The
position of $_{max}$ is included in Figure 11. (d) Tollmien-Schlichting
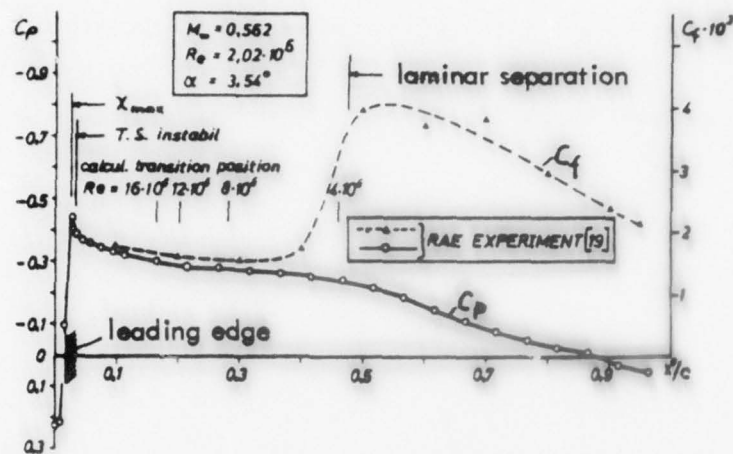
Figure 11. Results of application of stability and transition criteria.

instability appears just behind the weak suction peak for a Reynolds number $2.02 \cdot 10^6$. (e) At this Reynolds number no transition position (using Granville's criterium) has been found because separation was calculated. (f) For higher Reynolds numbers the transition positions have been calculated, and included in Figure 11. (g) An extrapolation of these positions to Re = $2.02 \cdot 10^6$ gives a fair agreement of the calculated transition point with the measured one at x^*/c 0.5.

5. CONCLUSION

Out of several problem areas of the large problem "transition in three-dimensional boundary layers" the calculation of laminar boundary layers on swept wings, and the investigation of known stability and transition criteria have been discussed.

The calculation of three-dimensional laminar boundary layers is fairly well advanced. Difficulties lie mostly in the external flow field representation and in the geometry of the wing or body.

Large difficulties exist concerning the understanding of the stability and transition mechanism in the boundary layers under considerations. Even the formulation of reliable prediction criteria has not been accomplished so far. Much more experimental and analytical work is necessary

in order to get more information about the possible flow situations. The thoughts and results discussed in this paper present part of the work on these problems at the DFVLR.

REFERENCES

1.   E. Krause, E. H. Hirschel, Th. Bothmann: "Numerische Stabilität dreidimensionaler Grenzschichtlösungen," ZAMM-Sonderheft 48, 1968.

2.   E. Krause, E. H. Hirschel, Th. Bothmann: "Differenzenformeln zur Berechnung dreidimensionaler Grenzschichten," DLR FB 69-66, 1969.

3.   E. Krause, E. H. Hirschel, Th. Bothmann: "Die numerische Integration der Bewegungsfleichungen dreidimensionaler, laminarer, kompressibler Grenzschichten," DGLR-Fachbuchreihe, 1969, Band 3, Braunschweig.

4.   E. Krause, E. H. Hirschel, Th. Bothmann: "Normal Injection in a Three-Dimensional Laminar Boundary Layer," AIAA J., Vol. 7, No. 2, 1969.

5.   E. Krause, E. H. Hirschel: "Exact Numerical Solutions for Three-Dimensional Boundary Layers," Lecture Notes in Physics, Vol. 8, Springer Verlag, 1971.

6.   E. Krause, E. H. Hirschel, W. Kordulla: "Fourth Order "Mehrstellen" - Integration for Three-Dimensional Turbulent Boundary Layers," Proceedings of the AIAA Computational Fluid Dynamics Conference, Palm Springs, 1973.

7.   E. Krause, W. Kordulla: "A Fourth Order Differential Prediction Method for Three-Dimensional Boundary Layers," in: L. F. East: "Computation of Three-Dimensional Turbulent Boundary Layers," FFA TN AE - 1211, 1975 (Euromech 60, Trandheim 1975).

8.   E. H. Hirschel: "The Influence of the Free-Stream Reynolds Number on Transition in the Boundary Layer on an Infinite Swept Wing," AGARD Rep. No. 602, 1973.

9.   E. H. Hirschel: "Theoretische Untersuchung von Transitionsphänomenen in der Grenzschicht eines unendlich gestreckten gepfeilten Flügels," DLR Mitt. 73-04, 1973.

10.   E. H. Hirschel: "Recommendations for Research Work on Transition in Boundary Layers," (Eurovisc Working Party on Transition in Boundary Layers), DFVLR-Techn. Memor. WT 1/75, Köln, 1975.

11.   E. H. Hirschel, U. Dallmann: "Suggestions for the Experimental Investigation of the Transition Laminar-Turbulent in Three-Dimensional Boundary Layers," DFVLR, 1B 351-74/13, 1974.

12.   S. R. Ahmed: "Berechnung des reibungslosen Strömungsfeldes von dreidimensionalen auftriebsbehafteten Tragflügeln, Rümpfen und Flügel-Rumpf-Kombinationen nach dem Panel-Verfahren," DLR-FB 73-102, 1973.

13. A. J. Karabelas, T. J. Hanratty: "Finite Difference Solution for Three-Dimensional Boundary Layers with Large Positive and Negative Crossflows," AIAA J., Vol. 9, No. 8, 1971.

14. J. E. Harris: "Calculation of Three-Dimensional Compressible Laminar and Turbulent Boundary Layers," NASA SP-347, Part 1, 1975.

15. A Mager: "Generalization of Boundary-Layer Momentum-Integral Equations to Three-Dimensional Flows including those of Rotating Systems," NACA Report 1967, 1952.

16. G. S. Raetz: "A Method of Calculating Three-Dimensional Laminar Boundary Layers of Steady Compressible Flows," Northrop-Aircraft, Inc. Rep. No. NAI-58-73 (BLC-114), 1957.

17. M. G. Hall: "Scale Effects in Flows over Swept Wings," RAE TR 71043 (1971).

18. D. A. Treadgold, J. A. Beasley: "Some Examples of the Application of Methods for the Prediction of Boundary-Layer Transition on Sheared Wings," AGARD Report R-602, 1972.

19. K. G. Winter, J. B. Moss: "Measurements of Pressure Distribution on a Half Model Wing Body Combination of 55° Sweep over a Wide Range of Reynolds Numbers," RAE TR 74149, 1974.

THE HYPERSONIC SLIP FLOW BOUNDARY LAYER
PAST A PARTLY HEATED FLAT PLATE

by

Ernest H. Hirschel, Wolfgang Geller
DFVLR, Köln, W. Germany

and

Francoise Martin
CNRS, Meudon, France

SUMMARY

The laminar hypersonic boundary layer at a flat plate in the region of viscous interaction is investigated for the case of a strong rise of the temperature of the plates surface at a certain distance downstream from the leading edge. The temperature rise takes place in a range of some boundary layer thicknesses. The theoretical investigation by means of a finite-difference solution of the governing equations, which are found by an order of magnitude analysis from the Navier-Stokes equations, and the energy equation, shows that already for a relatively small temperature rise the boundary layer assumptions are not longer valid. A pressure rise occurs both in tangential and normal direction near the plates surface. Depending on the amount and the steepness of the prescribed wall-temperature rise a pressure wave is formed, which lies almost parallel to the outer shock wave, and resembles for certain conditions also very much a shock wave. This pressure wave marks clearly the influence region which develops downstream of the region where the wall temperature is being changed. Once this wave is established the boundary layer assumptions are again valid since the normal pressure gradient is zero over the whole boundary-layer region between the surface of the plate and this wave. Particular results of the solution are compared qualitatively with results from an experimental investigation of the turbulent boundary layer on a nozzle wall with heat addition at a location at large distance from the nozzle throat.

1.   INTRODUCTION

The present theoretical study has been suggested by an experimental investigation by Pfeiffer and Will[1], who made measurements in the boundary layer of a hypersonic nozzle with and without heating of a part of the nozzle wall. The term "without heating" refers to the normally present nozzle wall condition, that is cooled wall according to the operation conditions of the wind tunnel. The objective of the work was to find out how the turbulent boundary layer is influenced by a strong heat addition through the nozzle wall.

The possible mechanism affecting a turbulent boundary layer have been discussed in[2]*, here we will concentrate on the results of the theoretical investigation only.

After studying the possible mechanism affecting the turbulent boundary layer it was decided to limit the investigation to the laminar case since the argument was, if there is a strong influence of the heating, as the experiment indicated, it must show up in the laminar case too, at least qualitatively.

2.   PROBLEM

In the present theoretical investigation it is studied how a stationary, laminar two-dimensional hypersonic boundary layer is influenced by heat addition through the wall. In accordance to[1] a fully developed boundary layer at a cooled wall at constant temperature is considered. At a station x_0 the wall temperature rises over a distance of two to six boundary layer thicknesses to a level 1.5 to 2 higher than upstream of the station x_0, Figure 1. Considered is the boundary layer at an infinitely thin flat plate in the region of viscous interaction.

Compressible boundary layers with heat addition through the wall have been studied extensively in boundary-layer theory (see for instance Reference 3). In the present case it is the question how a strong gradient of the wall temperature dT_w/dx will affect the boundary layer. It is to conjecture

---

*The present paper is a shortened and revised English version of Reference 2.
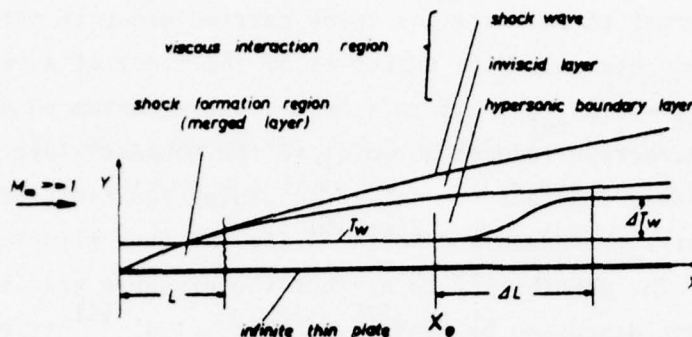
Figure 1. Schematic of the flow field.

that the boundary layer assumptions will be violated if the gradient is large enough. This seems to be very probable, since a heat addition is equivalent to a mass addition[4], which leads to displacement effects and to the creation of pressure gradients.

The experiment[1] has been made at a Mach number M = 8.68 and a unit Reynolds number Re = $3.9 \cdot 10^6$ m^{-1}. The resulting boundary layer is a hypersonic boundary layer with a relatively high density. It therefore appeared possible in order to study the heating effects to use the approach for hypersonic slip-flow boundary layers, which takes into account the momentum equation normal to the surface, rather than the Navier-Stokes equations. Very high gradients dT_w/dx certainly cannot be treated with this approach, since in that case the pressure gradient $\partial p/\partial x$ in the tangential momentum equation can no longer be neglected, as has been done in the method[5], which has been employed for this problem. The large advantage of the hypersonic slip-flow boundary approach over the Navier-Stokes approach is that the first leads to an initial-boundary value problem, which can be solved with a numerical marching procedure, whereas the latter leads to a pure boundary value problem, whose solution demands a much larger effort.

3. THE MATHEMATICAL MODEL

Hypersonic slip-flow boundary layers are characterized by the fact that all flow variables including the pressure have large gradients in direction normal to the surface. The order of magnitude analysis of the Navier-Stokes equations shows for such flows that the momentum equation for the

direction normal to the wall has to be carried along in the analysis if the square of the reference Mach number is of the order of a reference Reynolds number: $M^2_{ref} = 0(Re_{ref})$. If this holds, the momentum equation for the tangential direction reduces moreover to the boundary-layer equation without the pressure gradient. A set of governing equations of this kind has been used first by Rudman and Rubin[6] for the investigation of the merged layer flow. The possibility to neglect the pressure gradient term $\partial p/\partial x$ has first been discussed by Lees[7]. Cheng, et al.[8] tried to retain $\partial p/\partial x$ in the system of equations, but experienced numerical problems. The reason for this is that while retaining $\partial p/\partial x$ in the system of equations, but experienced numerical problems. The reason for this is that while retaining $\partial p/\partial x$ in the system of equations, it becomes elliptical-parabolic in the subsonic region, while without $\partial p/\partial x$ it always is of hyperbolic-parabolic character [9] and can be solved with a numerical marching procedure. The system of governing equations[5,6] and also[8], describes the flow from the surface of the flat plate up to the undisturbed outer flow, including the shock wave. In the present study the flow is calculated with the method[5] beginning at the leading edge through the merged layer into the region of viscous interaction. In the region of viscous interaction the one-layer approach is still used, although the shock wave is fully developed, and the slip flow is down to two or three percent.

4. RESULTS

The flow parameters from[1], which have been used in this investigation are: medium air, free-stream Mach number $M_\infty = 8.68$, unit Reynolds number $\overline{Re}_{\infty\ell} = 2.33 \cdot 10^6 m^{-1}$ (all not nondimensionalized variables are marked with a bar), static temperature of the free stream $\overline{T}_\infty = 53$ K, static pressure of the free stream $\overline{p}_\infty = 1.832 \cdot 10^{-3}$ bar, mean free path in the free stream $\overline{\lambda}_\infty = 0.564 \cdot 10^{-3}$ cm. The reference length is the length of the merged layer $\overline{L} = 0.07$ cm. The wall temperature is $\overline{T}_w$ - 361 K - constant for $0 \leqq \overline{x} \leqq \overline{x}_0$. Downstream of $\overline{x}_0 = 4\overline{L}$ the wall temperature rises sinoidal over the distance $\Delta\overline{L}/\overline{L}$ by the amount $\Delta\overline{T}_w$ remaining again constant after that. The length $\Delta\overline{L}/\overline{L}$ and the temperature rise $\Delta\overline{T}_w$ have been varied in order to find their influence on the flow field. Table 1 shows the pairs investigated. The mean temperatur rise $\Delta\overline{T}_w/\Delta\overline{L} = d\overline{T}_w/d\overline{x}$ has its smallest value

Table 1.   Pairs of the parameters $\Delta\bar{L}/\bar{L}$, $\Delta\bar{T}_w$.

case	1	2	3	4	5	6	7	8	9
$\Delta\bar{L}/\bar{L}$	3	2	1	3	2	1	3	2	1
$\Delta\bar{T}_w$ [K]	172	172	172	345	345	345	517	517	517

in case 1 and the highest in case 9.   In[1] the temperature rise was $\Delta\bar{T}_w$ = 517 K.

With the parameters of [1] very small scales of the flow field are determined.   The thickness of the whole layer investigated is $\bar{\delta}'$ = 0,07 cm at $\bar{x}_0$ = 4$\bar{L}$, and $\bar{\delta}'$ = 0,13 cm at $\bar{x}$ = 8$\bar{L}$.   The boundary layers thicknesses are $\bar{\delta}$= 0,04 cm and $\bar{\delta}$= 0,08 cm, respectively.

Since in the method[5] temperature-jump boundary conditions are employed along with the slip-flow conditions, the temperature of the gas at the wall $\bar{T}_{gw}$ is different from the wall temperature $\bar{T}_w$.   In Figures 2 and 3 the influence of the heating on the wall pressure $p_w = \bar{p}_w/\bar{p}_\infty$ and the temperature
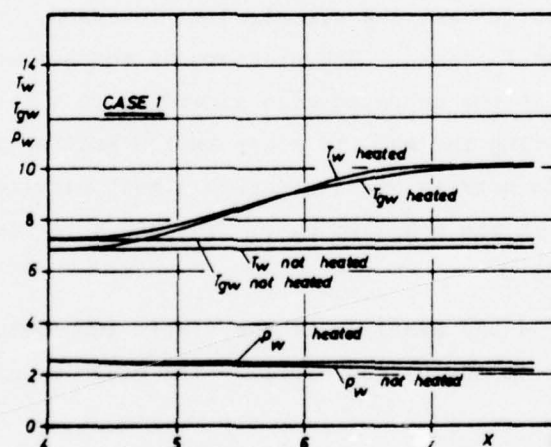
Figure 2.   Temperature of the gas T_{gw} and pressure p_w at the wall as function of x, case 1.

T_{gw} = $\bar{T}_{gw}/\bar{T}_\infty$ is shown for case 1 and case 9.   Included in the figures is the temperature of the wall T_w = $\bar{T}_w/\bar{T}_\infty$.
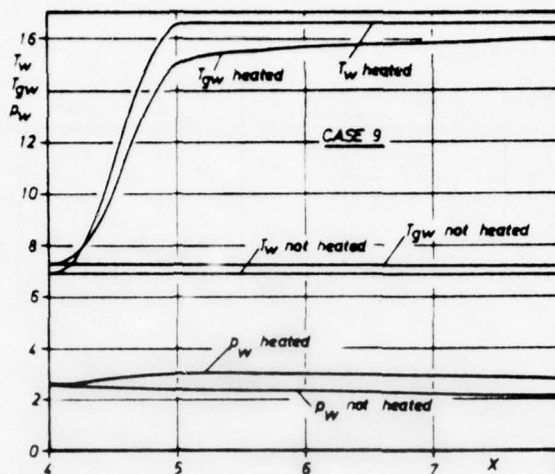
Figure 3. Temperature of the gas T_{ge} and pressure p_w at the wall as function of x, case 9.

In Figures 2 and 3 the results are given for both the heated and the unheated wall. The term "unheated" means as already stated in the introduction "operation condition" which actually is a cooled wall condition. Due to the temperature-jump allowed T_{gw} ang T_w are different. In the unheated case T_{gw} is larger than T_w but approaches the latter asymptotically. In the heated case the situation is reversed, but further downstream T_{gw} approaches T_w again. The pressure of the gas at the wall is still decreasing in the unheated case according to viscous interaction theory. While heating the wall it rises in the heating region and the curve appears downstream of this region almost parallel to the curve of the pressure in the unheated case. The pressure rise differs markedly in both cases.

In Figure 4 the profiles of the static temperature $T = \tilde{T}/\bar{T}_\infty$ in y-direction (= normal to the plates surface) are given at different stations x for case 9.

The profiles for the unheated case show the typical properties of hypersonic viscous interaction flows. At the outer edge the temperature rise takes place in the shock wave, and agrees well with the corresponding

274
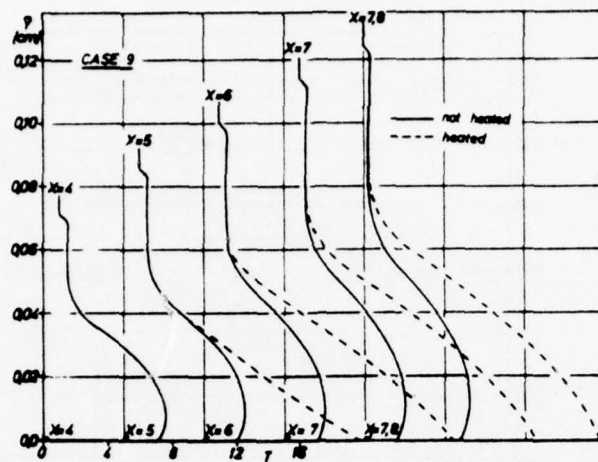
Figure 4.   Profiles of the static temperature T in y-direction at
different stations x, case 9.

Rankine-Hugoniot value[10]. It follows the inviscid layer beneath the
shock wave, which has no discernable energy dissipation and displays
therefore a temperature plateau, and finally near the surface we have
the typical temperature maximum of a hypersonic boundary layer. Rising
the wall temperature, here case 9, alters the temperature distribution
strongly- The maximim is now a relative maximum at the wall, in the
whole boundary layer region the temperature is higher than before, but
the temperature plateau remains unchanged in its larger part, indicating
a region of influence of the area, in which the temperature rises, which
lies between x = 4 and x = 5 in this case.

The profiles of the static pressure $p = \bar{p}_\infty$ in Figure 5 show more clearly
what happens to the flow field.

In the unheated case we again have the typical profiles which appear in
a viscous interaction flow. The pressure decreased beneath the shock
wave at the outer edge throughout the inviscid layer toward the region
near the wall. There the familiar feature $\partial p/\partial y = 0$ of the classical
boundary layer appears.

If the wall is heated the pressure at the surface rises as has already
been shown in Figures 2 and 3. Near the wall the flow exhibits larger
pressure gradients $\partial p/\partial y \neq 0$ for 4 < x < 7. For x > 7 again a pressure

275
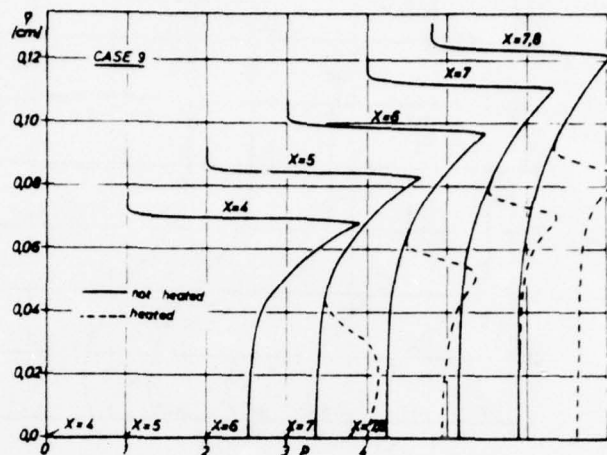
Figure 5. Profiles of the static pressure p in y-direction at different stations x, case 9.

plateau appears near the wall. The pressure rises in the direction toward the outer edge, goes through a maximum and drops then quite steeply to the pressure for the unheated case at the lower edge of the inviscid layer. Figure 5 shows that this pressure distribution is very similar to that of the shock wave at the outer edge.

The pressure drop has different steepness in the different cases. Figure 6 shows for the station x = 7.8 the pressure profiles for all nine cases. One can see that for increasing ΔT_w and decreasing ΔL the pressure drop becomes steeper.

Although it was not possible in the frame of this investigation to calculate further downstream, it appears from the present results that an embeded shock wave is created, if the amount of heat added as well as the gradient dT_w/dx is large enough. In any case a pressure wave is created, which lies almost parallel to the outer shock wave at the outer edge of the boundary layer, and which defines the region of influence of the area where the temperature has been risen. No statements are possible at this time about the behaviour of this pressure wave further downstream.

Figure 6 further shows that the parameter $\Delta \bar{T}_w$ govern the rise of the pressure niveau. The distance $\Delta \bar{L}$ govern the steepness of the imbedded shock wave toward the outer edge.

276
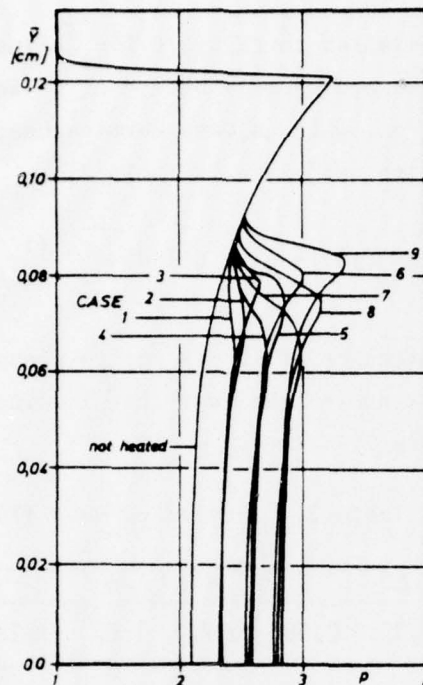
Figure 6. Profiles of the pressure p in y-direction at the station
x = 7.8 for all cases from Table 1.

The added amount of heat is also governed by the temperature rise.
Figure 7 shows the heat-flux

$$(4.1) \quad q_w = (\bar{q}_w/(\bar{k}_{ref} \, \bar{T}_\infty \, \sqrt{Re/L})) \quad (-k\partial T/\partial y - (\gamma - 1) \, M_\infty^2 \, Pr\mu\upsilon\partial n/\partial y)_w$$

as function of x for the different cases. Note that the heat flux con-
tains a slip-flow term (see for instance Reference 11).
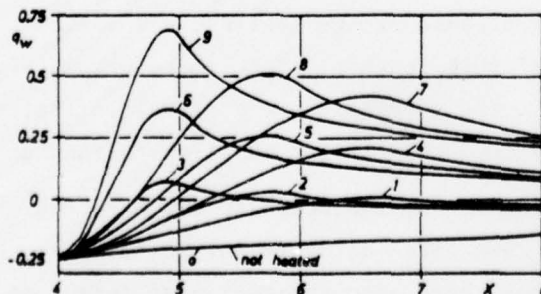
Figure 7. Wall heat transfer q_w as function of x for all cases.

277

The figure shows similar to Figure 6 the influence of $\Delta \bar{T}_w$. The maximum of q_w is always reached shortly before $\Delta \bar{L}$ is reached. This is due to the slip-flow part of q_w, which always carries heat out of the flow. The integration (results are given in Table 2)

$$(4.2) \quad Q = \int_{x_0}^{x_1} (q_{w_i}(\xi) - q_{w_o}(\xi))\, d\xi \qquad \begin{array}{l}\text{(i numbers the different cases;} \\ \text{o the unheated case; } x_0 = 4L, \\ x_1 = 7.8L)\end{array}$$

shows that the influence of $\bar{T}_w$ is not so prounced as it appears from Figure 6. This is due to the fact that x_1 lies too close to x_0, as can be seen from Figure 7.

Table 2. Integrated heat flux Q.

case	1	2	3	4	5	6	7	8	9
Q	0,43	0,52	0,58	0,92	1,07	1,22	1,42	1,67	1,9

Interesting is the fast drop of the heat flux after the maximum is reached, although the wall temperature remains on the new higher level. A return to the initial low wall temperature (finite hot spot) would drastically change the picture, also with respect to the imbedded shock wave.

The profiles of the tangential velocity component $u = \bar{u}/\bar{u}_\infty$ at different stations x in Figure 8 exhibit near the surface a small acceleration, whereas in the larger region of the boundary layer a velocity defect is present. This velocity defect is due to the rise of the density in the boundary layer because of the heating. Classical boundary layer theory does not reveal this feature, since there pressure variations are not accounted for. The profiles show a strong inflexional behaviour which will certainly lead to a fast transition to the turbulent state.

In Figure 9 profiles of the velocity component normal to the wall $v = \bar{v}\ \sqrt{Re_L}/\bar{u}_\infty$ are given at different stations x. As for the pressure profiles one sees here also the region of influence for the heated case. The steepness of the drop of the profiles for the heating case increases for increasing $\Delta T_w/\Delta L$, too.
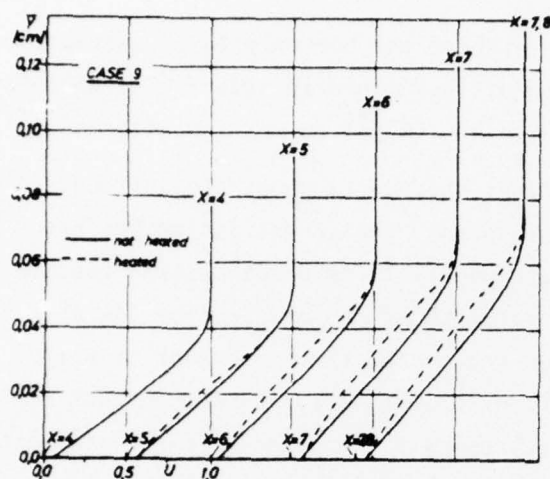
Figure 8. Profiles of the tangential velocity component u in y-direction at different stations x, case 9.
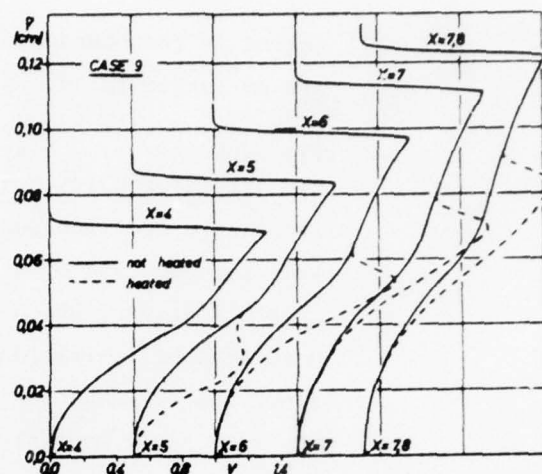
Figure 9. Profiles of the normal velocity component v in y-direction at different stations x, case 9.

Comparing the present computed results with the experimental results in Reference 1/2, one can see certain qualitative agreement. In Reference 1 a stronger acceleration of the tangential velocity component near the wall has been observed for the case of heat addition. The deceleration is observed in the experiment in the vicinity of M < 1, whereas the calculation shows this at M < 0,2. It is possible that the slip-flow conditions used in the calculation play a role. In Reference 1 a pressure rise has also been observed, but it is not so strong as the calculated one, and not visible that clear.

5. CONCLUSION

The theoretical investigation of a laminar hypersonic boundary layer past an infinitely thin flat plate shows, if heat is added through the plates surface at a certain position down-stream of the leading edge, that pressure changes near the surface appear, and a pressure wave is formed, which indicates the region of influence of the area, where the temperature has been risen. If the wall temperature has a very large gradient dT_w/dx, the pressure wave resembles a shock wave. In any case a larger

region in the boundary layer exists where the boundary layer assumptions are no longer valid. A similar result was found in Referenc 1, where a turbulent nozzle boundary layer with heat addition was investigated.

The present results don't allow final statements about the influence of local heat addition such as in hot spots. The investigation has been made for the case of a hypersonic boundary layer which allowed certain simplifications, which eased the solution of the problem considerably. More serious limitations are given because of the employment of slip-flow, and temperature-jump conditions at the wall, and perhaps due to the very small boundary layer thicknesses. The boundary layer stability problem which is connected with the point of inflexion profiles in the tangential velocity component in the heat addition case has not been treated.

For the experimental data in Reference 1 other limitations are present: the geometry of the flow was very complicated, since only a part of the nozzle in circumferential direction was heated, and the ratio of boundary layer thickness and nozzle diameter was very large with $\delta/R \approx 0.4$.

In order to get a more reliable understanding of the phenomena, which are undoubtly present, experiments are necessary in laminar and turbulent boundary layers in a larger Mach number region, and not only for hot spots which extend to infinity behind the temperature rise, as investigated here, but also for finite hot spots. Theoretical investigations using the Navier-Stokes equations will be possible only while employing asymptotic analysis. Further numerical experiments employing the Navier-Stokes equations can certainly clear up more the mechanism and can especially break down.

REFERENCES

1. H. Pfeiffer, E. Will: "Profile Measurements in a Hypersonic Turbulent Boundary Layer with Heat Transfer," Euromech Colloquium 43 on "Heat Transfer in Turbulent Boundary Layers with Variable Fluid Properties." Göttingen, Mai 1973.

2. E. H. Hirschel, F. Martin, W. Geller: "Die Hyperschall-Gleitströmungsgrenz-schicht an einer teilweise geheizten abenen Platte," Abhandlungen aus dem Aerodynamischen Institut der RWTH Aachen (E. Krause, Herausgeber), Heft 22, Sanderband, 1975.

3. H. Schlichting: "Boundary Layer Theory," McGraw-Hill, New York - Toronto - London, 1960.

4. D. Rues: "Über die Äquivalenz von Wärme-, Kraft- und Massequellen," ZAMP, Vol. 16, Fax. 4 (1965), pp. 522-526.

5. E. H. Hirschel: "Ein implizites Differenzenverfahren zur Berechnung hypersonischer Gleitströmungs-Grenzschichten," DLR FB 71-97 (1971).

6. S. Rudman, S. C. Rubin: "Hypersonic Viscous Flow over Slender Bodies Having Sharp Leading Edges," AIAA J. 6 (1968), No. 5, pp. 1169-1171.

7. L. Lees: "On the Boundary Layer Equations in Hypersonic Flow and their Approximate Solutions," J. of the Aeronautical Sciences, Vol. 20 (1953) No. 2, pp. 143-145.

8. H. K. Cheng, S. Y. Chen, R. Mobley, C. R. Huber: "On the Hypersonic Leading-Edge Problem in the Merged Layer Regime," in Rarefied Gas Dynamics, Suppl. 5, Vol. 1 (L. Trilling, H. Y. Wachmann, edgs.) New York: Academic Press, 1969.

9. E. H. Hirschel: "Untersuchung grenzschichtähnlicher Strömungen mit Druckgradienten bei hohen Antrömmachzahlen," DLF FB 76-22 (1976).

10. E. H. Hirschel: "The Influence of the Accommodation Coefficients on the Flow Variables in the Viscous Interaction Region of a Hypersonic Slip-Flow Boundary Layer," ZFW 20, 1972, H. 12, pp. 470-475.

11. E. H. Hirschel: "Die Strömung eines hochverdunnten dissoziierten Gases über eine ebene, vorn scharfe Platte," Diss. RWTH Aachen, DLR FB 70-60, 1970.

ADDITIONAL RESULTS ON SIMILAR
SOLUTIONS FOR TURBULENT FLOWS

by

H. Vollmers

Deutsche Forschungs- und Versuchsanstalt
für Luft- und Raumfahrt E. V.
Aerodynamische Versuchsanstalt Gottingen
Bunsenstrasse 10

At the previous DEA Meeting in 1975 a set of partial differential
equations describing plane and axisymmetric turbulent flows was
discussed (1). The equations include relations between mean
velocity field, Reynolds' stress, turbulent energy, and turbulent
length scale. They were transformed into ordinary differential
equations by similarity assumptions and solved numerically. The
following flow cases were treated:

1. The free plane jet in a fluid at rest,

2. the asymptotic plane wake,

3. the free mixing layer,

4. the fully developed plane flow in a channel,

5. the free round jet in a fluid at rest,

6. the fully developed flow in a cylindrical pipe.

Systematic variations of the coefficients, which were introduced
with the closure assumptions of the equations, were studied. One
set of values of the coefficients for all treated cases was obtained
by comparison of the solutions with experimental data. The work
was interrupted for nearly one year. When resuming the investiga-
tions, some new aspects appeared and lead to a change of two of the
coefficients. The coefficient k_q of the diffusion terms was
given a higher value, and as a consequence of this the coefficient
of a production term in the length scale equation was slightly

lowered. The change in k_q yields a physically more acceptable behavior of the solutions. For further details reference is made to the papers (2) or (3). The set of coefficient now reads:

$$c = 0.165; \quad c_L = 0.8; \quad k_q = 0.8; \quad \zeta = 0.98; \quad \zeta_2 = 1.2; \quad \zeta_3 = -1.5;$$
$$\alpha_L \approx 0.387; \quad k \approx 0.548.$$

The profiles of longitudinal or axial velocity $\bar{u}$, turbulent energy E, and turbulent length scale L computed with this set are plotted with a pertinent similarity coordinates in the following figures. Experimental values for mean velocity and turbulent energy are indicated by dashed lines. In some cases Prandtl's mixing length is shown as a dash pointed line with the mark 1 .

References

1.   Vollmers, H. and Rotta, J. C., Similar Solutions for Turbu-
        lent Energy and Turbulent Length Scale.

2.   Rotta, J. C. and Vollmers, H., "Aehnliche" Lösungen der
        Differentialgleichungen für gemittelte Geschwindigkeiten,
        Turbulenzenergie und Turbulenzlänge.

        DLR-FB 76-24 (1976).

3.   Vollmers, H. and Rotta, J. C., Similar Solutions for Turbu-
        lent Flow Fields Described by Mean Velocity, Turbulent Energy
        and Turbulent Length Scale.

        AIAA Paper No. 76-407 (1976).
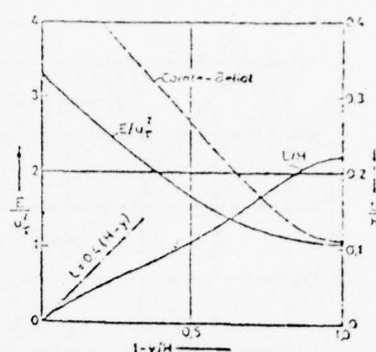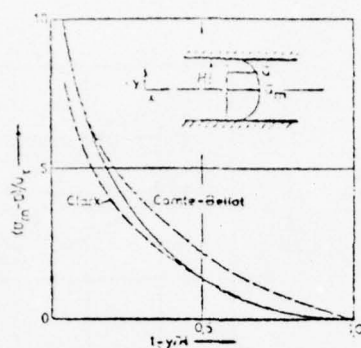
Profiles of mean velocity, turbulence energy and turbulence
length for the fully developed plane flow through a channel
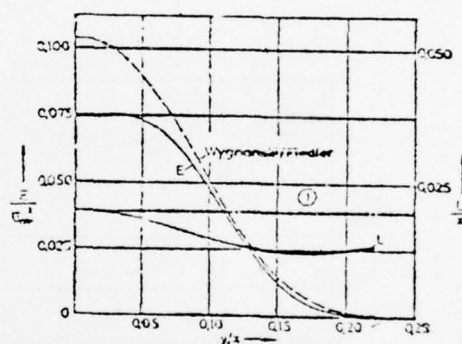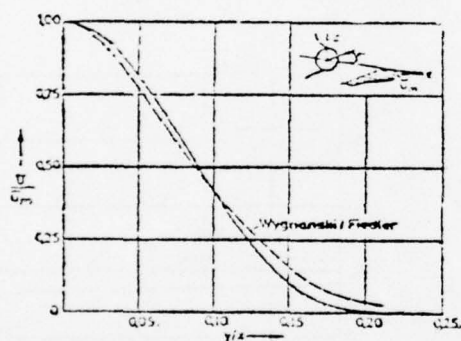
Profiles of mean velocity, turbulence energy and turbulence length
for the round free jet
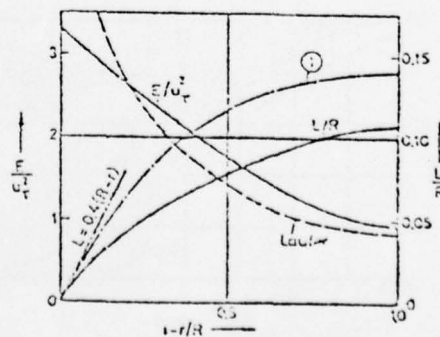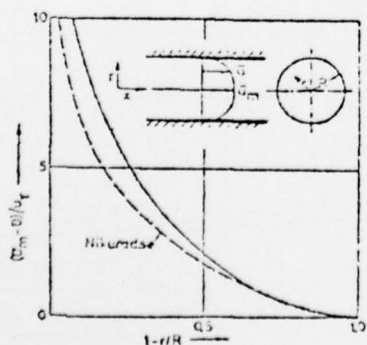
Profiles of mean velocity, turbulence energy and turbulence
length for the fully developed flow through a circular pipe
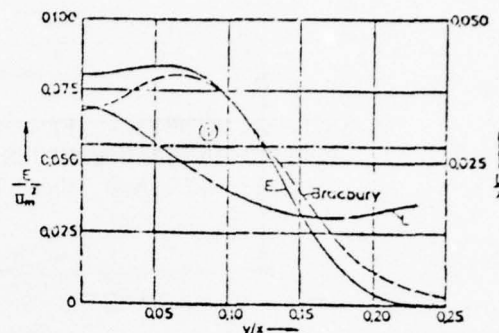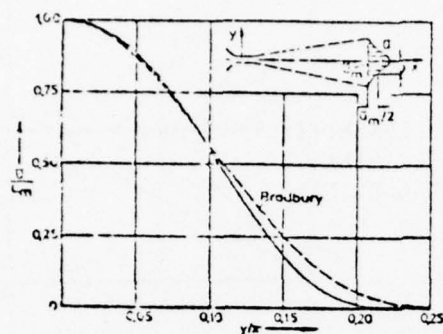
Profiles of mean velocity, turbulence energy and turbulence length for the plane free jet.
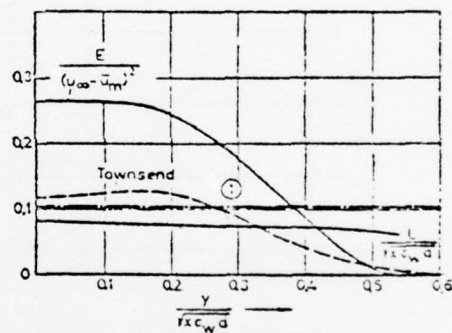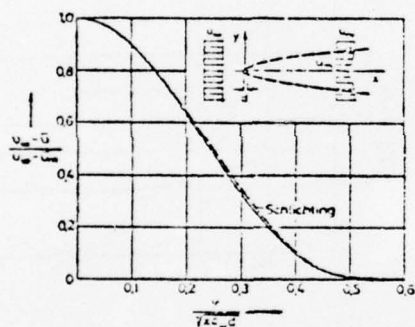
Profiles of mean velocity, turbulence energy and turbulence length for the plane wake.
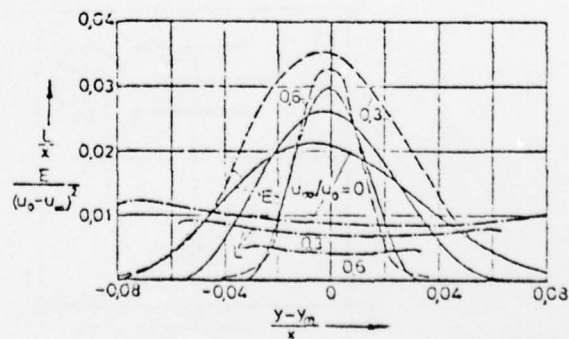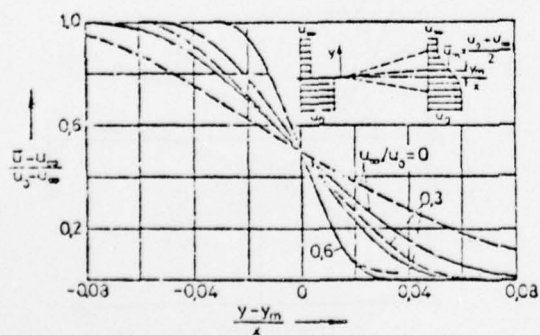
Profiles of mean velocity, turbulence energy and turbulence length for the free mixing layer for different velocity ratios.

AN INTEGRAL KINETIC-ENERGY-OF-TURBULENCE (IKET) METHOD
FOR CALCULATING COMPRESSIBLE RELAMINARIZATIONAL,
TRANSITIONAL, AND TURBULENT BOUNDARY-LAYER FLOWS

by

J. C. Adams, Jr. and B. K. Hodge
ARO, Inc.
von Karman Gas Dynamics Facility
Arnold Engineering Development Center
Air Force Systems Command
Tullahoma, Tennessee

Boundary - Layer Equations

Continuity: $\quad \dfrac{\partial}{\partial x} \bar{\rho}\, \bar{u} + \dfrac{\partial}{\partial y}\, \bar{\rho}\, V = 0 , \quad V = \bar{v} + \dfrac{\overline{\rho'\, v'}}{\bar{\rho}}$

X-Momentum: $\quad \bar{\rho}\, \bar{u}\, \dfrac{\partial \bar{u}}{\partial x} + \bar{\rho}\, V\, \dfrac{\partial \bar{u}}{\partial y} = -\dfrac{\partial \bar{p}}{\partial x} + \dfrac{\partial}{\partial y}\left[\bar{\mu}\left(1 + \dfrac{\mu_t}{\bar{\mu}} \right)\, \dfrac{\partial \bar{u}}{\partial y} \right]$

Y-Momentum: $\qquad\qquad\qquad\qquad \dfrac{\partial \bar{p}}{\partial y} = 0$

Energy: $\quad \bar{\rho}\, \bar{u}\, \dfrac{\partial \bar{h}}{\partial x} + \bar{\rho}\, V\, \dfrac{\partial \bar{h}}{\partial y} = \bar{u}\, \dfrac{\partial \bar{p}}{\partial x} + \bar{\mu}\left(1 + \dfrac{\mu_t}{\bar{\mu}} \right)\left(\dfrac{\partial \bar{u}}{\partial y} \right)^2$

$$+ \dfrac{\partial}{\partial y}\, \left[\left(\dfrac{\bar{\mu}}{Pr} + \dfrac{\mu_t}{Pr_t} \right)\, \dfrac{\partial \bar{h}}{\partial y} \right]$$

The IKET approach is used to compute the eddy viscosity μ_t.

288

IKET Equation:

$$\frac{d}{dx} \int_0^\delta 1/2 \; \bar{\rho} \; \bar{u} \; \overline{q^2} \; dy = -\int_0^\delta \left(\overline{\bar{\rho} \; u'v'} + \overline{\rho' u'v'} \right) \frac{\partial \bar{u}}{\partial y} \; dy$$

$$+ \int_0^\delta \overline{p' \frac{\partial v'}{\partial y}} \; dy \; - \int_0^\delta \left\{ \overline{p' u'} \left(\bar{u} \frac{\partial \bar{u}}{\partial x} + \bar{v} \frac{\partial \bar{u}}{\partial y} \right) + \bar{\rho} \; \overline{(u')^2} \frac{\partial \bar{u}}{\partial x} \right.$$

$$\left. + \bar{\rho} \; \overline{(v')^2} \; \frac{\partial \bar{v}}{\partial y} \right\} \; dy \; - \int_0^\delta \bar{\rho} \; \epsilon \; dy \; + \; E$$

where $\quad \bar{\rho} \; \epsilon$ = viscous dissipation of turbulent energy

$$1/2 \; \overline{q^2} = 1/2 \left[\overline{(u')^2} + \overline{(v')^2} + \overline{(w')^2} \right] = \text{Turbulent Kinetic Energy}$$

with E defined as

$$E = \left[\underbrace{1/2 \; \overline{q^2} \left(\bar{\rho} \; \bar{u} \; \frac{d\delta}{dx} - \bar{\rho} \; \bar{v} \right)}_{\text{I}} - \underbrace{\overline{p' v'} - 1/2 \; \bar{\rho} \; \overline{v' q^2} - 1/2 \; \overline{\rho' q^2 v'}}_{\text{II}} \right]_e$$

I   Free-Stream Turbulence Entrained by the Boundary Layer

II   Direct Absorption of Free Stream Acoustic Energy by the Boundary Layer

●   E Triggers Transition

Turbulence Model (Kolmogorov – Prandtl)

$$\tau_t = \mu_t \; \frac{\partial \bar{u}}{\partial y} = -\bar{\rho} \; \overline{u'v'} - \cancel{\rho' u' v'} \quad \text{Neglect}$$

where
$$\mu_t = C_\mu \; \bar{\rho} \; k^{1/2} \; \ell_\mu$$

$$k = 1/2 \; \overline{q^2}, \quad \ell_\mu \Rightarrow \text{Length Scale for Turbulent Shear Stress}$$

$$C_\mu \Rightarrow \text{Empirical}$$

$$\bar{\rho} \, \epsilon = \frac{C_D \; \bar{\rho} \; k^{3/2}}{\ell_D}$$

$$C_D \Rightarrow \text{Empirical}, \quad \ell_D \Rightarrow \text{Length Scale for Dissipation of Turbulent Energy}$$

Turbulent Structural Scales

$$-\overline{u'v'} = a_1 \; \overline{q^2} = 2a_1 k = \tau_t / \bar{\rho}$$

$$\overline{(u')^2} = a_2 \; \overline{q^2}$$

$$\overline{(v')^2} = a_3 \; \overline{q^2}$$

$$\overline{(w')^2} = (1 - a_2 - a_3) \; \overline{q^2}$$

$$a_2, a_3 \Rightarrow \text{Empirical}$$

$$a_1 = a_1(y)$$

290

Two - Layer Length Scale Model

Inner Region with Near Wall Damping:

$$\ell_\mu = y \, D_\mu$$

$$\ell_D = y \, D_D$$

$$a_1 = a_t \, D_a$$

$$D_\mu = 1 - \exp\,(-A_\mu \, R_t)$$

$$D_D = 1 - \exp\,(-A_D \, R_t)$$

$$D_a = 1 - \exp\,(-A_a \, R_t)$$

$$A_\mu, \, A_D, \, A_a, \, a_t \quad \blacktriangleright \quad Empirical$$

Local Turbulence Reynolds Number:

$$R_t = \frac{\bar{\rho} \, k^{1/2} \, y}{\bar{\mu}} = \frac{C_\mu}{2a_1} \, \frac{\bar{\rho} \, \ell_\mu \, y}{\bar{\mu}} \, \frac{\partial \bar{u}}{\partial y}$$

Outer Region:

$$\ell_\mu = Y$$

$$\ell_D = \lambda_D \, \delta$$

$$a_1 = a_t$$

$$\lambda_D, \, a_t \quad \blacktriangleright \quad Empirical$$

The outer region value of ℓ_μ, namely Y, is to be determined from the IKET equation.

291

Turbulence Model Constants

C_μ	0.2383
C_D	0.3777
a_t	0.150
a_2	0.566
a_3	0.150
A_μ	0.0160
A_D	0.18885
A_a	0.0469
λ_D	0.2069
Pr_t	0.90

Within the inner region

$$\ell_\mu = y \left[1 - \exp \left(- \frac{A_\mu \, C_\mu}{2a_1} \; \frac{\bar{\rho} \, \ell_\mu \, y}{\bar{\mu}} \; \frac{\partial \bar{u}}{\partial y} \right) \right]$$

$$a_1 = a_t \left[1 - \exp \left(- \frac{A_a \, C_\mu}{2a_1} \; \frac{\bar{\rho} \, \ell_\mu \, y}{\bar{\mu}} \; \frac{\partial \bar{u}}{\partial y} \right) \right]$$

Iteration using Newton's Method for systems required

Numerical Solution of the Compressible Turbulent Boundary-Layer Equations

● Implicit finite-difference method.

● Variable grid point spacing in both streamwise and body normal directions.

● Arbitrary wall temperature or adiabatic wall.

● Outer edge conditions input from a separate source; an inviscid analysis for example.

● Sutherland's Law for laminar viscosity (with Pr = 0.70).

● Thermally and calorically perfect gas model.

● Global iteration for ℓ_μ = Y required.

● Transition can be calculated using the acoustic energy entrained or turbulent flow forced at a specified location.

Nash-Webber Nozzle A, P_0 = 5 in. Hg. abs.

IKET Calculation of Turbulent
Boundary-Layer Relaminarization

294
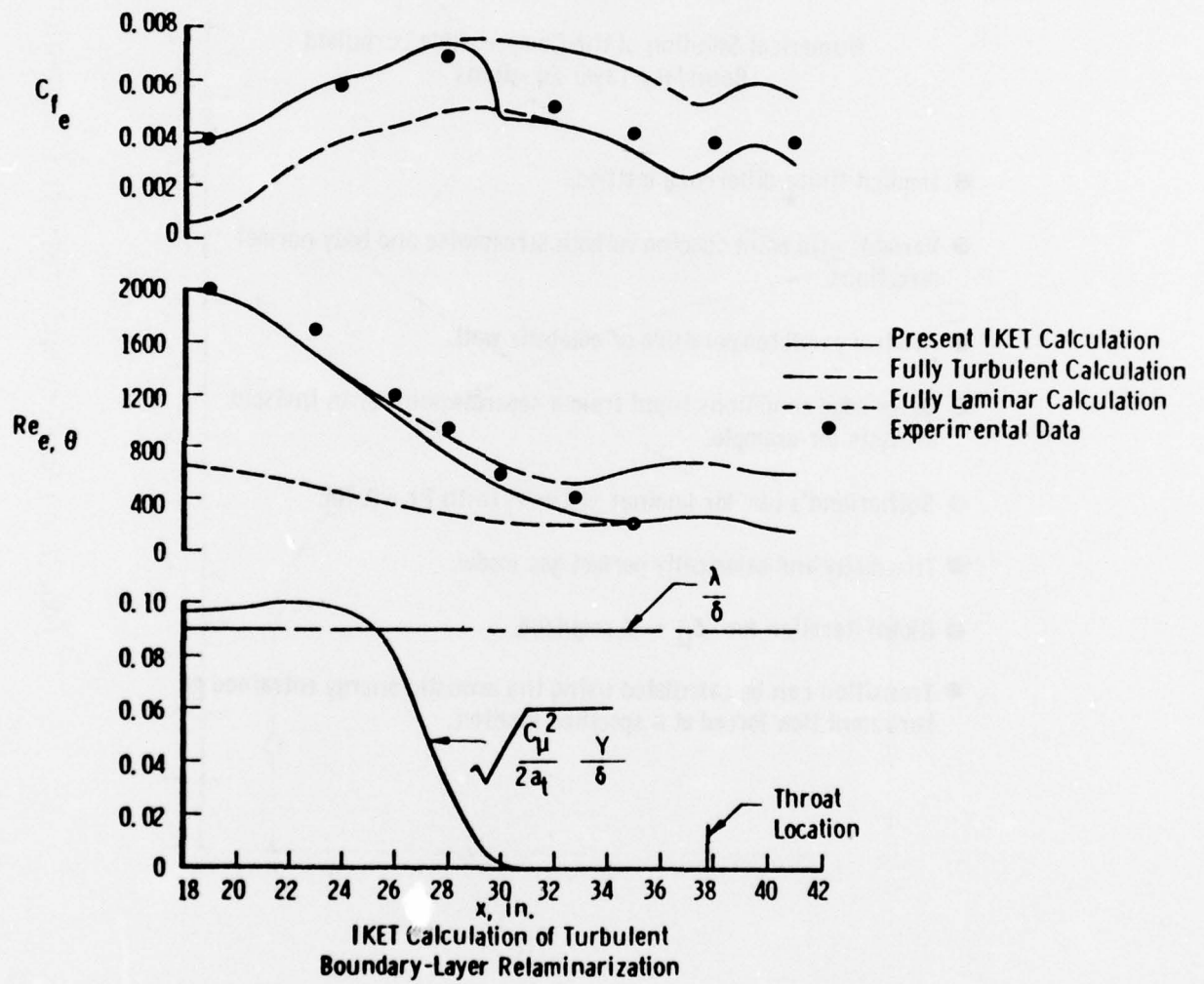
Hollow Cylinder, VKF Tunnel A

—— Present IKET Calculation Input
o Experimental Data from Gran, Lewis, and Kubota
(J. Fld. Mech. Vol. 66, 1974)
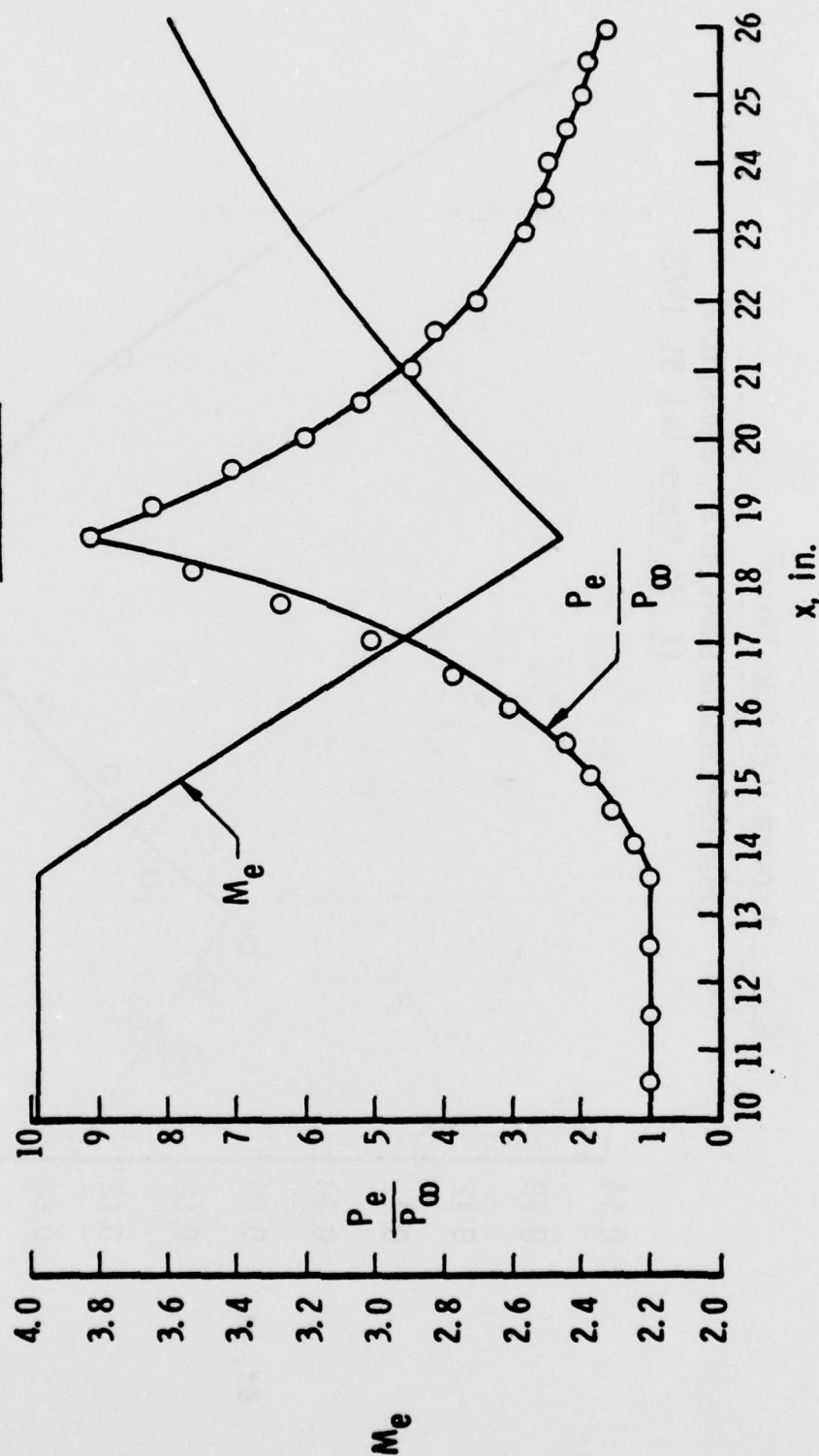
Edge Mach Number and Pressure Distribution

Displacement Thickness Distribution for Hot Wall Condition

Hollow Cylinder, VKF Tunnel A

—— Present IKET Calculation

○ □ Experimental Data Gran, Lewis, and Kubota
(J. Fld. Mech, Vol. 66, 1974)
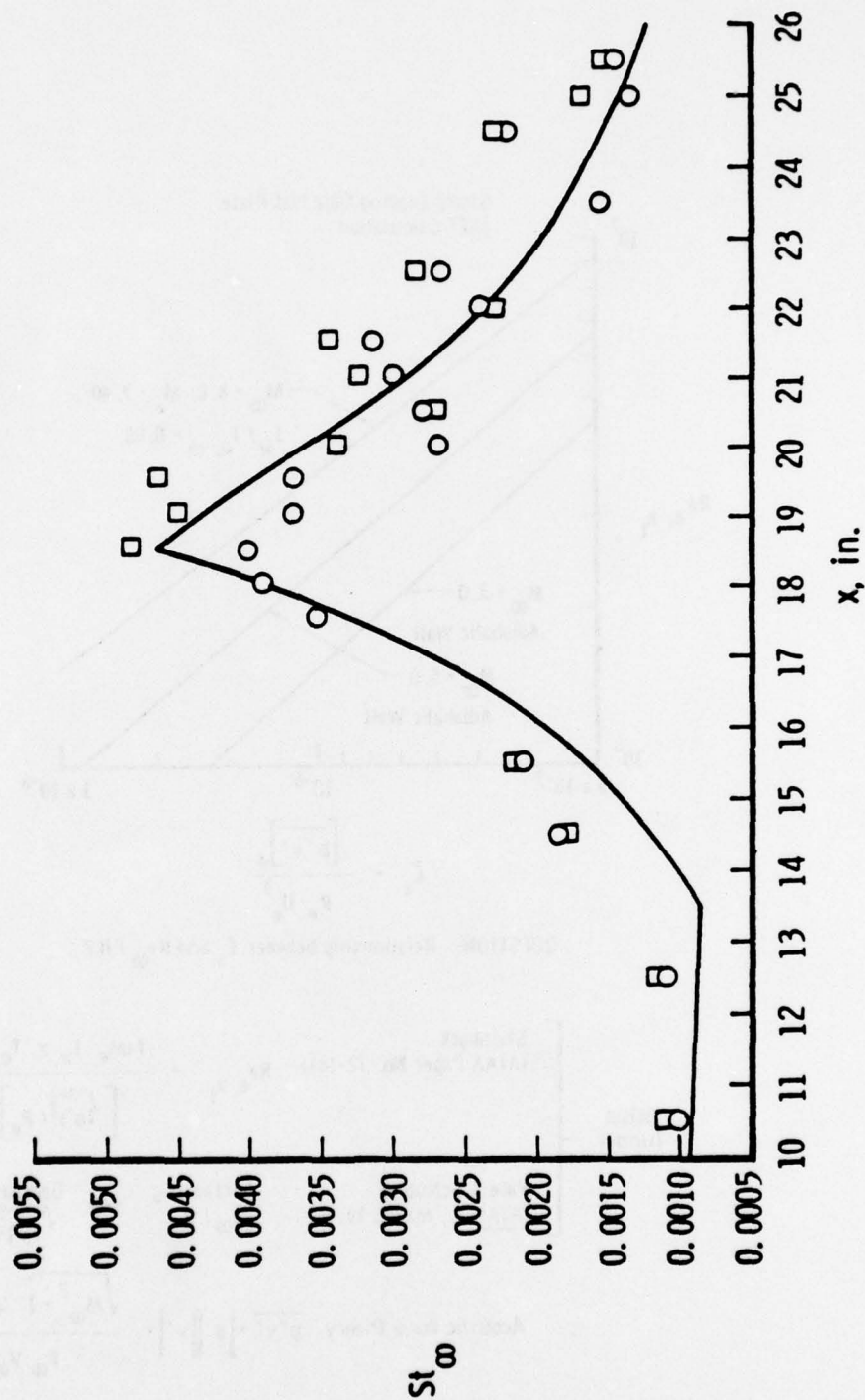
Stanton Number Distribution for Cold Wall Condition

St_∞

x, in.

Sharp Leading Edge Flat Plate
I KET Calculation

$$Re_{e, x_t}$$

$M_\infty = 8.0, \; M_e = 7.40$
$T_w / T_{0, \infty} = 0.80$

$M_\infty = 3.0$
Adiabatic Wall

$M_\infty = 5.0$
Adiabatic Wall

$$\bar{E}_e = \frac{\overline{\left[p'v'\right]}_e}{\rho_e U_e^3}$$
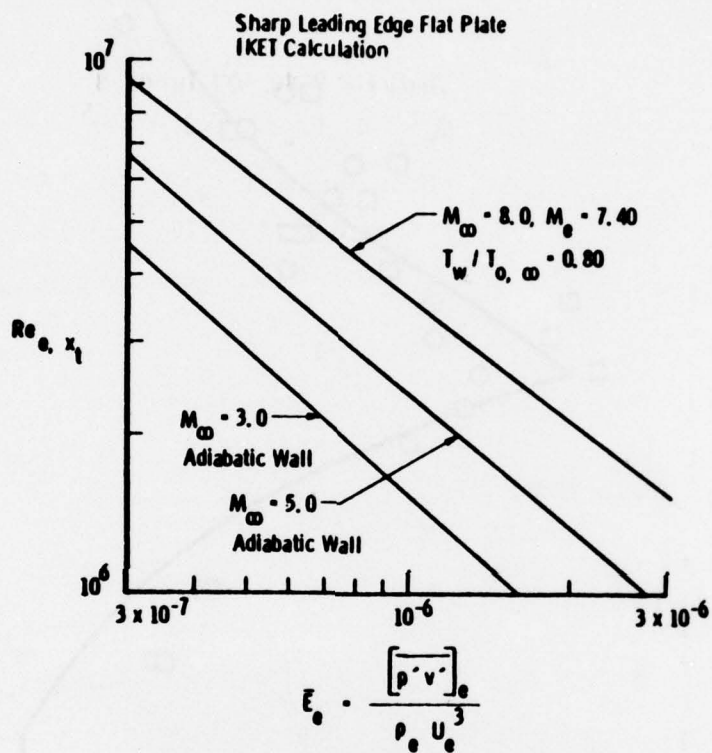
QUESTION: Relationship between E_e and Re_∞ / ft?

Wind Tunnel

Stainback
(AIAA Paper No. 72-181)

$$Re_{e, x_t} = \frac{f(M_e, T_w, \gamma, T_{0, \infty})}{\left[\sqrt{\overline{(p')^2}} / P_e\right]^n}, \quad n \sim O(1)$$

Pate & Schueler
(AIAA J., March 1969)

Increasing $Re_\infty / ft \rightarrow$ Decreasing $\sqrt{\overline{(p')^2}}$

Acoustic Wave Theory $\quad \overline{p'v'} = |p'||v'| = \dfrac{\sqrt{M_\infty^2 - 1} \; \overline{(p')^2}}{\rho_\infty V_\infty}$

298

Sharp Flat Plate, VKF Tunnel B
$M_e = 7.40$, Re_e / in. $= 2.35 \times 10^5$

——— IKET Calculation for $T_w / T_{0,\infty} = 0.80$
- - - - IKET Calculation for $T_w / T_{0,\infty} = 0.40$
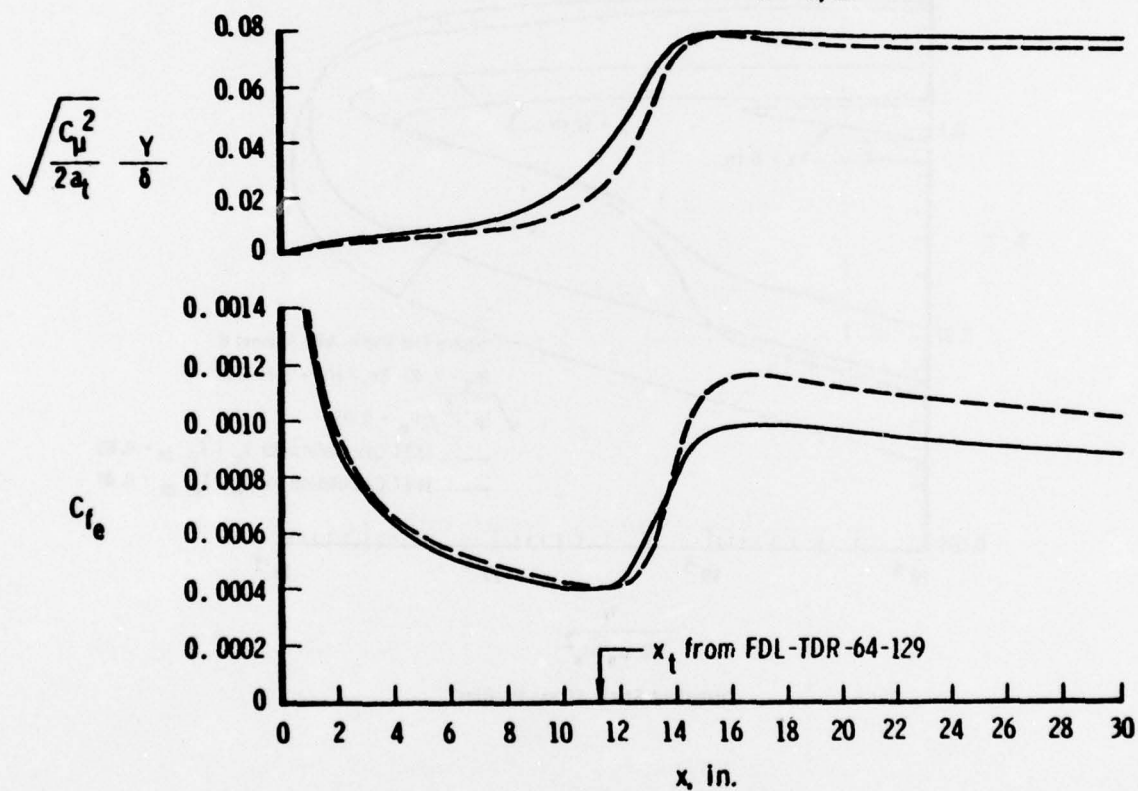
Laminar, Transitional, and Turbulent Outer Length Scale and Local
Skin Friction Distribution

Turbulent Shear Stress Profiles

| x, in. | Boundary-Layer Thickness δ, in. | |
	$T_w / T_{0,\infty}$ = 0.40	$T_w / T_{0,\infty}$ = 0.80
6	0.092	0.128
12	0.133	0.185
24	0.306	0.373

x = 6 in.

x = 12 in.

x = 24 in.

Sharp Flat Plate, VKF Tunnel B

M_e = 7.40, Re_e / in. = 2.35 x 10^5

$\sqrt{(p')^2} / P_e$ = 0.035

——— IKET Calculation for $T_w / T_{0,\infty}$ = 0.80

– – – IKET Calculation for $T_w / T_{0,\infty}$ = 0.40

y, in.

$$\frac{q}{1/2\ \rho_e\ U_e^2}$$

IKET Calculation
5 deg Half-Angle Sharp Cone
Adiabatic Wall

$\triangle$ ~ M_∞ = 3.0, Re_∞ / ft = 4.35 x 10^6
$\bigcirc$ ~ M_∞ = 5.00, Re_∞ / ft = 5.33 x 10^6
$\diamond$ ~ M_∞ = 5.00, Re_∞ / ft = 1.53 x 10^6

$\bar{E}_e$ vs. Re_{e, x_t} for 5 deg Half Angle Sharp Cone

The Effect of Acoustic Energy Absorption on a Turbulent Boundary Layer

REFERENCES

McDonald, H. and Camarata, F.J. "An Extended Mixing Length Approach for Computing the Turbulent Boundary Layer Development." Proceedings Computation of Turbulent Boundary Layers - 1968 AFOSR-IFP-Stanford Conference, Vol. 1, Stanford University, Stanford, California, August 1968, pp. 83-98.

Bradshaw, P., Ferriss, D.H., and Atwell, N.P. "Calculation of Boundary-Layer Development Using the Turbulent Energy Equation." Journal of Fluid Mechanics, Vol. 28, Pt. 3, May 1967, pp. 593-616.

Chan, Y.Y. "Comparison of Several Mixing Length Models for Turbulent Boundary-Layer Computations." National Research Council of Canada Aeronautical Report LR-531, March 1970.

Chan, Y.Y. "Turbulent Boundary-Layer Computations Based on an Extended Mixing Length Approach." AIAA Journal, Vol. 8, No. 10, October 1970, pp. 1873-1875.

Chan, Y.Y. "Compressible Turbulent Boundary Layer Computa tions Based on an Extended Mixing Length Approach." C.A.S.I. Transactions, Vol. 5, No. 1, March 1972, pp. 21-27.

McDonald, H. and Fish, R.W. "Practical Calculations of Trans-itional Boundary Layers." International Journal of Heat Mass Transfer, Vol. 16, No. 9, September 1973, pp. 1729-1744. See also AGARD-AG-164, December 1972, pp. 29-53.

Shamroth, S.J. and McDonald, H. "Assessment of a Transitional Boundary Layer Theory at Low Hypersonic Mach Numbers." NASA CR-2131, November 1972.

McDonald, H. and Kreskovsky, J.P. "Effect of Free Stream Turbulence on the Turbulent Boundary Layer." International Journal of Heat Mass Transfer, Vol. 17, No. 7, July 1974, pp. 705-716.

Laster, M.L. "Inhomogeneous Two-Stream Turbulent Mixing Using the Turbulent Kinetic Energy Equation." AEDC-TR-70-134, May 1970.

Bradshaw, P. and Ferriss, D.H. "Calculation of Boundary-Layer Development Using the Turbulent Energy Equation: Compressible Flow on Adiabatic Walls." Journal of Fluid Mechanics, Vol. 46, Pt. 1, March 1971, pp. 83-110.

Wolfshtein, M. "The Velocity and Temperature Distribution in One-Dimensional Flow with Turbulence Augmentation and Pressure Gradient." International Journal of Heat Mass Transfer, Vol. 12, No. 3, March 1969, pp. 301-318.

Townsend, A.A. "Equilibrium Layers and Wall Turbulence." Journal of Fluid Mechanics, Vol. 11, Pt. 1, August 1961, pp. 97-120.

Rose, W.C. and Murphy, J.D. "Ratio of Reynolds Shear Stress to Turbulence Kinetic Energy in a Boundary Layer." The Physics of Fluids, Vol. 16, No. 6, June 1973, pp. 935-937.

Mellor, G.L. and Herring, H.J. "A Study of Turbulent Boundary Layer Models. Part II, Mean Turbulent Field Closure." SC-CR-70-6125B, January 1971.

Warsi, Z.U.A. and Mertaugh, L.J. "Estimation of Turbulent Energy Dissipation Using Available Transfer Theories." AIAA Journal, Vol. 12, No. 2, February 1974, pp. 237-239.

Jones, W.P. and Launder, B.E. "The Prediction of Laminarization with a Two-Equation Model of Turbulence." International Journal of Heat Mass Transfer, Vol. 15, No. 2, February 1972, pp. 301-314.

Jones, W.P. and Launder, B.E. "The Calculation of Low-Reynolds-Number Phenomena with a Two-Equation Model of Turbulence." International Journal of Heat Mass Transfer, Vol. 16, No. 6, June 1973, pp. 1119-1130.

van Driest, E.R. "On Turbulent Flow Near a Wall." Journal of Aeronautical Sciences, Vol. 23, No. 11, November 1956, pp. 1007-1011, 1036.

Adams, J.C., Jr. "Numerical Calculation of the Subsonic and Transonic Turbulent Boundary Layer on an Infinite Yawed Airfoil." AEDC-TR-73-112, July 1973.

Nash-Webber, J.L. "Wall Shear-Stress and Laminarization in Accelerated Turbulent Compressible Boundary-Layers." MIT Gas Turbine Lab. Report No. 94, April 1968.

Lewis, J.E., Gran, R.L., and Kubota, T. "An Experiment on the Adiabatic Compressible Turbulent Boundary Layer in Adverse and Favorable Pressure Gradients." Journal of Fluid Mechanics, Vol. 51, Pt. 4, February 1972, pp. 657-672.

Gran, R.L., Lewis, J.E., and Kubota, T. "The Effect of Wall Cooling on a Compressible Turbulent Boundary Layer." Journal of Fluid Mechanics, Vol. 66, Pt. 3, November 1974, pp. 507-528.

Hahn, J.S. and Lutz, R. "Experimental Investigation of Turbulent Boundary Layers with Pressure Gradient and Heat Transfer at Mach Number 4." AEDC-TR-71-3, January 1971.

Deem, R.E., Erickson, C.R., and Murphy, J.S. "Flat-Plate Boundary-Layer Transition at Hypersonic Speeds." FDL-TDR-64-129, October 1964.

Pate, S.R. and Schueler, C.J. "Radiated Aerodynamic Noise Effects on Boundary-Layer Transition in Supersonic and Hypersonic Wind Tunnels." AIAA Journal, Vol. 7, No. 3, March 1969, pp. 450-457.

Bushnell, D.M. and Alston, D.W. "Calculation of Transitional Boundary-Layer Flows." AIAA Journal, Vol. 11, No. 4, April 1973, pp. 554-556.

Fischer, M.C. and Weinstein, L.M. "Cone Transitional Boundary-Layer Structure at M_e = 14." AIAA Journal, Vol. 10, No. 5, May 1972, pp. 699-701.

Potter, J.L. and Whitfield, J.D. "Boundary Layer Transition Under Hypersonic Conditions." AGARDograph 97, Part III, May 1965, pp. 1-61.

Stainback, P.C. "Effects of Wind-Tunnel Disturbances on Hypersonic Boundary-Layer Transition. Part I: Measurement of Transition Reynolds Numbers and Surface Fluctuating Pressures at a Local Mach Number of 5." AIAA Paper No. 72-181 presented at the AIAA 10th Aerospace Sciences Meeting, San Diego, California, January 1972.

A NUMERICAL STUDY OF SUPERSONIC VISCOUS CONE
FLOW AT HIGH ANGLE OF ATTACK†

by

David S. McRae*
Air Force Flight Dynamics Laboratory
Wright-Patterson Air Force Base, Ohio

ABSTRACT

Inviscid computations for supersonic flow about cones have proven
to be unstable at angles of attack greater than twice the cone half angle.
This limitation is overcome in the present study by inclusion of the
viscous effects in the governing equations. Solutions are obtained for
supersonic viscous flow over a sharp cone using the Navier-Stokes equations
subject to a conical symmetry assumption. The integration is carried out
by MacCormack's method for a 10° half angle cone at angles of attack
including 24° in nominal $M = 8$ flow. A physically based technique (normal
stress damping) is demonstrated for controlling starting transients and
for reducing or eliminating numerical oscillations at shock discontinuities.
Results are presented which show good engineering agreement with the
experimental study of Tracy. The general features which appear in the
experimental flow field also exist in the calculation, at a cost of only
40% additional computer time per mesh point over a comparable inviscid
calculation.

NOMENCLATURE

c   Local speed of sound

e   Total internal energy $(C_v T + v^2/2)$

K   Thermal conductivity

k $(\gamma - 1)/2\gamma$

m   Courant number

p   Pressure

$\dot{q}$ Heat transfer

R   Gas constant

r   Radial coordinate

T   Temperature

t   Time

u   Velocity in r direction

v   Velocity in θ direction

V   Total velocity $(u^2 + v^2 + w^2)^{\frac{1}{2}}$

w   Velocity in ϕ direction

∞ Free stream quantity

α Angle of attack

β Damping multiplier

γ ratio of specific heats (C_p/C_v)

θ Coordinate, conical angle

λ Second coefficient of viscosity $(-2/3\ \mu)$

μ Absolute viscosity

ρ Density

σ Normal Stress

τ Shear Stress

ϕ Coordinate, circumferential angle

Subscripts

c   Cone half angle

i   Time step number

j,k   Mesh point location

n   Normal direction

p   Pitot quantity

s   Surface quantity

t   Total quantity

1,2,3   Pertaining to r, θ, ϕ, direction

308

1. INTRODUCTION

Supersonic flow about cones has been a subject of interest to aero-
dynamicists for many years, both from their occurrence as a nose shape
for many aerodynamic configurations and from their use as a reentry ve-
hicle shape in current ICBMs. As a result of this interest, many attempts
have been made to accurately solve the flow field about conical shapes
with special emphasis on the lift-producing circular cone at angle of
attack. The present study evolved from an attempt to produce high angle
of attack cone flow solutions using the inviscid Euler equations. Al-
though successful results were obtained for angles of attack up to and
including 1½ times the cone half angle, much difficulty was encountered
at higher angles of attack with the inviscid boundary conditions in the
vicinity of the lee side imbedded shock wave. It was then shown that a
more accurate and less difficult representation of conical body flows
could be produced through the inclusion of viscous effects in the govern-
ing equations. This is done in a manner that allows solution of the
governing equations without undue amounts of computer time. The technique
developed should then be a candidate for replacing inviscid calculation
techniques for many applications.

This paper deals first with the approximation to the Navier-Stokes
equations and then with application of MacCormack's finite difference
technique. The solution technique is described along with a new method
for controlling starting transients and spurious oscillations around shock
wave discontinuities. The numerical results of the calculations are
then compared with supersonic cone flow experimental data for angles of
attack including 24° for a 10° half angle sharp cone.

2. FLUID FLOW EQUATIONS

The Navier-Stokes equations for a perfect gas can be written in
conservation law form for a spherical coordinate system as follows:

$$\vec{D}_t + \vec{E}_r + \vec{F}_\theta + \vec{G}_\phi + \vec{H} = 0 \tag{1}$$

where

$$\vec{D} = r^2 \, \text{Sin}\theta \begin{bmatrix} \rho \\ \rho u \\ \rho v \\ \rho w \\ \rho e \end{bmatrix}$$

$$\vec{E} = r^2 \, \text{Sin}\theta \begin{bmatrix} \rho u \\ \rho u^2 - \sigma_{11} \\ \rho uv - \tau_{12} \\ \rho uw - \tau_{13} \\ \rho ue + \dot{q}_r - u\,\sigma_{11} - v\tau_{12} - w\tau_{13} \end{bmatrix}$$

$$\vec{F} = r \, \text{Sin}\theta \begin{bmatrix} \rho v \\ \rho uv - \tau_{21} \\ \rho v^2 - \sigma_{22} \\ \rho wv - \tau_{23} \\ \rho ve + \dot{q}_\theta - u\tau_{21} - v\sigma_{22} - w\tau_{23} \end{bmatrix}$$

$$\vec{G} = r \begin{bmatrix} \rho w \\ \rho uw - \tau_{31} \\ \rho vw - \tau_{32} \\ \rho w^2 - \sigma_{33} \\ \rho we + \dot{q}_\phi - u\tau_{31} - v\tau_{32} - w\sigma_{33} \end{bmatrix}$$

$$\vec{H} = r \, \text{Sin}\theta \begin{bmatrix} 0 \\ -(\rho v^2 - \sigma_{22}) - (\rho w^2 - \sigma_{33}) \\ -\text{cot}\theta \ (\rho w^2 - \sigma_{33}) + (\rho uv - \tau_{12}) \\ \text{cot}\theta \ (\rho vw - \tau_{23}) + (\rho uw - \tau_{13}) \\ 0 \end{bmatrix}$$

The stress terms τ_{ij} and τ_{ij} will be defined in detail later. The equations are nondimentionalized by use of free stream total pressure and density and by the maximum adiabatic velocity for free stream total temperature.

Solution of the equation set in the form shown above would require very large amounts of machine time and capacity even for simple aerodynamic configurations. This has led researchers in the past to simplify the

310

equation set through removal of the stress terms (inviscid flow) and/or by reducing the number of dimensions to be considered in the problem. One class of flows which has been examined in detail through use of the Euler equations is that of supersonic inviscid flow over conical type bodies. These flows have the unique property that derivatives of all flow quantities are zero along rays passing through the apex of the conical surface.

Examination of experimental studies of supersonic flow over conical bodies[1-3] reveals that this behavior is approximately correct downstream from nose regions even when viscous effects are present. Therefore, in concert with an idea first broached by Anderson[4] for axial corner flow, the conically symmetric flow assumption is applied to all terms in the above equation set.

The resulting equation set is:

$$\vec{D}_t + \vec{F}_\theta + \vec{G}_\phi + \vec{H} = 0 \tag{2}$$

where:

(a) $\vec{D}, \vec{F}$, and $\vec{G}$ are unchanged except in the definition of the stress terms.

(b)
$$\left[\frac{\vec{E}}{r^2 \sin\theta} \right]_r = 0$$

(c)
$$\vec{H}' = \vec{H} + \frac{2\vec{E}}{r}$$

or $\vec{H}' =$

$$r\sin\theta \begin{bmatrix} 2\rho u \\ -(\rho v^2 - \sigma_{22}) - (\rho w^2 - \sigma_{33}) + 2(\rho u^2 - \sigma_{11}) \\ -\cot\theta \ (\rho w^2 - \sigma_{33}) + 3(\rho uv - \tau_{12}) \\ \cot\theta \ (\rho vs - \tau_{23}) + 3(\rho uw - \tau_{13}) \\ 2(\rho ue - u\sigma_{11} - v\tau_{12} - w\tau_{13}) \end{bmatrix}$$

311

These equations are non-dimensionalized as follows, with dimensional quantities denoted by primes:

$$u = \frac{u'}{V_{max}} \qquad v = \frac{v'}{V_{max}} \qquad w = \frac{w'}{V_{max}} \qquad (3)$$

$$p = \frac{p'}{P_{t_\infty}} \qquad \rho = \frac{\rho'}{t_\infty} \qquad t = \frac{t'}{r/V_{max}} \qquad T = \frac{T'}{T_{t_\infty}}$$

$$e = \frac{e'}{V_{max}^2} \qquad\qquad Re = \frac{V_{max}\, \rho_{t_\infty}\, r}{\mu}$$

$$V_{max} = \left(\frac{2\gamma}{\gamma-1} \quad R \quad T_{t_\infty}'\right)^{\frac{1}{2}} \qquad k = \frac{\gamma-1}{2\gamma}$$

It is significant that when time is nondimensionalized by the parameter r/V_{max} the metric r in equation (2) cancels except for the r contained in the Reynolds number. This results in all spherical radius scaling being contained in the Reynolds number. The net effect is that the calculation is carried out at a single (,) spherical surface with the distance of this surface from the cone apex effectively determined by the Reynolds number. (Figure 1).

The nondimensionalized stress terms are as follows after application of the conical symmetry assumption:

$$\tau_{12} = \tau_{21} = \frac{1}{Re}(u_\theta - v) \qquad\qquad\qquad (4)$$

$$\tau_{13} = \tau_{31} = \frac{1}{Re\,\sin\theta}(u_\phi - w\,\sin\theta)$$

$$\tau_{23} = \tau_{32} = \frac{1}{Re\,\sin\theta}\left[(w\,\sin\theta)_\theta - 2\,w\,\cos\theta + v_\phi\right]$$

$$\sigma_n = \lambda_{Re}\,(2\,u\,\sin\theta + (v\,\sin\theta)_\theta + w_\phi)$$

$$\lambda_{Re} = -\frac{2}{3Re}$$

$$\sigma_{11} = -kp + \frac{\sigma_n}{\sin}$$

$$\sigma_{22} = -kp + \frac{2}{Re}(v_\theta + u) + \frac{\sigma_n}{\sin\theta}$$

$$\sigma_{33} = -kp + \frac{2}{Re\,\sin\theta}(w_\phi + u\,\sin + v\,\cos\theta)$$

$$\qquad\qquad + \frac{\sigma_n}{\sin\theta}$$

312

The heat transfer terms are defined as follows:

$$\dot{q}_\theta = - \frac{1}{2RePr} \frac{\partial T}{\partial \theta} \qquad \dot{q}_\phi = - \frac{1}{2RePr} \frac{\partial T}{\partial \phi}$$

where $\quad Pr = \dfrac{\mu C_p}{K}$

The equation set utilized in the calculation then contains no derivative terms with respect to r (conical symmetry assumption) and has no explicit dependence on the r dimension except as appears implicitly in the Reynolds number.

3. THE NUMERICAL METHOD

The utility of MacCormack's[5] finite difference scheme for the solution of inviscid supersonic flows has been demonstrated in numerous studies[6-9]. More recent studies have also shown it to give excellent results for two-dimensional viscous flows with separation.[10-12] This scheme is applied in the manner set forth in[6], so no detailed development will be given here. The resulting MacCormack predictor and corrector steps for equation (2) are as follows:

$$\text{Predictor} \quad \tilde{D}_{j,k}^{i+1} = D_{j,k}^i - \frac{\Delta t}{\Delta \theta}(F_{j+1,k}^i - F_{j,k}^i) \tag{5}$$

$$- \frac{\Delta t}{\Delta \phi}(G_{j,k+1}^i - G_{j,k}^i) - \Delta t\, H_{j,k}'$$

$$\text{Corrector} \quad D_{j,k}^{i+1} = \frac{1}{2}\left[\tilde{D}_{j,k}^i + \tilde{D}_{j,k}^{i+1} - \frac{\Delta t}{\Delta \theta}(\tilde{F}_{j,k}^{i+1} - \tilde{F}_{j-1,k}^{i+1}) \right.$$

$$\left. - \frac{\Delta t}{\Delta \phi}(\tilde{G}_{j,k}^{i+1} - \tilde{G}_{j,k-1}^{i+1}) - \Delta t\, \tilde{H}_{j,k}'^{i+1} \right]$$

where $\sim$ indicates that the flow quantities are evaluated at the predictor level and $D_{j,k}^i$ implies $D(i\Delta t, j\Delta\theta, k\Delta\phi)$. The conservation law form of the equations requires first derivatives of the flow quantities at each mesh point in the computational domain in order to form the stress terms. These derivatives are obtained in two ways, depending on whether their direction agrees with the direction of the exterior derivative. If their direction agrees, one sided first differences opposite to the direction of the exterior differences are used at each mesh point. If not, central first differences are used. This results in no increase

in the number of mesh points needed over the inviscid solution (except for "corner" points) and gives standard central second differences for the second derivatives when combined into the Lax Wendroff form.

A complete stability analysis for MacCormack's method as applied to the Navier-Stokes equations has not been accomplished. However, useful estimates of allowable step sizes can be made through the use of linear theory and physical arguments. Claiming that the physical propagation of information cannot outstrip the numerical propagation of information cannot outstrip the numerical propagation results in the following Courant-Friedrich-Lewy (C.F.L.) condition[13]:

$$\Delta t_{cfl} \leq \left(\frac{1}{\frac{|v|}{\Delta\theta} + \frac{|w|}{\Delta\phi} + c \frac{(\Delta\theta^2 + \Delta\phi^2)^{\frac{1}{2}}}{\Delta\theta\Delta\phi}} \right)$$

where

$$c = (\frac{\gamma k p}{\rho})^{\frac{1}{2}}$$

The present study did not make continuous use of the CFL limit to control the time step size. Instead, the time step size for each run was frozen at a value which would insure no difficulty with the stability limit due to the use of normal stress damping (described in section 5). Based on experience gained in the study it can be stated that the time step should be:

$$\Delta t = m \, Min(\Delta t_{cfl}, \, \Delta t_{nsd}, \, \Delta t_{visc})$$

where $M \leq 1$

$$\Delta t_{nsd} = Min \left(\frac{\rho Re \, \Delta\theta^2}{2 \lceil \beta(2 + \frac{\lambda}{\mu}) \rceil} \right)$$

$$t_{visc} = Min \left(\frac{\Delta\theta^2 \, (\rho Re \, Pr)}{2\gamma} \right)$$

The portion of this analysis due to the stress terms is similar to that in Reference 14. In the present study $\Delta\theta << \Delta\phi$. The viscous effects on stability are therefore primarily determined by the θ step size. In case $\Delta\theta \simeq \Delta\phi$, more terms must be checked to insure stability. The validity of the analysis must then also be determined for non-split operators.

4.   THE SOLUTION TECHNIQUE

A body fixed coordinate system, with the origin at the cone apex (Figure 1) was used for the calculation. A finite difference mesh is

314

impressed on the (θ,ϕ) spherical surface at a distance r from the cone apex. It is on this surface that the calculation takes place, with viscous effects scaled by the Reynolds number based on the radius of the surface from the cone apex. Viscosity is obtained by Sutherland's formula. Mesh spacing on the surface was even for all runs. Lateral symmetry was used to reduce the extent of calculation to 180° of the surface in the ϕ direction.

The finite difference mesh was initialized with free stream values of the flow quantities at all points except for the body surface. Velocities there are set identically to zero and temperature is set to the experimentally determined value. Pressure at the surface is determined by evaluating the θ momentum equation at the body surface conditions and then substituting second order accurate one-sided finite differences into the result. This is then used to update pressure and (through use of the equation of state) density after both the predictor and the corrector steps of the integration. An ellipse, outboard of the anticipated bow shock location, is also impressed on the mesh to use as a cutoff for the calculation in the free stream region. The numerical integration then taked place in time with the steady state solution resulting after transients disappear from the flow field.

The convergence criteria, used to determine when the steady state was reached, measured differences of pressure, density, velocity and energy between time steps and stopped the calculation when these differences reached the fifth significant figure for all points in the flow field. Although this criteria is severe, previous experience by the author with inviscid conical flows revealed that instabilities can arise in the calculation even after changes in the flow field pressure become small as seen on a plotter or CRT display device. This criteria gave run times nearly twice as long as would have been necessary to obtain engineering values of surface pressure and should therefore remove possible doubts concerning the stability of the solutions obtained.

The outer boundary condition for the integration is the far field free stream. The bow shock wave was therefore captured which is allowed through use of conservation form of the governing equations. However,

315

at high angle of attack and Mach number, the bow shock strength becomes
such that the numerically-produced undamped oscillations at the shock
discontinuity will cause negative temperatures in the upstream flow with
subsequent solution instability. This instability occurs at a Mach number
normal to the shock wave of approximately three with dependence on mesh
size and Reynolds number. This value has been confirmed by Petty[15]
as well as in the present study. In order to overcome this difficulty,
a technique of numerical damping using the normal stress terms in the
governing equations was developed. This technique is described in the
following section.

5.   NORMAL STRESS DAMPING

Previous studies[6,7] using shock capturing finite difference tech-
niques have encountered oscillations in the vicinity of strong shock
waves which can cause solution instabilities. To overcome this difficulty,
artificial terms have been added to the governing equations to provide
necessary damping. In the present study, using the viscous equations
and shock capturing, oscillations were again encountered. This indicated
that the natural viscous terms are inadequate to overcome the series
truncation error at the existing mesh spacing. To damp these oscillations
without additional programming complexity, the normal stress terms (which
are in general large only near shock waves) were altered by increasing
the second coefficient of viscosity $(\lambda \geq - 2/3\mu)$. This resulted in elimin-
ation or reduction of the oscillations where desired. In addition to
improving the shock structure, it was found that normal stress damping
was extremely effective in removing instabilities caused by starting
transients which result from ill-suited initial conditions. The details
of implementation and conditions for proper use of this technique are
given below.

As shown in equation (4), the normal stress terms contain:

$$\sigma_n = \lambda_{Re}(\nabla \cdot \vec{V}) = - \frac{2}{3Re} \, (2u \sin\theta + (v\sin\theta)_\theta + w_\phi)$$

Normal stress damping results when $2u \sin\theta$ is removed and the
remainder of the term is multiplied by a factor β, where β is negative
(i.e. $\beta\sigma_n$). (A positive β does not produce the damping effect and makes

316

the calculation unstable except near one). The damping terms occur both in the energy equation and in the $\vec{H}'$ matrix resulting from the coordinate transformation. It was found that the most accurate solutions resulted from use of the damping multiplier in the derivative term only ($\vec{F}_\theta$ or $\vec{G}_\phi$) of the momentum equation most nearly normal to the shock wave for which damping is desired. Inclusion of the multiplier in the $\vec{H}'$ matrix or the energy equation produced some displacement of the solution. Also, it should be noted that in the steady limit,

$$\sigma_n = f\ (\nabla \cdot \vec{V}) = f\ (\vec{V} \cdot \frac{\nabla \rho}{\rho})$$

(through use of the continuity equation). This implies that normal stress damping cannot be used in the vicinity of compressible flow boundary layers without regard for possible changes in the density gradients.

In the present study, the damping multiplier (β) was unity over the lee 40° ($\phi = 140^\circ - 180^\circ$) of the flow, where viscous effects predominate. It was then varied smoothly around the cone from $\phi = 140^\circ$ in accord with the equation:

$$\beta\big|_\phi = 1 - \beta' \left[\frac{P_s\big|\phi - P_s\big|\phi = 140^\circ}{P_s\big|\phi = 0^\circ - P_s\big|\phi = 140^\circ} \right]^{\frac{1}{2}}$$

where s indicates body surface values and β' varied from 15 ($\alpha = 8^\circ$) to 130 ($\alpha = 24^\circ$). β was constant in the θ direction.

An example of the use of normal stress damping is given in Figure 2 for axisymmetric cone flow. The plot is a comparison of the computed static pressure in the θ direction with and without the inclusion of normal stress damping. In this case the damping is tailored in the θ direction by:

$$\beta = 1 - (\frac{P_s}{P_\infty})\ A1 - (\frac{P}{P_\infty})\ A2$$

where A1 = 9, A2 = 2. Although a small offset in pressure occurs outside the boundary layer, the surface pressure and shock position do not change appreciably when damping is applied.

Since shock wave discontinuities should ideally be fitted for greatest accuracy, the most recommended use for normal stress damping is controlling time like transients which cause calculation instabilities, especially in regions of strong expansion of the flow. In a cone flow

317

solution completed (but not included here) at the conditions M = 14.2,
$\theta c = 5.6^O$, $\alpha = 10^O$, $Re_x = .59 \times 10^6$, instabilities were encountered during
initial starting in the lee side expansion region which could not be
overcome until normal stress damping was used. Once the initial transients
were damped out, the normal stress damping was removed on the lee side
and the solution proceeded to convergence. The same type of difficulty
was encountered in a laser diffuser study[18]. Once normal stress damping
was used, the solution was started successfully and proceeded to
convergence.

6.   NUMERICAL RESULTS

A previous standard of comparison for calculations of laminar
viscous cone flows has been the experimental study of Tracy[10]. This
study was performed using a 10° half angle sharp cone in nominally
M = 8 flow. Data were presented at angles of attack from 0° to 24° at
4° intervals, with $Re_x = 0.4 \times 10^5$ and $Tw/T_{t_\infty} = 0.04$.

Solutions at Tracy's conditions, using implicit finite difference
techniques, have been obtained for the $\alpha = 12^O$ case by Lubard and
Helliwell[20] and for cases including $\alpha = 20^O$ by Lin and Rubin[21,22].
The present study has demonstrated converged solutions for angles of
attack of 0°, 8°, 12°, 20°, 24°. These solutions are presented and
compared with both the experimental data and previous available solutions.

Figures 3 through 6 show the surface pressure distributions of
Tracy compared with the results of the present study. The agreement is
generally good except near the windward centerline in the three higher
angles of attack. This discrepancy is attributed to an approximate 0.5^O
uncertainty in true angle of attack as noted by Tracy and to possible
surface pressure tap effects where the boundary layer is very thin in
relation to the tap diameter. The $\alpha = 20^O$ solution was reconverged at
$\alpha = 20.5^O$ to test the first possibility. The surface pressure at the
windward centerline regained only half of the 4.7% difference between
the experimental value and the $\alpha = 20^O$ solution. The windward centerline
surface pressure for the $\alpha = 12^O$ case obtained by Lubard and Helliwell
is essentially the same as that obtained in the present study.

Sample circumferential pitot surveys are presented in Figures 7
through 9. The angle in the θ direction for comparison with experiment
is defined by

$$\theta = \theta c + \text{Tan}^{-1} \left(\frac{Y}{3.45''}\right)$$

where Y is the normal distance to the cone surface in inches. Agreement
of the calculated values with experimental data is good except in the
vicinity of the captured shock and in a small region near the lee center-
line. Since the pitot surveys were made at constant height above the cone
surface, they will in most cases intersect the bow shock at some point
in the circumferential traverse. This appears in the plots as a sharp
rise from the free stream value (8.7×10^{-3}) to the maximum value for each
trace. Probe effects cause the character of this rise to appear remarkably
like that of the captured shock waves obtained in the present study, with
decrease in transition slope and loss of peak pressure caused by the
necessary damping present in the calculations. Note that the pitot pressure
transition centerpoint (the shock location criteria used by Tracy) of the
captured shock is virtually the same as would be determined from the
experimental pitot survey and that the pitot pressure quickly returns to
the proper magnitude on the high pressure side of the shock. The pitot
pressure discrepancy near the lee centerline can be evaluated more clearly
from Figure 10, which compares pitot pressure on the lee centerline for
the $\alpha = 24^{\circ}$ case. The discrepancy extends for approximately 6° to 7°
to either side of the lee centerline for this case. It is attributed to a
combination of the locally large pitot pressure drop due to finite model
nose radius and to nose effects resulting from the non-conical merged layer
region. Any persistent experimental nose effects would tend to be con-
centrated along the lee centerline as they are swept back along the cone.

To demonstrate the pressure distribution obtained through the shock
layer, Figure 11 shows static pressure in the θ direction at 60° intervals
around the cone for the $\alpha = 12^{\circ}$ case. The elevation above the cone sur-
face is given in radians in this and subsequent computer generated plots.
As noted in Section 5, the damping was not tailored in the θ direction
for these runs, so excess smearing of the shock is evident on the free
stream side. No appreciable harm is seen to result from this smearing.

319

The velocity vector plots in Figures 12 through 14 provide an indication of cross-flow streamline patterns and illustrate the relative magnitude of cross-flow velocity for all but the lowest momentum regions. The reverse flow region is thin in the $\alpha = 12^{\circ}$ case (Figure 12) with the vortical singularity (defined for this study as the cross flow stagnation point toward which streamlines converge) occurring near the edge of the viscous layer 3.2° above the cone surface. The cross-flow separation point is 17° from the lee centerline with the experimental point occurring at 24°. This difference is attributable to lack of resolution of the reverse flow region at this   in the present study, as both Lin and Rubin and Lubard and Helliwell obtained a value nearer that of experiment. This was supported in the present study by the fact that the separation points in the higher   runs (with more mesh points in the reverse flow regions) were virtually identical to those of experiment.

At $\alpha = 20^{\circ}$ (Figure 13) the extent of the reverse flow region and the position of the cross-flow separation point have reached limiting values, as no substantial changes in these can be seen in the $\alpha = 24^{\circ}$ run (Figure 14). This was noted for the separation point in both experiment and theory by Lin and Rubin[22]. However, the extent of the viscous region and the location of the vortical singularity continue to change as α increases. The vortical singularity is near the edge of the viscous layer for all cases in the present study in which it is lifted off.

Although agreement with experiment so far has been shown to be good, perhaps the best evaluation of the validity of the conical flow assumption for engineering solutions can be made through a pictorial representation of the flow field features. Figures 15 and 16 compare the overall results of the present study with the calculation of Lubard and Helliwell and Tracy's data. As shown in Figure 15, the position of the bow shock and viscous layer edge of the present study for this case are essentially those obtained by Lubard and Helliwell. Both studies tend to underestimate shock and viscous layer position at this   when compared with experiment. This is considered to be primarily due to the failure to account for nose tip effects as noted above. A weak supersonic region is present in the cross flow plane and is shown by the solid lines between viscous layer and bow shock. The vortical singularity position

320

is shown by the open oval symbol on the lee centerline. The structure of the $\alpha = 24^{\circ}$ case is more interesting (Figure 16). Supersonic cross flow is seen to exist over most of the field and is terminated by a complex sonic line/shock wave. The position of this line is nearer the lee centerline than shown by Tracy. The small amplitude oscillations present on the imbedded sonic line/shock as it nears the bow showk can be seen (through careful examination of Figure 14) to be caused by oscillations in velocity propagating through the supersonic cross flow region from the vicinity of the bow shock. The present study did not have sufficient resolution to determine the existence of the lambda portion of the imbedded shock, as shown by Tracy. However, its signature may be surmised in the hump present near $\phi = 150^{\circ}$ in the calculated viscous layer. The curious flat top present in the calculated viscous layer as compared to experiment is again attributed to the failure of the numerics to model non-conical nose effects.

In summary, the calculation is seen to model all features present in the experimental study, with the exception of the non-conical nose effects. The computer times are not excessive, ranging from 1.4 hours for the $\alpha = 12^{\circ}$ case to 1.6 hours for the $\alpha = 24^{\circ}$ on the CDC 6600. These times are based on a very stringent convergence criteria and represent an increase in time per mesh point calculated of only 40% over a comparable inviscid computer program.

7. CONCLUSIONS

Explicit finite difference solutions have been demonstrated for supersonic viscous cone flow at moderate and high angles of attack. These points are presented concerning the utility of the present technique:

(a) Agreement with experiment is generally quite good. Solution of the Navier-Stokes equations subject to the conical symmetry assumption is shown to model all features present in the experimental flow, with the exception of nose effects.

(b) Inviscid cone flow calculations at angles of attack greater than twice the cone half angle have proven to be unstable near the point where the high strength imbedded lee side shock waves reach the cone surface. The present technique does not exhibit that limitation, as the imbedded shock wave is physically modeled near the surface.

321

(c) Normal stress damping is shown to provide a physically based means to control spurious oscillations around shock waves without additional computer time. It is also very effective for control of starting transients due to ill-suited initial conditions.

The present technique, considering the good agreement with experiment and the removal of angle of attack limitations, provides a viable alternative to the use of the inviscid equations for the calculation of conical flows. A solution of this type could also be used to provide an accurate initial surface for space marching techniques.

8. ACKNOWLEDGEMENTS

The author gratefully acknowledges the advice and support of Dr. Wilbur L. Hankey and Dr. Milton E. Franke during the accomplishment of this work and also wishes to thank Dr. D.A. Anderson for many hours of fruitful discussion.

9. REFERENCES

[1] Cross, E.J., Jr., "Experimental and Analytical Investigation of the Expansion Flow Field Over a Delta Wing at Hypersonic Speeds," ARL 68-0027, 1968, Aerospace Research Laboratories, Wright-Patterson AFB, Ohio, Feb. 1968.

[2] Stetson, K.F., "Experimental Results of Laminar Boundary Layer Separation on a Slender Cone at Angle of Attack at $M_\infty = 14.2$," ARL 71-0127, Aerospace Research Laboratories, Wright-Patterson AFB, Ohio, Aug. 1971.

[3] Feldhuhn, R.E., "An Experimental Investigation of the Flowfield Around a Yawed Cone," AIAA Journal, Vol. 9, No. 6, June 1971, pp. 1074-1081.

[4] Anderson, D.A., "Comments on Numerical Solution of the Axial Corner Flow Problem for Laminar Flow," private communication.

[5] MacCormack, R.W., "The Effect of Viscosity in Hypervelocity Impact Cratering," AIAA 69-354, 1969, pp. 1-7.

[6] Kutler, P. and Lomax, H., "A Systematic Development of the Supersonic Flow Fields over and behind Wings and Wing-Body Configurations Using a Shock Capturing Finite Difference Approach," AIAA 71-99, 1971.

[7] Kutler, P., Reinhardt, W.A., and Warming, R.F., "Numerical Computation of Multi-shocked Three-Dimensional Flow Fields with Real Gas Effects," AIAA 72-702, 1972.

[8] Kutler, P., Warming, R.F., and Lomax, H., "Computation of Space
Shuttle Flowfields Using Noncentered Finite Difference Schemes,"
AIAA Journal, Vol. 11, No. 2, Feb. 1973, pp. 196-204.

[9] Kutler, P., "Numerical Solution for the Inviscid Supersonic Flow
in the Corner Formed by Two Intersecting Wedges," AIAA 73-677, 1973.

[10] Deiwert, G.S., "Numerical Simulation of High Reynolds Number
Transonic Flows," AIAA 74-603, 1974.

[11] Shang, J.S. and Hankey, W.L., Jr., "Numerical Solution of the Navier-
Stokes Equations for Supersonic Turbulent Flow over a Compression
Ramp," AIAA 75-4, 1975.

[12] Hung, C.M. and MacCormack, R.W., "Numerical Solutions of Supersonic
and Hypersonic Laminar Flows Over a Two Dimensional Compression
Corner," AIAA 75-2, 1975.

[13] MacCormack, R.W., "Numerical Solutions of the Interaction of a
Shock Wave with a Laminar Boundary Layer" Lecture Notes in Physics,
Vol. 8, Springer-Verlag, New York, 1971, p. 151.

[14] MacCormack, R.W. and Baldwin, B.S., "A Numerical Method for Solving
the Navier-Stokes Equations with Applications to Shock-Boundary
Layer Applications," AIAA 75-1, 1975.

[15] Petty, J.S., private communication.

[16] Baldwin, B.S. and MacCormack, R.W., "Numerical Solution of the Time
Dependent Compressible Navier-Stokes Equations in Inlet Regions,"
AIAA 74-558, 1974.

[17] Kutler, P., Sakell, L., and Aiello, G., "On the Shock-On-Shock Inter-
action Problem," AIAA 74-524, 1974.

[18] Knight, D.D. and Hankey, W.L., "Numerical Simulation of Nonchemically
Reacting Radial Supersonic Diffusion Laser," AIAA 76-60, AIAA
14th Aerospace Sciences Meeting, Washington, D.C., January 26-28, 1976.

[19] Tracy, R.R., "Hypersonic Flow over a Yawed Circular Cone," GALCIT
Memo No. 69, Graduate Aeronautical Laboratories, California Institute
of Technology, Pasadena, California, 1963.

[20] Lubard, S.C. and Helliwell, W.S., "Calculation of the Flow on a Cone
at High Angle of Attack," AIAA 73-636, 1973.

[21] Lin, T.C. and Rubin, S.G., "Viscous Flow over a Cone at Moderate
Incidence - 1 Hypersonic Tip Region," Computers and Fluids, Vol. 1,
pp. 37-57, 1973.

[22] Lin, T.C. and Rubin, S.G., "Viscous Flow over a Cone at Moderate
Incidence, Part 2, Supersonic Boundary Layer," Journal of Fluid
Mechanics, Vol. 69, part 3, pp. 593-620, 1973.
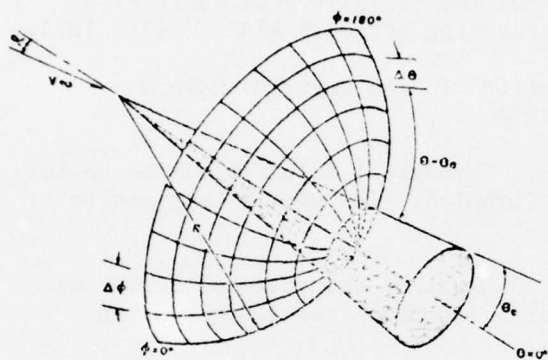
Figure 1. Finite Difference Mesh.
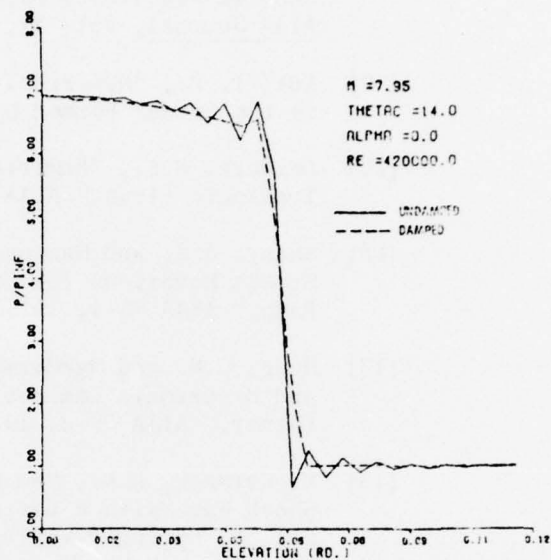
Figure 2. Static Pressure in θ Direction, Axisymmetric Flow.
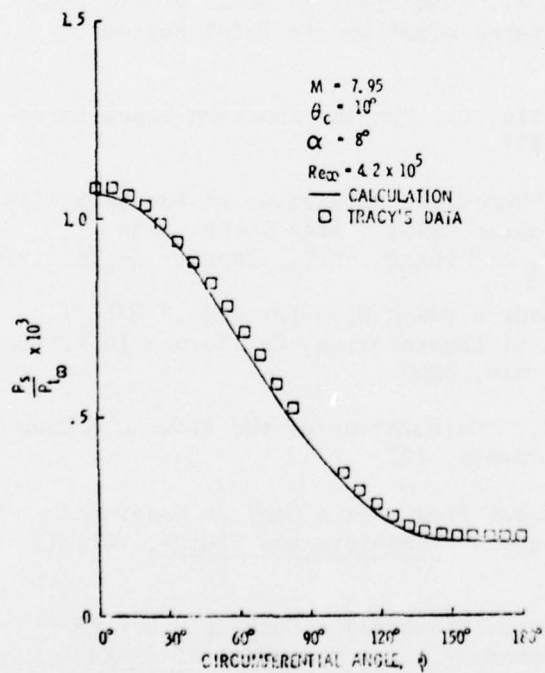
Figure 3. Surface Pressure Distribution at α = 8°.
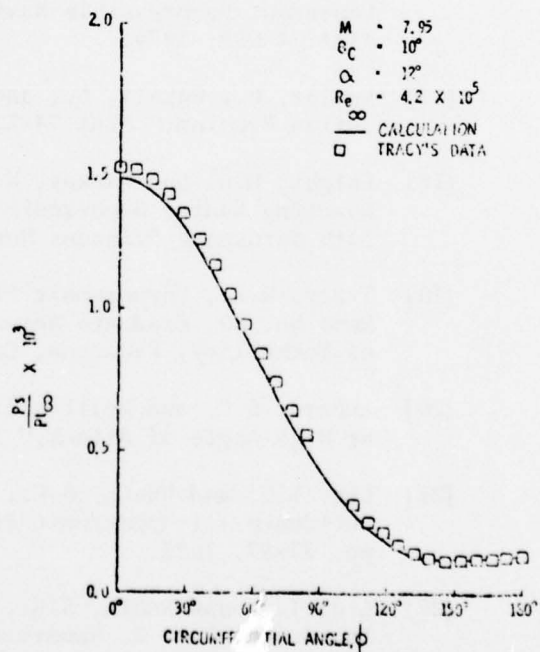
Figure 4. Surface Pressure Distribution at α = 12°.

324
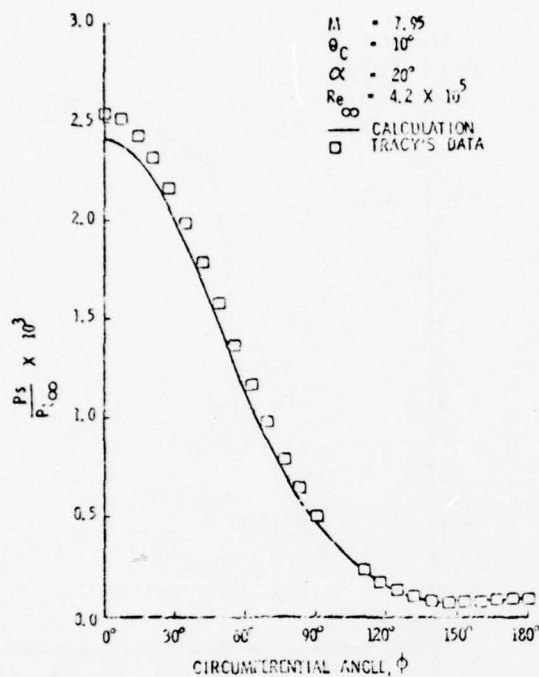
Figure 5. Surface Pressure Distribution at $\alpha = 20°$.
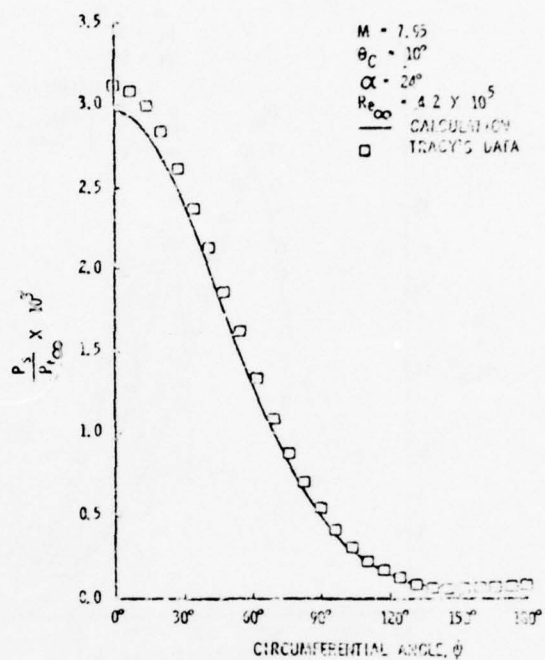
Figure 6. Surface Pressure Distribution at $\alpha = 24°$.
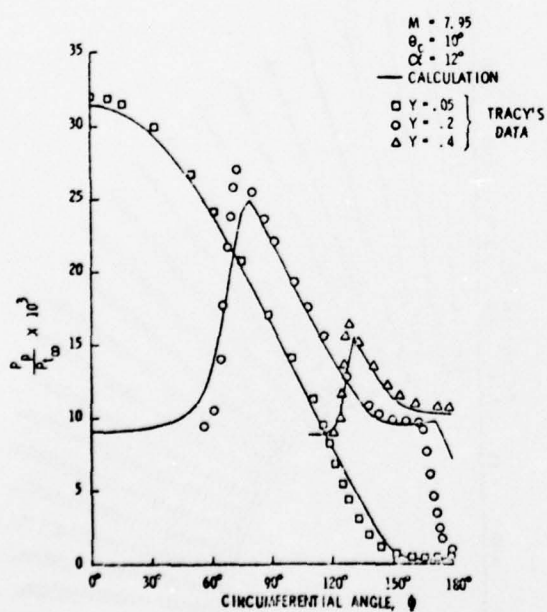
Figure 7. Pitot Pressure Surveys, $\alpha = 12°$.
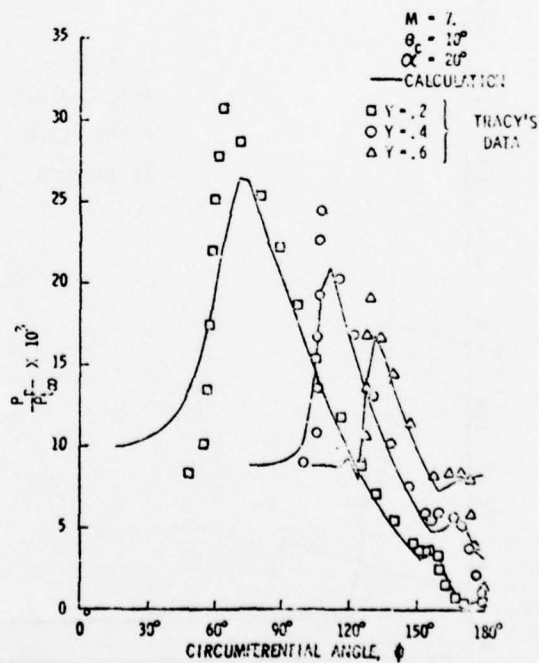
Figure 8. Pitot Pressure Surveys, $\alpha = 20°$.
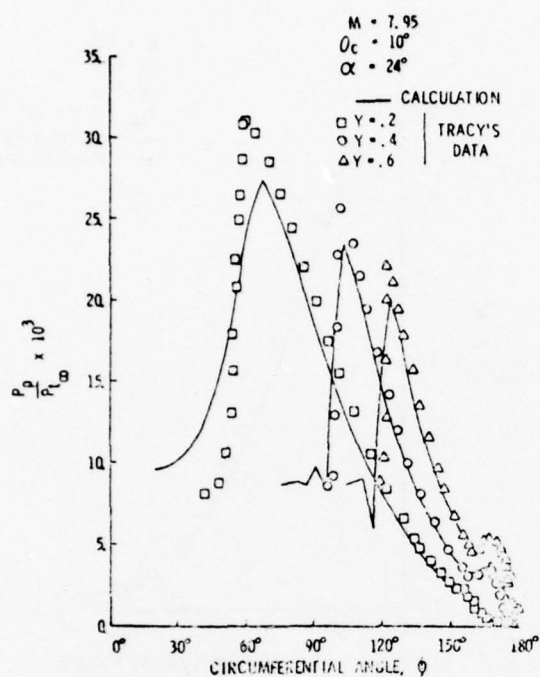
Figure 9. Pitot Pressure Surveys, $\alpha = 24^{\circ}$.
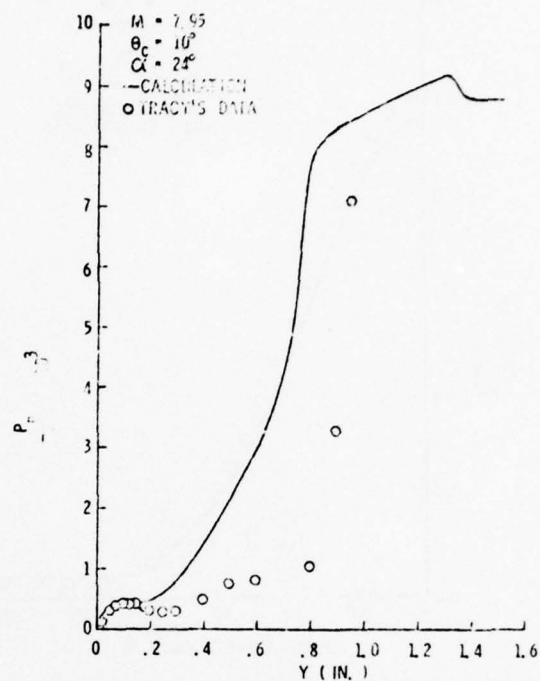
Figure 10. Pitot Pressure Along Lee Centerline, $\alpha = 24^{\circ}$.
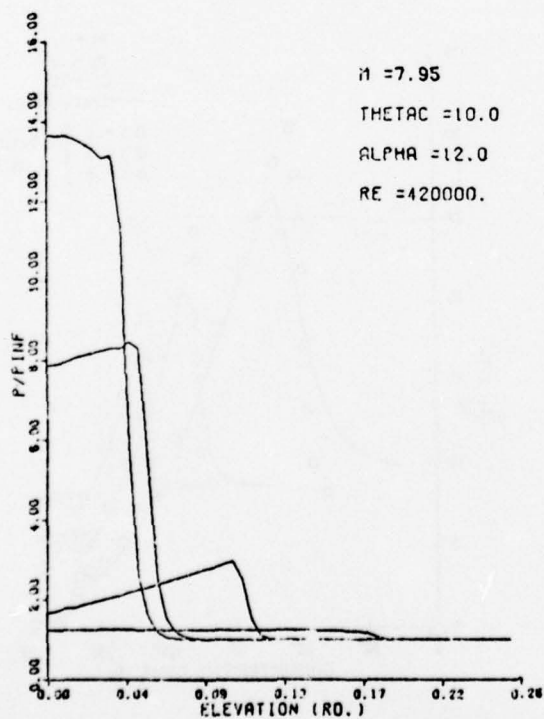
Figure 11. Static Pressure Distributions at 60° Circumferential Intervals
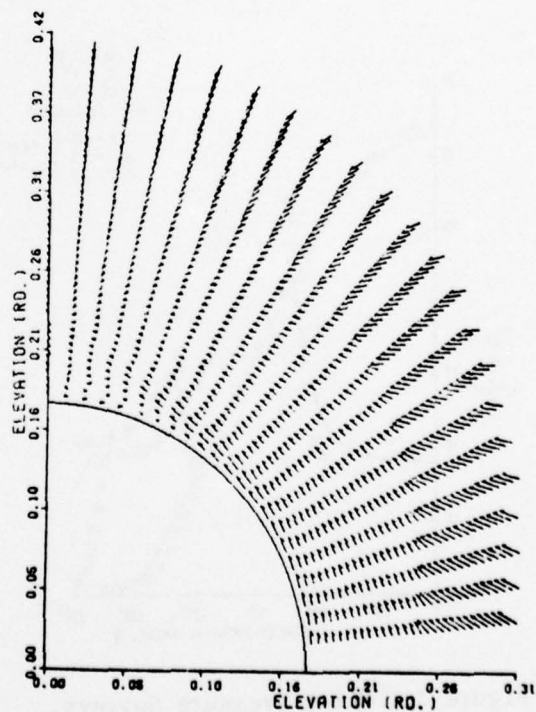
Figure 12. Velocity Vector Plot, $\alpha = 12^{\circ}$.

326
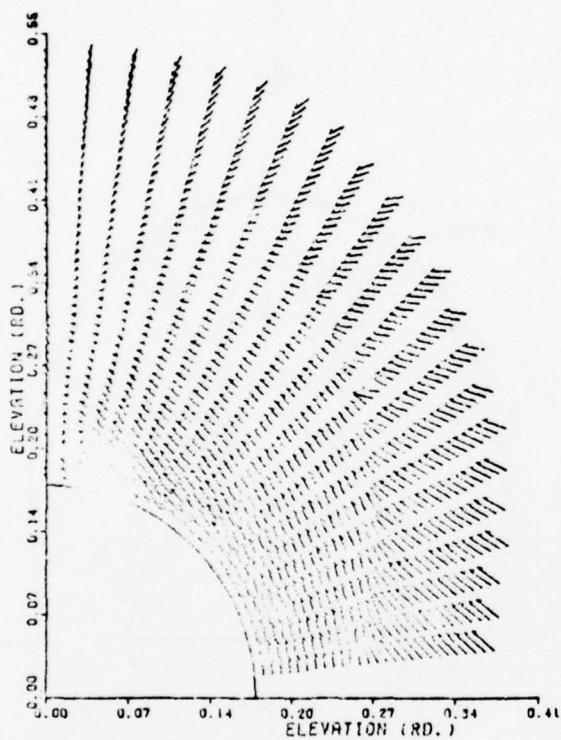
Figure 13. Velocity Vector Plot,
$\alpha = 20^{o}$.
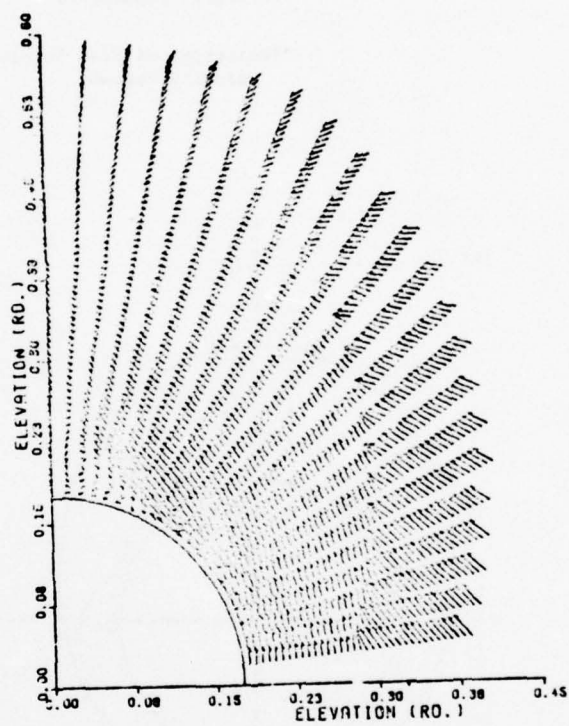
Figure 14. Velocity Vector Plot,
$\alpha = 24^{o}$.

$M = 7.95, \theta_c = 10^\circ$

	Tracy	Lubard, Helliwell	Present Calculation
Re	3.6×10^5		4.2×10^5
Shock, Sonic Lines	●	○	——
Viscous Layer	◇	◇	— — —
Separation	▲		∧
Vortical Singularity			◊
Projection of Free Stream Velocity Vector			⊕

$\alpha = 12^\circ$

$\alpha = 24^\circ$
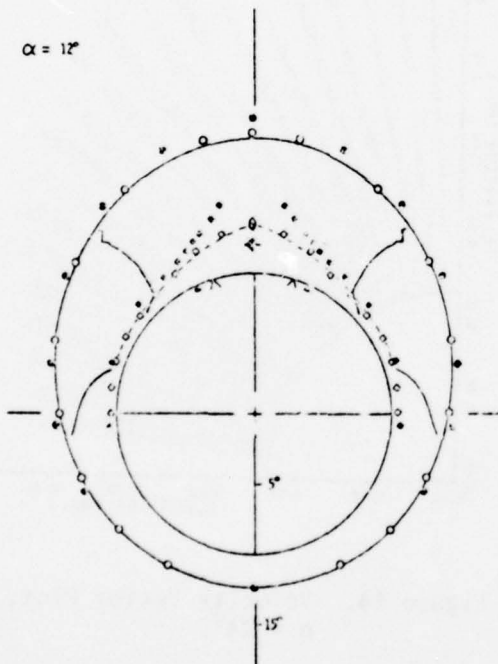
Figure 15. Comparative Features of the Cross Flow Field, $\alpha = 12^\circ$.
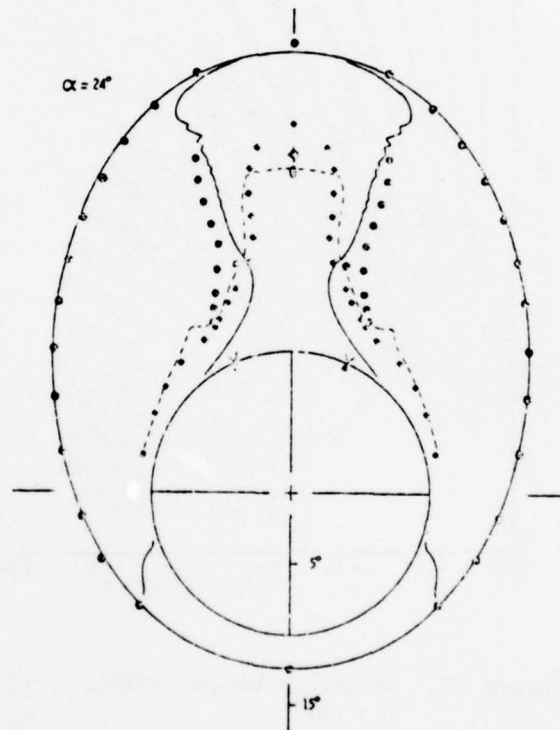
Figure 16. Comparative Features of the Cross Flow Field, $\alpha = 24^\circ$.

NUMERICAL STUDY OF SUPERSONIC TURBULENT
INTERACTING BOUNDARY LAYERS*

by

A. Polak, M.J. Werle, and S.D. Bertke
University of Cincinnati, Cincinnati, Ohio

1.   INTRODUCTION

The problem of turbulent boundary layer separation continues to be a major element in the design of efficient aerodynamic systems. This report summarizes the results of an attempt to solve such a problem numerically. Specifically, the separation and reattachment of a supersonic turbulent boundary layer from a flat surface with the necessary adverse pressure gradient field induced by a two dimensional ramp-type compression surface or a sine-wave shaped protuberance is considered. The method applied to the solution of this problem is a direct extension of that developed by Werle and Vatsa (Ref. 1) for the laminar supersonic separation problem. This approach uses the familiar interacting boundary layer equations solved with a novel solution technique wherein a time-like relaxation method produces the sought after "steady-state" solution of the governing equations.

In the present investigation it was found that the numerical method of Werle and Vatsa (Ref. 1) could be adapted to the turbulent case and in the process made more efficient. However, the present numerical results were found to severely misrepresent experimental data. After careful comparison of the present results for flow over a compression

ramp with available numerical solutions to the Navier Stokes equations (Ref. 2) it is concluded that the interacting boundary layer model fails most probably because it does not account for the penetration of the separation shock deep into the viscous boundary layer.

2. METHOD OF SOLUTION

The basic approach is numerical in nature. It centers around the numerical solutions of the turbulent interacting boundary-layer equations. The method is essentially an implicit finite difference scheme written for the similarity form of the governing equations and marches from some initial station aft along the surface to the terminal point of interest. To account for the boundary value nature of the problem Werle and Vatsa (Ref. 1) have added the time dependent concept, similar to the one used for the solution of elliptic partial differential equations. The present extension of this approach to the turbulent boundary layers involves inclusion of an eddy viscosity model into the solution scheme. Two such models are considered, the equilibrium eddy viscosity model as delineated by Cebeci and Smith (Ref. 3) and the relaxation model as applied by Shang and Hankey (Ref. 2).

In an effort to develop an efficient and numerically stable scheme capable of handling flow fields of present interest a number of modifications to the numerical algorithm were made. Specifically, the following important steps have been taken.

a. The numerical stability and convergence rate of the algorithm has been enhanced by introducing a new difference representation in the continuity equation. It has only recently been recognized (Ref. 4) that the longitudinal derivatives in the continuity equation provide a path for interacting flows to propagate information upstream. To accommodate this numerically requires the use of some sort of a forward difference procedure.

b. The reliability of the present algorithm was enhanced by adopting the "upwind differencing" concept. In the reversed

flow region upwind differencing is used in the longitudinal
direction for the convective terms in order to satisfy the
stability requirements. This eliminates the so-called
"artificial convection" concept used earlier (Refs. 1 and 5).
This modification is significant because the velocities in
the reversed flow regions are larger in the turbulent case
than in the laminar. Furthermore, the upwind differencing
scheme was found helpful in the direction normal to the
surface in the convection dominated outer regions of the
boundary layer.

The calculation commences with certain initial conditions and then
through the time dependent approach (Ref. 1) the steady state solu-
tion for a given set of boundary conditions is sought. In the pre-
sent calculations the initial conditions were set by taking the
ramp angle, or the amplitude of the sine-wave protuberance to be
zero (a flat plate) in the first sweep. Subsequent time sweeps are
conducted with the ramp angle, or wave amplitude increased gradually
by a small amount. After the desired geometry is reached (after
the first 10-15 sweeps) the time-like relaxation process is continued
until the flow properties are relaxed to their final state.

3.   SUMMARY OF RESULTS

Examples from the calculated results are presented for supersonic
separated flows over a compression ramp and for flow over a sine-
wave protuberance. These geometries are sketched in Figure 1.

To obtain the current solutions in the separated region it is first
necessary to obtain initial conditions at some point ahead of the
ramp-plate or protuberance-plate junctures. These are obtained from
a laminar-transitional-fully turbulent calculation. Temperature and
velocity profiles and displacement surface derivatives are punched
onto data cards to serve as the initial input data for the separation
studies. Whenever comparisons are made with other calculation methods
and/or experimental data it is essential that these profiles be
practically the same.

3.1 Compression Ramp

The first example considered here serves also as a test case of this study of supersonic ramp induced separation. In this case initial flow profiles obtained at s = 0.9 were used to initialize a region of calculation extending from s = 0.9 to s = 1.2 with a longitudinal step-size of 0.006. There were 65 points distributed across the boundary layer in a geometrically expanding grid. A "sharp" version of the ramp was employed with ramp angle of 25° and ramp actually starting at s = 0.996.

To attain the ramp angle configuration of 25°, calculations were initialized at ramp angle of 0° and the time-like relaxation process continued with the ramp angle increased 3° after each pass through the mesh. Thus after 9 time iterations the configuration reached and held its final state and the fluid state continued to relax to its final state. This process is shown in Figure 2 when the surface pressure at the corner location is shown as a function of time iteration number. These calculations were performed with an equilibrium eddy viscosity model with the downstream boundary condition taken as the inviscid pressure level there. Note that once the ramp attains its final level (9 iterations) it takes approximately 50 more iterations for the pressure to attain its "steady state". Other flow properties relax more slowly and usually 60 iterations were needed after the configuration was frozen to attain a totally satisfactory "steady state" solution. These calculations, with a grid of 3,000 points were performed in less than five minutes of computer time on the IBM 376-168.

The resulting surface pressure distributions obtained from the present approach using an equilibrium eddy viscosity model are compared with experimental data (Ref. 6) and Navier Stokes solutions (Ref. 2) in Figure 3. The accompanying skin friction distributions are shown in Figure 4. The pertinent observation from these results is that both the interacting boundary layer and Navier Stokes solutions misrepresent the experimental data.

It has been reasoned by previous investigators of turbulent viscous interactions that the fault for this deficiency is to be found in the

eddy viscosity model itself. Shang and Hankey (Ref. 2) have found that the use of the so-called "relaxation eddy viscosity" concept provided nearly perfect alignment of the numerical Navier Stokes results and experimental data. The extreme case of this model is to simply use the "frozen" eddy viscosity concept whereby the eddy viscosity profile is held fixed downstream from a point ahead of the strongly interacting region. Results from the use of this model are shown in Figures 5 and 6 for both the present method and the Navier Stokes solution of Ref. 2. It is clearly seen that while the Navier Stokes codes show a sensitivity to this concept the interacting boundary layer method does not.

After careful scrutiny of all the aspects of the numerical results it was found that the principle difference in the two results seemed completely isolated in the embedded shock wave structure observed in the Navier Stokes calculations. The present version of the interacting boundary layer concept does not allow for any penetration of the shock into the viscous region with all the flow compression taking place at the outer edge of the boundary layer only. It appears that the next stage of development for the interacting boundary layer model must involve inclusion of a shock wave like structure into the viscous flow region solution.

3.2 Sine-Wave Protuberance

An attempt is currently being made to extend an earlier study (Ref. 7) of laminar separated boundary layers over two-dimensional protuberances to the turbulent regime. The main interest in this study is focused on very thick separated turbulent boundary layers. In such a case the protuberance is buried deeply in the boundary layer and the flow disturbance at the boundary layer edge is smaller than in the case of thin boundary layers. Separation shocks, if they occur will be much weaker, hence the difficulty mentioned earlier for sharp corner ramps is not expected to arise. However, a new problem not yet resolved has emerged. This has to do with a very slow convergence rate of the time-like relaxation solution method. For moderately thick turbulent boundary layers a "steady state" solution is obtained in about 60

time iterations (five minutes of computer time). For the identical
free stream conditions but very thick boundary layer the computer
time level is unacceptable at the present (about 240 iterations are
required, or 20 minutes of CPU time).

Two case studies, one for a relatively thin (δ = 0.01, δ/h = 0.33)
and the second for a very thick separated turbulent boundary layer
(δ = 0.187, δ/h = 3.1) are presented. In both cases the free stream
flow conditions correspond to a set of NASA test data (Ref. 8). The
free stream Mach number and static temperature are 2.5 and T_∞ = 252°R
respectively. The Reynolds number based on free stream conditions and
a reference length L^* = 15.25 cm is Re_∞ = 1.647 x 10^6. The sine-wave
protuberance profile is given by $y = \frac{h}{2}\{1 - \cos[\frac{2\pi}{w}(x - x_o)]\}$, where he
is the height and w is the width of the protuberance. In both case
studies w = 0.24. Calculations were performed with T_w/T_o = 0.81, Pr =
0.72, and Pr_T = 0.9 and an equilibrium eddy viscosity model.

For the first example an initial profile was produced from a flat
plate laminar-transitional-turbulent calculation at the station x =
3.0, with 41 normal grid points distributed according to a geometrical
progression. Subsequently, with this profile a calculation for a sine-
wave placed between x = 3.55 and x = 3.79, with h = 0.03 was made. In
the longitudinal direction 71 grid points were taken with a stepsize
Δs = 0.02. The full height of the protuberance was achieved gradually
after 11 time iterations. Figure 7 shows that, as in case of the
compression ramp, the fluid state relaxes to a final state in about
60 iterations. The resulting skin friction distribution is shown in
Figure 8. A separation bubble appears at the forward junction of the
plate and protuberance.

For the second case of the thick separated turbulent boundary layer the
initial profile was obtained from a noninteracting calculation to
correspond to the boundary layer as it develops along the wall of the
UPWT Langley Tunnel. The location of the initial profile is at s = 72.96
with the corresponding displacement thickness of 2.8 cm. The ADI
algorithm was subsequently employed between this station and s = 74.56
using 81 grid points in the s direction (Δs = 0.02) with 53 point
variable mesh in the normal direction. Figure 9 shows the slow

334

eddy viscosity model itself. Shang and Hankey (Ref. 2) have found that the use of the so-called "relaxation eddy viscosity" concept provided nearly perfect alignment of the numerical Navier Stokes results and experimental data. The extreme case of this model is to simply use the "frozen" eddy viscosity concept whereby the eddy viscosity profile is held fixed downstream from a point ahead of the strongly interacting region. Results from the use of this model are shown in Figures 5 and 6 for both the present method and the Navier Stokes solution of Ref. 2. It is clearly seen that while the Navier Stokes codes show a sensitivity to this concept the interacting boundary layer method does not.

After careful scrutiny of all the aspects of the numerical results it was found that the principle difference in the two results seemed completely isolated in the embedded shock wave structure observed in the Navier Stokes calculations. The present version of the interacting boundary layer concept does not allow for any penetration of the shock into the viscous region with all the flow compression taking place at the outer edge of the boundary layer only. It appears that the next stage of development for the interacting boundary layer model must involve inclusion of a shock wave like structure into the viscous flow region solution.

3.2 Sine-Wave Protuberance

An attempt is currently being made to extend an earlier study (Ref. 7) of laminar separated boundary layers over two-dimensional protuberances to the turbulent regime. The main interest in this study is focused on very thick separated turbulent boundary layers. In such a case the protuberance is buried deeply in the boundary layer and the flow disturbance at the boundary layer edge is smaller than in the case of thin boundary layers. Separation shocks, if they occur will be much weaker, hence the difficulty mentioned earlier for sharp corner ramps is not expected to arise. However, a new problem not yet resolved has emerged. This has to do with a very slow convergence rate of the time-like relaxation solution method. For moderately thick turbulent boundary layers a "steady state" solution is obtained in about 60

333

convergence rate for the skin friction at s = 73.44. When compared
to the previous case this represents a fourfold increase in computer
time for the same number of mesh points. The skin friction distribu-
tion for this case is shown in Figure 10. It is seen that ahead of
the protuberance the skin friction drops and a small separation region
develops on the front face of the wave.

Experimental data for identical flow conditions with a train of
waves are available (Ref. 8). A corresponding calculation for a
train of waves can in principle be accomplished at this time, but
would require a substantial increase in the number of grid points,
thus in computer time. Therefore, the detailed comparison with these
data are postponed until the improvement in the convergence rate
is achieved.

4.   CONCLUSIONS AND RECOMMENDATIONS

The capability of the numerical method to handle turbulent separated
flows was demonstrated. While this method is efficient it appears
that for the ramp induced separation problem the interaction model
must be adjusted to accommodate the phenomenon of shock wave penetra-
tion into the boundary layer. This aspect of the separation process
was apparently not important in the laminar flow problem (Ref. 1)
because of the relatively weak shocks occurring there. Neither is
this issue believed to be dominant for flow of thick turbulent boundary
layers over protuberances such as considered here. However, before
the method can be considered operational for handling flow fields over
a train of protuberances typical of present interest, the convergence
rate of the time-like relaxation method must be increased.

REFERENCES

1.   Werle, M.J. and Vatsa, V.N., "A New Method for Supersonic
      Boundary Layer Separations," AIAA Journal, pp. 1491-1497,
      November 1974.

2.   Shang, J.S. and Hankey, W.L., Jr., "Numerical Solution for
      Supersonic Turbulent Flow Over a Compression Ramp," AIAA
      Journal, Vol. 13, pp. 1368-1374, October 1975.

3. Cebeci, T., "Calculation of Compressible Turbulent Boundary Layers with Heat and Mass Transfer," AIAA Journal, Vol. 9, pp. 1091-1098, June 1971.

4. Davis, R.T. and Werle, M.J., "Numerical Methods for Interacting Boundary Layers," Paper to be presented at 25th Heat Transfer and Fluid Mechanics Institute, University of California, Davis, California, June 21-23, 1976.

5. Werle, M.J., Polak, A., Vatsa, V.N., and Bertke, S.D., "Finite Difference Solutions for Supersonic Separated Flows," appearing in Flow Separation, AGARD CP 168, 1975.

6. Law, C.H., "Supersonic Turbulent Boundary-Layer Separation," AIAA Journal, Vol. 12, pp. 794-797, June 1974.

7. Polak, A., Werle, M.J., Vatsa, V.N., and Bertke, S.D., "Supersonic Laminar Boundary-Layer Flow Past a Wavy-Wall with Multiple Separation Regions," Rept. AFL 74-12-15, Dept. of Aerospace Engineering, University of Cincinnati, Cincinnati, Ohio, December 1974, to be published in Journal of Spacecraft and Rockets.

8. Brandon, A.J., Masek, R.V., and Dunavant, J.C., "Aerodynamic Heating to Corrugation Stiffened Structures in Thick Turbulent Boundary Layers," AIAA Journal, Vol. 13, No. 11 (1975), pp. 1460-1466.

$$Y = \frac{h}{2}\{1 - \cos[\frac{2\pi}{W}(X - X_o)]\}$$

$$Y = \frac{\bar{X}^3 \tan\theta_R}{B + C\bar{X} + \bar{X}^2}$$

$X_o = 0.996$
$C = 0.004$
$B = C^2/4$
$\bar{X} = X - X_o$
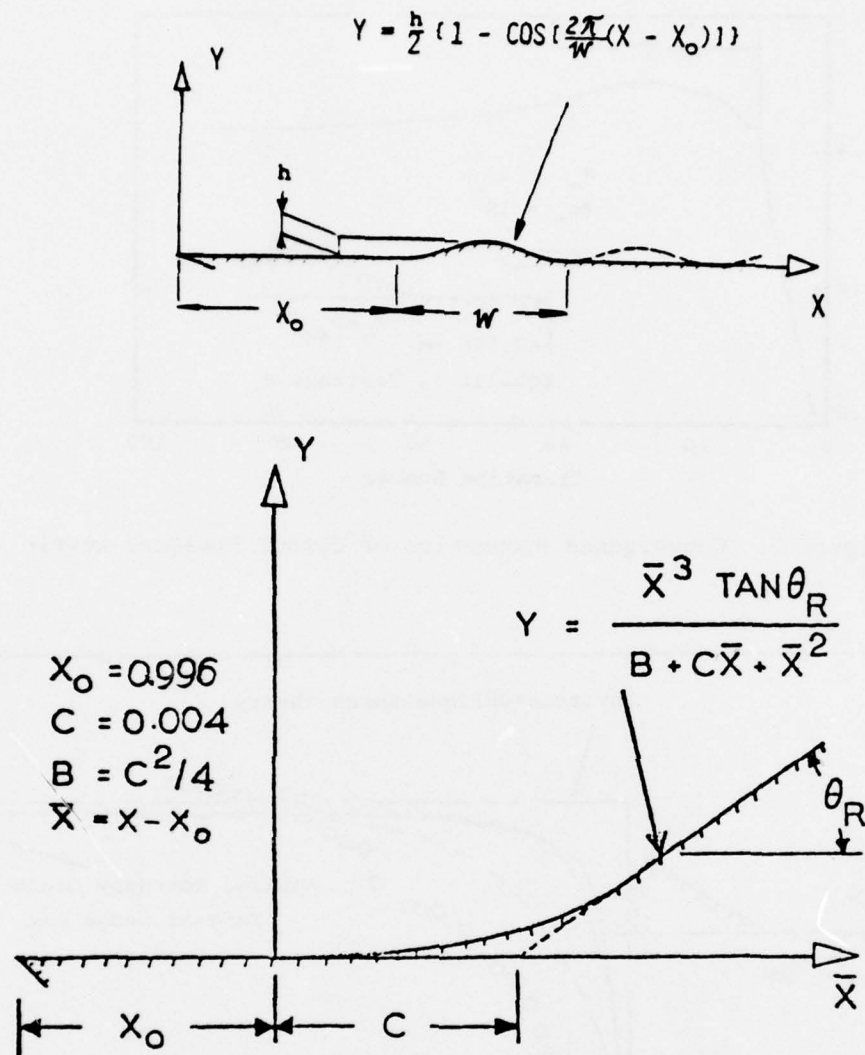
Figure 1. Surface Geometry.

337
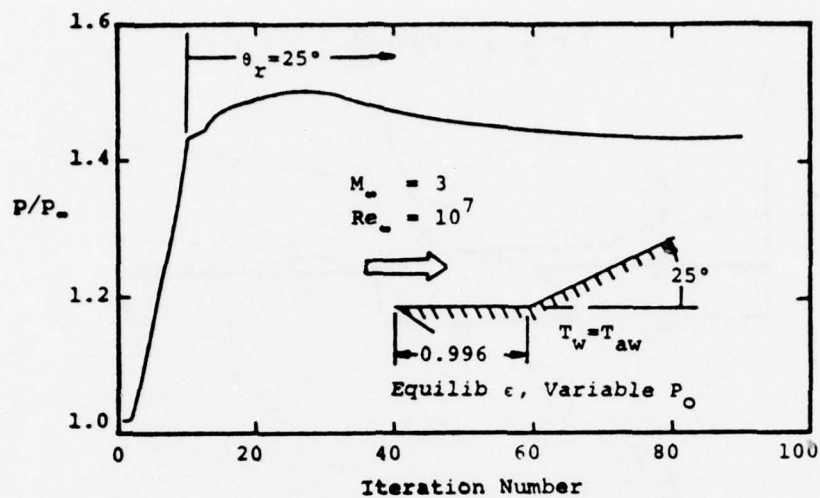
Figure 2. Convergence Properties of Corner Pressure Level.
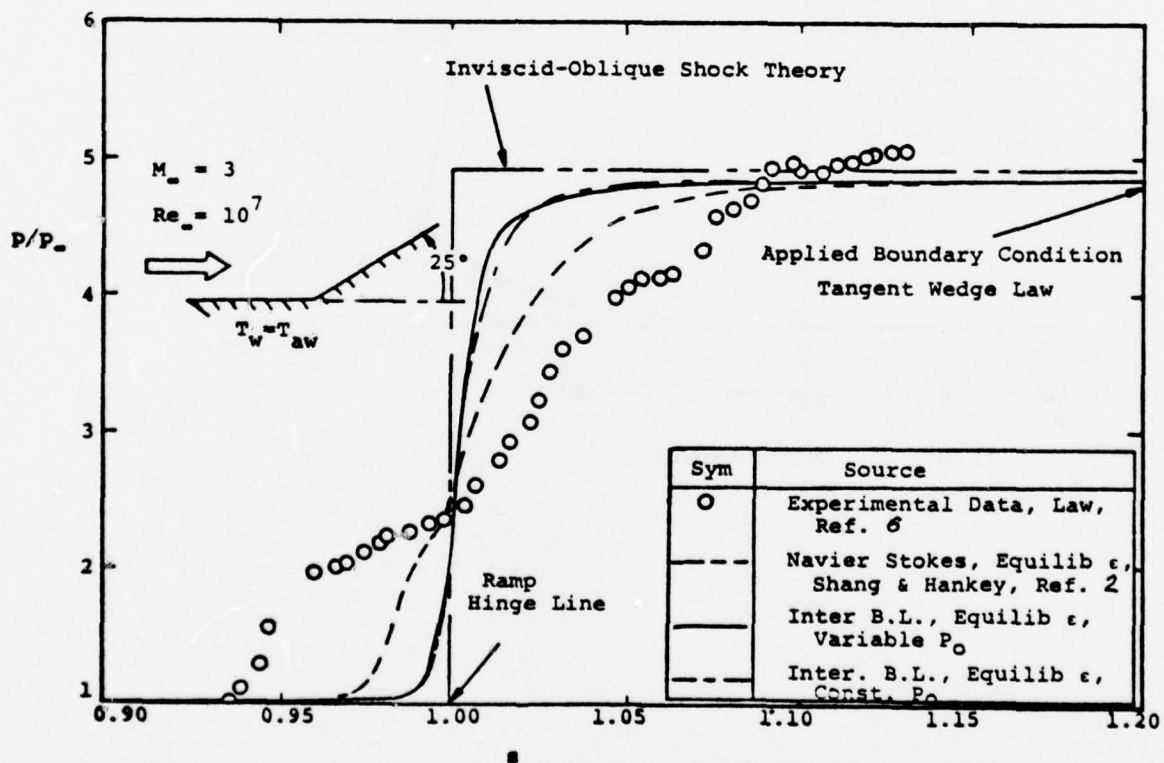
Figure 3. Comparison of Theoretical and Experimental Surface Pressures for ARL Ramp - Equilibrium Eddy Viscosity Model.
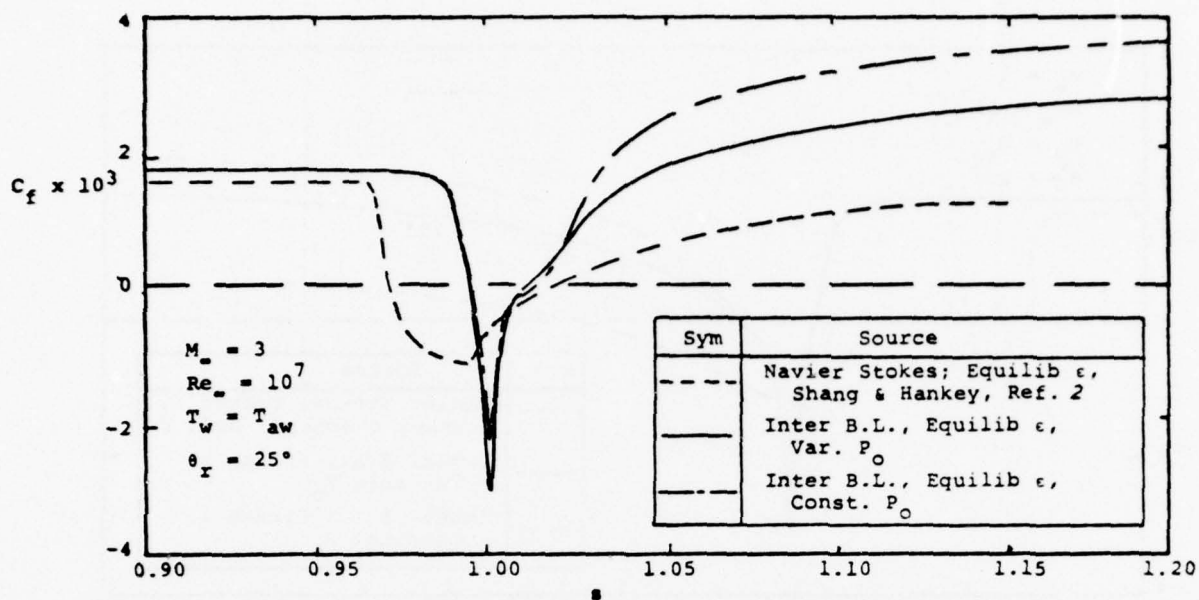
Figure 4.   Comparison of Theoretical Skin Friction Distribution
For ARL Ramp - Equilibrium Eddy Viscosity Model.
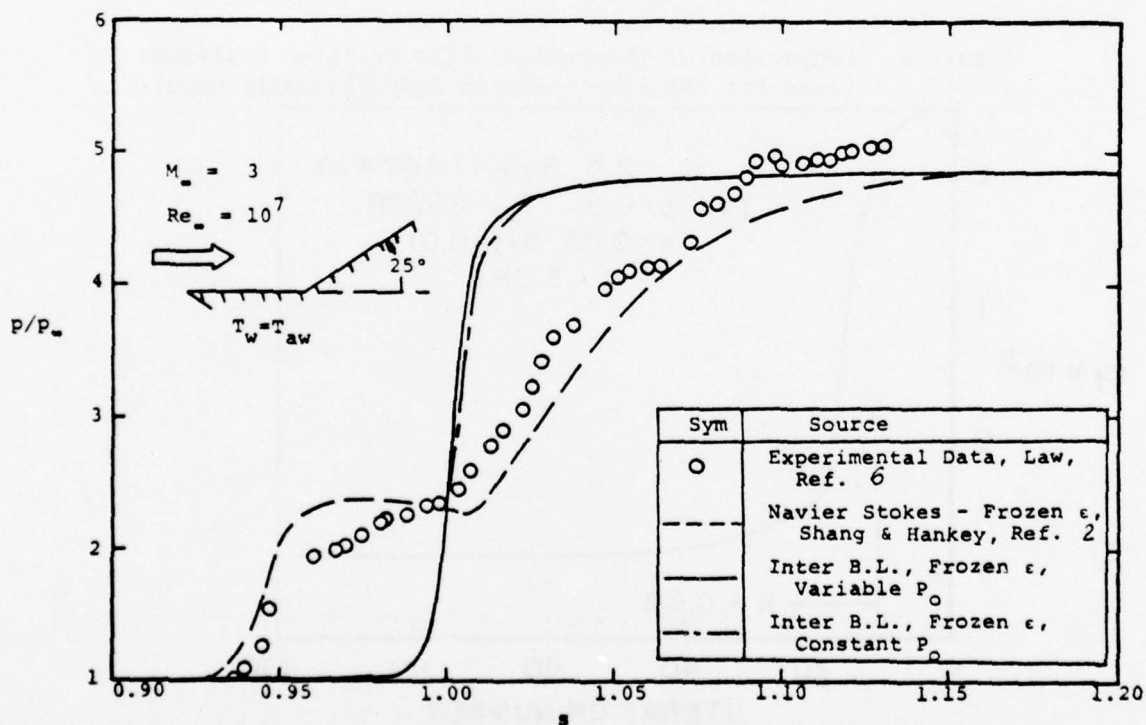
Figure 5.   Comparison of Theoretical and Experimental Surface
Pressures For ARL Ramp - Frozen Eddy Viscosity Model.

339
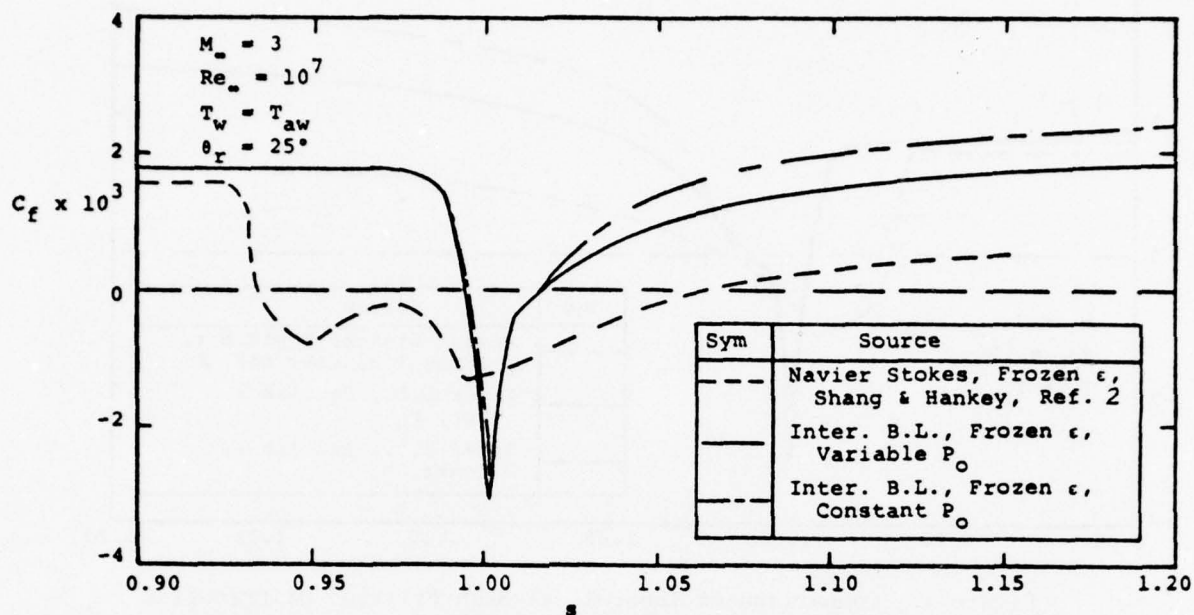
Figure 6. Comparison of Theoretical Skin Friction Distributions For ARL Ramp - Frozen Eddy Viscosity Model.
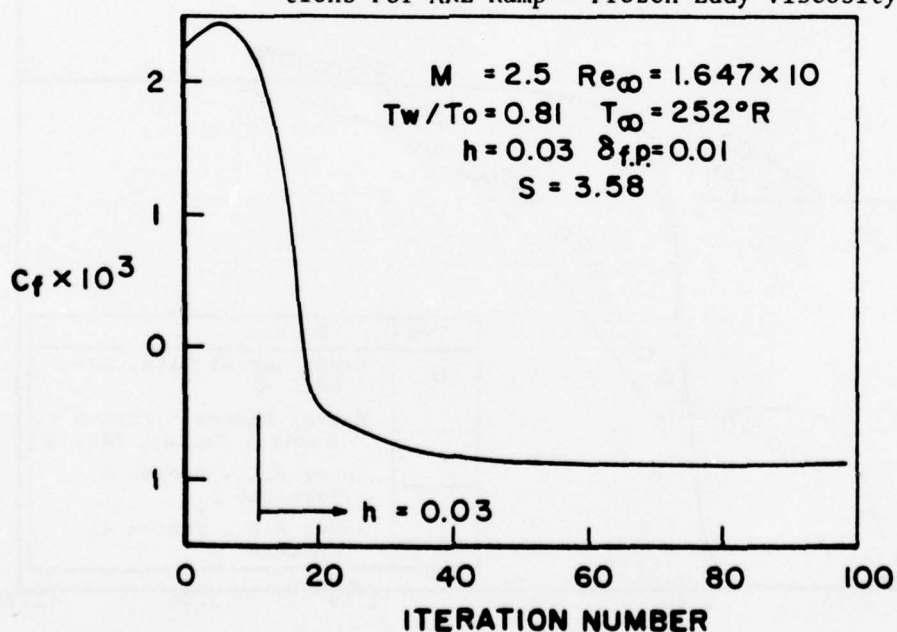
Figure 7. Convergence Properties of Skin Friction - Thin Boundary Layer.

$M_\infty = 2.5$ $Re_\infty = 1.647 \times 10^6$
$T_w/T_o = 0.81$ $T_\infty = 252°R$
$\delta_{f.p.} = 0.01$

$h = 0.03$

$h = 0.0$

$y = 0.015 \left\{ 1 - \cos\left[\frac{}{} (X - 3.55) \right] \right\}$
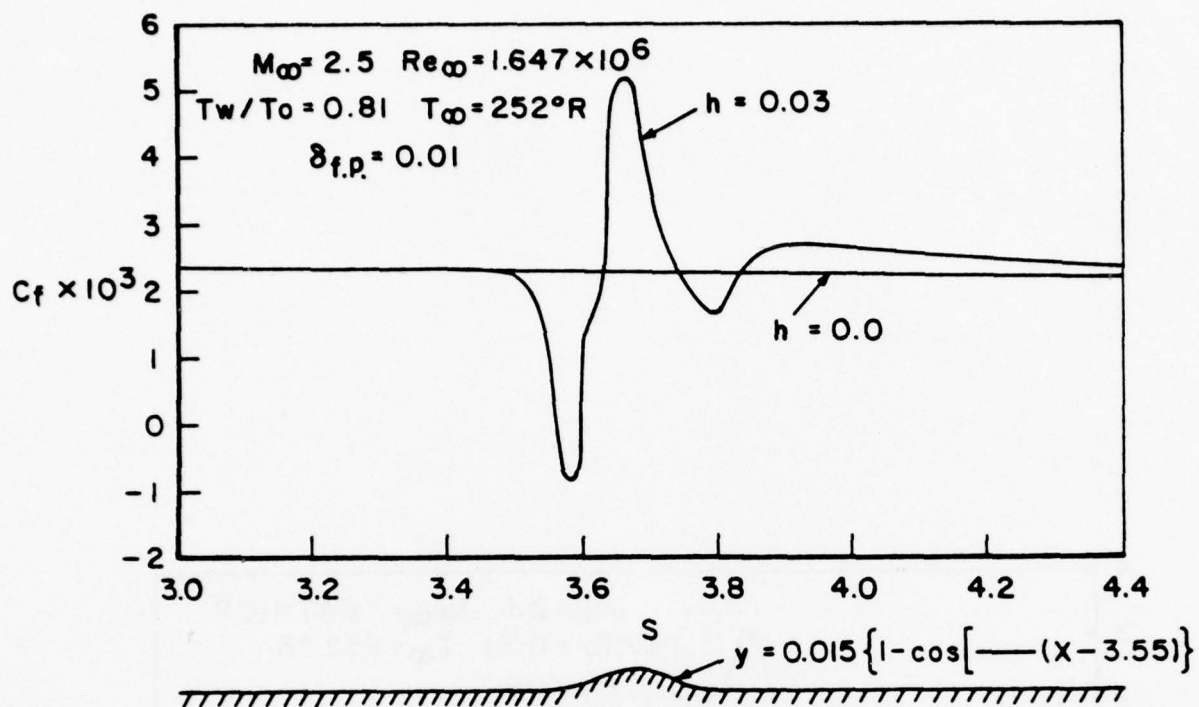
Figure 8.   Skin Friction Distribution - Thin Boundary Layer.

$M_\infty = 2.5$ $Re_\infty = 1.647 \times 10^6$
$T_w/T_o = 0.81$ $T_\infty = 252°R$
$h = 0.06$ $\delta_{f.p.} = 0.187$
$S = 73.44$

$h = 0.06$

ITERATION NUMBER
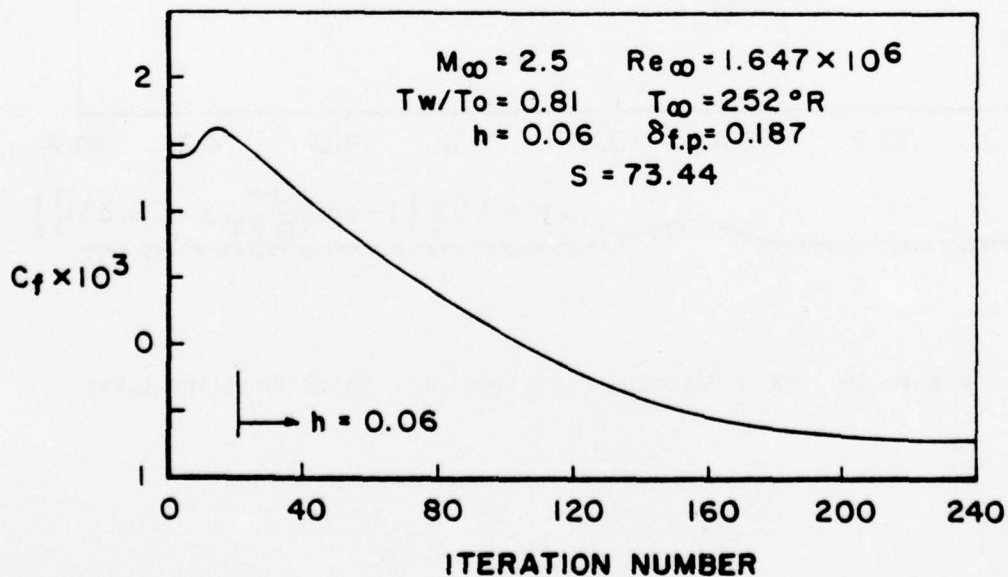
Figure 9.   Convergence Properties of Skin Friction - Thick
Boundary Layer.

341
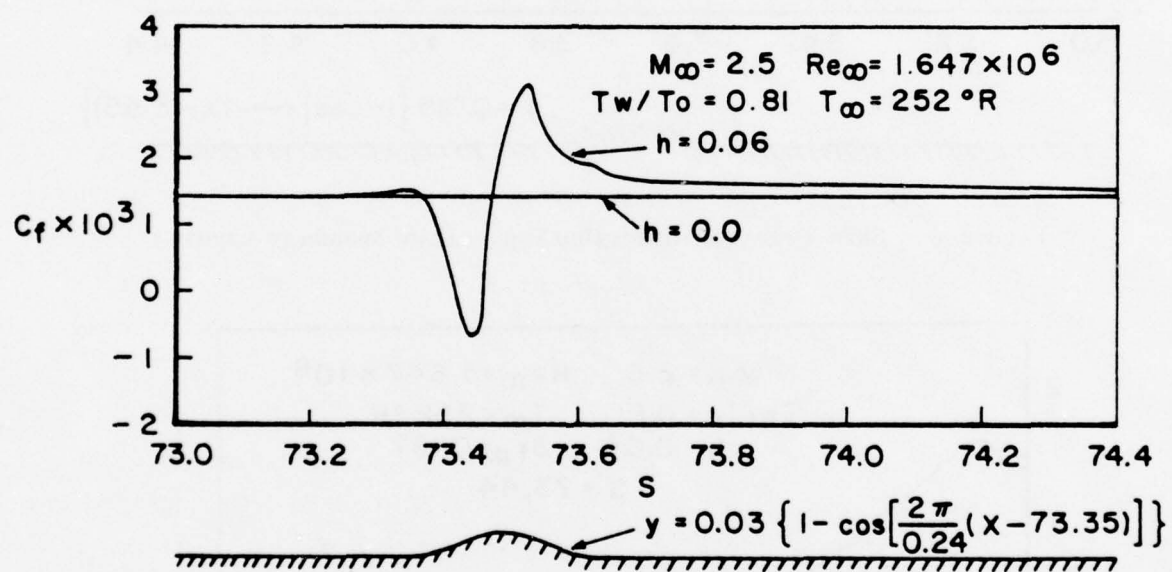
Figure 10.   Skin Friction Distribution - Thick Boundary Layer.

NUMERICAL SIMULATION OF SHOCK WAVE - TURBULENT BOUNDARY LAYER INTERACTION

by

J.S. Shang* and W.L. Hankey, Jr.**
Air Force Flight Dynamics Laboratory
Wright-Patterson Air Force Base, Ohio

and

C. Herbert Law[†]
Air Force Aero Propulsion Laboratory
Wright-Patterson Air Force Base, Ohio

ABSTRACT

Numerical solutions of the Navier-Stokes equations are presented for the interactions of a shock wave and a turbulent boundary layer. The turbulent closure is provided by a relaxation eddy viscosity model which approximates the response of turbulence to a severe pressure gradient. The relaxation eddy viscosity model was successfully applied for a series of compression ramp configurations in a previous investigation by the authors. In the present analysis, further verification of the eddy viscosity model is attempted by investigating shock impingement on a turbulent boundary layer. Computations were performed for shock generators varying from 7.93° to 12.17°, at a free-stream Mach number of 2.96 and a Reynolds number of 1.2×10^7. Numerical results obtained with MacCormack's scheme were compared with experimental measurements of the surface pressure distribution and the location of the separation and reattachment points. The density distribution throughout the entire interacting flowfield was also compared with experimental results obtained from holographic interferograms. In general, all essential features of the experimental observation were duplicated by the numerical computation.

---

* Aerospace Engineer, Flight Mechanics Division. Member AIAA
** Senior Scientist, Flight MEchanics Division. Member AIAA
† Aerospace Engineer, Turbine Engine Division. Member AIAA

NOMENCLATURE

C_f	Skin friction coefficient
D	Van Driest damping factor, Equation 14
e	Specific energy
e_i	Specific internal energy, $c_v T$
F, G	Vector fluxes in mean flow equations
h	Maximum vertical dimension of the computational domain
L	Length of the leading plate, 1 ft.
p	Static pressure
P_r	Molecular Prandtl number
P_{r_t}	Turbulent Prandtl number
S	Distance along the surface
t	Time
T	Temperature
u, v	Velocity components in Cartesian coordinates
u_{max}	Maximum velocity in the shock layer
U	Vector of conserved properties in mean flow equations
x, y	Cartesian coordinates
δ	Boundary layer thickness
$\delta s.g$	Deflection angle of the shock generator referenced to the unperturbed freestream
ϵ	Eddy viscosity coefficient
λ	Relaxation eddy viscosity length scale, Equation 21
μ	Molecular viscosity coefficient
τ_{ij}	Components of the stress matrix

Subscripts

e	Denotes properties evaluated at the external stream
o	Denotes properties evaluated at the location immediately upstream of the interaction region
w	Denotes properties evaluated at the wall
∞	Denotes properties evaluated at the unperturbed freestream

1.   INTRODUCTION

In recent years significant progress has been made in the numerical
analysis of supersonic flows with strong viscous-inviscid interaction.
Two geometries which have received considerable attention are the flat
plate-ramp configuration and shock impingement on a plate. The sufficiently
large pressure gradient generated either by the ramp geometry or the
incident shock wave induces boundary layer separation. The complex flow-
field is characterized by the strong interaction of the viscous dominated
region adjacent to the wall with the inviscid freestream. Qualitative
similarity has been observed for laminar, transitional and turbulent flows.

All available techniques in fluid mechanics research have been used
to describe laminar viscous-inviscid interactions. Numerical solutions
either by means of interacting boundary-layer equations[1,2,3] or Navier-
Stokes equations[4,5,6,7] have produced convincing results and reached
favorable agreement with experimental measurements. Analytical results
also have been obtained. In this regard, the mathematical structure of
the separation region has been given by Stewartson and Williams[8] while
numerical investigations based upon the asymptotic theory have been
successfully carried out by Burggraf et al.[9,10]

Unfortunately, for turbulent flow we have not as yet been able to
solve the interacting flowfield as conclusively. The major difficulty
can be easily identified as the lack of an accurate turbulence model for
the viscous-inviscid interacting flowfield. In spite of the inherent
shortcoming, Wilcox[11] first demonstrated the feasibility of numerically
solving the turbulent interacting problem. In his work, an explicit time-
marching first-order finite difference scheme (AFTON 2pt code) incorporating
Saffman's turbulence model[12] was used. Baldwin and MacCormack[13] also
numerically solved a shock boundary layer interaction problem in the
hypersonic regime using two different eddy viscosity models.[12,14]
In their work, a multi-layered grid spacing was used to achieve suitable
numerical resolution near the wall. Horstman, Kussoy, Coakley, Rubesin,
and Marvin[15] performed a combined experimental and numerical investigation
of a chock-wave induced flow separation over an axisymmetric configuration.
They devised a modification of the diffusion eddy viscosity model by use

of their experimental measurements. The comparison between data and calculations by the modified eddy viscosity model reflects reasonable agreement. Shang and Hankey[16,17] also adopted MacCormack's numerical scheme to solve the viscous-inviscid interaction problem in a compression corner with a relaxation eddy viscosity model. The numerical results in comparison with Law's data[18] indicated an improvement over Wilcox's calculation[11] of the compression ramp (mainly in the prediction of the upstream pressure propagation) and a substantial improvement over the result by the conventional equilibrium eddy viscosity model.[14,16,17]

The relaxation eddy viscosity model is first of all an engineering approximation. In concept, it approximates the experimental observation that in a highly decelerated or accelerated turbulent flow, the Reynolds shear stress remains nearly frozen at its initial value while being convected along streamlines[19,20] and then exponentially approaches a new equilibrium state.[20] In practical implementation, the relaxation eddy viscosity model parallels Bradshaw's[21] extra-rate-of-strain correction and also is similar to Rose and Johnson's suggestion for a mixing length correction.[22] An outstanding feature of this turbulence model is its simplicity in that only one additional parameter is required (λ, a time-like length scale which describes the exponential decay of the eddy viscosity distribution) and as a result pays no penalty in computing time. In numerical computation, an initial streamwise location for which the relaxation phenomenon is initiated also requires specification. The relaxation eddy viscosity model has been successfully demonstrated for a series of compression ramp configurations. Further substantiation of this concept is still needed, particularly if an exact description of the turbulent structure is not feasible for some time to come.

The objectives of the present effort are to demonstrate the sensitivity of the relaxation length scale in the turbulence model and to develop an engineering method capable of predicting the turbulent viscous-inviscid interactions including flow separation. Since there are few numerical results[11,13,15] and essentially no analytical work to compare and verify accuracy, the substantiation must be obtained from comparison with experimental measurements. However, one should realize that the resolution of suspected three-dimensional influences has not as yet been

completely delineated for all the existing experiments.[23,24] Therefore, the specific comparison of experimental data and numerical calculations must concentrate on the essential features of the interaction problem.

2. GOVERNING EQUATIONS

The governing equations of the present analysis are the unsteady compressible Navier-Stokes equations in terms of mass-averaged variables.[11,13,15] The turbulent closure is provided by the relaxation eddy viscosity model and the turbulent Prandtl number.

$$\frac{\partial U}{\partial t} + \frac{\partial F}{\partial x} + \frac{\partial G}{\partial y} = 0 \tag{1}$$

The vector components are:

$$U = \begin{Bmatrix} \rho \\ \rho u \\ \rho v \\ \rho e \end{Bmatrix} \tag{2}$$

$$F = \begin{Bmatrix} \rho u \\ \rho u^2 - \sigma_{xx} \\ \rho uv - \tau_{xy} \\ (\rho e - \sigma_{xx})u - \tau_{xy} \cdot v - \dot{q}_x \end{Bmatrix} \tag{3}$$

$$G = \begin{Bmatrix} \rho v \\ \rho uv - \tau_{xy} \\ \rho v^2 - \sigma_{yy} \\ (\rho e - \sigma_{yy})v - \tau_{xy} \cdot u - \dot{q}_y \end{Bmatrix} \tag{4}$$

where the apparent stress components are given by:

$$\sigma_{xx} = -p + 2(\mu + \epsilon) \frac{\partial u}{\partial x} - \frac{2}{3}(\mu + \epsilon)\left(\frac{\partial u}{\partial x} + \frac{\partial v}{\partial y}\right) \tag{5a}$$

$$\sigma_{yy} = -p + 2(\mu + \epsilon) \frac{\partial v}{\partial y} - \frac{2}{3}(\mu + \epsilon)\left(\frac{\partial u}{\partial x} + \frac{\partial v}{\partial y}\right) \tag{5b}$$

$$\tau_{xy} = \tau_{yx} = (\mu + \epsilon)\left(\frac{\partial u}{\partial y} + \frac{\partial v}{\partial x}\right) \tag{6}$$

$$\dot{q}_x = \gamma(\mu/p_r + \epsilon/p_{r_t}) \frac{\partial ei}{\partial x} \tag{7a}$$

$$\dot{q}_y = \gamma(\mu/p_r + \epsilon/p_{r_t}) \frac{\partial ei}{\partial y} \tag{7b}$$

The mean specific total energy is as follows:[13,16,17]

$$e = C_v T + (u^2 + v^2)/2 \tag{8}$$

Auxiliary relationships included in the system of equations are the equation of state for a perfect gas and Sutherland's viscosity equation.

The associated boundary conditions are prescribed as follows: The initial condition and upstream boundary condition are prescribed at the freestream value for all the dependent variables.

$$U(0, x, y) = U_\infty$$
$$U(t, x_i, y) = U_\infty \tag{9}$$

At the downstream boundary, the component of the gradient of the dependent variables in the streamwise direction is set to zero:

$$\frac{\partial U}{\partial x} = 0 \tag{10}$$

The outer boundary conditions for the present analysis consists of two segments,[16] upstream and downstream of the incident shock. The boundary condition on the former is satisfied by permitting the flow to approach its unperturbed freestream value.

$$U(t,x,h) = U_\infty \tag{11}$$

The boundary condition on the segment downstream of the incident shock is fulfilled by the Rankine-Hugoniot relations.

$$U(t,x,h) = U(M_\infty, \delta s.g) \tag{12}$$

The anticipated reflected shock is permitted to pass through the downstream segment of the computational domain. Therefore, no additional prescribed boundary condition is required.

The boundary conditions on the solid contour are given as the non-slip condition for velocity.

$$u(t,x,0) = 0 \tag{13}$$
$$v(t,x,0) = 0 \tag{14}$$

and the adiabatic wall

$$\left. \frac{\partial T}{\partial y} \right|_{y=0} = 0 \tag{15}$$

348

The pressure at the wall is obtained by satisfying the compatible condition.

$$\frac{\partial p}{\partial y}\Big|_{y=0} = \left[\frac{\partial}{\partial x}\ (\mu\frac{\partial u}{\partial y}) + \frac{\partial}{\partial y}\ (\frac{4}{3}\ \mu\frac{\partial v}{\partial y}) - \frac{\partial}{\partial y}\ (\frac{2}{3}\ \mu\frac{\partial u}{\partial x})\right]_{y\ =\ 0} \tag{16}$$

3. EDDY VISCOSITY MODEL

The relaxation eddy viscosity model consists of a system of three equations. The local equilibrium eddy viscosity coefficient is described by the Cebeci-Smith's model[14]

In the inner region:

$$\varepsilon_{eq(i)} = \rho k^2 y^2 D^2\ \left|\frac{\partial u}{\partial y}\right| \tag{17}$$

where k is the von Karman constant (0.4) and D is the Van Driest damping factor:

$$D = 1 - \exp\ (-y\ \frac{\sqrt{|\tau w|}}{\rho_w}\ /26\ \nu_w) \tag{18}$$

The outer region, Clauser's defect law gives

$$\varepsilon_{eq(o)} = 0.0168\ \rho u_{max}\ \delta_i^* \tag{19}$$

δ_i^* is the kinematic displacement thickness (also the basic scaling for the outer layer).

$$\delta_i^* = \int_o^h\ (1 - \frac{u}{u_{max}})\ dy \tag{20}$$

One notes that the reference velocity is taken as u_{max} in the calculation of the kinematic displacement thickness (δ_i^*) to prevent a possible numerical anomaly in the transient phase of the computations. More importantly, one must also appreciate that the outer edge of an interacting boundary layer cannot be readily defined, and for this reason the intermittency correction of the wake region is also omitted.

In the relaxation eddy viscosity model, the flow "history" effects, or more precisely, the Reynolds stress relaxation phenomenon, is described by a simple algebraic equation for the eddy viscosity coefficient

$$\varepsilon = \varepsilon_o + (\varepsilon_{eq.} - \varepsilon_o)\ e^{-(\frac{\Delta x}{\lambda})} \tag{21}$$

349

where ε denotes the relaxing eddy viscosity coefficient. The local equilibrium value of the eddy viscisity ε_{eq} is generated by equations (17) and (19). The distance between the initial station and the calculated station is indicated as Δx, while the parameter λ is the relaxation length scale. The value for ε_o is defined as the eddy viscosity at an upstream location for which the relaxation phenomena is initiated. This reference station for defining ε_o was selected at $x/L = .9027$ for all the computations presented which corresponds to about seven boundary-layer thicknesses upstream of the intersection of the shock wave and the wall.

The relaxation parameter λ, which is a measure of the memory of stress-containing eddies is the only free parameter to describe numerically the relaxation phenomenon. In the present analysis, the sensitivity of the relaxation length scale will be domonstrated by utilizing two values of λ; namely $\lambda = 10\delta_o$ and $\lambda = 20\delta_o$. The former has been used exclusively in References 16 and 17.

Equation (21) is a particular solution of a rate equation suggested by Bradshaw[21] in his study on the effects of streamline curvature in turbulent flow. Equation (21) is also similar to the relaxation equation for the mixing length suggested by Rose and Johnson.[22] According to Bradshaw[21], the relaxation length parameter λ is a function of y to take into account different turbulent scalings in the inner and outer regions. He postulated that the fine eddy structure near the wall quickly achieves an equilibrium state while the outer region requires a longer period to readjust. However, in carrying out this concept for turbulent interactions in a previous investigation[17], little numerical difference was observed.

4. NUMERICAL PROCEDURE

MacCormack's[4,6] alternating-direction-explicit numerical scheme is adopted in the present analysis. Two numerical damping terms are included specially designed to eliminate nonlinear instabilities. One of these recently implemented by MacCormack and Baldwin, is applied to the convective terms[6] while for flowfields containing severe pressure gradients such as in this boundary-layer-shock wave interaction, a fourth-order smoothing term[4,6,7,13] is necessary. The detailed description of the numerical smoothing procedure can be obtained in Reference 4.

A major difficulty encountered in the numerical analysis is the determination of the resolution required for engineering accuracy. The basic requirement is to adequately resolve all significant features of the flow. The commonly accepted criteria of a mesh Reynolds number of the order of two is impractical for the present analysis[6] but also seems to be unnecessary.[16,17] For turbulent flow the high velocity gradients near the wall dictate an extremely fine mesh spacing to achieve adequate numerical resolution. The exponential stretching of the grid-spacing immediately adjacent to the wall combined with a coarser constant step-size in the outer region is used in the normal direction of the main flow.[4,16,17]

In the present analysis, the entire flowfield is divided into two overlapping computational domains. In the first domain, the development of a turbulent boundary layer over a flat plate is calculated. The interacting region is contained within the second computational domain which overlaps the first region. The calculations are joined at $x = .8749$ ft. from the leading edge. A 64x30 calculation mesh system is employed for both computational domains. The mesh point distribution in the normal coordinate includes 18 points in an exponentially varying inner region (Δy min = 10^{-4} ft.) and 12 points in the constant step-size outer region with Δy of 3.65×10^{-3} ft. However, for the interaction zone (the second computational domain) the grid-spacing in the streamwise direction is reduced from that of the first computational domain by a factor of three to give a Δx of 3.98×10^{-3} ft. Thus, the computational inviscid-viscous interaction zone has a physical dimension of about $20\delta \times 5\delta$.

The present calculation was performed on a CDC 6600 computer for which nearly full use was made of the available memory core. Increasing the dimensions of the inviscid-viscous interaction zone is still possible by simply overlapping additional computational domains. A similar procedure also can be used to perform a partial truncation error analysis. However, one feels that the basic issue of numerical resolution should be a separate and systematic effort and is beyond the scopy of the present study. The convergence criteria required to obtain the asymptotic steady state solution was defined to be one tenth of one percent change in consecutive skin friction coefficient calculations. The criterion is reached generally in about two hours for the cases investigated.

5.   DISCUSSION OF RESULTS

As indicated earlier, a primary objective of the study is to investi-
gate the sensitivity of the previous developed[16,17] relaxation eddy
viscosity model through comparison with experimental data for the shock
impingement problem. Numerical solutions were obtained for the experimental
conditions of Law.[24] General features of the computed flowfield were
found to be very similar to that of the ramp configuration. (See Figure 1).

Numerical solutions are presented in three groups. First the entire
flowfields of the compression ramp and shock-boundary layer interaction are
presented. The second group of results are intended to reveal the numerical
sensitivity of the relaxation length parameter, λ, by comparing the sur-
face pressure and location of the separation and reattachment points with
experimental measurements.[24] In the last group, detailed flowfield
prediction in terms of the density contour are compared with the holographic
interferograms.

In Figure 1, two density contour graphs are presented together for
the entire flowfield around a 25° compression ramp and a shock-boundary
layer interaction. The incident shock is induced by a 12.27° shock wave
generator so that the inviscid pressure rise will be identical to the
25° ramp. The computed density contour graphs reproduce all the essential
features of the supersonic interacting flowfield. For the compression
ramp, a well-defined turbulent boundary layer is separated from the leading
plate by the upstream pressure propagation. The separation shock penetrates
well within the turbulent boundary layer. As the flow negotiates the
corner and subsequentially reattaches on the ramp, the reattachment shock
wave system also appears. The separation shock and reattachment shock
waves eventually coalesce downstream of the reattachment point. The shock-
boundary layer interacting flowfield possesses nearly the identical
general characteristics to that of the compression ramp. The expansion
region imbedded between the separation shock and the reattachment shock
waves of the shock-boundary layer interaction is substantially larger and
more obvious than the ramp configuration. In this sense, Green[23] has
correctly pointed out that the wave system produced by an incident oblique
shock may be considered to be a variant of the compression ramp configuration.

352

An obvious short-coming of the numerical solution is also revealed in the calculation of the incident shock. In "shock capturing", the thin incident oblique shock wave is smeared into a region with finite dimensions. In future work it is recommended that this drawback be remedied by implementing a "shock fitting" scheme for the incident shock.[25,26,27] A "shock fitting" scheme in conjunction with the Navier-Stokes equations was successfully demonstrated recently by Tannehill, Holst and Pakich[27] in their work on viscous blunt body flows with an impinging shock.

Although the computed incident shock yields the accurate shock wave angle, the smearing of the shock creates a difficulty in the determination of an accurate coordinate reference point.[4,6,11,17,23] For that reason, the separation point is used as the coordinate origin consistently throughout the analysis.

The surface pressure distribution and regions of flow separation of a 25° ramp and shock-boundary layer interaction generated by a 12.27° wedge are presented together with the experimental data[18,24] in Figure 2. The compression ramp data and numerical solution were recorded for a Reynolds number of 10^{7}. The shock impingement data were collected for a Reynolds number of 1.2×10^{7}. The Mach number is identical for both cases. The overall agreement between the experiment and the computed pressure distribution is acceptable with the ramp configuration results being slightly better than for shock impingement. The maximum deviation between the pressure data and the calculated value is about 15% based upon the downstream pressure. For both cases, the most serious discrepancy between data and computed results is in the region between the pressure plateau and reattachment point.

In the next group of presentations (Figures 3, 4, 5, and 6), the sensitivity of the relaxation length parameter, λ, in predicting the surface pressure distribution and location of separation and reattachment is demonstrated. The data were obtained for four different incident shock strengths by changing flow deflection angles of the shock generator. The deflection angles are given as 7.93° (Figure 3), 8.90° (Figure 4), 9.87° (Figure 5), and 10.83° (Figure 6). Two numerical computations with different relaxation length scales $\lambda = 10\delta_{o}$ and $\lambda = 20\delta_{o}$ were performed for all the cases considered.

The differences between the calculations of $\lambda = 10\delta_o$ and $\lambda = 20\delta_o$ are concentrated around the flow separation and the reattachment regions. Doubling the relaxation length parameter λ produces only a maximum change in pressure level and the size of the reverse flow region of about 20 percent. The calculations with $\lambda = 20\delta_o$ produces better agreement with Law's data than the numerical solutions with $\lambda = 10\delta_o$. Serious disparity appears only in the prediction of the pressure plateau and in the reattachment region (Figures 3, 4, 5, and 6). Part of the discrepancy is possibly caused by the approximation of Reynolds stress by the eddy viscosity coefficient, particularly in the separated region. Detailed experimental measurements of the Reynolds stress are needed in the reverse-flow region to resolve this issue.

The difference between the numerical results is exclusively produced by the different relaxation length scales. However, the possible source of the differences between the numerical results and experimental results cannot be easily identified. According to Green[23] and Law,[28] substantial variations exist between experimental measurements performed under supposedly similar conditions in different facilities.[23,28,29] This problem is particularly acute for shock wave-boundary layer interaction investigations. Nevertheless, it is generally agreed that the discrepancies are primarily due to three-dimensional effects, but a specific evaluation has not been accomplished. It can be stated, however, that the numerical results are well within the experimental uncertainty of the measurements.

As in the investigation of compression ramps, one can follow the progression of increasing incident shock strength to observe the development of a pressure plateau and the "dual'minima" behavior in the skin friction coefficient distributions (Figure 3 through Figure 6). The overall agreements between data and the numerical prediction is considered to be acceptable for engineering application.

On Figures 7, 8, 9, and 10, comparisons are made between measured and calculated flowfield density distributions. The calculated density contours are compared with the experimental holographic interferograms and the calculated density profiles at several selected streamwise locations are compared with measured profiles obtained from the interferograms. The holographic interferograms contain the three-dimensional effects which

emanate from the corner region near the wind tunnel sidewalls. Upstream of the interaction region, these effects are minimal. However, in the interaction zone and downstream the errors can be quite significant if three-dimensional effects are not accounted for. The detailed data reduction procedure for obtaining density profiles from the interferograms is discussed in Reference 30. Although this procedure estimates the three-dimensional effects, actual measurements of density can be as much as 15 to 20% error. However, spatial resolution is quite accurate, to within 0.005 inches. The numerical solutions duplicate the essential features of the flowfield and in general are within the uncertainty envelope of the experimental data.

The density contour plots and interferograms are in general agreement. The computed density contours (Figures 7, 8, 9, and 10) indicate clearly the incident shock penetrates deeply into the turbulent boundary layer. The severe adverse pressure gradient causes boundary layer separation. The separation not only induces an upstream pressure propagation but also triggers a family of compression wavelets which coalesce to form the separation shock. An imbedded expansion region immediately follows to compensate for the over compression. As the separated shear layer re-attaches to the plate, the shear layer realigns with the plate and induces a second group of compression wavelets which coalesce to form the reattachment shock. Far downstream of the shock impingement point, the turbulent boundary layer reemerges into a highly compressed region. The separation and reattachment shock eventually coalesce to form the classic reflected shock wave. The numerical results accurately predict the incident shock strength and overall pressure rise (See Figures 3, 4, 5, and 6) for the inviscid pressure asymptotes). However, the contour plots and density profiles reveal considerable shock smearing produced by the present coarse grid size employed in the inviscid region. (In principle, an improvement in the definition of the incident shock wave is possible by adopting a "shock fitting" scheme). [27] For the impinging shock of relatively weak strength a good agreement of density profiles between experiments and calculations is obtained. In summary, this present effort demonstrates the feasibility of computing the interaction of a shock wave with a turbulent boundary layer.

6. CONCLUSION

After completing the compression ramp study[16,17] further verification
of the relaxation turbulence model was deemed appropriate. Therefore, shock
impingement on a turbulent boundary layer was studied. A comparison of
the numerical solutions with experimental measurements by Law[24,28] was
made. A parametric study of the relaxation length scale λ, showed the
value of $20 \, \delta_o$ to be superior to $10 \, \delta_o$ as previously used for the study
of compression ramps. Comparison of the pressure, skin friction distribution,
and density contours with experiment exhibited good engineering agreement.

Improvements on the present analysis were identified and recommended
for future work.

a. Due to the large step size of the grid, the incident shock
was smeared which propagated an error downstream. A "shock fitting
scheme[25,26,27] is recommended to eliminate this deficiency.

b. An improvement of the turbulence model in the separated region
is recommended in order to improve the agreement in the pressure plateau
region.

7. REFERENCES

[1]   Dwoyer, D.L., "Supersonic and Hypersonic Two-Dimensional Laminar Flow
       Over a Compression Corner" Proceedings AIAA Computational Fluid
       Dynamics Conference, July 1973, p. 69.

[2]   Werle, J.J. and Vatsa, V.N., "Numerical Solution of Interacting
       Supersonic Boundary Layer Flows Including Separation Effects"
       ARL tr 73-0162. Aerospace Research Laboratories, Wright-Patterson
       AFB, Ohio, December 1973.

[3]   Carter, J.E., "Solutions for Laminar Boundary Layers with Separation
       and Reattachment" AIAA Paper 74-583, AIAA 7th Fluid and Plasma
       Dynamics Conference, Palo Alto, California, June 17-19, 1974.

[4]   MacCormack, R.W., "Numerical Solutions of the Interaction of a Shock
       Wave with a Laminar Boundary Layer" Lecture Notes in Physics, Vol. 8,
       Springer-Verlag, New York, 1971, p. 151.

[5]   Carter, J.E., "Numerical Solution of the Supersonic Laminar Flow
       Over a Two-Dimensional Compression Corner" Lecture Notes in Physics,
       Vol. 19, Springer-Verlag, New York, 1973, p. 69.

[6]   MacCormack, R.W. and Baldwin, B.S., "A Numerical Method for Solving
       the Navier-Stokes Equations With Application to Shock-Boundary
       Layer Interactions" AIAA Paper 75-1, AIAA 13th Aerospace Sciences
       Meeting, Pasadena, California, January 20-22, 1975.

[7] Hung, C.M. and MacCormack, R.W., "Numerical Solutions of Super-
      sonic and Hypersonic Laminar Flows Over a Two-Dimensional Com-
      pression Corner" AIAA Paper 75-2, AIAA 13th Aerospace Sciences
      Meeting, Pasadena, California, January 20-22, 1975.

[8] Stewartson, K. and Williams, P.G., "Self-Induced Separation"
      Proc. Roy. Soc. A213, 1969, p. 181.

[9] Burggraf, O.R., "Asymptotic Theory of Separation and Reattachment
      of a Laminar Boundary Layer on a Compression Ramp" AGARD-CPP-168,
      AGARD Conference on Flow Separation, Göttingen, Germany, May 1975,
      p. 101.

[10] Jensen, J., Burggraf, O.R., and Rizzetta, D.P., "Asymptotic
      Solution for Supersonic Viscous Flow Past a Compression Corner"
      Proceedings of 4th International Conference on Numerical Methods
      in Fluid Dynamics, Boulder, Colorado, June 1974.

[11] Wilcox, D.C., "Numerical Study of Separated Turbulent Flows,"
      AIAA Paper 74-584, AIAA 7th Fluid and Plasma Dynamics Conference,
      Palo Alto, California, June 17-19, 1974.

[12] Saffman, P.G. and Wilcox, D.C., "Turbulence Model Predictions for
      Turbulent Boundary Layer" AIAA Journal, Vol. 12, No. 4, April 1973,
      p. 541.

[13] Baldwin, B.S. and MacCormack, R.W., "Numerical Solution of the
      Interaction of a Strong Shock Wage with a Hypersonic Turbulent
      Boundary Layer" AIAA Paper 74-558, AIAA 7th Fluid and Plasma
      Dynamics Conference, Palo Alto, California, June 17-19, 1974.

[14] Cebeci, T., Smith, A.M.O., and Mosinskis, G., "Calculations of
      Compressible Adiabatic Turbulent Boundary Layer" AIAA Journal,
      Vol. 8, No. 11, 1970, p. 1974.

[15] Horstman, C.C., Kussoy, M.I., Coakley, T.J., Rubesin, M.N., and
      Marvin, J.G., "Shock-Wave Introduced Turbulent Boundary-Layer
      Separation at Hypersonic Speeds" AIAA Paper 75-4, AIAA 13th Aero-
      space Sciences Meeting, Masadena, California, January 20-22, 1975.

[16] Shang, J.S. and Hankey, W.L., Jr., "Numerical Solution of the
      Navier-Stokes Equations for Supersonic Turbulent Flow Over a Com-
      pression Ramp" AIAA Paper 75-3, AIAA 13th Aerospace Sciences
      Meeting, Pasadena, California, January 20-22, 1975.

[17] Shang, J.S. and Hankey, W.L., Jr., "Supersonic Turbulent Flows
      Utilizing the Navier-Stokes Equations" AGARD-CPP-168, AGARD
      Conference on Flow Separation, Gottingen, Germany, May 1975, p. 23-1

[18] Law, C.H., "Supersonic Turbulent Boundary-Layer Separation" AIAA
      Journal, Vol. 12, No. 6, June 1964, p. 794.

[19] Deissler, R.G., "Evolution of a Moderately Short Turbulent Boundary Layer in a Severe Pressure Gradient" Journal Fluid Mechanics, Vol. 64, Part 4, 1974, p. 763.

[20] Narasimha, R. and Prabhu, A., "Equilibrium and Relaxation in Turbulent Wakes" Journal of Fluid Mechanics, Vol. 54, Part 1, 1972, p. 1.

[21] Bradshaw, P., "Effects of Streamline Curvature on Turbulent Flow" AGARDograph No. 169, (AGARD-AG-169), August 1973.

[22] Rose, W.E. and Johnson, D.A., "A Study of Shock-Wave Turbulent Boundary Layer Interaction Using Laser Velocimeter and Hot-wire Anemometer Techniques" AIAA Paper 74-95, AIAA 12th Aerospace Sciences Meeting, Washington, D.C., January 30-February 1, 1974.

[23] Green, J.E., "Interaction Between Shock Waves and Turbulent Boundary Layer" Progress in Aerospace Sciences, Vol. 11, pp. 235-340, Pergamon Press, 1970.

[24] Law, C.H., "Supersonic Shock Wave - Turbulent Boundary Layer Interactions" AIAA Paper 75-832, AIAA 8th Fluid and Plasma Dynamics Conference, Hartford, Connecticut, June 16-18, 1975.

[25] Kutler, P., Reinhardt, W.A., and Warming, R.F., "Multi-Shocked, Three-Dimensional Supersonic Flowfields with Real Gas Effects" AIAA Journal, Vol. 11, No. 5, May 1973, pp. 657-664.

[26] Moretti, G., "Floating Shock Fitting Technique Imbedded Shocks in Unsteady Multi-Dimensional Flows" Proceedings of the 1974 Heat Transfer and Fluid Mechanics Institute, Stanford University Press, 1974, p. 184.

[27] Tannehill, J.C., Holst, T.L., and Rakich, J.V., "Numerical Computation of Two-Dimensional Viscous Blunt Body Flows with an Impinging Shock" AIAA Paper 75-154, AIAA 13th Aerospace Sciences Meeting, Pasadena, California, January 20-22, 1975.

[28] Law, C.H., "Two-Dimensional Compression Corner and Planar Shock Wave Interactions with a Supersonic, Turbulent Boundary Layer" ARL TR 75-0157, Aerospace Research Labs, Wright-Patterson AFB, Ohio, February 1975.

[29] Reda, D.C. and Murphy, J.D., "Shock-Wave - Turbulent Boundary Layer Interactions in Rectangular Channels, Part II: The Influence of Sidewall Boundary Layers on Incipient Separation and Scale of the Interaction", AIAA Paper 73-234, 11th Aerospace Sciences Meeting, Washington, D.C., 10-12 January 1973.

[30] Havener, A.G. and Radley, J.J., "Supersonic Wind Tunnel Investigations Using Pulsed Laser Holography" ARL 73-0148, Aerospace Research Laboratories, Wright-Patterson AFB, Ohio, October 1973.
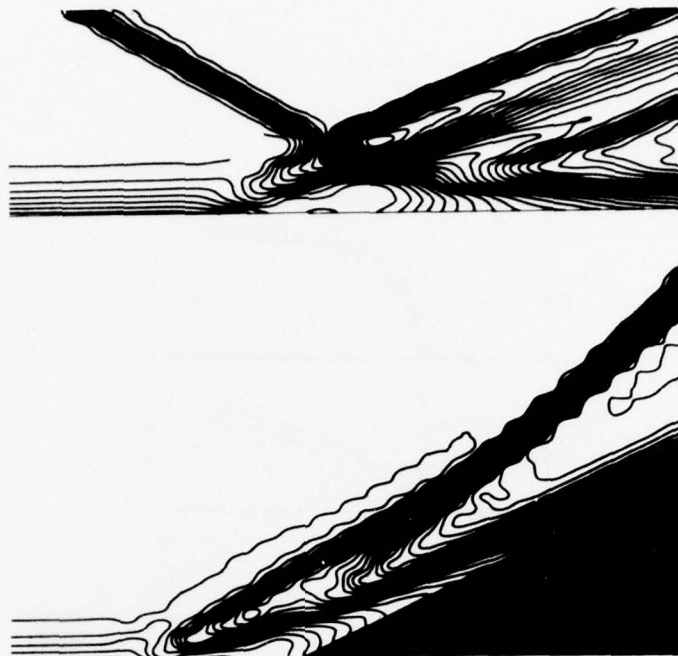
Figure 1. Density Contour Graph of a Compression Ramp (25°) and Shock-Turbulent Boundary Layer Interaction (12.27°) for the Same Inviscid Pressure Rise.
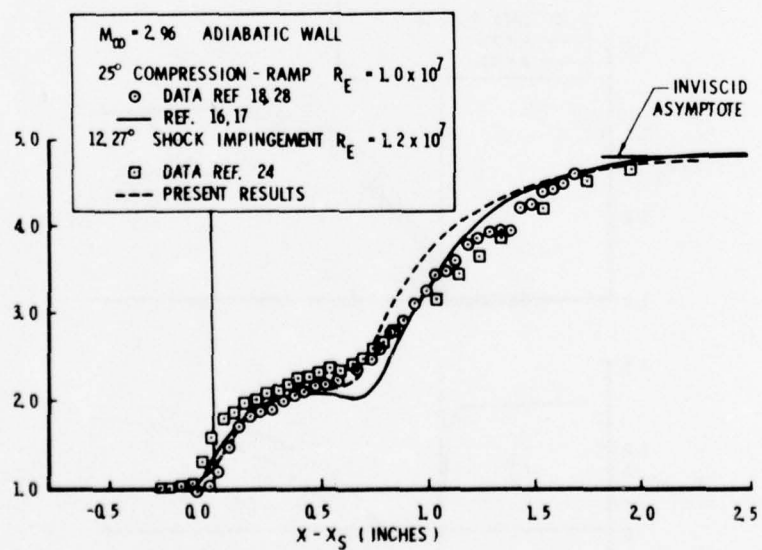
Figure 2. Comparison of Surface Pressure Distribution Between a Compression Ramp (25°) and Shock-Turbulent Boundary Layer Interaction (12.27°)
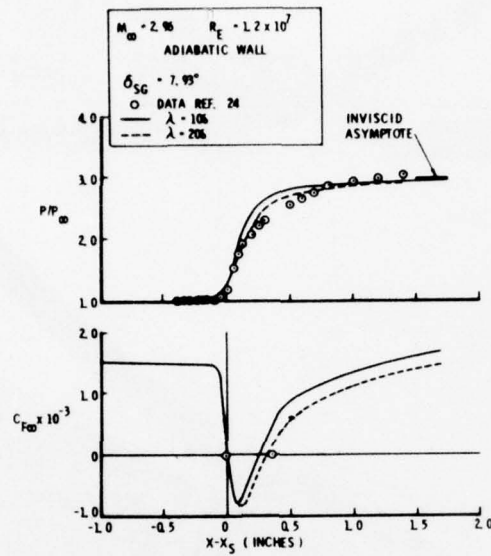
Figure 3.   Comparison of Skin-Friction Coefficient and Surface Pressure Distribution, $\delta s.g = 7.93^{O}$.
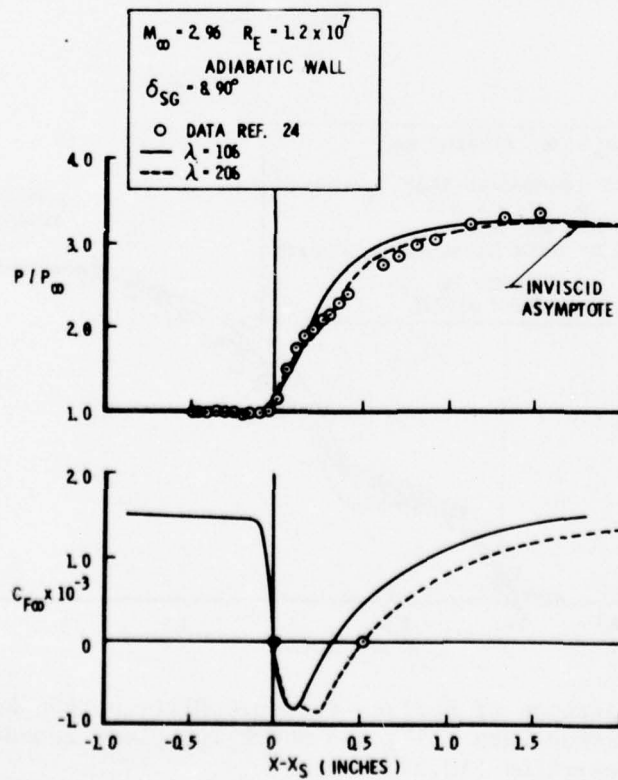
Figure 4.   Comparison of Skin-Friction Coefficient and Surface Pressure Distribution, $\delta s.g = 8.90^{O}$.

360
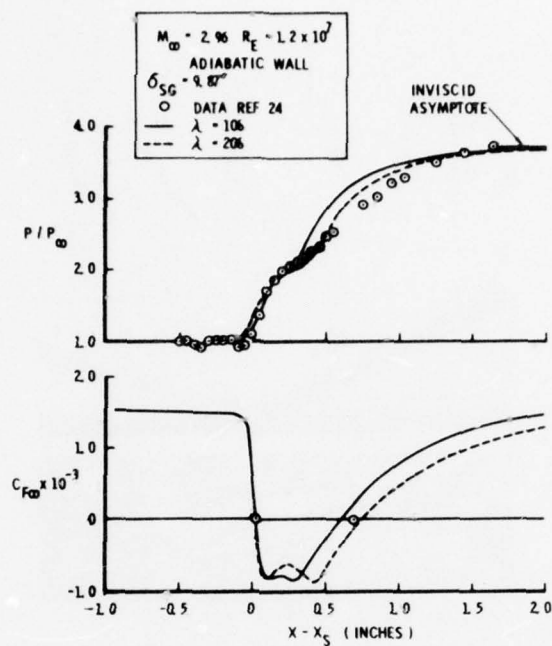
Figure 5. Comparison of Skin-Friction Coefficient and Surface Pressure Distribution, δs.g = 9.87°.
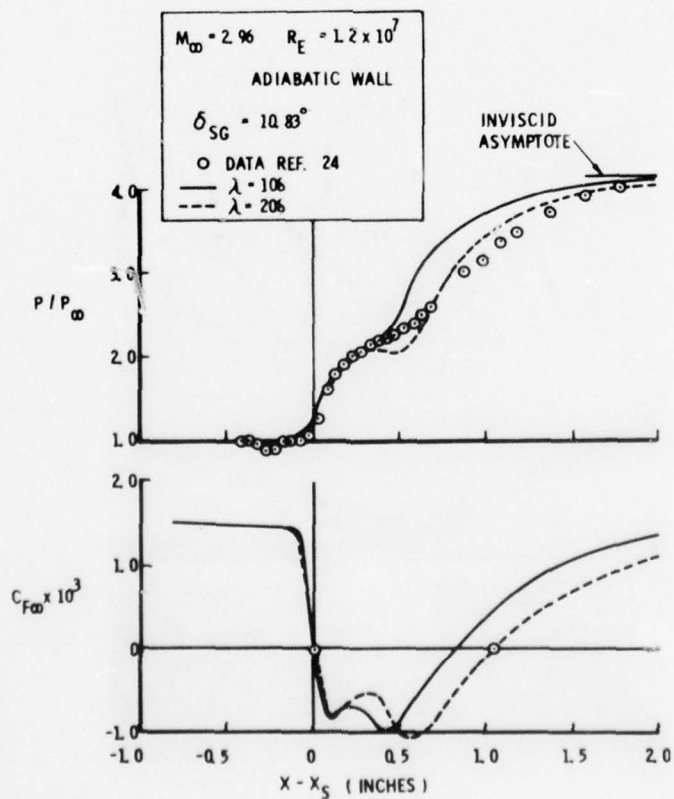
Figure 6. Comparison of Skin-Friction Coefficient and Surface Pressure Distribution, δs.g = 10.83°.
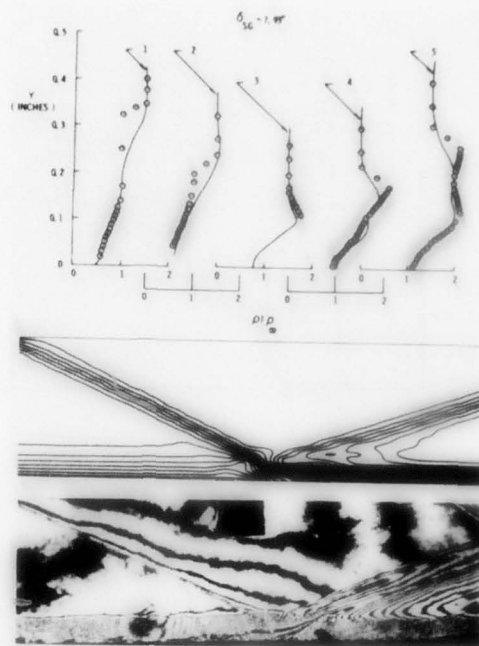
Figure 7.   Comparison of Density Contours Holographic Interferogram
and Density Profiles, δs.g = 7.93°.
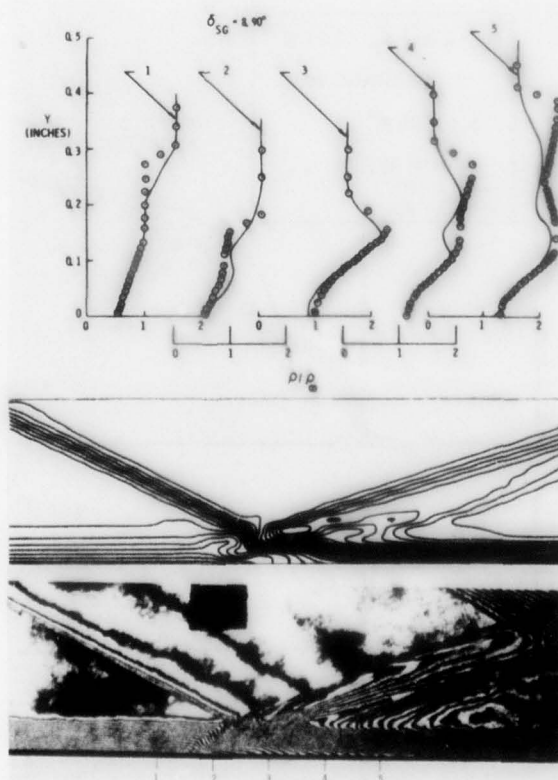
Figure 8.   Comparison of Density Contours Holographic Interferogram
and Density Profiles, δs.g = 8.90°.
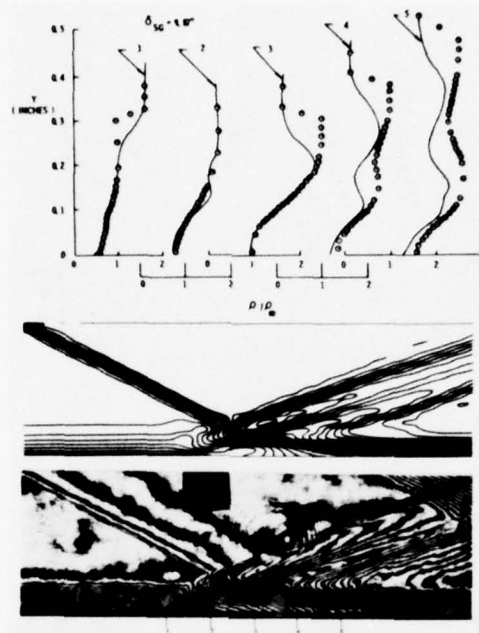
Figure 9.   Comparison of Density Contours Holographic Interferogram and Density Profiles, δs.g = 9.87°.
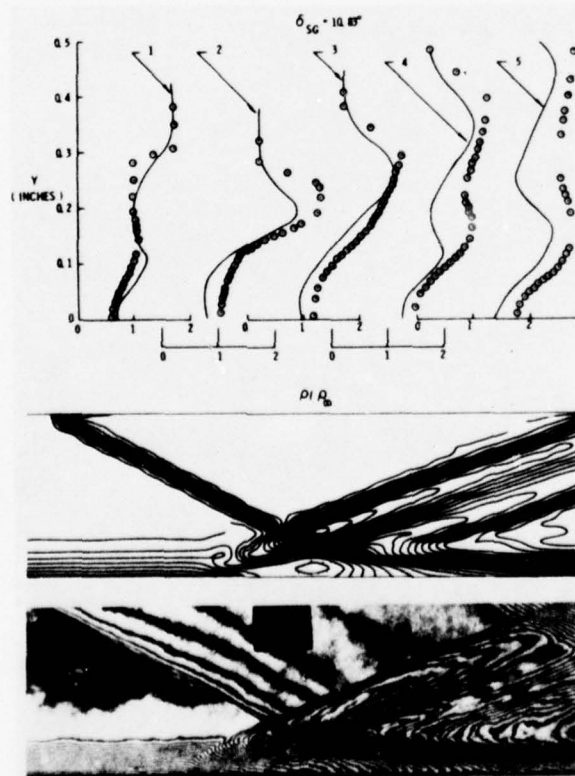
Figure 10.   Comparison of Density Contours Holographic Interferogram and Density Profiles, δs.g = 10.83°.

363

A RATIONAL THEORY FOR THE PRESSURE DRAG
OF AN AIRFOIL IN SUBSONIC FLOW

by

K. Gersten
Ruhr University
Bochum, FRG

and

J.F. Gross
University of Arizona
Tucson, Arizona

ABSTRACT

A rational theory is developed to determine the pressure drag of an
airfoil in subsonic flow. The pressure drag results from an integration
of the pressure distribution over the contour of the airfoil. This
pressure distribution is the same as that resulting from the potential
flow over the same airfoil except for a small region in the neighborhood
of the trailing edge. The difference in the pressure distributions
results from an interaction between the turbulent boundary layer and the
inviscid outer flow. The calculation of this difference follows a triple-
deck approach suggested by Melnick for the flow in the neighborhood of the
trailing edge. The flow in the outer layer or upper deck is inviscid but
rotational. Calculation of this flow field requires the solution of a
Poisson differential equation which yields the correction to the potential
flow pressure distribution.

A result of the theory is the relationship of the pressure drag and the
Reynolds number. It is shown that the pressure drag decreases more
rapidly than the friction drag as the Reynolds number increases. Numer-
ical results are given for the symmetric Joukowsky airfoil. The theory
developed here for symmetric airfoils and incompressible flow can be
extended to asymmetric airfoils and compressible flows.

I.   INTRODUCTION

The total resistance of a body is composed of the friction drag and the pressure drag. The friction drag results from the integration of the wall shear stress over the surface of the airfoil and the pressure drag is due to a corresponding integration of the appropriate component of static pressure around the airfoil. It is well known that the classical Prandtl boundary layer theory can provide a determination of the friction drag at high Reynolds numbers with great accuracy as long as no separation occurs along the body. However, to the present time, no rational theory has been proposed for calculating the pressure drag for the flow around a body for subsonic flow without boundary layer separation.

In previous theories, the pressure distributions around bodies were determined neglecting the boundary layer effects and then the pressure drag for inviscid subsonic flow was shown to be zero. This is called d'Alembert's Paradox. Therefore, the pressure drag results from the boundary layer and, in fact, is a boundary layer effect of higher order since the Prandtl boundary layer theory cannot be used to calculate the pressure drag.

The pressure drag is a typical example of a viscous interaction effect. As a result of the finite thickness of the boundary layer, a pressure distribution in the region near the trailing edge of the airfoil occurs which is different from the pressure distribution in the inviscid flow. This difference in the pressure near the trailing edge of the airfoil is responsible for the pressure drag. In the case of those bodies on whose surface no boundary layer separation occurs, the pressure drag can become 10%-20% of the total drag depending on the geometry of the airfoil and on the location of transition.

Prandtl[1] had in principle discussed how a boundary layer theory of higher order could be formulated to explain displacement-thickness effects. Accordingly, the boundary layer for an inviscid outer flow is first calculated. The resulting distribution of the displacement thickness along the airfoil determined in this way is then added to the airfoil thickness. For this fictitious airfoil, a new pressure distribution can be obtained using inviscid theory. The boundary layer which results from

366

this new airfoil will have a displacement thickness that is somewhat
different from the former so that a subsequent correction is required.
Using this method, the final pressure distribution can be obtained only
using an iterative technique. This final distribution will depend
critically on the strong interaction between the outer flow and the
boundary layer.

It turns out that the theory which has been discussed above breaks down
near the trailing edge of the airfoil. The reason is as follows: the
inviscid flow contains a singularity at the trailing edge of the profile.
Here we consider only symmetric profiles with zero angle of attack with
a cusp at the trailing edge (the trailing edge angle is equal to 0 - see
Figure 1). The airfoil has the same properties as a symmetric Joukowsky
profile in the region near the trailing edge. A finite velocity exists
at the trailing edge, but the gradient dU/dx directly behind the trailing
edge is infinitely large, see Figure 1 and Equation (24b). This
singularity leads to the result that in the second-order theory dis-
cussed above, the wake can be described by a distribution of sources
whose intensity at the trailing edge becomes infinitely large. As a
result of this, the velocities at the trailing edge become infinitely
large and this result is physically impossible.

In order to avoid this basic difficulty, several empirical engineering
approximations have been proposed. So, for example, Thwaites[2] suggests
that the calculations of the pressure distribution for the inviscid flow
should not be made on the contour of the airfoil itself, but at the dis-
tance of the boundary layer thickness from the surface. The distribution
of the boundary layer thickness and the thickness of the wake can then
be obtained from a classical boundary layer calculation. From this
method, it is shown that the correction for the pressure distribution
occurs only in a very small region near the trailing edge. It is
important, therefore, to obtain this correction through analysis of the
local flow in the region of the trailing edge. It is also necessary to
take into account the interaction between the inviscid outer flow and
the boundary layer on the surface, in the neighborhood of the trailing
edge.

It is well known from the theory of the laminar boundary layer, that in those places where singularities occur (leading edge of the flat plate, cusp profiles, separation) the boundary layer in the region close to the singularity, generally consists of three different layers. This so-called triple deck concept has been described by K. Stewartson[3]. The calculations of these different layers can be obtained using the method of matched asymptotic expansions in order to solve the singular perturbation problem. The flows in which the triple deck concept is useful are specific problems in which strong interaction occurs between the inviscid outer flow and the boundary layer. This interaction takes place in the outer layer (upper deck) in which the frictional effects can be neglected. The details regarding the corresponding theories of the flows in the region of the trailing edge of the flat plate or over cusp airfoils can be found in References 4 to 7.

In recent years, these perturbation methods have also been applied to the turbulent boundary layer. With the help of the method of matched asymptotic expansions, the classical turbulent boundary layer could be described in a general asymptotic theory for turbulent perturbations at large Reynolds numbers (see References 10 to 12). It has been shown that the law of the wall and the velocity-defect profile are the first order terms in an asymptotic expansion of the velocity profile for large Reynolds numbers. From this, it is possible to obtain fully developed turbulent boundary layers as first order solutions which are valid for the limiting case of $Re \to \infty$.

The concept of the triple-deck boundary layer has also been applied to turbulent boundary layers in which strong interactions occur between the outer flow and the boundary layer.

T.C. Adamson, Jr. and A. Feo[8] and R.E. Melnick and B. Grossman[9] have studied the interaction of shock waves with the turbulent boundary layer. R.E. Melnick and R. Chow[4] studied the problem of trailing edge in order to calculate friction correction to the lift. It is important then to study the application of the triple-deck model for the turbulent boundary layer at the trailing edge in order to determine the pressure drag of airfoils in subsonic flow.

A rational theory will be developed to calculate the pressure drag of symmetrical airfoils using the concept of the triple-deck model for the turbulent boundary layer in the region of the trailing edge. Incompressible flow will be assumed in order to simplify the analysis. An extension to asymmetric airfoils as well as to compressible flow is possible in principle and will be completed in the near future. The development of the theory in this paper follows closely the work of R.E. Melnick and R. Chow. [4]

II. THE TRIPLE-DECK FOR THE TRAILING EDGE

It can be seen in Figure 1 that the pressure drag results from a modification of the pressure distribution given by the inviscid flow in the region of the trailing edge. It is sufficient, therefore, to consider only the neighborhood of the trailing edge in a region whose dimensions will be of the order of magnitude of the boundary layer thickness δ_o at the trailing edge. The flow in the neighborhood of the trailing edge is shown schematically in Figure 2. The turbulent boundary layer entering the trailing-edge region consists of two layers: the inner layer where the law of the wall is valid and the outer layer where the law of the wake is valid. According to the asymptotic theory of turbulent boundary layers discussed above, the perturbation parameter

$$\varepsilon = \frac{u_{\tau_o}}{U_\infty} = \sqrt{\frac{\tau_{w_o}}{\rho U_\infty^2}} = \sqrt{\frac{1}{2} C_{fo}} \tag{1}$$

is described by the dimensionless friction felocity. Here the value of the friction velocity at the trailing edge is given by index o and evaluated at the entrance of the boundary into the trailing-edge region. The thickness of the boundary layer is then given by the order of magnitude ε

$$\frac{\delta_o}{L} = O(\varepsilon) \tag{2}$$

where the chord length of the airfoil L is the non-dimensionalizing length. Correspondingly, the stretching of the interaction region is also of the order of magnitude ε. It can be seen in Figure 2 that the boundary layer in the interaction region consists of the following three layers:

369

1. An outer layer in which the inviscid flow is rotational. In this region, the interaction between the inviscid, irrotational outer flow (potential flow) and the turbulent boundary layer takes place. The normal distances from the wall in this layer are also of the order of magnitude ε.

2. An inner layer adjacent to the wall which is a continuation of the wall layer of the incoming turbulent boundary layer. In this layer, the total stress in the boundary layer is a constant, that is, independent of the distance from the wall.

3. A middle (or blending layer) layer. This layer is necessary in order to match the Reynolds stresses that appear in the outer flow with the stresses that appear in the inner layer.

It will be seen that the outer layer in the interaction region must be studied more closely since a pressure field occurs here which is different from the pressure field of the inviscid theory and this difference represents the required correction for the pressure distribution for the airfoil. The basis for the calculation of the flow in this region is to use the time-independent Navier-Stokes equation:

$$\frac{\partial u}{\partial x} + \frac{\partial v}{\partial y} = 0 \tag{3a}$$

$$u\,\frac{\partial u}{\partial x} + v\,\frac{\partial u}{\partial y} = -\frac{1}{\rho}\frac{\partial p}{\partial x} + \nu\Delta u + \frac{1}{\rho}\left(\frac{\partial \sigma_x}{\partial x} + \frac{\partial \tau_{xy}}{\partial y}\right) \tag{3b}$$

$$u\,\frac{\partial v}{\partial x} + v\,\frac{\partial v}{\partial y} = -\frac{1}{\rho}\frac{\partial p}{\partial y} + \nu\Delta v + \frac{1}{\rho}\left(\frac{\partial \tau_{yx}}{\partial x} + \frac{\partial \sigma_y}{\partial x}\right) \tag{3c}$$

where is the Laplace operator and the stress tensor due to the turbulent fluctuation velocity components is given by

$$\begin{pmatrix} \sigma_x & \tau_{xy} \\ \tau_{yx} & \sigma_y \end{pmatrix} = - \begin{pmatrix} \rho\overline{u'^2} & \rho\overline{u'v'} \\ \rho\overline{u'v'} & \rho\overline{v'^2} \end{pmatrix} \tag{4}$$

Outside the region near the wall, the viscous shear stresses can be neglected with regard to the turbulent shear stresses.

We consider new coordinates for the region of interest in Figure 2:

$$X = \frac{1}{\epsilon} \frac{x - L}{L} \quad , \quad Y = \frac{1}{\epsilon} \frac{y}{L} \tag{5}$$

which are of order 1 in the interaction region. If we introduce these coordinates into Equations (3a)-(3c), neglect laminar friction terms, and recall that the order of magnitude of the turbulent stresses are $0(\epsilon^2)$, one obtains for the limit $\epsilon \to 0$:

$$\frac{\partial u}{\partial X} + \frac{\partial v}{\partial Y} = 0 \tag{6a}$$

$$u \frac{\partial u}{\partial X} + v \frac{\partial u}{\partial Y} = -\frac{1}{\rho} \frac{\partial p}{\partial X} \tag{6b}$$

$$u \frac{\partial v}{\partial X} + v \frac{\partial v}{\partial Y} = -\frac{1}{\rho} \frac{\partial p}{\partial Y} \tag{6c}$$

The flow is, therefore, described by the equations for inviscid flow but it is not irrotational. Furthermore, the vorticity of the oncoming turbulent boundary layer must be considered in this region.

It is well known that one can define a stream function

$$u = \frac{\partial \psi}{\partial y} \quad , \quad v = -\frac{\partial \psi}{\partial x} \tag{7}$$

Elimination of the pressure terms in Equation (6a)-(6c) leads to the so-called vorticity transport equation:

$$\frac{\partial \psi}{\partial Y} \frac{\partial \Delta \psi}{\partial X} - \frac{\partial \psi}{\partial X} \frac{\partial \Delta \psi}{\partial Y} = 0 \tag{8}$$

The vorticity ω as defined by Equation (9) is related to the stream function ψ as follows:

$$\omega = \frac{1}{2} \left(\frac{\partial v}{\partial X} - \frac{\partial u}{\partial Y} \right) \tag{9}$$

$$\omega = -\frac{1}{2} \Delta \psi \tag{10}$$

so that Equation (8) can also be written as

$$u \frac{\partial \omega}{\partial X} + v \frac{\partial \omega}{\partial Y} = 0 \tag{11}$$

This shows that the vorticity is constant along a stream-line.

An asymptotic expansion will now be postulated for the stream function in which the perturbation parameter is given by Equation (1). The stream function in the potential flow in the neighborhood of the trailing edge can be given by the following expression:

$$\psi(x,\bar{y}) = \psi_O + U_O\bar{y} + U_OLA \left[\left(\frac{x-L}{L}\right)^2 + \left(\frac{\bar{y}}{L}\right)^2\right]^{3/4} \sin\frac{3}{2}\theta \qquad (12)$$

with

$$\theta = \tan \frac{\bar{y}}{x-L} \qquad (13)$$

Here ψ_O is the value of the stream function at the trailing edge ($x = L$, $\bar{y} = 0$) and U_O is the velocity at the same point. A is a dimensionless factor which depends only on the geometry of the airfoil. It is assumed that the contour of the airfoil in the region of the trailing edge contains a cusp and this contour can be expressed in the following way:

$$\frac{y_c}{L} = A \left(\frac{L-x}{L}\right)^{3/2} \qquad (14)$$

For Joukowsky's airfoil, A is a function only of the relative thickness of the profile. The coordinate $\bar{y}$ is the distance from the chord not from the surface. For $x < L$, therefore, a new coordinate

$$y = \bar{y} - \bar{y}_c \qquad (15)$$

will be introduced. Then Equation (12) yields:

$$\psi(x,y) = \psi_O + U_Oy + U_OLA \left(\frac{L-x}{L}\right)^{3/2} + U_OLA \left[\left(\frac{x-L}{L}\right)^2\right.$$

$$\left. + \left(\frac{\bar{y}}{L}\right)^2\right]^{3/4} \sin\frac{3}{2}\theta \qquad (16)$$

$$\theta = \tan^{-1} \frac{y + AL \left(\frac{L-x}{L}\right)^{3/2}}{x-L} \qquad (17)$$

For fixed x L, the stream function for small y can then be expanded to yield the following:

$$\theta = \pi - \frac{\bar{y}}{L-x} = \pi + \frac{\bar{y}}{x-L} \qquad (18)$$

$$\sin\frac{3}{2}\theta = -\cos\left(\frac{3}{2}\frac{\bar{y}}{L-x}\right) = -1 + \frac{9}{8}\left(\frac{\bar{y}}{L-x}\right)^2 - \ldots \qquad (19)$$

372

$$\psi(x,y) = \psi_0 + U_0 y + U_0 LA \left(\frac{L-x}{L}\right)^{3/2} + U_0 LA \left(\frac{x-L}{L}\right)^{1/2}\left[1 + \frac{3}{4}\left(\frac{\bar{y}}{x-L}\right)^2\right.$$

$$\left. + \ldots\right] \bullet \left[-1 + \frac{9}{8}\left(\frac{\bar{y}}{L-x}\right)^2 - \ldots\right] \tag{20}$$

$$\psi(x,y) = \psi_0 + U_0 y + \frac{3}{8} U_0 LA \left(\frac{x-L}{L}\right)^{3/2}\left(\frac{y}{x-L}\right)^2 + \ldots$$

For $y = 0$, the stream function takes on the constant value $\psi = \psi_0$ which is to be expected. If one introduces the coordinates from Equation (5), then the following equations result:

$$\frac{\psi}{\varepsilon U_0 L} = \Psi = \Psi_0 + Y + \varepsilon^{1/2} \frac{3}{8} A \frac{Y^2}{|X|^{1/2}} \quad \text{for } X < 0 \tag{21}$$

$$\frac{\psi}{\varepsilon U_0 L} = \Psi = \Psi_0 + Y + \varepsilon^{1/2} \frac{3}{2} A \left[X^2 + Y^2\right]^{3/4} \frac{Y}{X} \tag{22}$$

$$\text{for } X > 0$$

For a general solution, $\psi(X,Y)$ of Equation (8), the following asymptotic expansion can be used:

$$\frac{\psi}{\varepsilon U_0 L} = \Psi = Y + \varepsilon^{1/2} \Psi_{inv}(X,Y) + \varepsilon \Psi_{BL}(Y) + \varepsilon^{3/2} \Psi'(X,Y) + \ldots \tag{23}$$

For simplification, $\Psi_0 = 0$. The first 2 terms of the expansion represent the inviscid solution represented by Equations (21) and (22). In this case, the expressions for Ψ are given by:

$$\Psi_{inv} = \frac{3}{8} A \frac{Y}{|X|^{1/2}} \qquad X < 0 \tag{24a}$$

$$\Psi_{inv} = \frac{3}{2} A \left[X^2 + Y^2\right]^{3/4} \frac{Y}{X} \approx \frac{3}{2} AX^{1/2} Y \qquad X > 0 \tag{24b}$$

The inviscid flow is only slightly perturbed by the small shear flow in the region of the wall. The term proportional to ε results from the entering turbulent boundary layer and will be determined through the defect of the velocity profile of that turbulent boundary layer.

The turbulent boundary layer will be characterized by the following velocity profile:

$$u(y) = u_{T_0}\left[\frac{1}{\kappa} \ln y^* + B_0 + \frac{\tilde{\pi}}{\kappa}\left(1 - \cos \pi \frac{y}{\delta_0}\right)\right]$$

$$\text{where } y^* = \frac{y u_{T_0}}{\nu} \tag{25}$$

and $\quad U_o = u_{\tau o} \left[\dfrac{1}{\kappa} \ln \dfrac{\delta_o u_{\tau o}}{\nu} + B_o + \dfrac{2\tilde{\pi}}{\kappa} \right]$

$\tilde{\pi}$ is Cole's wake parameter for the velocity profile. For zero pressure gradient, the value is given by $\tilde{\pi} = 0.5$. Von Karman gave the constant as $\kappa = 0.4$.

The defect part of the velocity profile is given by:

$$u(y) - U_o = u_{\tau o} \left[\dfrac{1}{\kappa} \ln \dfrac{y}{\delta_o} - \dfrac{\tilde{\pi}}{\kappa} \left(1 + \cos \pi \dfrac{y}{\delta_o} \right) \right] \qquad (26)$$

and is, according to Equation (1), also proportional to ε. The corresponding stream function Ψ_{BL} that is obtained in Equation (23) has the same order of magnitude. The correction for the stream function which is effectively that for the pressure distribution is proportional to $\varepsilon^{3/2}$.

Analogous to Equation (23), it is possible to obtain asymptotic expansions for both velocity components u and v:

$$\dfrac{u}{U_o} = U = 1 + \varepsilon^{1/2} U_{inv}(X,Y) + \varepsilon U_{BL}(Y) + \varepsilon^{3/2} U'(X,Y) + \dots \qquad (27)$$

$$\dfrac{v}{U_o} = V = \varepsilon^{1/2} V_{inv}(X,Y) + \varepsilon^{3/2} V'(X,Y) + \dots \qquad (28)$$

According to Equation (26), $U_{BL}(Y)$ may be written:

$$U_{BL}(Y) = \begin{cases} \dfrac{1}{\kappa} \ln \dfrac{Y}{\delta_T} - \dfrac{\pi}{\kappa} \left(1 + \cos \pi \dfrac{Y}{\delta_T} \right) & Y < \delta_T \\[2em] 0 & Y > \delta_T \end{cases} \qquad (29)$$

where $\quad \delta_T = \dfrac{\delta_o}{\varepsilon L} \qquad (30)$

Since the boundary layer profile $U_{BL}(Y)$ is taken to be independent of X, the v components in the boundary layer disappear as a result of the continuity equation and, therefore, the term of the v expansion proportional to ε vanishes. If the expansions in Equations (23), (27), and (28), are substituted into Equation (11), then using

$$\Omega = -\dfrac{1}{2} \Delta \Psi = \varepsilon U_o L \omega$$

and $\quad \Delta Y = 0, \Delta \Psi_{inv} = 0 \quad ; \quad \dfrac{\partial}{\partial x} (\Delta \Psi_{BL}) = 0 \qquad (31)$

374

one obtains

$$[1 + \varepsilon^{1/2} U_{inv} + \varepsilon U_{BL} + \varepsilon^{3/2} U'] \frac{\partial}{\partial X} [\varepsilon^{3/2} \Delta \Psi' + \ldots]$$

$$+ [\varepsilon^{1/2} V_{inv} + \varepsilon^{3/2} V' + \ldots] \frac{\partial}{\partial Y} [\varepsilon \Delta \Psi_{BL} + \varepsilon^{3/2} \Delta \Psi' \tag{32}$$

$$+ \ldots] = 0$$

From this, we obtain:

$$\varepsilon^{3/2} \quad \frac{\partial}{\partial X} \Delta \Psi' + V_{inv} \frac{\partial}{\partial Y} \frac{d^2 \Psi_{BL}}{dY^2} \quad + \ldots = 0 \tag{33}$$

Equations (21) and (27), together with Equation (7) yield:

$$U = \frac{\partial \Psi}{\partial Y} , \quad V = - \frac{\partial \Psi}{\partial X} \tag{34}$$

It can be shown that integrating Equation (33) with X yields:

$$\Delta \Psi' = + \Psi_{inv} \quad \frac{d^2 U_{BL}}{dY^2} \tag{35}$$

This is a Poisson equation. The right side is a known function which is given by Equations (24) or (29). It can be considered to be the vorticity Ω' of the modified flow. Analogous to Equation (11), one then obtains

$$\Delta \Psi' = -2 \Omega' \quad (X,Y) \tag{36}$$

with

$$\Omega' = - \frac{1}{2} \Psi_{inv} \frac{d^2 U_{BL}}{dY^2} \tag{37}$$

Equation (36) is to be solved with the following boundary conditions:

$$X^2 + Y^2 \rightarrow \infty : \quad \Psi' \quad (X,Y) = 0 \tag{38}$$

$$Y = 0 \quad V' (X,0) = - \frac{\partial \Psi'}{\partial X} = 0 \tag{39}$$

The solution of Equation (26) is composed of a particular solution and a solution of the homogeneous (Laplace equation) equation:

$$\Psi' (X,Y) = \Psi'_o (X,Y) + \Psi'_1 (X,Y) \tag{40}$$

A particular solution can be obtained as follows:

$$\Psi_1 (X,Y) = - \frac{1}{\pi} \iint \Omega' (\xi,\eta) \ln \bar{R} \, d\xi d\eta \tag{41}$$

The solution for the V' component along the line y = 0 is given by:

$$V' (X,0) = \frac{1}{\pi} \iint \frac{\partial}{\partial Y} (\ln \bar{R}) \Omega' \, d\xi d\eta = - \frac{1}{\pi} \iint \frac{\partial}{\partial \eta} (\ln \bar{R}) \Omega' \, d\xi d\eta \tag{42}$$

375

where $\quad \overline{R} = \sqrt{(X -\xi)^2 + (Y - \eta)^2}$ $\hspace{4cm}$ (43)

The function $\Psi'_o (X,Y)$ has to satisfy the Laplace equation

$$\Delta\Psi'_o = 0 \hspace{6cm} (44)$$

and along $Y = 0$, the induced V' velocity component given by Equation (42) has to be compensated.

One may consider the V' velocity to be represented by a series of sources or sinks along the X-axis having an intensity equal to $\dfrac{V'}{2}$. The solution of Equation (44) can then be carried out by the determination of the induced velocity field resulting from these source or sink distributions. When the function $\Psi' (X,Y)$ is determined, one can obtained directly the U' component of the perturbation velocity:

$$U' = \frac{\partial\Psi'}{\partial Y} \hspace{6cm} (45)$$

For the inviscid velocity distribution, one can then obtain:

$$u(x,y) = u_{pot} + \varepsilon^{3/2} U_o U' \;\; (X,Y) \hspace{4cm} (46)$$

Index pot refers to the potential flow.

The pressure can then be determined from the Bernoulli equation and this yields the expression:

$$C_p = \frac{p - p_\infty}{\frac{\rho}{2} U^2_\infty} = 1 - \left(\frac{u}{U_\infty}\right)^2 = 1 -\left(\frac{u_{pot}}{U_\infty}\right)^2$$
$$- 2 \; \frac{u_{pot}}{U_\infty} \; \varepsilon^{3/2} \; \frac{U_o}{U_\infty} \; U' \;\; (X,0) \hspace{3cm} (47)$$

or $\quad C_p(x) = Cp_{pot} -2\varepsilon^{3/2} \; \dfrac{u_{pot}(x,0)}{U_\infty} \; \dfrac{U_o}{U_\infty} \; U' \;\; (X,0)$ $\hspace{2cm}$ (48)

The pressure coefficient, $C_p(x)$ yields the pressure drag coefficient through integration:

$$C_{DP} = \frac{D_p}{\frac{\rho}{2} U^2_\infty L} = 2 \int_o^1 C_p(x) \; \frac{d\overline{y}_c}{dx} \; d\left(\frac{x}{L}\right) \hspace{2cm} (49)$$

where $y_c(x)$ is the contour of the body. According to d'Alembert's Paradox, the integration over $c_{p\,pot}$ yields no contribution. Therefore,

$$C_{DP} = -4 \; \varepsilon^{3/2} \frac{U_o}{U_\infty} \int_o^1 \frac{u_{pot}}{U_\infty} \; U' \;\; (X,0) \; \frac{d\overline{y}_c}{dx} \; d\frac{x}{L} \hspace{1cm} (50)$$

Since $D\bar{y}_c/dx < 0$ in the region of the trailing edge, the pressure drag is positive for positive values of $U'(X,o)$. If the coordinate X is introduced into Equation (5), then one obtains the following expression from Equation (50):

$$C_{DP} = -4\epsilon^{5/2} \frac{U_o}{U_\infty} \int_\infty^o \frac{u_{pot}(X,0)}{U_\infty} U'(X,0) \frac{d\bar{y}_c}{dx} dX \qquad (51)$$

If we assume that the integral for a given airfoil is a constant, then we obtain

$$C_{D_P} = C \epsilon^{5/2} \qquad (52)$$

or corresponding to Equation (1):

$$C_{DP} = C_1 C_{fo}^{5/4} \qquad (53)$$

If we assume that the friction coefficient C_{fo} at the trailing edge remains proportional to the value at the trailing edge of a flat plate, then one obtains with the help of an interpolation formula from Schlichting:[13]

$$C_{DP} = C_2 [2 \log Re - 0.65]^{-2.875} \qquad (54)$$

where

$$Re = \frac{U_\infty L}{\nu} \qquad (55)$$

Using an interpolation formula from Schultz-Grunow, the result is

$$C_{DP} = C_3 (\log Re)^{-3.23} \qquad (56)$$

The coefficient for the friction drag is given by

$$C_{DF} = \frac{D_F}{\frac{\rho}{2}U_\infty^2 L} = 2 \int_0^1 C_f(x) d\frac{X}{L} \qquad (57)$$

If we assume that $C_f(x)$ is proportional to C_{fo}, then the ratio of the pressure drag and friction drag is given by

$$\frac{C_{DP}}{C_{DF}} = C_4 \cdot \epsilon^{1/2} = C_5 C_{fo}^{1/4} = C_6 [2 \log Re - 0,65]^{-0,575}$$
$$= C_7 [2 \log Re]^{-0.646} \qquad (58)$$

With increasing Reynolds number, the ratio of pressure coefficient to friction coefficient will decrease. The pressure drag will then continue to decrease faster than the friction drag.

For the symmetric Joukowsky airfoil with 15% thickness ratio and with transition at 15% chord length, the following values can be determined:

$$C_1 = 5,5 \qquad C_2 = 1,9 \qquad C_3 = 0,58 \qquad C_4 = 1,3$$

$$C_5 = 1,1 \qquad C_6 = 0,86 \qquad C_7 = 0,69$$

Re	C_{fo}	ε	C_D	C_{DF}	C_{DP}	$\dfrac{C_{DP}}{C_{DF}}$
10^6	$1,6.10^{-3}$	0,028	0,0100	0,0082	0,0018	0,22
10^7	$1,1.10^{-3}$	0,023	0,0068	0,0057	0,0011	0,19

The value of the total drag ($Re = 10^7$) is in good agreement with results in Reference 14.

REFERENCES

1. Prandtl, L., "Aerodynamic Theory," Durrand, W.F., Ed., Springer Verlag, Berlin, 1935.

2. Thwaites, B., "Incompressible Aerodynamics," Oxford, 1960.

3. Stewartson, K., "Multistructured Boundary Layers on Flat Plates and Related Bodies" in Advances in Applied Mechanics, Academic Press, New York, p. 146-234, 1974.

4. Melnik, R.E. and R. Chow, "Asymptotic Theory of Two Dimensional Trailing Edge Flows," Grumman Research Department Report RE-510J, November 1975.

5. Stewartson, K., "On the Flow Near the Trailing Edge of a Flat Plate II," Mathematika, Vol. 16, 1969.

6. Messiter, A.F., "Boundary Layer Flow Near the Trailing Edge of a Flat Plate," SIAM J. Appl. Math., Vol. 18, 1970.

7. Brown, S.N. and K. Stewartson, "Trailing Edge Stall," J. Fluid Mech., Vol. 42, 1970.

8. Adamson, T.C., Jr., and A. Feo, "Interactions Between a Shock Wave and a Turbulent Boundary Layer in Transonic Flow," SIAM J. App. Math., Vol. 29, No. 1, July 1975.

9. Melnik, R.E. and B. Grossman, "Analysis of the Interaction Between a Weak Normal Shock Wave with a Turbulent Boundary Layer," AIAA Paper 74-598, 1974.

10. Mellor, G.L., "The Large Reynolds Number Asymptotic Theory of Turbulent Boundary Layers," Int. J. Eng. Sci., Vol. 10, 1972.

11. Yanjik, K., "Asymptotic Theory of Turbulent Shear Flows," J. Fluid Mech., Vol. 42, 1970.

12. Bush, W.B. and F. Fendell, "Asymptotic Analysis of Turbulent Channel and Boundary Layer Flow," J. Fluid Mech., Vol. 56, 1972.

13. Schlichting, H., "Boundary Layer Theory," McGraw-Hill, New York, 1955.

14. Smith, A.M.O. and T. Cebecci, "Remarks on Methods for Predicting Viscous Drag," in "Aerodynamic Drag," AGARD-CPP-124, 1973.
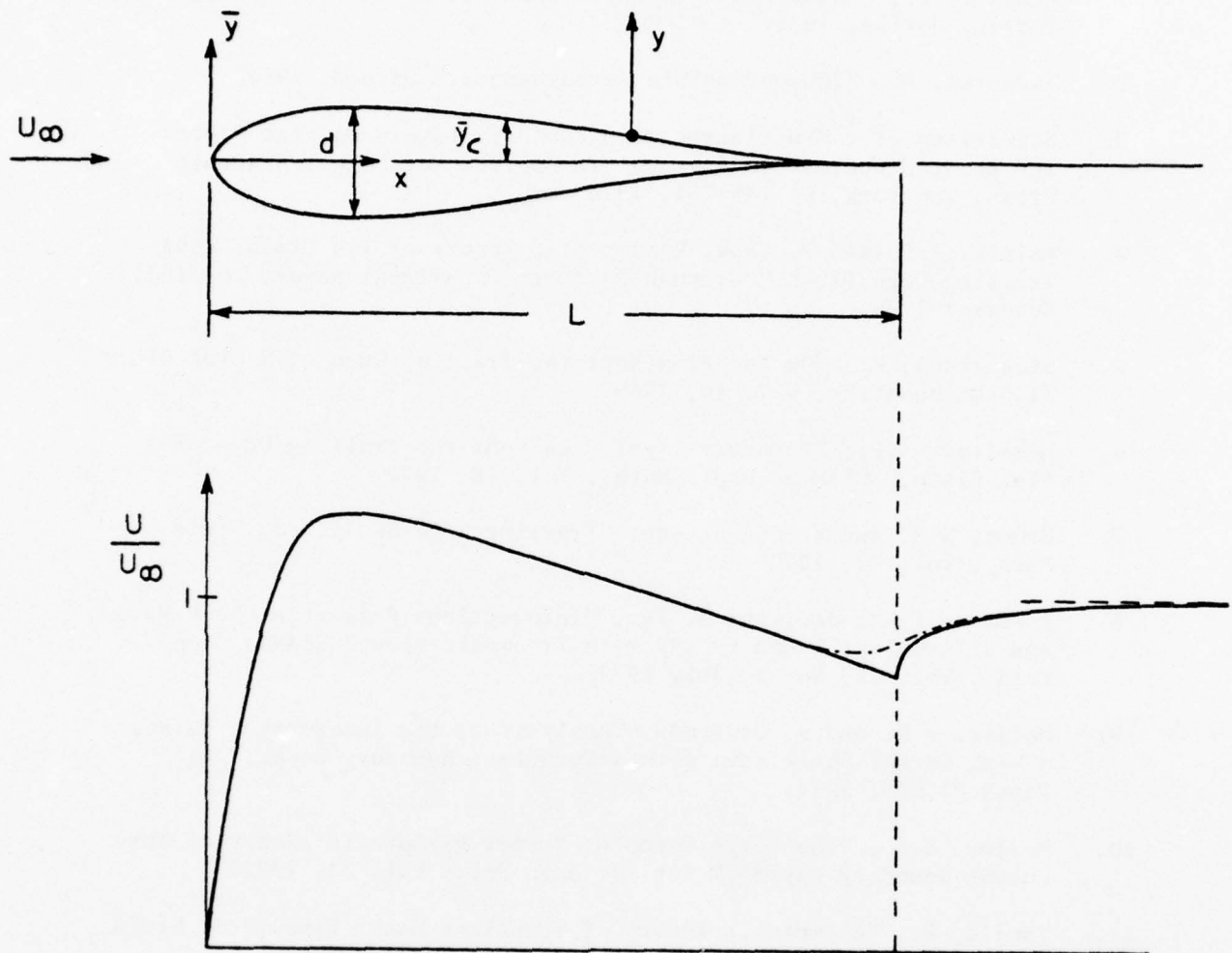
FIGURE 1

FIGURE I. VELOCITY DISTRIBUTION ON THE CONTOUR OF A SYMMETRIC
JOUKOWSKY AIRFOIL AT ZERO ANGLE OF ATTACK

——————   INVISCID FLOW

—·—·—·—   INCLUDING OUTER FLOW TURBULENT BOUNDARY
LAYER INTERACTION NEAR TRAILING EDGE

FIGURE 2

Effect of inviscid flow on turbulent boundary layer

Interaction of inviscid flow and turbulent boundary layer

Effect of inviscid flow on turbulent wake

POTENTIAL FLOW

POTENTIAL FLOW

$O(\epsilon)$

WAKE

POTENTIAL FLOW

$O(\epsilon)$

INVISCID ROTATIONAL FLOW

BLENDING LAYER $O(\epsilon^2)$

WALL LAYER $O(\epsilon\hat{\epsilon})$

$O(\epsilon)$

POTENTIAL FLOW

OUTER BOUNDARY LAYER $O(\epsilon)$
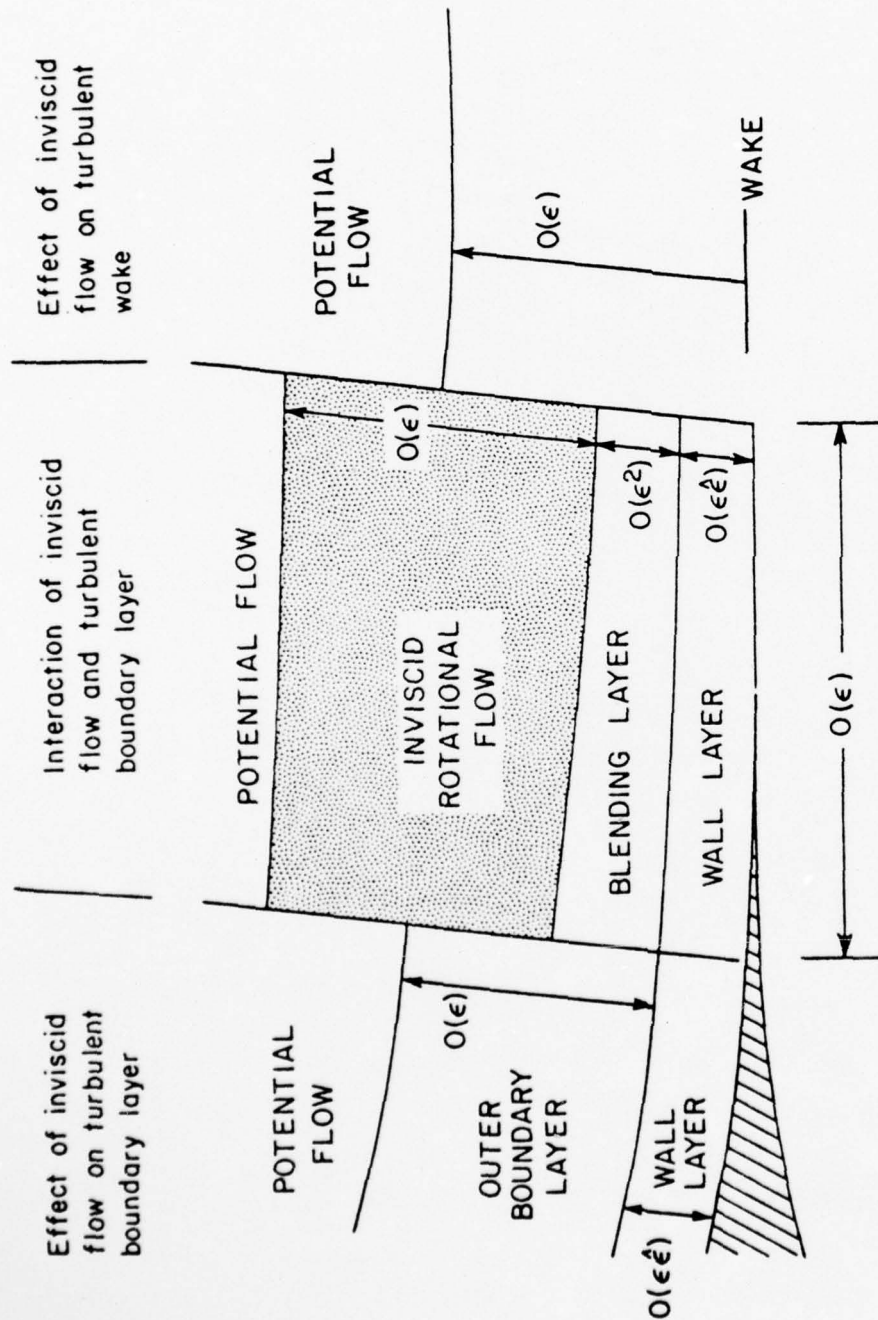
WALL LAYER

$O(\epsilon\hat{\epsilon})$

FIGURE 2. STRUCTURE OF THE FLOW FIELD NEAR THE TRAILING EDGE OF A SYMMETRICAL AIRFOIL

$$\epsilon = \frac{u_{\tau o}}{U_\infty} = \sqrt{\frac{\tau_{wo}}{\varsigma U\infty^2}} = \sqrt{\frac{C_{fo}}{2}}$$

INDEX o REFERS TO THE TRAILING EDGE

$$\hat{\epsilon} = (\epsilon^2 Re)^{-1}$$

DETERMINATION OF TURBULENCE TRANSPORT PROPERTIES
IN A MACH 4.9 TURBULENT SEPARATED FLOW USING
THE LASER DOPPLER VELOCIMETER

by

Robert L. P. Voisinet and William J. Yanta
Naval Surface Weapons Center
White Oak Laboratory
Silver Spring, Maryland

INTRODUCTION

This paper describes a continuation of the separated flow field
measurements which have been presented in Reference 1. The turbulent
transport properties in the separated flow were evaluated to comple-
ment the mean flow measurements obtained previously. The technique
of using the laser doppler velocimeter (LDV) to obtain turbulent
transport properties is described in Reference 2. Comparisons of
the data are made with the transport terms calculated from the time-
averaged conservation equations using measured mean flow inputs as
described in Reference 3.

EXPERIMENTAL SETUP

LDV measurements were made in the NSWC Boundary Layer Channel at five
locations along the test plate corresponding to 61, 70, 74, 80, and
86 inches downstream of the nozzle throat. The first two measuring
stations are located ahead of the interaction, the next two are
within the interaction region, and the last is downstream of reattach-
ment (see Fig. 1). The supply temperature was 600°R, the wall
temperature near adiabatic, and the supply pressure was 5 atmospheres

except for two profiles which were obtained for 1 and 10 atmospheres at X=61 inches.

The LDV system used in the tests is commonly referred to as the dual scatter or differential Doppler system and is described in some detail in Reference 2.

RESULTS

The turbulent shear stress distributions ahead of the interaction are shown in Figure 2 and compared with the zero-pressure-gradient data of Reference 3. The effect of Reynolds number on the distributions is minimal. The measured distributions are lower than the data of Reference 3 which may be due to the strong favorable pressure gradient history in the flow.

The longitudinal turbulence intensity distributions are presented in Figure 3. A sharp increase in the turbulence intensity is seen at $Y/\delta \approx 0.3$ for the profiles downstream of separation. This peak remains high even for the profile downstream of reattachment. The question might arise as to whether the measured fluctuations are due to turbulence or flow unsteadiness. It is interesting to note how the freestream turbulence level remains low. One might expect the free-stream turbulence to increase accordingly if the flow was unsteady.

The turbulent shear stress distributions are shown in Figure 4. Again a peaking of the distribution occurs for those profiles downstream of separation and is evident for the profile downstream of reattachment. The shear stress distributions for those locations inside the separation bubble are negative. For the profile downstream of reattachment the shear stress near the wall projects to a positive value again. The mixing length distributions are shown in Figure 5.

CONCLUSIONS

The Laser Doppler Velocimeter has been shown to be a viable tool for the measurement of a complex separated flow field. The LDV velocity measurements show good agreement with mean flow measurements obtained using conventional probes and the turbulence properties show good correlation with other data.

384

REFERENCES

1. Voisinet, R.L.P., "An Experimental Investigation of the Turbulent Boundary Layer Separation Induced by a Continuous Flow Compression," AGARD CP 168 on "Flow Separation" 27-30 May 1975

2. Yanta, W.J. and Lee, R.E., "Measurements of Mach 3 Turbulence Transport Properties on a Nozzle Wall," AIAA Journal, Vol. 14, No. 6, June 1976

3. Lee, R.E. and Smith, R.A., "Evaluation of Mach 5 Nozzle Wall Turbulent Transport Models," AIAA Journal, Vol. 13, No. 2., February 1975, pp 177-184

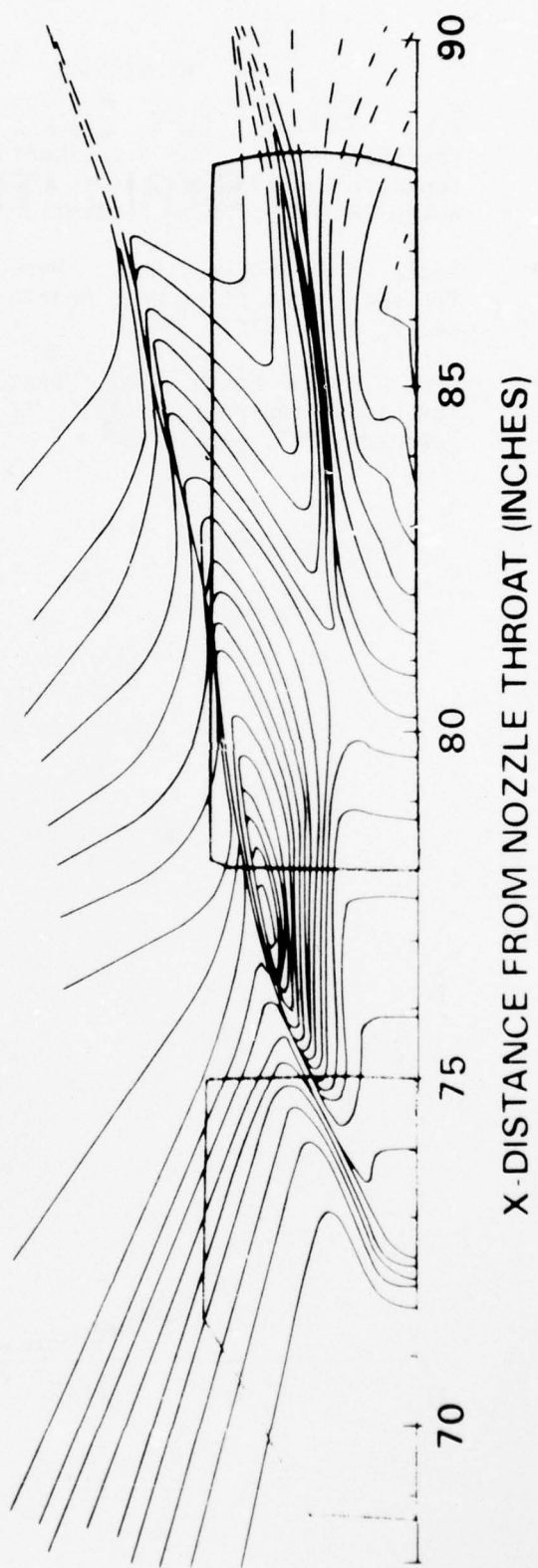# SCHLIEREN PHOTOGRAPHS AND STATIC PRESSURE ISOBAR MAPPING

X-DISTANCE FROM NOZZLE THROAT (INCHES)

Figure 1

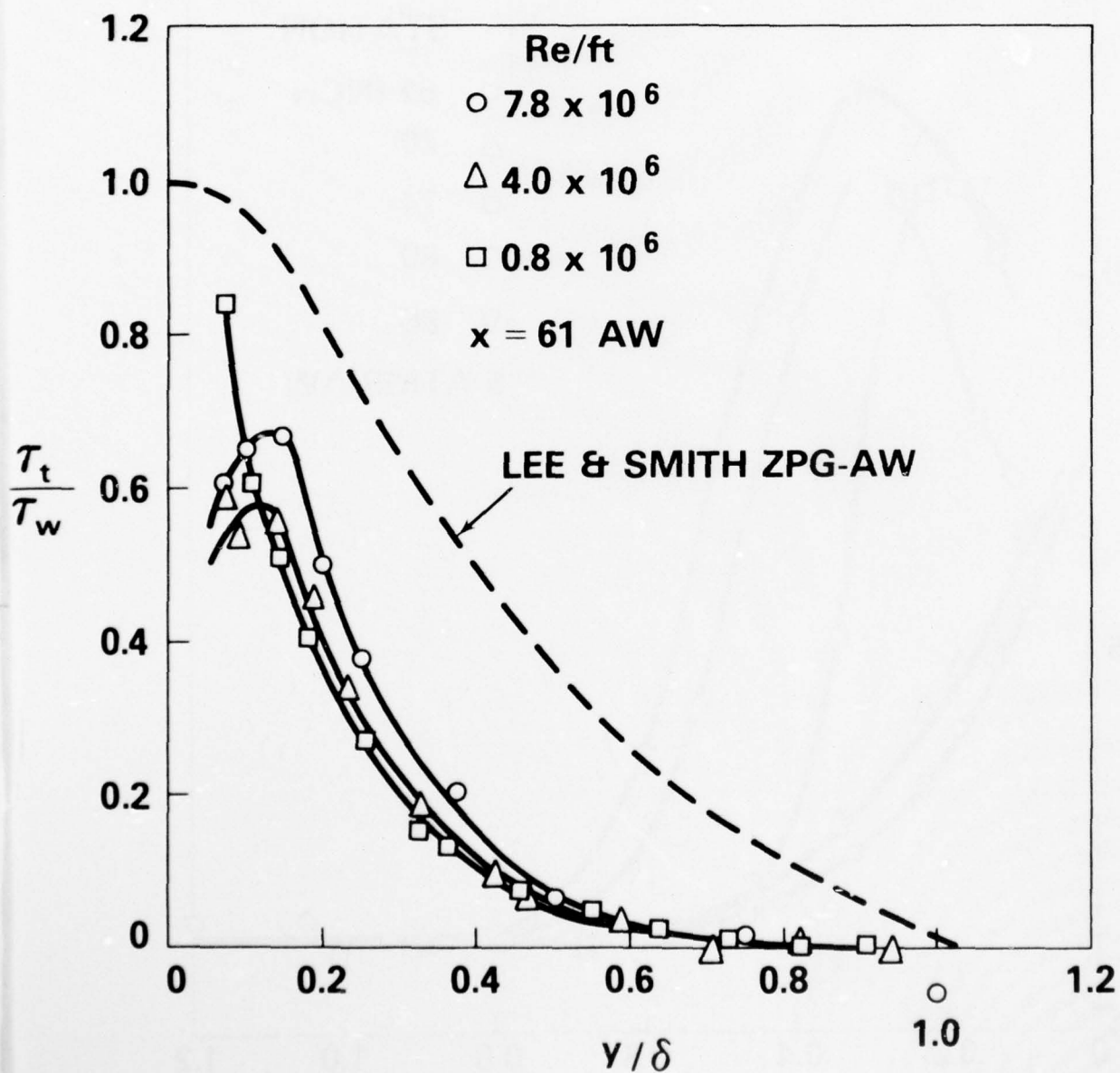# TURBULENT SHEAR STRESS DISTRIBUTIONS

Figure 2

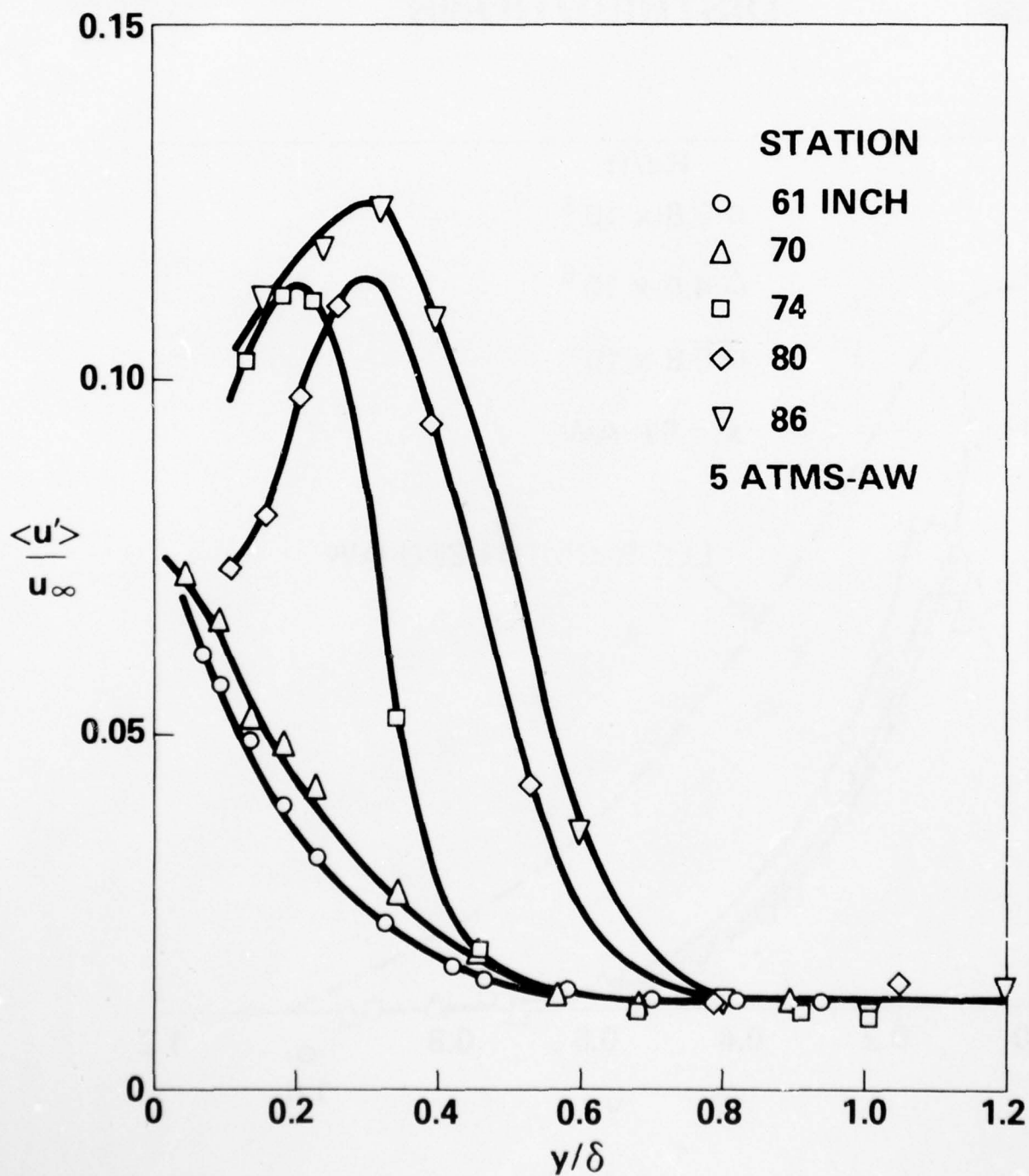# TURBULENCE INTENSITY
DISTRIBUTIONS (LONGITUDINAL)

Figure 3
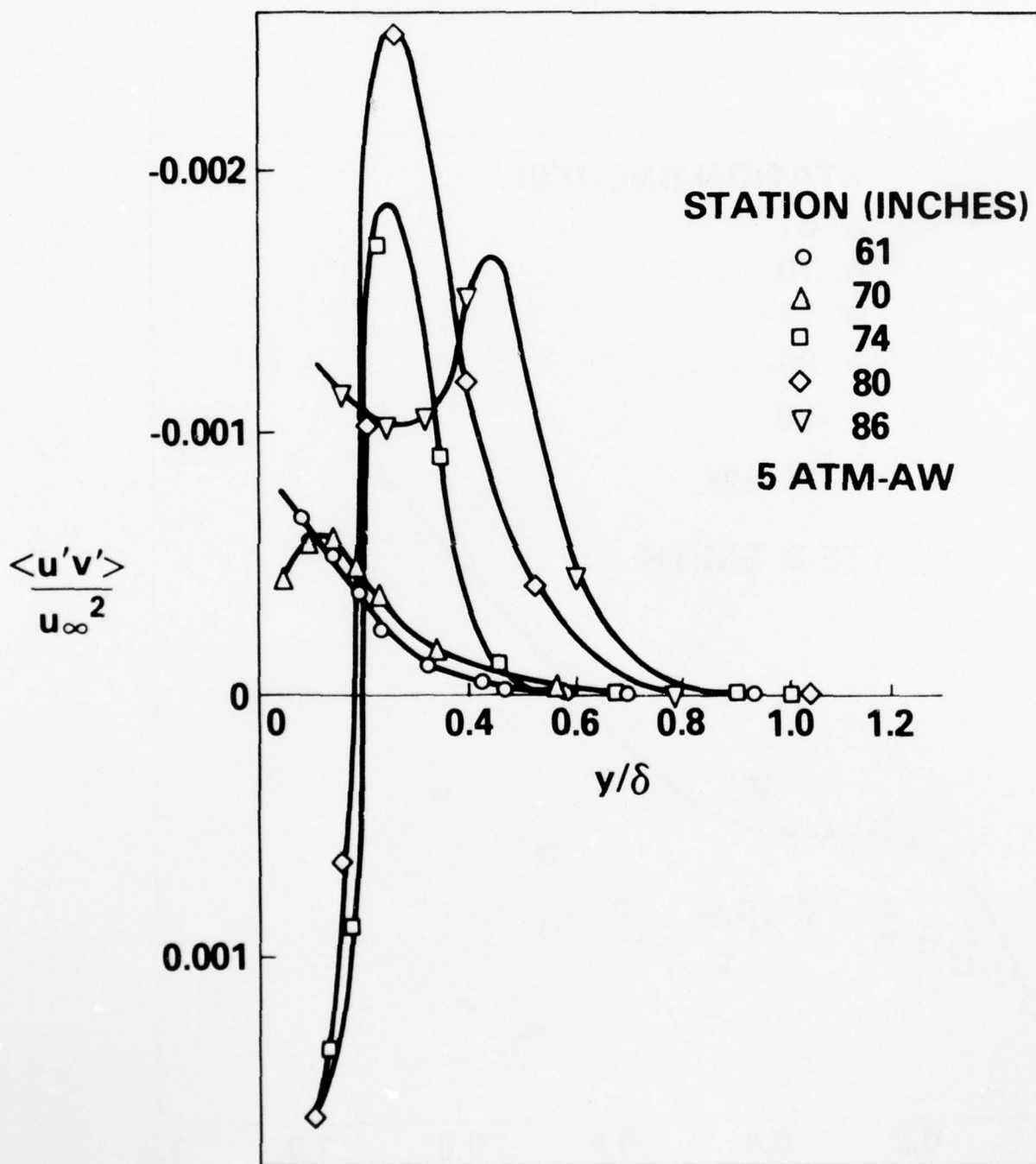
TURBULENT SHEARING STRESS DISTRIBUTIONS
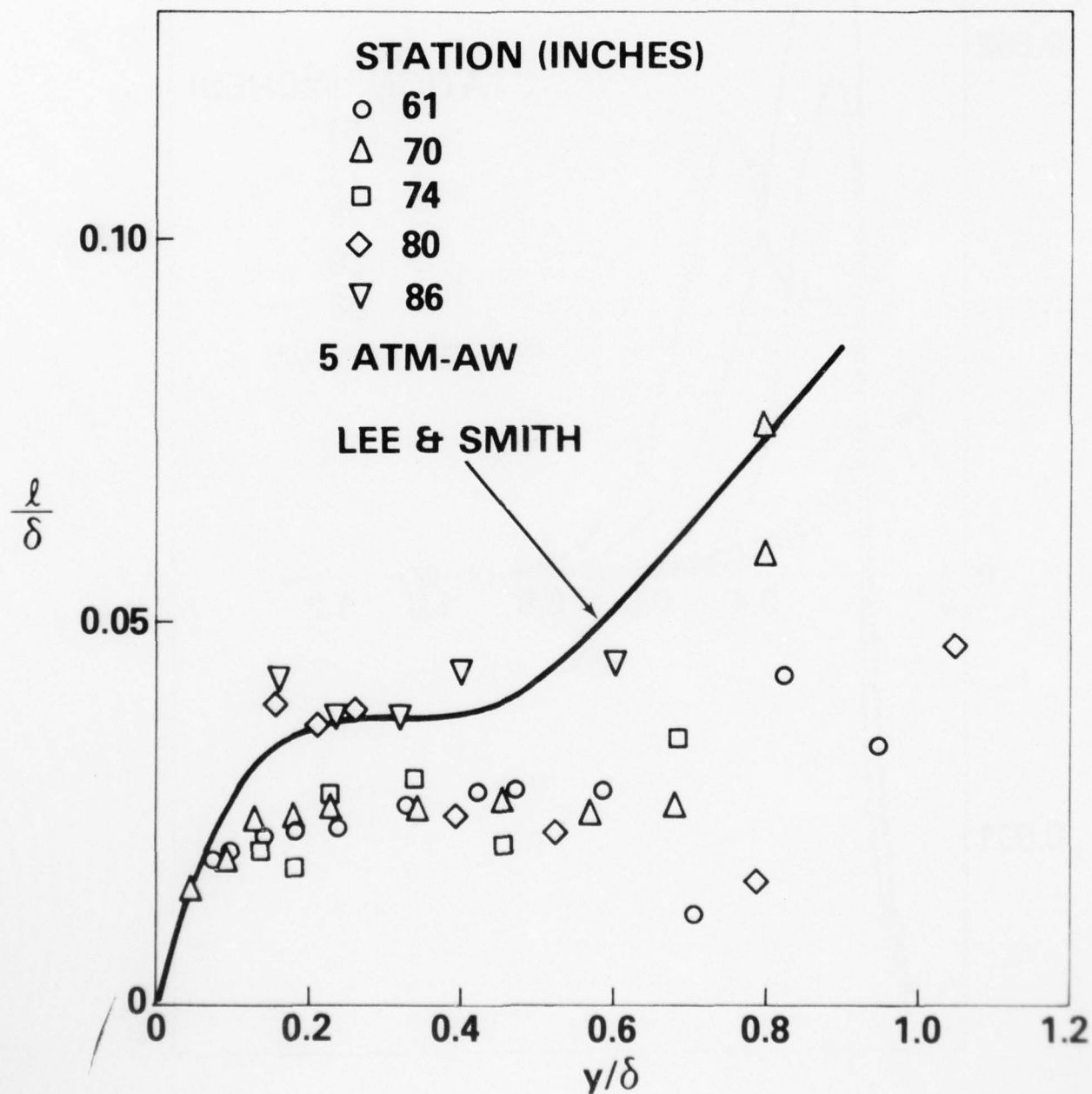

Figure 4

MIXING LENGTH DISTRIBUTION

Figure 5
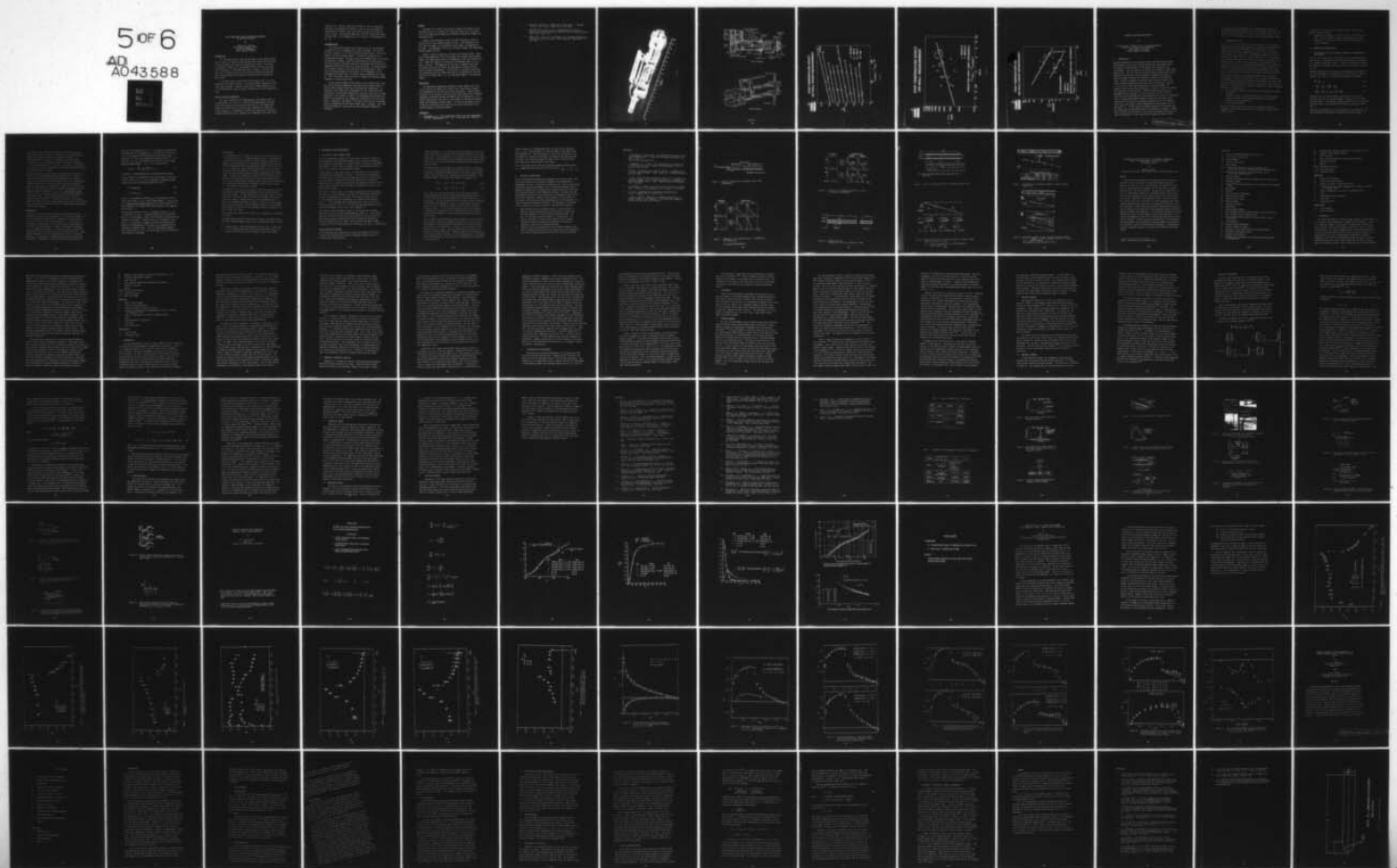
STEP TEMPERATURE EFFECTS ON DIRECT MEASUREMENT
OF SKIN-FRICTION DRAG

by

Robert L.P. Voisinet
Naval Surface Weapons Center
White Oak Laboratory
Silver Spring, Maryland

INTRODUCTION

It is well known that a local discontinuity in the surface tempera-
ture of a body will markedly influence the heat transfer from the fluid
to the body region over which the discontinuity exists. This effect
is especially evident in the measurement of heat transfer using plug-
type calorimeters in high-speed wind-tunnel testing. A similar local
"hot spot" condition can occur in skin-friction balance testing when
small surface elements are thermally insulated from the surrounding
main surface.

A literature survey revealed only one reference (Ref. 1) to this
temperature step effect on drag. Its results showed a negligible effect
(less than 2 percent). However, recent tests at NSWC indicated errors
in the measured wall shear as high as 30 percent for a 100°R temperature
step.

FACILITY AND TEST CONDITIONS

Tests were conducted in the NSWC Boundary Layer Channel (Ref. 2)
at Mach numbers of 2.9 and 4.9. Skin-friction measurements were made
on the flat nozzle wall test plate of the facility. The supply tem-
perature was 760°R and the test plate was cryogenically cooled with
liquid nitrogen to a temperature of 160°R thus simulating a "cold wall"
condition where the wall-to-adiabatic-wall temperature ratio was of the

order of 0.25. The test setup for the Mach 4.9 case is essentially the same as was reported in Reference 3 and the test procedure and techniques for the Mach 3 case were similar, except for a change in nozzle contour. The Reynolds number was varied by changing the supply pressure from 1 to 10 atmospheres at M = 4.9 and 1 to 2 atmospheres at M = 2.9.

INSTRUMENTATION

The skin-friction balance used in these tests was one developed at NSWC for use in a cryogenically cooled environment. The balance, pictured in Figure 1, is of the self-nulling type whereby a 0.781-inch diameter circular floating element is continually recentered by a servo-feedback system. The basic design of the NSWC balance is described in Reference 4; however, significant modifications have been made to the basic design to increase sensitivity and decrease the pressure and temperature drift which existed in the early design. The unique feature of the balance design is the "clam shell" mechanism which is used to cool the floating element of the balance to the temperature of the surrounding test plate prior to taking a shear measurement (see Figure 2). This "clam shell" device was used to regulate the floating element temperature in the present tests.

If the floating element of the balance is not cooled during a test run, the equilibrium temperature which the balance element attains is several hundred degrees above the surrounding wall temperature. By obtaining a wall shear stress measurements at this condition and for successively cooler element temperatures using the "clam shell" cooling mechanism, a plot similar to Figure 3 can be generated which shows the effect of the element-to-wall temperature difference on the wall shear stress. From plots like Figure 3, the ideal wall shear can be obtained from an extrapolation of the data to where $T_{wall} = T_{element}$. The slope of this extrapolation line gives the error per degree temperature difference.

RESULTS

The effect of a locally "hot" balance element with respect to the surrounding wall is to increase the local wall shear stress in proportion to the magnitude of temperature difference between the element and surrounding wall.

Figure 4 shows the Mach 4.9 and 2.9 results plotted in terms of absolute error versus Reynolds number per foot. The magnitude of the error does not appear to be dependent on Mach number nor magnitude of the shear. The magnitude of the error decreases slightly with decreasing Reynolds number per foot.

Figure 5 shows the same data in terms of the percent error. Since the absolute magnitude of the error changes only slightly with Reynolds number, the figure merely depicts the magnitude of the local shear variation. Shown for comparison is the data of Westkaemper (Ref. 1) for a Mach 5 condition. The magnitude of that data is somewhat lower than the present data but well within the experimental accuracy of skin-friction balance measurements. In particular, it should be noted that the percentage error can become very large as the magnitude of the wall shear stress becomes small, i.e., for high Mach numbers or low Reynolds numbers.

CONCLUSIONS

An experimental program was conducted at Mach numbers of 4.9 and 2.9 to evaluate the effects of a locally "hot" shear-balance element on the magnitude of the wall shear stress measurement. Results showed the effect of an increase in the local wall shear stress with increasing temperature difference between the element and surrounding wall. The absolute magnitude of this error is only slightly a function of Reynolds number and independent of Mach number. As such the percentage error is a function of absolute shear stress and can reach high values at low Reynolds numbers or high Mach numbers.

REFERENCES

1.   Westkaemper, J.C., "Step Temperature Effects on Direct Measurements of Drag," _AIAA Journal_, Vol. 1, No. 7, July 1963, pp. 1708-1710.

2.   Lee, R.E., Yanta, W.J., Leonas, A.C., and Carner, J., "The NOL
      Boundary Layer Channel," NOLTR 66-185, Nov. 1966.

3.   Voisinet, R.L.P. and Lee, R.E., "Measurements of a Mach 4.9
      Zero-Pressure Gradient Turbulent Boundary Layer with Heat Transfer,"
      NOLTR 72-232, Sept. 1972.

4.   Bruno, J.R., Yanta, W.J., and Risher, D.B., "Balance for Measuring
      Skin-Friction in the Presence of Heat Transfer," NOLTR 69-56,
      June 1969.

Figure 1
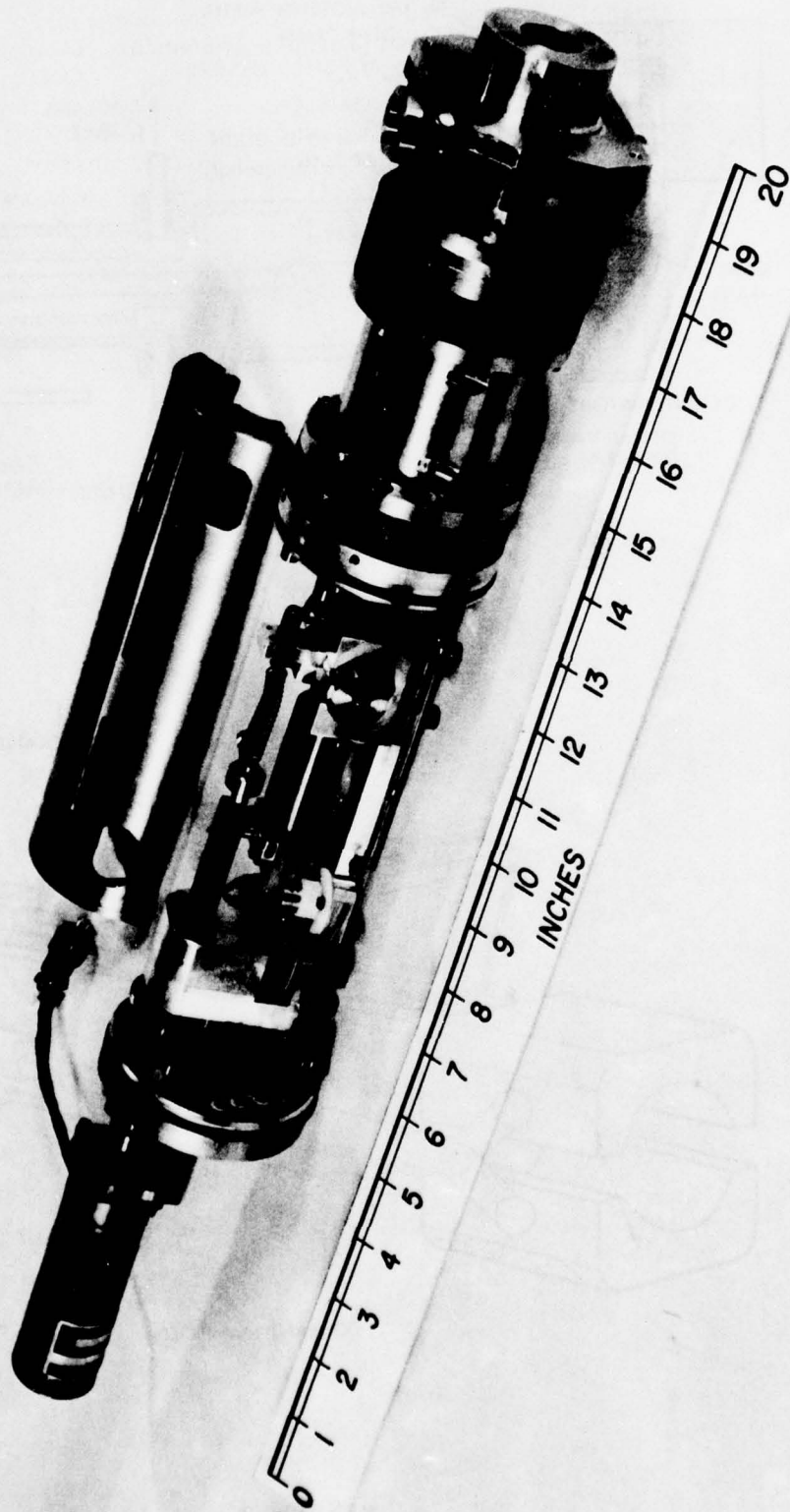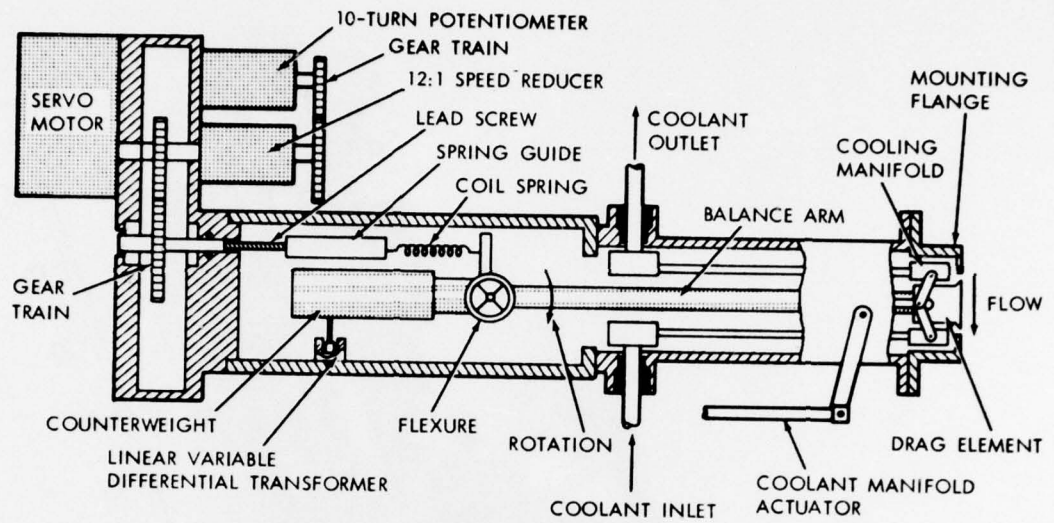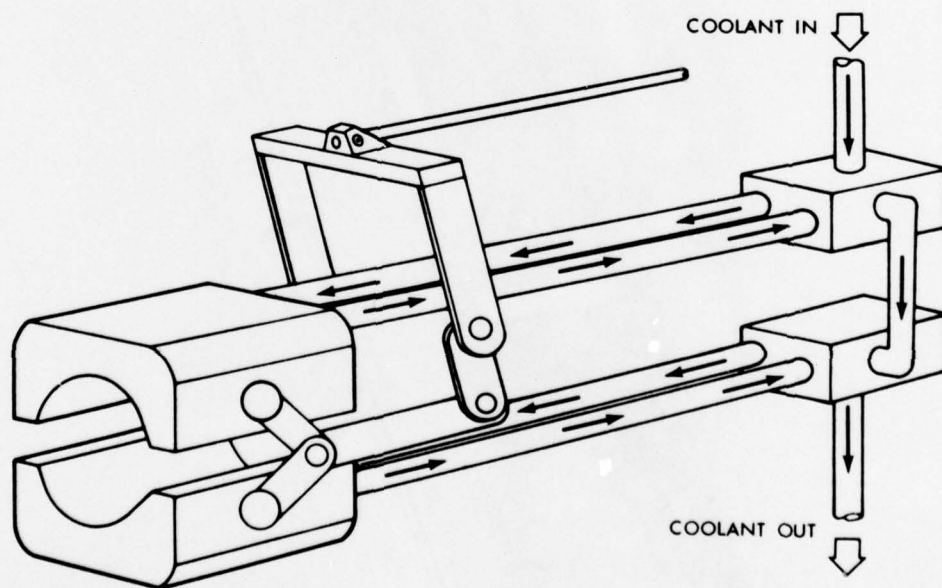
BALANCE SCHEMATIC

COOLANT MANIFOLD

Figure 2

396

STEP TEMPERATURE EFFECT
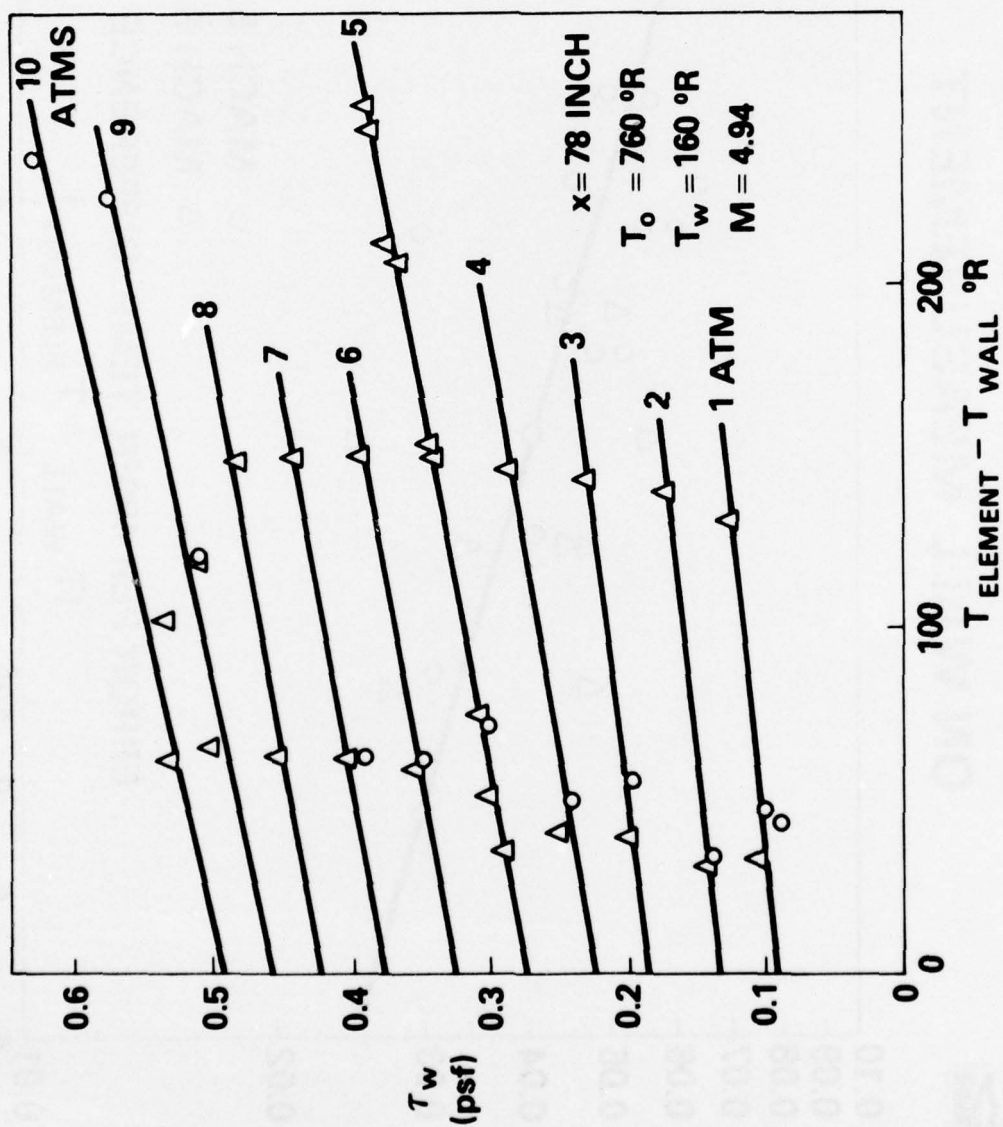# ON WALL SHEAR MEASUREMENT

Figure 3
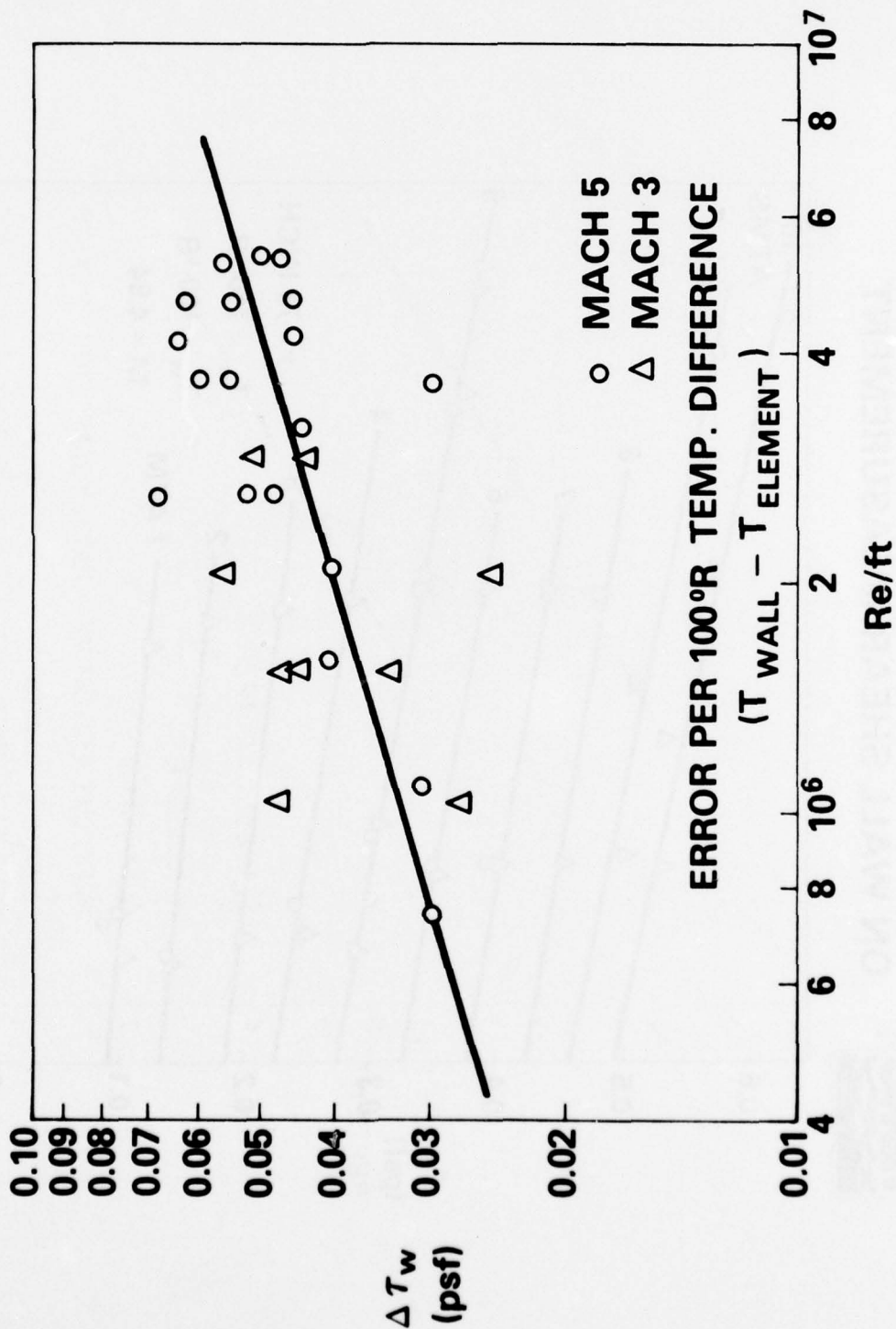
STEP TEMPERATURE EFFECT ON WALL MEASUREMENT

Figure 4
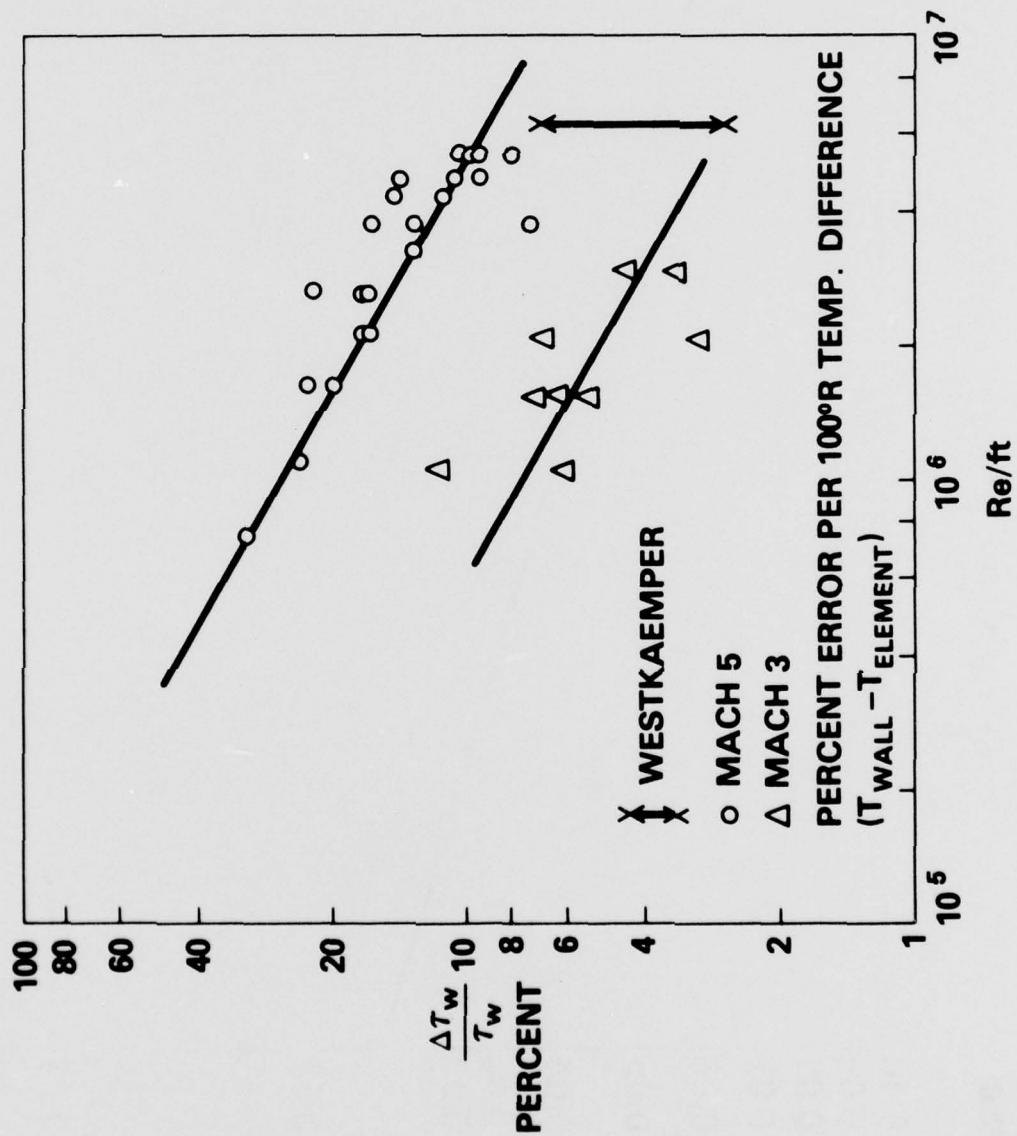
STEP TEMPERATURE EFFECT
ON WALL SHEAR MEASUREMENT

Figure 5

399

BOUNDARY LAYERS WITH RELAXATION

by

V. Vasanta Ram, H. Herwig, and F. von Schulz-Hausmann
Institute of Thermo- and Fluiddynamics
Ruhr-University Bochum
Federal Republic of Germany

1. INTRODUCTION

Prediction methods for the turbulent boundary layer hitherto proposed
and developed, have met with limited success when the boundary layer
in question has been subject to disturbances like separation and
reattachment. Such disturbances are however not uncommon in engineering
applications. The root cause for the unsatisfactory performance of the
methods can be traced to the experimentally supported fact that the
separation bubble disturbs the turbulence structure of the boundary
layer. Prediction methods on the other hand invariably contain, for
closure reasons, hypotheses which imply that the turbulence structure
is in a state of local equilibrium that is suitably defined. An
example of such an equilibrium hypothesis is the wall similarity implied
the logarithmic law of the wall. Prediction methods based on such
hypotheses may be expected to yield satisfactory results as long as
the effect of the disturbances on the quantities of interest is negligible.
There is enough experimental evidence to point out that these "local
equilibrium" laws are not an adequate representation for the boundary
layer for a considerable distance downstream of reattachment, see for
Equation[1,2]. In this region it becomes necessary to incorporate into
the methods the "relaxation process of the turbulence structure," without
which satisfactory description of the turbulent boundary layer does not
seem to be possible. In the light of this experience there is need

to study closely the development of the boundary layer subject to a
disturbance with particular attention to its turbulence structure. The
object of this short paper is to report on the present status of work
done in this area by the group of authors at the Ruhr-University Bochum.

2. FRAMEWORK FOR STUDY

First, it is useful to recall some essential features of the turbulent
boundary layer that has not undergone any significant disturbances (or
where disturbances have died down). The characteristics of such a
boundary layer, broadly termed *"boundary layers close to equilibrium"*
may be summarized as follows [3]. The turbulent boundary layer can be
thought of as comprising of two distenct regions, viz. the outer wake-
like region and the inner wall region. The turbulence structure of the
boundary layer as a whole reveals characteristics observed in free-
shear flows as well as in wall-bounded turbulent flows, the former being
dominant in the outer region and the latter in regions closer to the
wall. The outer region has a long memory meaning thereby that distur-
bances in this region die down more slowly than in the inner region[4].

Our framework for study of the turbulent boundary layer subject to
disturbances is based on the conjecture that in spite of disturbances
to the turbulence structure the two-layer concept might still hold, with
different relaxation mechanisms for the outer and inner layer, see also
Reference 3. More precisely we thought it worthwhile to adopt an approach
through the following steps.

a. The relaxation behaviour of the outer and inner region is studied
   separately.
b. Attempt to relate the relaxation behaviour of the outer region
   to that in a wake, and the relaxation behaviour in the inner
   region to that in channel flow.
c. Piece the two together.

There is a distinct possibility that the two-layer concept may be
inadequate. Additional layers will have to be added if found so from
further studies.

According to the spirit of this scheme this paper contains results under two heads as follows.

A. Computational attempts for the outer part of the boundary layer with a "relaxation model" that has been developed for wakes.

B. Experiments in "relaxing" channel flow with a step change in surface roughness.

A. RELAXATION IN OUTER REGION

3. THE OUTER REGION OF THE TURBULENT BOUNDARY LAYER DOWNSTREAM OF REATTACHMENT

The test case choosen for the outer region of the turbulent boundary layer subject to disturbances was the flow downstream of reattachment on a backward-facing step, Figure 1. Detailed experimental results on this geometrical configuration were available to the authors, see Reference 1.

Findings presented in this section are the outcome of our attempts to trace the development of the profiles of the mean velocity u and the turbulent shear stress through the following set of equations:

$$\frac{\partial u}{\partial x} + \frac{\partial v}{\partial y} = 0 \tag{1a}$$

$$u \frac{\partial u}{\partial x} + v \frac{\partial u}{\partial y} = U_o \frac{dU_o}{dx} + \frac{1}{\rho} \frac{\partial \tau}{\partial y} \tag{1b}$$

$$u \frac{d\tau}{dx} + v \frac{\partial \tau}{\partial y} = A(\tau - \tau_{eq}) + \frac{\partial}{\partial y} (\nu_\tau \frac{\partial \tau}{\partial y}) \tag{1c}$$

Equations (1a,b) are the boundary layer equations (in the usual notation) with the viscous terms dropped. Equation (1c) is a shear stress equation. A few comments regarding the terms in the shear stress equation as well as our motivation for using this form are in order here.

The model stress Equation (1c) was proposed by R. Narasimha et al.,[5] while studying the relaxation of turbulence structure in wakes. It

was found satisfactory when describing both the mean velocity and shear-stress profiles in wakes. In Equation (1c)τ_{eq} represents the shear-stress distribution when the turbulence structure is in equilibrium, $A[\frac{1}{s}]$ is related to a relaxation time for turbulence structure and ν_τ a "stress diffusion" term. The system of equations is closed if the quantities A, τ_{eq}, and ν_τ are defined. Points that are important in the definition of these quantities have been discussed by R. Narasimha and A. Prabhu[5].

Our motivation for using this shear-stress equation was, besides its simplicity, the following physically plausible reason. Since it is more or less established and generally agreed that the turbulence structure in the outer part of the boundary layer is not significantly different from that in a wake we may expect that their relaxation behaviour, when subject to disturbances, would also be similar to each other. Translation of this physical concept into mathematical terms would mean that the quantities A, τ_{eq}, and ν_τ when suitably scaled should be the same for wakes and for the flow in the outer region of the boundary layer. In this approach the question of scaling is perhaps the most crucial one. A detailed discussion of this point is beyond the scope of this short resumé, but we shall return to it briefly later, after presenting some results of our "computational experiments" with this model equation.

Computations

In Figures 2 and 3 typical mean velocity and shear-stress profiles obtained by solving the set of Equations (1a-c) have been plotted. The circles indicate our measurements (cf. Reference 1, DEA-proceedings 1975) on a 10 mm step. The starting station $x = x_o$ is at $x_o/H = 17$ (H denotes the step height, $x = 0$ is at the step), starting profiles for u and are from experiments. Further, the solution of Equation (1a-c) is sought in a region $y > y_o$, with y_o the wall distance where the Reynolds shear-stress profile at the starting station $\tau(x_o, y)$ goes through a maximum. The x-wise distribution of u and τ at the inner boundary $y = y_o$ required as a boundary condition was also taken from measurements. Furthermore, since the equations are not valid up to

the wall the distribution of v at $y = y_0$ needs to be prescribed. We thought that the v-component at $y = y_0$ would not be grossly in error if the departure from equilibrium of the inner layer is neglected (the inner layer approaches equilibrium faster!), so we obtained v at $y = y_0$ by using the law of the wall with the <u>measured wall-shear stress</u>. v at $y = y_0$ is then given by

$$v(x,y_0) = - \frac{du_\tau}{dx} y_0 (\frac{1}{\kappa} \ln\frac{u_\tau y_0}{\nu} + C) \qquad (2)$$

The numerical scheme employed was the Crank-Nicholson method.

Figure 3 shows the distribution of the shear stress τ and of the velocity defect $w = U_0 - u$ at a station $\frac{x}{H} = 42$ obtained through computation using the following values for A and ν_τ:

$$A = 0.00082 \; U_0/\theta \qquad (3a)$$

$$\nu_\tau = 0.552 \; w_0 \; \delta_w \qquad (3b)$$

where θ is the momentum thickness, δ_w is the "thickness" of the outer layer (from $y = y_0$ to a wall distance where $u = 0.98 \; U_0$) and w_0 the <u>characteristic shear velocity</u> for the defect profile. We have obtained w_0 by fitting Coles' wake function to the computed defect profile.

The functional forms of A and ν_τ in Equation (3a,b) (i.e., the scaling laws for A and ν_τ) have been taken over from those for wakes (cf. R. Narasimha). They will be briefly discussed under the section "scaling laws". However, prior to a discussion of this point it is instructive to gather a picture of the qualitative pattern of the dependance of the result on the magnitude of the constants in Equation (3a,b). This is illustrated in Figure 4 which shows plots of w and τ at a station $\frac{x}{H} = 30$ for the values of the constants as indicated.

Scaling Laws

It is appropriate at this stage to enter into a brief discussion of the scaling laws for A and ν_τ, given by Equation (3a,b). The product w_o δ_w in Equation (3b) conveys that the "stress diffusion coefficient ν_τ" <u>scales</u> in the same manner as the conventional kinematic eddy viscosity. It must be emphasized that the conventional kinematic eddy viscosity ν_e ($\tau = \nu_e \rho \frac{\partial u}{\partial y}$) and the stress diffusion coefficient ν_τ are not by this definition said to be identical. Instead of the constant multiplying factor one could envisage a function of the dimensionless wall distance $(\frac{y-y_o}{\delta_w})$. However, this complication seemed to us to be unnecessary at this stage of investigation since it has been established that wakes as well as the outer region of boundary layers (both close to equilibrium) are satisfactorily described by a "constant" eddy-viscosity concept, i.e., independant of the normal coordinate.

The quantities to be used in the scaling law for the relaxation time in Equation (3a) deserve deeper investigation, which would go beyond the scope of this paper. It would suffice here to say that whereas for wakes this choice of U_o and θ seems to be intuitively obvious (both are constants for a wake at constant pressure), for the boundary layer the choice of the momentum thickness θ, which is subject to a steady change even at constant pressure, involves ambiguity and hence is questionable. Provisionally we have used the local momentum thickness in Equation (3a) which changes only slowly.

We may temporarily summarize the results of our computational experiments as follows:

The simple model equation for shear stress, Equation (3c) might suffice to handle turbulent boundary layers with a disturbed turbulence structure if

a. a proper choice of the scaling quantities for A and ν_τ is made; and
b. if the relaxation behaviour of the inner region, which enters the boundary conditions for the outer region is taken into account.

406

B. RELAXATION IN THE INNER REGION

4. RELAXATION IN WALL-BOUNDED FLOWS

Due to the fundamental importance of relaxation in the wall region for
the development of the turbulent boundary layer disturbed by separation
and subsequent reattachment, we naturally wanted to study this phenomenon
and thought it is best done in a simple case of wall-bounded turbulent
flow, viz. the flow in a two-dimensional channel.

A long channel of large aspect ratio (1:25) was built for this purpose.
Its dimensions are indicated in Figure 4. The walls were covered with
sand paper up to a certain section; downstream of this section the walls
were left smooth. We desired to study the mean flow and turbulence
quantities in the transition region where the turbulence structure under-
goes a change, relaxing from the rough wall turbulence structure to the
smooth wall structure.

The flow in a channel with a step change in roughness has been studied
prior to us - to our knowledge - by Jacobs [6] and by Tani and Makita[7].
In Jacob's experiments only one wall of the channel of aspect ratio
1:3 was roughened and his measurements are of mean velocity profiles
alone [6]. Tani and Makita have studied the mean flow as well as the
turbulence quantities $\overline{u'^2}$, $\overline{v'^2}$, and $\overline{u'v'}$ with both the mutually facing
walls of the channel (aspect ratio 1:10) roughened [7].

Experiments of Tani and Makita as well as our present the following
physical picture of the relaxation phenomenon (Figure 5). The pressure
gradient at the wall adjusts itself most rapidly to the new state, the
mean-velocity profile following next and the turbulence quantities
adjusting themselves still slower. One may define relaxation lengths
in respect of each of these quantities, denoted L_p, $L_{\overline{u}}$, and L_τ , respectively.

Present Status of our Work

The streamwise pressure gradient at the wall and profiles of the mean
velocity have been measured, profiles of Reynolds shear stress are
currently under investigation.

Plotted in Figure 6 are the measured pressure distribution at the wall and the development of the mean-velocity profile from the rough to the smooth state. Our measurements are in substantial qualitative agreement with those of Tani and Makita, one noteworthy qualitative feature being the local rise in pressure immediately following the step change from rough to smooth.

Of primary interest in the study of a relaxation process is the law of decay and the relaxation length contained in the law. Our preliminary theoretical investigations suggested that in the middle region of the channel, away from the walls, the departure from the asymptotic (fully developed smooth) state might follow simply an exponential law:

$$u(x,y) - u_g(y) = f(y) \exp \left(-\frac{x}{L_{\bar{u}}}\right) \tag{4a}$$

$$\tau(x,y) - \tau_g(y) = g(y) \exp \left(-\frac{x}{L_\tau}\right) \tag{4b}$$

$u_g(y)$ and $\tau_g(y)$ are the mean-velocity and shear-stress profiles corresponding to the fully developed smooth walled channel flow, $f(y)$ and $g(y)$ are functions with the dimensions of velocity and stress respectively. The form of Equations (4a,b) further provides a procedure to determine from experiments - that is, if the measured quantities obey this law - the relaxation lengths for mean velocity and shear stress, $L_{\bar{u}}$ and L_τ. It may be noted in passing that in the absence of a framework such as Equations (4a,b) the determination of relaxation length from measurements is rather uncertain and ambiguous and hence unsatisfactory.

We have analyzed our measurements hitherto conducted as well as those of Tani and Makita within this framework and the results are in Figure 7. (Measurements of Tani and Makita were available to us only on a small-sized graph in their publication, so there is some uncertainty in the numerical values.) Figure 7 shows the departure for velocity $u(x,y)$ - $u_g(y)$ on a semilogarithmic plot. Keeping in mind the preliminary nature of our data reduction at present, the form of the equation is encouraging. The relaxation length $L_{\bar{u}}$ in the two sets of experiments are in the table in the same figure.

Figure 8 shows on a semilogarithmic plot the shear-stress departure $\tau(x,y) - \tau_g(y)$ from experiments of Tani and Makita, taken again from their publication. (Our measurements of shear-stress profiles are not yet complete!) Even here the prospect for Equation (4b) does not seem to be bad. The relaxation length for shear stress L_τ obtained after data reduction has been entered in the figure.

It is of interest to note that the relaxation length for mean velocity $L_{\bar{u}}$ is roughly two-thirds of that for shear stress L_τ $(\dfrac{L_{\bar{u}}}{H} \simeq 6, \quad \dfrac{L_\tau}{H} \simeq 9)$.

5. OUTLINE OF FUTURE WORK

It has already been established by experiments by us and by others that the salient feature of the turbulent boundary layer downstream of reattachment is that its turbulence structure is not close to equilibrium. The obvious conclusion herefrom is that a prediction procedure that is capable of handling such a boundary layer should necessarily incorporate the relaxation process of the turbulence structure. We would like our experiments and analysis to be viewed only as intermediate steps on the road to this objective. However, from an analysis of our work up to the present, both theoretical and experimental, we feel encouraged to go further along the path hitherto persued. The following is only meant to focus attention on what we believe are the main steps involved.

a. When dealing with any relaxation process, a basic question is about the relation between the various relaxation lengths and the flow parameters of the problem like Reynolds number. We wish to term these relations broadly as "scaling laws". We propose (and hope!) to obtain these scaling laws by careful theoretical analysis supported by experiments on simple con- figurations like flow in a channel and wake.

b. Develop a theoretical framework for the turbulent boundary layer with a disturbed turbulence structure that explicitly incorporates the distinct relaxation behavior of the inner and outer regions.

References

1. P. Wauschkuhn, V. Vasanta Ram: Die turbulente Grenzschicht hinter einem Ablösungsgebiet. Zeitschrift für Flugwissenschaften, 23, Heft 1, 1975.
   See also DEA Proceedings 1975.

2. P. Bradshaw, F. Y. F. Wong: The reattachment and relaxation of a turbulent shear layer. Journal of Fluid Mechanics, Vol. 52, part. 1, 1972, 113-135.

3. D. Coles: The young persons guide to the data. Computation of turbulent boundary layers - 1968. AFOSR-IFP. Stanford Conference, Vol. II, 1-45.

4. I. Tani: Review of some experimental results on the response of a turbulent boundary layer to sudden perturbations. Computation of turbulent boundary layers - 1968. AFOSR-IFP-Stanford Conference, Vol. I, 483-494.

5. R. Narasimha, A. Prabhu: Equilibrium and relaxation in turbulent wakes. Journal of Fluid Mechanics, Vol. 54, part 1, 1972, 1-38.

6. W. Jacobs: Umformung eines turbulenten Geschwindigkeits-profils. ZAMM 19, Heft 2, 1939, 87-100.

7. I. Tani, H. Makita: Response of a turbulent shear flow to a stepwise change in wall roughness. Zeitschrift für Flugwissen-schaften 19, Heft 8/9, 1971, 335-339.
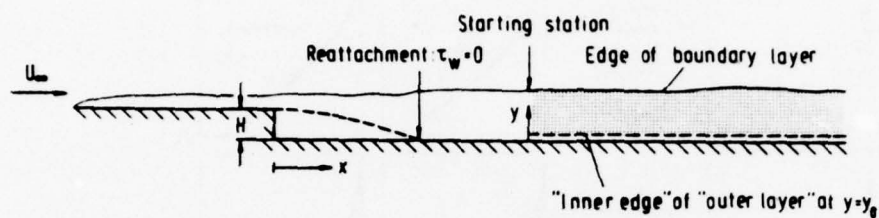
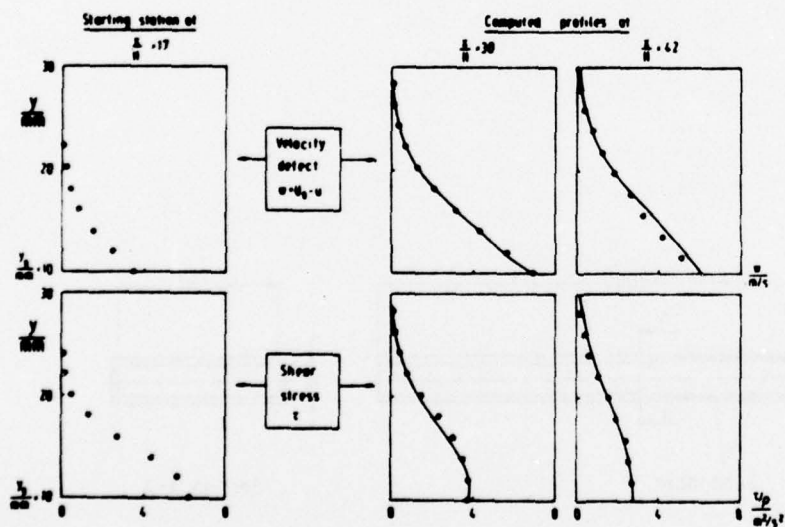Figure 1. Region of computation for boundary layer after reattachment.

Figure 2. Computed w- and τ-profiles with a = 0.00082 U_o/θ
ν_τ = 0,552 $w_o\,\delta_w$

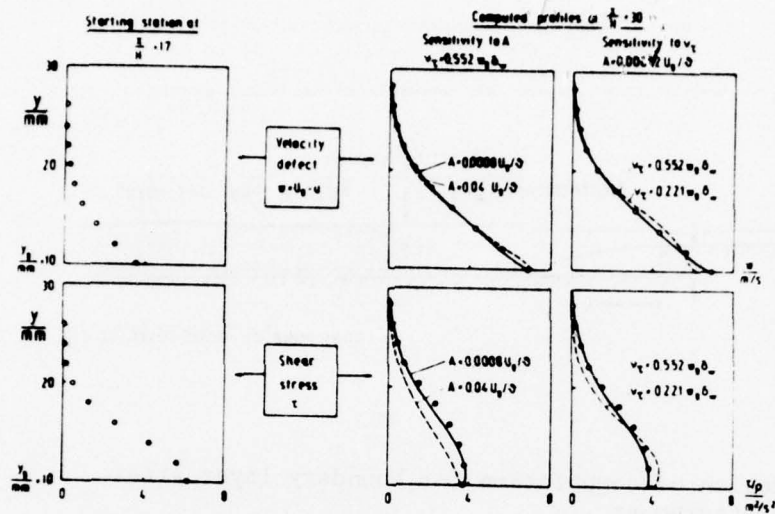(o indicates measurements)

Figure 3. Sensitivity of computed profiles to A and ν_τ
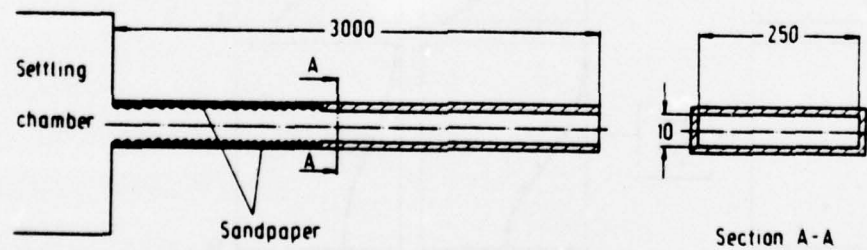(o indicates measurements)

Figure 4. Channel flow rig
(Drawing not to scale, dimensions in mm)

Physical quantity	Wall pressure gradient dp/dx	Mean velocity $\bar{u}(y)$	Shear stress $\tau(y)$
Relaxation length	L_p	$L_{\bar{u}}$	L_τ
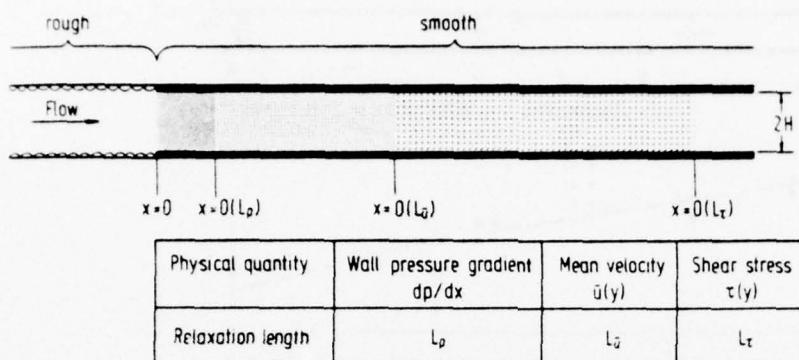
Note: Physical quantity reaches asymptotic value over a distance of the order of its relaxation length

Figure 5. Scheme of relaxation process in turbulent channel flow.
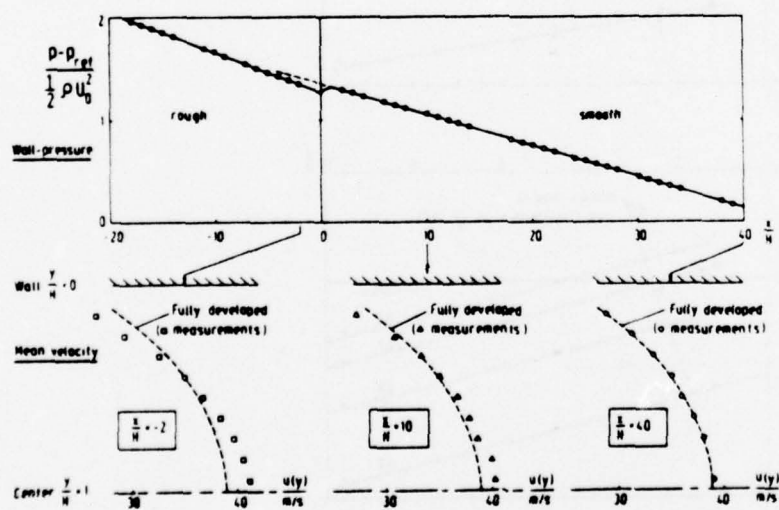
Figure 6. Measured wall pressure and mean velocity in rough to smooth channel flow at U_o = 39 m/s.

(U_o - velocity at center line of fully developed smooth channel flow)

413

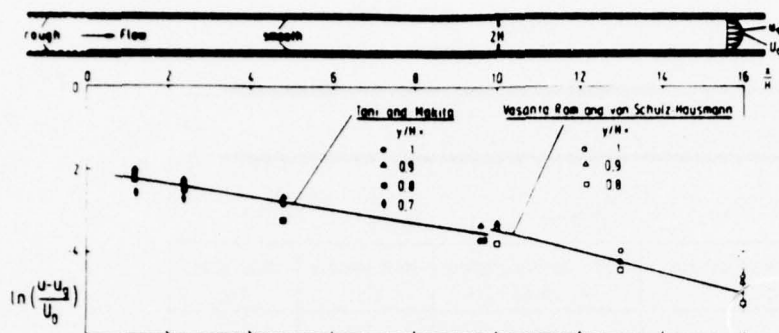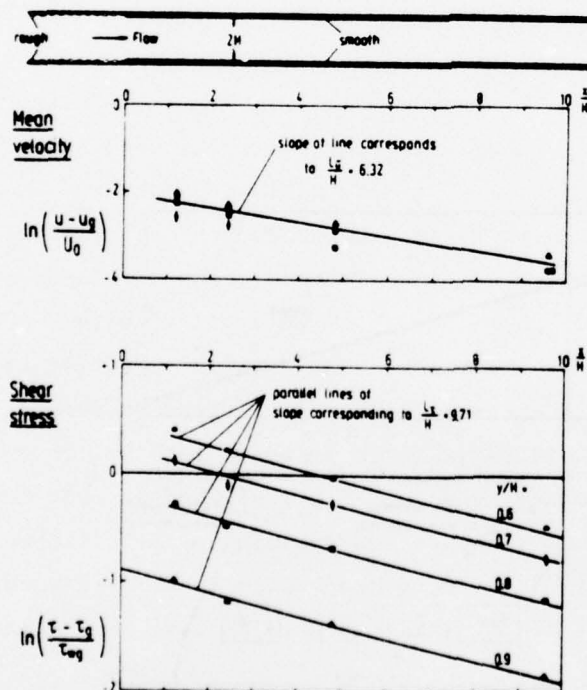Figure 7. Determination of relaxation length in rough to smooth channel flow.

Figure 8. Relaxation lengths for mean velocity and shear stress.
u_g, τ_g - asymptotic (fully developed) profiles in smooth walled channel.
Measurements by Tani and Makita (1971).

414

EXPERIMENTS PLANNED SPECIFICALLY FOR DEVELOPING TURBULENCE MODELS IN COMPUTATIONS OF FLOW FIELDS AROUND AERODYNAMIC SHAPES

by

Joseph G. Marvin[*]
Ames Research Center, NASA, Moffett Field, California 94035, USA

SUMMARY

Building-block experiments and companion numerical simulations intended to verify and guide turbulence modeling are described. Emphasis is given to a series of experiments and computations being used to enhance modeling development for the shock-wave turbulent-boundary-layer interaction problem. Experiments and computations for the exact experimental geometry are presented for Mach and Reynolds number ranges encompassing those associated with full-scale vehicles in transonic, supersonic, and hypersonic flight. Results are given for transonic flow over a circular-arc airfoil undergoing shock-wave-induced, boundary-layer separation, for supersonic flow along a tube wall undergoing a normal-shock-wave-induced, boundary-layer separation, and for supersonic and hypersonic flows undergoing oblique-shock-wave-induced, boundary-layer separation. The detailed experimental data and computations, which use the complete Navier-Stokes equations, are discussed with emphasis on their role in establishing the concept of turbulence modeling. The main conclusion established is that turbulence modeling progress can be achieved by combining numerical simulations with carefully controlled building-block experiments. Extending this concept to complete aircraft is the step to be achieved in the next decade.

---

*Chief, Experimental Fluid Dynamics Branch

NOTATIONS

A   Van Driest damping parameter, Equation (5)

C_F skin-friction coefficient

C_H Stanton Number

C_p pressure coefficient

c   chord length

d_k distance from location of initial pressure rise to
        location of the knee in the pressure distribution curve

d_s distance from location of initial pressure rise to
        location of separation point

e   internal energy

h   distance from wing centerline to upper or lower tunnel wall

L   relaxation length

ℓ_s distance from initial pressure rise to location of reattachment
        point

M   Mach number

p   pressure

q   kinetic energy of turbulence

R   reattachment location

$\overline{R}$ radius of test section

Re   Reynolds number

S   separation location

T   temperature

t   wing maximum thickness

u   mass-averaged velocity parallel to wall in axial direction

v   mass-averaged velocity normal to wall

w   mass-averaged velocity parallel to wall normal to axial
        direction

x   axial distance

Δx distance between mesh points

y   distance normal to surface

Z_s distance of shock extent relative to wing centerline

γ Klebenoff intermittency factor

δ boundary-layer thickness

δ_o boundary-layer thickness at first measuring station ahead
        of interaction

416

δ_u boundary-layer thickness upstream of interaction ($x = 0$)

δ_1^* kinematic displacement thickness

ϵ eddy viscosity

ϵ_u eddy viscosity immediately upstream of interaction

μ molecular viscosity

ρ density

$\rho\overline{v'u'}$ turbulent shear stress

τ, τ_{xr} total shear stress

$<(\ )>$ root mean square

Subscripts

c   based on chord length

i,j   indices in tensor notation

k   value at the knee in the pressure curve

o   location of incident shock impingement on surface in absence of a boundary layer

s   value at shock wave; also value of separation point

t   total

u   value upstream of interaction

w   wall value

∞ free-stream value

Superscripts

$(\bar{\ })$ time averaged

$(\ )'$ fluctuating value

1. INTRODUCTION

The rapid development of faster, larger computers has been paralleled by an equally rapid development of computational aerodynamics. Table 1 is a simplified summary of the status of computational aerodynamics that illustrates its rapid development, particularly since the start of this decade. The stage of approximation of the governing equations has been divided into four progressively more complex categories, culminating with the viscous time-dependent Navier-Stokes equations. Beginning in the 1930's and progressing through the 1960's, inviscid linearized theory in various refined stages has been used to design many of the current aircraft. Many limitations in this theory required

417

that much of the configuration design be accomplished experimentally, however. In the 1970's, development of inviscid nonlinear theory advanced more rapidly and is nearing completion. Computations for transonic and hypersonic flight have been made for realistic aerospace vehicle geometries (notable examples are References 1-3). The major limitation of these computations is that they cannot handle separated flows. To provide that capability, the next stage of equation approximation requires utilization of the time-averaged Navier-Stokes equations or their approximation. Such computations for turbulent flows, which are ubiquitous and very important in most aerospace vehicle applications, are in the early stages of development. The limitation of these computations is the accuracy of the turbulence model used to complete the system of governing equations; that item now paces the development. Once this stage of approximation reaches the point of practical utility, it is expected that computations using the complete Navier-Stokes equations in time-dependent form will begin their development, but an advanced computer is essential before practical computations become available because the resolution scale for the smaller turbulent eddies precludes the use of any current computers. Thus, within the next decade, it could be possible to numerically simulate the flow about complete aircraft shapes including important viscous effects. Then, performing complimentary roles, the computer and the large wind tunnel can significantly reduce the time and cost required to develop new aerospace vehicles[4].

The Navier-Stokes equations are the basic governing equations used to describe most fluid mechanics phenomena. They apply to problems involving turbulent flow, but to avoid the difficulty of describing every discrete turbulent motion possible, they are usually time averaged. Time averaging eliminates some of the information -ontained in the equations and, moreover, results in more unknowns than governing equations through the introduction of apparent Reynolds stresses for the actual transfer of momentum by velocity fluctuations. Therefore, the extra unknowns must be represented by physically plausible combinations of quantities for which transport equations are expressed in terms of constants or empirical functions considered as known or

δ_u boundary-layer thickness upstream of interaction $(x = 0)$

δ_i^* kinematic displacement thickness

ε eddy viscosity

ε_u eddy viscosity immediately upstream of interaction

μ molecular viscosity

ρ density

$\rho\overline{v'u'}$ turbulent shear stress

τ, τ_{xr} total shear stress

$<(\ )>$ root mean square

Subscripts

c   based on chord length

i,j   indices in tensor notation

k   value at the knee in the pressure curve

o   location of incident shock impingement on surface in absence of a boundary layer

s   value at shock wave; also value of separation point

t   total

u   value upstream of interaction

w   wall value

∞ free-stream value

Superscripts

$(\tilde{\ })$ time averaged

$(\ )'$ fluctuating value

1. INTRODUCTION

The rapid development of faster, larger computers has been paralleled by an equally rapid development of computational aerodynamics. Table 1 is a simplified summary of the status of computational aerodynamics that illustrates its rapid development, particularly since the start of this decade. The stage of approximation of the governing equations has been divided into four progressively more complex categories, culminating with the viscous time-dependent Navier-Stokes equations. Beginning in the 1930's and progressing through the 1960's, inviscid linearized theory in various refined stages has been used to design many of the current aircraft. Many limitations in this theory required

417

expressible in terms of the mean variables. The problem of reducing the unknowns to equal the number of equations is referred to as the "closure problem"; the process of expressing the unknowns as transport equations in terms of empirical functions or constants is referred to as "turbulence modeling."

Historically, progress in turbulence modeling has been slow and deliberate, and has relied substantially on a few carefully controlled experiments performed over a range of test conditions. Such experiments could be called "building-block experiments" because they provided the gage for establishing the credibility of computational techniques, but, more importantly, because they provided physically meaningful concepts that were used to enhance heuristic modeling ideas. The conference on the computation of turbulent flows held at Stanford University in 1968[5] used many of the classic experiments to assess progress in predicting incompressible, attached, turbulent flows. Later that same year, the conference on compressible turbulent flows held at Langley Research Center[6] concluded that very few, if any, compressible flow experiments in the building-block category were being performed.

Relying on historical perspective, if progress in modeling is to be made, it will come through combining a broad experimental effort with computational techniques and modeling ideas[5]. However, for compressible flow, the problems are more complex because Mach number must be included in the list of variables. Figure 1 shows the Mach-Reynolds number domain for aerospace vehicles and it gives an indication of the range of conditions over which adequate turbulence modeling must be provided. The upper limit on Reynolds number based on vehicle length[7] is shown as well as the upper limit based on wing chord. Mach number varies between subsonic and hypersonic, encompassing the range encountered by commercial passenger vehicles and NASA's Space Shuttle Vehicle. Figure 2 compares the domain of available experiments that can be used to test turbulence modeling concepts with that for the vehicles. The shaded area represents partially documented experiments where zero- or mild-pressure gradients were impressed on the flow. Reference 8 summarizes available experiments and their measurements. Most of these earlier experiments were performed at lower Reynolds numbers, which made it

difficult for the analysts to confidently predict Reynolds number trends for actual flight conditions and, in most cases, not enough meaningful data were available in any single experiment to assess modeling concepts confidently. Thus, the situation remains somewhat the same as for the development of linearized theory, where designers rely mainly on experiment for their vehicle development. The unshaded area in Figure 2 represents the domain of more recent experiments where shock-induced separation was studied and where specific attempts to document the complete flow-field features have been made or are under way. These latter experiments and companion computations, which to-gether are being used to establish adequate turbulence models for designers, are discussed subsequently. Another disturbing consideration is the lack of large-scale facilities that can operate at Reynolds num-bers high enough to verify complete vehicle designs at the proper Reynolds number[7].

If the concept of numerical simulation of flow fields over complete aircraft is to become a reality, the ability to predict flow-field be-haviors at flight Reynolds numbers and Mach numbers must be developed. This paper illustrates how the computer and the wind tunnel are being used to develop turbulence models for a complex class of fluid-dynamics problems, i.e., turbulent boundary-layer separation caused by the inter-action of a shock wave with a boundary layer. Such a study can be viewed as an early predecessor of the larger problem of using the computer and the wind tunnel to develop real aircraft shapes at reduced cost and time. The first portion of this paper reviews the essential elements of turbulence modeling. Since experiments are an essential part of the concepts established, some recent developments in instrumentation are reviewed to establish confidence in our ability to measure quantities that can guide the modeling processes. Thereafter, the modeling con-cepts and experimental results are compared and conclusions drawn.

2. ELEMENTS OF TURBULENCE MODELING

Turbulence is a random, dissipative, three-dimensional phenomenon that involves many characteristic scales. While the Navier-Stokes equations contain all the necessary elements of the physics involved

420

in the processes, practical solutions are possible only if approximate forms of the equations are used. Of the myriad of possible approximations, the Reynolds-averaged form[9] of these equations has proven the most fruitful and probably will continue to be so for some time. However, averaging introduces unknowns and, in order to close the equations, it is essential that certain terms be modeled.

The objective of turbulence modeling is to provide the designer with useful tools for confidently predicting the behavior of turbulent flows. The basic three elements leading to this objective - are experiments, intuitive modeling concepts, and the computer code - shown in Figure 3. Each element is essential, and they are not easily separated. The process could start with the modeling concept or with the experiments. Historically, the process began with experimental observations that later led to modeling concepts. This trend is beginning to change in that model development and experiment are being performed in parallel and coordinated efforts. Once the modeling concepts are established, the computer code can be assembled. This particular sequence is essential for complicated equation systems because the modeling concepts can often alter the order of the equation system or method of solution. Once the code has been established, it can be compared with and verified by the experiments. If the experiments provide enough detail, they can guide changes in the modeling concepts and the process is continued until the predictive capability of the code can be established and provided to the designer. An important aspect of the computation code development is that it be directed specifically to the geometry of the experiment and that it use exact experimental initial conditions so that no doubt can be cast on the comparative results.

Experiments that support the modeling process can be classified according to the type of closure proposed. Bradshaw[10] broadly classified these closures as first and higher order, corresponding, respectively, to closures either where second-order correlations like the Reynolds stresses are expressed in terms of first-order correlations like the mean velocity, viz., algebraic mixing length or eddy viscosity formulations, or where third- and higher-order correlations are expressed in terms of second- and higher-order correlations by introducing additional

421

appropriate transport equations. Table 2 gives the elements of the experiments required, depending on the type of equation closure. Verification experiments by their nature require documentation of mean and surface quantities over the practical ranges of flight Mach and Reynolds numbers. These experiments are useful for any closure technique used. First-order modeling experiments are those that require measurements of the shear stress and heat fluxes across the flow field because these quantities provide insight into concepts used to model these terms and provide closure. Such experiments can, but need not be, attempted over the complete Mach and Reynolds number ranges because the verification experiments can test the ability of the model to perform outside the domain where, e.g., the shear stresses have been measured. They must be performed at Reynolds numbers sufficiently high to establish fully developed turbulence. Higher-order modeling experiments require that fluctuating measurements be made across the flow field. Depending on the order of the closure, more and more information on the fluctuating field must be ascertained. As for any modeling experiment, data need not be acquired over the complete Mach and Reynolds number domain provided verification experiments are available. Ideally, one well-conceived experiment could suffice for all three types listed in Table 1. Moreover, the same experimental apparatus and instrumentation can be used to eliminate experimental uncertainties. Coles[11] emphasized this latter aspect when commenting on the flows used as the basis for the Stanford Conference. He also emphasized the need for redundancy of measurement, complete documentation for future reference, and the elimination of three-dimensional uncertainties by, for example, testing axisymmetric configurations.

3. INSTRUMENTATION DEVELOPMENTS

Verification and modeling experiments for incompressible flows have been available for some time. Compressibility introduces complexities into the modeling concepts as well as the experiments. The complexity in the experiments results from the hostile test environment of high Reynolds numbers and high Mach numbers as well as in the use

and interpretation of fluctuating measurement devices. Recent instru-
mentation developments and techniques have made it possible to perform
modeling experiments at high Reynolds numbers and Mach numbers. Results
from two such experiments are given in Figures 4 and 5.

Figure 4 shows the results from several experiments where shear
stress measurements were made across turbulent boundary layers without
pressure gradients. The boundary-layer-edge Mach number in these ex-
periments ranged from subsonic through hypersonic. The solid line in-
dicates the expected variation of the normalized total shear stress
shown in Reference 12 to be independent of edge Mach number. The mea-
surements, obtained with hot-wire and hot-film anemometers and a laser
velocimeter, show the variation of the turbulent component of shear
stress. Except for the decreases near the wall ($y/\delta < 0.3$) due mainly
to the relatively large probe size and not the difference between the
total and turbulent magnitudes of shear, the data agree reasonably well
with the expected trends in shear distribution. Work is in progress
to resolve the differences near the wall and some success has been
achieved (Reference 13, e.g., use of a split-film anemometer minimizes
the probe scale effects and suppresses the decrease to a location much
nearer the wall). From such data, mixing lengths or eddy viscosities
in the outer regions of a turbulent boundary layer can be determined
for use in first-order modeling concepts.

Figure 5 shows the results of measurements of the fluctuating
velocities and densities across a high-speed subsonic turbulent
boundary layer[14]. These data were obtained with hot-wire and hot-
film anemometers operating at high overheats so that the sensitivities
to various fluctuations can be separated[14]. The solid lines are the
usual ratios 4:3:2 for $(<\mu'>)^2 : (<w'>)^2 : (<v'>)^2$ in incompressible flows.
The compressible measurements agree reasonably well with the ratios
obtained for incompressible flow. Reasonably accurate measurements
for the fluctuating components of the velocity field in compressible
flows can be expected. Also, for modeling purposes, it might only be
necessary to obtain trends in these quantities with parameter changes
such as pressure gradient, Reynolds number, and Mach number rather
than absolute magnitudes.

Recent advances in wall skin-friction measurements techniques have also been reported [15]. Results obtained using these surface-mounted hot-wire gages of the Ludwig type are presented later. The advantage of these gages is that they can be used in either laminar or turbulent flows and they are insensitive to pressure-gradient effects.

4.   EXPERIMENTS

Some of the building-block experiments now being used to predict the behavior of turbulent boundary layers undergoing separation after their interaction with an incident shock wave are described. Each experiment, in which there is a significant coupling of the viscous and inviscid flow fields, has a companion computer simulation that uses the complete time-average, Navier-Stokes equations and requires a large fast computer for their solution. The experiments, in various degrees of completeness at this time, cover a wide range of Mach number and Reynolds number.

4.1   Transonic Regime

The first two experiments involve transonic flows with particular interest directed toward shock-boundary-layer interactions on wings. Figure 6(a) shows the experimental arrangement for a verification experiment [16] being performed on a wing that spans the test section of a high Reynolds number channel recently built at Ames Research Center. The facility operates in a blow-down mode, and the freestream Mach number can be adjusted before or during tests by a translating wedge that acts as a downstream choke. The upper and lower walls are contoured so that strong shocks would not extend to the walls and choke the flow. A thick circular-arc wing (Figure 6(b)) was chosen to allow local airfoil Mach numbers to achieve values where shock-induced separation would occur, but without having the shock extend more than about 2/3 of the distance between the wing and the outer wall. Surface pressures for various Mach numbers and Reynolds numbers have been obtained [16] as well as surface skin friction at specific Reynolds numbers. Still to be obtained are mean velocity data and more skin-friction data.

424

The wing experiment resulted in both shock-induced and trailing-edge-induced separation, depending on the free-stream Mach number. Data were obtained to Reynolds numbers, based on chord length, of 17×10^6. At intermediate Mach numbers, some unsteadiness in the flow field occurred. The results are discussed in detail in Reference 16. Reynolds-number effects for both the trailing edge and shock-induced separation were not significant beyond Reynolds numbers of 10×10^6 based on wing chord. Some results obtained when shock-induced separation occurred are given in Figure 7. Oil-flow patterns (lower portion of the figure) illustrate the two-dimensionality of the flow and the detail in the region downstream of separation. The shadowgraph view near the inter-action clearly illustrates shock-induced separation. The pressure ratios downstream of the shock are below C_p^*, indicating that the flow is slightly supersonic and suggesting the presence of an oblique shock (also apparent in the shadowgraph). Figure 8 presents the air-foil pressures at several Reynolds numbers and the skin-friction measurements at a single Reynolds number. The skin-friction measure-ments were obtainedrecently by Rubesin and Okuno using surface-mounted wire gages specifically developed for this experiment [15]. The location of separation, determined from the oil-flow photograph, is shown on the abscissa of the skin-friction plot. This location also corresponds to the location of the knee in the pressure curve down-stream of the shock. The comparison with the computation is discussed subsequently.

Figure 9 shows the physical arrangement of another transonic flow experiment [17] being used for code verification and model concept development. These tests are also being conducted in the Ames high Reynolds number channel. Supersonic flow was developed at the entrance of an axisymmetric test section and a normal shock wave was positioned at a fixed location by adjusting the location of a downstream shock generator. The relative distance between the shock wave and the down-stream shock generator was always about 1 m. Experimental verification data were obtained for Reynolds numbers, based on distance along a wall to the location of the shock wave, between 9×10^6 and 290×10^6. Over this range of Reynolds number, Mach number varied between 1.35 and 1.45

425

because of the differences in wall boundary-layer growth. With this arrangement, data are also being obtained at constant shock Mach number by allowing the shock position to vary along the tube surface when the Reynolds number is varied. A complete flow documentation, including turbulence measurements, has been performed at a Reynolds number of 37×10^6 where the corresponding Mach number ahead of the shock wave was 1.44.

Examples of the data are presented in Figures 10 and 11. Additional results, including velocity profiles and velocity fluctuation data, are given in Reference 17. The shock position is located at $x/\delta_u = 0$. The pressure rises rapidly downstream of the shock wave and causes separation, after which it increases gradually. The corresponding skin friction is reduced ahead, reverses sign in the separated region, and then increases thereafter. The shear stress data (Figure 11) were obtained with a supported cross-wire anemometer specially designed to withstand the high dynamic pressures encountered in this experiment [17]. The maximum shear stress in the boundary layer shows a significant increase after the shock wave and then decreases downstream toward the value expected for a mild adverse pressure gradient. Downstream of the shock wave beyond the effective boundary layer, some measurable shear was evident. It reverses sign because the mean velocity profiles are retarded, probably resulting from a coalescence of com-pression waves ahead of the shock wave [17] . In this flow, the height of the separated zone was very small and no details were measured in the reversed-flow region.

Documentation of the mean flow over a wide range of Reynolds numbers is now under way. These data will be used to assess the ability of the turbulence model to predict Reynolds-number effects on quantities such as interaction lengths, pressure rise to separation, and the effects of Mach number on incipient separation. An example of this is shown in Figure 12 wherein the pressure rise in separation, as determined from the location of the knee in the pressure curve [18], and the normalized interaction lengths, as determined by measuring the distances from the beginning of the pressure rise to the location of the knee in the pressure curve and to the point of reattachment,

are plotted as a function of Reynolds number. For these data, the test Mach number varied somewhat because the shock was always at the same axial location in the test section. The normalized data indicate that the pressure rise to separation is unaffected by Reynolds number and that the length of the interaction scales with the initial boundary-layer thickness. Additional data of this type are being obtained for a constant shock Mach number by allowing the shock position to change along the tube surface when the Reynolds number is changed.

4.2 Supersonic Regime

One experiment being used to verify the computations in the supersonic regime is the adiabatic shock-impinging flow originally reported by Reda and Murphy [19]. Figure 13 is a schematic of the test arrangement. Shock waves of varying strength were impinged on a M = 3 boundary layer developed along a tunnel wall. For some tests, the shocks were strong enough to separate the flow on the tunnel wall. Mean-flow profiles and surface-pressure data were reported originally. Since the original work was completed, skin-friction data have been inferred from the profile data [20] and shear distribution upstream and downstream of an interaction without separation were measured [21]. Currently, measurements throughout a separated region, such as velocity fluctuations, shear distributions, and surface skin friction, are being documented.

The surface pressure, normalized by the upstream total pressure, and indirectly inferred wall shear stress for a separated flow case are shown in Figure 14. Separation and reattachment points from oil-flow photographs are indicated. The pressure data have a plateau near the separation. Data for various shock strength [19] will be used to assess the ability of the Navier-Stokes codes to predict the onset of separation.

4.3 Hypersonic Regime

At the hypersonic speeds, the axisymmetric shock expansion boundary-layer interaction flow described in Reference 22 is being used to guide turbulence modeling concepts. The experiment is sketched in Figure 15. The leading edge of the shock generator was varied

between 5⁰ and 20⁰. Measurements in the axial direction were made in finely spaced steps by traversing the shock generator in the axial direction during the tests. Complete flow documentation, including turbulence measurements across the flow field, is available for shock generator angles of 7⁰ and 15⁰ where unseparated and fully separated interactions occurred, respectively. Surface pressure, skin friction, and heat transfer are available for other generator angles and will be used to verify the ability of the turbulence model to predict the effects of shock strength on separation at hypersonic speeds.

The surface pressure, skin friction, and heat transfer for separated flow are shown in Figure 16. Separation and reattachment points obtained from pitot-pressure measurements on probes near the surface facing both upstream and downstream [22] are shown. The pressure increases through the interaction region to a plateau near separation and then rises farther after reattachment. The skin friction decreases, then rises downstream of reattachment. The heat transfer rises continually. The decay in pressure skin friction, and heat transfer downstream of the interaction results from the expansion fan emanating from the corner of the generator.

Fluctuating turbulence properties to be used to guide modeling changes were measured across the boundary layer at four locations through the interaction [23]. An example of the measurements is shown in Figure 17, where the shear stresses at the four measurement locations are plotted. It was not possible to obtain shear measurements in the reversed-flow region of the separation bubble at the second measurement station so the expected trend has been sketched. The measurements show many of the same features as for the transonic test shown previously in Figure 11. Through the interaction, the maximum level of shear stress near the separated region increases significantly. Downstream of reattachment, $(x - x_o)/\delta_o > -1$, the shear profiles do not differ in shape from those usually found in zero or slightly favorable pressure gradients. Turbulence memory apparently persists only for about five boundary-layer thicknesses beyond the initial rise in pressure [23].

428

5. FLOW-FIELD SIMULATIONS

The flow fields experimentally investigated have each been programmed for numerical simulation on a CDC-7600 computer. Each program uses the mass-averaged form of the time-dependent Navier-Stokes equations[24] and solves them with the MacCormack time-marching explicit scheme with splitting[25]. The complete Navier-Stokes equations were used because the viscous and inviscid flows interact significantly; use of approximate solution techniques would only introduce uncertainty when evaluating the ability of the turbulence models to predict measured trends with Mach number and Reynolds-number variations.

Each of the programs and solution techniques have been reported on separately and their details are not addressed here. Only the general form of the equations is presented and some of the terms in the equations affected by the turbulence assumptions are discussed briefly. Then the results are compared with experimental data.

Written in divergence form for the axisymmetric geometry shown in Figure 9, the governing equations are[17]:

$$\frac{\partial U}{\partial t} + \frac{\partial F}{\partial x} + \frac{1}{R-y}\frac{\partial G}{\partial y} = \frac{H}{R-y} \tag{1}$$

$$U = \begin{pmatrix} \rho \\ \rho u \\ \rho v \\ e \end{pmatrix} \quad ; \qquad F = \begin{pmatrix} \rho u \\ \rho u^2 + \sigma_{xx} \\ \rho uv + \tau_{xr} \\ u(e + \sigma_{xx}) + v\tau_{xr} + q_x \end{pmatrix}$$

$$G = \overline{(R-y)} \begin{pmatrix} \rho v \\ \rho uv + \tau_{xr} \\ \rho v^2 + \sigma_{rr} \\ r(e + \sigma_{rr}) + u\tau_{xr} + q_y \end{pmatrix} ; \quad h = \begin{pmatrix} 0 \\ 0 \\ \sigma_{\theta\theta} \\ 0 \end{pmatrix} \tag{2}$$

429

Solutions to the above equations are advanced in time until steady-state solutions are achieved. The turbulence terms to be modeled appear in the axial, radial, and azimuthal stress terms, σ_{xx}, σ_{rr}, and $\sigma_{\theta\theta}$, respectively, and in the heat-flux and shear-stress terms, q_x, q_y and τ_{xr}, respectively[17], e.g.,

$$-\tau_{xr} = \mu_T \left(\frac{\partial u}{\partial y} + \frac{\partial v}{\partial x} \right) \tag{3}$$

Turbulence effects are then introduced by using a scalar eddy viscosity coefficient,

$$\mu_T = \mu + \varepsilon \tag{4}$$

The turbulent thermal conductivity is related to the eddy viscosity by introducing a turbulent Prandtl number that is held constant for each computation. The choice of introducing an eddy viscosity description was dictated by two considerations. First, the initial objective of the computations was to simply asses the ability of the codes to compute a strong viscid-inviscid interaction such as that imposed when a shock wave separates a turbulent boundary layer and, to accomplish this within the numberical framework already established for laminar flows[26], the implementation of a Boussinesq effective viscosity[27] formulation was straightforward. Second, the economies of computation using a Navier-Stokes code required that the simplest turbulence model available be used, otherwise excessive computation times would make the assessment of even the first objective difficult. While the purpose of this paper is not to discuss recent advances in computation techniques, it can be reported that the basic MacCormack code has been speeded up by one order of magnitude[28] or more, depending on the problem under consideration. This was made possible by rearranging equation terms into inviscid and viscid combinations that allow further splitting into inviscid and viscid operators. The inviscid operators can be advanced in time steps larger than those dictated by CFL stability condition by introducing certain characteristics terms; the viscous terms are advanced implicitly. While the solutions may not be rigorously accurate in time, their steady-state solutions are. This

major computational advance now makes it economically feasible to include higher-order modeling concepts into the codes for testing against the experimental data and this is now under way.

A baseline turbulence model has been used to determine whether the codes can predict the qualitative features of the flow fields. Essentially, the baseline model is a two-layer, eddy viscosity model that uses mixing length with Van Driest damping in the inner region and an eddy viscosity that scales on the incompressible displacement thickness in the outer region[22]. In equation form, in the inner region:

$$\epsilon_i = \rho(0.4y)^2 \left[1 - \exp\frac{-y}{A}\right]^2 \left|\frac{\partial u}{\partial y} \quad \frac{\partial v}{\partial x}\right| \tag{5}$$

where

$$\frac{1}{A} = \frac{[\rho_w \mu_w| \quad (\partial u/\partial y)_w|]^{1/2}}{26\mu_w}$$

and, in the outer region,

$$\epsilon_o = 0.0168 \, \rho u_e \delta_i^*/\gamma \tag{6}$$

In Equation (6), δ_i^* and γ are the kinematic displacement thickness and the Klebenoff intermittency, respectively[22]. As will be shown, solutions using the baseline model indicate that the computations can indeed predict all the qualitative features of the flow field, but improvements in the baseline model are required before quantitative features can be predicted.

Modifications to improve the predictions using the Boussinesq formulation have been guided by experiments in two separate approaches, both resulting in essentially the same findings. The first used experimental data to introduce an axial dependence on the baseline model constants throughout the interaction zone[22]. Results with this technique showed improvement but the generalization to other flows was limited. Essentially, the experimental results of Reference 22 showed that, in the separation zone, the effective mixing lengths in the wall region were smaller than those predicted by the baseline model and downstream they were higher. Both results seem to indicate that the corresponding effective eddy viscosities were lower and higher

431

than the baseline values within and downstream of the interaction, respectively. The second approach introduced the concept of relaxation into the model[21;29]. This relaxation concept was postulated on the basis of comparisons with experimental pressure data (as in Reference 29) or on the basis of interpretation of turbulence measurements (as in References 21 and 23). The latter measurements showed that the turbulence took a finite distance to equilibrate with the changes in mean flow through the interaction. This finite distance is somewhat different for each flow, and apparently depends on Mach and Reynolds numbers. In equation form, relaxation can be described either on a global or a point-by-point departure from the baseline model as follows:

$$\varepsilon = \varepsilon_u + (\varepsilon_{eq} - \varepsilon_u)[1 - \exp \frac{-x}{L}] \tag{7}$$

or

$$\varepsilon(x) = \varepsilon(x - \nabla x) + [\varepsilon_{eq}(x) - \varepsilon(x - \Delta x)][1 - \exp(-\frac{\Delta x}{L})] \tag{8}$$

where ε_{eq} is evaluated using the baseline formulation with locally determined mean flow properties and L is an arbitrary relaxation length.

Each of the experimentally determined flow fields has been computed using the baseline and relaxation models, then they are compared with the data in each of the figures introduced previously. In each application, the investigator introduced some differences in the details of applying the baseline and relaxation models described above. These details are discussed in the references cited. The observed trends of interest here are not thought to be affected by these differences, however.

5.1   Transonic Regime

The data from the transonic-wing experiment are compared with the computations in Figure 8. With the baseline model, the overall features of the flow field are predicted reasonably well. For example, the trend of increasing airfoil peak Mach number with Reynolds number is predicted, as is separation due to shock interaction. Downstream of the shock, where the flow separates, the

432

pressure recovery is overpredicted because the predicted shock wave is normal, whereas the experimental shock wave is oblique. A comparison of the predicted and measured skin friction at Re = 10^7 further illustrates the differences in that region as the location of predicted separation is downstream of that location determined from the oil-flow photographs. Use of the relaxation concept[30] with one boundary-layer thickness for L (relaxation length) tends to shift the location of the shock wave closer to the leading edge, reduces the peak Mach number and resulting shock strength, but the pressure recovery is still overpredicted. (Solutions using other choices for L did not improve the results[30].) Relaxation model solutions were not computed at the higher Reynolds number, but closer agreement with the separation location would be expected. For lower Mach numbers, where the flow is not separated but where viscous effects are still important, the computations using the baseline model compare very favorably with the data, except at the trailing edge where extensive separation occurred[30].

Comparisons of the computations with the data from the normal shock-wave experiment are presented in Figures 10 to 12. As mentioned in Reference 17, the height of the separation zone was fairly small, but the length of separation was large, perhaps 6-12 boundary-layer thicknesses, depending on the techniques of measurement. The pressure prediction agrees well with the data. The skin friction is underestimated downstream. Including local relaxation with a relaxation length, L, of 10 boundary-layer thicknesses in the turbulence model [i.e., Equation (8)] resulted in poorer agreement in the skin friction downstream and no significant changes in the pressure rise. The shear distributions obtained using the global relaxation model are compared with the data in Figure 11 at three locations downstream of the wave. Similar results were obtained with the baseline and local relaxation models. The computations fail to predict the significant increase in shear at the first station and, evidently, this continues to affect the prediction downstream. The effects of Reynolds number on the interaction are compared in Figure 12. The predicted separation pressures and length of interaction to the separation point are compared with the experimental pressure and length evaluated at the knee in the pressure curve.

433

The trends with Reynolds number are predicted reasonably well. The separation point from the computations occurs upstream of the knee in the pressure curve. The overall length of the interaction is underpredicted. All calculations shown in this figure were made recently by J. R. Viegas using the new faster version of the MacCormack code[28]. These new calculations took less than 10 minutes on a CDC-7600, whereas the first computations[17] took about 5 hours on the same computer.

5.2 Supersonic Regime

Comparisons for the oblique-shock interaction using the baseline and relaxation turbulence models are shown in Figure 14. For the oblique-shock interaction, the baseline model predicts the overall pressure rise reasonably well and also predicts separation. However, no appreciable upstream influence in the pressure and no plateau are indicated in the calculations because the size of the separation bubble is underpredicted. Introducing the relaxation concept with $L = 5$ boundary-layer thicknesses corrects this deficiency because it lowers the effective eddy viscosity near the separation, thus increasing the size of the separated zone, which in turn introduces a plateau in the pressure rise curve. The location of separation is predicted with the relaxation model, but the reattachment location is too far downstream. The comparison with the wall shear downstream of reattachment where the boundary layer thins may appear better than is the actual case because these computations were made with a relatively coarse grid, and in the downstream locations the first computation point away from the wall was in the logarithmic region of the turbulent boundary layer. Since the method used to obtain derivatives at the wall requires calculated points within the sublayer region, the predicted shear is expected to be lower than the measurements, and the results would be similar to those for the transonic normal-shock comparisons.

5.3 Hypersonic Regime

In Figure 16, the predicted results and experimental data are compared. As with the supersonic oblique-shock interaction, the baseline model prediction reproduces the overall trends in the data but is deficient in the separated region. Recent calculations by

434

T. J. Coakley using a relaxation model with L = 5 boundary-layer thicknesses (as indicated by the turbulence measurements from Reference 23) improve the situation somewhat. (See, e.g., Figure 17 and the previous discussion of Figure 17.) The height of the separation is greater and the resulting upstream influence leads to a plateau in the pressure. The location where skin friction begins to decrease is predicted, but the extent of the separation in the axial direction is overpredicted significantly, much as for the supersonic example. The heat t-ansfer is underpredicted throughout the inter-action region with either model.

From an examination of all the comparisons, general observations about the computations can be made. In most cases, the pressure rise can be predicted reasonably well with a simple eddy viscosity description for the turbulence. The exception is for the transonic wing where the shock-induced separation was very large and extended from the foot of the shock beyond the trailing edge. The eddy viscosity concept is deficient in providing the proper details within the separated zone and this, in turn, apparently affects the entire flow field when the separation zones are large, viz., the oblique-shock cases. Introducing relaxation tends to improve the situation somewhat because it decreases the eddy viscosity in the region of separation, resulting in an increase in the height of the separation. However, the net decrease in eddy viscosity persists beyond the separated zone even for short relaxation lengths, and the codes underpredict the skin friction downstream. Interpretation of the modeling experiments indicates the need for an increase in effective eddy viscosity downstream of reattachment. Therefore, improved turbulence models that more closely reflect the experimental findings must be introduced before realistic simulations can be made.

6.   CONCLUDING REMARKS

Experiments of two types needed to achieve the objectives of numerically simulating, highly interacting turbulent flows were described. These experiments were classified as verification and modeling experiments: verification experiments that measure mean flow and surface quantities could suffice for checking the code's ability to predict correctly over a range of Mach and Reynolds

435

numbers, whereas turbulence modeling experiments require, in addition to mean-flow measurements, that fluctuating measurements be made to the degree of complexity called for in the order of the modeling closure technique. From the numerical simulation viewpoint, the lowest-order closure technique is more desirable because the complexity of the numerical procedures and the computation times can be reduced.

Progress in modeling turbulence for the computer codes using the Navier-Stokes equations has been limited so far to modifications of the simple eddy viscosity descriptions because the computation times have been excessive. Recent developments in the method for solving the Navier-Stokes equations have altered that situation because the computations have been speeded up by several orders of magnitude. Computer simulations that use higher-order modeling concepts are forthcoming, and it is expected that these will more closely resemble the experimentally observed results.

REFERENCES

1.   Bailey, F. R.; and Ballhaus, W. F.: Comparisons of Computed
     and Experimental Pressures for Transonic Flows About Isolated
     Wings and Wing-Fuselage Configurations. SP-347, Vol. II, 1975,
     pp. 1213-1232, NASA.

2.   Rakich, J. V.; and Pegot, E. G.: Flow Field and Heating on the
     Windward Side of the Space Shuttle Orbiter. SP-347, Vol. II,
     1975, pp. 1377-1394, NASA.

3.   Marconi, F.; Yaeger, L.; and Hamilton, H. H.: Computation of
     High-Speed Inviscid Flows About Real Configurations. SP-347,
     Vol. II, 1975, pp. 1411-1456, NASA.

4.   Chapman, D. R.; Mark, H.; and Pirtle, M. W.: Computers vs.
     Wind Tunnels for Aerodynamic Flow Simulation. Astronautics
     and Aeronautics, Vol. 13, No. 4, April 1975, pp. 22-30.

5.   Kline, S. J.; Morkovin, M. V.; Sovran, G.; Cockrell, J. D.;
     Coles, D. E.; and Hirst, E. A., editors: Proceedings -
     Computation of Turbulent Boundary Layers - 1968 AFOSR-IFP-
     Standard Conference, Vols. I and II. August 1968.

6.   Anon: Compressible Turbulent Boundary Layers. SP-216, 1968,
     NASA.

7.   Jones, J. Lloyd, Jr.: Problems of Flow Simulation in Wind
     Tunnels. AIAA Paper 69-660, 1969.

8.   Waltrup, P. J.; and Schetz, J. A.: Supersonic Turbulent
     Boundary Layer Subjected to Adverse Pressure Gradients. AIAA
     Journal, Vol. II, No. 1, Jan. 1973, pp. 50-57.

9.   Reynolds, O.: On the Dynamicay Theory of Incompressible
     Viscous Fluids and the Determination of the Criterion, Phil.
     Trans. A 186, pp. 123-161, or Papers 2, 535.

10. Bradshaw, P.: The Understanding and Prediction of Turbulent
     Flow. The Aeronautical Journal, Vol. 76, No. 739, July 1972.

11. Coles, D. E.: A Young Person's Guide to the Data, Proceedings -
     Computation of Turbulent Boundary Layers - 1968. AFOSR-IFP-
     Standord Conference, Vol. II, 1968, pp. 1-45.

12. Sandborn, V. A.: A Review of Turbulence Measurements in
     Compressible Flow. TM X-62,337, March 1974, NASA.

13. Sandborn, V. A.; and Seegmiller, H. L.: Evaluation of Mean
     and Turbulent Velocity Measurement in Subsonic Accelerated
     Boundary Layers. TM X-62,488, Sept. 1975, NASA.

14. Horstman, C. C.; and Rose, W. C.: Hot-Wire Anemometry in
     Transonic Flow. TM X-62,495, Dec. 1975, NASA.

15. Rubesin, Morris, W.; Okuno, Arthur F.; Mateer, George G.; and Brosh, Aviel: A Hot-Wire Surface Gage for Skin Friction and Separation Detection Measurements. TM X-62,465, July 1975, NASA.

16. McDevitt, J. B.; Levy, L. L.; and Deiwert, G. S.: Transonic Flow About a Thick Circular-Arc Airfoil. AIAA Paper 75-878, 1975.

17. Mateer, G. G.; Brosh, A.; and Viegas, J. R.: A Normal Shock-Wave Turbulent Boundary-Layer Interaction at Transonic Speeds. AIAA Paper 76-161, 1976.

18. Seddon, J.: The Flow Produced by Interaction of a Turbulent Boundary Layer With a Normal Shock Wave of Strength Sufficient to Cause Separation. ARC R & M 3502, March 1960.

19. Reda, D. C.; and Murphy, J. D.: Shock-Wave Turbulent Boundary-Layer Interactions in Rectangular Channels, Part II: The Influence of Sidewall Boundary Layers on Incipient Separation and Scale of the Interaction. AIAA Paper 73-234, 1973.

20. Rubesin, M. W.; Murphy, J. D.; and Rose, W. O.: Wall Shear in Strongly Retarded and Separated Compressible Turbulent Boundary Layers. AIAA Journal, Vol. 12, No. 10, Oct. 1975, pp. 1442-1444.

21. Rose, W. C.; and Johnson, D. A.: A Study of Shock-Wave Turbulent Boundary-Layer Interaction Using Laser Velocimenter and Hot-Wire Anemometer Techniques. AIAA Paper 74-95, 1974.

22. Marvin, J. G.; Horstman, C. C.; Rubesin, M. W.; Coakley, T. J.; and Kussoy, M. I.: An Experimental and Numerical Investigation of Shock-Wave Induced Turbulent Boundary-Layer Separation at Hypersonic Speeds. AGARD Conference Proceedings No. 168 on Flow Separation, May 1975.

23. Mikulla, V.; and Horstman, C. C.: Turbulence Measurements in Hypersonic Shock-Wave Boundary-Layer Interaction Flows. AIAA Paper 76-162, Jan. 1976.

24. Rubesin, M. W.; and Rose, W. C.: The Turbulent Mean-Flow Reynolds-Stress, and Heat Flux Equations in Mass-Averaged Dependent Variables. TM X-62,248, March 1973, NASA.

25. MacCormack, R. W.; and Baldwin, B. S.: A Numerical Method for Solving the Navier-Stokes Equations with Application to Shock-Boundary Layer Interactions. AIAA Paper 75-1, 1975.

26. MacCormack, R. W.: Numerical Solution of the Interaction of a Shock Wave with a Laminar Boundary Layer. Lecture Notes in Physics, Vol. 8, Springer-Verlag, New York, 1971, pp. 151-163.

27. Boussinesq, J.: Theorĭc de L'écoulement Tourbillant, Memoires Presentés Par Divers Savants Sciences Mathématique et Physiques, Académic Des ciences, Paris, France, Vol. 23, 1877, p. 46.

28. MacCormack, R. W.: A Rapid Solver for Hyperbolic Systems of
    Equations. Paper to be presented at the 5th International
    Conference on Numerical Methods in Fluid Dynamics held at
    Twente University of Technology, Enschede, The Netherlands,
    June 28-July 2, 1976.

29. Shang, J. S.; and Hankey, W. L., Jr.: Numerical Solution of the
    Navier-Stokes Equations for Supersonic Turbulent Flow Over a
    Compression Corner. AIAA Paper 74-4, 1975.

30. Deiwert, G. S.: Computation of Separated Transonic Turbulent
    Flows. AIAA Paper 75-829, June 1975.

TABLE 1.   STATUS OF COMPUTATIONAL AERODYNAMICS

TYPE OF EQUATION CLOSURE	TYPE OF EXPERIMENT	DOCUMENTED QUANTITIES	TEST CONDITIONS
FIRST ORDER OR HIGHER ORDER	VERIFICATION	$C_F, C_H, p_W, \bar{T}, \bar{u}, \bar{v}, \bar{w}, <q_\infty>$	TO FLIGHT MACH AND REYNOLDS NO.
FIRST ORDER	FIRST ORDER MODELING	$C_F, C_H, p_W, \bar{T}, \bar{u}, \bar{v}, \bar{w}, <q_\infty>$ $\rho \overline{v'u'}, \rho \overline{T'v'}$	REPRESENTATIVE FLIGHT MACH AND REYNOLDS NO.
HIGHER ORDER	HIGHER ORDER MODELING	$C_F, C_H, p_W, \bar{T}, \bar{u}, \bar{v}, \bar{w}, <q_\infty>$ $\rho \overline{v'u'}, \rho \overline{T'v'}$ $u', v', w', q, \overline{v'q'}, \frac{\partial u_i}{\partial x_j} \ldots$	REPRESENTATIVE FLIGHT MACH AND REYNOLDS NO.

TABLE 2.   ELEMENTS OF WELL-DOCUMENTED BUILDING-BLOCK EXPERIMENTS

STAGE OF APPROXIMATION	READINESS TIME PERIOD			LIMITATIONS	PACING ITEM
	2D AIRFOILS	3D WINGS	3D AIRCRAFT		
INVISCID LINEARIZED	1930's	1950's	1960's USED IN CURRENT AIRCRAFT DESIGN	SLENDER CONFIGURATIONS SMALL ANGLE OF ATTACK PERFECT GAS NO TRANSONIC FLOW NO HYPERSONIC FLOW NO FLOW SEPARATION	
INVISCID NONLINEAR	1971	1973	1976 ? DEVELOPMENT NEARING COMPLETION	NO FLOW SEPARATION	CODE DEVELOPMENT
VISCOUS TIME AVERAGED	1975	1977 ?	1979 ? EARLY STAGE OF DEVELOPMENT	ACCURACY OF TURBULENCE MODEL	TURBULENCE MODELING
VISCOUS TIME DEPENDENT		MID 1980's		ACCURACY OF NAVIER – STOKES EQS.	DEVELOPMENT OF ADVANCED COMPUTER

440
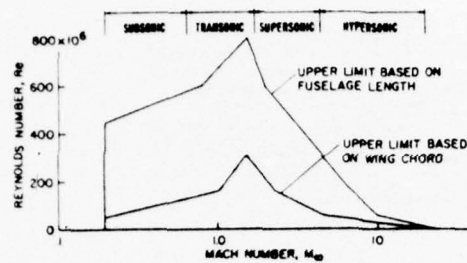
Figure 1. Mach and Reynolds number domain for aerospace vehicles.
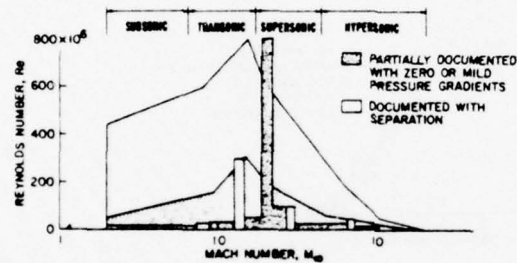
Figure 2. Mach and Reynolds number domain for experiments compared with that for aerospace vehicles.
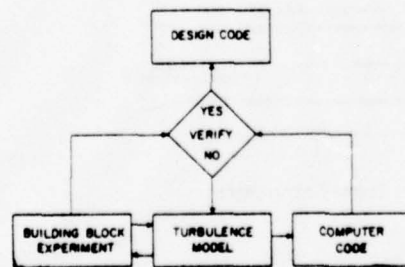
Figure 3. Process of physical modeling for computer code development.
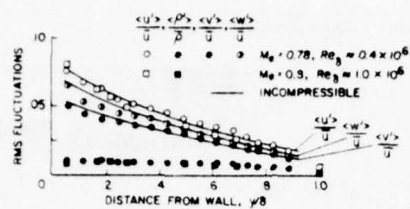
Figure 4.   Shear-stress measurements in compressible flows.
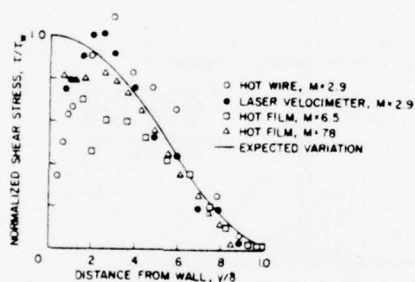
Figure 5.   Normalized rms velocity and density fluctuations
across a compressible turbulent boundary layer.

(a)   Overall arrangement

(b)   Wing design
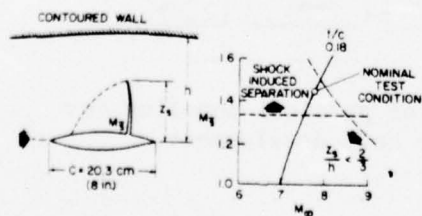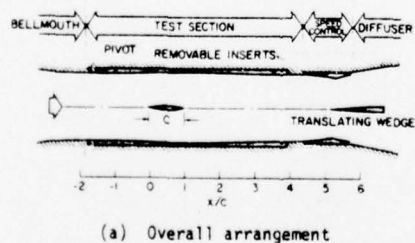
Figure 6.   Experimental arrangement for a transonic wing
undergoing shock-induced separation.

442

PRESSURE DISTRIBUTION   SHADOWGRAPH

OIL FLOW PATTERNS
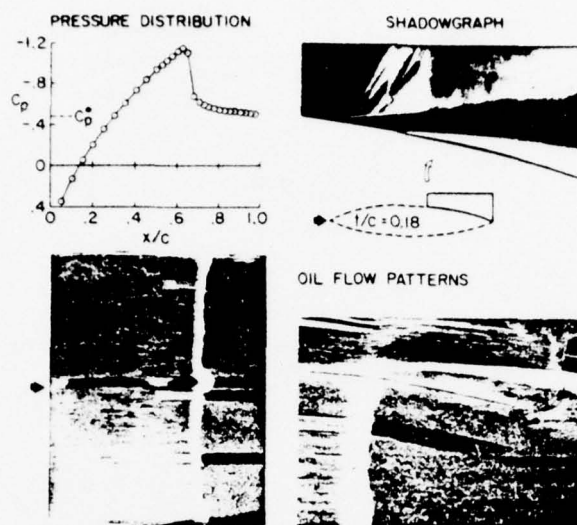
Figure 7.   Shock-induced boundary-layer separation experiment
            on a bioconvex circular-arc airfoil;
            Re = 10.3×10^6, M_∞ = 0.786.
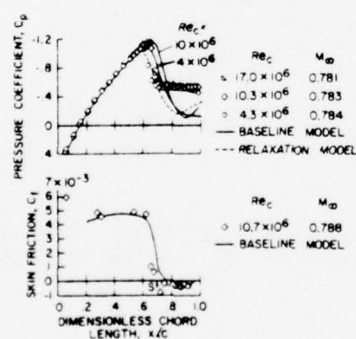
Figure 8.   Results from the shock-induced separation
            experiment on a bioconvex circular-arc airfoil.
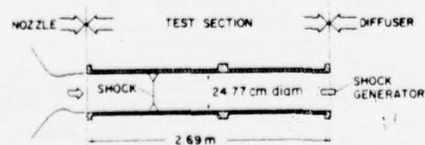
Figure 9.   Experimental arrangement for a normal-shock-wave,
            turbulent boundary-layer experiment with
            separation.

443
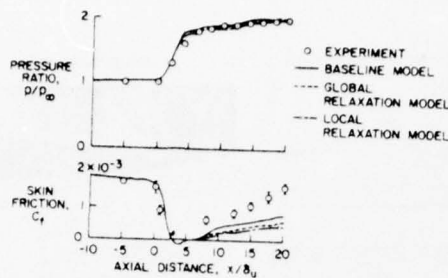
Figure 10. Results from the normal-shock-wave experiment, $M_\infty = 1.44$ and $Re_x = 37\times10^6$.
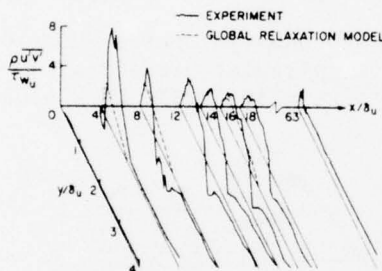
Figure 11. Shear-stress profiles from the normal--shock-wave experiment, $M_\infty = 1.44$ and $Re_x = 37\times10^6$.
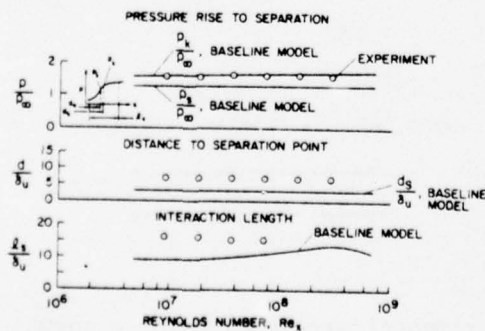
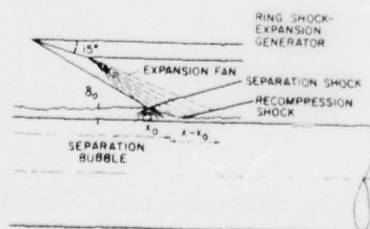Figure 12. Effect of Reynolds number on pressure rise to separation and on various interaction lengths.

444
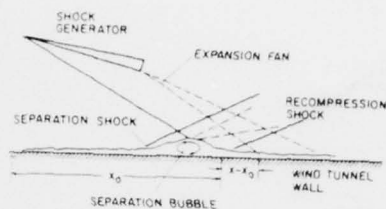
Figure 13. Experimental arrangement for a supersonic oblique-shock-wave, boundary-layer interaction experiment, $M_\infty = 3.0$ and $Re_{\delta_0} = 9.73 \times 10^5$.
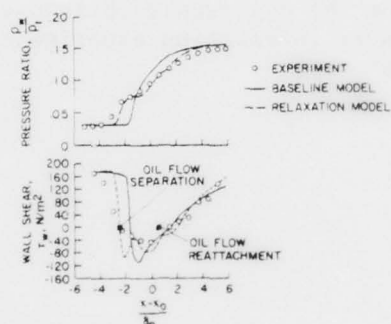
Figure 14. Results from the supersonic oblique-shock-wave, boundary-layer interaction experiment, $M_\infty = 3.0$ and $Re_{\delta_0} = 9.73 \times 10^5$.
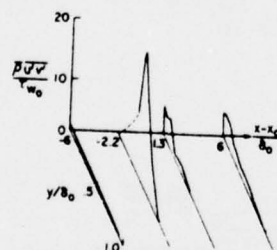

Figure 15. Experimental arrangement for an axially symmetric hypersonic oblique shock-expansion, boundary-layer interaction experiment, $M_\infty = 6.9$ and $Re_x = 13 \times 10^6$.

445
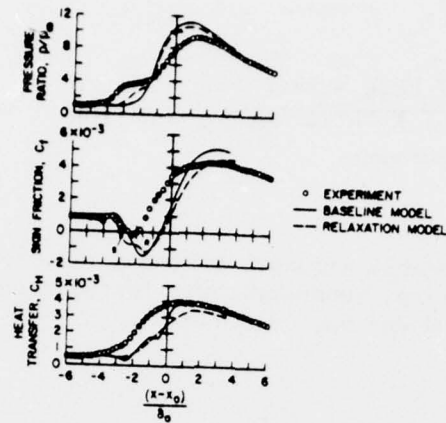
Figure 16.   Results from the hypersonic oblique-shock-expansion, boundary-layer interaction experiment, M_∞ = 6.9 and Re_x = 13×10^6.

Figure 17.   Shear-stress distributions for the hypersonic oblique-shock-expansion, boundary-layer interaction experiment, M_∞ = 6.9 and Re_x = 13×10^6.

446

TURBULENT FLOW NEAR A WALL BASED ON A
TURBULENT KINETIC ENERGY EQUATION[*]

by

D. L. Whitfield[†]
ARO, Inc.
Arnold Air Force Station, Tennessee

[†]Supervisor, Analysis Section, 16T/S Projects, Propulsion Wind
Tunnel Facility, Arnold Engineering Development Center, Arnold
Air Force Station, Tennessee 37389.

OBJECTIVE

AN ANALYTICAL INVESTIGATION OF TURBULENT FLOW
NEAR A SMOOTH IMPERMEABLE WALL

APPROACH

1. RELATE THE REYNOLDS STRESS TO THE TURBULENT
    KINETIC ENERGY

2. ASSUME THE TOTAL SHEAR STRESS IS CONSTANT
    NEAR THE WALL

3. SOLVE THE MOMENTUM AND TURBULENT KINETIC
    ENERGY EQUATIONS ANALYTICALLY

$$\rho U \frac{\partial e}{\partial x} + \rho V \frac{\partial e}{\partial y} = \frac{\partial}{\partial y}\left[\left(\mu - \frac{\rho\langle uv\rangle}{\partial U/\partial y}\right)\frac{\partial e}{\partial y}\right] - \rho\langle uv\rangle\frac{\partial U}{\partial y} - \frac{Ce}{L^2}\left(\mu - \frac{\rho\langle uv\rangle}{\partial U/\partial y}\right)$$

Using $\qquad \tau = \mu\frac{\partial U}{\partial y} - \rho\langle uv\rangle \qquad$ and $\qquad e = e(U)$

$$\left(\rho U \frac{\partial U}{\partial x} + \rho V \frac{\partial U}{\partial y}\right)\frac{de}{dU} = \frac{\partial}{\partial y}\left(\tau\frac{de}{dU}\right) - \rho\langle uv\rangle\frac{\partial U}{\partial y} - \frac{Ce}{L^2}\frac{\tau}{\partial U/\partial y}$$

448

$$\tau \, \frac{d^2 e}{dU^2} - \rho \, \langle uv \rangle - \frac{C \, e}{L^2} \, \frac{\tau}{(\partial U / \partial y)^2} \approx 0$$

$$- \langle uv \rangle \sim L^2 \left(\frac{\partial U}{\partial y} \right)^2$$
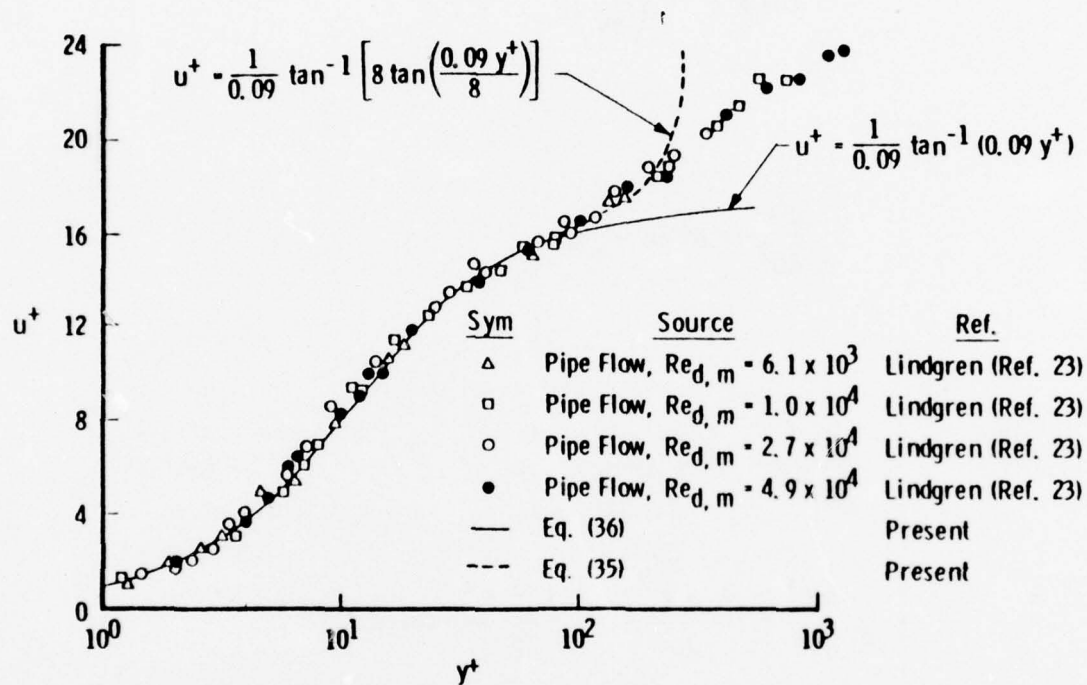
$$\tau \, \frac{d^2 e}{dU^2} + a^2 \rho e = \beta \tau$$

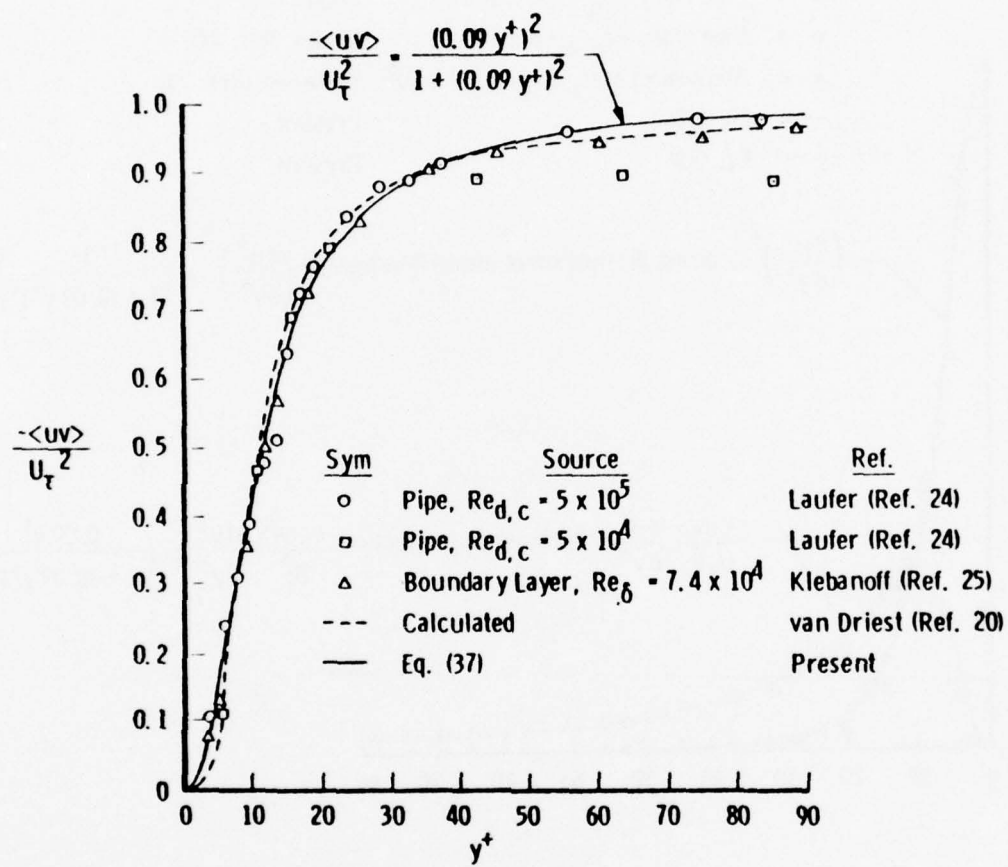$$\frac{du^+}{dy^+} = 1 - \frac{- \langle uv \rangle}{U_\tau^2}$$

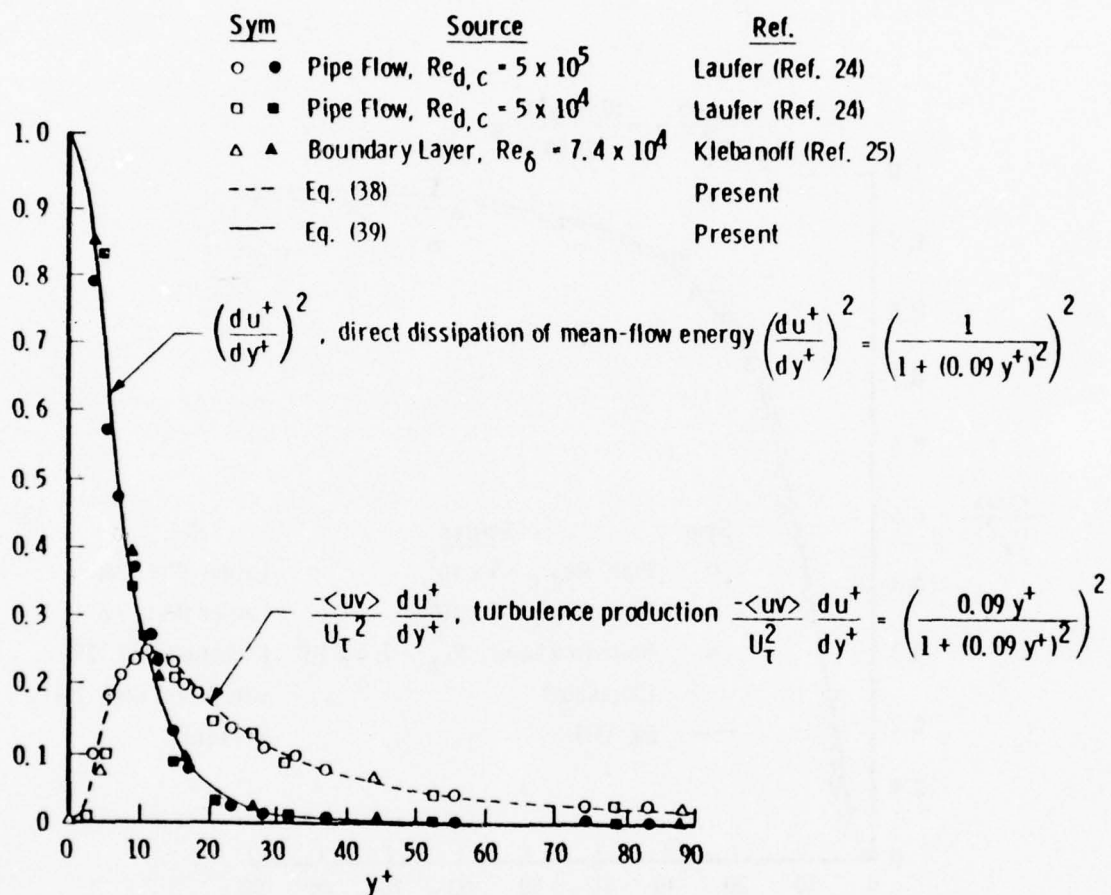$$\frac{du^+}{dy^+} = \frac{1 + \epsilon^2}{2} + \frac{1 - \epsilon^2}{2} \, \cos(a \, u^+)$$

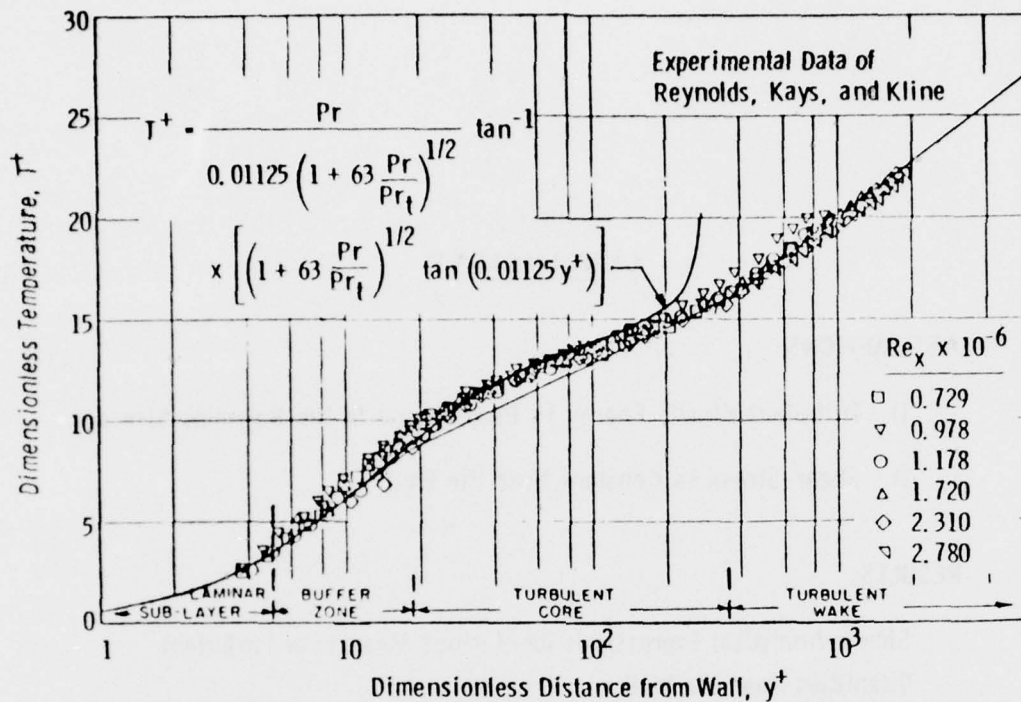$$y^+ = \frac{2}{\epsilon a} \, \tan^{-1} \left[\epsilon \tan \left(\frac{a u^+}{2} \right) \right]$$

$$y^+ = \frac{8}{0.09} \, \tan^{-1} \left[\frac{1}{8} \tan (0.09 \, u^+) \right]$$
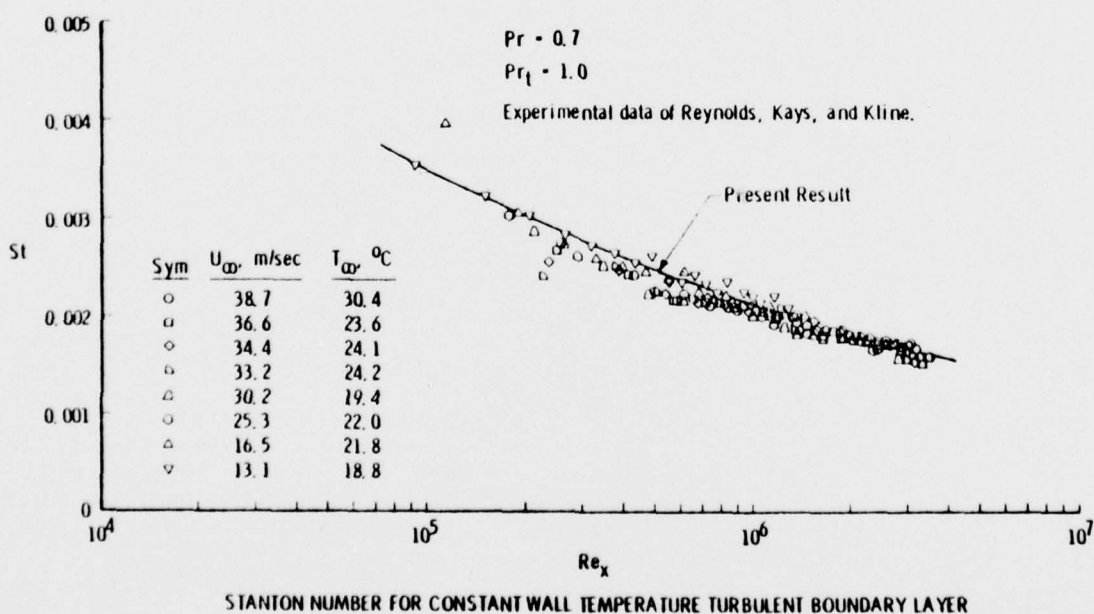
$$y^+ = \frac{1}{0.09} \, \tan (0.09 \, u^+)$$

$$u^+ = \frac{1}{0.09} \tan^{-1}\left[8 \tan\left(\frac{0.09\, y^+}{8}\right)\right]$$

$$u^+ = \frac{1}{0.09} \tan^{-1}(0.09\, y^+)$$

Sym	Source	Ref.
△	Pipe Flow, $Re_{d,m} = 6.1 \times 10^3$	Lindgren (Ref. 23)
□	Pipe Flow, $Re_{d,m} = 1.0 \times 10^4$	Lindgren (Ref. 23)
○	Pipe Flow, $Re_{d,m} = 2.7 \times 10^4$	Lindgren (Ref. 23)
●	Pipe Flow, $Re_{d,m} = 4.9 \times 10^4$	Lindgren (Ref. 23)
——	Eq. (36)	Present
- - -	Eq. (35)	Present

$$\frac{-\langle uv \rangle}{U_\tau^2} = \frac{(0.09\,y^+)^2}{1 + (0.09\,y^+)^2}$$

Sym	Source	Ref.
○	Pipe, $Re_{d,c} = 5 \times 10^5$	Laufer (Ref. 24)
▢	Pipe, $Re_{d,c} = 5 \times 10^4$	Laufer (Ref. 24)
△	Boundary Layer, $Re_\delta = 7.4 \times 10^4$	Klebanoff (Ref. 25)
---	Calculated	van Driest (Ref. 20)
—	Eq. (37)	Present

451

$\left(\dfrac{du^+}{dy^+}\right)^2$, direct dissipation of mean-flow energy $\left(\dfrac{du^+}{dy^+}\right)^2 = \left(\dfrac{1}{1+(0.09\,y^+)^2}\right)^2$

$\dfrac{-\langle uv\rangle}{U_\tau^{\,2}}\dfrac{du^+}{dy^+}$, turbulence production $\dfrac{-\langle uv\rangle}{U_\tau^2}\dfrac{du^+}{dy^+} = \left(\dfrac{0.09\,y^+}{1+(0.09\,y^+)^2}\right)^2$

y^+

452

$$T^+ = \frac{Pr}{0.01125\left(1 + 63\,\frac{Pr}{Pr_t}\right)^{1/2}}\,\tan^{-1}$$

$$\times\left[\left(1 + 63\,\frac{Pr}{Pr_t}\right)^{1/2}\tan\left(0.01125\,y^+\right)\right]$$

Experimental Data of
Reynolds, Kays, and Kline

$Re_x \times 10^{-6}$

Sym	$Re_x \times 10^{-6}$
⊡	0.729
▽	0.978
○	1.178
△	1.720
◇	2.310
▽	2.780

LAMINAR SUB-LAYER · BUFFER ZONE · TURBULENT CORE · TURBULENT WAKE

Dimensionless Distance from Wall, y^+

UNIVERSAL FLAT-PLATE TEMPERATURE PROFILE. PRANDTL NUMBER, 0.7
TURBULENT PRANDTL NUMBER, 1.0.

Pr = 0.7
Pr_t = 1.0
Experimental data of Reynolds, Kays, and Kline.

Present Result

Sym	U_∞, m/sec	T_∞, °C
○	38.7	30.4
◻	36.6	23.6
◇	34.4	24.1
◻	33.2	24.2
△	30.2	19.4
◌	25.3	22.0
△	16.5	21.8
▽	13.1	18.8

Re_x

STANTON NUMBER FOR CONSTANT WALL TEMPERATURE TURBULENT BOUNDARY LAYER

453

CONCLUSIONS

ASSUMPTIONS:

1) Turbulent Kinetic Energy Is Proportional to the Reynolds Stress

2) Shear Stress Is Constant Near the Wall

RESULTS:

Simple Analytical Expressions for Various Mean Flow Turbulent
Quantities Near the Wall

SOME EFFECTS OF SCALE AND REYNOLDS NUMBER
ON THE TRANSONIC SHOCK - BOUNDARY LAYER INTERACTION*

by

John D. Lee
The Ohio State University
The Aeronautical and Astronautical Research Laboratory
Columbus, Ohio

The reaction of the boundary layer to compression in the transonic range often produces an extensive effect upon the flow field near a vehicle and hence upon the aerodynamic forces. The phenomenon will remain poorly understood and unpredictable until there is available a body of reliable experimental evidence from which accurate conclusions may be drawn, and against which theoretical predictions may be compared. The influences of Reynolds number and of scale are particularly important at the conditions under which most simulation is conducted. Usually these conditions are such that the boundary layer is relatively thicker than in flight, even at the same Reynolds number. Thus it is necessary to know if the differences are important, i.e., whether the simulation is adequate.

Various experiments have been performed in the transonic wind tunnels of the OSU-AARL to acquire data on the influence of Reynolds number and scale using bodies and airfoils. The results from a number of these are used here to illustrate the variety of effects even in relatively simple flows. Data presented are from airfoil models in two tunnels: the 6 in. by 22 in. airfoil tunnel which is essentially interference-free and the 4 in. by 10 in. airfoil tunnel which is used for wide variations in Reynolds number. Boattail-body data are also shown from tests conducted in the 9 in. by 12 in. tunnel, which is also operated over a 15:1 range in Reynolds number.

Pressure distributions on a section of the C-141 wing in flight tests (as reported in AFFDL-TR-68-84) were simulated on an airfoil model, a typical comparison being that shown in Figure 1. The results of varying the Reynolds number for the flow over this model are seen in Figure 2 to be quite small; other conditions showed larger variations in the location of the shock, that in Figure 3 being the greatest. Data from a section of a different shape shown in Figure 4 show even less sensitivity to Reynolds number variations in the range tested (6 to 60 x 10^6).

Boattail pressure distributions showed an insensitivity to variations in Reynolds number (Figure 5) until a dummy sting was added for partial simulation of an engine exhaust (Figure 6). The resultant trend with Reynolds number can then be identified with the local interaction with the sting, whereas the shock-boundary layer interaction remained almost unaffected as with no sting. In the case of a boattail of larger angle (Figure 7) where the boundary layer was completely separated at the site of the shock, no dependence on Reynolds number was noticed.

A test program using models of the NACA 0012 profile produced information on the behavior of the flow field for this type of airfoil in supercritical flow, into a lower range of Reynolds numbers than reported for the other models. Since flow in this channel (the 6 in. by 22 in. airfoil tunnel) is almost entirely free of interference for models with chords less than 8 inches, it provides a means of data comparison for scale as well as Reynolds number effects. Figures 8 and 9 show the lack of interference present in both subcritical and supercritical flow.

In the example cases where C_p-distributions are compared (Figures 10 through 13) in the Reynolds number range from 2 to 8 million and for models having chords of 3 inches and 6 inches, the details can be discerened by careful examination. Several

456

possibilities are illustrated for this range of Reynolds number:

(a) Little or no variation with Re or scale.

(b) A smooth variation with Re.

(c) Variations related to both scale and Reynolds number.

(d) Shock-interactions on both upper and lower surfaces, interfering with each other.

By comparing the data from the two models, a small scale effect appeared in some cases in that the effective Reynolds number for the smaller model was apparently higher than the calculated value.

Over the range of such interactions, realistic comparisons and analysis can be obtained only if a very tight control is maintained over Mach number (to ± 0.002) and attack angle (to ± 0.05°) since, under some conditions, the flow field is extremely sensitive to both of these parameters. The variation of integrated lift and pitching moment over the Mach number range, as given in Figure 14, reflects the sensitivity to Mach number in the case of the NACA 0012 profile. Such information is a necessary prerequisite to a detailed study of the local interactions.

457
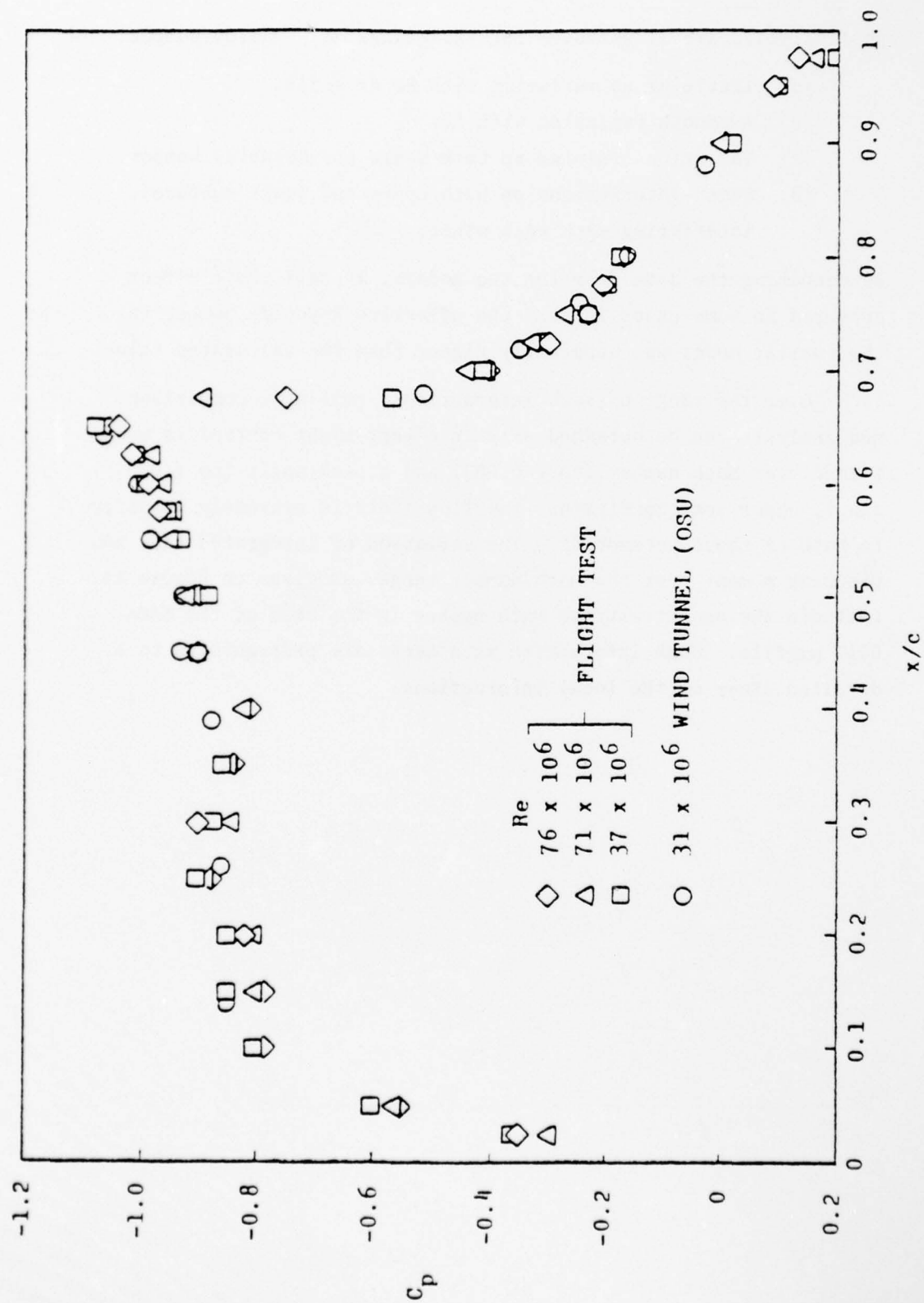
Figure 1. Flight Test Data From Suction Surface of C-141 (eta = 0.389) Wing (Ref. AFFDL-TR-68-84) in Comparison With Wind Tunnel Data (M = 0.81), Tunnel $\alpha = 5^{\circ}$)

458
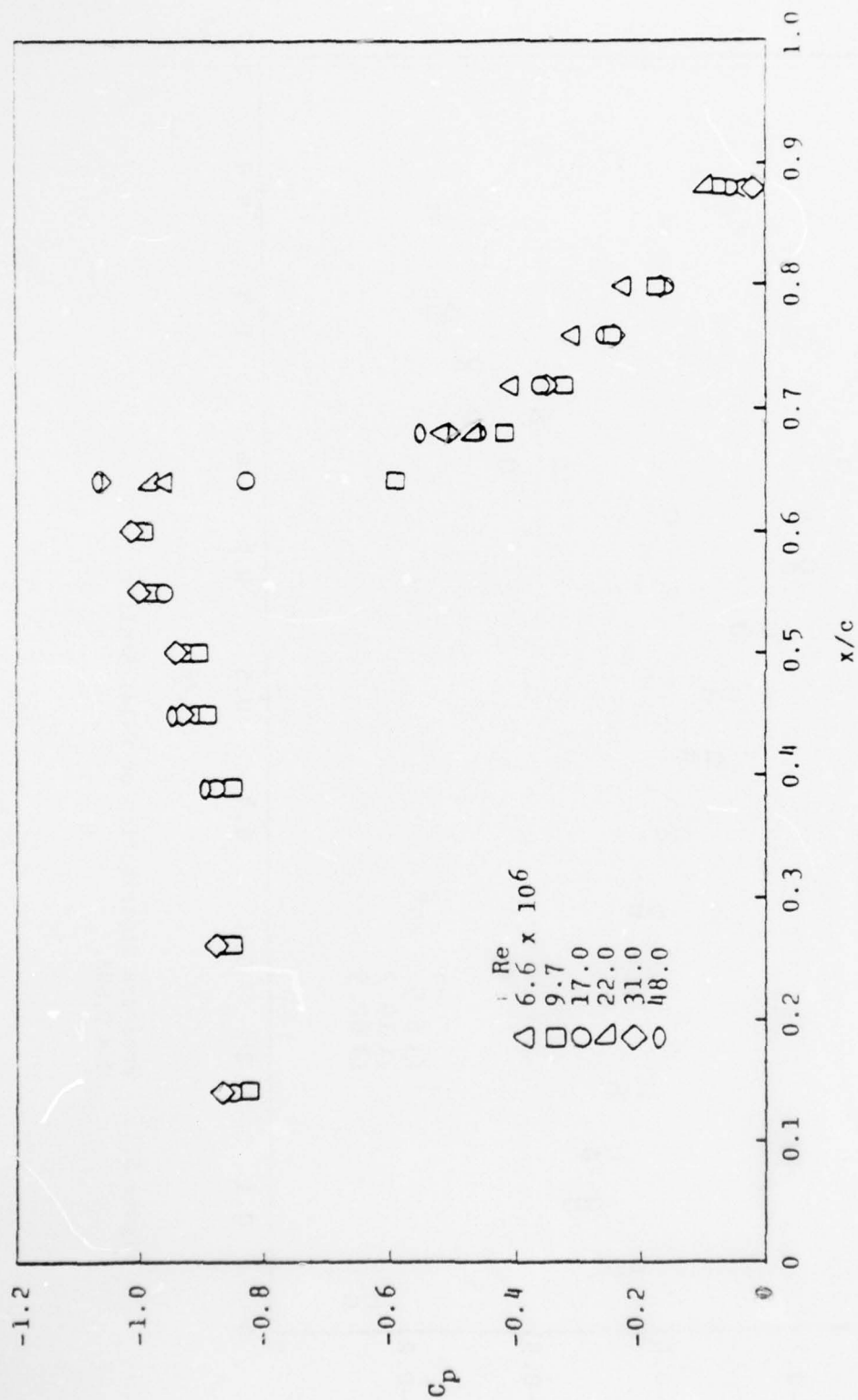
Figure 2.   Pressure Distributions on Suction Surface of C-141 Section.
M = 0.81, α = 5° (Variation With Reynolds Number) (Compare
Flight Test Data, Figure 1).
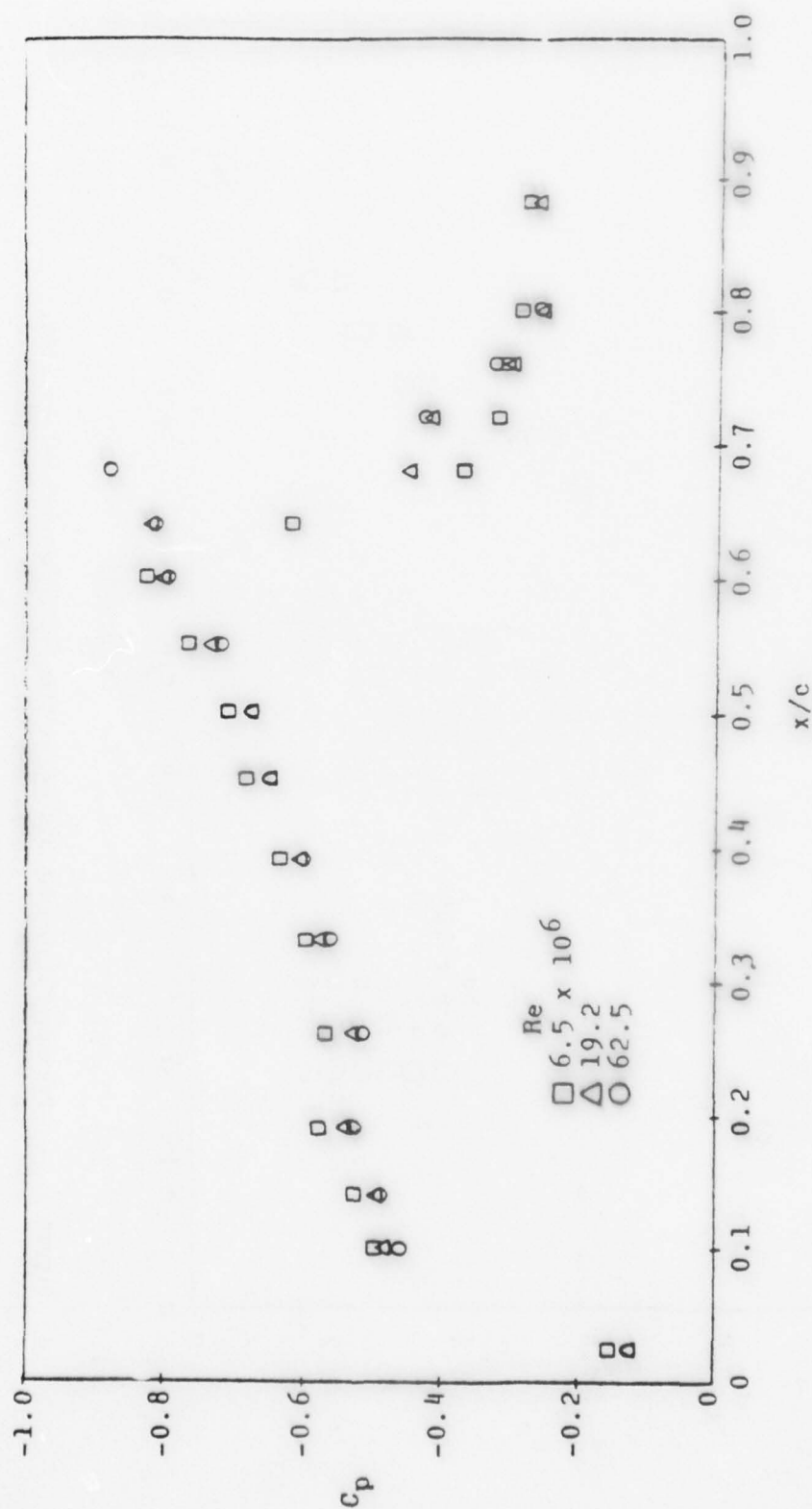
Figure 3. Pressure Distribution on C-141 Section.
M = 0.893.
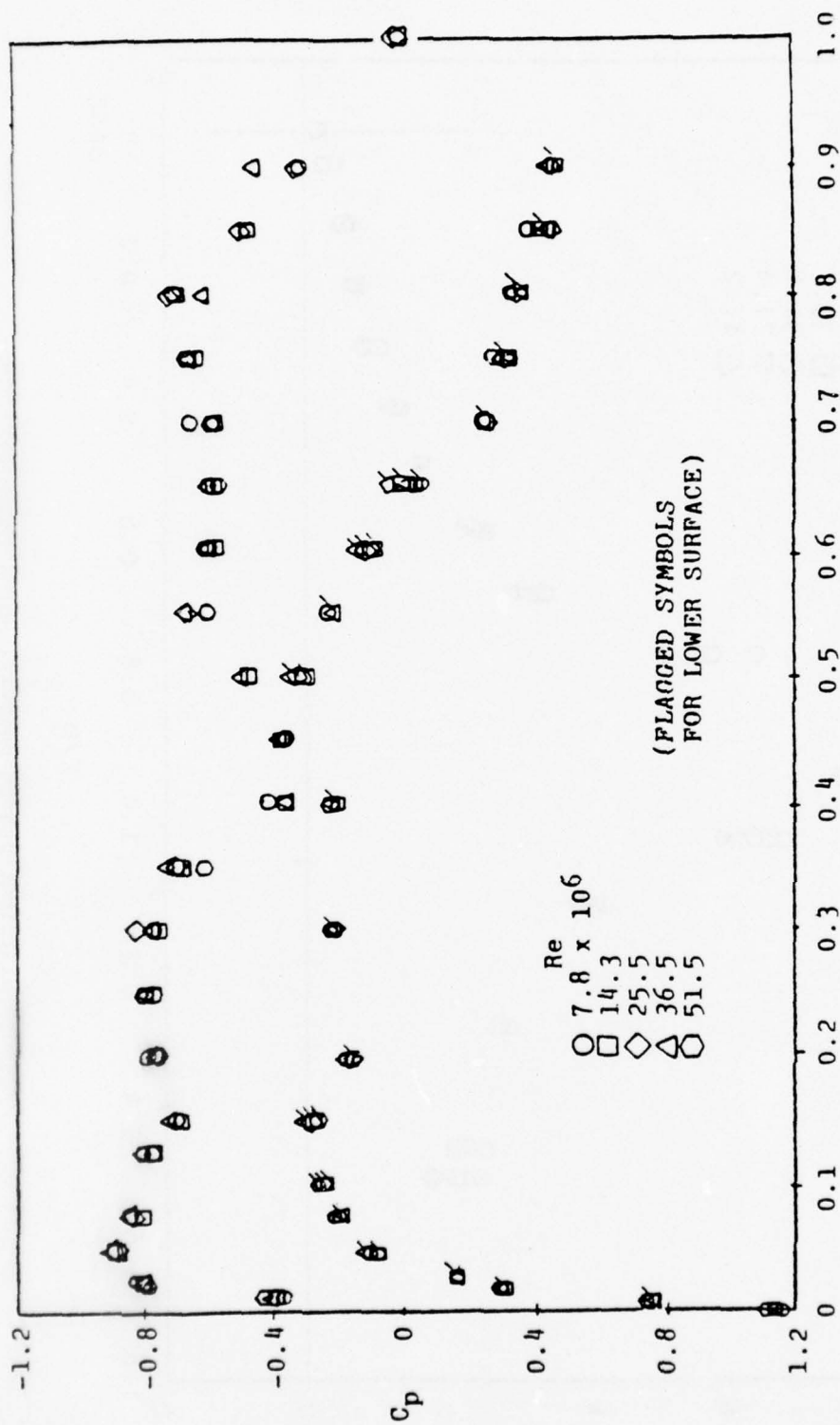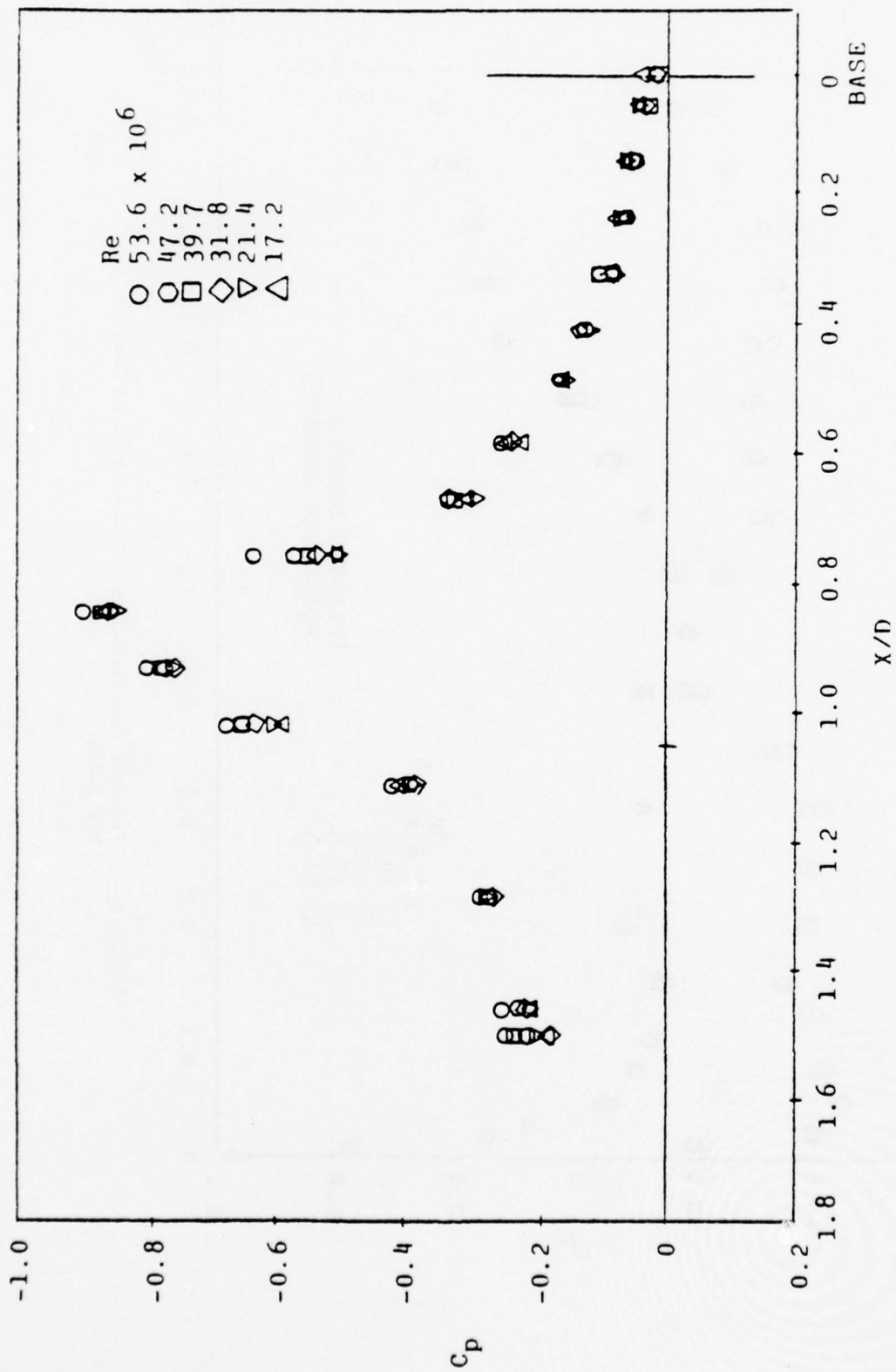
Figure 4.   Pressure Distributions on Supercritical Section.
M = 0.800.

461

Figure 5. Pressure Distributions On Boattail No. 2 (Nom. 15°), No Sting. Variation With Reynolds Number at Mach No. 0.82.
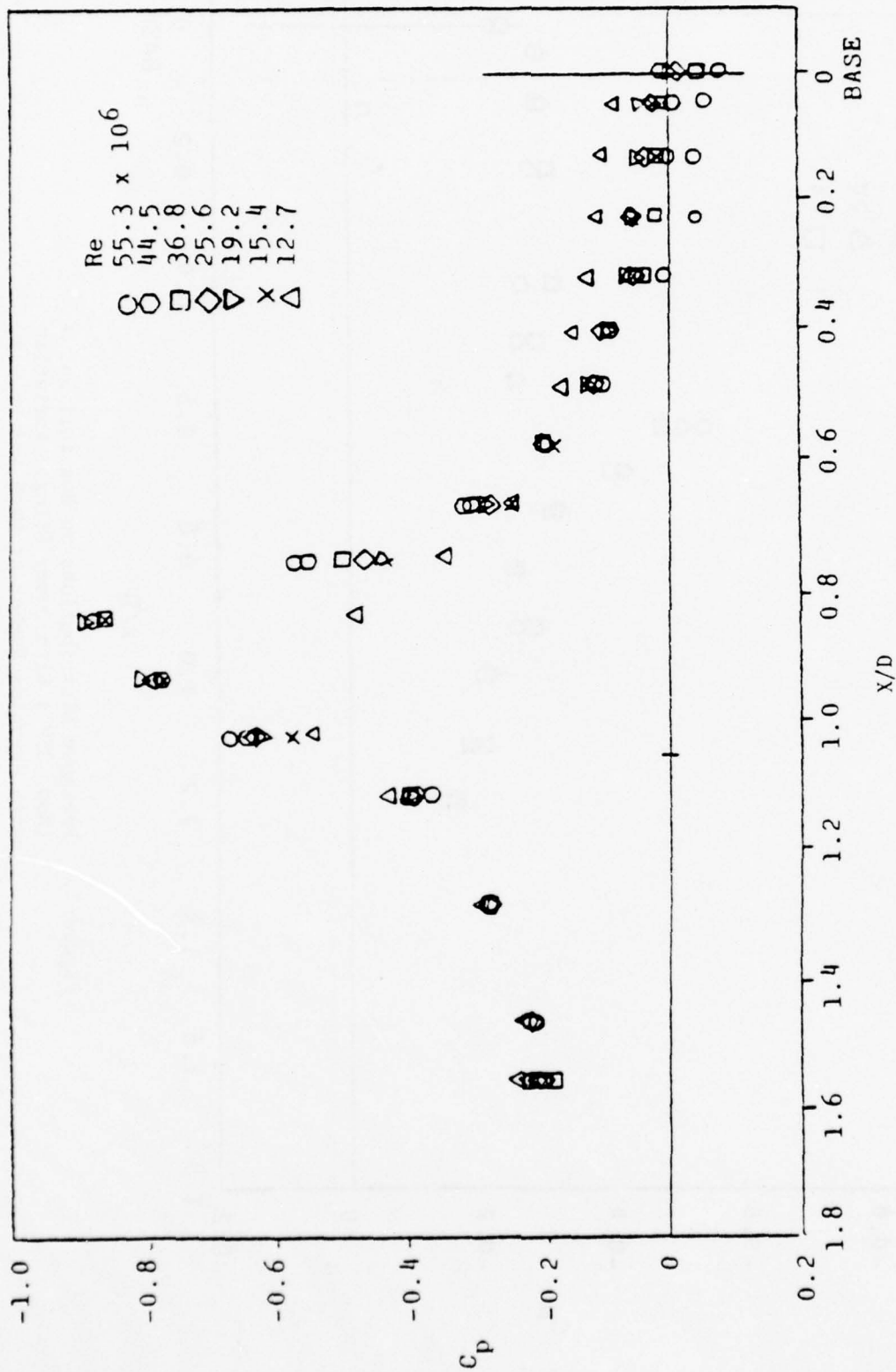
Figure 6.   Pressure Distributions On Boattail No. 2 (Nom. 15°) With
Dummy Sting.   Variation With Reynolds Number at Mach
No. 0.81.

463
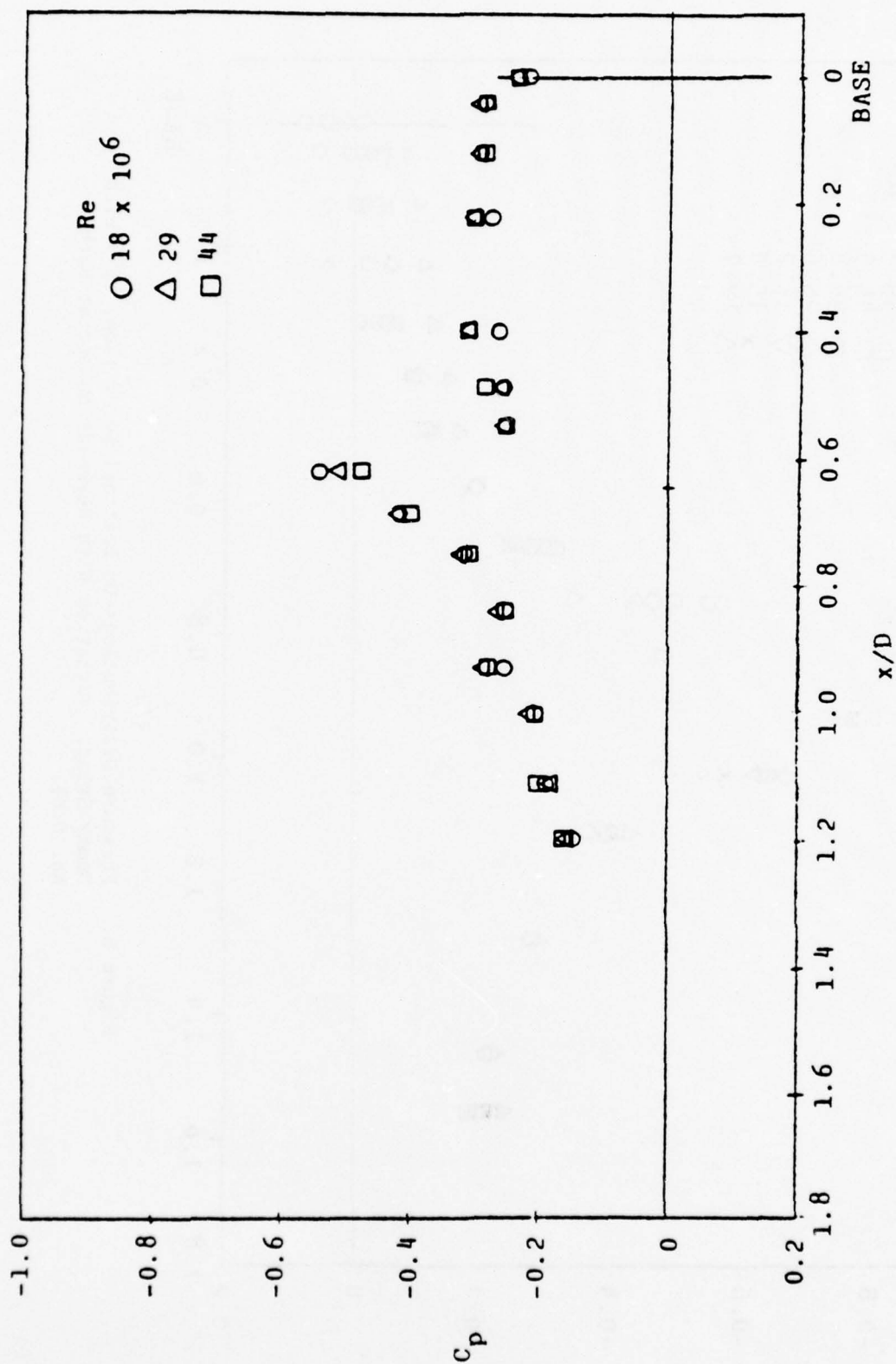
Figure 7. Pressure Distributions on Boattail No. 3 (Nom. 25°) With Dummy Sting. Variation with Reynolds Number at Mach Number 0.81.
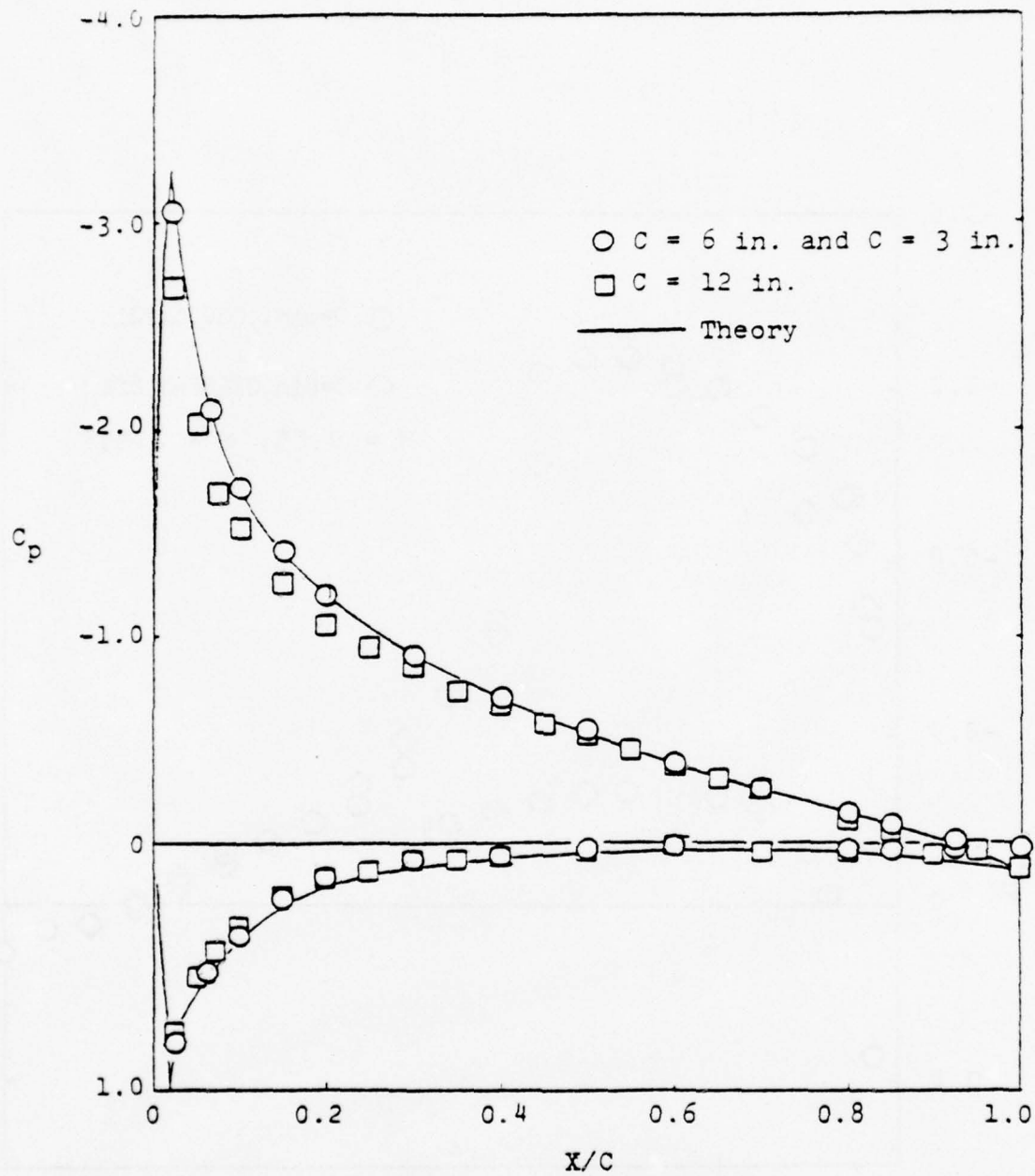
Figure 8. Pressure Distributions on the 0012 Profile
at $M = 0.35$, $\alpha = 8^o$ Showing Lift Interference
on the $C = 12$ in. Model.
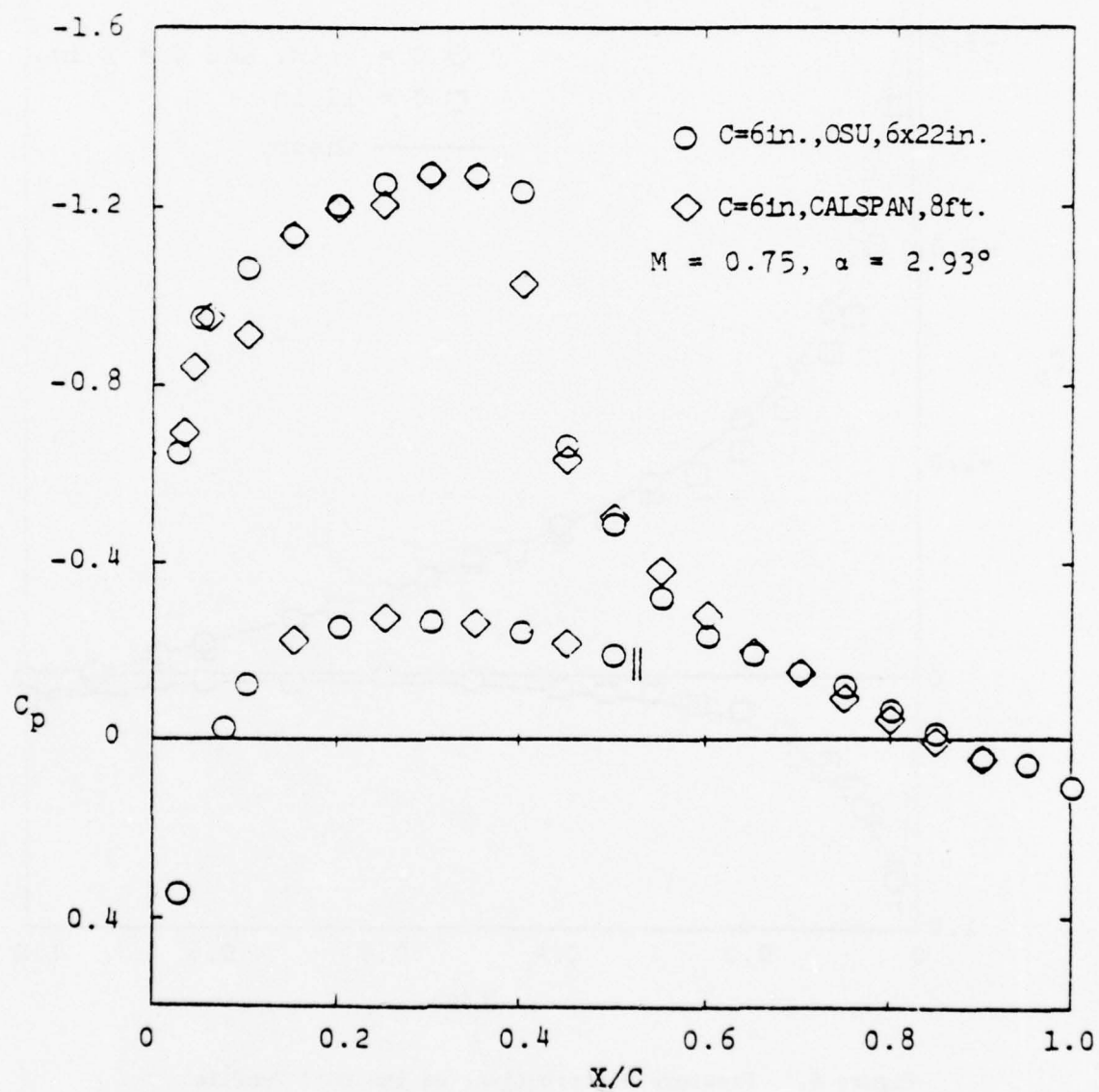
Figure 9. Comparison of Pressure Distributions at M = 0.75,
α = 2.93°. (alternated for lower surface, terminated
at X/C = 0.5 for clarity).
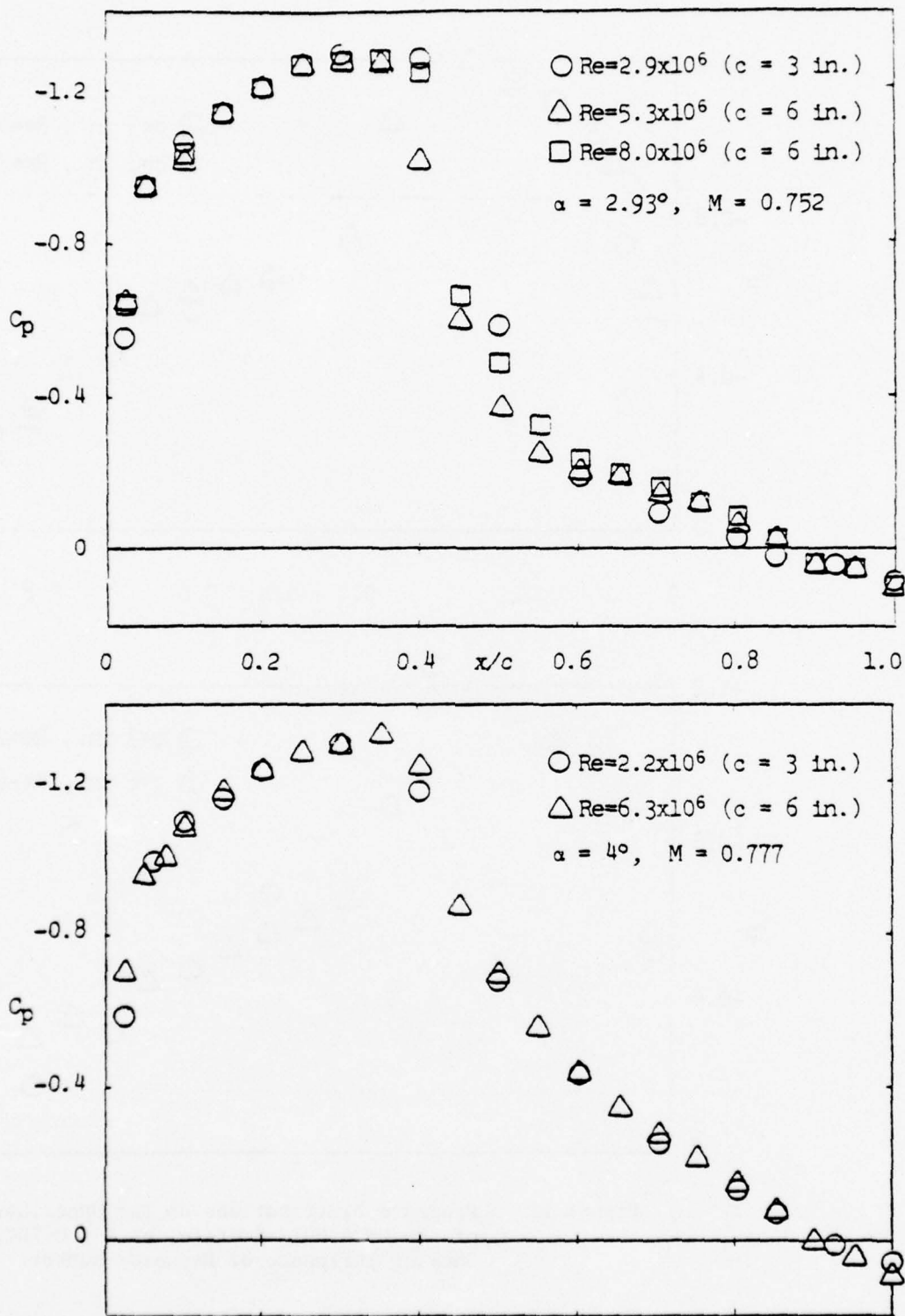
Figure 10. Pressure Distributions on the Upper Surface
of the NACA 0012 Profile Showing Negligible
Scale and Reynolds Number Effects.
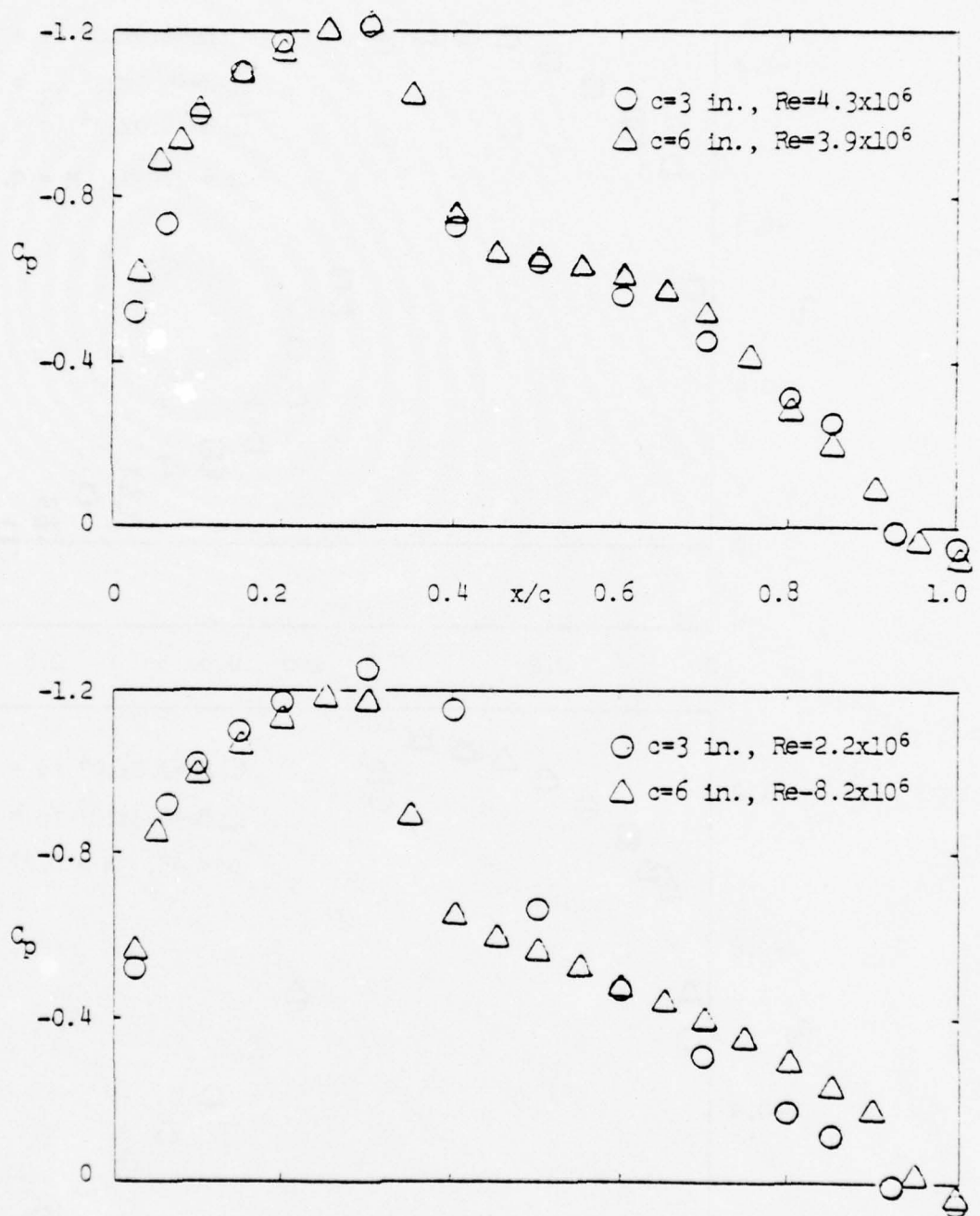
Figure 11.   Pressure Distributions on the Upper Surface
of the NACA 0012 Profile, at M = 0.794, α = 4.0°,
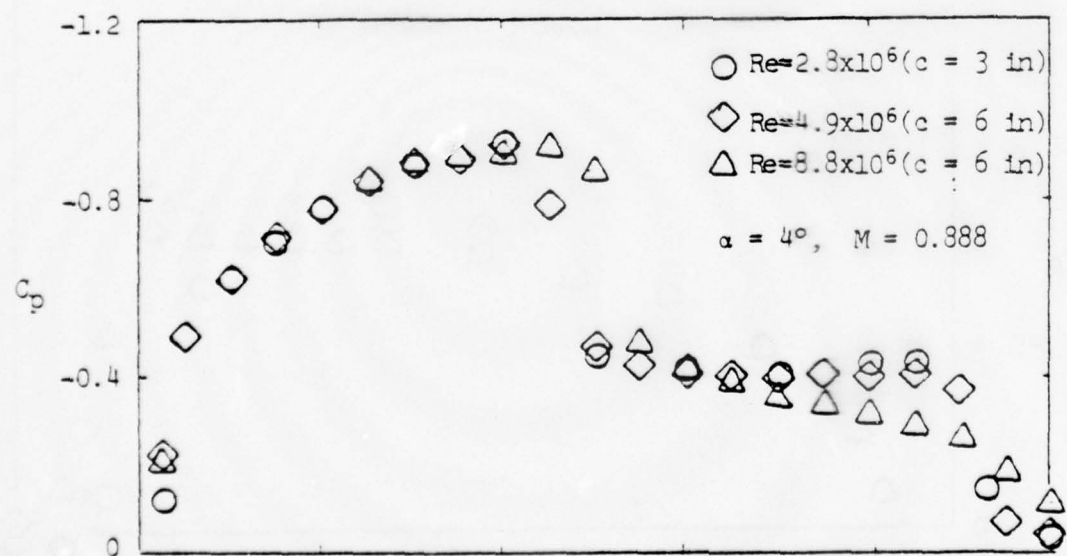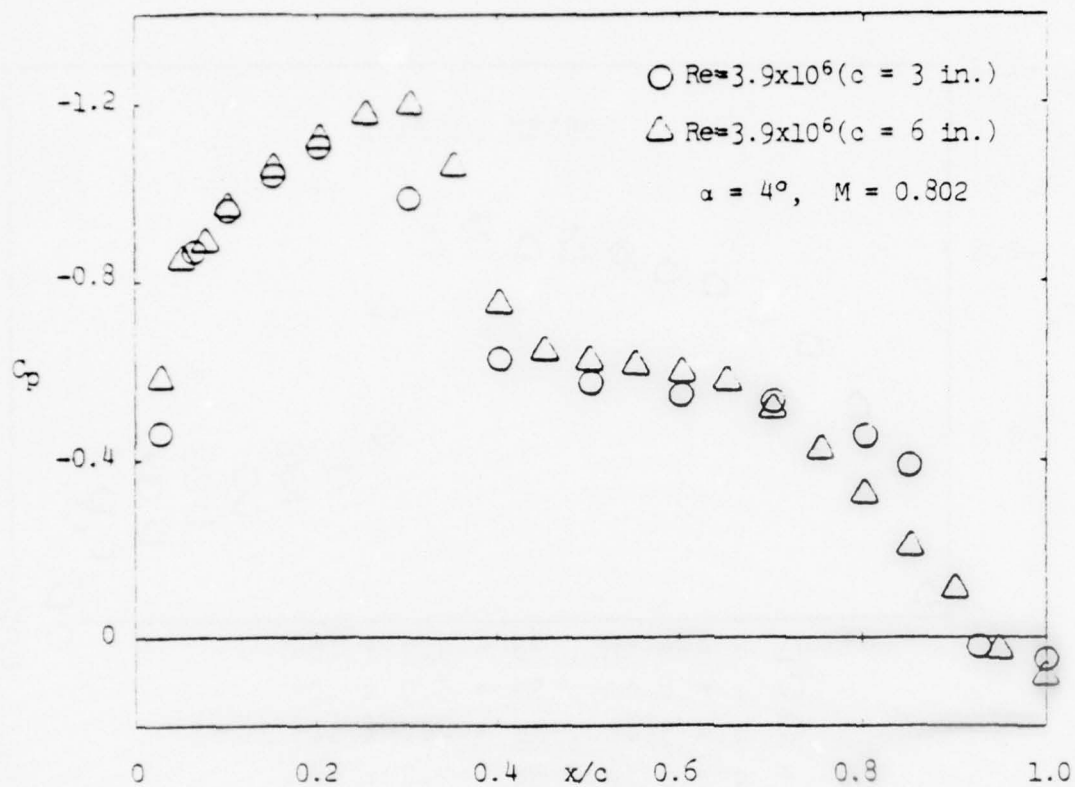Showing Influence of Reynolds Number.

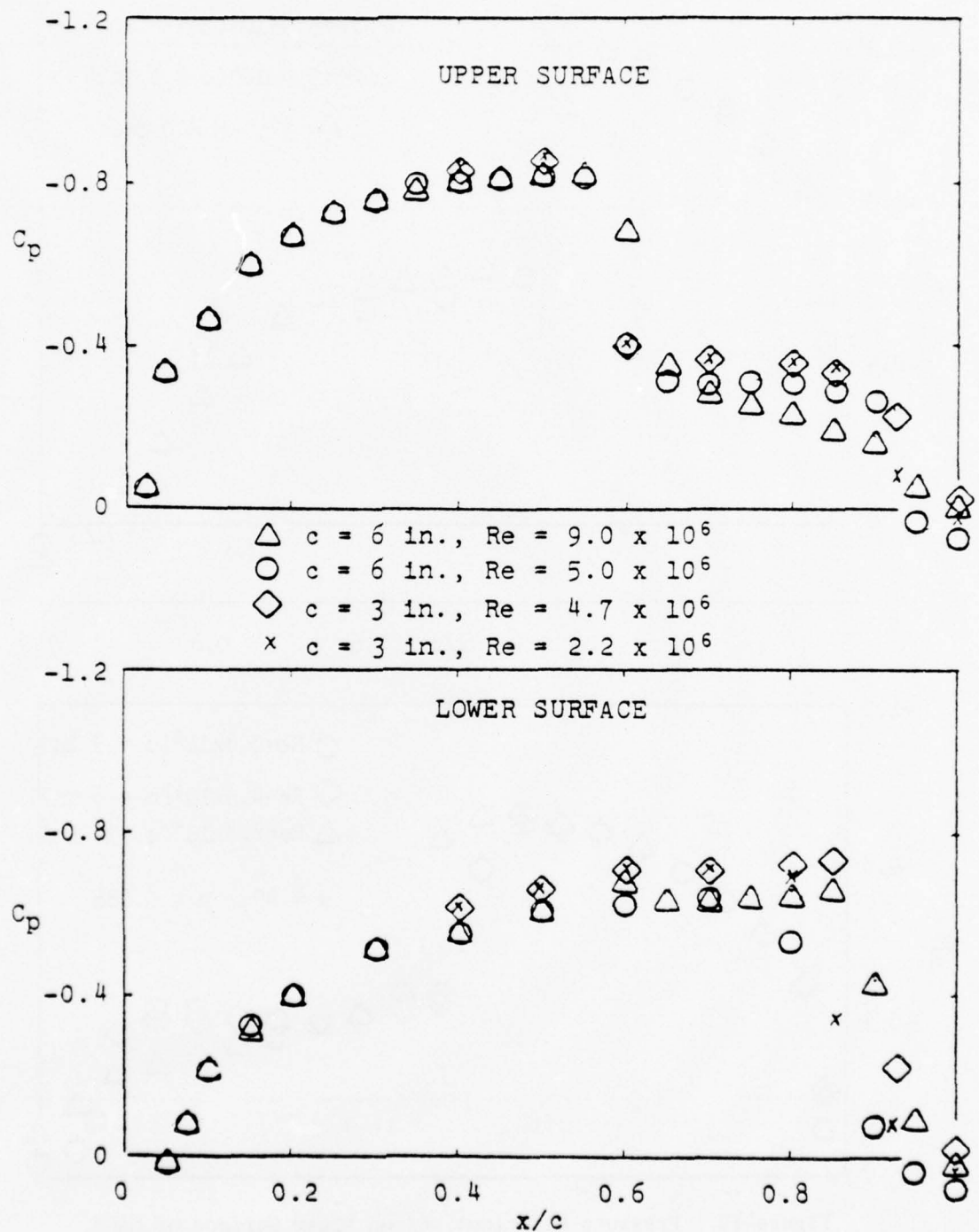Figure 12. Pressure Distributions on Upper Surface of NACA 0012 Profile: Effects From Scale and Reynolds Number.

469

Figure 13.   Pressure Distributions on Both Surfaces of the
NACA 0012 Profile, M = 0.891, α = 2.0°, Showing
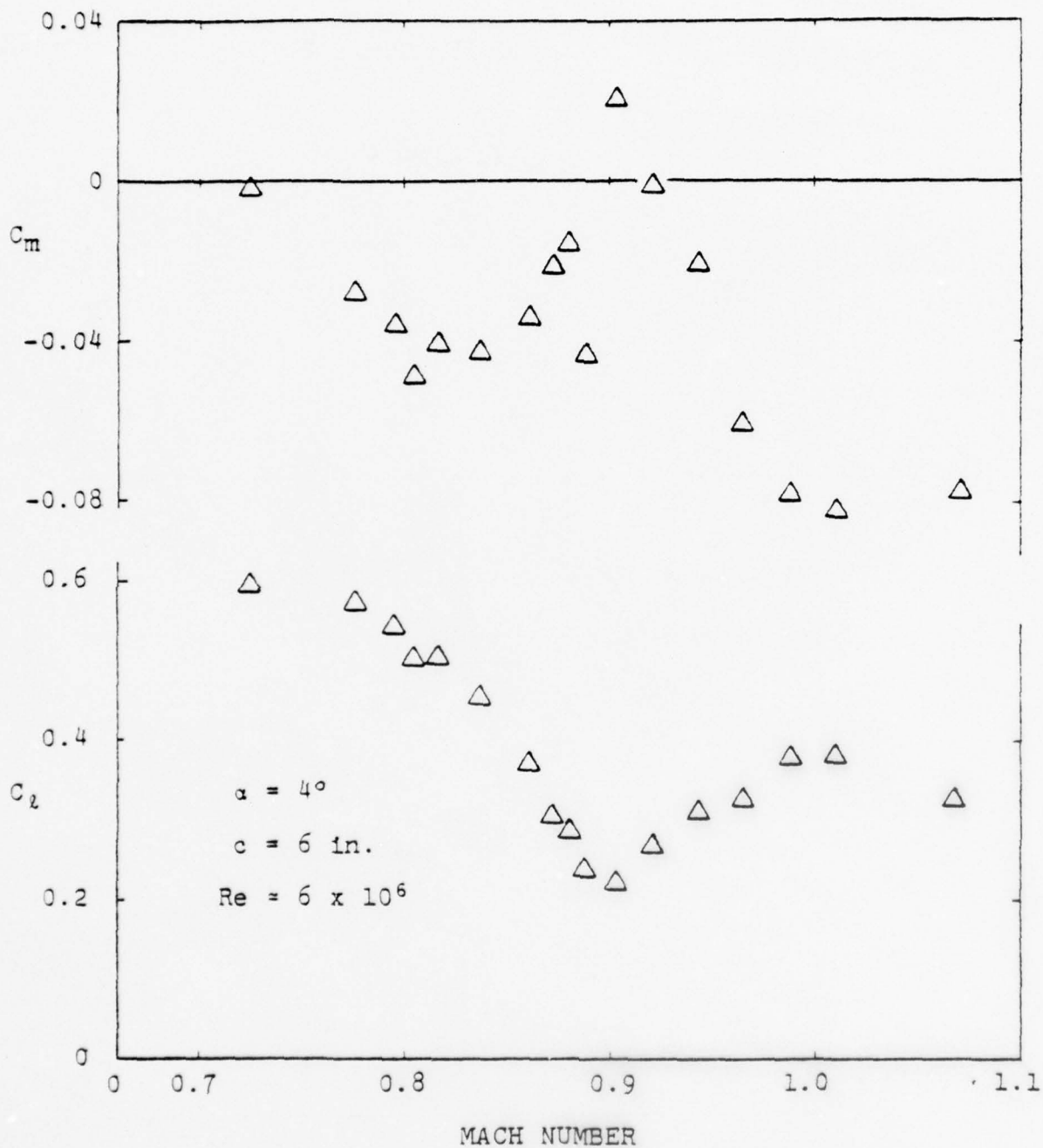Scale and Reynolds Number Effects.

Figure 14.   Lift and Pitching Moment (quarter-chord) on the
NACA 0012 Section in the Supercritical Range.
c = 6 in., Re $\simeq$ 6 x 10^6, α = 4°.

471

TURBULENT BOUNDARY LAYER MEASUREMENTS ON A
SPINNING TANGENT-OGIVE-CYLINDER AT ANGLE OF
ATTACK

by

J. E. Danberg
University of Delaware
Newark, DE

and

W. B. Sturek
U. S. Army Ballistic Research Laboratories
Aberdeen Proving Ground, MD

ABSTRACT

Experimental measurements of the tripped turbulent boundary
layer profile characteristics on a yawed, spinning tangent-ogive-
cylinder model are described. The profile measurements were made
using a flattened total head probe at 30° increments completely
about the azimuthal plane for three longitudinal stations at M=3,
$\alpha=4°$, $\omega=0$, and 10,000 RPM. Wall static pressure measurements were
obtained in order to compute velocity profiles from the measured
total head pressure. The data have been analyzed according to "law
of the wall-law of the wake" concepts using a least squares fitting
technique. The effect of azimuthal position is revealed in the
growth of the wake parameter by a factor of two from the wind to the
lee-side. A small but consistent effect of spin is also apparent.

LIST OF SYMBOLS

C_s Law of the wall profile parameter

κ Prandtl mixing length constant   0.4

T   Temperature

u   Longitudinal velocity component

u_s A velocity seale parameter

u_τ Wall shear velocity $= (\tau_\omega/\rho_\omega)^{1/2}$

$\tilde{u}$ Transformed velocity (see eqn. (2))

y   Coordinate normal to surface

β $(T_{aw}-T_w) \, / \, (T_{te}-T_w)$

δ Boundary layer thickness

δ_s A boundary layer thickness parameter

ν Kinematic viscosity

π_s Law of the wake profile parameter

ρ Density

Subscripts

aw   Adiabatic wall

e   Edge of the boundary layer

t   Total temperature

w   Wall

1.   INTRODUCTION

The U.S. Army Ballistic Research Laboratories is interested
in the boundary layer development on yawed, spinning slender bodies
of revolution for application to the design of artillery projectiles
in general and for gaining further knowledge of the Magnus effect in
particular.   Reference 1 presents some experimental evidence showing
the significant effect that the boundary layer configuration has on
the Magnus force experienced by a yawed, spinning body of revolution
as well as a discussion of the influence of Magnus on the aero-
dynamic stability of a spin stabilized projectile.   Turbulent boundary
layer development over non-spinning bodies of revolution is also of
interest to the Army in the aerodynamics of missiles.

Recent advances in computational fluid dynamics have resulted
in increased effort toward computation of three dimensional boundary
layer development.   References 2-5 report three dimensional, laminar,
and turbulent compressible boundary layer computations for bodies
of revolution.   Comparisons of the computations to experimental
boundary layer profile data have indicated encouraging agreement with
the experimental data.   This indicates that the numerical techniques
are working well; however, comparisons to detailed profile data have
only been made for cone models.   Comparisons to cone data do not
test the computation technique's ability to cope with effects such
as longitudinal pressure gradient or changes in wall curvature.
Experimental data for comparison to theoretical computations of three
dimensional compressible turbulent boundary layer development avail-
able in the literature are extremely scarce.   References 6 and 7
report experimental measurements of the compressible turbulent
boundary layer on yawed cones.   Similar experimental measurements
for a more general body configuration such as an ogive-cylinder are
not available in the open literature.

The objective of this experimental effort is to obtain detailed
turbulent boundary layer profile data that will be useful for com-
parisons with theoretical computations.   This paper describes
measurements of the tripped turbulent boundary layer on a yawed,

475

spinning tangent-ogive-cylinder model. Measurements were made for the model spinning at a rate of 10,000 RPM and also while the model was not spinning. These measurements were made at three longitudinal stations on the cylinder portion of the model for azimuthal stations completely about the circumference of the model in thirty degree increments.

2. THE EXPERIMENT

2.1 Test Facility

The tests were run in the BRL Supersonic Wind Tunnel No. 1[8]. This is a symmetric, continuous flow, closed circuit facility with a flexible plate nozzel. The test section has a height of 38 cm and a width of 33 cm. The nominal tunnel operating conditions were $M = 3.0$, $p_o = 0.299 \times 10^6$ Pa, and $T_o = 308°K$. The total pressure was maintained within $\pm 1°K$ during each individual test run. The Reynolds number based on model length was 7.4×10^6.

2.2 Model

The model used was a seven caliber long tangent-ogive-cylinder with a one-caliber ogive section. The diameter of the model was 5.08 cm. A schematic drawing showing the model geometry is given in Figure 1. The model was suspended on ball bearings and an internal air driven turbine was used to drive the model in spin. The model was made of high strength aluminum alloy and was highly polished. The model was dynamically balanced to a tolerance of 2.1 gram-cm. A boundary layer trip consisting of a 0.64 cm wide band of #80 sand grit was placed 2.5 cm from the tip of the model.

2.3 Survey Mechanism

The survey mechanism was designed to drive the probe perpendicular to the axis of the model. The probe is positioned by a cam that is rotated using an electric motor mounted within the angle-of-attack crescent. Since the survey mechanism is attached to the angle of attack crescent, the probe is driven perpendicular to the axis of the model for any angle of attack setting. The azimuthal position is determined by selecting predrilled mounting holes placed at 30°

476

its. The number of azimuthal position changes was kept to
_um by obtaining data at positive and negative angles of
.

The survey mechanism was calibrated by using a dial indicator
_dicate the displacement of the probe support in thousandths of
_nch to establish a table of displacement versus electrical output
_nal from the probe drive mechanism. In the data reduction procedure
_vided difference interpolation was used to determine the y position
_r a given electrical signal. The coordinate system is indicated in
_igure 2.

2.4   Test Procedure

Total head surveys were made of the boundary layer at three
longitudinal positions along the cylinder portion of the model for
an angle of attack of 4°, M = 3, and for spin rates of zero and
10,000 RPM. The total head probe used had a flattened tip. The
probe tip has an opening of 0.076 mm with a lip thickness of 0.025 mm
and was 2.5 mm in width. The probe was positioned to measure the
pressure along lines parallel to the model axis.

The surveys were made by starting the measurements well beyond
the edge of the boundary layer--at $y \sim 1.25$ cm whereas the largest
δ was about 0.65 cm. The pressure signal from the total head probe
was measured using a strain gage transducer that was calibrated within
$\pm$ 0.025 percent of its full scale range--0-25 psi (0-0.172 X 10^6 Pa).
Measurements were made while holding the probe in a fixed position
after allowing approximately thirty seconds for the pressure signal
to stabilize. The position of the model surface was detected by
electrical signal when the probe contacted the surface of the non-
spinning model. Immediately following the survey for the model not
spinning, the model was spun to 10,000 RPM and another survey made
again starting from well beyond the outer edge of the viscous region.
The model spin rate was held constant within $\pm$ 50 RPM during the
survey using an automatic control on the air supply to the driving
turbine. These surveys were stopped close to, but not touching, the
model surface in order to preclude damage to the model surface or the
total head probe. Each survey consisted of 35-40 data points.

increments. The number of azimuthal position changes was kept to a minimum by obtaining data at positive and negative angles of attack.

The survey mechanism was calibrated by using a dial indicator to indicate the displacement of the probe support in thousandths of an inch to establish a table of displacement versus electrical output signal from the probe drive mechanism. In the data reduction procedure divided difference interpolation was used to determine the y position for a given electrical signal. The coordinate system is indicated in Figure 2.

2.4   Test Procedure

Total head surveys were made of the boundary layer at three longitudinal positions along the cylinder portion of the model for an angle of attack of $4°$, $M = 3$, and for spin rates of zero and 10,000 RPM. The total head probe used had a flattened tip. The probe tip has an opening of 0.076 mm with a lip thickness of 0.025 mm and was 2.5 mm in width. The probe was positioned to measure the pressure along lines parallel to the model axis.

The surveys were made by starting the measurements well beyond the edge of the boundary layer--at y ~ 1.25 cm whereas the largest δ was about 0.65 cm. The pressure signal from the total head probe was measured using a strain gage transducer that was calibrated within $\pm$ 0.025 percent of its full scale range--0-25 psi (0-0.172 X 10^6 Pa). Measurements were made while holding the probe in a fixed position after allowing approximately thirty seconds for the pressure signal to stabilize. The position of the model surface was detected by electrical signal when the probe contacted the surface of the non-spinning model. Immediately following the survey for the model not spinning, the model was spun to 10,000 RPM and another survey made again starting from well beyond the outer edge of the viscous region. The model spin rate was held constant within $\pm$ 50 RPM during the survey using an automatic control on the air supply to the driving turbine. These surveys were stopped close to, but not touching, the model surface in order to preclude damage to the model surface or the total head probe. Each survey consisted of 35-40 data points.

477

2.5   Wall Static Pressure Measurements

Measurements of wall static pressure have been made in order to
compute velocity profiles from the measurements of total pressure
distribution through the boundary layer. The model used for the wall
pressure measurements was a non-spinning model identical in outside
dimensions to that used for the boundary layer surveys. Wall pressure
taps were located at nine (9) positions on the cylinder portion of the
model. The inside diameter of the wall pressure taps was 0.0599 cm.
The model and strut support were mounted in the roll head mechanism
which allows the model to be rotated in azimuth from ϕ = -90° to
ϕ = 180°. Measurements were obtained for angles of attack from
0° to 10° for 10° increments in azimuthal position. The pressure
leads from the model were approximately 3 meters in length and were
connected to a pressure scanner unit. Each pressure transducers are
calibrated within $\pm$ 0.25 percent of their full scale range of 0-5
psia (0-.0344 X 10^6 Pa).

2.6   Data Reduction

The Mach number distribution within the boundary layer has
been calculated from measured values of total pressure and wall
static pressure using the Rayleigh pitot formula. Velocity and
density profiles have been calculated from the Mach number profiles
assuming a linear variation of $(T_t - T_{aw}) / (T_{te} - T_{aw})$ vs u/u_e
where the adiabatic wall temperature was calculated assuming a
recovery factor of 0.88. Integral properties of the boundary layer
were calculated by integrating the profile data using a Fortran
subroutine which fits a curve to the tabulated data.

3.   DISCUSSION OF THE RESULTS

Examples of the velocity profile data for zero spin are shown
in Figures 3, 4, and 5. These profiles clearly show the growth of
the boundary layer in the azimuthal and longitudinal directions.
Unusual inflection points are noticeable in several of the profiles,
particularly in Figure 4 for ϕ = 0° and ϕ = 180°. This behavior
suggests the presence of vortices submerged within the boundary layer

478

or a tendency to approach separation. This behavior, however, is not strongly evident at the next downstream station shown in Figure 5. Laser light water vapor flow visualization studies revealed a vortical structure submerged within the boundary layer on the lee side of the model near the base. Boundary layer separation was not indicated until the angle of attack reached 6°.

Wall static pressure measurements for four azimuthal stations at $\alpha = 4°$ are shown in Figure 6. These data indicate that the azimuthal pressure gradient changes from always favorable near the nose of the model to favorable and adverse as the base of the model is approached. The longitudinal pressure gradient changes from mildly favorable on the windside of the model to strongly adverse as the lee-side of the model is approached. The influence of the longitudinal and circum-ferential adverse pressure gradients is seen in the rapid growth of the lee-side boundary layer profiles shown in Figures 4 and 5.

The integral properties of the boundary layer are shown in Figures 7, 8, and 9. These data indicate that little effect of spin is evident except at the last station. Figure 9 shows that the effect of spin is to decrease the boundary layer thickness on the side where surface spin and the inviscid cross flow are in the same direction; whereas the boundary layer is more thick on the side where the surface spin and inviscid cross flow are in opposite directions. The growth of the boundary layer in the circumferential and longi-tudinal directions is shown in the plots of δ^* and θ. The plots of the form factor, H, indicate little effect of longitudinal or cir-cumferential station. The form factor is, however, consistently greater for the spinning model.

4.   PROFILE CHARACTERIZATION

An attempt has been made to gain additional information about the characteristics of the measured velocity profiles using "law of the wall" and "law of the wake" turbulent boundary layer concepts. The procedure used is based on the method proposed in Reference 9 where a least square fitting technique is employed to determine certain profile parameters. The form of the assumed profile is based

on the work of Cole's[10] in incompressible flow in which the boundary
layer is found to have a wall region in which the velocity is depen-
dent on a velocity scale, u_s, and a length scale ν_w/u_s and a wake
region which is also dependent on u_s but the length scale is a
boundary layer thickness, δ_s. The following functional relationship
was used in the data reduction:

$$\tilde{u}/u_s = \underbrace{\ln(u_s y/\nu_w) + c_s}_{\text{law of the wall}} + \underbrace{2\pi_s \sin^2(\pi y/2\delta_s)}_{\text{law of the wake}} \tag{1}$$

Compressibility effects are accounted for, at least approximately,
using the results of the Prandtl-Van Driest[11] mixing length analysis
in which the compressible flow velocity, u, is transformed into an
equivalent incompressible form through

$$\tilde{u} = \int_o^u \sqrt{\rho/\rho_w} \; du \tag{2}$$

which is evaluated numerically from the measured Mach number profiles
and assuming: (a) constant pressure across the boundary layer, (b)
perfect gas equation of state, (c) adiabatic relationship between
Mach number, total and static temperature and (d) the Crocco tempera-
ture-velocity equation:

$$(T_t - T_w) \; / \; (T_{te} - T_w) = \beta(u/u_e) + (1-\beta) \; (u/u_e)^2 \tag{3}$$

$$\beta = (T_{aw} - T_w) \; / \; (T_{te} - T_w)$$

In Equation (1) there are four parameters; u_s, C_s, π_s and δ_s
which are determined so as to minimize the rms deviation between the
profile measurements and the analytical curve. It should be noted
that the form of the "law of the wall" used here is not valid in the
laminar sublayer region near the wall. Data close to the wall which
systematically deviate from the semilogrithmic relation are omitted
from the fitting procedure. The equation is also not valid when the

480

velocity becomes uniform at the edge of the boundary layer. Only data corresponding to y values less than δ are used in the curve fitting, where δ is defined as the value of y at which the derivative of equation (1) (du/dy) is zero. The boundary layer thickness δ is typically ten percent larger than δ_s.

The more conventional form of Equation (1), for example as used by Coles[10], is related to Equation (1) when

$$u_s = u_\tau / \kappa \qquad (4)$$

where
κ = Prandtl's mixing length constant

u_τ = wall shear velocity = $\sqrt{\tau_w / \rho_w}$

As a consequence the usual constant in the logrithmic wall law is related to C_s by

$$C_s = C\kappa + \ln \kappa \qquad (5)$$

The change in definition of these two parameters is desirable for the present purposes because κ can not be determined solely from velocity profile data unless accurate data in the laminar sublayer is obtained. However, if κ is assumed known ($\kappa \sim .4$ approximately) then Equation (4) may be used to determine the wall shear stress.

Equation (1) is found to adequately describe a wide range of two-dimensional turbulent boundary layer measurements except, of course, in the laminar sublayer. Most two-dimensional profiles can be represented in this way with a root-mean-square deviation of less than $\pm.03$ in $\tilde{u}/u_s$. This corresponds to about $\pm.3$ percent of the maximum flow velocity at the edge of the boundary layer which is approximately the error expected in the transducers used for the pressure measurements. The fit of the three-dimensional boundary layers considered here was typically the same with the maximum rms deviation of .09. Figure 10 illustrates the quality of the fit obtained with the present data. The figure shows the variation of the velocity profiles with azimuthal position for the most rearward

481

station (6 calibers from the nose) on the non-spinning model. The thickening of the boundary layer on the leeward side (180°) is evident as well as a significant increase in the size of the wake region of the profile. The profiles obtained on the spinning model at 10,000 RPM are essentially the same as for the non-spinning case.

5. AZIMUTHAL DISTRIBUTION OF PROFILE PARAMETERS

In Figure 11 the wake region profile parameter, π_s, is shown plotted against azimuthal position for the most rearward station (X/D=6). The maximum velocity increase relative to the logrithmic law is proportional to π_s and the leeward side (180°) is more than twice that on the windward side (0°). The level on the windward side is comparable with the accepted incompressible value of π_s = .55[12] for zero pressure gradient flow. A survey of compressible flow, zero pressure gradient data indicated a value of π_s = .81[9] but the data base included a number of surveys taken on wind tunnel nozzle walls and these contain significant history effects which cause the value of π_s to vary with facility Mach number[13]. Thus the value of π_s on the windward side of the model is essentially that of a zero pressure gradient, two dimensional boundary layer. On the leeward side π_s is more characteristic of an adverse pressure gradient situation. In addition to the variation of π_s with azimuthal angle, there is also a small but consistent effect of spin. At 10,000 RPM the curves are slightly displaced in the direction of rotation.

Figure 12 shows the strong variation of the wall region parameter, C_s, with azimuthal position. The general level of C_s on the leeward side is approximately 1.0 which is quite close to the incompressible zero pressure gradient value of 1.16 (C = 5.5, $\kappa = 0.4$). On the windward side C_s is over three times larger. Zero pressure gradient data from a number of sources[9] indicate a mean value of 1.8 from both flat plate and nozzle wall results but with a large degree of scatter which may indicate that history effects are important. These results as well as those for π_s show that the character of the turbulent boundary layer on the leeward side between 120° to 240° is quite different from that on the windward side of the model.

482

5.   SUMMARY

An experimental effort has been described in which measurements of the three-dimensional turbulent boundary layer and wall static pressure distribution have been obtained for a yawed, spinning slender body of revolution in supersonic flow. The measurements provide a unique set of flow field data for comparison with theoretical computations of boundary layer development and inviscid flow fields. Several observations made upon examination of these data are listed below.

(a) A spin rate of 10,000 RPM has only a slight effect on the measured boundary layer profile characteristics for the tripped turbulent boundary layer.

(b) The circumferential velocity component experiences a favorable pressure gradient from the wind to the lee-side at forward positions on the model; but the pressure gradient changes from favorable to adverse at rearward stations as the lee-side is approached.

(c) A least square curve fitting technique has been used to characterize the measured velocity profiles in terms of four parameters which are related to the "law of the wall" and "law of the wake" regions of a turbulent boundary layer. The wake parameter, π_s, and the wall parameter, C_s, show strong variation around the model associated with the effects of angle of attack. One effect of spin rate is found to be a shift in the wake profile parameter distribution in the direction of spin.

References

1. W. B. Sturek, "Boundary-Layer Distortion on a Spinning Cone," AIAA Journal, Vol. 11, No. 3, March 1973, pp. 395-395.

2. T. C. Lin and S. G. Rubin, "A Two-Layer Model for Coupled Three Dimensional Viscous and Inviscid Flow Calculations," AIAA Paper No. 75-853, presented at the AIAA Fluid and Plasma Dynamics Conference, Hartford, Connecticut, June 1975.

3. J. C. Adams, Jr., "Finite-Difference Analysis of the Three-Dimensional Turbulent Boundary Layer on a Sharp Cone at Angle of Attack in a Supersonic Flow," AIAA Paper No. 72-186 presented at the AIAA 10th Aerospace Sciences Meeting, San Diego, California, January 1972.

4. H. A. Dwyer and B. R. Sanders, "Magnus Forces on Spinning Supersonic Cones--Part I: The Boundary Layer," AIAA Paper No. 75-193, presented at the AIAA 13th Aerospace Sciences Meeting, Pasadena, California, January 1975.

5. J. E. Harris, "An Implicit Finite-Difference Procedure for Solving the Three-Dimensional Compressible Laminar, Transitional, and Turbulent Boundary-Layer Equations," NASA SP-347, March 1975, pp. 19-40.

6. W. J. Rainbird, "Turbulent Boundary Layer Growth and Separation on a Yawed Cone," AIAA Journal, Vol. 6, No. 12, December 1968, pp. 2410-2416.

7. M. E. Fisher and L. M. Weinstein, "Turbulent Compressible Three-Dimensional Flow Profiles," AIAA Journal, Vol. 12, No. 2, February 1974, pp. 131-132.

8. J. C. McMullen, "Wind Tunnel Testing Facilities at the Ballistic Research Laboratories," BRL Memorandum Report No. 1292, U. S. Army Ballistic Research Laboratories, Aberdeen Proving Ground, Maryland, July 1960. AD 244180.

9. J. E. Danberg, "A Re-evaluation of Zero Pressure Gradient Compressible Turbulent Boundary Layer Measurements," Proceedings CP-93, AGARD Fluid Dynamics Specialists Meeting on "Turbulent Shear Flows," 1971.

10. D. E. Coles, "The Law of The Wake in Turbulent Boundary Layers," J. Fluid Mechanics, Vol. 1, Part 2, 1956, pp. 191-226; also see D. E. Coles and E. A. Hirst, "Proceedings AFOSR-IFP-Stanford Conference on Computation of Turbulent Boundary Layers - 1968", Vol. II, pp. 1-45.

11.   E. R. van Driest, "Turbulent Boundary Layers in Compressible Fluids," J. Aero. Sci., Vol. 18, No. 3, 1951, pp. 145-160.

12.   D. E. Coles, "The Turbulent Boundary Layer in a Compressible Fluid", RAND Corp., Report R-403-PR, 1962.

13.   J. E. Danberg, "Some Supersonic Wind Tunnel Nozzel Boundary Layer Characteristics", BRL Memorandum Report (to be published) U. S. Army Ballistic Research Laboratories, Aberdeen Proving Ground, Maryland.

NOTE: ALL DIMENSIONS IN CALIBERS

DIA = 5.08 cm

Figure 1. Tangent-Ogive-Cylinder Model.
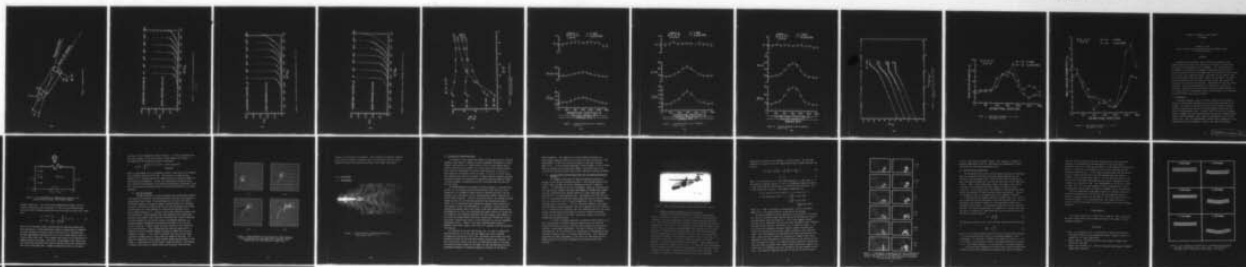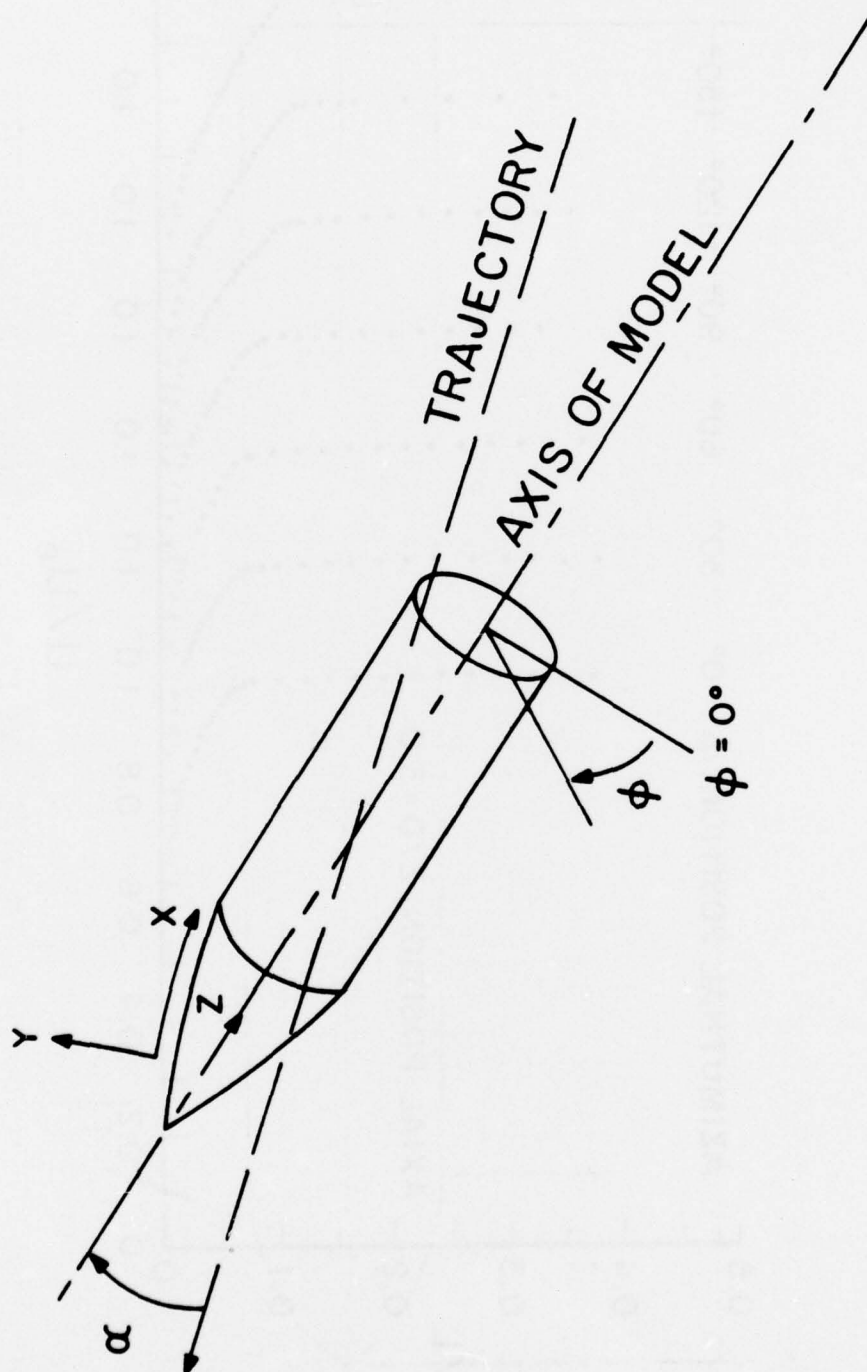
Figure 2. Coordinate System.
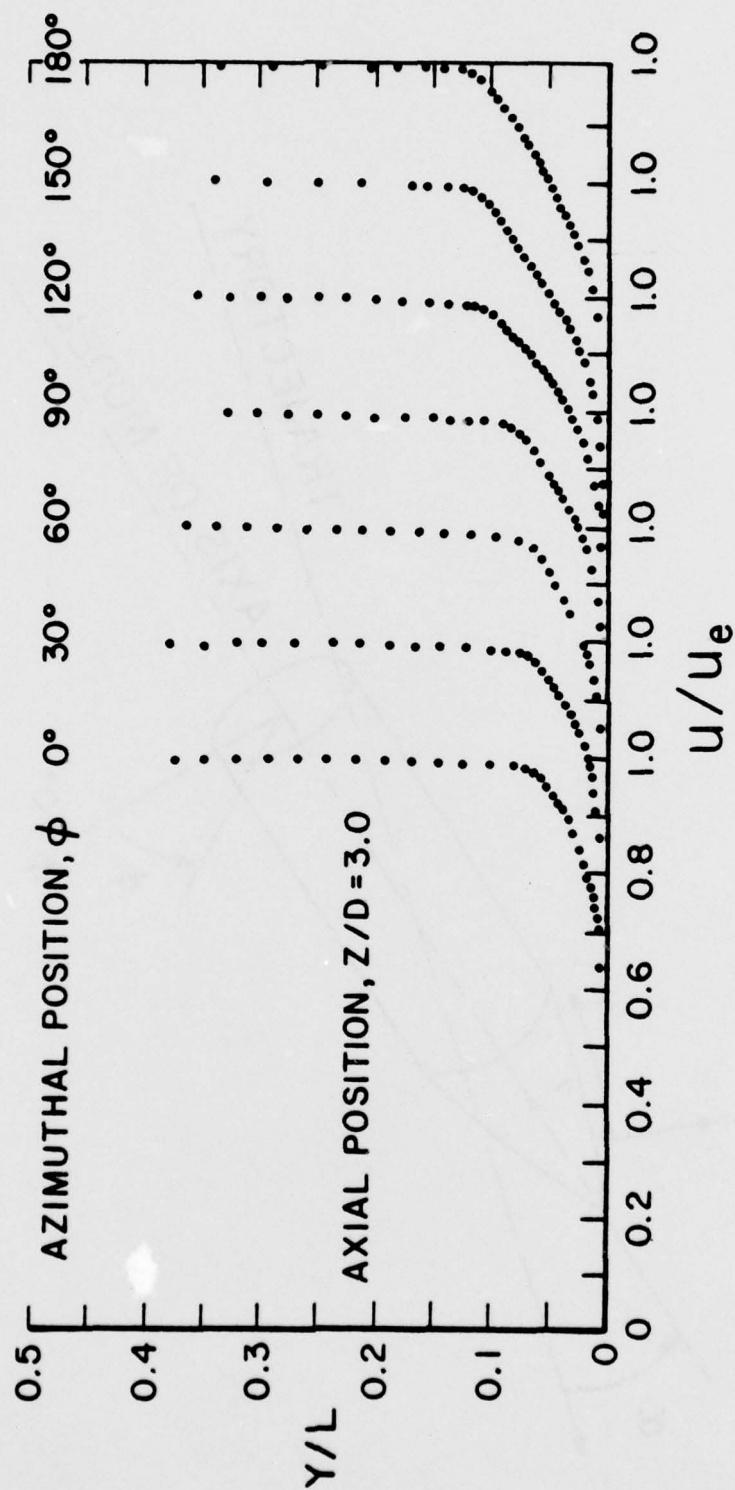
Figure 3. Velocity Profiles versus Azimuthal Position.

(Z/D = 3)
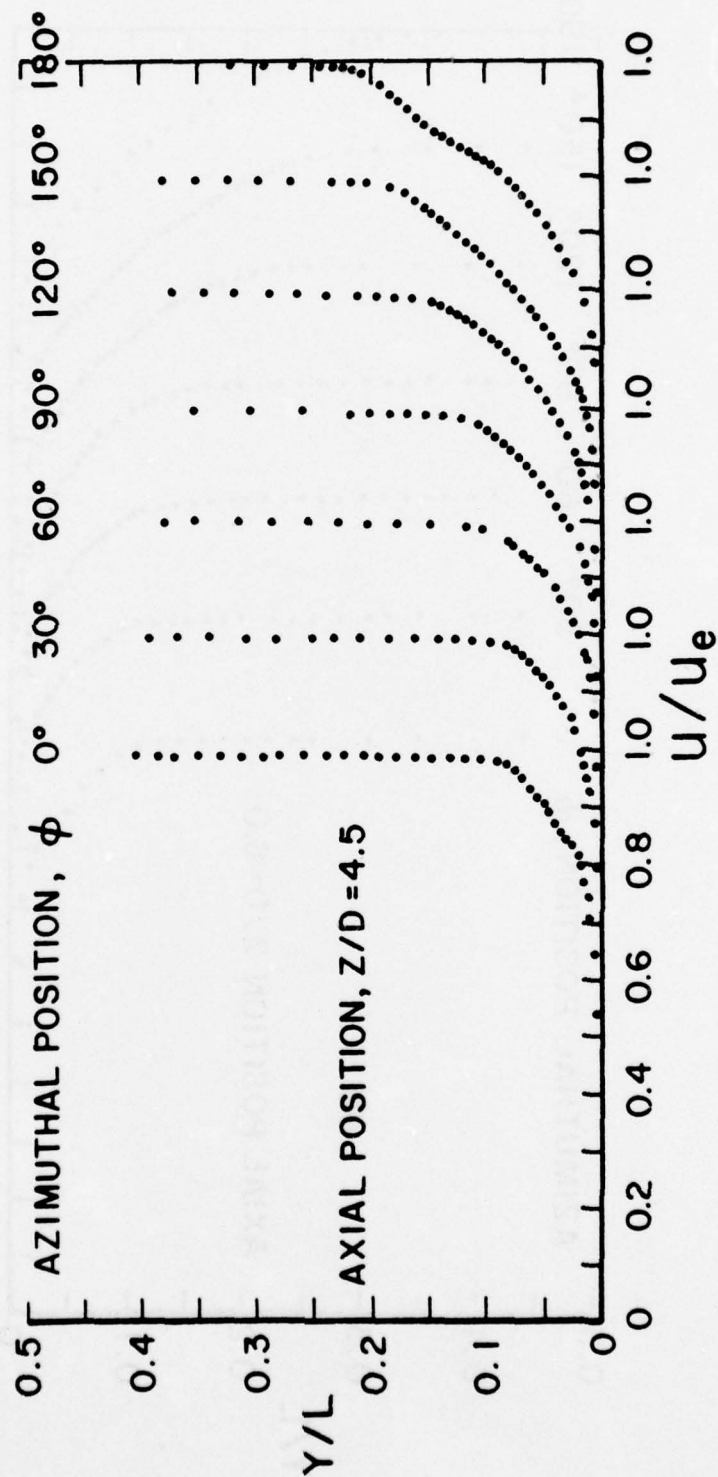
Figure 4. Velocity Profiles versus Azimuthal Position. (Z/D = 4.5)
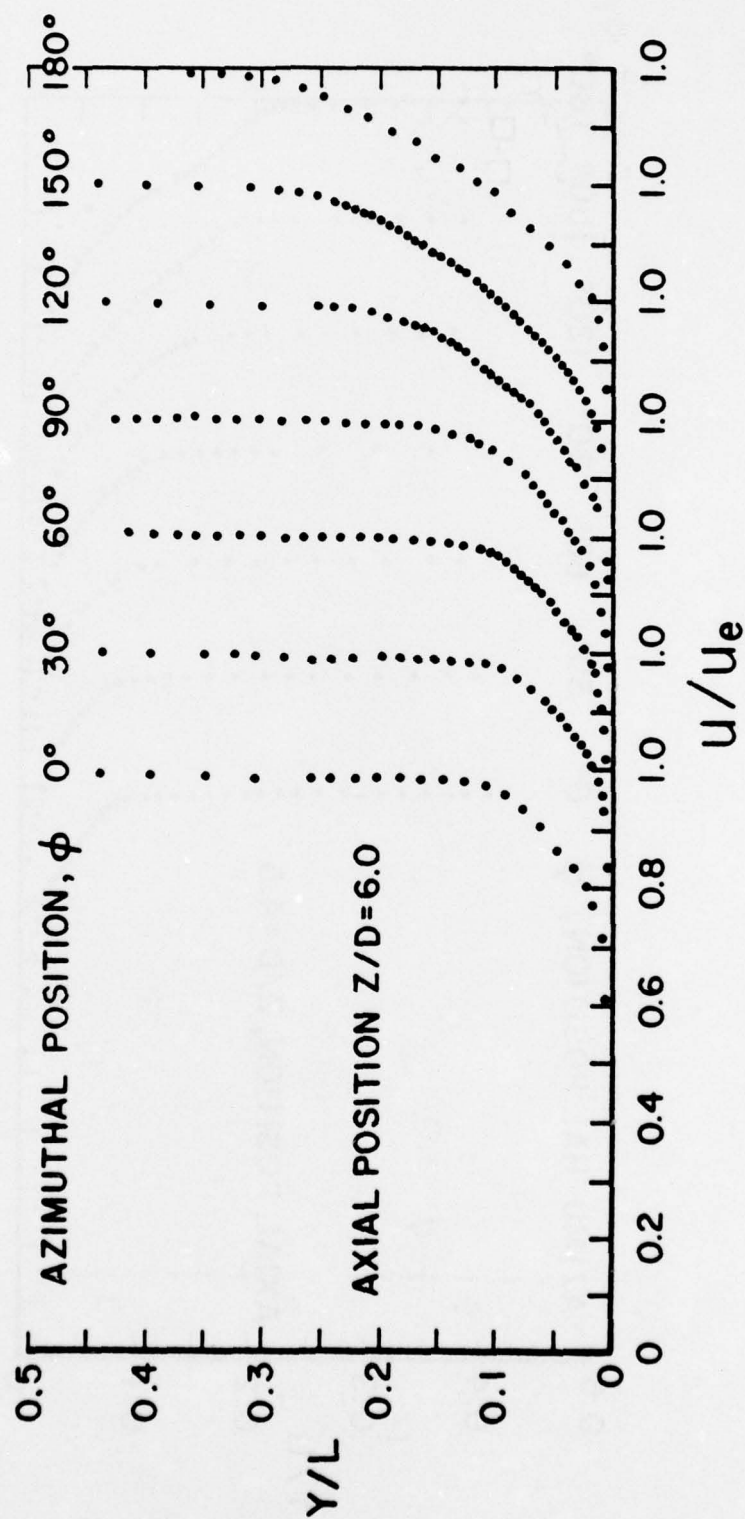
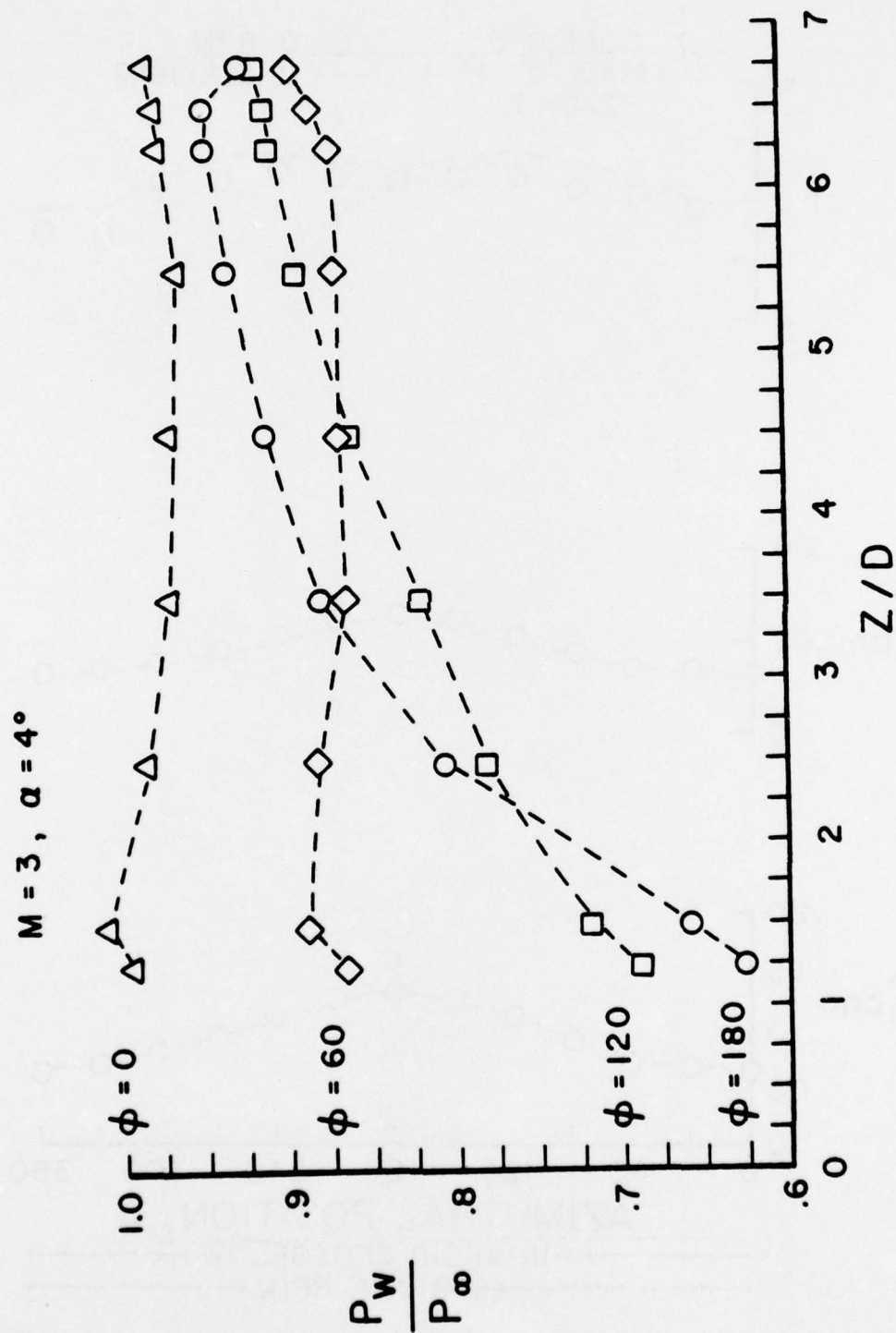Figure 5. Velocity Profiles versus Azimuthal Position (Z/D = 6.0)

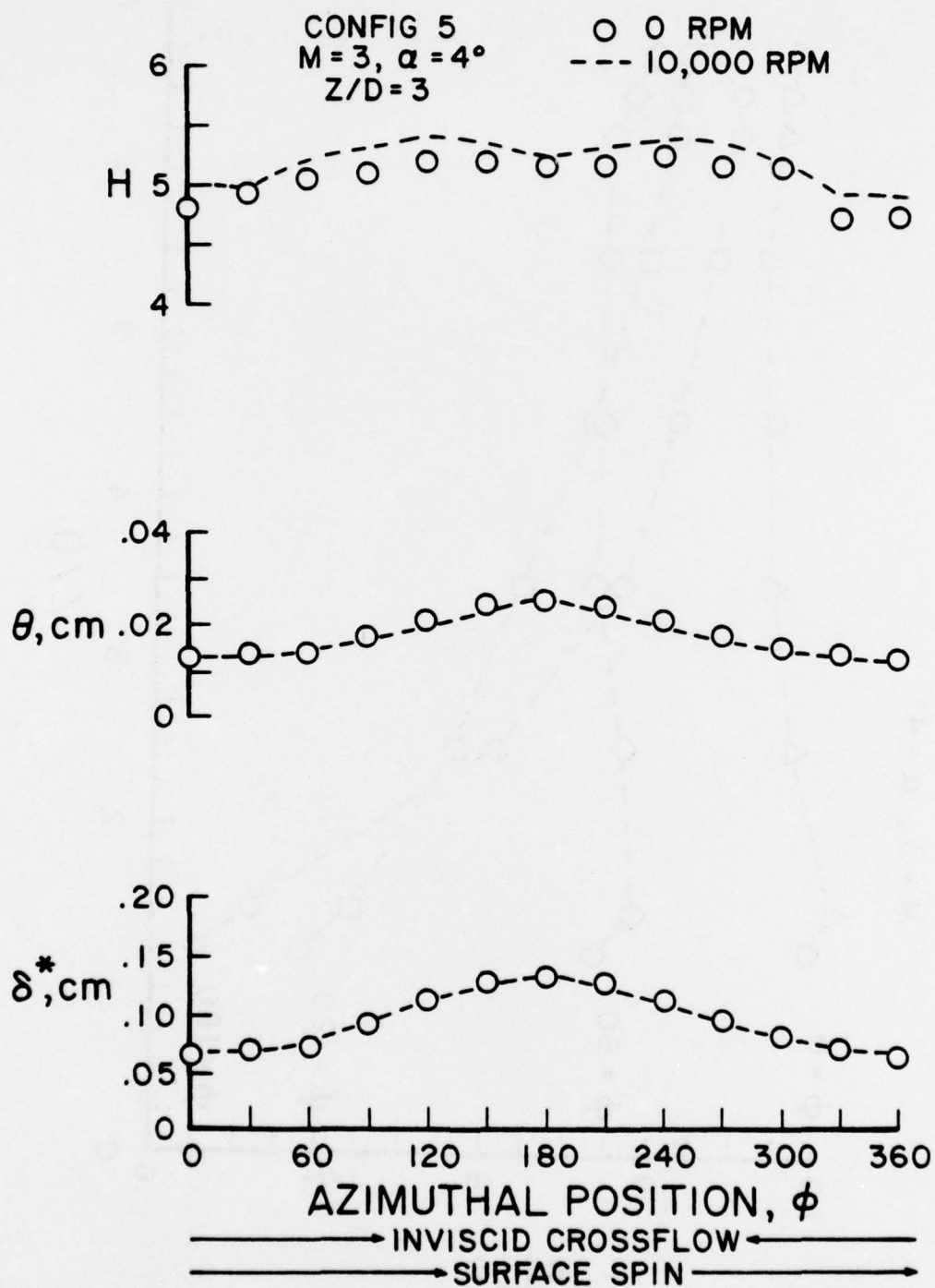Figure 6. Surface Static Pressure Distribution
(Non-spinning Model)

491

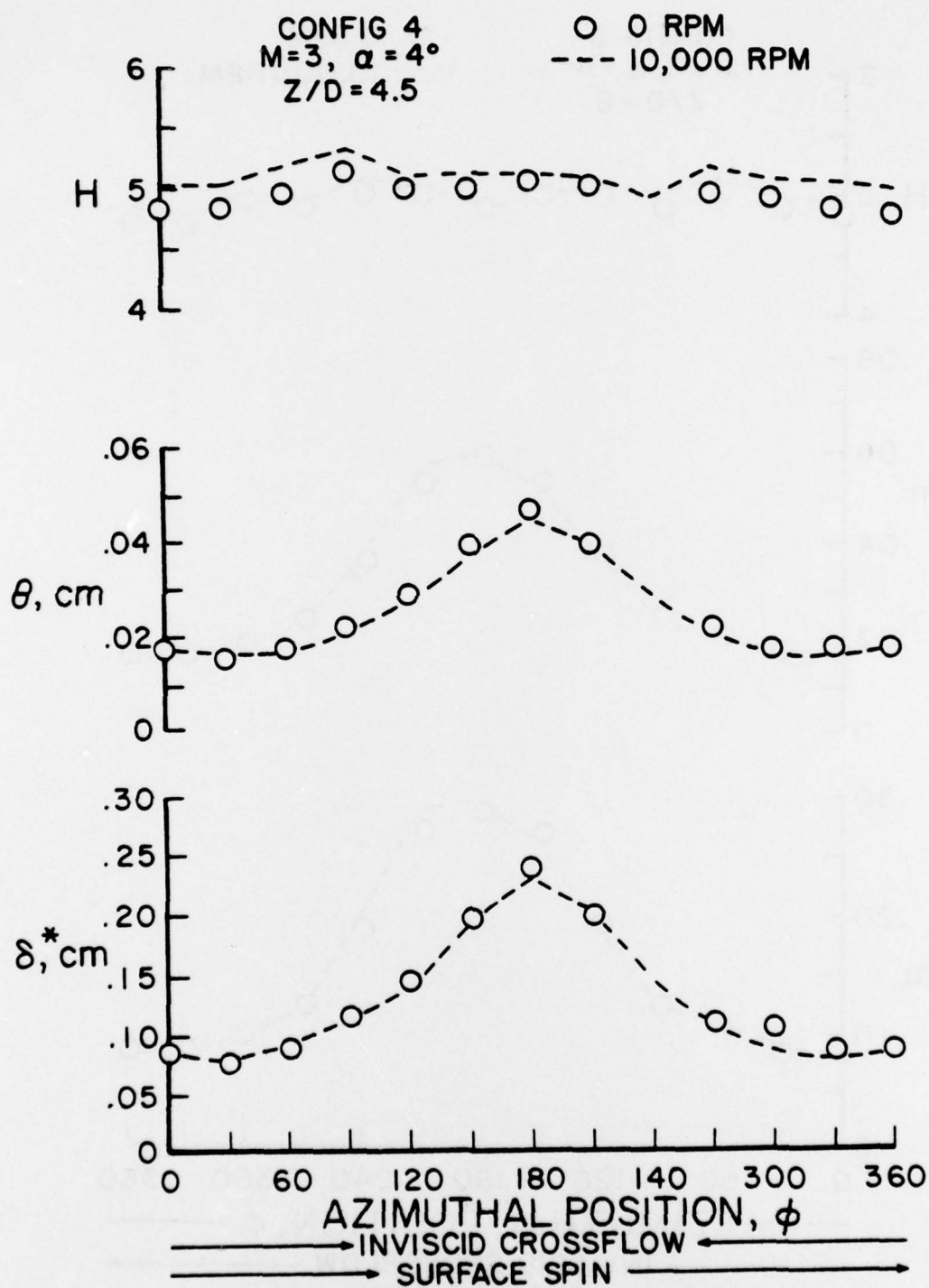Figure 7. Integral Boundary Layer Parameters
(Z/D = 3).

492

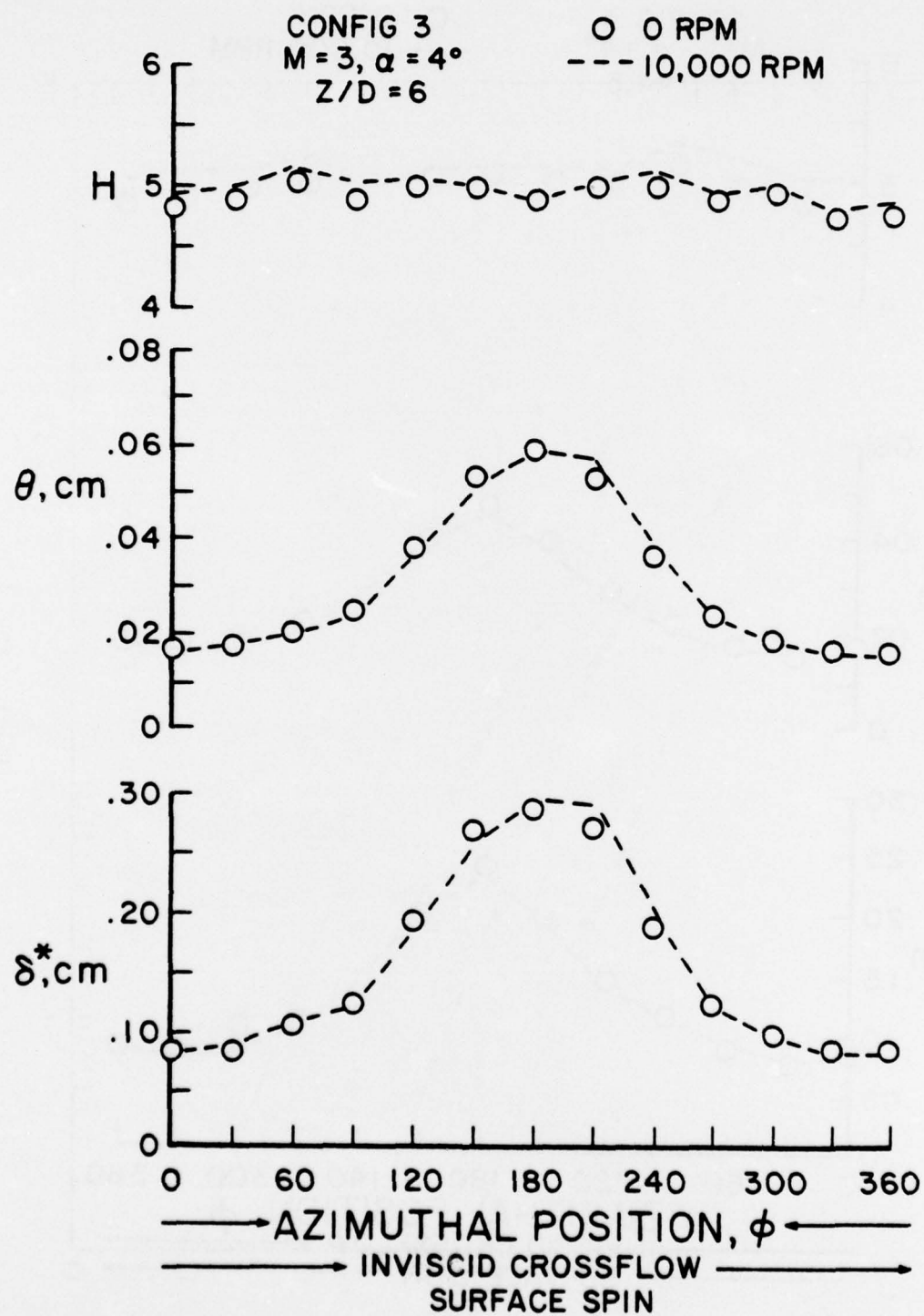Figure 8. Integral Boundary Layer Parameters
(Z/D = 4.5).

493

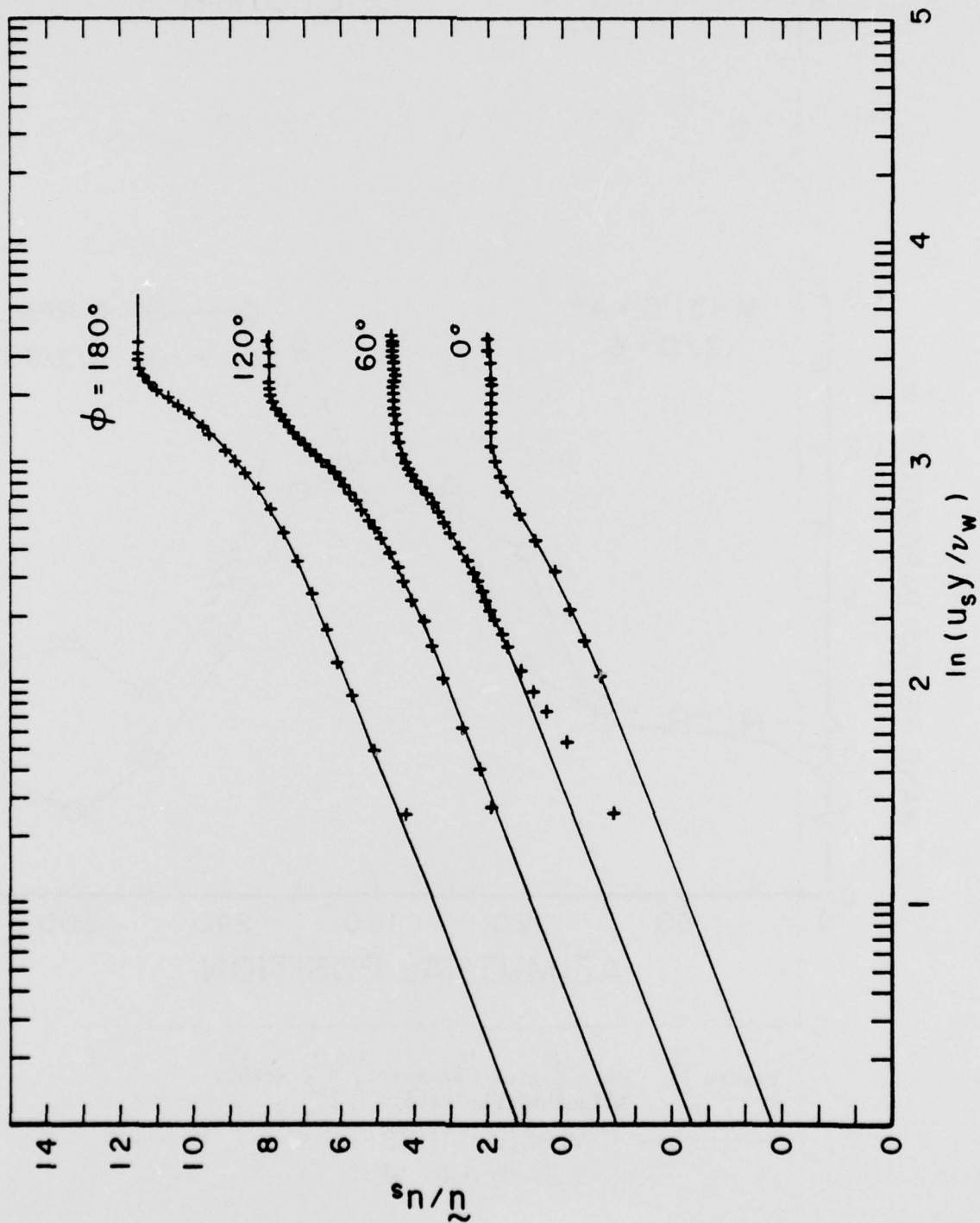Figure 9. Integral Boundary Layer Parameters
(Z/D = 6.0).

494

Figure 10. Velocity Profiles in Law-of-the Wall Coordinates (Z/D = 6.0, w = 0.0).

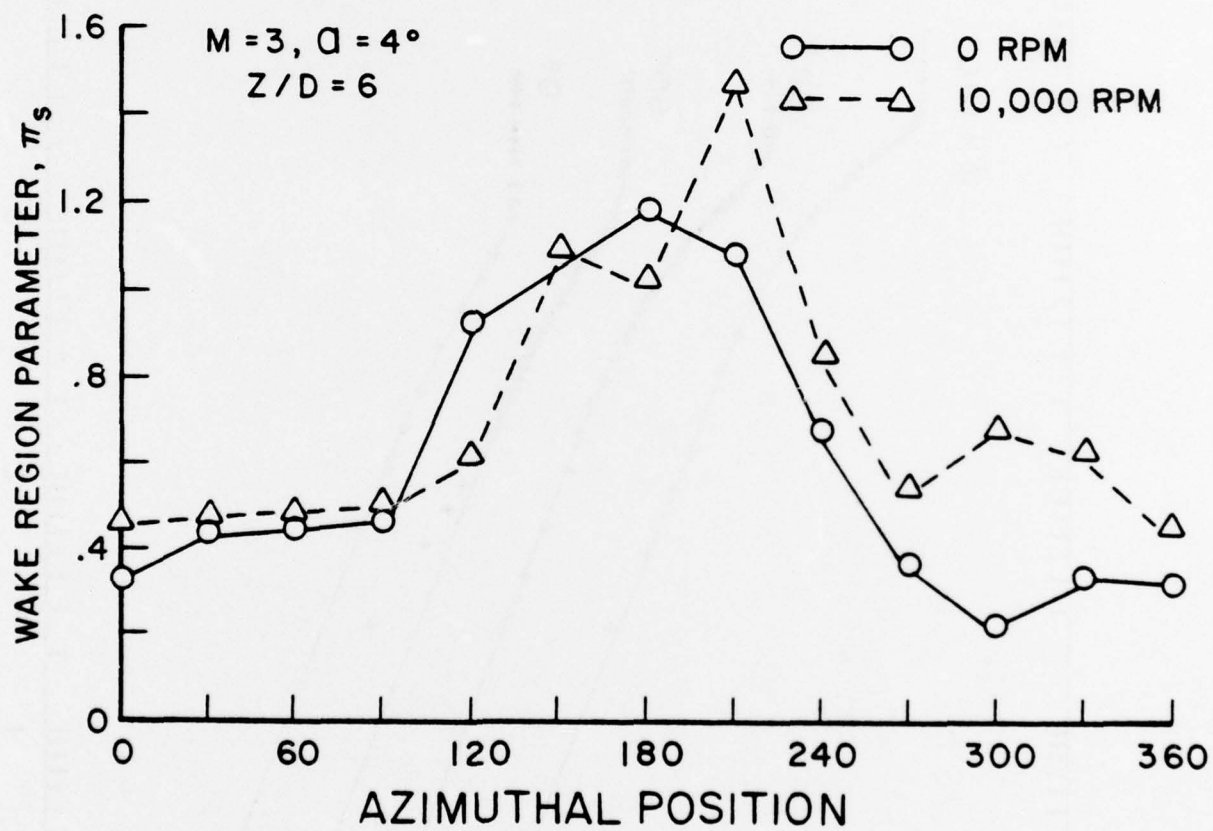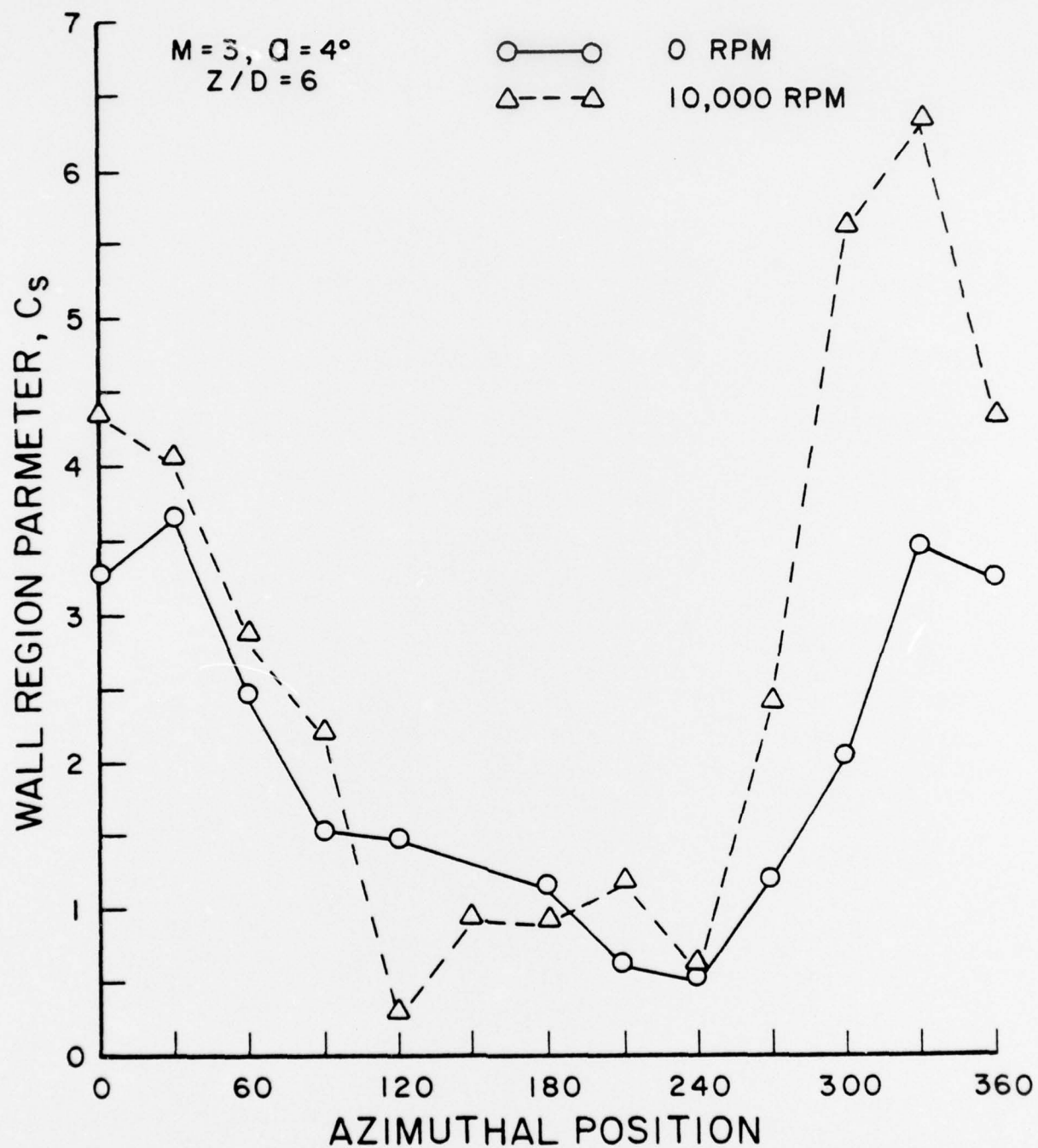Figure 11. Wake Region Parameter, π_s, versus
Azimuthal Position.

Figure 12. Wall Region Parameter, C_s, versus
Azimuthal Position.

497

PROGRESS IN NUMERICAL FLUID DYNAMICS
AT DTNSRDC

by

Joanna W. Schot
David W. Taylor Naval Ship Research and Development Center
Bethesda, Maryland

ABSTRACT

Highlights are presented of some of the work in numerical fluid
dynamics which has recently been completed at the David W. Taylor Naval
Ship Research and Development Center (DTNSRDC). This work involves the
development of new numerical and computer techniques for solving both
viscous and inviscid fluid flow problems which are pertinent to the research
goals of this Data Exchange Agreement. References are also made to some
of the related work being done under contract for the Center. The topics
discussed include free surface potential flow, viscous and interacting
flows, and fluid-structure interactions. Combinations of spectral, finite-
difference, and finite-element methods are employed in the numerical
approaches. Applications of these methods to the performance analysis of
air-cushion vehicles, conventional ships, rotating plates, and circulation-
controlled airfoils are briefly discussed.

1. Introduction

This paper highlights some of the work in numerical fluid dynamics
which has recently been completed and is being further developed at the
DTNSRDC. As the name of the Center indicates, our research is directed
toward the analysis and solution of ship performance problems and the
design of improved naval ships. The word "ship" is used in the broadest
sense to encompass not only conventional designs but also advanced-concept
vehicles such as hydrofoil craft, twin-hull configurations, and surface-
effect ships. Thus, ship hydrodynamics problems form a large part of our
numerical work in fluid dynamics. However, many important problems

involving the aerodynamic properties of higher-speed surface ships, air-cushion vehicles, and carrier-based aircraft must also be solved. Fortunately, from the numerical point of view, techniques developed to solve aerodynamic problems can often be applied to hydrodynamics problems, and conversely. It is the aim of this paper to call attention to recently developed numerical methods and computer techniques which can be further exploited to solve diverse problems pertinent to the research goals of this Data Exchange Agreement.

The areas of research to be discussed in the following sections are potential flow with free surface conditions, viscous-inviscid interacting flows, viscous flows based on the full Navier-Stokes equations, and fluid-structure interactions.

2. Free Surface Potential Flow

The problem of computing the non-lifting potential flow past an arbitrary three-dimensional body has been solved by the source-sink method of Hess and Smith [1], developed under contract for DTNSRDC. This method is regularly used in the process of solving aerodynamic and hydrodynamic problems at the Center, especially the improved programs developed by Dawson [2] and Dawson and Dean [3] known as the XYZ Potential Flow Program with various options. These improved programs compute on-body streamlines for input to boundary layer programs, use a more accurate source calculation which reduces leakage for internal flows, and provide special input-checking for accurate definition and paneling of the body surface. However, these popular methods can not handle potential flow problems with a free surface, such as the wave motion at an air-sea interface. Since naval ships operate in, slightly above, or below this interface, methods for solving potential flow problems with free surface conditions are important. In the past few years various methods, both analytical and numerical, for solving these problems in two and three spatial dimensions have been investigated under the Center's Numerical Ship Hydrodynamics Program. The forthcoming Proceedings of the First International Conference on Numerical Ship Hydrodynamics, sponsored by DTNSRDC in October 1975, will contain many papers on this subject. Two of these investigations, on the moving surface pressure distribution problem and the thin ship problem, are summarized below.

500

a) Moving Surface Pressure Distribution

Haussling and Van Eseltine [4] have developed a combination of finite-difference and spectral (Fourier series) methods to solve transient potential flow problems with both linear and nonlinear free surface conditions. The basic problem which they solved is the flow generated by a pressure disturbance $p(x,z,t)$ moving across a free surface denoted by $y = \eta(x,z,t)$, where t is time and an (x,y,z)-coordinate system is used. Figure 1 illustrates the two-dimensional version of the computational region and the boundary conditions employed. The coordinate system moves with the disturbance. The two-dimensional initial/boundary value problem in the moving reference frame with nonlinear free surface conditions is written in the form

$$\phi_{xx} + \phi_{yy} = 0 \quad -\ell < x < \ell, \; -d < y < \eta \tag{1}$$

$$\eta_t = -U\eta_x - \phi_x\eta_x + \phi_y \quad \text{at} \quad y = \eta \tag{2}$$

$$\phi_t = -U\phi_x - \frac{1}{F_r^2}\eta - \frac{1}{2}(\phi_x^2 + \phi_y^2) - \frac{\delta}{F_r^2}p \quad \text{at} \quad y = \eta \tag{3}$$

$$\phi_x = 0 \quad \text{at} \quad x = \pm\ell \tag{4}$$

$$\phi_y = 0 \quad \text{at} \quad y = -d \tag{5}$$

$$\phi = 0, \; \eta = -\delta p \quad \text{at} \quad t = 0 \tag{6}$$

where $\phi(x,y,t)$ is the velocity potential and subscripts x, y, and t denote differentiation with respect to these independent variables. The dimensionless parameters are the Froude number $F_r = U/(gL)$, based on the length of the pressure disturbance L, and $\delta = P/\rho gL$, where U is the speed of the disturbance, g is the gravitational acceleration, ρ is the constant density of the fluid, and P is the maximum surface pressure. The pressure disturbance may be arbitrarily specified. Haussling and Van Eseltine evaluated both a spectral method and a finite-difference method for solving the Laplace equation. For the time-advancement they used an over-all marching scheme which coupled the solution of the Laplace equation with numerical approximations to the time-dependent free-surface
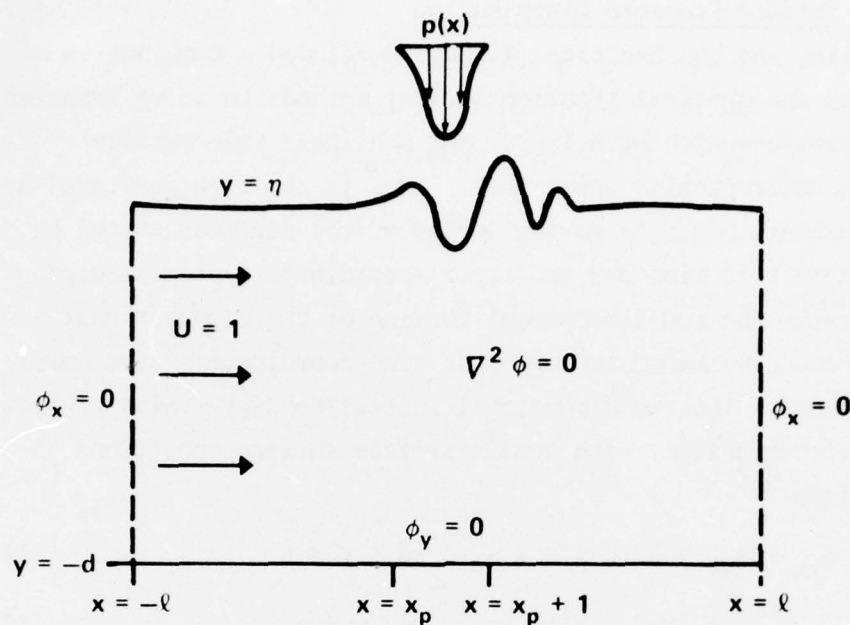
Figure 1. The Two-dimensional Computational Region for the Moving Surface Pressure Distribution Problem.

boundary conditions. For solving three-dimensional problems, the free surface conditions given by Equations (2) and (3) were linearized and replaced by the following expressions which are valid for small wave slopes only

$$
\left.
\begin{aligned}
\eta_t &= -U\eta_x + \phi_y \\
\phi_t &= -U\phi_x - \frac{1}{F_r^2}\eta - \frac{\delta}{F_r^2}p
\end{aligned}
\right\} \quad \text{at} \quad y = 0 \qquad (7)
$$

Based on the favorable results obtained and the experience gained with these approaches, a three-dimensional computer program known as ACVWAVES has been developed by Haussling and Van Eseltine [5] to calculate the unsteady hydrodynamic characteristics of an air-cushion vehicle (ACV) or surface-effect ship (SES). This program uses Fourier series expansions to compute the wave resistance, side force, yawing moment, total power, and wave elevations associated with vehicles moving on arbitrary trajectories over calm or disturbed seas. Computer-generated pictures of the waves

obtained by this program are shown in Figure 2. In this calculation the
ACV, which appears as the small square in each frame of the figure, is
represented by the following pressure distribution

$$p(y=0) = \begin{cases} \sin^2(\pi x^*)\ \sin^2(\pi z^*) & 0 \leq x^* \leq 1 \text{ and } 0 \leq z^* \leq 1 \\ 0 & \text{otherwise} \end{cases}$$

where a right-handed (x,y,z) coordinate system is used, and (x^*,z^*) denotes
the coordinates moving with the ACV. The results, as stated by the
authors in [5], indicate that their scheme provides an efficient means for
analyzing ACV hydrodynamics. By use of a theory which relates an arbi-
trary pressure distribution to the surface elevation and the motions of the
ACV, the pressure distribution could be adjusted realistically as the ship
maneuvers.

b) Thin Ship Problems

Another approach to solving transient three-dimensional potential
free surface flow problems has been developed by Ohring [6] and applied to
conventional "thin" ships. This work makes use of a very fast finite-
difference scheme for solving the Laplace equation which is an outgrowth
of earlier research in viscous fluid flow by Lugt and Ohring, who studied
the efficiency of various methods for constructing solutions of the
Navier-Stokes equations [7]. Using a fourth-order difference operator and
thin ship theory, Ohring computed the time-dependent three-dimensional
potential flow around a thin ship with linearized free surface conditions.
The direct method for solving the system of difference equations is a
modified diagonal decomposition technique which makes use of the fast
Fourier transform. Ohring's paper [6] gives details of this scheme and
the results obtained. Three-dimensional wave patterns generated in a
channel by Ohring's THINSHIP computer program are shown from an aerial
viewpoint in Figure 3. The time T=3 indicates that the ship has moved
upstream a distance equal to three times the length of the ship. The
region of computation, which extends farther downstream than shown in the
figure, is represented by 129 grid points along the length of the channel,
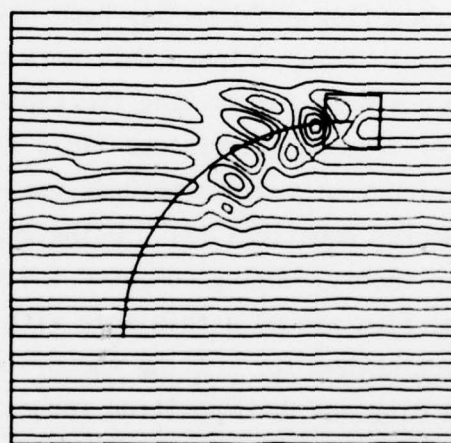17 points across half the channel width, and 64 points from the water
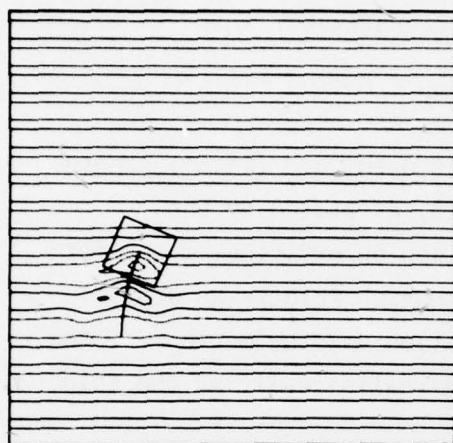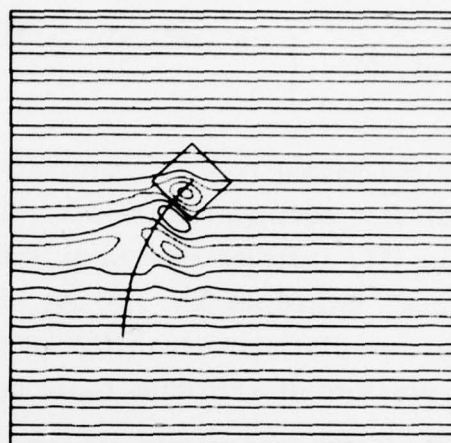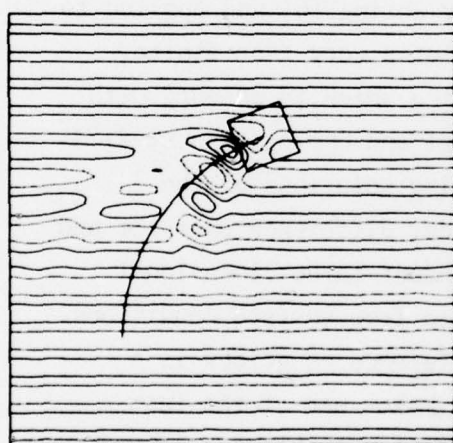
Figure 2. Wave Elevations at Four Successive Times Generated by an ACV Moving Over a Disturbed Area. Negative values (depressions) are represented by broken lines.

surface to the bottom of the channel. This extensive calculation required less than five minutes of computer time on the CDC 6600, and the results compare favorably with patterns generated by ship model experiments.
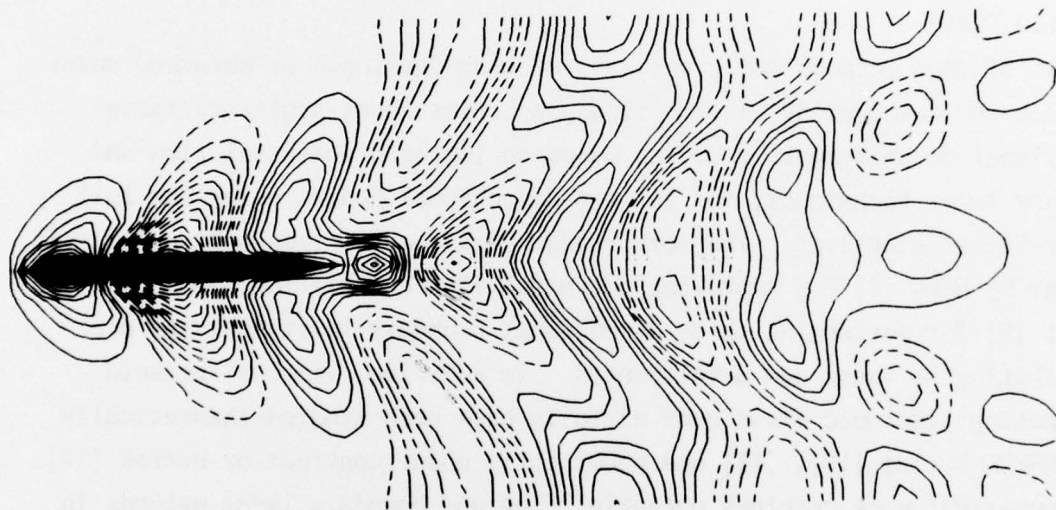
———— ELEVATION

– – – – DEPRESSION

Figure 3. Aerial View of 3-D Waves Generated by a
Thin Ship at Time T = 3.0.

3. Viscous and Interacting Flows

In addition to the established methods of applying potential flow and boundary layer theory to compute viscosity-dependent aerodynamic or hydrodynamic characteristics of naval vehicles, more accurate methods which provide flow details are needed for certain types of new design problems. Drag reduction requirements for higher speed helicopters, vertical or short takeoff and landing (V/STOL) aircraft, as well as for faster ships and submarines have made it necessary to obtain improved computer programs, including programs for automatically generating detailed geometric models of actual hardware configurations and the associated numerical mesh for the flow field.

At DTNSRDC methods and programs are being developed or obtained under contract for calculating viscous flow properties about arbitrary three-dimensional or axisymmetric bodies based on improved potential flow and boundary layer techniques, and for two-dimensional bodies using the full Navier-Stokes equations. The more recent work done at the Douglas Aircraft Company by Hess [8] for improving potential flow calculations and by Cebeci [9] for performing three-dimensional boundary layer analyses are contributing to these new developments. In addition, viscous-inviscid interacting transonic flows over airfoils have been studied theoretically at DTNSRDC by Tai [10], [11] and numerically under contract by Dvorak [12]. This numerical work combines potential flow and boundary layer methods in an iterative procedure which calculates interactions between the viscous and inviscid regions and results in the prediction of viscosity dependent aerodynamic forces. However, even these improved methods based on boundary layer theory cannot solve classes of problems involving separated flow regions.

As discussed at the last DEA meeting [13], in order to compute the detailed behavior of viscous flow development and vortex shedding, including the variation in drag, lift, and moment coefficients with time, accurate solutions of the full Navier-Stokes equations are required. For this reason fully viscous flows past two-dimensional bodies at an angle of attack have been studied at the Center by Lugt and Haussling [14] who developed techniques for obtaining numerical solutions of the Navier-

Stokes equations. The comparison of various numerical methods for solving these equations which was carried out by Lugt and Ohring [7] led these authors to solve the difficult problem of flow past rotating plates [15]. In the following paragraphs, recent progress in two of these areas of research will be described; namely, interacting flows over circulation-controlled airfoils and viscous flows past rotating cylinders.

a) Viscous-Inviscid Interacting Flows over Circulation-Controlled Airfoils

An example of the need for improved numerical methods for solving viscous-inviscid interacting flows is the detailed design of the V/STOL X-wing aircraft, an artists conception of which is shown in Figure 4. As described by one of its designers, Robert M. Williams [16], this new aircraft concept, now under development at DTNSRDC and Lockheed Aircraft Corporation, will operate either as a rotary wing high-speed helicopter or as a fixed-wing aircraft. The boundary layer over the airfoils is controlled by using the concept known as reverse velocity blowing in which a thin jet of air is ejected tangentially over the rounded trailing edge of the airfoil. This jet suppresses boundary layer separation and permits the positioning of the rear stagnation point to optimize lift. As pointed out by Williams [16], the technology base for the X-wing concept has been derived from about six years of related circulation control rotor research at the Center and earlier studies in the United Kingdom and the United States.

In order to perform successful circulation control analysis for the X-wing aircraft, accurate numerical methods which can take into account the effects of airfoil curvature and separation are required in addition to wind tunnel experiments. The work of Dvorak [12] and his colleagues has led to a procedure for calculating viscous/potential flow interaction analysis which is a useful numerical tool. Other numerical approaches are under development at the Center for improving the aerodynamic analysis of aircraft equipped with circulation-controlled airfoils.
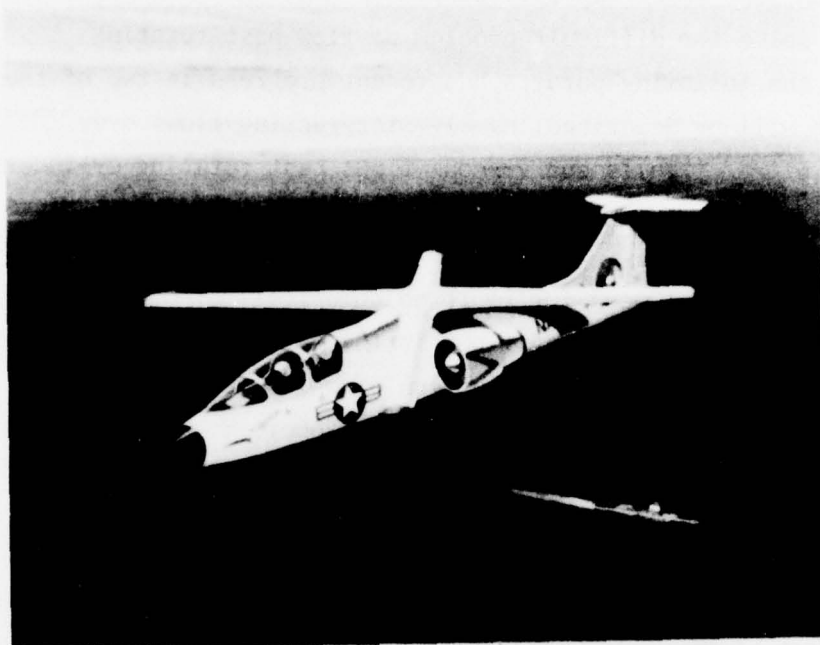
Figure 4. The Circulation Control X-wing V/STOL Aircraft Concept

b) Rotating Elliptic Cylinders in a Viscous Fluid

Numerical solutions of laminar flow fields around rotating elliptic cylinders in a fluid at rest or in a parallel stream have been obtained by Lugt and Ohring and preliminary results have been published [15]. These authors constructed solutions of the stream function-vorticity formulation of the Navier-Stokes equations using the DuFort-Frankel scheme for the vorticity equation and the Hockney direct method for the Poisson equation. In their recently completed paper [17] the transient period from the abrupt start of the rotation to a later time is investigated by calculating streamlines and equivorticity lines as well as the drag, lift and moment coefficients. For purely rotating cylinders oscillatory behavior is observed and explained by these authors. Bodies rotating in a parallel stream are studied for two cases: (1) when the vortex developing at the retreating edge of the thin ellipse appears on the upstream side of the edge and (2) when it appears on the downstream side of the edge. The cylinder is assumed to be infinitely long so that a two-dimensional

formulation in elliptical coordinates (η, θ) may be used. For the body rotating in a parallel flow, the dimensionless Navier-Stokes equations are written

$$\frac{\partial \omega}{\partial t} + \frac{1}{h^2} [- \frac{\partial}{\partial \eta} (\frac{\partial \psi}{\partial \theta} \omega) + \frac{\partial}{\partial \theta} (\frac{\partial \psi}{\partial \eta} \omega)] = \frac{2}{Re} \nabla^2 \omega \qquad (8)$$

$$\nabla^2 \psi = \omega, \qquad (9)$$

where ω is the vorticity, ψ is the stream function, t is the time, ∇^2 is the Laplacian operator, and $Re = 2\,a\,U/\nu$ is the Reynolds number in which a is the focal length of the ellipse, U is the free stream velocity, and ν is the kinematical viscosity. The boundary conditions are:

On the surface of the ellipse $\eta = \eta_1$: $\psi = 0$ and $\partial \psi / \partial \eta = 0$

In the outer flow field $\eta = \eta_\infty$: $\quad \frac{1}{h} \frac{\partial \psi}{\partial \theta} = \cos(\theta - t/Ro)$

$$\frac{1}{h} \frac{\partial \psi}{\partial \eta} = \sin(\theta - t/Ro)$$

$$+ \frac{1}{hRo}(\cosh \eta \sinh \eta)$$

where $\alpha(t) = t/Ro$ is the angle of attack and $Ro = U/\Omega a$ is the Rossby number with Ω the angular velocity of the tip of the ellipse.

The above problem was solved numerically on a grid of 97 x 96 points. The choice of reference frames and the details of the numerical results are presented by Lugt and Ohring [17]. One of the computer-plotted pictures of the streamlines and vorticity lines included in this reference, obtained for the case Re = 200 and Ro = 0.5, is shown in Figure 5. In this figure the coordinate reference frame is fixed to the body with regard to translation, but the body rotates relative to this reference frame. This time sequence occurred during the fourth revolution of the body. Such pictures are useful for analyzing the complex flow fields generated by the interference of the plate with the shed vortices as the plate continues to rotate. The computer program, ROTAPLATE, developed by Lugt and Ohring to perform these sophisticated calculations requires less than an hour of computing time on an IBM 360-91 for each complete revolution. Such speed was made possible only by the use of the fast direct
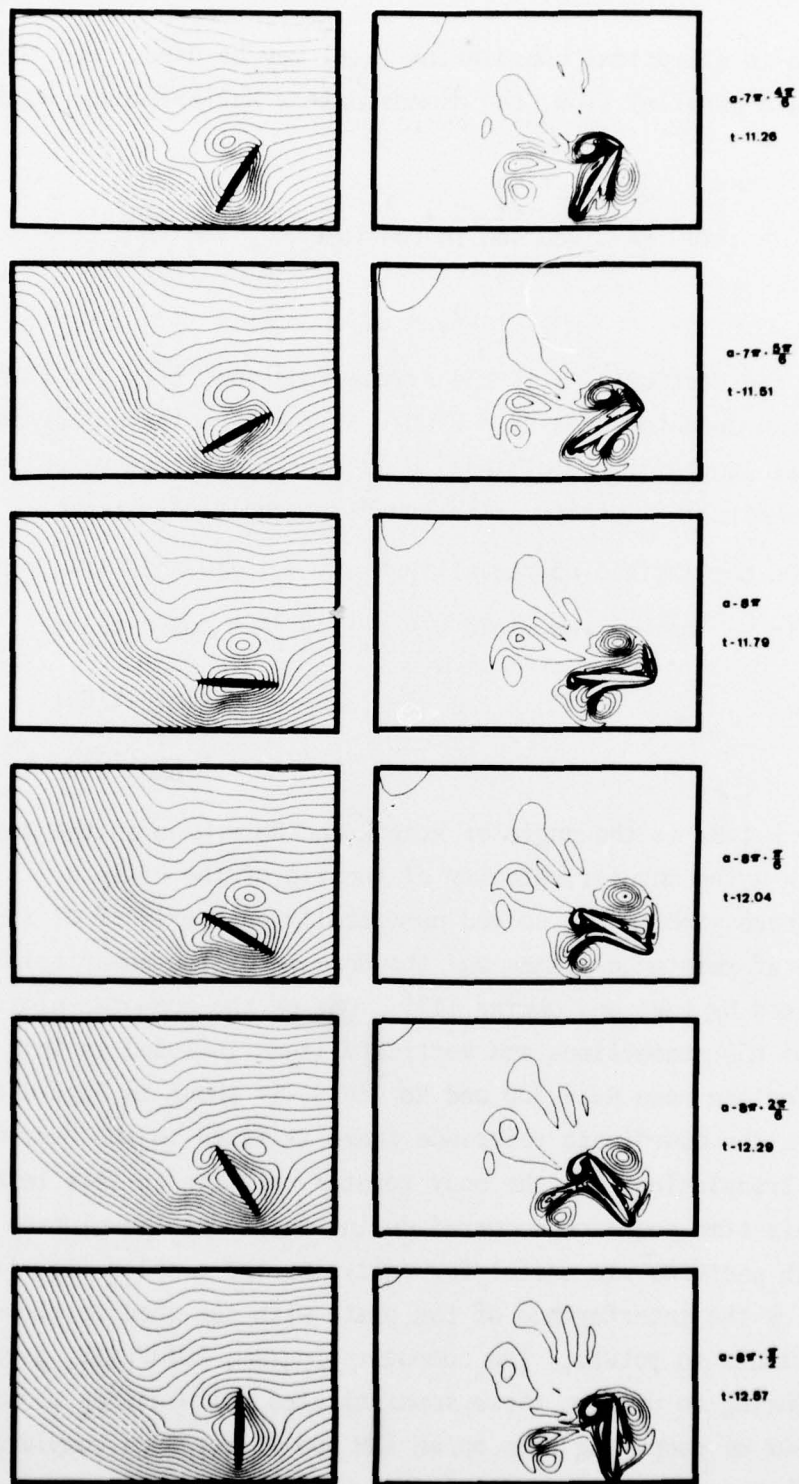
Figure 5. A Time-Sequence of Streamlines and Lines of Constant Vorticity for an Elliptical Cylinder Rotating in a Parallel Stream with Re = 200 and Ro = 0.5. The angle of attack α is indicated for the various time values.

Poisson solver based on Hockney's method. This program is therefore a powerful computational tool for investigating the phenomenon of autorotation and for calculating aerodynamic noise.

4. Fluid-Structure Interactions

The flow problems discussed in the foregoing sections were formulated under the assumption that the solid bodies remain undeformed by the actions of the surrounding fluid. There are many types of problems in which interactions between the fluid and the solid body must be taken into account. Those of naval importance include, for example, flow-induced vibrations, ship silencing, and shock response of ships and other structures. At the Center efforts are underway to develop improved formulations and solutions of fluid-structure interaction problems. Progress can already be cited in the dynamic analysis of submerged structures.

A method which uses standard versions of NASTRAN [18], [19], [20] for the calculations has been developed by Everstine and others [21], [22] for determining the transient response of a ring-stiffened cylinder to an underwater nuclear blast. A finite-element approach is used to model the cylinder in an acoustic medium which is assumed to be initially stationary. The fluid is assumed to be compressible and inviscid, with the pressure p satisfying the wave equation

$$\nabla^2 p = \frac{1}{c^2} \frac{\partial^2 p}{\partial t^2} \tag{10}$$

The boundary conditions at the fluid-structure interface may be specified by

$$\frac{\partial p}{\partial n} = - \rho \frac{\partial^2 u_n}{\partial t^2} \tag{11}$$

where n is the outward normal from the solid at the fluid-solid interface, ρ is the fluid mass density, and u_n is the normal component of the displacement. At rigid walls, equation (11) reduces to $(\partial p / \partial n) = 0$. At a free surface, in the absence of waves, the boundary condition is given by $p = 0$. In the above notation, t is the time and ∇^2 the Laplace operator.

In this particular formulation the fluid effects can be treated using an approximation which mathematically uncouples the structural response

from the fluid in the sense that the fluid pressure at the fluid-solid interface is determined only from the motion of the solid surface. References [21] and [22] provide the details of the numerical calculations. Figure 6 illustrates a time-sequence of the results obtained with the decoupling approximation. In this figure the shock wave from the nuclear blast is moving from the top of the page downward past the circular cylinder. Each rectangle after time t = 0.0 sec shows the effect of the blast on the rigid-body displacement and the elastic deformation of the cylinder at an instant in time. The displacements are scaled by a factor of about 2500. The real time modeled in this calculation was 5 milli-seconds which required about 45 minutes of computer time on the CDC 6600.

With the advancements being made in both finite-element and finite-difference techniques for solving fluid flow and structural analysis problems, improved methods for the study of fluid-solid interactions are being investigated. It is anticipated that this rather new area of research may have some impact on the future program of this Data Exchange Agreement.

Acknowledgments

It is with pleasure that I would like to thank Dr. Hans J. Lugt and the other authors whose work has been described in this paper for their valuable assistance.

References

1. Hess, J.L. and Smith, A.M.O., "Calculation of Nonlifting Potential Flow About Arbitrary Three-Dimensional Bodies," Douglas Aircraft Co. Report No. E.S. 40622, March 1962.

2. Dawson, Charles, "The LARC Potential Flow Program," DTNSRDC Report AML-22-68, June 1968.

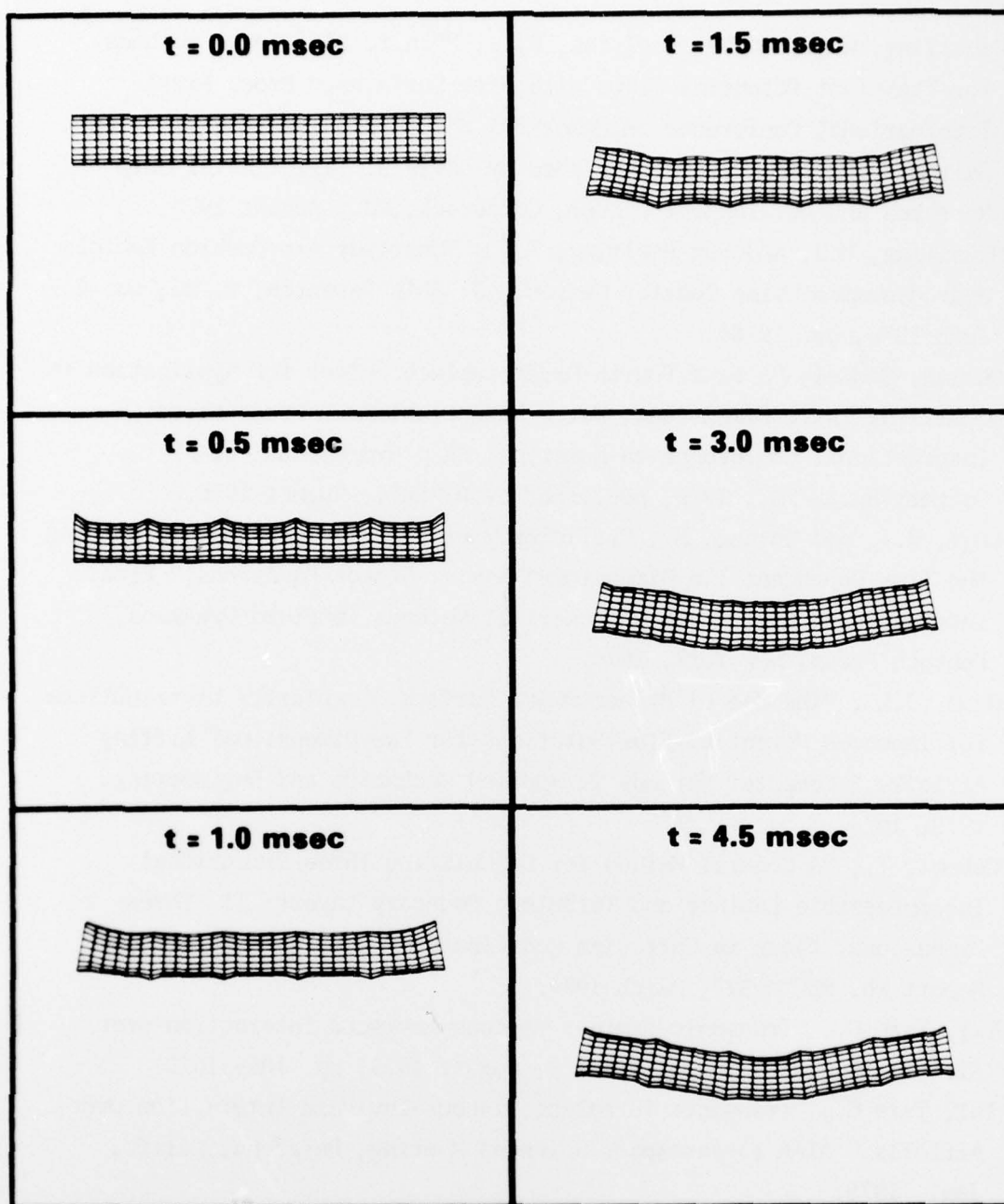3. Dawson, C.W. and Dean, J.S., "The XYZ Potential Flow Program," DTNSRDC Report 3892, June 1972.

Figure 6. Time Sequence of the Response of a Submerged Ring-Stiffened
Cylinder to Shock Wave from a Nuclear Blast. The direction of
the shock wave is from the top of the page to the bottom.

4. Haussling, H.J. and Van Eseltine, R.T., "Finite-Difference Methods for Transient Potential Flows with Free Surfaces," Proc. First International Conference on Numerical Ship Hydrodynamics, Gaithersburg, Md., 1975, published by David W. Taylor Naval Ship Research and Development Center, Carderock, Md., August 1976.

5. Haussling, H.J. and Van Eseltine, R.T., "Unsteady Air Cushion Vehicle Hydrodynamics Using Fourier Series," J. Ship Research, v. 20, no. 2, June 1976, pp. 79-84.

6. Ohring, Samuel, "A Fast Fourth-Order Laplace Solver for Application to Numerical Three-Dimensional Water Wave Problems," Proc. First International Conference on Numerical Ship Hydrodynamics, Gaithersburg, Md., 1975, published by DTNSRDC, August 1976.

7. Lugt, H.J. and Ohring, S., "Efficiency of Numerical Methods in Solving the Time-Dependent Two-Dimensional Navier-Stokes Equations," Proc. International Conference on Numerical Methods in Fluid Dynamics, Pentech Press, New York, 1974.

8. Hess, J.L., "The Use of Higher-Order Surface Singularity Distributions for Improved Potential Flow Solutions for Two-Dimensional Lifting Airfoils," Computer Methods in Applied Mechanics and Engineering, v. 5, 1975.

9. Cebeci, T., "A General Method for Calculating Three-Dimensional Incompressible Laminar and Turbulent Boundary Layers: II Three-Dimensional Flows in Cartesian Coordinates," Douglas Aircraft Co. Report No. MDC J6517, March 1974.

10. Tai, Tsze C., "Transonic Laminar Viscous-Inviscid Interaction over Airfoils," AIAA J., v. 13, no. 8, August 1975, pp. 1065-1072.

11. Tai, Tsze C., "Transonic Turbulent Viscous-Inviscid Interaction over Airfoils," AIAA 13 Aerospace Sciences Meeting, Pasadena, Calif., Jan. 1975.

12. Dvorak, F.A., "Viscous/Potential Flow Interaction Analysis for Circulation Controlled Airfoils," Analytical Methods, Inc. Report No. 75-01, Dec. 1975.

13. Schot, Joanna W., "Computer Solutions of the Navier-Stokes Equations of Viscous Fluid Motion," Boundary Layer Effects 4th US-FRG Meeting, Forschungsbericht aus der Wehrtechnik BMVg-FBWT 75-21, 1975.

14. Lugt, H.J. and Haussling, H.J., "Laminar flow past an abruptly accelerated elliptic cylinder at 45° incidence," J. Fluid Mech., v. 65, part 4, (1974), pp. 711-734.

15. Lugt, H.J. and Ohring, S., "Rotating Thin Elliptic Cylinder in a Parallel Viscous Fluid Flow," Proc. Fourth International Conference on Numerical Methods in Fluid Dynamics, Boulder, 1974. Lecture Notes in Physics, v. 35, Springer-Verlag, Heidelberg, 1975, pp. 257-262.

16. Williams, Robert M., "Application of Circulation Control Rotor Technology to a Stopped Rotor Aircraft Design," First European Rotorcraft and Powered Lift Aircraft Forum, Univ. of Southampton, England, 22-24 September 1975.

17. Lugt, H.J. and Ohring, S., "Rotating Elliptic Cylinders in a Viscous Fluid at Rest or in a Parallel Stream." (To appear.)

18. Butler, T.G. and Michel, D., "NASTRAN: A Summary of the Functions and Capabilities of the NASA Structural Analysis Computer System," NASA Report SP-260, Washington, D.C., 1971.

19. Raney, J.P. and Weidman, D.J., "NASTRAN Overview: Development, Dynamics Application, Maintenance, Acceptance," The Shock and Vibration Bulletin, 42, Part 5, Jan. 1972, pp. 109-127.

20. "The NASTRAN Theoretical Manual," NASA Report SP-221(03), Washington, D.C., March 1976.

21. Everstine, G.C., Schroeder, E.A., and Marcus, M.S., "The Dynamic Analysis of Submerged Structures," NASTRAN: Users' Experiences, NASA Report TM X-3278, Sept. 1975, pp. 419-429.

22. Everstine, G.C., "A NASTRAN Implementation of the Doubly Asymptotic Approximation for Underwater Shock Response," Proceedings of the Fifth NASTRAN Users' Colloquium (to be held at NASA Ames Research Center), October 1976.

CONCLUDING REMARKS

by

Alfred Walz
University of Karlsruhe, Karlsruhe Germany

These two-days of very concentrated and "compressed" Data
Exchange Meetings clearly displayed the fact that the past year's
work was indeed a very successful one.

The tendency to support the understanding of the complex
inter-acting pheonomena by numerical solutions of the 3-dimensional
Navier-Stokes equations has dominated many papers presented by the
participants from the United States and the Federal Republic of
Germany.

In addition, very successful and intense efforts have been
reported such as experimental and numerical studies with reference
to turbulent boundary layers, transitional problems, heat trans-
fer, etc.

In reflecting on the results of this meeting, it can be
safely stated that the efforts of all the participants have con-
tributed greatly to this data exchange program. The aim of this
program is to resolve the various thermo-fluidynamic characteris-
tics of external and internal flow fields encountered at high Mach
number and high Reynolds number flight conditions of the not too
distant future.

CONCLUDING REMARKS

by

Anthony W. Fiore
Air Force Flight Dynamics Laboratory
Wright-Patterson Air Force Base, Ohio

On behalf of the United States Air Force and the Flight
Dynamics Laboratory, I would like to thank everyone for contributing
to this data exchange program. The papers and data presented by
scientists of both the Federal Republic of Germany and the United
States will contribute greatly to the advancement of the know-
ledge of flight at high Mach numbers and Reynolds numbers.

Both the experimental and theoretical efforts have produced
favorable results in helping to explain some problems which have
been technically obscure in the past. Needless to say, more work
is required but in a new direction. This new direction has been
included in the new statement of work which I have recently sub-
mitted for purposes of extending this DEA for a period of approx-
imately five additional years. The problems of interest in the
United States reflect requirements for various new weapon systems.
These requirements make it necessary to continue the studies on
laminar, transitional, and turbulent boundary layers. The speed
range of interest extends from subsonic to hypersonic Mach numbers.
The investigations should include both experimental and theoreti-
cal research; however, instead of looking at 2-dimensional flow
fields over simple configurations such as a flat plate, we are now
putting the emphasis on 3-dimensional flow fields common to more
realistic configurations. These configurations should be wings
and wing-body combinations representative of real flight vehicles.
Some specific problems are (1) separated flow fields over wings
at very high lift coefficients, (2) boundary layer problems en-
countered at supersonic and hypersonic speeds and very high
Reynolds numbers where shock wave interaction became pronounced,
and (3) various methods of decreasing the surface shear stress
and total drag in order to decrease fuel consumption. I am sure
that you can think of other problem areas as well.

With reference to our next D.E.A. meeting, it has been decided that it should be held on 28/29 April 1977 in Gottingen, Germany. In closing, I wish to thank everyone for coming to Dayton. In particular, I wish to thank our Germany colleagues for coming such a long distance for this meeting.